Functional approaches to Fermi polarons in cold atomic gases and solid-state systems

Marcel Gievers
PhD Thesis
2025

Functional approaches to Fermi polarons in cold atomic gases and solid-state systems

Marcel Gievers

A dissertation submitted
to the Faculty of Physics at the
Ludwig-Maximilians-Universität München
for the degree of
DOCTOR RERUM NATURALIUM

Munich, January 9, 2025

First referee: Prof. Dr. Jan von Delft
Second referee: Prof. Dr. Richard Schmidt
Day of submission: January 9, 2025
Day of the oral examination: February 20, 2025

The cover page shows the formation of a polaron cloud as presented in the supplemental materials of our paper on Rydberg atom spectroscopy. Also I have grown and evolved over the years of my PhD and became stronger inside. As the polaron, I try to carry this strength out into the world, but I have not reached the stationary limit yet.

Zusammenfassung (Summary in German)

Wenn ein attraktives Störstellenatom in ein Fermigas aus ultrakalten Atomen eingetaucht wird, so formt sich ein Fermi-Polaron. Dies ist ein prominentes Quasiteilchen und liefert ein faszinierendes Beispiel für einen korrelierten Quanten-Vielteilchenzustand. In dieser Dissertation benutzen wir verschiedene funktionale Ansätze, um physikalische Systeme zu beschreiben, die mit dem Fermi-Polaron-Problem zusammenhängen.

Zunächst stellen wir eine neue Messmethode vor, um korrelierte ultrakalte atomare Gase mithilfe von Rydberg-Anregungen zu untersuchen. Wenn das Störstellenatom zu einem Rydberg-Zustand angeregt wird, verursacht es die Bildung von ultralangreichweitigen Rydberg-Molekülen mit den umgebenden Gasatomen. In Radiofrequenz-Spektren gibt die Besetzung dieser molekularen Zustände Auskunft über die Dichte- und Energieeigenschaften des umgebenden Mediums. Wir rekonstruieren Dichteprofile aus Absorptionsspektren, die mithilfe der funktionalen Determinanten-Methode berechnet werden, und veranschaulichen, dass die Rydbergatom-Spektroskopie eine *in-situ*-Messung des Fermi-Polarons ermöglicht. Des Weiteren diskutieren wir, wie diese Methode benutzt werden kann, um die zeitaufgelöste Formierung eines Fermi-Polarons und Eigenschaften einer BCS-Supraflüssigkeit zu untersuchen.

Der Hauptteil dieser Dissertation widmet sich der Entwicklung von feldtheoretischen Methoden wie der funktionalen Renormierungsgruppe (fRG) und dem Parquet-Formalismus. In der Quantenfeldtheorie werden allgemeine Wechselwirkungen zwischen zwei Teilchen in der Vierpunkt-Vertexfunktion modelliert, die ein hochgradig kompliziertes Objekt hinsichtlich ihrer Frequenzabhängigkeit ist. Eine Aufteilung der Vertexfunktion in Austauschprozesse einzelner Bosonen (SBE, aus dem Englischen *single-boson exchange*) ist geeignet, um die Vertexfunktion numerisch zu behandeln, und bietet eine intuitive physikalische Interpretation der Wechselwirkungsprozesse. Wir verallgemeinern den SBE-Formalismus auf den Fall mit zwei unterscheidbaren Teilchenarten und entwickeln ein numerisches Programm, um die zugehörigen Vertexfunktionen für Probleme ohne Impulsabhängigkeit auszurechnen. Exakte Formeln für das Hubbard-Modell auf einem Gitterpunkt in Anwesenheit eines Magnetfeldes bieten dabei einen praktischen Anhaltspunkt. Darüber hinaus bewerten wir verschiedene selbstkonsistente Summierungsmethoden, um Potenzgesetze eines statischen Fermi-Polarons zu untersuchen. Hierbei zeigen wir, dass der Parquet-Formalismus die Singularität an der Fermikante in Röntgenabsorptionsspektren von Metallen auf Genauigkeit bis zum subführenden Logarithmus auflösen kann, wenn Austauschprozesse zwischen mehreren Bosonen miteinbezogen werden.

Im Zusammenhang mit der fRG leiten wir Multiloop-Flussgleichungen für die SBE-Vertices her und zeigen, wie eine Cutoff-Abhängigkeit in der nackten Wechselwirkung eine

flexiblere Behandlung von bosonischen Propagatoren ermöglicht. Wir präsentieren eine Anwendung der fRG im SBE-Formalismus für das zweidimensionale Hubbard-Modell. Im Verlauf der Arbeit ordnen wir die bisherigen fRG-Untersuchungen von Fermi-Polaronen ein und erörtern, wie diese in zukünftigen Nachforschungen erweitern werden können.

Summary (Summary in English)

When an attractive impurity atom is immersed in a Fermi gas of ultracold atoms, a Fermi polaron is formed. This is a paradigmatic quasi-particle and serves as a fascinating example of a correlated quantum many-body state. In this dissertation, we use different functional approaches to describe physical systems related to the Fermi polaron problem.

In the first part, we present a new measurement technique for probing correlated ultracold atomic gases by using Rydberg excitations. When the impurity atom is excited to a Rydberg state, it induces the formation of ultralong-range Rydberg molecules with the surrounding gas atoms. In radio-frequency spectra, the occupation of these molecular states provides information about the density and energy properties of the surrounding medium. We reconstruct density profiles from absorption spectra, calculated using the functional determinant approach, and demonstrate that Rydberg atom spectroscopy allows for an *in situ* measurement of the Fermi polaron. Furthermore, we discuss how this technique can be applied to probe the time-dependent formation of a Fermi polaron and to analyze properties of a BCS superfluid.

The main part of this dissertation is dedicated to the development of field-theoretical methods like the functional renormalization group (fRG) and the parquet formalism. In quantum field theory, general interactions between two particles are incorporated in the four-point vertex function, which is a highly complicated object in terms of its frequency dependence. A decomposition of the vertex function into single-boson exchanges (SBE) offers a convenient way of handling the vertex function numerically and provides an intuitive physical interpretation of interaction processes. We generalize the SBE formalism to the case of two distinct particle types and develop a numerical program to compute the corresponding vertex functions for problems without momentum dependence. Exact formulas for a single-site Hubbard model in the presence of a magnetic field offer a practical testing case. Moreover, we evaluate various self-consistent summation techniques to analyze the power-law behavior of a static Fermi polaron. Hereby, we show that the parquet formalism may resolve the Fermi-edge singularity in X-ray absorption spectra of metals up to subleading logarithmic accuracy when including multi-boson exchange processes.

In the context of fRG, we derive multiloop flow equations for the SBE vertices and demonstrate how a cutoff dependence in the bare interaction provides a more flexible treatment of bosonic propagators. We include an application of fRG in the SBE formalism for the two-dimensional Hubbard model. Along the way, we classify the hitherto existing analyses of Fermi polarons using fRG and explain how these can be extended in future investigations.

List of Publications

This dissertation is based on the following journal articles, listed in chronological order:

[P1] *Multiloop flow equations for single-boson exchange fRG*
Marcel Gievers, Elias Walter, Anxiang Ge, Jan von Delft, Fabian B. Kugler
Sec. 3.3.2   arXiv:2201.04878   Eur. Phys. J. B **95**, 108 (2022)

[P2] *Probing polaron clouds by Rydberg atom spectroscopy*
Marcel Gievers, Marcel Wagner, Richard Schmidt
Sec. 2.3.2   arXiv:2306.03627   Phys. Rev. Lett. **105**, 053401 (2024)

[P3] *Subleading logarithmic behavior in the parquet formalism*
Marcel Gievers, Richard Schmidt, Jan von Delft, Fabian B. Kugler
Sec. 5.1.2   arXiv:2411.07226   Phys. Rev. B **111**, 085151 (2025)

[P4] *Single-boson exchange formulation of the Schwinger-Dyson equation and its application to the functional renormalization group*
Miriam Patricolo, **Marcel Gievers**, Kilian Fraboulet, Aiman Al-Eryani, Sarah Heinzelmann, Pietro M. Bonetti, Alessandro Toschi, Demetrio Vilardi, Sabine Andergassen
Sec. 4.5.2   arXiv:2411.11661   SciPost Phys. **18**, 078 (2025)

There are two more articles in preparation whose contents are briefly presented in Secs. 2.5 and 3.5. Furthermore, the author was involved in the following journal articles, which were published during the PhD studies, but are not part of this dissertation:

[P5] *Shape effects of localized losses in quantum wires: Dissipative resonances and nonequilibrium universality*
Thomas Müller, **Marcel Gievers**, Heinrich Fröml, Sebastian Diehl, Alessio Chiocchetta
arXiv:2105.01059   Phys. Rev. B **104**, 155431 (2021)

[P6] *Quantum wires with local particle loss: Transport manifestations of fluctuation-induced effects*
Marcel Gievers, Thomas Müller, Heinrich Fröml, Sebastian Diehl, Alessio Chiocchetta
arXiv:2312.12656   Phys. Rev. B **110**, 205419 (2024)

Acknowledgments

Anyone who believes that a PhD is an achievement of the individual is greatly mistaken in our times. The work I am presenting in this dissertation emerged through collaborations with many people, was shaped by countless discussions and accompanied by their personal support. When I came to Munich and started my PhD in October 2020, the pandemic had not yet reached its most dramatic point. Within the following years, the global political situation had become more critical and also my supervisors lived through personal challenges. In all that time I was accompanied by many great people to help me making the best out of the situation. In retrospect, I can truly say that my PhD and the years in Munich belong to the greatest experiences I had in my life and this I primarily owe to all the wonderful people I met and who supported me all along. Let me mention some of them in the next few paragraphs.

My greatest thanks go to my supervisors, Jan von Delft and Richard Schmidt, who guided me through the whole time of my PhD and became truthful mentors to me. I did not only learn a lot from their valuable scientific input, but also from their strategies of conducting research projects. They gave me a lot of trust and freedom, which helped me to pursue on the aspects of my research I found the most interesting. Fortunately, they engaged in the experiment of supervising me together so in my project I could combine the exciting physics of cold atomic gases with elaborate numerics from solid state theory. Being part of two complementary groups was a fascinating and unique experience, which I am extremely grateful for!

I would like to thank everyone who contributed to the scientific results I have gained in the years of my PhD: Fabian Kugler for guiding me through several projects, Anxiang Ge and Dominik Kiese for helping me with setting up the multi-boson exchange solver, and I thank Elias Walter, Nepomuk Ritz, and Marc Ritter for further instructive advice regarding programming. I am very grateful for the collaboration with Sabine Andergassen and her group; in particular, I had many insightful discussions with Kilian Fraboulet, Miriam Patricolo, and Aiman Al-Eryani. I am very pleased that this way I could build up scientific connections beyond the groups I am affiliated with. Moreover, I thank Benedikt Schneider and Johannes Halbinger for interesting discussions about quantum field theory, Marcel Wagner and Márton Kanász-Nagy for introducing me to the physics of Rydberg atoms, Xin Chen and Eugen Dizer for many interesting discussions about polaron physics. Finally, I am grateful to Emilio Ramos Rodríguez for continuing my project on Rydberg atom spectroscopy.

I acknowledge support from the Max Planck Research School for Quantum Science and Technology (IMPRS-QST). I really enjoyed the many informative and social events they

Table of contents

1. Introduction

> *"The beginning is the most important part of the work."*
>
> *Plato*

1.1. Motivation

In the last century, science has eagerly pursued the question of what binds the world in its innermost essence[1] and has found far-reaching answers. The standard model of particle physics culminating in the more recent experimental verification of the Higgs boson accurately predicts the smallest compounds of matter and their interactions. After the discovery of the DNA, it is understood how living organisms encode their genes and pass them on. Still, the precise knowledge about these microscopic scales does not imply an understanding of emergent and complex phenomena on macroscopic scales. An explanation of high-temperature superconductivity, the implementation of large-scale quantum systems for reliable quantum computation and the treatment of diseases resulting from genetic defects, to name a few, remain formidable challenges of the present day.

Strongly correlated quantum particles in condensed matter give rise to a plethora of fascinating emergent phenomena whose characteristics cannot intuitively be described in a single-particle picture. The precise description of how the individual 10^{23} particles in a piece of metal behave is out of reach, however, this is not necessary at all. With the focus on emergent phenomena, the problem can be reduced enormously if only essential collective degrees of freedom are taken into account. In this dissertation, we refine existing field-theoretical methods for more effective computations of collective behavior in quantum many-body systems.

An effective way to approach quantum many-body systems is by analyzing impurities and their interactions with the environment, for example, a single atom hybridizing with a non-interacting bath of surrounding atoms. The mentioned scenario induces the formation of polarons, which are quasi-particles of the dressed impurities characterized by a density enhancement around the impurities and distinct energy states. Just as dust particles in the air promote the formation of steam above a hot cup of tea, impurities give rise to a wealth of interesting phenomena in quantum physics: Magnetic impurities in metals induce the Kondo effect, impurity atoms enable the formation of topological states as in the quantum Hall effect, and more generally, most of the technology of our time

---

[1]"Was die Welt im Innersten zusammenhält", to put it in the words of Goethe's Faust.

is based on the doping of semiconductors using impurity atoms. Starting from a single impurity atom, the description may be generalized successively. Thus, our investigations on Fermi polarons, i.e., quasi-particles around impurities in Fermi gases, may pave the way to understand more general quantum systems like imbalanced mixtures of different fermionic atoms on a more profound level.

Resolving the full frequency dependence of interactions between different particles is a challenging task. Over the years, various computational methods were developed to reduce the exponentially large Hilbert space of quantum many-body systems in an effective way, each coming with its own benefits and limitations. The most prominent examples are quantum Monte-Carlo samples, which are very versatile, but come with the sign problem for fermions, and the widely used density functional theory (DFT), which comes with limited predictions for strong correlations. In this dissertation, we use two complementary methods to describe physics related to Fermi polarons:

For a single heavy impurity, the Fermi polaron problem can be solved numerically exactly by the functional determinant approach (FDA). This is a widely used method to compute radio-frequency spectra of ultracold atomic gases. On the one hand, it gives a non-perturbative description in real times and frequencies including bound states and long-range potentials like that of a Rydberg atom. On the other hand, it is limited to the case of a single stationary impurity in a bath of effectively non-interacting particles, which extremely restricts the applicability of the method. Our FDA analysis gives a first good estimate for experimentally measurable quantities like the polaron's density profile.

For a more sophisticated description, we use the functional renormalization group (fRG) and the parquet formalism, two field-theoretical approaches, to compute the full renormalized interactions between two particles. These methods *per se* are not bound by the system size and are applicable to interacting particles at arbitrary densities including the dynamics of multiple impurities. However, limited computational resources force us to make restrictions in our numerical analyses. We compute correlation functions within the Matsubara formalism, which restricts our predictions to the thermal equilibrium and requires analytical continuation to give experimentally measurable quantities in real frequencies. Furthermore, truncations of the correlation functions make them inherently perturbative in the interaction strengths. Specifically, bound states are exceptionally tough to take into account.

Collective behavior in condensed matter systems is often characterized by bosonic excitations such as magnons, Cooper pairs, and excitons (to mention only a few). For the most part of this dissertation, we refine the single-boson exchange formalism (SBE), which was introduced in the context of the Hubbard model to decompose the frequency dependence of the full two-particle interaction vertex into effective bosonic processes. This description saves numerical costs tremendously and allows for more flexibility in the field-theoretical description. We generalize this formalism to many-body systems including two distinct particle types and evaluate its applicability in the context of power-law behavior in metals.

Of course, we are not able to tackle emergent phenomena, which were mentioned at

the beginning, in their full complexity. Still, the insights and developed methods in this dissertation may contribute to future investigations of quantum impurity models and may help to extend them to more general quantum systems composed of distinct particles.

1.2. Outline

We start with a review on ultracold atomic gases and the physics of Fermi polarons in Chapter 2. There, we outline different theoretical methods to compute their characteristic features. The main focus in this chapter is on our proposed measurement technique to probe the density profile of a Fermi polaron using Rydberg atom spectroscopy. We use the functional determinant approach (FDA) for this, which is a suitable method to compute absorption spectra around heavy impurities. At the end, we sketch how Rydberg atom spectroscopy can be applied to examine further quantities such as the time-dependent formation of a Fermi polaron and the energy gap of a BCS superfluid.

In Chapter 3, we introduce the main methods used in this dissertation, namely the functional renormalization group (fRG) and the parquet formalism. In a general framework, we discuss flow equations for bosonic propagators and three-point vertices as they appear in a Hubbard–Stratonovich field theory. Then, we discuss their connection to the so-called single-boson exchange (SBE) formalism, for which we derive multiloop fRG flow equations. At the end, we develop a technique to better control the flow of fermionic and bosonic degrees of freedom along the fRG flow by introducing a scale dependence on the bare interaction vertex.

Chapter 4 focuses on how the SBE formalism can be implemented numerically. For this, we specifically consider a fermionic action with two distinct particle types and a local interaction. We present our numerical code for solving the parquet equations and the fRG flow. Finally, we give an application of our formalism to the two-dimensional Hubbard model.

The preliminary stage for a general solution of the Fermi polaron problem using the SBE formalism is obtained by neglecting the dynamics of the impurity. In such an analysis, the momentum degrees of freedom can be completely integrated out. In Chapter 5, we examine how diagrammatic techniques can predict the power-law behavior of polarons around static impurities. In particular, we analyze the Fermi-edge singularity and Anderson's orthogonality catastrophe. Thus, polaron physics also appears in metals when a local electron is excited from a deep valence band into the Fermi gas of conduction-band electrons. By analyzing the logarithmic behavior in that model, we make statements about the strengths and weaknesses of our developed diagrammatic techniques.

A full computation of the Fermi polaron properties in the SBE formalism goes beyond the scope of this dissertation. Nevertheless, in Chapter 6 we discuss first steps toward such a general treatment when the momentum of the impurity is taken into consideration.

To conclude this dissertation, in Chapter 7 we summarize the key results and outline future research directions.

2. Fermi polarons from heavy impurities

"It is the theory which decides what can be observed."
Albert Einstein[1]

An attractive impurity atom immersed in a Fermi gas gives rise to the formation of a *polaron*, one of the most iconic quasi-particles. While energy properties of Fermi polarons have been studied for decades, their direct experimental observation *in situ* has not been realized yet. After reviewing the key properties of ultracold atomic gases and Fermi polaron physics, we propose a new experimental method to measure the density profiles of Fermi polarons by using Rydberg atom spectroscopy. We observe an enhancement in the density around the impurity, which represents the *polaron cloud*. Due to the strongly correlated nature of the polaron, each particle contributes to the polaron cloud, but intriguingly, in total, only up to one additional particle is contained in it. We finally discuss how our method can be extended to measure the time-dependent formation of a polaron cloud and properties of a BCS superfluid. The computational method used in this chapter is the functional determinant approach (FDA). This is a relatively straightforward numerical method for computing spectra in the limit of immobile impurities.

2.1. Review of physical concepts

2.1.1. Ultracold atomic gases

Since the experimental realization of a Bose–Einstein condensate (BEC) in 1995 [AEM⁺95, DMA⁺95], which was awarded with the Nobel Prize six years later, ultracold atomic gases have emerged as a versatile and indispensable platform for the exploration of quantum many-body systems. With their high degree of controllability, they opened plenty of research directions and became the ideal tool for simulating theoretical concepts of condensed matter physics like quantum impurity problems or the Hubbard model realized in optical lattices. Thus, they follow Richard Feynman's proposal that quantum many-body problems should be simulated by other (better controlled) quantum systems [Fey82].

---

[1]As found in the original: "Erst die Theorie entscheidet darüber, was man beobachten kann."; see Werner Heisenberg's "Der Teil und das Ganze: Gespräche im Umkreis der Atomphysik", specifically the chapter titled "Die Quantenmechanik und ein Gespräch mit Einstein (1925-1926)".

Here, we focus on the most important aspects. For further reading regard the following review articles [BDZ08, CGJT10, BDN12] and PhD theses [Pun09, Die23, Chr23, Mil24, Wag24].

Ultracold gases are characterized by an inter-particle length d shorter than the de Broglie wavelength $\lambda_{\text{dB}} = h/p$ of the quantum particles. The technologies of laser cooling and optical traps, which were awarded with the Nobel Prize in 1997, were essential for the rapid development of ultracold atomic gases. With these technologies, the systems can be cooled down to temperatures of a few nano-Kelvin. In typical experiments, dilute vapors of neutral alkaline atoms are prepared in a magnetic or optical trap. The simple electronic structure of those atoms makes them suitable for the laser cooling technology. The interaction between alkali atoms is well described by a Lennard–Jones potential,

$$V(r) \simeq \frac{C_{12}}{r^{12}} - \frac{C_6}{r^6}, \quad C_{12}, C_6 > 0. \tag{2.1}$$

The strong repulsive interaction $\sim r^{-12}$ is related to the Pauli principle whereas the attractive interaction $\sim -r^{-6}$ originates from van der Waals forces mediated by the polarizability of induced dipoles. The interactions are thus short-ranged and are classified by the van der Waals length $l_{\text{vdW}} \simeq 5\,\text{nm}$. The characteristic length scales are summarized as [BPD12]

$$r_{\text{atom}} \ll l_{\text{vdW}} = \left(\frac{2m_r C_6}{\hbar^2}\right)^{1/4} \ll d = n^{-1/3} \lesssim \lambda_{\text{dB}} = \sqrt{\frac{2\pi\hbar^2}{mk_{\text{B}}T}} \ll l_{\text{osc}} = \sqrt{\frac{\hbar}{m\omega_0}}. \tag{2.2}$$

Here, $r_{\text{atom}} \simeq 10^{-10}\,\text{m}$ is the size of the atoms, m_r the reduced mass for the scattering potential $V(r)$, Eq. (2.1), $n \simeq 10^{-12}\,\text{cm}^{-3}$ the particle density and l_{osc} the oscillator length of the harmonic trap of frequency ω_0.

The large de Broglie wavelength λ_{dB} prevents the particles from resolving the precise shape of the scattering potential such that interactions are mainly determined by a single parameter, namely the s-wave scattering length a, whose precise definition is given below [cf. Eq. (2.7)]. The scattering length can be tuned via a uniform magnetic field near *Feshbach resonances*. The use of Feshbach resonances allows for the high flexibility in ultracold atomic gases as both attractive and repulsive interactions of arbitrary strength can be straightforwardly simulated.

The collective behavior of ultracold gases is commonly probed by spectroscopy experiments. These are based on the transitions between atomic hyperfine states, which occur after emission or absorption of respective photons. While radio-frequency spectroscopy involves photons with negligible momentum, Raman spectroscopy includes momentum transfer at the scattering process and thus allows for the determination of momentum-resolved spectra.

2.1.2. Scattering theory

Important concepts of ultracold atomic gases are already understood from the scattering theory between two particles c and d [SN11, Zha21].

The Schrödinger equation in relative coordinates reads

$$\left[-\frac{1}{2m_r} \boldsymbol{\nabla}^2 + V(\boldsymbol{r}) - E \right] \psi(\boldsymbol{r}), \quad \boldsymbol{\nabla}^2 = \partial_r(r^2 \partial_r) - \hat{\boldsymbol{l}}^2, \tag{2.3}$$

with the reduced mass $m_r = m_c m_d/(m_c + m_d)$ and the angular-momentum operator $\hat{\boldsymbol{l}}$ whose eigenfunctions are given by spherical harmonics $\hat{\boldsymbol{l}}^2 Y_{lm}(\Omega_{\boldsymbol{r}}) = l(l+1)Y_{lm}(\Omega_{\boldsymbol{r}})$. For a centro-symmetric potential $V(\boldsymbol{r}) = V(r)$, the Schrödinger equation (2.3) is solved by the ansatz

$$\psi_{klm}(\boldsymbol{r}) = \langle \boldsymbol{r}|klm\rangle = Y_{lm}(\Omega_{\boldsymbol{r}})\frac{u_{kl}(r)}{r}, \tag{2.4}$$

where the radial part $u_{kl}(r)$ solves the one-dimensional Schrödinger equation

$$u_{kl}''(r) + 2m_r \left[E - V(r) + \frac{1}{2m_r r}l(l+1) \right] u_{kl}(r) = 0. \tag{2.5}$$

The term including the angular-momentum quantum number l yields the centrifugal barrier, which favors scattering between particles of lower angular momenta. Let us further assume that the scattering potential has a finite interaction range r_0 where $V(r < r_0) = 0$ [cf. the van der Waals potential, Eq. (2.1)]. Outside this range $r > r_0$, Eq. (2.5) is solved by a linear combination of spherical Bessel functions $j_l(kr)$ and spherical Neumann functions $n_l(kr)$.

Far from the center, the s-wave channel behaves as $u_{k0}(r) \overset{r\to\infty}{\longrightarrow} A\sin(kr+\delta_k)$, where A is a constant and δ_k is the phase shift of the asymptotically free wave function. Considering the ultracold temperatures, we assume a small incoming energy of the scattering state $k^2/(2m_r)$ compared to the energy scale of the potential $1/(2m_r r_0^2)$ giving $kr_0 \ll 1$. Inserting the asymptotic form into the boundary conditions of the wavefunction at $r = r_0$ yields

$$\left.\frac{u_{k0}'(r < r_0)}{u_{k0}(r < r_0)}\right|_{r=r_0} = \left.\frac{u_{k0}'(r > r_0)}{u_{k0}(r > r_0)}\right|_{r=r_0} = \frac{k\cos(kr_0 + \delta_k)}{\sin(kr_0 + \delta_k)} \overset{kr_0 \to 0}{\longrightarrow} \frac{k}{\tan\delta_k}. \tag{2.6}$$

Assuming that the inner part of the wave function $u_{k0}(r < r_0)$ does not depend strongly on the energies of the scattering states, it is justified to perform the expansion

$$\frac{k}{\tan\delta_k} = -\frac{1}{a} + r_{\text{eff}}k^2 + \mathcal{O}(k^4). \tag{2.7}$$

Here we introduced the *s*-wave *scattering length* a and the *effective range* r_{eff}. The same expansion also appears in the *s*-wave contribution of the *scattering amplitude* $f_k(\Omega_{\boldsymbol r})$, which gives another way of handling the asymptotic form of the wave function:

$$\psi(\boldsymbol{r}) \overset{|\boldsymbol{r}|\to\infty}{\longrightarrow} \mathrm{e}^{\mathrm{i}\boldsymbol{k}\boldsymbol{r}} + f_k(\Omega_{\boldsymbol r})\frac{\mathrm{e}^{\mathrm{i}kr}}{r} \tag{2.8a}$$

$$\Rightarrow f_{k,l=0}(\Omega_{\boldsymbol r}) \simeq \frac{\mathrm{e}^{2\mathrm{i}\delta_k} - 1}{2\mathrm{i}k} = -\frac{1}{\mathrm{i}k - k/\tan\delta_k} \simeq -\frac{1}{\mathrm{i}k + 1/a - r_{\text{eff}}k^2 + \mathcal{O}(k^4)}. \tag{2.8b}$$

For our purposes, it is sufficient to neglect r_{eff} so we can assume a delta potential $V(\boldsymbol{r}) = g\delta(\boldsymbol{r})$. When relating g to a, it is necessary to introduce an ultraviolet momentum cutoff λ to regularize the divergence coming from the delta potential. This is handled in the T-matrix approach, which is explained in the following.

The Schrödinger equation (2.3) in a scattering problem is typically reformulated as the Lippmann–Schwinger equation,

$$|\psi^{\pm}\rangle = |\phi\rangle + G_0^{\pm}\hat{V}|\psi^{\pm}\rangle, \quad G_0^{\pm}(\omega) = (\omega \pm \mathrm{i}0^+ - \hat{H}_0)^{-1}, \tag{2.9}$$

where $|\psi^{\pm}\rangle$ is the full outgoing/ingoing scattering state and $|\phi\rangle$ is the free state. Furthermore, $\hat{H}_0$ refers to the free Hamiltonian and $\hat{V}$ to the scattering potential. The self-consistency of Eq. (2.9) can be expressed in terms of the so-called *transition matrix* or short T matrix, defined by

$$\hat{V}|\psi^+\rangle = \hat{V}(\hat{\mathbb{1}} - G_0^+\hat{V})^{-1}|\phi\rangle \equiv \hat{T}|\phi\rangle \Rightarrow \hat{T} = \hat{V} + \hat{T}G_0^+\hat{V}. \tag{2.10}$$

For a delta potential $V(\boldsymbol{r}) = g\delta(\boldsymbol{r})$, the T matrix is written as [Zha21]

$$\begin{aligned}
T(\omega) &= \frac{g}{1 - \frac{g}{V}\sum_{\boldsymbol{k}}\frac{1}{\omega - \boldsymbol{k}^2/(2m_r)}} \\
&= \left[\frac{1}{g} + \frac{1}{V}\sum_{\boldsymbol{k}}\frac{1}{\boldsymbol{k}^2/(2m_r)} - \frac{1}{V}\sum_{\boldsymbol{k}}\left(\frac{1}{\omega - \boldsymbol{k}^2/(2m_r)} + \frac{1}{\boldsymbol{k}^2/(2m_r)}\right)\right]^{-1} \\
&= \left[\frac{1}{g} + \frac{1}{V}\sum_{\boldsymbol{k}}\frac{1}{\boldsymbol{k}^2/(2m_r)} + \frac{\mathrm{i}\sqrt{2m_r\omega}\,m_r}{2\pi}\right]^{-1}.
\end{aligned} \tag{2.11}$$

Here, the divergent terms from the momentum sum are extracted. The T matrix is related to the scattering amplitude, Eq. (2.8), as $T = -2\pi/m_r f_{l=0}$. From identifying the term $\mathrm{i}\sqrt{2m_r\omega}$ with $\mathrm{i}k$, we get the relation between the effective parameter g and the physical scattering length a:

$$\frac{1}{g} = \frac{m_r}{2\pi a} - \frac{1}{V}\sum_{\boldsymbol{k}}\frac{2m_r}{\boldsymbol{k}^2}. \tag{2.12}$$

In the microscopic theory, the effective parameter g needs to be adjusted together with the divergent momentum sum. To this end, the dependence on the ultraviolet momentum cutoff λ can be compensated by a cutoff dependence of g in such a way that Eq. (2.12) is fulfilled and the physics is described correctly by the scattering length a. The relation between the effective coupling strength g and the scattering length a is essential for the description of ultracold Fermi mixtures including Fermi polarons.

2.1.3. Fermi polarons

Mixtures of fermions are ubiquitous in physics. They range from the electron gas in metals to the nuclear gas in neutron stars. We focus here on a mixture of two particle types c and d with masses m_c and m_d and fermionic operators $\hat{c}_{\boldsymbol{k}}$ and $\hat{d}_{\boldsymbol{k}}$. As discussed previously, the van der Waals interaction, Eq. (2.1), in ultracold atomic gases is well represented by a delta potential $V(\boldsymbol{r} - \boldsymbol{r}') \propto g\delta(\boldsymbol{r} - \boldsymbol{r}')$ with the coupling constant g[2]. In momentum representation, the Hamiltonian reads

$$\hat{H} = \sum_{\boldsymbol{k}} \hat{c}_{\boldsymbol{k}}^{\dagger} \frac{\boldsymbol{k}^2}{2m_c} \hat{c}_{\boldsymbol{k}} + \sum_{\boldsymbol{k}} \hat{d}_{\boldsymbol{k}}^{\dagger} \frac{\boldsymbol{k}^2}{2m_d} \hat{d}_{\boldsymbol{k}} + \frac{g}{V} \sum_{\boldsymbol{k},\boldsymbol{k}',\boldsymbol{q}} \hat{c}_{-\boldsymbol{k}}^{\dagger} \hat{d}_{\boldsymbol{k}+\boldsymbol{q}}^{\dagger} \hat{d}_{\boldsymbol{k}'+\boldsymbol{q}} \hat{c}_{-\boldsymbol{k}'}, \qquad (2.13)$$

with the volume factor V. In general, the two particle types come with different masses m_c and m_d yielding a mass imbalance $\alpha = (m_d - m_c)/(m_c + m_d)$. The corresponding chemical potentials μ_c and μ_d are tuned in such a way that the respective densities n_c and n_d might be different. An imbalance in densities is described by the polarization $P = (n_c - n_d)/(n_c + n_d)$. Hereby, we always assume c to be the majority particles and d the minority particles, i.e., $n_c \geq n_d$. Interactions within a particle type, i.e., c with c and d with d can be neglected as scattering states of higher angular momenta $l > 0$ are energetically suppressed at low temperature while s-wave scattering $l = 0$ within one particle type is not allowed because of Pauli's exclusion principle.

A well understood limit of a Fermi mixture is the balanced case where the chemical potentials $\mu_c = \mu_d$ and thus the densities $n_c = n_d$ coincide, yielding a vanishing polarization $P = 0$. Such a system exhibits the rich physics of the BEC-BCS crossover [Zwe11, CSPR+18], which was successively realized in several experiments [GRJ03, CBA+04, MPY+19]. Below a critical temperature, the atoms form a BCS superfluid consisting of Cooper pairs formed by a c and d particle. At weak coupling, this system is well described by the theory of superconductivity by Bardeen, Cooper and Schrieffer (BCS) from 1957 [BCS57] (see also Sec. 2.5), which was awarded with a Nobel Prize in 1972. For $1/(k_{\mathrm{F}}a) \ll 0$, the Cooper pairs are weakly bound and their constituents are separated by a distance $\xi \sim \Delta^{-1} \sim \exp[1/(k_{\mathrm{F}}|a|)]$ determined by the gap parameter Δ and the scattering length a. Consequently, in that regime the inter-particle

---

[2]As van der Waals interactions are attractive, the coupling constant $g < 0$ is negative in the microscopic model. Still, in our effective description, its sign can vary and is determined by the value of the scattering length a [cf. Eq. (2.12)].
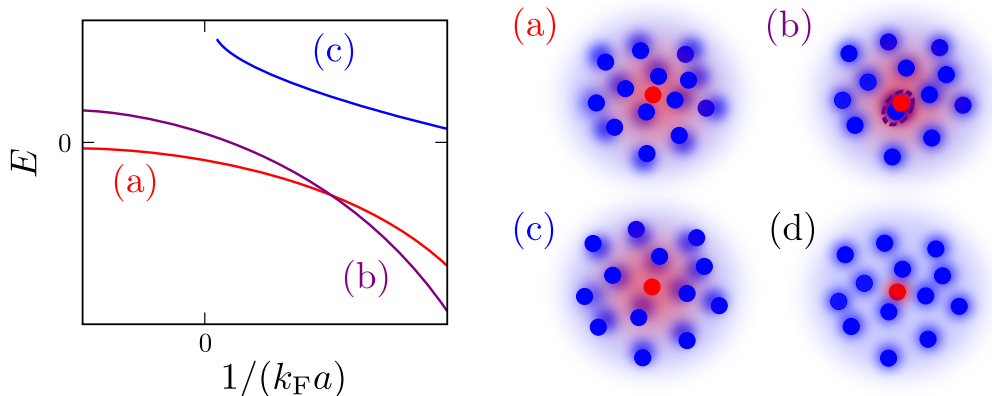
Figure 2.1.: The three branches of the Fermi polaron problem. On the left, the energies E of the different polaron branches are illustrated in dependence on the inverse scattering length $1/(k_{\mathrm{F}}a)$. The respective lines correspond to (a) the attractive polaron (red), (b) the molaron (purple), and (c) the repulsive polaron (blue). On the right, we sketch the the atomic clouds of majority particles (blue circles) with the impurity (red circle). The collective behavior is symbolized by the red area. In the attractive branch (a), the gas particles are attracted by the impurity while, for the repulsive branch (c), they are repelled. The molaron (b) contains a molecule consisting of the impurity and one gas particle (symbolized by the dashed purple ellipse). For comparison, we also show the non-interacting case (d), which is adiabatically connected to the attractive polaron branch for $1/(k_{\mathrm{F}}a) \to -\infty$.

spacing $d \sim 1/k_{\mathrm{F}}$ (cf. Eq. (2.2) as $n \propto k_{\mathrm{F}}^3$) is much smaller than the extent of Cooper pairs. For $a > 0$, the particles can form additional bound states. For $1/(k_{\mathrm{F}}a) \gg 0$, the bound state formation is favored and the physics is governed by tightly bound bosonic molecules that form a BEC, instead of the loosely bound Cooper pairs [Zwe11].

The focus in this dissertation is on the limit $P = 1$ with a single d particle embedded in a Fermi gas of c particles. This case exhibits the formation of a Fermi polaron, a collective state of the impurity entangled with excitations of the bath particles. The polaron is a paradigm for the concept of a quasi-particle. For reviews about the Fermi polaron problem, see Refs. [MZB14, SKI$^+$18, LC24]. Originally, polarons were introduced by Landau in 1933 [Lan33, LP48] as electrons moving in a solid material being dressed by lattice distortions. They were further investigated in this context by Fröhlich in 1954 [Frö54]. Since its first observation using radio-frequency spectroscopy of an ultracold atomic gas formed by ^{6}Li atoms [SWSZ09], polaron physics has experienced a resurgence of interest and has continuously been part of active research. Moreover, polarons occur in the rich zoo of quasi-particles in atomically thin semiconductors, so-called van der Waals materials [SBC$^+$17, FSIS20], and are even formed in neutron stars [FGH$^+$14].

Figure 2.1 summarizes the most important concepts of the Fermi polaron problem. The low-energy physics is essentially described by three different states. The most iconic is the

attractive polaron. This is the typical quasi-particle, which consists of the impurity being dressed by a cloud of excited atoms that are attracted toward the impurity center. For $1/(k_{\mathrm{F}}a) \to -\infty$, the polaron is adiabatically connected to the non-interacting case where the bare impurity forms a non-interacting product state with the Fermi sea. Secondly, there is the so-called *molaron* branch [DMCS24]. Here, the impurity forms a molecule with one of the majority particles. The molaron is characterized by a dressing cloud around the molecule. Depending on the scattering length a, the ground state is either given by the attractive polaron or the molaron. The physics is characterized by the so-called polaron-to-molecule transition between these two states. The bound state that is responsible for the presence of the molaron is hard to describe by perturbative approaches. The first excited state where this bound state is not occupied and the dressing cloud around the impurity consists of atoms repelled from the center is known as the *repulsive polaron.* Toward the unitary regime where the scattering length diverges $1/(k_{\mathrm{F}}a) = 0$, the repulsive polaron becomes unstable. The repulsive polaron branch was predicted in an fRG study [SE11] and later observed experimentally using radio-frequency spectroscopy [KPV+12, KZJ+12].

The following approach using variational wavefunctions, known as the *Chevy ansatz* [Che06, CRLC07, TC12], has become the most widely used technique to describe the energy branches of the Fermi polaron:

$$|\mathrm{pol}(\boldsymbol{p})\rangle = \alpha_{\boldsymbol{p}}\hat{d}_{\boldsymbol{p}}^{\dagger}|\mathrm{FS}_N\rangle + \sum_{\substack{|\boldsymbol{k}| > k_{\mathrm{F}}, \\ |\boldsymbol{q}| < k_{\mathrm{F}}}} \alpha_{\boldsymbol{p},\boldsymbol{k},\boldsymbol{q}}\hat{d}_{\boldsymbol{p}+\boldsymbol{q}-\boldsymbol{k}}^{\dagger}\hat{c}_{\boldsymbol{k}}^{\dagger}\hat{c}_{\boldsymbol{q}}|\mathrm{FS}_N\rangle. \qquad (2.14)$$

The first term describes the simple impurity coexisting with the Fermi sea and the second term is formed by the impurity in the presence of a particle-hole excitation. To describe the molaron branch, another type of variational wavefunction has been introduced [MC09, PDZ09]:

$$|\mathrm{mol}(\boldsymbol{p})\rangle = \sum_{|\boldsymbol{k}|>k_{\mathrm{F}}} \beta_{\boldsymbol{p},\boldsymbol{k}}\hat{c}_{-\boldsymbol{k}}^{\dagger}\hat{d}_{\boldsymbol{k}+\boldsymbol{p}}^{\dagger}|\mathrm{FS}_{N-1}\rangle, \qquad (2.15)$$

where a molecular state consisting of a c and d particle is put on top of the Fermi sea containing $N - 1$ particles. The variational parameters $\alpha_{\boldsymbol{p}}, \beta_{\boldsymbol{p},\boldsymbol{k}}$, etc. are computed by minimizing the expressions $\langle \mathrm{pol}(\boldsymbol{p})|(\hat{H} - E)|\mathrm{pol}(\boldsymbol{p})\rangle$ and $\langle \mathrm{mol}(\boldsymbol{p})|(\hat{H} - E)|\mathrm{mol}(\boldsymbol{p})\rangle$. The Chevy ansatz is equivalent to a non-self-consistent T matrix approach [PG18], which is underlined by our data shown in Chapter 6. To extend the predictability of the Chevy ansatz, one can include higher orders of particle-hole excitations [LC24], however, this comes with an increasing computational effort.

Over the years, plenty of experiments have been set up using different spectroscopy techniques to observe energy properties of different polaron configurations [NNJ+09, SWSZ09, KPV+12, KZJ+12, CJL+16, SVM+17, YPM+19, ALS+20, NSF+20, FBD+21,

BHF[+]24]. Besides the Chevy ansatz, Fermi polarons were theoretically analyzed by different T-matrix approaches [PDZ09, HL24], diagrammatic Monte–Carlo methods [PS08, VRH14, KP14, KP15], the functional renormalization group (fRG) [SE11, Sch13, MRS22, MS24] and the functional determinant approach (FDA) [KSN[+]12, SKI[+]18]. In this dissertation, we want to pave the way of describing polarons by more elaborate field-theoretical approaches. As they are not limited to specific particle densities and zero temperature, field-theoretical approaches are a promising tool for an extension to the more general case of imbalanced mixtures of fermions. However, as we will see, in practice, many diagrammatic approaches rely on the weak-coupling limit.

The concept of quasi-particles greatly simplifies the description of quantum many-body systems as it focuses on the most relevant composite constituents. Quantum impurity problems such as the formation of a single polaron are the starting point for moving toward the full interacting quantum many-body system as more impurities can be successively included. The more general case of Fermi mixtures with arbitrary imbalances $0 < P < 1$ is not yet explored in great detail. The competition of several phenomena such as the formation of polarons, molecules and Cooper pairs makes them difficult to describe. Nevertheless, in this dissertation, we want to lay the theoretical foundations toward a more general description of imbalanced Fermi mixtures.

2.2. Functional determinant approach

In this section, we explain the functional determinant approach (FDA), which is a widely used method to compute radio-frequency spectra for quantum states around static impurities. Here, we sketch the derivation and the most important features. For further reading, we recommend Refs. [LLL96, Kli03, SKI[+]18, Wan23]. The method describes polaron physics exactly in the limit of an immobile impurity (or equivalently an infinitely massive one). It is not limited to ground-state physics and can be used for arbitrary temperatures and densities of the medium.

In the typical scenario, we have a Fermi gas of particles described by the many-body wave function $|\Psi\rangle$ coupled to an impurity described by its occupancy $|\sigma\rangle$ ($|0\rangle$ for a non-interacting impurity and $|1\rangle$ for an interacting one). The total wavefunction is given by the product $|\sigma\rangle \otimes |\Psi\rangle$ and the total Hamiltonian consists of individual parts, which depend on the occupancy of the impurity. For our example with two impurity states, it reads

$$\hat{H} = \sum_{\sigma=0,1} |\sigma\rangle\langle\sigma| \otimes \hat{H}_\sigma = |0\rangle\langle 0| \otimes \hat{H}_0 + |1\rangle\langle 1| \otimes \hat{H}_1. \tag{2.16}$$

The above Hamiltonian is obtained from the polaron Hamiltonian, Eq. (2.13), when the momenta corresponding to the minority particles $\hat{d}_{\boldsymbol{k}}^\dagger, \hat{d}_{\boldsymbol{k}}$ are omitted and only two states for the impurity are left over (namely, $|1\rangle = \hat{d}^\dagger|0\rangle$ and $|0\rangle$ with $\hat{d}|0\rangle = 0$). The momenta

in the interaction term $g/V\,\hat{d}^\dagger\hat{d}\sum_{\boldsymbol{k},\boldsymbol{k}'}\hat{c}_{\boldsymbol{k}}^\dagger\hat{c}_{\boldsymbol{k}'}$ are therefore completely decoupled. In the case of a single immobile impurity, the Fermi polaron can thus be described as a Fermi gas situated around a static external potential $\hat{v}$. Consequently, the Hamiltonian of the Fermi gas is a bilinear operator,

$$\hat{H}_1 = \sum_{i,j}\langle i|\hat{h}_1|j\rangle\hat{c}_i^\dagger\hat{c}_j, \tag{2.17}$$

and the system is exactly solvable. Here, we have expressed the many-body operator $\hat{H}_1$ (acting on the Fermi gas) through the single-particle operator $\hat{h}_1$ using the fermionic creation and annihilation operators $\hat{c}_i^\dagger, \hat{c}_j$, written in the single-particle basis states $|i\rangle$ and $|j\rangle$. Physical observables in such a system can be expressed through Slater determinants including the single-particle states.

Typically, the single-particle Hamiltonian $\hat{h}_1$ consists of a trivial part and a potential part, i.e., $\hat{h}_1 = \hat{h}_0 + \hat{v}$ and can be diagonalized using new basis states $|\alpha\rangle$. Thus, we write $\hat{h}_1 = \sum_\alpha[h_1]_\alpha\hat{n}_\alpha$ where the number operator is expressed with respect to this new basis, i.e., $\hat{n}_\alpha = \hat{c}_\alpha^\dagger\hat{c}_\alpha$. Let us assume a finite Hilbert space with M states. Corresponding Fock states are written as $|n_1, ..., n_M\rangle$. For fermions, the occupation numbers of the individual states are $n_{\alpha=1,...,M} \in \{1, 0\}$. The number operator $\hat{n}_\alpha$ is thus an eigenstate of the Fock states with the respective occupation numbers $\hat{n}_\alpha|n_1, ..., n_M\rangle = n_\alpha|n_1, ..., n_M\rangle$. Writing the trace $\operatorname{tr}e^{\hat{H}_1}$ in terms of these Fock states yields

$$\operatorname{tr}e^{\hat{H}_1} = \sum_{n_1,...,n_M}\langle n_1, ..., n_M|e^{\sum_\alpha[h_1]_\alpha\hat{n}_\alpha}|n_1, ..., n_M\rangle = \sum_{n_1,...,n_M}\prod_\alpha\langle n_1, ..., n_M|e^{[h_1]_\alpha\hat{n}_\alpha}|n_1, ..., n_M\rangle$$

$$= \sum_{n_1,...,n_M}\prod_\alpha e^{[h_1]_\alpha n_\alpha} = \prod_\alpha\left(\sum_{n_\alpha}e^{[h_1]_\alpha n_\alpha}\right). \tag{2.18}$$

For fermions, the final sum is evaluated as $\sum_{n_\alpha=0,1}e^{[h_1]_\alpha n_\alpha} = 1 + e^{[h_1]_\alpha}$ such that the whole trace is given as a determinant over the single-particle operator $\hat{h}_i$:

$$\operatorname{tr}e^{\hat{H}_1} = \prod_\alpha(1 + e^{[h_1]_\alpha}) = \det(\hat{\mathbb{1}} + e^{\hat{h}_1}). \tag{2.19}$$

Importantly, the last expression is independent of the single-particle basis used, i.e., $\hat{h}_1$ does not need to be represented by a diagonal matrix.

We can always describe a product of exponential functions $e^{\hat{X}_1}e^{\hat{X}_1}\cdots e^{\hat{X}_n}$ as a single exponential $e^{\hat{Y}}$ using the Baker–Campbell–Hausdorff formula. Applying the above steps in the eigenbasis of the new operator $\hat{Y}$ allows a generalization of Eq. (2.19) to

$$\operatorname{tr}\left(e^{\hat{X}_1}e^{\hat{X}_2}\cdots e^{\hat{X}_n}\right) = \det\left(\hat{\mathbb{1}} + e^{\hat{x}_1}e^{\hat{x}_2}\cdots e^{\hat{x}_n}\right). \tag{2.20}$$

The bilinear many-body operators $\hat{X}_i$ are replaced by their single-particle counterparts $\hat{x}_i$. Equation (2.20) is referred to as *Klich's formula* [Kli03]. For bosons, the derivation is analogous; only the occupation numbers n_α can be arbitrarily high such that the summation in Eq. (2.18) yields the geometric series and Klich's formula includes two additional minus signs, i.e., $\mathrm{tr}\left(\mathrm{e}^{\hat{X}_1}\mathrm{e}^{\hat{X}_2}\cdots\mathrm{e}^{\hat{X}_n}\right) = \left[\det(\hat{\mathbb{1}} - \mathrm{e}^{\hat{x}_1}\mathrm{e}^{\hat{x}_2}\cdots\mathrm{e}^{\hat{x}_n})\right]^{-1}$.

Generally, the time evolution of a state $|\sigma\rangle \otimes |\Psi_{\mathrm{gas}}\rangle$ under the Hamiltonian $\hat{H}$, Eq. (2.16), is given by

$$|\Psi(t)\rangle = \mathrm{e}^{-\mathrm{i}\hat{H}t}(|\sigma\rangle \otimes |\Psi_{\mathrm{gas}}\rangle) = |\sigma\rangle \otimes \mathrm{e}^{-\mathrm{i}\hat{H}_\sigma t}|\Psi_{\mathrm{gas}}\rangle. \tag{2.21}$$

In Ramsey interferometry experiments, one performs time-dependent measurements with respect to the occupation of the impurity. The measurement technique typically consists of two steps: By a first pulse, the impurity is brought from the non-interacting state $|0\rangle$ into a superposition $(|0\rangle + |1\rangle)/\sqrt{2}$. Then, one applies a second pulse with a finite phase shift and determines the hyperfine state of the impurity (i.e., a measurement of the Pauli matrix $\hat{\sigma}_z = |0\rangle\langle 0| - |1\rangle\langle 1|$). This procedure yields the *Ramsey signal* $S(t) = \langle\Psi_0(t)|\Psi(t)\rangle$, which is an overlap between the time-evolved state with an unoccupied impurity state $|0\rangle$ and a time-evolved state with an interacting impurity state $|1\rangle$ [CJL+16]. Initially, the gas particles form a Fermi sea $|\Psi_{\mathrm{gas}}\rangle = |\mathrm{FS}\rangle$ so the overlap contains both the Hamiltonian $\hat{H}_1$ including the interaction potential and the unperturbed Hamiltonian $\hat{H}_0$. We have

$$S(t) = \langle\Psi_0(t)|\Psi(t)\rangle = \langle\mathrm{FS}|\mathrm{e}^{\mathrm{i}\hat{H}_0 t}\mathrm{e}^{-\mathrm{i}\hat{H}_1 t}|\mathrm{FS}\rangle = \mathrm{tr}\left(\hat{\rho}\,\mathrm{e}^{\mathrm{i}\hat{H}_0 t}\mathrm{e}^{-\mathrm{i}\hat{H}_1 t}\right). \tag{2.22}$$

Here, we expressed the Fermi gas through its density matrix $\hat{\rho} = |\mathrm{FS}\rangle\langle\mathrm{FS}| = \mathrm{e}^{-\beta(\hat{H}_0 - \mu\hat{N})}/Z$ with the partition function $Z = \mathrm{tr}\,\mathrm{e}^{-\beta(\hat{H}_0 - \mu\hat{N})}$. Using Klich's formula (2.20) yields

$$S(t) = \det\left(\hat{\mathbb{1}} + \mathrm{e}^{-\beta(\hat{h}_0 - \mu\hat{\mathbb{1}})}\mathrm{e}^{\mathrm{i}\hat{h}_0 t}\mathrm{e}^{-\mathrm{i}\hat{h}_1 t}\right) = \det\left(\hat{\mathbb{1}} - n_{\mathrm{F}}(\hat{h}_0) + n_{\mathrm{F}}(\hat{h}_0)\mathrm{e}^{\mathrm{i}\hat{h}_0 t}\mathrm{e}^{-\mathrm{i}\hat{h}_1 t}\right), \tag{2.23}$$

where we used the Fermi–Dirac distribution function $n_{\mathrm{F}}(\varepsilon) = 1/(1 + \mathrm{e}^{\beta(\varepsilon-\mu)})$.

After solving the single-particle Schrödinger equations for the system with a trivial impurity $|0\rangle$, i.e., $\hat{h}_0|n\rangle = \varepsilon_n|n\rangle$, and for the system with the interacting impurity $|1\rangle$, i.e., $\hat{h}_1|\alpha\rangle = E_\alpha|\alpha\rangle$, the Ramsey signal $S(t)$ is computed via a determinant over the matrix M. We write M in the basis of the non-interacting eigenstates,

$$\langle n|M(t)|n'\rangle = [1 - n_{\mathrm{F}}(\varepsilon_n)]\delta_{nn'} + n_{\mathrm{F}}(\varepsilon_n)\mathrm{e}^{\mathrm{i}\varepsilon_n t}\sum_\alpha \langle n|\alpha\rangle\mathrm{e}^{-\mathrm{i}E_\alpha t}\langle\alpha|n'\rangle. \tag{2.24}$$

Thus, we obtain $S(t) = \det M(t)$. While the overlaps $\langle n|\alpha\rangle$ can be precomputed, the determinants of Eq. (2.24) need to be evaluated individually for each time step. If individual time steps are not correlated, this can be performed via parallelization.

In a radio-frequency spectroscopy experiment, the impurity is flipped from the state

$|0\rangle$ to $|1\rangle$, which is evoked by a radio-frequency pulse $\hat{V} \sim \mathrm{e}^{\mathrm{i}\omega t}\hat{\Omega}$ where $\hat{\Omega}$ is the transition operator $\hat{\Omega} = |1\rangle\langle 0| \otimes \hat{\mathbb{1}}$. The absorption spectrum is given by *Fermi's golden rule*:

$$A(\omega) = 2\pi \sum_{i,f} p_i \left|\langle f|\hat{\Omega}|i\rangle\right|^2 \delta[\omega - (E_f - E_i)]. \tag{2.25}$$

At zero temperature, the total initial state is fixed to $|i\rangle = |0\rangle \otimes |\mathrm{FS}\rangle$ and, as a result, the sum does not need to run over several initial states i anymore. The final state $|f\rangle = |f_{\mathrm{imp}}\rangle \otimes |f_{\mathrm{FS}}\rangle$ is more general. Since $2\pi\delta(\omega) = \int \mathrm{d}t\, \mathrm{e}^{\mathrm{i}\omega t}$ and $|\mathrm{FS}\rangle$ and $|f_{\mathrm{FS}}\rangle$ are many-body eigenstates of $\hat{H}_0$ and $\hat{H}_1$ [cf. Eq. (2.16)], we can rewrite Fermi's golden rule as

$$A(\omega) = \int \mathrm{d}t\, \mathrm{e}^{\mathrm{i}(\omega - E_f + E_i)t} \sum_f \langle i|\hat{\Omega}^\dagger|f\rangle\langle f|\hat{\Omega}|i\rangle = \int \mathrm{d}t\, \mathrm{e}^{\mathrm{i}\omega t} \sum_f \langle i|\mathrm{e}^{\mathrm{i}\hat{H}t}\hat{\Omega}^\dagger|f\rangle\langle f|\mathrm{e}^{-\mathrm{i}\hat{H}t}\hat{\Omega}|i\rangle. \tag{2.26}$$

The sum over all final states $|f\rangle$ can now be carried out and the impurity degrees of freedom, $|0\rangle$ and $|1\rangle$, with the two transition operators $\hat{\Omega}$ evaluated straightforwardly:

$$A(\omega) = \int_{-\infty}^{\infty} \mathrm{d}t\, \mathrm{e}^{\mathrm{i}\omega t}\langle \mathrm{FS}|\mathrm{e}^{\mathrm{i}\hat{H}_0 t}\mathrm{e}^{-\mathrm{i}\hat{H}_1 t}|\mathrm{FS}\rangle = 2\mathrm{Re}\int_0^{\infty} \mathrm{d}t\, \mathrm{e}^{\mathrm{i}\omega t}\langle \mathrm{FS}|\mathrm{e}^{\mathrm{i}\hat{H}_0 t}\mathrm{e}^{-\mathrm{i}\hat{H}_1 t}|\mathrm{FS}\rangle$$
$$= 2\mathrm{Re}\int_0^{\infty} \mathrm{d}t\, \mathrm{e}^{\mathrm{i}\omega t}S(t). \tag{2.27}$$

We conclude that the absorption spectrum is obtained via a Fourier transform of the Ramsey signal $S(t)$, Eq. (2.23). In practice, the upper limit is approximated by a finite time $t_{\mathrm{max}} \sim 1/\delta E$, which corresponds to a minimal energy scale δE for a resolution of the final spectra. This computation is performed by a fast Fourier transform [cf. App. A].

   Another quantity that we compute with the FDA is the density of the Fermi gas. We are interested in the stationary density distribution,

$$n_\sigma(\boldsymbol{r}) = \mathrm{tr}\left(\hat{\rho}_\sigma \hat{c}_{\boldsymbol{r}}^\dagger \hat{c}_{\boldsymbol{r}}\right) = \frac{1}{Z_\sigma}\mathrm{tr}\left(\mathrm{e}^{-\beta(\hat{H}_\sigma - \mu\hat{N})}\hat{c}_{\boldsymbol{r}}^\dagger \hat{c}_{\boldsymbol{r}}\right), \tag{2.28}$$

where the density matrix $\hat{\rho}_\sigma$ is evaluated with respect to the fixed impurity state $|\sigma\rangle$. To compute Eq. (2.28), we use a special case of Klich's formula (cf. Eq. (S33) in the SM of Ref. [P2]):

$$\mathrm{tr}\left(\mathrm{e}^{\hat{X}_1}\hat{X}_2\right) = \left.\frac{\mathrm{d}}{\mathrm{d}a}\right|_{a=0}\mathrm{tr}\left(\mathrm{e}^{\hat{X}_1}\mathrm{e}^{\hat{X}_2}\right) = \left.\frac{\mathrm{d}}{\mathrm{d}a}\right|_{a=0}\det\left(\hat{\mathbb{1}} + \mathrm{e}^{\hat{x}_1}\mathrm{e}^{\hat{x}_2}\right)$$
$$= \det(\hat{\mathbb{1}} + \mathrm{e}^{\hat{x}_1})\,\mathrm{tr}\left([\hat{\mathbb{1}} + \mathrm{e}^{\hat{x}_1}]^{-1}\mathrm{e}^{\hat{x}_1}\hat{x}_2\right). \tag{2.29}$$
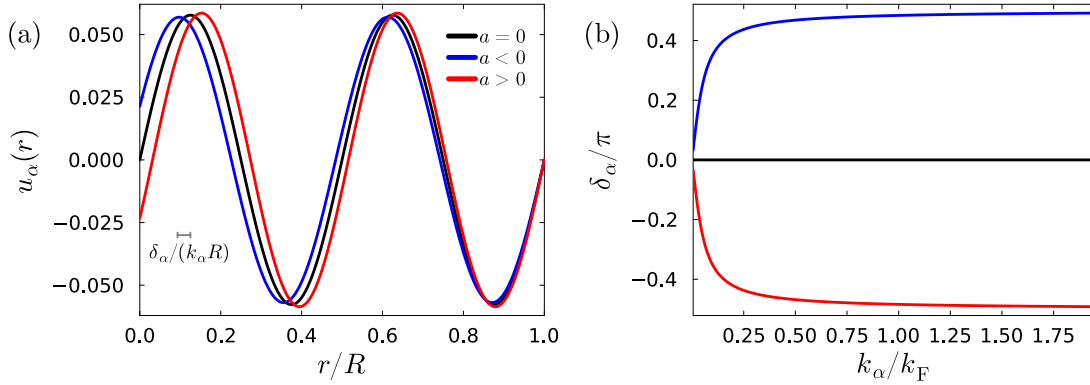
Figure 2.2.: Illustration of the phase shift δ_α. (a) Radial part $u_\alpha(r)$ of the single-particle wave function $\psi_{\alpha lm}(\boldsymbol{r})$, Eq. (2.34), at $\alpha = 4$ for different values of the scattering length $ak_F = 0, -20, 20$. (b) Corresponding phase shifts δ_α as a function of the momentum k_α.

Here, we used Jacobi's formula,

$$\frac{\mathrm{d}}{\mathrm{d}a} \det A(a) = \det[A(a)] \operatorname{tr}\left(A(a)^{-1}\frac{\mathrm{d}A(a)}{\mathrm{d}a}\right), \tag{2.30}$$

to differentiate the determinant. Suppose $\hat{X}_1 = -\beta(\hat{H}_\sigma - \mu\hat{N})$ in Eq. (2.29) is a bilinear operator represented in the basis states $|i\rangle$ and $|j\rangle$ [cf. Eq. (2.17)], then we take

$$\hat{X}_2 = \hat{c}_{\boldsymbol{r}}^\dagger \hat{c}_{\boldsymbol{r}} = \sum_{i,j} \hat{c}_i^\dagger \langle i|\boldsymbol{r}\rangle\langle\boldsymbol{r}|j\rangle \hat{c}_j, \tag{2.31}$$

to evaluate the density $n(\boldsymbol{r})$, Eq. (2.28), as

$$n_\sigma(\boldsymbol{r}) = \frac{1}{Z_\sigma} \det(\hat{\mathbb{1}} + \mathrm{e}^{-\beta(\hat{h}_\sigma - \mu)}) \langle\boldsymbol{r}|(\hat{\mathbb{1}} + \mathrm{e}^{-\beta(\hat{h}_\sigma - \mu)})^{-1}\mathrm{e}^{-\beta(\hat{h}_\sigma - \mu)}|\boldsymbol{r}\rangle = \langle\boldsymbol{r}|n_F(\hat{h}_\sigma)|\boldsymbol{r}\rangle. \tag{2.32}$$

Here, we canceled the partition function with the determinant and identified the term in the expectation value as the Fermi–Dirac distribution. After solving the Schrödinger equation $\hat{h}_\sigma|\alpha\rangle = E_\alpha|\alpha\rangle$, the density takes the form (cf. Eq. (S35) in the SM of Ref. [P2]):

$$n_\sigma(\boldsymbol{r}) = \sum_\alpha n_F(E_\alpha) |\langle\alpha|\boldsymbol{r}\rangle|^2. \tag{2.33}$$

So it is a sum over the occupation numbers with the corresponding wave functions in real space, which is rather intuitive.

In Fig. 2.3, we present our data for Fermi polarons formed by a heavy impurity, i.e., $m_d/m_c \to \infty$, which we obtained from the FDA. These are similar to those discussed
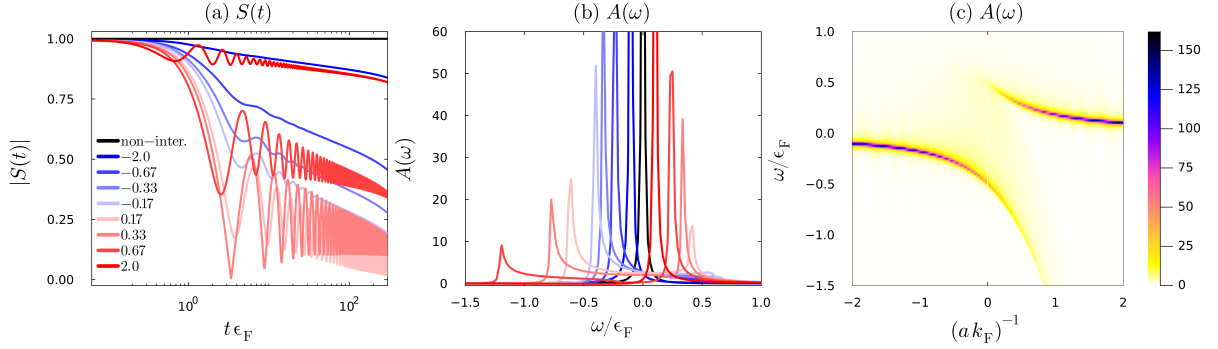
Figure 2.3.: Quantities of the Fermi polaron computed using the FDA: (a) Ramsey signals $S(t)$, Eq. (2.23), and (b) absorption spectra $A(\omega)$, Eq. (2.27), for different values of the dimensionless inverse scattering length $1/(ak_\mathrm{F})$ marked by different colors. (c) Absorption spectra $A(\omega)$ as a colorplot depending on the inverse scattering length $1/(ak_\mathrm{F})$. We use $T/\varepsilon_\mathrm{F} = 0.001$, $Rk_\mathrm{F} = 600$, $n_\mathrm{max} = 375$, and $t_\mathrm{max}\varepsilon_\mathrm{F} = 300$. Similar results were obtained in Refs. [KSN+12] and [SKI+18].

in Refs. [KSN+12] and [SKI+18]. We solve the three-dimensional Schrödinger equations $\hat{h}_0|\boldsymbol{n}\rangle = \varepsilon_{\boldsymbol{n}}|\boldsymbol{n}\rangle$ and $\hat{h}_1|\boldsymbol{\alpha}\rangle = E_{\boldsymbol{\alpha}}|\boldsymbol{\alpha}\rangle$ for a radial interaction potential $V(\boldsymbol{r}) = V(r)$ in a finite system of radius R using the quantum numbers $\boldsymbol{\alpha} = (\alpha, l, m)$. The total wave functions are expressed as

$$\psi_{\alpha lm}(\boldsymbol{r}) = \langle \alpha lm|\boldsymbol{r}\rangle = Y_{lm}(\Omega_{\boldsymbol{r}})\frac{u_{\alpha l}(r)}{r}. \tag{2.34}$$

In comparison to Eq. (2.4), the continuous variable k is replaced by the discrete parameter α due to the finite system size. The overlaps $\langle \boldsymbol{n}|\boldsymbol{\alpha}\rangle$ appearing in the Ramsey signal, Eq. (2.24),

$$\langle nlm|\alpha l'm'\rangle = \int_{\boldsymbol{r}} \langle nlm|\boldsymbol{r}\rangle\langle \boldsymbol{r}|\alpha l'm'\rangle = \int_{\Omega_{\boldsymbol{r}}} Y_{lm}^*(\Omega_{\boldsymbol{r}})Y_{l'm}(\Omega_{\boldsymbol{r}})\int_0^R \mathrm{d}r\, u_{nl}(r)u_{\alpha l'}(r)$$
$$\equiv \delta_{ll'}\delta_{mm'}\langle nl|\alpha l\rangle, \tag{2.35}$$

are determined by the one-dimensional integrals $\langle nl|\alpha l\rangle$ over the radial parts as the contribution of spherical harmonics is trivial. Details on the functions $u_{\alpha l}(r)$ are discussed extensively in Sec. S1 in the SM of Ref. [P2], including a delta potential and a finite-well potential.

For Fermi polarons, it is sufficient to assume a zero interaction range, which is exclusively described by the s-wave scattering length. Thus, only the contributions with zero angular momentum $l = 0 = m$ provide a non-trivial contribution to the Ramsey signal $S(t)$, Eqs. (2.22)–(2.24), and we just write α instead of $(\alpha, 0, 0)$. The scattering length enters the radial part of the wave function via the phase shift δ_α, which is self-consistently

determined by the following equation (cf. Eq. (S13) in the SM of Ref. [P2]):

$$k_\alpha R + \delta_\alpha = \alpha\pi, \quad \delta_\alpha = -\arctan(k_\alpha a). \tag{2.36}$$

Figure 2.2 illustrates that for negative scattering lengths $a < 0$ the phase shift is positive such that the corresponding eigenenergy is lowered, i.e., $E_\alpha = k_\alpha^2/(2m) = (\alpha\pi - \delta_\alpha)^2/(2mR^2)$. The radial part of the wave function $u_{\alpha 00}(r)$ is torn toward the center. For positive scattering lengths $a > 0$ we have the opposite behavior; here the eigenenergies are increased and the corresponding wavefunction is repelled at the center. For positive scattering lengths there exists an additional bound state with energy $\varepsilon_b = -1/(2ma^2)$.

By knowing the eigenenergies E_α and overlaps $\langle\alpha|n\rangle$ between the non-interacting $|n\rangle$ and interacting wave functions $|\alpha\rangle$, we can evaluate the matrix elements $\langle n|M(t)|n'\rangle$, Eq. (2.24), and compute the Ramsey signal $S(t)$, Eq. (2.23). This proves itself as the bottleneck of the numerics as $S(t)$ includes determinants over the dense matrices $M(t)$ for every single time step. On the contrary, obtaining the absorption spectra $A(\omega)$ from fast Fourier transform, Eq. (2.27), is numerically straightforward. As discussed in Sec. S5 of the SM of Ref. [P2], the finite system size R is accompanied by a finite resolution of energies $\delta\varepsilon \sim \pi k_F/(mR)$ and gives an upper time limit $t_{\max} \sim 2mR/k_F$ for the Fourier integral of the Ramsey signal.

In Fig. 2.3, we show Ramsey signals $S(t)$ and absorption spectra for various inverse scattering lengths $1/(ak_F)$. As discussed in the literature [KSN+12, SKI+18], the existence of the bound state for $a > 0$ leads to additional strong oscillations in the Ramsey signal and to an additional peak at positive frequencies of the absorption spectrum. This refers to the repulsive polaron, which is an excited state where the bound state is not occupied, in contrast to all the upwards shifted energy states of the gas particles. The attractive polaron branch at negative frequencies is the many-body ground state. Note that in the limit of an immobile impurity, which is considered in the FDA, there is no polaron-to-molecule transition. The decay of the Ramsey signal [cf. Fig. 2.3(a)] and the spectral peaks [cf. Fig. 2.3(b)] are characterized by a power-law behavior and thus correspond to Anderson's orthogonality catastrophe [And67]. We will extensively discuss this matter in Chapter 5.

2.3. Rydberg atom spectroscopy

Many interesting effects in ultracold atomic gases occur on sub-optical length scales $\lesssim 300$ nm (e.g., the size of polarons, the distance of Cooper pairs in superfluids and the extension of Feshbach molecules). As optical probes are typically limited in resolution by their wavelength, it remains challenging to conduct time-resolved and *in situ* measurements of respective correlation functions. In recent years, Rydberg excitations have been providing a versatile platform for experiments in atomic quantum gases. In this section, we present a new measurement technique for the hitherto unexplored density

profile of a Fermi polaron by making use of the fact that the radius $r_{\text{Ryd}} = 50\text{--}500$ nm of typical Rydberg atoms matches the typical length scale of the polaron cloud. The density profile of the polaron can be determined from the occupancy of bound states between the fermionic gas atoms and the Rydberg electron. Rydberg excitations are created by optical light so we found an elegant way of converting optical excitations into a probe at sub-optical wavelengths. As a result, the absorption spectra do not only give information about the size of a Fermi polaron, but, as we show, also provide an astonishingly accurate measure for its overall density profile.

2.3.1. Overview

Rydberg atoms are excited atoms with one or more electrons occupying a very high principal number $n_{\text{Ryd}} \gtrsim 50$. By now, there have been many experimental realizations of Rydberg atoms using various atomic isotopes [BBN$^+$09, AGHW10, WML$^+$10, GRS$^+$12, SLE$^+$16]. The outermost electron, also called *Rydberg electron*, can be approximately described by the wavefunctions of a hydrogen atom with a screened charge of the atomic nucleus. It was shown that the Rydberg electron mediates an effective interaction potential for the neutral atomic in the environment [DG87, GDS00]. When the Rydberg electron itself is in an *s*-wave state, this potential is given by

$$V_{\text{Ryd}}(r) = \frac{2\pi a_e}{m_e} |\psi_{n_{\text{Ryd}}}(r)|^2, \tag{2.37}$$

where a_e is the *s*-wave scattering length of the Rydberg electron with the respective gas particles and m_e is the mass of the electron. The approximate wavefunction of the Rydberg electron $\psi_{n_{\text{Ryd}}}$ with principal number n_{Ryd} and zero angular momentum $l_{\text{Ryd}} = 0$ yields

$$\psi_{n_{\text{Ryd}}}(r) = \frac{1}{\sqrt{4\pi r}} \frac{W_{\nu,1/2}[2r/(\nu a_0)]}{\sqrt{a_0 \nu^2 \Gamma(\nu + 1)\Gamma(\nu)}}, \quad \text{with } \nu = n_{\text{Ryd}} - \delta_0. \tag{2.38}$$

The screening effect of the nucleus is incorporated in the so-called quantum defect δ_0 that depends on the isotope of the Rydberg excitation. Furthermore, Eq. (2.38) includes the Bohr radius a_0, the Whittaker function $W_{\kappa,\mu}(z)$ and the Gamma function $\Gamma(z)$.

Figure 2.4(a) illustrates the potential $V_{\text{Ryd}}(r)$, Eq. (2.37), which exhibits many oscillations (see blue line). The most pronounced minimum is located around the Rydberg radius r_{Ryd} and hosts a deeply bound state (see dashed red line). Its binding energy ε_{RM} typically lies in the MHz regime and therefore exceeds the other energy scales of the many-body system (cf. App. B.1). When a previously non-interacting atom in a many-body state is excited to a Rydberg state [cf. Fig. 2.4(b)], gas particles in the vicinity of the Rydberg radius (white dashed circle) can occupy the bound state and form so-called *ultralong-range Rydberg molecules* [GDS00, DAD$^+$15, Eil19, FHS20]. Actually the Rydberg atom is being dressed by many excitations of atoms in the vicinity and thus
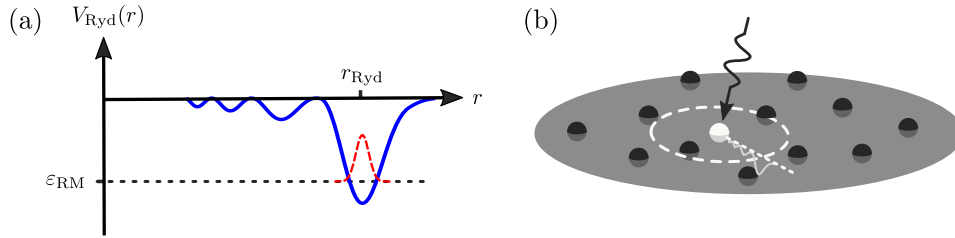
Figure 2.4.: (a) Sketch of the Rydberg-molecular potential $V_{\mathrm{Ryd}}(r)$ (blue) as a function of the distance to the impurity r. At the Rydberg radius r_{Ryd}, the outermost minimum is located hosting the Rydberg-molecular state with binding energy $\varepsilon_{\mathrm{RM}}$. (b) Sketch of a Rydberg atom located in a Fermi sea briefly after the excitation. The dimer-molecular state affects atoms close to the Rydberg radius r_{Ryd} (white dashed circle) (see also Fig. 6.1 in Ref. [Wag24]).

itself forms a polaron [SLN+16, CSW+18, SWD+18]. Due to strong long-range interactions, atoms nearby a Rydberg atom cannot be excited to a Rydberg state themselves, which is known as the *Rydberg blockade* mechanism. Thus, Rydberg atoms cannot be put arbitrarily close to each other. When the Rydberg blockade distance is much larger than the inter-particle separation of the surrounding atoms, the atoms effectively interact with a single Rydberg atom. This is the realization of a quantum impurity problem [SSD16].

The general idea of our technique is that the Rydberg excitation can be used as a sub-optical microscope to probe correlation functions of quantum many-body states. When the laser, which excites the impurity to the Rydberg state, is detuned by the binding energy $\varepsilon_{\mathrm{RM}}$, the corresponding Rydberg molecule is formed [cf. Fig. 2.4(b)]. Thus, there is a direct connection between the absorption of photons at a certain frequency and the formation of Rydberg molecules. Those, on the other hand, can only form if gas particles are located at a distance of the Rydberg radius r_{Ryd} from the impurity. This Rydberg atom spectroscopy provides information about the pair correlation function evaluated at the distance r_{Ryd} [Wag24]. Since r_{Ryd} is directly related to the easily tunable principal number n_{Ryd}, it is possible to scan through the various distances from the impurity.

The overall experimental procedure is shown in Fig. 2.5. The impurity atom takes three different states: At the beginning it is in the non-interacting state $|0\rangle$ (green) and the surrounding is given by a simple Fermi sea. At a time $t_0 + 0^+$, the impurity is excited to the state $|1\rangle$ (yellow), which interacts via short-range interaction with the fermionic medium and induces the formation of a polaron cloud (red). The latter is characterized by an enhancement of the density around the impurity. At a time $t_1 \gg 1/\varepsilon_{\mathrm{F}}$, the polaron formation is complete and the system is in a quasi-stationary state. That is exactly the state we want to probe. So finally, the impurity is excited to the Rydberg state $|\mathrm{R}\rangle$ (white). As discussed before, this leads to the formation of Rydberg molecules at a distance r_{Ryd} to the impurity. The occupancy of the Rydberg molecule depends on the
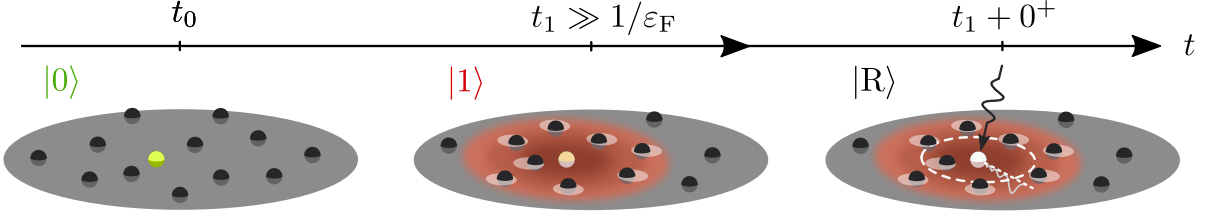
Figure 2.5.: Measurement protocol for the Rydberg spectroscopy experiment (see also Fig. 7.2 in Ref. [Wag24]). At the beginning, a Fermi gas is prepared with the impurity in the non-interacting state $|0\rangle$. A radio-frequency pulse at a time $t_0 + 0^+$ brings the impurity to the locally interacting state $|1\rangle$, which induces the formation of a polaron cloud. After the polaron cloud formation is completed, an additional pulse excites the impurity to the Rydberg-atomic state $|\mathrm{R}\rangle$.

density of the polaron cloud. The Hamiltonian, Eq. (2.16), is extended to

$$\hat{H} = \hat{\mathbb{1}} \otimes \hat{H}_0 + \sum_{\sigma=1,\mathrm{R}} |\sigma\rangle\langle\sigma| \otimes \hat{V}_\sigma, \quad \hat{H}_0 = \sum_{\boldsymbol{k}} \varepsilon_{\boldsymbol{k}} \hat{c}_{\boldsymbol{k}}^\dagger \hat{c}_{\boldsymbol{k}}, \quad \hat{V}_\sigma = \int_{\boldsymbol{r}} V_\sigma(\boldsymbol{r}) \hat{c}_{\boldsymbol{r}}^\dagger \hat{c}_{\boldsymbol{r}}, \qquad (2.39)$$

where $V_1(\boldsymbol{r})$ is a delta potential characterized by the scattering length a and $V_{\mathrm{R}}(\boldsymbol{r})$ is the long-range Rydberg potential, Eq. (2.37).

As a first step, we need to solve the Schrödinger equation $\hat{h}_{\mathrm{R}}|\boldsymbol{\alpha}_{\mathrm{R}}\rangle = E_{\boldsymbol{\alpha}_{\mathrm{R}}}|\boldsymbol{\alpha}_{\mathrm{R}}\rangle$ with the single-particle Hamiltonian $\hat{h}_{\mathrm{R}} = \hat{h}_0 + \hat{v}_{\mathrm{R}}$. Since the Rydberg potential is long-range, it becomes crucial to include higher angular momenta in the wavefunction $\langle\boldsymbol{\alpha}_{\mathrm{R}}|\boldsymbol{r}\rangle$, Eq. (2.34). The diagonalization is performed using a discretization of the Laplace operator (cf. Sec. S1.D in the SM of Ref. [P2]).

After determining the overlaps $\langle\boldsymbol{\alpha}_{\mathrm{R}}|\boldsymbol{\alpha}_1\rangle$ of the eigenstates $|\boldsymbol{\alpha}_{\mathrm{R}}\rangle$ including the Rydberg potential V_{R} and the eigenstates $|\boldsymbol{\alpha}_1\rangle$ including the polaron potential V_1, we compute the Ramsey signal, Eq. (S32) in the SM of Ref. [P2], similar to Eq. (2.22)–(2.24). Hereby, we need a good resolution in time $\delta t < 2\pi/|\varepsilon_{\mathrm{RM}}|$ in order to reproduce the Rydberg molecular dimer peak.

Our absorption spectra $A(\omega)$, Eq. (2.25), which are obtained by Fourier transformation of the Ramsey signal $S(t)$, Eq. (2.27), show two characteristic features:

First, their peak positions are shifted by the energies of the attractive polaron [cf. Fig. 2.3(b)–(c)]. This can be demonstrated by the single-particle energies illustrated in Fig. 2.6. The absorption spectra do not only record the energy of the Rydberg molecular bound state $\varepsilon_{\mathrm{RM}}$, but take into account every single energy shift of the scattering states, which add up to the polaron energy according to Fumi's theorem (cf. Eq. (S37) in the SM of Ref. [P2]). Our measurement technique thus gives an unconventional, yet completely new method to detect polaron energies.

Second, and more importantly, the weight of the dimer peaks gives information about the value of the density at distance r_{Ryd} to the Rydberg impurity. By repeating the
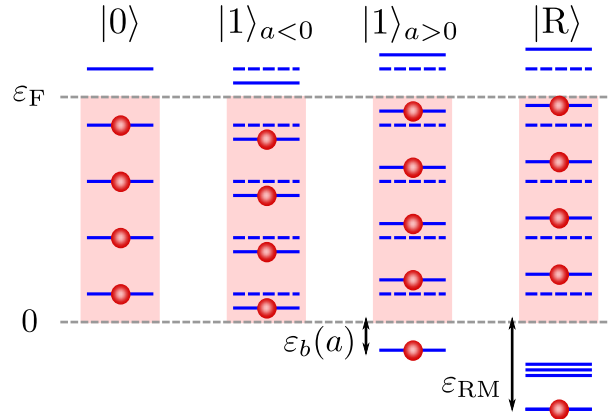
Figure 2.6.: Illustration of the single-particle energy levels of the Fermi gas. On the left, we have the case of an unoccupied impurity $|0\rangle$ with the non-interacting energies ε_n. In the presence of an impurity with a local potential, the energy levels E_α are shifted upwards ($a < 0$) or downwards ($a > 0$). In the case of $a > 0$, there is an additional bound state with energy ε_b. In the presence of a Rydberg potential, there are several non-universal bound states. We form our system in such a way that the binding energy $\varepsilon_{\mathrm{RM}}$ corresponding to the Rydberg-molecular state is the lowest.

measurement for different principal values n_{Ryd}, one can reconstruct the density profile of the polaron cloud quite accurately. Nicely, the weights of the peaks are robust against other factors such as a finite temperature (cf. Sec. S4.D in the SM of Ref. [P2]) or recoil effects of a slowly moving impurity [CJL+16, LLP19]. This suggests that our proposed measurement technique should also be applicable beyond the limit of an immobile impurity.

To conclude, we give the first example of a correlated quantum many-body state, which can be probed by Rydberg atom spectroscopy, namely the Fermi polaron. Our proposed measurement technique can be realized in the experimental setups in the groups of T. Pfau in Stuttgart and T. C. Killian at Rice University. Moreover, it seems reasonable to extend the idea of the Rydberg atom microscopy to other correlated systems. In Sec. 2.5, we briefly discuss on the perspective of probing a BCS superfluid.

Probing polaron clouds by Rydberg atom spectroscopy

by

M. Gievers[1,2], M. Wagner[3], and R. Schmidt[3]

[1]Arnold Sommerfeld Center for Theoretical Physics, Center for NanoScience, and

Munich Center for Quantum Science and Technology, Ludwig-Maximilians-Universität

München, 80333 Munich, Germany

[2]Max Planck Institute of Quantum Optics, 85748 Garching, Germany

[3]Institut für Theoretische Physik, Universität Heidelberg, 69120 Heidelberg, Germany

Probing Polaron Clouds by Rydberg Atom Spectroscopy

Marcel Gievers[1,2,*] Marcel Wagner,[3] and Richard Schmidt[3]

[1]*Arnold Sommerfeld Center for Theoretical Physics, Center for NanoScience, and Munich Center for Quantum Science and Technology, Ludwig-Maximilians-Universität München, 80333 Munich, Germany*
[2]*Max Planck Institute of Quantum Optics, 85748 Garching, Germany*
[3]*Institut für Theoretische Physik, Universität Heidelberg, 69120 Heidelberg, Germany*

In recent years, Rydberg excitations in atomic quantum gases have become a successful platform to explore quantum impurity problems. A single impurity immersed in a Fermi gas leads to the formation of a polaron, a quasiparticle consisting of the impurity being dressed by the surrounding medium. With a radius of about the Fermi wavelength, the density profile of a polaron cannot be explored using *in situ* optical imaging techniques. In this Letter, we propose a new experimental measurement technique that enables the *in situ* imaging of the polaron cloud in ultracold quantum gases. The impurity atom induces the formation of a polaron cloud and is then excited to a Rydberg state. Because of the mesoscopic interaction range of Rydberg excitations, which can be tuned by the principal numbers of the Rydberg state, atoms extracted from the polaron cloud form dimers with the impurity. By performing first principle calculations of the absorption spectrum based on a functional determinant approach, we show how the occupation of the dimer state can be directly observed in spectroscopy experiments and can be mapped onto the density profile of the gas particles, hence providing a direct, real-time, and *in situ* measure of the polaron cloud.

Mixtures of quantum particles are ubiquitous in physics, ranging from neutron matter [1] and the BCS-BEC crossover in atomic gases [2] to superconducting phases in solid-state physics [3]. Quantum mixtures have been investigated for many decades, but more recently, drastic progress in the controllability of experiments with ultracold atomic gases allows for new insights into a plethora of physical phenomena. In the limit of an extremely imbalanced quantum mixture, a single impurity is immersed in a Fermi gas. This leads to the formation of Fermi polarons, quasiparticles formed of gas particles which dress the impurity [4–7]. Even though many polaronic properties are understood to a great extent [4–29], a direct observation of the polaron dressing cloud in continuum systems has been out of reach.

Fermi polarons are generated by the short-range interaction between a Fermi gas and impurity particles, which in cold atoms can be tuned by Feshbach resonances. The size of the resulting polaron dressing cloud is of the order of the Fermi wavelength, i.e., $r_c \sim k_F^{-1}$. For typical densities of ultracold atoms, i.e., $\rho_0 = 10^{11}$–10^{13} cm^{-3}, the relevant length scales lie in the suboptical regime, $r_c \sim 100$–500 nm, which hinders gaining insight into the

real-space structure of these fundamentally important quasiparticles.

In this Letter, we demonstrate how to overcome this challenge enabling an *in situ* measurement of the polaron cloud in cold atom experiments. To this end, we propose a new measurement technique to explore the density profile around the impurity by use of atomic Rydberg states. Key to the idea is the use of the long-range interaction between the Rydberg atom and the bath particles. This interaction is generated by the outermost electron on the Rydberg orbit [30] and induces the formation of ultralong-range Rydberg molecules (ULRMs), i.e., deeply bound states of atoms inside the interaction potential [31–38]. Intriguingly, the extent of the Rydberg atoms of $r_{\mathrm{Ryd}} = 50$–500 nm matches precisely the typical size of the polaron dressing cloud. Hence, by tuning the principal quantum numbers n_{Ryd} of the Rydberg excitation, the binding length of ULRMs is tuned through the polaron cloud (cf. Fig. 1). ULRMs can thus serve as a precision sensor inserted into the polaron cloud. The occupation of ULRMs is detected via a straightforward measurement of the *optical* linear response absorption and can be mapped onto the *suboptical* size of the polaron cloud. Because of its fermionic nature, our method differs from recent probing of a BEC with Rydberg impurities; as for the fermionic systems studied here, the number of particles in the Rydberg radius remains always small [37,39,40].

We calculate Rydberg absorption spectra in the presence of a polaron cloud around the impurity using a functional
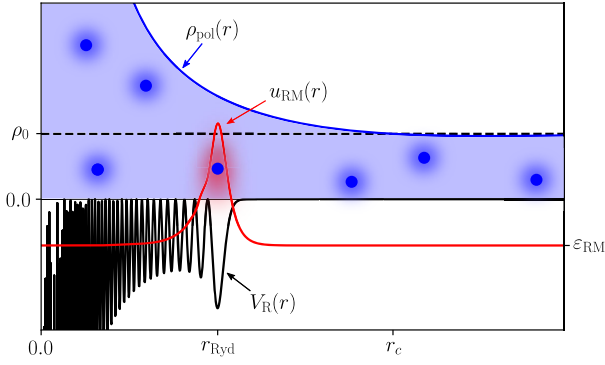
FIG. 1. A Rydberg atom in a polaron cloud. The bath density $\rho_{\text{pol}}(r)$ (blue line) is increased at the center compared to the background density ρ_0 (dashed line). The Rydberg potential $V_R(r)$ (black line) is tuned such that the outermost bound state $u_{\text{RM}}(r)$ (red line) at r_{Ryd} is situated near the polaron cloud radius r_c.

determinant approach [41–43]. The Rydberg blockade mechanism [44] ensures that our single-impurity calculations are applicable. While our approach becomes exact in the limit of heavy impurities immersed in a gas of lighter atoms, the idea of Rydberg sensing of polaron clouds can be extended to arbitrary mass ratios [45,46]. We show that, when the Rydberg excitation is immersed in a polaron cloud, the weight of the peak in the Rydberg absorption spectrum corresponding to the ULRM ground state gives direct access to the density evaluated at a distance r_{Ryd} from the impurity. This way, the complete density profile of polaron clouds, which so far eluded experimental observations, can be mapped out by use of a simple Rydberg spectroscopy experiment.

Model.—We consider a Fermi gas combined with a single charge-neutral and immobile impurity atom. The impurity can be brought into three states $\sigma \in \{0, 1, R\}$. For $\sigma = 0$, the impurity is not interacting with the bath particles. For $\sigma = 1$, the impurity interacts with the bath particles via a short-range interaction that induces the formation of a Fermi polaron [47]. For $\sigma = R$, the impurity is in the Rydberg state, which evokes the long-range interaction with the bath particles. The Hamiltonian reads:

$$\hat{H} = \hat{\mathbb{1}} \otimes \hat{H}_0 + \sum_{\sigma=1,R} |\sigma\rangle\langle\sigma| \otimes \hat{V}_\sigma, \quad (1a)$$

$$\hat{H}_0 = \sum_k \varepsilon_k \hat{c}_k^\dagger \hat{c}_k, \quad \hat{V}_\sigma = \int_r V_\sigma(r)\hat{c}_r^\dagger \hat{c}_r. \quad (1b)$$

Here, $\hat{c}_k^\dagger, \hat{c}_k$ are fermionic operators of the gas and $|\sigma\rangle$ is the state of the impurity. When the impurity is in the state $|\sigma\rangle$, the time evolution of the fermionic gas is given by the Hamiltonian $\hat{H}_\sigma = \hat{H}_0 + \hat{V}_\sigma$, acting only on the fermionic subspace.

We propose the following procedure. At the beginning, the impurity is in the noninteracting state $|0\rangle$ and the bath particles form a Fermi sea $|\text{FS}\rangle$, yielding the many-body state $|\psi(t_0)\rangle = |0\rangle \otimes |\text{FS}\rangle$. By a radio-frequency (rf) pulse, the impurity is then switched to the short-range interacting state, i.e., $|\psi(t_0 + 0^+)\rangle = |1\rangle \otimes |\text{FS}\rangle$. Time evolution leads to the formation of the polaron cloud around the impurity atom. After sufficiently long dephasing time, the system is well described by $|\psi(t_1)\rangle = |1\rangle \otimes |\text{pol}\rangle$. Finally, by driving an optical transition, the impurity atom is transferred to the Rydberg state, i.e., $|\psi(t_1 + 0^+)\rangle = |R\rangle \otimes |\text{pol}\rangle$. This way, the Rydberg atom is, by construction, exactly placed in the center of the polaron cloud as illustrated in Fig. 1.

We simulate the impurity in the $|1\rangle$ state by a delta potential with an s-wave scattering length a [41,48]. The potential in the $|R\rangle$ state, which is generated by scattering of the Rydberg electron with the bath particles, is given by [30]

$$V_R(r) = \frac{2\pi\hbar^2 a_e}{m_e} |\psi_{n_{\text{Ryd}}}(r)|^2. \quad (2)$$

Here, $\psi_{n_{\text{Ryd}}}(r)$ is the wave function of an s-wave Rydberg electron with principal number n_{Ryd} and scattering length a_e between an electron and neutral atoms of the background gas [48]. Because of the nonlocal potential $V_R(r)$, there is a finite overlap between the polaron cloud and bound states inside $V_R(r)$ (cf. Fig. 1).

For the calculation of physical quantities, we use the functional determinant approach, which is a standard method for determining spectra [45]. Specifically, the density $\rho_\sigma(r, t)$ around the impurity in state $|\sigma\rangle$ is obtained by a Klich formula [48,53,55]:

$$\rho_\sigma(r, t) = \text{tr}[\hat{\rho}(t)\hat{c}_r^\dagger \hat{c}_r] = \langle r|e^{-i\hat{h}_\sigma t} n_F(\hat{h}_0) e^{i\hat{h}_\sigma t}|r\rangle, \quad (3)$$

where $n_F(\varepsilon) = (e^{\beta(\varepsilon-\mu)} + 1)^{-1}$ is the Fermi-Dirac distribution with inverse temperature β and chemical potential μ and we set $\hbar = 1 = k_B$. The single-particle operator $\hat{h}_\sigma$ corresponds to the Hamiltonian of the gas particles $\hat{H}_\sigma$.

The absorption spectrum of the Rydberg atom inside the polaron is obtained from Fermi's golden rule,

$$A_{\text{pol}}(\omega) = 2\pi \sum_f |\langle f|\text{pol}\rangle|^2 \delta[\omega - (E_f - E_i)]$$

$$= 2\text{Re} \int_0^\infty dt\, e^{i\omega t} \langle\text{pol}|e^{i\hat{H}_1 t} e^{-i\hat{H}_R t}|\text{pol}\rangle, \quad (4)$$

where the gas is initially in the polaron state $|\text{pol}\rangle$ with total energy E_i and $|f\rangle$ represent the complete set of final states of the gas in presence of the Rydberg impurity $|R\rangle$ with total energies E_f.

We obtain the absorption spectrum as the Fourier transform of the Ramsey signal [22,48], which is calculated as a

time-dependent Slater determinant [41,43,48]. Through $\hat{H}_1$ and $\hat{H}_R$, $A_{pol}(\omega)$ depends on both the Rydberg principal quantum number n_{Ryd} and the scattering length a of the polaron. In the following, we consider the system at zero temperature [56] and express physical quantities in terms of the Fermi momentum k_F and Fermi energy ε_F, respectively [48]. Still, our method is robust against finite temperature as it depends only on the weight of spectral peaks and not their widths [48].

Fermi polaron cloud.—Before turning to its observation, we first describe the formation of the polaron cloud in the initial state of the system. In particular, we are interested in the stationary density profile, which is established after a hold time $t_1 \gg 1/\varepsilon_F$ [48]. In that limit, the density profile Eq. (3) close to the impurity is well described by the ground state of the Hamiltonian $\hat{H}_1$ and given by

$$\rho_{pol}(\boldsymbol{r}) = \langle \boldsymbol{r}|n_F(\hat{h}_1)|\boldsymbol{r}\rangle. \tag{5}$$

Because of spherical symmetry, the density depends only on the distance to the impurity, i.e., $\rho_{pol} = \rho_{pol}(r)$.

Figure 2 shows the density of the polaron cloud as a function of the inverse dimensionless scattering length $(ak_F)^{-1}$ measured with respect to the background density, $\rho_0 = k_F^3/(6\pi^2)$. For $a < 0$, the single-particle wave functions are drawn toward the impurity, resulting in a density enhancement near $r = 0$. This enhancement is accompanied by Friedel-like oscillations farther away from the impurity [see also Fig. 2(b)]. On the contrary, for $a > 0$, the single-particle scattering wave functions are pushed away from the impurity. However, the bound state emerging at positive scattering length still leads to an overall enhancement of the density near the impurity [42]. Note that the particle density is formally divergent at $r = 0$, which is an artifact of the contact interaction and not present for physical finite-range potentials [48]. However, for all our considerations, the delta impurity is a valid approximation as the usual van der Waals length of the atoms is much shorter than the size of the Rydberg state. Importantly, the integrated number of particles in the polaron cloud converges to a well-defined, finite number, also in the limit of contact interaction.

We define the region with an increased particle density around the impurity as the *polaron cloud*. The size r_c of the polaron cloud, visualized by a green line in Fig. 2(a), is determined by the first crossing of $\rho_{pol}(r_c) = \rho_0$ and it is of the order of the Fermi wavelength.

The number of particles contributing to the polaron cloud N_c is given by the integrated number of excess atoms within the volume defined by r_c, i.e., $N_c = N_{pol}(r_c) - N_0(r_c)$ [48]. Note that the number of particles contributing to the polaron cloud is at most one particle despite the infinitely many particle-hole excitations required to obtain the exact many-body solution [57]. This is confirmed by a
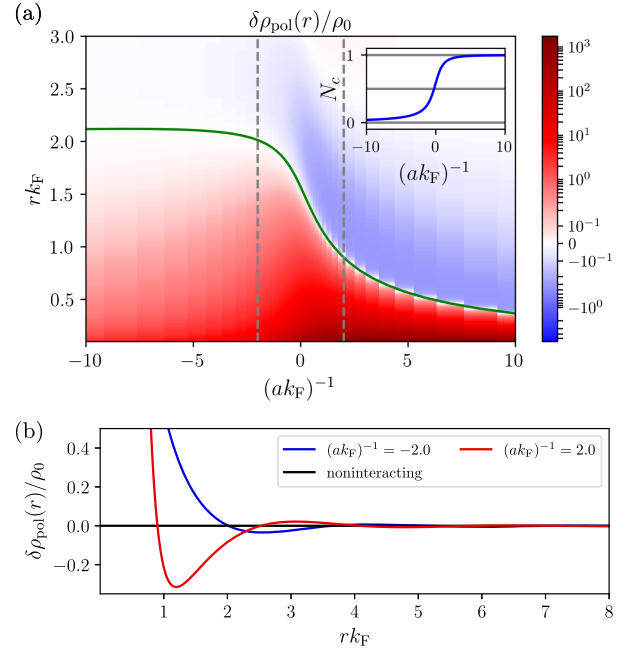
FIG. 2. (a) Polaron density profiles $\delta\rho_{pol}(r) = \rho_{pol}(r) - \rho_0$ in dependence on the inverse scattering lengths $(ak_F)^{-1}$ measured in terms of ρ_0. The size of the polaron cloud r_c is marked in green. The integrated number of excess particles in the cloud N_c is shown in the inset. Note that the color plot is semilogarithmic. (b) Polaron cloud density for two exemplary scattering lengths marked as gray dashed lines in the upper plot.

thermodynamic consideration using Fumi's theorem [22,48]. However, although the number of contributing particles is small, it is the enormous density increase at the center that results in a significant effect in absorption spectroscopy in the presence of the Rydberg excitation.

We note that the real-time evolution of the polaron cloud formation can be obtained in a similar fashion by directly applying Eq. (3). While the corresponding absorption spectra, which then track the real-time formation of the polaron cloud, can also be calculated using linear response theory, in this Letter we focus on the quasistationary limit [cf. Eq. (5)].

Rydberg atom spectroscopy.—Let us now describe the Rydberg absorption spectra in the presence of a polaron cloud. The potential $V_R(r)$ in Eq. (2) features a pronounced minimum at the Rydberg radius r_{Ryd} (see Fig. 1). This minimum supports a spatially confined bound state leading to a prominent dimer peak in the absorption spectrum [32,33,38,43,44,48]. We refer to that state as the *Rydberg molecule (RM)* to differentiate it from higher excited bound states. The Rydberg radius r_{Ryd} can be tuned by the principal quantum number n_{Ryd} and is characteristic for the atomic species of the impurity (in our case ^{87}Rb).

A typical absorption spectrum calculated in the presence of the polaron cloud is shown in Fig. 3(a). The visible peaks
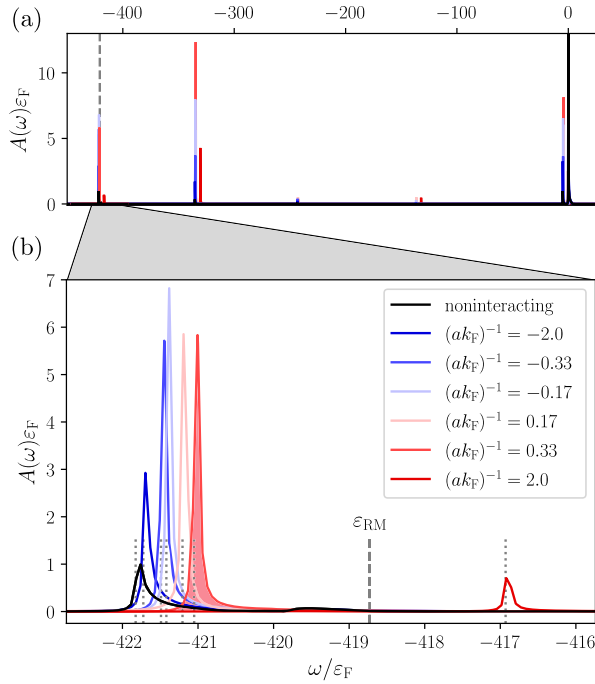
FIG. 3. (a) Absorption spectrum of a Rydberg impurity with $n_{\mathrm{Ryd}} = 60$ generated in polarons of different inverse scattering lengths $(ak_{\mathrm{F}})^{-1}$ at background density $\rho_0 = 5 \times 10^{11}$ cm^{-3}. The binding energy $\varepsilon_{\mathrm{RM}}$ is marked as a dashed gray line. (b) Magnification of the RM peak: Peak positions ω_{peak} Eq. (7) are marked by gray dotted lines. The red shaded region below the curve for $(ak_{\mathrm{F}})^{-1} = 0.33$ indicates the value of the corresponding peak weight I_{pol}. The calculations are performed for a ^{87}Rb impurity in ^{40}K particles.

correspond to the various bound states between the Rydberg atom and bath particles. For $a = 0$, the density ρ_0 is spatially constant in the initial state and one recovers the results for a single Rydberg impurity in a Fermi gas [38,43]. Because of its good overlap with the scattering states of the Fermi gas, the RM with binding energy $\varepsilon_{\mathrm{RM}}$ (indicated by the dashed vertical line) has the largest oscillator strength.

For $a \neq 0$, a Fermi polaron is formed in the initial state. In this case the RM peak does not necessarily remain the most prominent peak of the spectrum. This can be understood from the increased density close to the impurity that causes bound states localized more closely to the impurity to have a larger overlap with the polaron's scattering states.

Looking closer at the RM response [cf. Fig. 3(b)], we observe two key changes in the spectrum that enable the spectroscopy of polarons: (a) the weight of the peaks is modified and (b) their position is shifted. In order to associate the weight of the RM peak with the polaron cloud density at distance r_{Ryd}, we perform an integral over a frequency window that encompasses the dimer peak [see exemplary shaded region in Fig. 3(b)]:
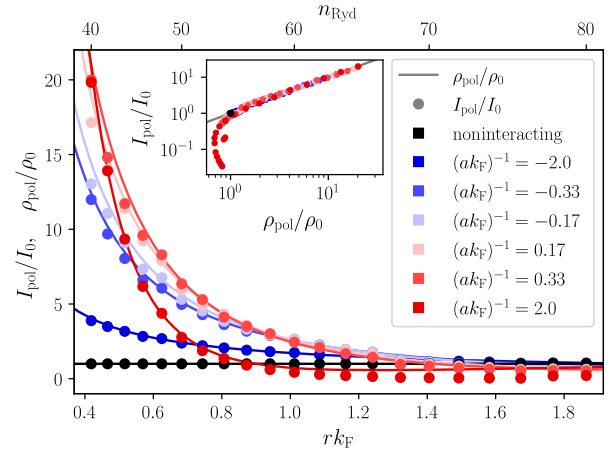
FIG. 4. Normalized density profiles $\rho_{\mathrm{pol}}(r)/\rho_0$ Eq. (5) for polaron clouds formed at inverse scattering lengths $(ak_{\mathrm{F}})^{-1}$ (solid lines) compared to the integrated dimer response $I_{\mathrm{pol}}(r_{\mathrm{Ryd}})/I_0(r_{\mathrm{Ryd}})$ Eq. (6) (dots). The latter corresponds to the Rydberg radius through the respective principal numbers, i.e., $r_{\mathrm{Ryd}}(n_{\mathrm{Ryd}})$. We use a fixed $\rho_0 = 5 \times 10^{11}$ cm^{-3}. The inset shows the dependence between I_{pol}/I_0 and the densities $\rho_{\mathrm{pol}}/\rho_0$. Apart from deviations for small densities, the data points show a tight relation, which is underlined by the gray line marking identity. The calculations are performed for a ^{87}Rb impurity in ^{40}K particles.

$$I_{\mathrm{pol}}(n_{\mathrm{Ryd}}) = \int_{\mathrm{peak}} \mathrm{d}\omega \, A_{\mathrm{pol}}(n_{\mathrm{Ryd}}, \omega). \qquad (6)$$

For absorption spectra at different principal numbers and scattering lengths, we calculate the integrated weight as a function of the principal number, i.e., $I_{\mathrm{pol}}(n_{\mathrm{Ryd}})$. Crucially, since n_{Ryd} is directly related to r_{Ryd}, these values are associated with the density ρ_{pol} at the respective distance. The comparison of $I_{\mathrm{pol}}(n_{\mathrm{Ryd}}) = I_{\mathrm{pol}}(r_{\mathrm{Ryd}})$ with $\rho_{\mathrm{pol}}(r)$ is shown in Fig. 4, where we normalized the signal strength and density by the noninteracting values $I_0(r_{\mathrm{Ryd}})$ and ρ_0. We find striking agreement between the integrated weights of the dimer peaks $I_{\mathrm{pol}}(r_{\mathrm{Ryd}})/I_0(r_{\mathrm{Ryd}})$ and the densities $\rho_{\mathrm{pol}}(r)/\rho_0$. The strong correlation between both quantities is further analyzed in the inset of Fig. 4. Especially for larger density values, the mapping from absorption response to polaron cloud densities works exceptionally well. As our procedure depends only on the integrated spectral weight, it is robust against broadening effects on the spectrum, i.e., finite temperatures [45,48], mobile impurities [46], and the finite lifetime of the Rydberg excitation [35].

Our predictions are made in units of the Fermi momentum, i.e., $r_c = r_c(k_{\mathrm{F}})$. Hence, another way of tuning the location of the Rydberg radius r_{Ryd} relative to the polaron cloud is by changing the overall density of the medium $\rho_0 = k_{\mathrm{F}}^3/(6\pi^2)$. The discussion of density profiles reconstructed using this

alternative method is provided in the Supplemental Material [48].

The shifted positions of the RM peaks (cf. Fig. 3) allow us to directly measure the energy of attractive Fermi polarons. The peak position is given by

$$\omega_{\text{peak}} = \varepsilon_{\text{RM}} - E_{\text{pol}}(a) + E_{\text{pol,R}}(n_{\text{Ryd}}), \qquad (7)$$

which makes the argument evident. First, the RM peak energy is reduced by the energy of the attractive polaron $E_{\text{pol}}(a)$ in the initial state [22]. Second, the presence of the Rydberg impurity shifts the single-particle energies of the Fermi gas itself once more, resulting in an additional polaron shift given by $E_{\text{pol,R}}(n_{\text{Ryd}})$. It is quite noticeable that our absorption spectra thus simultaneously provide two complementary properties of the polaron: it resolves its energy as well as its real-space density profile.

Conclusion.—We have proposed a new technique for probing the dressing cloud of polarons using Rydberg spectroscopy. ULRMs are the key feature enabling the approach. They are formed at a specific distance from the impurity and lead to dimer peaks that can be uniquely identified in absorption spectra. When tuning the principal number n_{Ryd} of the Rydberg state, the location of the ULRM is changed and the integrated weight of its dimer peaks directly corresponds to the density of gas particles. While we focused on the case of Fermi polarons, our procedure is general and can be extended to mobile impurities featuring molaron states [58], and other correlated many-body states such as Bose polarons [59–62] or polarons created in BCS superfluids [63]. Thus, the proposed technique paves the way to completely new observations in experiments with ultracold atoms that can probe length scales beyond the optical regime in an *in situ* fashion.

Finally, by employing deeply bound states as a probe, the proposed spectroscopy allows for observing dynamics on timescales that are ultrafast compared to the typical scales of the underlying many-body system. This allows us, for example, to investigate the formation of the polaron cloud in real time. In theory, this can be simulated by considering the linear response to the switch-on of the impurity similar to pump-probe spectroscopy.

*Corresponding author: m.gievers@lmu.de

[1] M. Kutschera and W. Wójcik, Phys. Rev. C **47**, 1077 (1993).

[2] W. Zwerger, *The BCS-BEC Crossover and the Unitary Fermi Gas* (Springer Science & Business Media, New York, 2011), Vol. 836.

[3] J. R. Schrieffer and J. S. Brooks, *Handbook of High-Temperature Superconductivity* (Springer, New York, 2007).

[4] N. V. Prokof'ev and B. V. Svistunov, Phys. Rev. Lett. **81**, 2514 (1998).

[5] N. Prokof'ev and B. Svistunov, Phys. Rev. B **77**, 020408(R) (2008).

[6] A. Schirotzek, C.-H. Wu, A. Sommer, and M. W. Zwierlein, Phys. Rev. Lett. **102**, 230402 (2009).

[7] P. Massignan, M. Zaccanti, and G. M. Bruun, Rep. Prog. Phys. **77**, 034401 (2014).

[8] F. Chevy, Phys. Rev. A **74**, 063628 (2006).

[9] R. Combescot, A. Recati, C. Lobo, and F. Chevy, Phys. Rev. Lett. **98**, 180402 (2007).

[10] C. Mora and F. Chevy, Phys. Rev. A **80**, 033607 (2009).

[11] M. Punk, P. T. Dumitrescu, and W. Zwerger, Phys. Rev. A **80**, 053605 (2009).

[12] S. Nascimbène, N. Navon, K. J. Jiang, L. Tarruell, M. Teichmann, J. McKeever, F. Chevy, and C. Salomon, Phys. Rev. Lett. **103**, 170402 (2009).

[13] S. Zöllner, G. M. Bruun, and C. J. Pethick, Phys. Rev. A **83**, 021603(R) (2011).

[14] M. Koschorreck, D. Pertot, E. Vogt, B. Fröhlich, M. Feld, and M. Köhl, Nature (London) **485**, 619 (2012).

[15] C. Kohstall, M. Zaccanti, M. Jag, A. Trenkwalder, P. Massignan, G. M. Bruun, F. Schreck, and R. Grimm, Nature (London) **485**, 615 (2012).

[16] A. Wenz, G. Zürn, S. Murmann, I. Brouzos, T. Lompe, and S. Jochim, Science **342**, 457 (2013).

[17] J. Vlietinck, J. Ryckebusch, and K. Van Houcke, Phys. Rev. B **87**, 115133 (2013).

[18] W. Ong, C. Cheng, I. Arakelyan, and J. E. Thomas, Phys. Rev. Lett. **114**, 110403 (2015).

[19] R. S. Christensen and G. M. Bruun, Phys. Rev. A **91**, 042702 (2015).

[20] F. Scazza, G. Valtolina, P. Massignan, A. Recati, A. Amico, A. Burchianti, C. Fort, M. Inguscio, M. Zaccanti, and G. Roati, Phys. Rev. Lett. **118**, 083602 (2017).

[21] M. Sidler, P. Back, O. Cotlet, A. Srivastava, T. Fink, M. Kroner, E. Demler, and A. Imamoglu, Nat. Phys. **13**, 255 (2017).

[22] R. Schmidt, M. Knap, D. A. Ivanov, J.-S. You, M. Cetina, and E. Demler, Rep. Prog. Phys. **81**, 024401 (2018).

[23] Z. Yan, P. B. Patel, B. Mukherjee, R. J. Fletcher, J. Struck, and M. W. Zwierlein, Phys. Rev. Lett. **122**, 093401 (2019).

[24] N. Darkwah Oppong, L. Riegger, O. Bettermann, M. Höfer, J. Levinsen, M. M. Parish, I. Bloch, and S. Fölling, Phys. Rev. Lett. **122**, 193604 (2019).

[25] G. Ness, C. Shkedrov, Y. Florshaim, O. K. Diessel, J. von Milczewski, R. Schmidt, and Y. Sagi, Phys. Rev. X **10**, 041019 (2020).

[26] H. S. Adlong, W. E. Liu, F. Scazza, M. Zaccanti, N. D. Oppong, S. Fölling, M. M. Parish, and J. Levinsen, Phys. Rev. Lett. **125**, 133401 (2020).

[27] I. Fritsche, C. Baroni, E. Dobler, E. Kirilov, B. Huang, R. Grimm, G. M. Bruun, P. Massignan, Phys. Rev. A **103**, 053314 (2021).

[28] P. E. Dolgirev, Y.-F. Qu, M. B. Zvonarev, T. Shi, and E. Demler, Phys. Rev. X **11**, 041015 (2021).

[29] F. Scazza, M. Zaccanti, P. Massignan, M. M. Parish, and J. Levinsen, Atoms **10**, 55 (2022).

[30] N. Y. Du and C. H. Greene, Phys. Rev. A **36**, 971 (1987).

[31] C. H. Greene, A. S. Dickinson, and H. R. Sadeghpour, Phys. Rev. Lett. **85**, 2458 (2000).

[32] V. Bendkowsky, B. Butscher, J. Nipper, J. P. Shaffer, R. Löw, and T. Pfau, Nature (London) **458**, 1005 (2009).

[33] B. Butscher, J. Nipper, J. B. Balewski, L. Kukota, V. Bendkowsky, R. Löw, and T. Pfau, Nat. Phys. **6**, 970 (2010).

[34] B. J. DeSalvo, J. A. Aman, F. B. Dunning, T. C. Killian, H. R. Sadeghpour, S. Yoshida, and J. Burgdörfer, Phys. Rev. A **92**, 031403(R) (2015).

[35] F. Camargo, J. D. Whalen, R. Ding, H. R. Sadeghpour, S. Yoshida, J. Burgdörfer, F. B. Dunning, and T. C. Killian, Phys. Rev. A **93**, 022702 (2016).

[36] F. Camargo, R. Schmidt, J. D. Whalen, R. Ding, G. Woehl, Jr., S. Yoshida, J. Burgdörfer, F. B. Dunning, H. R. Sadeghpour, E. Demler, and T. C. Killian, Phys. Rev. Lett. **120**, 083401 (2018).

[37] K. S. Kleinbach, F. Engel, T. Dieterle, R. Löw, T. Pfau, and F. Meinert, Phys. Rev. Lett. **120**, 193401 (2018).

[38] J. D. Whalen, S. K. Kanungo, R. Ding, M. Wagner, R. Schmidt, H. R. Sadeghpour, S. Yoshida, J. Burgdörfer, F. B. Dunning, and T. C. Killian, Phys. Rev. A **100**, 011402(R) (2019).

[39] M. Schlagmüller, T. C. Liebisch, H. Nguyen, G. Lochead, F. Engel, F. Böttcher, K. M. Westphal, K. S. Kleinbach, R. Löw, S. Hofferberth et al., Phys. Rev. Lett. **116**, 053001 (2016).

[40] C. Veit, N. Zuber, O. A. Herrera-Sancho, V. S. V. Anasuri, T. Schmid, F. Meinert, R. Löw, and T. Pfau, Phys. Rev. X **11**, 011036 (2021).

[41] M. Knap, A. Shashi, Y. Nishida, A. Imambekov, D. A. Abanin, and E. Demler, Phys. Rev. X **2**, 041020 (2012).

[42] R. Schmidt, J. D. Whalen, R. Ding, F. Camargo, G. Woehl, Jr., S. Yoshida, J. Burgdörfer, F. B. Dunning, E. Demler, H. R. Sadeghpour, and T. C. Killian, Phys. Rev. A **97**, 022707 (2018).

[43] J. Sous, H. R. Sadeghpour, T. C. Killian, E. Demler, and R. Schmidt, Phys. Rev. Res. **2**, 023021 (2020).

[44] R. Löw, H. Weimer, J. Nipper, J. B. Balewski, B. Butscher, H. P. Büchler, and T. Pfau, J. Phys. B **45**, 113001 (2012).

[45] M. Cetina, M. Jag, R. S. Lous, I. Fritsche, J. T. Walraven, R. Grimm, J. Levinsen, M. M. Parish, R. Schmidt, M. Knap et al., Science **354**, 96 (2016).

[46] W. E. Liu, J. Levinsen, and M. M. Parish, Phys. Rev. Lett. **122**, 205301 (2019).

[47] We use here the terminology of polarons also in the infinite impurity mass limit where Anderson's orthogonality leads formally to a vanishing polaron quasiparticle weight [22]. For the physics of the polaron cloud formation this is, however, not relevant here.

[48] See Supplemental Material at http://link.aps.org/supplemental/10.1103/PhysRevLett.132.053401 for additional details, which includes Refs. [22,30,41–43,49–54].

[49] J. J. Sakurai and J. Napolitano, *Modern quantum mechanics*, revised edition (Addison-Wesley, Boston, 2011).

[50] I. Bloch, J. Dalibard, and W. Zwerger, Rev. Mod. Phys. **80**, 885 (2008).

[51] C. E. Burkhardt and L. J. Leventhal, The quantum defect, in *Topics in Atomic Physics* (Springer, New York, 2006), pp. 214–229, 10.1007/0-387-31074-6_11.

[52] M. T. Eiles, Phys. Rev. A **98**, 042706 (2018).

[53] I. Klich, An elementary derivation of Levitov's formula, in *Quantum Noise in Mesoscopic Physics*, edited by Y. V. Nazarov (Springer Netherlands, Dordrecht, 2003), pp. 397–402.

[54] R. S. Lous, I. Fritsche, M. Jag, B. Huang, and R. Grimm, Phys. Rev. A **95**, 053627 (2017).

[55] K. Schönhammer, Phys. Rev. B **75**, 205329 (2007).

[56] To be precise, we have run our calculations at $T = 0.001\varepsilon_F$.

[57] P. W. Anderson, Phys. Rev. Lett. **18**, 1049 (1967).

[58] O. K. Diessel, J. von Milczewski, A. Christianen, and R. Schmidt, arXiv:2209.11758.

[59] N. B. Jørgensen, L. Wacker, K. T. Skalmstang, M. M. Parish, J. Levinsen, R. S. Christensen, G. M. Bruun, and J. J. Arlt, Phys. Rev. Lett. **117**, 055302 (2016).

[60] M.-G. Hu, M. J. Van de Graaff, D. Kedar, J. P. Corson, E. A. Cornell, and D. S. Jin, Phys. Rev. Lett. **117**, 055301 (2016).

[61] Z. Z. Yan, Y. Ni, C. Robens, and M. W. Zwierlein, Science **368**, 190 (2020).

[62] L. A. Peña Ardila, N. B. Jørgensen, T. Pohl, S. Giorgini, G. M. Bruun, and J. J. Arlt, Phys. Rev. A **99**, 063607 (2019).

[63] J. Wang, X.-J. Liu, and H. Hu, Phys. Rev. Lett. **128**, 175301 (2022).

Supplemental Material: Probing Polaron Clouds by Rydberg Atom Spectroscopy

Marcel Gievers,[1,2] Marcel Wagner,[3] and Richard Schmidt[3]

[1] *Arnold Sommerfeld Center for Theoretical Physics, Center for NanoScience,*
and Munich Center for Quantum Science and Technology,
Ludwig-Maximilians-Universität München, 80333 Munich, Germany
[2] *Max Planck Institute of Quantum Optics, 85748 Garching, Germany*
[3] *Institut für Theoretische Physik, Universität Heidelberg, 69120 Heidelberg, Germany*
(Dated: August 27, 2024)

In this document, we provide details on the methods and parameters we have used in order to produce the data shown in the main text. In Sec. I we give the single-particle eigenfunctions for the system in presence of different impurities. Sec. II motivates the functional determinant approach (FDA) expressions for the investigated quantities: density profiles discussed in Sec. III and Ramsey signals which are used to compute the absorption spectra discussed in Sec. IV. We conclude this supplement in Sec. V with a brief comment on our numerical accuracy.

I. SPHERICALLY SYMMETRIC POTENTIALS

All the FDA calculations [S1–S3] are performed in the bases of single-particle solutions for the Schrödinger equations with the respective impurities. The solution of single-particle impurity problems is a standard quantum-mechanical exercise [S4]. Still, for the sake of completeness and to settle our notation, we provide here the respective eigenfunctions and overlaps used in our FDA computations.

We consider a single-particle Hamiltonian $\hat{h}_\sigma$ with a spherically symmetric potential $\hat{v}_\sigma$:

$$\hat{h}_\sigma = \frac{\hat{\boldsymbol{p}}^2}{2m} + \hat{v}_\sigma, \tag{S1a}$$

$$\frac{\hat{\boldsymbol{p}}^2}{2m} = -\frac{1}{2m}\boldsymbol{\nabla}^2 = -\frac{1}{2mr^2}\left[\partial_r(r^2\partial_r) - \hat{\boldsymbol{l}}^2\right]. \tag{S1b}$$

The eigenfunctions of the angular-momentum operator $\hat{\boldsymbol{l}}^2$ are the spherical harmonics $\hat{\boldsymbol{l}}^2 Y_{lm} = l(l+1)Y_{lm}$. With the wave function

$$\langle \boldsymbol{r}|klm\rangle = Y_{lm}(\Omega_{\boldsymbol{r}})\frac{u_{kl}(r)}{r}, \tag{S2}$$

the problem is reduced to a one-dimensional Schrödinger equation:

$$u_{kl}''(r) + 2m\left[E - V_{\sigma,\text{eff}}(r)\right]u_{kl}(r) = 0, \tag{S3a}$$

$$V_{\sigma,\text{eff}}(r) = V_\sigma(r) + \frac{1}{2mr^2}l(l+1). \tag{S3b}$$

Its radial solutions $u_{kl}(r)$ form an orthonormal basis and depend on the respective impurity potential $\hat{v}_\sigma$. We write the eigenfunctions of the free problem as $|\boldsymbol{n}\rangle$, i.e.,

$\hat{h}_0|\boldsymbol{n}\rangle = \varepsilon_n|\boldsymbol{n}\rangle$, and the solutions of the impurity problem as $|\boldsymbol{\alpha}\rangle$, i.e., $\hat{h}_\sigma|\boldsymbol{\alpha}\rangle = E_{\sigma,\boldsymbol{\alpha}}|\boldsymbol{\alpha}\rangle$. Here, $\boldsymbol{n}, \boldsymbol{\alpha}$ include the quantum numbers referring to momentum and angular momentum.

A. Noninteracting case

For a noninteracting impurity $|0\rangle$ with $V_0(r) = 0$, we use the basis of free states

$$u_{nl}(r) = \mathcal{N}_{nl}\, r\, j_l(k_{nl}r), \tag{S4}$$

with the spherical Bessel functions $j_l(x)$. As our system is limited to a sphere of radius R, we enforce $\psi_{klm}(|\boldsymbol{r}| = R) = 0$ such that the momenta are discretized,

$$k_{nl} = z_{nl}/R. \tag{S5}$$

Here, z_{nl} is the nth zero of the lth spherical Bessel functions, i.e., $j_l(z_{nl}) = 0$. The normalization factor $\mathcal{N}_{nl}$ yields

$$\mathcal{N}_{nl} = \frac{\sqrt{2}}{\sqrt{R^3[j_{l+1}(z_{nl})]^2}}, \tag{S6}$$

which comes from the definite integral over spherical Bessel functions

$$\int_0^R dr\, r^2 j_l(k_{nl}r)j_{l'l}(k_{n'l}r) = \delta_{nn'}\frac{R^3}{2}[j_{l+1}(z_{nl})]^2. \tag{S7}$$

For zero angular momentum, we have $Y_{00} = 1/\sqrt{4\pi}$, $j_0(x) = \sin x/x$, $z_{n0} = n\pi$ and $\mathcal{N}_{n0} = \sqrt{2/R}\,k_{n0}$. So the total wave function reads:

$$u_{n0}(r) = \sqrt{\frac{2}{R}}\sin(k_n r), \tag{S8a}$$

$$\langle \boldsymbol{r}|n00\rangle = \frac{1}{\sqrt{2\pi R}}\frac{\sin(k_n r)}{r}, \quad k_n = \frac{n\pi}{R}. \tag{S8b}$$

The general integral over two radial wave functions is given by:

$$\int_0^r dr'\, |u_{nl}(r')|^2 = \mathcal{N}_{nl}^2\int_0^r dr'\, r'^2[j_l(k_{nl}r')]^2$$
$$= \mathcal{N}_{nl}^2\frac{r^3}{2}\left\{[j_l(k_{nl}r)]^2 - j_{l-1}(k_{nl}r)j_{l+1}(k_{nl}r)\right\}. \tag{S9}$$

This is used to calculated the number of particles within a certain radius $N(r)$, see Eq. (S36) below.

For the s-wave case, Eq. (S9) can be simplified to:

$$\int_0^r \mathrm{d}r' \, |u_{n0}(r')|^2 = \frac{2}{R} \left[\frac{r}{2} - \frac{\sin 2k_n r}{4k_n} \right]. \quad \text{(S10)}$$

B. Delta impurity

For the interacting impurity $|1\rangle$ described by a delta potential $V_1(r) = \frac{a}{2mr^2} \delta(r) \partial_r(r...)$ [S5], the radial wave function is given by a combination of spherical Bessel functions $j_l(kr)$ and Neumann functions $y_l(kr)$

$$u_{kl}(r) = \mathcal{N}_{kl} r \left[\cos \delta_l(k) j_l(kr) - \sin \delta_l(k) y_l(kr) \right]. \quad \text{(S11)}$$

Again, the confinement of the sphere only allows discrete momenta $k_{\alpha l}$.

As the delta impurity is local, it affects only the s-wave contribution. With $y_0(x) = -\cos(x)/x$, the corresponding radial wave function is given by:

$$u_{\alpha 0}(r) = \sqrt{\frac{2}{R}} A_\alpha \sin(k_\alpha r + \delta_\alpha), \quad \text{(S12a)}$$

$$A_\alpha = \sqrt{\frac{R}{2}} \frac{\mathcal{N}_\alpha}{k_\alpha} = \left(1 + \frac{\sin 2\delta_\alpha}{2k_\alpha R} \right)^{-1/2}. \quad \text{(S12b)}$$

The phase shift δ_α is connected to the s-wave scattering length a and fulfills the following conditions together with the momentum k_α:

$$k_\alpha R + \delta_\alpha = \alpha \pi, \quad \delta_\alpha = - \arctan(k_\alpha a). \quad \text{(S13)}$$

The total wave function becomes:

$$\langle \boldsymbol{r} | \alpha 00 \rangle = A_\alpha \frac{1}{\sqrt{2\pi R}} \frac{\sin(k_\alpha r + \delta_\alpha)}{r}. \quad \text{(S14)}$$

The overlap integrals of the radial functions (S12a) with the noninteracting ones (S8a) are given by:

$$\langle n|\alpha \rangle = \int_0^R \mathrm{d}r \, u_{n0}(r) u_{\alpha 0}(r) = \frac{2A_\alpha}{R} \frac{k_n}{k_n^2 - k_\alpha^2} \sin \delta_\alpha. \quad \text{(S15)}$$

Here and in the following, we use the abbreviation $\langle n|\alpha \rangle \equiv \langle n00|\alpha 00 \rangle$.

For positive scattering lengths $a > 0$, we have an additional bound state with a negative binding energy. The corresponding radial wave function is derived by replacing k_α by $\mathrm{i}\kappa = \mathrm{i}/a$. With $\delta = -\mathrm{i}\kappa R = -\mathrm{i}\,\mathrm{artanh}(\kappa a)$, we conclude:

$$u_b(r) = -\sqrt{\frac{2}{R}} A_b \sinh[\kappa(r - R)], \quad \text{(S16a)}$$

$$A_b = \left(\frac{\sinh(2\kappa R)}{2\kappa R} - 1 \right)^{-1/2} \quad \text{(S16b)}$$

$$\Rightarrow u_b(r) = \frac{\sqrt{2\kappa}(\mathrm{e}^{-\kappa r} - \mathrm{e}^{-\kappa(2R-r)})}{\sqrt{1 - 4\kappa R \mathrm{e}^{-2\kappa R} - \mathrm{e}^{-4\kappa R}}}. \quad \text{(S16c)}$$

The second form is crucial for the numerics as large numbers $\sim \mathrm{e}^{\kappa R}$ are canceled.

Similar to Eq. (S15), the overlap integrals of the radial bound state function Eq. (S16a) with the noninteracting ones are given by:

$$\langle n|b \rangle = \frac{2A_b}{R} \frac{k_n}{k_n^2 + \kappa^2} \sinh \kappa R$$

$$= \frac{2}{R} \frac{k_n}{k_n^2 + \kappa^2} \frac{\sqrt{\kappa R}(1 - \mathrm{e}^{-2\kappa R})}{(1 - 4\kappa R \mathrm{e}^{-2\kappa R} - \mathrm{e}^{-4\kappa R})^{1/2}}. \quad \text{(S17)}$$

In analogy to Eq. (S10), the integrals over two radial wave functions yield:

$$\int_0^r \mathrm{d}r' \, |u_{\alpha 0}(r')|^2$$
$$= \frac{2}{R} A_\alpha^2 \left(\frac{r}{2} - \frac{\sin[2(k_\alpha r + \delta_\alpha)] - \sin(2\delta_\alpha)}{4k_\alpha} \right), \quad \text{(S18a)}$$

$$\int_0^r \mathrm{d}r' \, |u_{b0}(r')|^2$$
$$= \frac{1 - \mathrm{e}^{-2\kappa r} - \mathrm{e}^{-2\kappa R}(\mathrm{e}^{-2\kappa R} - \mathrm{e}^{-2\kappa(R-r)} + 4\kappa r)}{1 - \mathrm{e}^{-4\kappa R} - 4\kappa R \mathrm{e}^{-2\kappa R}}. \quad \text{(S18b)}$$

C. Spherical-well potential

As mentioned in the main text, the density in presence of a delta impurity diverges at the center. To make sure that this does not affect the spectra, we have performed analogous computations of spectra corresponding to a polaron formed in presence of a spherical-well potential. Here, the divergent density is cured. A spherical well of radius d is described by the potential $V_1(r < d) = V_0 < 0$ and $V_1(r > d) = 0$. Inside the well $r < d$, the radial functions $u_{Kl}(r)$ are given by the spherical Bessel functions with momentum $K = \sqrt{2m(E - V_0)}$ [cf. Eq. (S4)]. Outside the well $r > d$, the radial functions $u_{kl}(r)$ are given by a linear combination of spherical Bessel and Neumann functions [cf. Eq. (S11)]

$$u_{Kl}(r < d) = A_{Kl} r \, j_l(Kr), \quad \text{(S19a)}$$
$$u_{kl}(r > d) = B_{kl} r \, j_l(kr) + C_{kl} r \, y_l(kr). \quad \text{(S19b)}$$

From the continuous differentiability at the well edge $r = d$ and the boundary condition at $r = R$, we receive the following general relations for the coefficients A_{Kl}, B_{kl} and C_{kl}

$$A_{Kl} \, j_l(Kd) = B_{kl} j_l(kd) + C_{kl} y_l(d) \quad \text{(S20a)}$$
$$A_{Kl} K \, j_{l+1}(Kd) = k \left[B_{kl} j_{l+1}(kd) + C_{kl} y_{l+1}(kd) \right], \quad \text{(S20b)}$$
$$0 = B_{kl} \, j_l(kR) + C_{kl} \, y_l(kR), \quad \text{(S20c)}$$

where we have used $\mathrm{d}_x j_l(x) = l/x \cdot j_l(x) - j_{l+1}(x)$ as property of differentiated spherical Bessel functions. For

$l = 0$, which is in particular interesting for local impurities, the conditions (S19)-(S20) lead to the following relation

$$k_\alpha \cos[k_\alpha(R-d)]\sin(K_\alpha d)$$
$$+ K_\alpha \cos(K_\alpha d)\sin[k_\alpha(R-d)] = 0, \qquad \text{(S21)}$$

which is valid for discrete values of momenta k_α and K_α with the corresponding energies $E_\alpha = k_\alpha^2/(2m) = K_\alpha^2/(2m) + V_0$. Eq. (S21) is solved numerically and the momenta are inserted into the radial functions:

$$u_{\alpha 0}(r) = A_\alpha \begin{cases} \sin(K_\alpha r)/K_\alpha & r < d \\ \frac{\cos(K_\alpha d)}{\cos[k_\alpha(R-d)]}\sin[k_\alpha(r-R)]/k_\alpha & r > d \end{cases},$$
$$\text{(S22a)}$$

$$A_\alpha = \sqrt{8(K_\alpha k_\alpha)^3}\left\{4k_\alpha^3 K_\alpha d - 2k_\alpha^3 \sin(2K_\alpha d)\right.$$
$$+ 4K_\alpha k_\alpha(R-d)[K_\alpha^2 \cos^2(K_\alpha d)$$
$$+ k_\alpha^2 \sin^2(K_\alpha d)] + 2k_\alpha K_\alpha^2 \sin(2K_\alpha d)$$
$$- 2K_\alpha^2 k_\alpha \cos[2k_\alpha(R-d)]\sin(2K_\alpha d)$$
$$- K_\alpha[K_\alpha^2 - k_\alpha^2 + (K_\alpha^2 + k_\alpha^2)\cos(2K_\alpha d)]$$
$$\left. \times \sin[2k_\alpha(R-d)]\right\}^{-1/2}. \qquad \text{(S22b)}$$

The value for the coefficient A_α is determined from normalization of the wave function.

The scattering length a of the spherical well can be determined from the relations $\tan\delta_l(k) = -C_{kl}/B_{kl}$ and $\lim_{k\to 0} k\cot\delta_0(k) = -a^{-1}$, which gives:

$$a = \lim_{k\to 0}\frac{1}{k}\frac{C_{k0}}{B_{k0}} = d + \frac{2mV_0\tan(\sqrt{-2mV_0}d)}{\sqrt{-2mV_0}^3}. \qquad \text{(S23)}$$

We solve this equation numerically for V_0 at a fixed value of d to obtain the scattering length a. Due to the periodicity of the tangent, negative scattering lengths a are found for $2mV_0 \in (-\pi^2/(4d^2), 0)$ and positive ones for $2mV_0 \in (-9\pi^2/(4d^2), -\pi^2/(4d^2))$.

There are bound states with $V_0 < E_b < 0$ where k_α is replaced by the imaginary number $i\kappa_b = \sqrt{-2mE_b}$ while $K_b = \sqrt{2m(E_b - V_0)}$ stays positive. The analogous expressions of Eqs. (S21)-(S22) are

$$\kappa_b \sin(K_b d) + K_b \cos(K_b d)\tanh[\kappa_b(R-d)] = 0,$$
$$\text{(S24a)}$$

$$u_{b0}(r) = A_b \begin{cases} \sin(K_b r)/K_b & r < d \\ -\frac{\cos(K_b d)}{\kappa_b}e^{-\kappa_b(r-d)}\frac{1-e^{-2\kappa_b(R-r)}}{1+e^{-2\kappa_b(R-d)}} & r > d \end{cases},$$
$$\text{(S24b)}$$

$$A_b = 2\sqrt{\kappa_b^3 K_b^3}(1 + e^{-2\kappa_b(R-d)})$$
$$\times \left\{2K_b^3\cos^2(K_b d)\left[1 - e^{-4\kappa_b(R-d)}\right.\right.$$
$$\left. -4\kappa_b(R-d)e^{-2\kappa_b(R-d)}\right]$$
$$\left. +\kappa_b^3\left(1+e^{-2\kappa_b(R-d)}\right)^2[2K_b d - \sin(2K_b d)]\right\}^{-1/2}.$$
$$\text{(S24c)}$$

At most, there can be $\lfloor\sqrt{-2mV_0}d/\pi\rfloor$ bound states due to the periodicity of the oscillating function. We take potential depths V_0 such that there is only one bound state for positive scattering lengths.

Analogously to Eqs. (S15) and (S17), the overlaps for these wave functions have an analytical expression

$$\langle n|\alpha\rangle = \sqrt{\frac{2}{R}}A_\alpha\left[\frac{k_n\cos k_n d\sin K_\alpha d - K_\alpha\cos K_\alpha d\sin k_n d}{K_\alpha(K_\alpha^2 - k_n^2)}\right.$$
$$\left. + \cos K_\alpha d\frac{-k_\alpha\cos[k_\alpha(R-d)]\sin k_n d - k_n\cos k_n d\sin[k_\alpha(R-d)] + k_\alpha\sin k_n R}{k_\alpha\cos[k_\alpha(R-d)](k_n^2 - k_\alpha^2)}\right], \qquad \text{(S25)}$$

$$\langle n|b\rangle = \sqrt{\frac{2}{R}}A_b\left[\frac{K_b\cos K_b d\sin k_n d - k_n\cos k_n d\sin K_b d}{K_b(k_n^2 - K_b^2)}\right.$$
$$\left. - \cos K_b d\frac{(1 + e^{-2\kappa_b(R-d)})\kappa_b\sin(k_n d) + (1 - e^{-2\kappa_b(R-d)})k_n\cos k_n d - 2e^{-\kappa_b(R-d)}\kappa_b\sin k_n R}{\kappa_b(k_n^2 + \kappa_b^2)(1 + e^{-2\kappa_b(R-d)})}\right]. \qquad \text{(S26)}$$

D. Rydberg impurity

The potential $V_R(\boldsymbol{r})$, generated by the impurity in the Rydberg state, depends on the wave function of the Rydberg electron $\psi_{R,nlm}(\boldsymbol{r}) = Y_{lm}(\Omega_{\boldsymbol{r}})u_{R,nl}(r)/r$, where the radial wave functions can be approximated in terms of Whittaker functions [S6]

$$u_{R,nl}(r) = \frac{W_{\nu,l+1/2}[2r/(\nu a_0)]}{\sqrt{a_0\nu^2\Gamma(\nu+l+1)\Gamma(\nu-l)}}, \text{ with } \nu = n - \delta_l.$$
$$\text{(S27)}$$

The level shifts of the energies $E_{nl} \propto -1/[2(n-\delta_l)^2]$ are specific for the atom type. For an impurity of ^{87}Rb, we have $\delta_{l=0} = 3.13$ [S7].
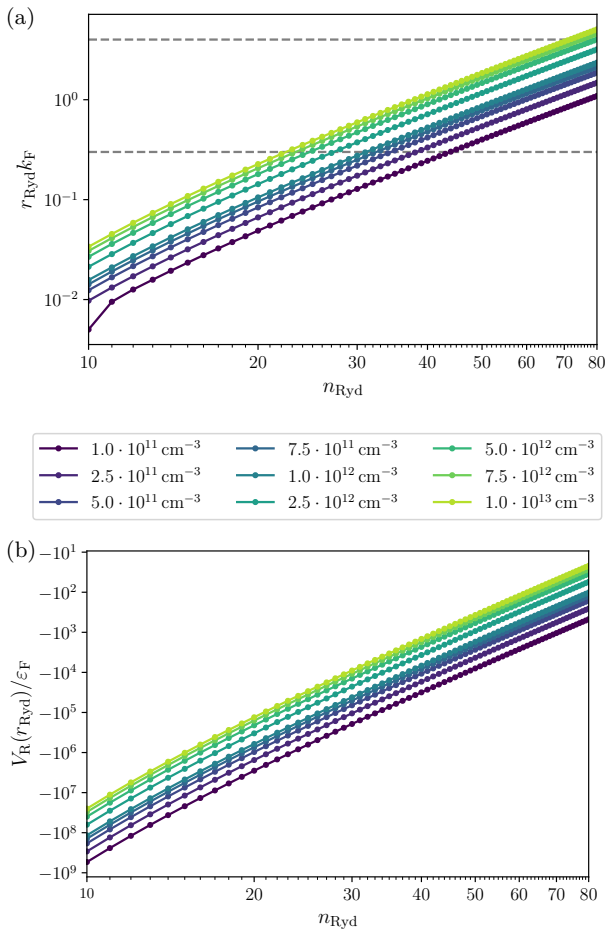
Figure S1. Characteristics of the Rydberg potential $V_R(r)$ of a ^{87}Rb impurity in a gas of ^{40}K particles measured in units of ε_F for different principal quantum numbers n_{Ryd} of the outermost electron and different values of densities ρ_0 (colors). The upper panel shows the positions $r_{Ryd} \sim n_{Ryd}^2$ of the dimer minimum and the lower panel the corresponding potential depth $V_R(r_{Ryd})$. These plots help to choose the right principal numbers n_{Ryd} and densities ρ_0 for the experimental procedure.

We consider the spherically symmetric potential $V_R(r)$ for an s-wave Rydberg electron, which in total yields:

$$V_R(r) = \frac{\hbar^2 a_e}{2m_e r^2} \frac{\{W_{\nu,1/2}[2r/(\nu a_0)]\}^2}{a_0 \nu^2 \Gamma(\nu+1)\Gamma(\nu)}, \quad \nu = n_{Ryd} - \delta_0.$$
(S28)

The electron scattering length with ^{40}K atoms is $a_e = -15a_0$ [S8]. The potential $V_R(r)$ Eq. (S28) diverges at the center and is highly oscillating for large principal numbers n_{Ryd}. It is characterized by a deep minimum located at the Rydberg radius r_{Ryd}. This minimum induces the localized bound state corresponding to the Rydberg molecule. The position of this bound state r_{Ryd} as well as the corresponding potential depth $V_R(r_{Ryd})$ are cru-

cial for our proposed measurement technique. They can be tuned by the principal number n_{Ryd} or the density ρ_0 measured in units of k_F^3. In Fig. S1 we show the dependencies of the Rydberg radius r_{Ryd} and the potential depth $V_R(r_{Ryd})$ on the principal quantum number n_{Ryd} and the overall density ρ_0 in units of the Fermi momentum k_F for gas particles of ^{40}K. For observing a polaron's density profile, the region $r_{Ryd}k_F = 0.3-4.0$ is of particular interest. From Fig. S1, we conclude that reasonable principal numbers for our measurement technique are around $n_{Ryd} = 25 - 80$ while densities should be at around $\rho_0 = 10^{10}-10^{13}$ cm^{-3}.

In the presence of the Rydberg potential $V_R(r)$ Eq. (S28), the radial part of the Schrödinger equation (S3) is solved by exact diagonalization of the single-particle Hamiltonian $\hat{h}_R$ for a discrete position grid r_i with $i = 1, 2, ..., N$ where $r_1 = 0$ and $r_N = R$. To satisfy the boundary condition $u_{\alpha l}(r_N) = 0$, we only diagonalize the Hamiltonian $[\hat{h}_R]_{ij}$ with $i, j = 1, 2, ..., N-1$. As we allow for a combination of linear grids r_i with higher resolution in the center, we take into account different steps $\delta r_i^+ = r_{i+1} - r_i$ and $\delta r_i^- = r_i - r_{i-1}$ with $\delta r_1^+ = \delta r_1^-$. Concretely, we use the following discretized Laplacian:

$$[\hat{h}_R]_{i,i} = \frac{1}{4m}\left[\frac{1}{(\delta r_i^+)^2} + \frac{2}{\delta r_i^+ \delta r_i^-} + \frac{1}{(\delta r_i^-)^2}\right] + V_{\sigma,\text{eff}}(r_i),$$

$$[\hat{h}_R]_{i,i-1} = -\frac{1}{4m}\left[\frac{1}{(\delta r_i^-)^2} + \frac{1}{\delta r_i^+ \delta r_i^-}\right],$$

$$[\hat{h}_R]_{i,i+1} = -\frac{1}{4m}\left[\frac{1}{(\delta r_i^+)^2} + \frac{1}{\delta r_i^+ \delta r_i^-}\right].$$
(S29)

Furthermore, we divide the eigenfunctions $u_{\alpha l}(r_i)$ by the discrete integral $\sqrt{\int_r (u_{\alpha l}(r))^2}$ in order to fulfill their normalization.

Fig. S2 shows the Rydberg potential $V_R(r)$ for different principal numbers n_{Ryd} as well as the outermost bound state $u_{RM}(r)$, which is located at the Rydberg radius. We see that for higher principal numbers the wave function $u_{RM}(r)$ is smeared out. This leads to a less precise value for the position r in the reconstructed density profiles. As we are primarily interested in the dimer peak corresponding to the outermost bound state and not in deeply bound states closer to the center at higher energy scales, our description of the Rydberg potential $V_R(r)$ does not need to be precise close to the center. In order to lower the numerical effort, we therefore cut the potential in the center as seen in Fig. S2. This does not have an impact on our spectra.
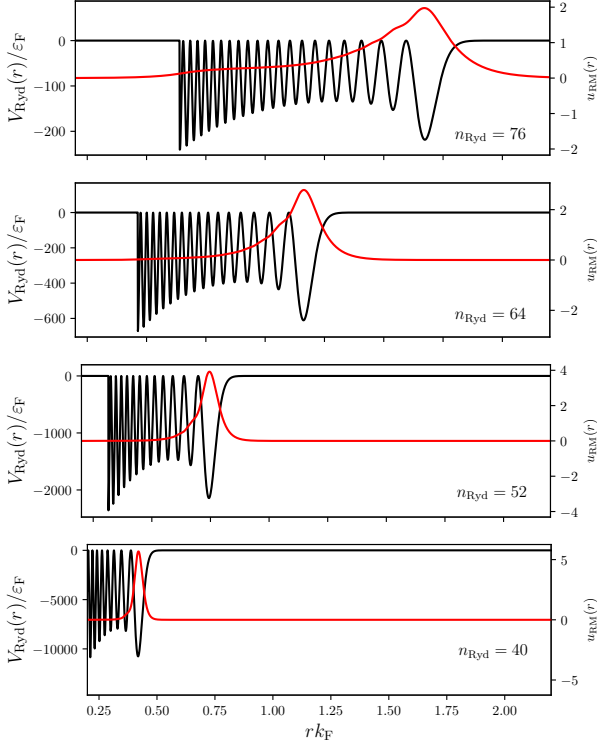
Figure S2. Radial wave functions $u_{\mathrm{RM},l=0}(r)$ of the bound state corresponding to the last minimum in the Rydberg potential $V_{\mathrm{R}}(r)$ for different principal numbers n_{Ryd}. The data are calculated for a Rydberg impurity of ^{87}Rb in a gas of ^{40}K atoms at particle density $\rho_0 = 5 \times 10^{11}\,\mathrm{cm}^{-3}$.

II. FUNCTIONAL DETERMINANT APPROACH

Klich's formula [S9] allows the calculation of a trace $\mathrm{tr}(\mathrm{e}^{\hat{X}})$, where $\hat{X}$ is a bilinear operator, i.e.,

$$\hat{X} = \sum_{i,j} \langle i|\hat{x}|j\rangle \hat{c}_i^\dagger \hat{c}_j. \qquad (S30)$$

Here, $\hat{x}$ is the corresponding single-particle operator. For the case of fermionic operators $\hat{c}_i^\dagger$, $\hat{c}_j$, Klich's formula takes the form:

$$\mathrm{tr}(\mathrm{e}^{\hat{X}}) = \det(\hat{\mathbb{1}} + \mathrm{e}^{\hat{x}}). \qquad (S31)$$

This makes it possible to calculate expectation values over products of exponentials, i.e.,

$$
\begin{aligned}
S_{\sigma_1\sigma_2}(t) &= \langle \mathrm{e}^{\mathrm{i}\hat{H}_{\sigma_1}t}\mathrm{e}^{-\mathrm{i}\hat{H}_{\sigma_2}t}\rangle_{\sigma_1} \\
&= \frac{\mathrm{tr}[\mathrm{e}^{-\beta(\hat{H}_{\sigma_1}-\mu\hat{N})}\mathrm{e}^{\mathrm{i}\hat{H}_{\sigma_1}t}\mathrm{e}^{-\mathrm{i}\hat{H}_{\sigma_2}t}]}{\mathrm{tr}[\mathrm{e}^{-\beta(\hat{H}_{\sigma_1}-\mu\hat{N})}]} \\
&= \det[\hat{\mathbb{1}} - n_{\mathrm{F}}(\hat{h}_{\sigma_1}) + n_{\mathrm{F}}(\hat{h}_1)\mathrm{e}^{\mathrm{i}\hat{h}_{\sigma_1}t}\mathrm{e}^{-\mathrm{i}\hat{h}_{\sigma_2}t}].
\end{aligned}
\qquad (S32)
$$

$S_{\sigma_1\sigma_2}(t)$ is the Ramsey signal when the impurity is prepared in state $|\sigma_1\rangle$ and then switched to the state $|\sigma_2\rangle$.

Furthermore, the Klich formula,

$$\mathrm{tr}(\hat{c}_i^\dagger \hat{c}_j \mathrm{e}^{\hat{X}}) = \langle j|\frac{\mathrm{e}^{\hat{x}}}{\hat{\mathbb{1}} + \mathrm{e}^{\hat{x}}}|i\rangle \det(\hat{\mathbb{1}} + \mathrm{e}^{\hat{x}}), \qquad (S33)$$

allows the calculation of densities. If the state is prepared at an impurity $|0\rangle$ with density matrix $\hat{\rho}_0$ and then evolved in presence of the impurity $|\sigma\rangle$, the corresponding density is evaluated as

$$
\begin{aligned}
\rho_\sigma(\boldsymbol{r},t) &= \mathrm{tr}[\hat{\rho}_{0\sigma}(t)\hat{c}_{\boldsymbol{r}}^\dagger \hat{c}_{\boldsymbol{r}}] \\
&= \frac{\mathrm{tr}[\mathrm{e}^{-\mathrm{i}\hat{H}_\sigma t}\mathrm{e}^{-\beta(\hat{H}_0-\mu\hat{N})}\mathrm{e}^{\mathrm{i}\hat{H}_\sigma t}\hat{c}_{\boldsymbol{r}}^\dagger \hat{c}_{\boldsymbol{r}}]}{\mathrm{tr}[\mathrm{e}^{-\beta(\hat{H}_0-\mu\hat{N})}]} \\
&= \langle \boldsymbol{r}|\mathrm{e}^{-\mathrm{i}\hat{h}_\sigma t}n_{\mathrm{F}}(\hat{h}_0)\mathrm{e}^{\mathrm{i}\hat{h}_\sigma t}|\boldsymbol{r}\rangle.
\end{aligned}
\qquad (S34)
$$

Eqs. (S32) and (S34) are the relations we use to calculate the densities and absorption spectra in the main text.

III. DETAILS ON DENSITY PROFILES

In this section, we provide details for the calculation of the density profiles of the polaron cloud.

The stationary density of the polaron $\rho_{\mathrm{pol}}(\boldsymbol{r})$ given in the main text is calculated by an expansion of the single-particle eigenstates $\langle \boldsymbol{r}|\boldsymbol{\alpha}\rangle = Y_{lm}(\Omega_{\boldsymbol{r}})u_{\alpha l}(r)/r$ with eigenenergies $E_{\boldsymbol{\alpha}}$ of the respective impurity problem

$$
\begin{aligned}
\rho_{\mathrm{pol}}(\boldsymbol{r}) &= \sum_{\boldsymbol{\alpha}} \langle \boldsymbol{r}|\boldsymbol{\alpha}\rangle n_{\mathrm{F}}(E_{\boldsymbol{\alpha}})\langle \boldsymbol{\alpha}|\boldsymbol{r}\rangle \\
&= \frac{1}{4\pi r^2}\sum_{\alpha l}(2l+1)n_{\mathrm{F}}(E_{\alpha l})|u_{\alpha l}(r)|^2.
\end{aligned}
\qquad (S35)
$$

Here, the sum over m has been executed as a sum over spherical harmonics so only the radial contributions $u_{\alpha l}(r)$ are left, which are discussed in detail in Sec. I.

The number of particles within a certain radius r is given by the integral over the density and can be expressed as an integral over the radial wave functions

$$N_{\mathrm{pol}}(r) = \sum_{\alpha l}(2l+1)n_{\mathrm{F}}(E_{\alpha l})\int_0^r \mathrm{d}r'\,|u_{\alpha l}(r')|^2. \qquad (S36)$$

This expression is used to determine the number of particles N_c contributing to the polaron clouds, shown in the main text. The respective expressions for the integrated wave functions are provided by Eqs. (S9) and (S18).

Fig. S3 shows density profiles of polaron clouds for different inverse scattering lengths $(ak_{\mathrm{F}})^{-1}$. These curves supplement the plots provided in the main text. We see the extreme increase of the density around the center. This is the region we identify as the "polaron cloud". Further away from the impurity some Friedel-like oscillations appear which fade away quite fast. At distances $rk_{\mathrm{F}} \gtrsim 5$, the effect of the interacting impurity is not visible anymore such that the polaron densities ρ_{pol} coincide with the plateau value ρ_0.
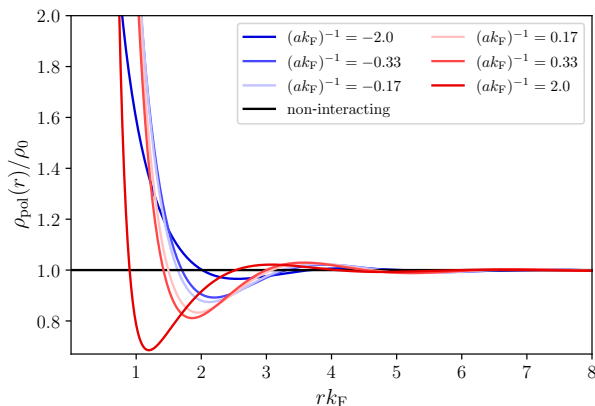
Figure S3. Density profiles $\rho_{\rm pol}(r)$ Eq. (S35) in the presence of a delta impurity with different inverse s-wave scattering lengths $(ak_{\rm F})^{-1}$.

A. Particle number from Fumi's theorem

This section discusses the usefulness of our empirical definition for the polaron cloud (cf. Fig. 2 in the main text). We define the polaron radius r_c as the first crossing between the density profile $\rho_{\rm pol}(r)$ with the background density ρ_0, i.e., $\rho_{\rm pol}(r_c) = \rho_0$. In the thermodynamic limit, the particle number N_c inside the polaron cloud can be derived from Fumi's theorem (cf. App. C in [S10]).

For $a < 0$, the single-particle energies E_α are lowered compared to the corresponding values ε_n of the noninteracting system. The energy of the attractive polaron is then determined by the sum over all occupied energy differences $E_{\alpha=n} - \varepsilon_n$. This can be expressed in terms of the phase shift δ_α Eq. (S13)

$$E_{\rm pol} = \sum_n n_{\rm F}(\varepsilon_n) \cdot (E_{\alpha=n} - \varepsilon_n) \simeq -\frac{\pi}{mR^2} \sum_n n_{\rm F}(\varepsilon_n)\, n\delta_n.$$

(S37)

Here, in the last step $\delta_n^2 \ll 2n\pi|\delta_n|$ is used as the phase shift is bounded by π. In the thermodynamic limit, i.e., $R \to \infty$, the energy differences $\Delta\varepsilon_n \equiv \varepsilon_n - \varepsilon_{n-1} = (2n-1)\pi^2/(2mR^2)$ are infinitesimal and we arrive at Fumi's theorem [S10], which is an integral expression including the polaron energy and the phase shift

$$E_{\rm pol} \underset{R \to \infty}{=} -\frac{1}{\pi} \int_0^\infty {\rm d}\varepsilon\, n_{\rm F}(\varepsilon)\delta(\varepsilon).$$

(S38)

Suppose the chemical potential μ is fixed and the impurity is switched from $|0\rangle$ to $|1\rangle$. The free energy is reduced by an amount of $E_{\rm pol}$, which generates an increase of N_c particles in the system. N_c again can be calculated by a thermodynamic relation of the grand-canonical ensemble

$$N_c = -\frac{\partial E_{\rm pol}}{\partial \mu} = \frac{1}{\pi} \int_0^\infty {\rm d}\varepsilon\, \frac{\partial n_{\rm F}(\varepsilon)}{\partial \mu}\delta(\varepsilon).$$

(S39)
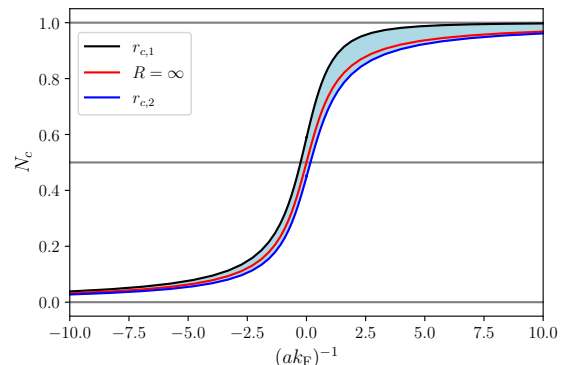
Figure S4. Integrated number of particles inside the polaron cloud $N_c = N_{\rm pol}(r_c) - N_0(r_c)$ [cf. Eq. (S36)] compared to the number at $R \to \infty$ Eq. (S40) extracted from thermodynamic considerations (red line). The black curve corresponds to the integrated number up to the first crossing $\rho_{\rm pol}(r_c) = \rho_0$ and the blue curve to the second crossing.

For zero temperature, this yields the phase shift at the Fermi energy $\varepsilon_{\rm F}$:

$$N_c = \frac{\delta(\varepsilon_{\rm F})}{\pi} = -\frac{1}{\pi}\arctan(k_{\rm F}a).$$

(S40)

For $a > 0$, due to the occupation of the additional boundstate, the energy of the attractive polaron $E_{\rm pol}$ Eq. (S38) is includes the binding energy and N_c Eq. (S40) is increased by 1.

Fig. S4 compares the particle number N_c from the main text [cf. Eq. (S36)], which empirically is determined by an integral over the density up to the polaron cloud radius r_c, with the thermodynamic equivalent N_c Eq. (S40). The qualitative agreement is undeniable. However, an integration only up to the first crossing $\rho_{\rm pol}(r_c) = \rho_0$ overestimates the particle number in the polaron whereas an integration up to the second crossing underestimates it.

To conclude, our defined polaron cloud, namely the region of extreme density increase up to the radius r_c, may not be exactly identified with the actual polaron defined from thermodynamic properties. Still, the similarity between the integrated number N_c with the corresponding number from Fumi's theorem suggests that the region of increased density gives a useful description of the polaron, which is actually a many-body state of the entire system.

B. Effect of finite angular-momentum states

Fig. S5 shows how many angular momentum states need to be taken into account in the summation in Eq. (S35) in order to reach the predicted density plateau ρ_0 for the case of a noninteracting impurity $|0\rangle$. We conclude that in order to reach a plateau of radius r, one
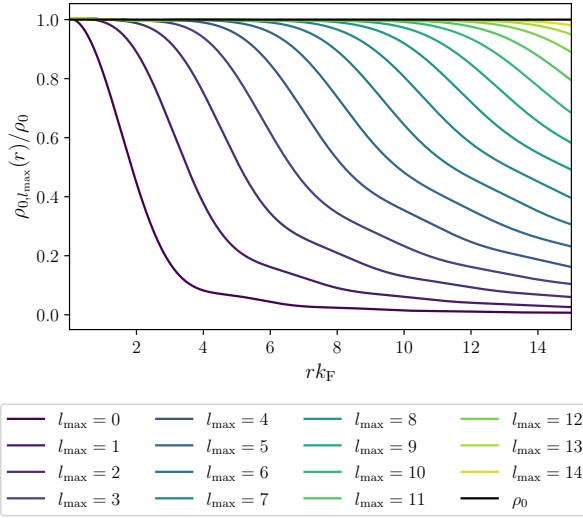
Figure S5. Noninteracting densities $\rho_0(r)$ are shown when the summation in Eq. (S35) is limited by different maximal angular momenta $l_{\max}$. The data are compared to the exact value $\rho_0 = k_F^3/(6\pi)^2$.

has to take into account about $l/(k_F r)$ angular momenta. This is important for the calculation of Rydberg spectra. Since the Rydberg radii in our calculations do not exceed $r_{\text{Ryd}} k_F = 3.0$, it is sufficient to consider only angular momentum states up to $l_{\max} = 8$ in all our calculations.

C. Effect of finite system size

The finite system size R also modifies the density plateau. At the center, i.e., $r = 0$, only the s-wave states contribute to the density. Furthermore, as $\lim_{r\to 0} \sin^2(k_n r)/r^2 = k_n^2 = (n\pi)^2/R^2$ [cf. Eq. (S8a)], we find a closed expression for the density summation in Eq. (S35) at zero temperature

$$\rho_0(r=0) = \frac{\pi}{2R^3} \sum_n \Theta(\mu - \frac{n^2\pi^2}{2mR^2})n^2$$
$$= \frac{\pi}{12R^3} n_{\max}(n_{\max}+1)(2n_{\max}+1), \quad \text{(S41)}$$

where $n_{\max} = \lfloor k_F R/\pi \rfloor$. We want to take large system sizes R such that the constant density value $\rho_0 = k_F^3/(6\pi^2)$ is reached at the center. In order to reach 1% accuracy for the densities around the center, we take a system size of $Rk_F = 400$.

D. Effect of finite impurity range

Finally, let us elaborate that the divergent density at the center $r = 0$ can be cured by a finite interaction range of the impurity. To do so, in Fig. S6 we show
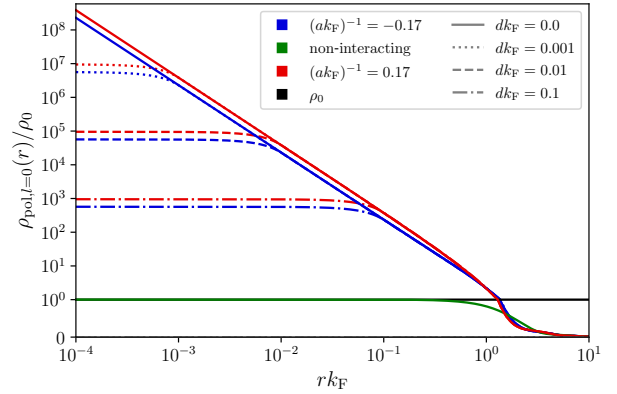
Figure S6. The s-wave contributions $\rho_{\text{pol},l=0}(r)$ of the polaron density Eq. (S35) are plotted for a spherical-well impurity potential with different interaction radii d. Here, $d = 0.0$ refers to the solution of the delta impurity. The colors mark different inverse scattering lengths $(ak_F)^{-1}$ and the line styles represent the interaction radii d. As a reference, the density plateau ρ_0 is shown in black. We conclude that within the range of a finite interaction radius d the density value is just cut off.

the s-wave contributions of the density Eq. (S35) when using the radial wave functions $u_{\alpha l}(r)$ for a spherical-well potential of different extents $d > 0$ [cf. Eqs. (S22) and (S24)]. We conclude that in the range of the square-well potential $r < d$, the densities are cut to a finite value so the divergent densities are under control. However, this does not lead to a prominent change of the resulting absorption spectra. Hence, it is sufficient to keep the eigenbasis in presence of the delta impurity.

E. Polaron cloud formation

We want to elaborate on the statement that the stationary density profile of the polaron cloud Eq. (S35) indeed emerges in the long-time limit $t \gg 1/\varepsilon_F$. For this, we use the more general time-dependent density $\rho(\boldsymbol{r}, t)$ Eq. (S34). An expansion in single-particle wave functions leads to:

$$\rho(\boldsymbol{r}, t) = \sum_{\boldsymbol{\alpha}, \boldsymbol{\alpha}', \boldsymbol{n}} \langle \boldsymbol{r}|\boldsymbol{\alpha}\rangle e^{-iE_{\boldsymbol{\alpha}}t} \langle \boldsymbol{\alpha}|\boldsymbol{n}\rangle n_F(\varepsilon_{\boldsymbol{n}}) \langle \boldsymbol{n}|\boldsymbol{\alpha}'\rangle e^{iE_{\boldsymbol{\alpha}'}t} \langle \boldsymbol{\alpha}'|\boldsymbol{r}\rangle$$

$$= \sum_{\boldsymbol{n}} n_F(\varepsilon_{\boldsymbol{n}}) \left| \sum_{\boldsymbol{\alpha}} e^{-iE_{\boldsymbol{\alpha}}t} \langle \boldsymbol{\alpha}|\boldsymbol{n}\rangle \langle \boldsymbol{r}|\boldsymbol{\alpha}\rangle \right|^2. \quad \text{(S42)}$$

In analogy to Eq. (S35), the sum over m can be executed by a sum over spherical harmonics and the density only
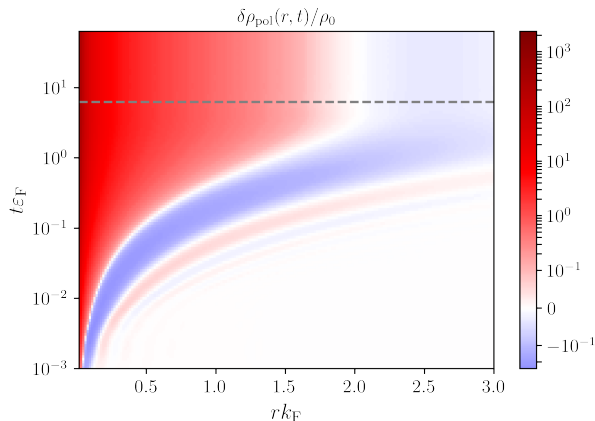
Figure S7. Time-dependent density profile $\delta\rho_{\rm pol}(r,t) = \rho_{\rm pol}(r,t) - \rho_0$ Eq. (S43) for an inverse scattering length $(ak_{\rm F})^{-1} = -2.0$. The actual polaron cloud formation is complete at $t = 2\pi/\varepsilon_{\rm F}$, which is marked by the gray dashed line.

depends on the radial component

$$\rho(r,t) = \frac{1}{4\pi r^2} \sum_{nl} (2l+1) n_{\rm F}(\varepsilon_{nl})$$
$$\times \left| \sum_{\alpha} {\rm e}^{-{\rm i}E_{\alpha l}t} \langle \alpha l | nl \rangle u_{\alpha l}(r) \right|^2. \quad \text{(S43)}$$

For a delta impurity, of course, only the s-wave contribution is affected by the time dependence. Fig. S7 illustrates the formation of a polaron cloud in real time for an exemplary scattering length. The polaron cloud grows with increasing time and is surrounded by fading oscillations until at a time scale inverse to the Fermi energy $t \lesssim 2\pi/\varepsilon_{\rm F}$ it reaches its final size. Hence, for a high enough hold time $t_1 \gg 1/\varepsilon_{\rm F}$, we expect the system to be in a steady state, where Eq. (S35) is applicable for the density profile.

IV. DETAILS ON ABSORPTION SPECTRA

A. Relation between $S(t)$ and $A(\omega)$

To show the relation between the Ramsey signal $S_{\sigma_1\sigma_2}$ Eq. (S32) and the absorption spectrum $A_{\rm pol}(\omega)$ given in the main text, we follow Ref. [S2], only here the impurity is switched from $|1\rangle$ to $|{\rm R}\rangle$. The absorption spectrum is calculated by Fermi's golden rule where the initial state is the polaron $|\psi_i\rangle = |1\rangle \otimes |{\rm pol}\rangle$ and the final state is in the presence of the Rydberg impurity $|\psi_f\rangle = |{\rm R}\rangle \otimes |f\rangle$. The perturbation flips the state of the impurity into the Rydberg state and vice versa, i.e., $\hat{\Omega} = (|1\rangle\langle{\rm R}| + {\rm h.c.}) \otimes \hat{\mathbb{1}}$. By rewriting the delta function in Fermi's golden rule as

a time integral, one obtains:

$$A_{\rm pol}(\omega) = 2\pi \sum_f |\langle \psi_f | \hat{\Omega} | \psi_i \rangle|^2 \delta[\omega - (E_f - E_i)]$$
$$= \sum_f \int_{-\infty}^{\infty} {\rm d}t\, {\rm e}^{{\rm i}\omega t} \langle \psi_i | {\rm e}^{{\rm i}E_i t} \hat{\Omega} | \psi_f \rangle \langle \psi_f | {\rm e}^{-{\rm i}E_f t} \hat{\Omega} | \psi_i \rangle. \quad \text{(S44)}$$

Alternatively, by inserting $\hat{\Omega}$ and using the fact that the impurity does not contribute to the total energies E_i, E_f, the form given in the main text is obtained. $|\psi_i\rangle$ and $|\psi_f\rangle$ are eigenstates with eigenenergies E_i and E_f, respectively. Furthermore, the time evolution of the gas in the presence of the impurity $|\sigma\rangle$ is given by the Hamiltonian $\hat{H}_\sigma$ acting only on the subspace of the Fermi gas

$$\langle \psi_i | {\rm e}^{{\rm i}E_i t} = \langle 1| \otimes \langle {\rm pol}| {\rm e}^{{\rm i}\hat{H}_1 t}, \quad \text{(S45a)}$$
$$\langle \psi_f | {\rm e}^{-{\rm i}E_f t} = \langle R| \otimes \langle f| {\rm e}^{-{\rm i}\hat{H}_{\rm R} t}, \quad \text{(S45b)}$$

such that the overall absorption spectrum reads

$$A_{\rm pol}(\omega) = \sum_f \int_{-\infty}^{\infty} {\rm d}t\, {\rm e}^{{\rm i}\omega t} \langle {\rm pol}| {\rm e}^{{\rm i}\hat{H}_1 t} |f\rangle \langle f| {\rm e}^{-{\rm i}\hat{H}_{\rm R} t} |{\rm pol}\rangle. \quad \text{(S46)}$$

The sum over all possible final configurations for the gas $|f\rangle$ gives an identity so that, in total, the absorption spectrum is the Fourier transform of the Ramsey signal $S_{1{\rm R}}(t)$ Eq. (S32). By separating the integration into negative and positive times, it is straightforward to bring the expression into the form which is given in the main text

$$A_{\rm pol}(\omega) = 2{\rm Re} \int_0^{\infty} {\rm d}t\, e^{{\rm i}\omega t} S_{1{\rm R}}(t). \quad \text{(S47)}$$

For numerical stability, we multiply the integrand with an exponential decay $f_\gamma(t) = {\rm e}^{-\gamma t}$ (in our numerical calculations we use $\gamma = 0.03\,\varepsilon_{\rm F}$). Eq. (S47) is calculated by fast Fourier transformation (FFT) up to a maximal time $t_{\rm max}$, which needs to be chosen high enough to give a good resolution in frequency space (cf. Sec. V).

B. Details on the Ramsey signal

The determinant for the Ramsey signal [cf. Eq. (S32)],

$$S_{1{\rm R}}(t) = \det[\hat{\mathbb{1}} - n_{\rm F}(\hat{h}_1) + n_{\rm F}(\hat{h}_1){\rm e}^{{\rm i}\hat{h}_1 t}{\rm e}^{-{\rm i}\hat{h}_{\rm R} t}], \quad \text{(S48)}$$

can be calculated by introducing the single-particle eigenstates $|\boldsymbol{\alpha}_\sigma\rangle$ in presence of the local polaronic impurity $\sigma = 1$ and the long-ranged Rydberg impurity $\sigma = {\rm R}$ with corresponding eigenenergies $E_{\alpha_\sigma l}$, i.e., $\hat{h}_\sigma |\boldsymbol{\alpha}_\sigma\rangle = E_{\alpha_\sigma l} |\boldsymbol{\alpha}_\sigma\rangle$. In the eigenbasis of the polaron states $|\boldsymbol{\alpha}_1\rangle$,

Figure S8. Ramsey signals $S(t)$ of a Rydberg atom with $n_{\mathrm{Ryd}} = 60$ in a polaron formed at different inverse scattering lengths $(ak_{\mathrm{F}})^{-1}$. The fine oscillations with periods $\tau = 2\pi/|\omega_{\mathrm{peak}}|$ correspond to the dimer peak of the Rydberg molecules. The loss of spectral weight at $t = 0$ is due to the omission of highly energetic bound states, but does not affect the quality of the dimer peaks.

the matrix elements for the calculation of the determinant are:

$$\langle \boldsymbol{\alpha}_1 | [\hat{\mathbb{1}} - n_{\mathrm{F}}(\hat{h}_1) + n_{\mathrm{F}}(\hat{h}_1)\mathrm{e}^{\mathrm{i}\hat{h}_1 t}\mathrm{e}^{-\mathrm{i}\hat{h}_{\mathrm{R}}t}] | \boldsymbol{\alpha}_1' \rangle$$

$$= \delta_{ll'}\delta_{mm'}\left[[1 - n_{\mathrm{F}}(E_{\alpha_1 l})]\delta_{\alpha_1\alpha_1'} \right.$$

$$\left. + n_{\mathrm{F}}(E_{\alpha_1 l})\mathrm{e}^{\mathrm{i}E_{\alpha_1 l}t}\sum_{\alpha_{\mathrm{R}}}\langle \alpha_1 l | \alpha_{\mathrm{R}} l \rangle \mathrm{e}^{-\mathrm{i}E_{\alpha_{\mathrm{R}} l}t}\langle \alpha_{\mathrm{R}} l | \alpha_1' l \rangle \right].$$
(S49)

The overlaps $\langle \alpha_1 l | \alpha_{\mathrm{R}} l \rangle$ and $\langle \alpha_{\mathrm{R}} l | \alpha_1' l \rangle$, respectively, are analogous to the expressions in Eqs. (S15) and (S17), only for the eigensystem in the presence of the Rydberg impurity. They are obtained by numerical integration.

The whole expression Eq. (S49) is diagonal in the angular-momentum quantum numbers l and m due to the conversation of angular momentum. Let us call the term within the brackets in Eq. (S49) $M_{\alpha_1\alpha_1' l}$. As it is the same for each of the $2l + 1$ blocks corresponding to the magnetic quantum number m, the total determinant in Eq. (S49) is calculated analogously to that in Ref. [S3]

$$S(t) = \det(\delta_{ll'}\delta_{mm'}M_{\alpha_1\alpha_1' l}) = \prod_{l=0}^{\infty}[\det(M_{\alpha\alpha' l})]^{2l+1}.$$
(S50)

We provide the Ramsey signals of a Rydberg atom in different polaron clouds in Fig. S8. The fine oscillations

Figure S9. Normalized density profiles $\rho_{\mathrm{pol}}(r)/\rho_0$ for different polaron clouds with inverse scattering lengths $(ak_{\mathrm{F}})^{-1}$ (solid lines) are compared to the integrated dimer peaks $I_{\mathrm{pol}}(r_{\mathrm{Ryd}})/I_0(r_{\mathrm{Ryd}})$ (dots), which correspond to the Rydberg radius through the respective overall density, i.e., $r_{\mathrm{Ryd}}(\rho_0)$. The inset shows the analysis of the dependence between the integrated absorption peak weights I_{pol}/I_0 and the corresponding densities $\rho_{\mathrm{pol}}/\rho_0$.

have a period of $\tau = 2\pi/|\omega_{\mathrm{peak}}|$ and correspond to the dimer peaks at ω_{peak} in the absorption spectra. In order to resolve absorption peaks at high frequency values, it is essential to resolve the time dependence of the Ramsey signal $S(t)$ optimally (cf. Sec. V).

We see that our calculated Ramsey signals do not take into account enough eigenstates in order to reach the exact value $S(t = 0) = 1$. This is due to the fact that the Rydberg impurity generates a lot of more deeply bound states with more overlap to the polaron's bound states or the polaron's scattering states, which we do not take into account (cf. Sec. I D). As we are primarily concerned about the overlap with the outermost Rydberg molecular state, the missing weight in the global spectrum does not affect our final results.

C. Reconstructed density by tuning ρ_0

In the main text, we have mentioned that the polaron's density can also be reconstructed from Rydberg spectroscopy for fixed principal number n_{Ryd} and different background densities ρ_0. Such a plot is provided in Fig. S9.

In the experimental setup, the Rydberg radius r_{Ryd} is of course fixed for a specific atom type and principal number n_{Ryd}, regardless of the density ρ_0 of the surrounding medium. However, the polaron's density profile is determined by the Fermi momentum of the gas. As we give physical quantities in units of the Fermi momentum, the relative size between the Rydberg impurity at fixed n_{Ryd}
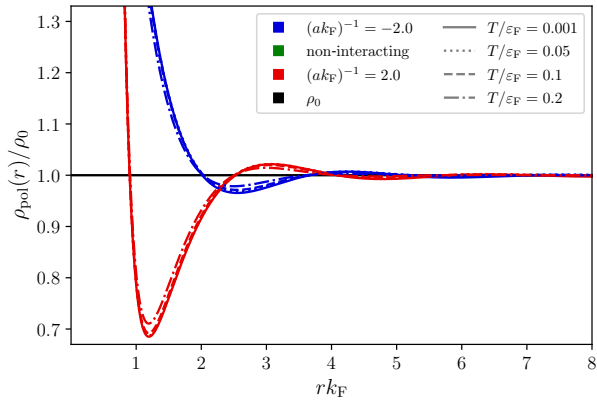
Figure S10. Density profiles $\rho_{\mathrm{pol}}(r)$ Eq. (S35) in the presence of a delta impurity with different inverse s-wave scattering lengths $(ak_{\mathrm{F}})^{-1}$ and temperatures T.

and the polaron with radius $r_c \sim k_{\mathrm{F}}^{-1}$ changes when tuning the background density $\rho_0 = \rho_0(k_{\mathrm{F}})$. This has already been clarified in Fig. S1, where different density values ρ_0 lead to different Rydberg radii r_{Ryd} in units of the Fermi momentum.

Fig. S9 is analogous to the plot given in the main text, only here we have fixed the principal number to $n_{\mathrm{Ryd}} = 59$ and associated the position dependence rk_{F} by changing the overall density ρ_0 as discussed before. When changing the overall density, the shape of the dimer peaks differ much more from one to the other than when changing the principal numbers [S3]. That is why overall the data in Fig. S9 are more noisy than those provided in the main text. However, the agreement between integrated weights and density values is still obvious. The two complementary methods give more flexibility in the experimental realization and underline the validity of our technique.

D. Effect of finite temperature

In this section, we elaborate that a finite temperature does not have a significant impact on our data. Thus, our method is robust against temperatures used in typical ultracold atomic gases. First of all, FDA does not have any conceptual limitation to zero temperature. Temperature only enters in the Fermi distribution $n_{\mathrm{F}}(\varepsilon)$, which is included in the density $\rho_{\mathrm{pol}}(\boldsymbol{r})$ Eq. (S35) and the Ramsey signal $S_{\sigma_1,\sigma_2}(t)$ Eq. (S32).

Fig. S10 shows the density profiles of polaron clouds $\rho_{\mathrm{pol}}(r)$ for different temperatures T. For higher temperatures, the chemical potential μ is lowered such that the background density $\rho_0 = k_{\mathrm{F}}^3/(6\pi^2)$ is kept constant. At $T = 0.05\,\varepsilon_{\mathrm{F}}$, which is basically the state of the art for fermionic quantum mixtures [S11], the difference to $T = 0.001\,\varepsilon_{\mathrm{F}}$, which is used in the rest of our work, is barely visible. We compare these density values to those
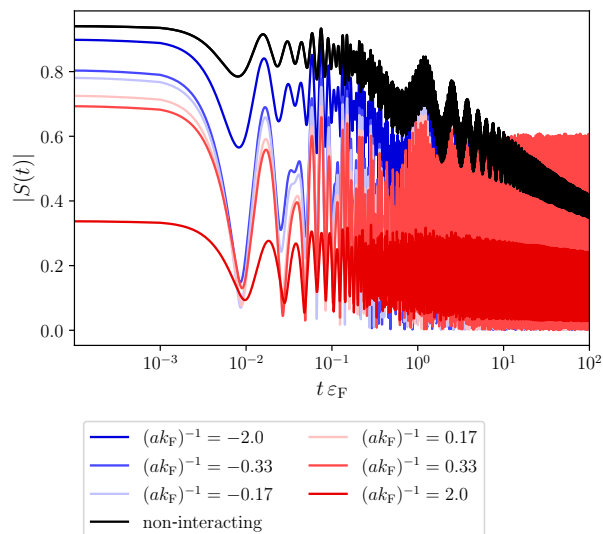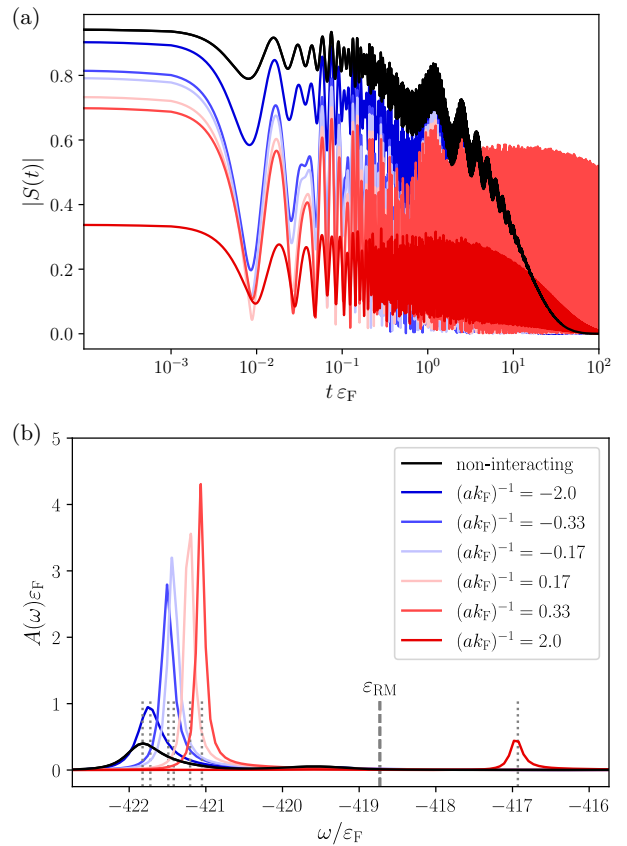

Figure S11. (a) Ramsey signals $S(t)$ of a Rydberg atom with $n_{\mathrm{Ryd}} = 60$ in a polaron formed at different inverse scattering lengths $(ak_{\mathrm{F}})^{-1}$ for a temperature $T = 0.2\,\varepsilon_{\mathrm{F}}$. (b) RM peaks of the corresponding absorption spectrum. The peak positions ω_{peak} are marked by gray doted lines and the binding energy $\varepsilon_{\mathrm{RM}}$ by a dashed gray line.

at $T = 0.1\,\varepsilon_{\mathrm{F}}$ and $T = 0.2\,\varepsilon_{\mathrm{F}}$, which are typical temperatures of Fermi polaron experiments. With increasing temperature, the density enhancement in the center as well as the accompanied oscillations are softened. This can be explained by the averaging over various statistical realizations. However, already here we see that this is only a slight effect so our probe barely changes with temperature.

To validate that our method of determining density profiles from Rydberg atom spectroscopy stays stable, we provide Ramsey signals, absorption spectra and the reconstructed density profiles (cf. Figs. S11 and S12) in analogy to those given in the main text, only here for a temperature $T = 0.2\,\varepsilon_{\mathrm{F}}$.

For a finite temperature, the Ramsey signals $S_{\mathrm{pol}}(t)$ decay faster [cf. Fig. S11(a)] as the orthogonality catastrophe is not fulfilled anymore [S1]. This leads to a broadening of the dimer response peaks in the absorption spectra [cf. Fig. S11(b)]. Note that, due to the finite temperature, the peaks are no longer asymmetrically cut on the
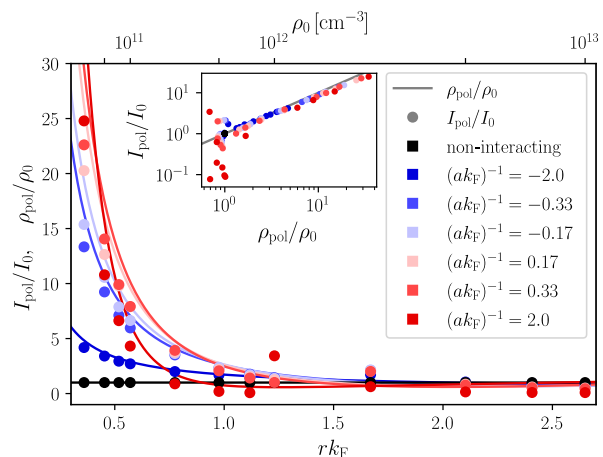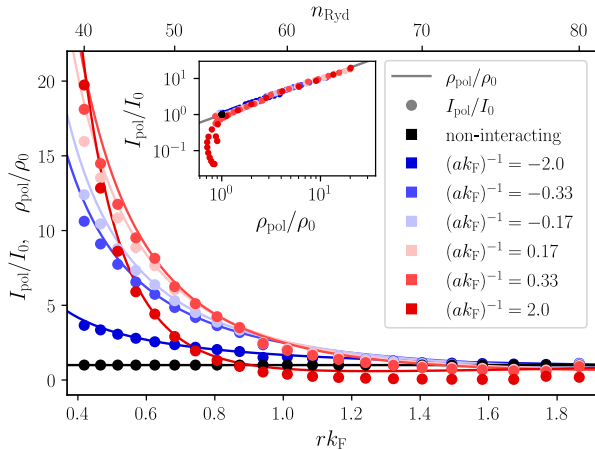
Figure S12. Normalized density profiles $\rho_{\mathrm{pol}}(r)/\rho_0$ for different polaron clouds with inverse scattering lengths $(ak_{\mathrm{F}})^{-1}$ (solid lines) are compared to the integrated dimer peaks $I_{\mathrm{pol}}(r_{\mathrm{Ryd}})/I_0(r_{\mathrm{Ryd}})$ (dots). The latter corresponds to the Rydberg radius through the respective principal numbers, i.e., $r_{\mathrm{Ryd}}(n_{\mathrm{Ryd}})$. We use a fixed $\rho_0 = 5 \times 10^{11}\,\mathrm{cm}^{-3}$ and a finite temperature $T = 0.2\,\varepsilon_{\mathrm{F}}$. The inset shows the dependence between I_{pol}/I_0 and the densities $\rho_{\mathrm{pol}}/\rho_0$.

left, but their shape is more Gaussian-like. The positions of the peak's maxima, however, do not change and reveal the polaron energy [cf. Eq. (7) in the main text].

The tight relation between the integrated dimer response I_{pol} and the actual density ρ_{pol} is still recovered for $T = 0.2\,\varepsilon_{\mathrm{F}}$. This is illustrated in Fig. S12, whose similarity to the plot at $T = 0.001\,\varepsilon_{\mathrm{F}}$ given in the main text is undeniable. This is due to the fact that our method only relies on the integrated spectral weight of the dimer response I_{pol}, which is basically unaffected by a finite temperature in contrast to the actual shape of the peak.

In a more realistic setting, the absorption spectra might be broadened also through other effects like the finite lifetime of the Rydberg excitation or the mobility of the impurity. Similar to the effect of a finite temperature, we expect our method to be robust as long as these effects do not significantly change the spectral weight of the dimer response.

V. NUMERICAL ACCURACY

In this section, we briefly mention how we choose our numerical parameters in order to achieve high accuracy in the calculated quantities. The choice of l_{max} and R is already motivated in Secs. III B and III C, respectively.

The maximal number α_{max} of single-particle scattering states $u_{\alpha l}(r)$ is chosen such that enough states above the Fermi energy are taken into account. For a brief estimate, we consider the noninteracting impurity $|0\rangle$ at zero temperature and angular momentum. The highest radial quantum number for n, which needs to be considered in the calculations, is determined by the Fermi momentum

$$\frac{k_{n_{\mathrm{max}}}^2}{2m} = \frac{n_{\mathrm{max}}^2 \pi^2}{2mR^2} \geq z\,\varepsilon_{\mathrm{F}} \Rightarrow n_{\mathrm{max}} \geq \sqrt{z}\frac{k_{\mathrm{F}}R}{\pi}. \quad \text{(S51)}$$

To increase precision, we want to take into account the doubled amount of maximal energy, i.e., $z = 2$, such that $n_{\mathrm{max}} = \lfloor \sqrt{2}k_{\mathrm{F}}R/\pi \rfloor$ states are considered. In our calculations, we use $Rk_{\mathrm{F}} = 400$ and $n_{\mathrm{max}} = 250 = \alpha_{\mathrm{max}}$.

Let us now discuss the maximal time, we can take into account in the Ramsey signals $S(t)$ used in the Fourier transform for the absorption spectrum Eq. (S47). For this, we again consider the noninteracting system. Because of the finite system size, there is a difference of discrete momenta, i.e., $\delta k = \pi/R$, which leads to a differences of energies, i.e., $\delta E = k/m \cdot \delta k = \pi k/(mR)$. The largest difference in energy $\delta\varepsilon_{\mathrm{max}}$ provides an upper time limit for the Ramsey signal $t_{\mathrm{max}} \leq 2\pi/\delta\varepsilon_{\mathrm{max}}$ before finite-size effects occur. With $k_{\mathrm{max}} = k_{\mathrm{F}}$, we thus have:

$$t_{\mathrm{max}} \leq \frac{2mR}{k_{\mathrm{F}}}. \quad \text{(S52)}$$

In natural units, i.e., $2m = 1 = k_{\mathrm{F}}$, the maximal time is just given by the system size $t_{\mathrm{max}} \leq R$. For our data we use $t_{\mathrm{max}} = 100$.

The maximal time, however, corresponds to a finite frequency resolution $\delta\omega$ when taking the numerical Fourier transform. Thus, the absorption spectra $A(\omega)$ are not resolved more accurately than the maximal energy accuracy. In natural units, i.e., $2m = 1 = \varepsilon_{\mathrm{F}}$, this takes the values $\delta\omega \sim 2\pi/R$.

On the other hand, the resolution of the Ramsey signals (cf. Fig. S8) corresponds to a maximal frequency ω_{max} in the absorption spectrum reached by the FFT. This maximal frequency has to be larger than the binding energy of the Rydberg molecule, i.e., $\omega_{\mathrm{max}} > |\varepsilon_{\mathrm{RM}}|$ such that the dimer peak is included in the spectrum. This corresponds to a minimal time resolution of the Ramsey signal

$$\delta t < \frac{2\pi}{\omega_{\mathrm{max}}} = \frac{2\pi}{|\varepsilon_{\mathrm{RM}}|}. \quad \text{(S53)}$$

In fact, the resolution of our data is affected by the system size R. In addition, we need extremely well resolved Ramsey signals in order to reach high accuracy in the absorption spectra for the highly energetic values of the dimer peaks.

[S1] M. Knap, A. Shashi, Y. Nishida, A. Imambekov, D. A. Abanin, and E. Demler, Phys. Rev. X **2**, 041020 (2012).

[S2] R. Schmidt, J. D. Whalen, R. Ding, F. Camargo,

G. Woehl, Jr., S. Yoshida, J. Burgdörfer, F. B. Dunning, E. Demler, H. R. Sadeghpour, and T. C. Killian, Phys. Rev. A **97**, 022707 (2018).

[S3] J. Sous, H. R. Sadeghpour, T. C. Killian, E. Demler, and R. Schmidt, Phys. Rev. Res. **2**, 023021 (2020).

[S4] J. J. Sakurai and J. Napolitano, *Modern quantum mechanics, revised edition* (Addison-Wesley, Boston, 2011).

[S5] I. Bloch, J. Dalibard, and W. Zwerger, Rev. Mod. Phys. **80**, 885 (2008).

[S6] N. Y. Du and C. H. Greene, Phys. Rev. A **36**, 971 (1987).

[S7] C. E. Burkhardt and J. J. Leventhal, The quantum defect, in *Topics in Atomic Physics* (Springer, New York, 2006) pp. 214–229.

[S8] M. T. Eiles, Phys. Rev. A **98**, 042706 (2018).

[S9] I. Klich, An elementary derivation of Levitov's formula, in *Quantum Noise in Mesoscopic Physics*, edited by Y. V. Nazarov (Springer Netherlands, Dordrecht, 2003) pp. 397–402.

[S10] R. Schmidt, M. Knap, D. A. Ivanov, J.-S. You, M. Cetina, and E. Demler, Reports on Progress in Physics **81**, 024401 (2018).

[S11] R. S. Lous, I. Fritsche, M. Jag, B. Huang, and R. Grimm, Phys. Rev. A **95**, 053627 (2017).

2.4. Time-dependent formation of a polaron cloud

In the following two sections, we provide two interesting extensions of our measurement technique for probing correlated quantum states via Rydberg atom spectroscopy. Firstly, we discuss how Fermi polarons form after the interactions of the impurity atom are switched on and how this information is contained in absorption spectra. Secondly, we deal with a completely different quantum state, which can be observed by our measurement technique, namely a BCS superfluid.

In the previous section, we mentioned that the typical time scale for the formation of a polaron cloud is $t_1 = 2\pi/\varepsilon_F$ (cf. Fig. S6 in the SM of Ref. [P2]). With the numbers for a cold-atomic gas of ^{40}K atoms, provided in Eq. (B.4), this yields $t_1 \simeq 0.83$ ms, which is very slow compared to the other time scales of the Rydberg spectroscopy experiment. Thus, after exciting the impurity from the non-interacting state $|0\rangle$ to the locally interacting state $|1\rangle$, it takes some time until the system is in the quasi-stationary state of the Fermi polaron. We illustrate this in Fig. 2.7. As an extension of the proposed experiment in Sec. 2.3, one can also excite the impurity from $|1\rangle$ to $|R\rangle$ before the polaron cloud has been completely formed, i.e., at a time $t < t_1$. As a result, by varying t, one would get access to the dynamics of the polaron cloud formation.

Let us first give a formula of the time-dependent density distribution of the polaron cloud within the FDA. We are interested in the scenario where at a time t_0 the system is prepared in the state $|\Psi(t_0)\rangle = |0\rangle \otimes |\text{FS}\rangle$. Then, by a radio-frequency pulse, the impurity is suddenly switched to the interacting state, but the Fermi gas has not yet reacted, i.e., the total state is given by $|\Psi(t_0 + 0^+)\rangle = |1\rangle \otimes |\text{FS}\rangle$. This state now evolves in time according to the polaron Hamiltonian $\hat{H}_1$ [cf. Eqs. (2.16) and (2.21)],

$$|\Psi(t > t_0)\rangle = \mathrm{e}^{-\mathrm{i}\hat{H}t}|\Psi(t_0 + 0^+)\rangle = |1\rangle \otimes \mathrm{e}^{-\mathrm{i}\hat{H}_1 t}|\text{FS}\rangle \xrightarrow{t \gg 1/\varepsilon_F} |1\rangle \otimes |\text{pol}\rangle, \qquad (2.40)$$

which leads to the formation of the polaron cloud (cf. Fig. 2.7). In the subspace of the Fermi gas, the time-dependent density is evaluated with the density matrix
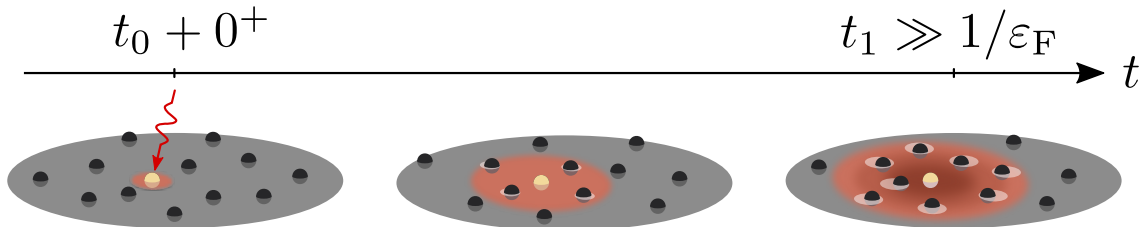
Figure 2.7.: Time-dependent formation of a polaron cloud. At a time t_0, the impurity is suddenly changed from $|0\rangle$ to $|1\rangle$ by a radio-frequency pulse, which induces the formation of a polaron cloud. After a time scale $t_1 \gg 1/\varepsilon_F$, the formation of the polaron cloud is completed and the system is situated in a quasi-stationary state.

$\hat{\rho}(t) = \mathrm{e}^{-\mathrm{i}\hat{H}_1 t}|\mathrm{FS}\rangle\langle\mathrm{FS}|\mathrm{e}^{\mathrm{i}\hat{H}_1 t}$:

$$n(\boldsymbol{r}, t) = \frac{1}{Z_0}\mathrm{tr}\left(\mathrm{e}^{-\mathrm{i}\hat{H}_1 t}\mathrm{e}^{-\beta(\hat{H}_0 - \mu\hat{N})}\mathrm{e}^{\mathrm{i}\hat{H}_1 t}\hat{c}_{\boldsymbol{r}}^{\dagger}\hat{c}_{\boldsymbol{r}}\right) = \langle\boldsymbol{r}|\mathrm{e}^{-\mathrm{i}\hat{h}_1 t}n_{\mathrm{F}}(\hat{h}_0)\mathrm{e}^{\mathrm{i}\hat{h}_1 t}|\boldsymbol{r}\rangle, \qquad (2.41)$$

where we use similar steps as in Eqs. (2.28)–(2.32) (see also Eq. (S34) in the SM of Ref. [P2]). After solving the Schrödinger equation for the non-interacting $\hat{h}_0|\boldsymbol{n}\rangle = \varepsilon_{\boldsymbol{n}}|\boldsymbol{n}\rangle$ and interacting case $\hat{h}_1|\boldsymbol{\alpha}\rangle = E_{\boldsymbol{\alpha}}|\boldsymbol{\alpha}\rangle$, this is expressed as a sum (cf. Eq. (S38) in the SM of Ref. [P2]):

$$n(\boldsymbol{r}, t) = \sum_{\boldsymbol{n}} n_{\mathrm{F}}(\varepsilon_{\boldsymbol{n}})\left|\sum_{\boldsymbol{\alpha}}\mathrm{e}^{-\mathrm{i}E_{\boldsymbol{\alpha}}t}\langle\boldsymbol{\alpha}|\boldsymbol{n}\rangle\langle\boldsymbol{r}|\boldsymbol{\alpha}\rangle\right|^2. \qquad (2.42)$$

During the polaron cloud formation, the system is not in an eigenstate of the full Hamiltonian. Hence, Fermi's golden rule, Eq. (2.25), cannot be applied straightforwardly. Following the steps used in Sec. 5.7 in Ref. [SN11], we derived a generalized form of the absorption spectrum (cf. App. B.2). Here we found a generalized expression for the absorption spectrum:

$$A(\omega, t) \simeq 2\pi\sum_{f,n}|\langle f|\hat{\Omega}|n\rangle\langle n|i(t)\rangle|^2\delta(\omega + E_f - E_n). \qquad (2.43)$$

Compared to the conventional Fermi's golden rule, there is an additional summation over eigenstates $|n\rangle$ of the Hamiltonian $\hat{H}$, Eq. (2.16). With $|i(t)\rangle = |\Psi(t)\rangle$, Eq. (2.40), the absorption spectrum can be expressed as a double time integral over an expression, which resembles a Ramsey signal [cf. derivation of Eq. (B.22)][3]:

$$A(\omega, t) = \int \mathrm{d}t_1\,\mathrm{e}^{\mathrm{i}\omega t_1}\int \mathrm{d}t_2\,\mathrm{tr}\left(\hat{\rho}_0\,\mathrm{e}^{\mathrm{i}\hat{H}_1(t+t_1+t_2)}\mathrm{e}^{-\mathrm{i}\hat{H}_{\mathrm{R}}t_1}\mathrm{e}^{-\mathrm{i}\hat{H}_1(t_2+t)}\right), \qquad (2.44)$$

with the density matrix given by the Fermi sea $\hat{\rho}_0 = |\mathrm{FS}\rangle\langle\mathrm{FS}|$. The integrand can thus be expressed by a Klich formula (2.20) as a functional determinant:

$$\mathrm{tr}\left[\hat{\rho}_0\,\mathrm{e}^{\mathrm{i}\hat{H}_1(t+t_1+t_2)}\mathrm{e}^{-\mathrm{i}\hat{H}_{\mathrm{R}}t_1}\mathrm{e}^{-\mathrm{i}\hat{H}_1(t_2+t)}\right] = \det\left[\hat{\mathbb{1}} - n_{\mathrm{F}}(\hat{h}_0) + n_{\mathrm{F}}(\hat{h}_0)\mathrm{e}^{\mathrm{i}\hat{h}_1(t+t_1+t_2)}\mathrm{e}^{-\mathrm{i}\hat{h}_{\mathrm{R}}t_1}\mathrm{e}^{-\mathrm{i}\hat{h}_1(t_2+t)}\right].$$
$$(2.45)$$

This expression can be computed in a similar way as the Ramsey signal for the Rydberg spectroscopy experiment in Sec. 2.3. The additional time integral over t_2 and the time dependence t of the polaron cloud formation complicate the corresponding numerics. However, the computations are similar to those already implemented. We have not

---

[3]Note that the second time integral over t_2 originates from a Kronecker delta symbol and is therefore taken over a finite range $\int \mathrm{d}t_2... = \frac{1}{2\pi}\int_0^{2\pi}\mathrm{d}t_2....$

further pursued on an evaluation of the time-dependent absorption function $A(\omega, t)$, Eq. (2.44), but with the input we give here it should be possible. Thus, we even assume that the time-dependent formation of a polaron cloud could be detected as well in a Rydberg spectroscopy experiment.

2.5. Rydberg atom spectroscopy of a BCS superfluid

The content of this section is part of the following paper in preparation:

Probing BCS superfluids by Rydberg atom spectroscopy

Emilio Ramos Rodríguez, **Marcel Gievers**, Richard Schmidt

The interaction of impurities with fermionic excitations in superconductors is one of the paradigmatic problems of solid state physics. In this section, we present an ongoing project on how the proposed Rydberg atom spectroscopy in Sec. 2.3 can be applied to probe characteristic properties of a BCS superfluid. Recently, Ramsey signals and absorption spectra of a short-range impurity in a BCS superfluid were analyzed via the FDA [WLH22]. There it was seen that due to the energy gap Δ, which is needed to break Cooper pairs, multiple particle-hole excitations are energetically unfavored and Anderson's orthogonality catastrophe is prevented yielding a quasi-particle for the polaron. It stands to reason that embedding a Rydberg excitation can provide even more information on the BCS superfluid. We are interested in the competition between the extension of a Cooper pair and the Rydberg molecule, and the physics in different scales of temperatures and densities.

In the total Hamiltonian of the Rydberg spectroscopy experiment, Eq. (2.39), the Hamiltonian of the gas particles $\hat{H}_0$ is now replaced by the BCS mean-field Hamiltonian where the gap parameter $\Delta = g/V \sum_{\boldsymbol{k}} \langle \hat{c}_{-\boldsymbol{k},\downarrow} \hat{c}_{\boldsymbol{k},\uparrow} \rangle$ is introduced:

$$
\begin{aligned}
\hat{H}_{\mathrm{BCS}} - \mu\hat{N} &= \sum_{\boldsymbol{k},\sigma=\uparrow,\downarrow} \xi_{\boldsymbol{k}} \hat{c}_{\boldsymbol{k}\sigma}^{\dagger} \hat{c}_{\boldsymbol{k}\sigma} + \frac{g}{V} \sum_{\boldsymbol{k},\boldsymbol{k}',\boldsymbol{q}} \hat{c}_{-\boldsymbol{k},\uparrow}^{\dagger} \hat{c}_{\boldsymbol{k}+\boldsymbol{q},\downarrow}^{\dagger} \hat{c}_{\boldsymbol{k}'+\boldsymbol{q},\downarrow} \hat{c}_{-\boldsymbol{k}',\uparrow} \\
&\simeq \sum_{\boldsymbol{k}} \left(\hat{c}_{\boldsymbol{k},\uparrow}^{\dagger}, \hat{c}_{-\boldsymbol{k},\downarrow} \right) \begin{pmatrix} \xi_{\boldsymbol{k}} & \Delta \\ \Delta^* & -\xi_{\boldsymbol{k}} \end{pmatrix} \begin{pmatrix} \hat{c}_{\boldsymbol{k},\uparrow} \\ \hat{c}_{-\boldsymbol{k},\downarrow}^{\dagger} \end{pmatrix} + \sum_{\boldsymbol{k}} \xi_{\boldsymbol{k}} - \frac{V|\Delta|^2}{g},
\end{aligned} \qquad (2.46)
$$

with $\xi_{\boldsymbol{k}} = \boldsymbol{k}^2/(2m) - \mu$. Importantly, the Hilbert space of gas particles is doubled as now two spin degrees of freedom $\hat{c}_{\uparrow,\boldsymbol{k}}$ and $\hat{c}_{\downarrow,\boldsymbol{k}}$ are included. In the following, we assume the gap parameter to be real $\Delta^* = \Delta$ and constant in space.

The Hamiltonian, Eq. (2.46), is diagonalized by a Bogoliubov transformation,

$$
\begin{pmatrix} \hat{c}_{\boldsymbol{k},\uparrow} \\ \hat{c}^{\dagger}_{-\boldsymbol{k},\downarrow} \end{pmatrix} = \begin{pmatrix} u^*_{\boldsymbol{k}} & v_{\boldsymbol{k}} \\ -v^*_{\boldsymbol{k}} & u_{\boldsymbol{k}} \end{pmatrix} \begin{pmatrix} \hat{\gamma}_{\boldsymbol{k},+} \\ \hat{\gamma}^{\dagger}_{-\boldsymbol{k},-} \end{pmatrix}, \quad |u_{\boldsymbol{k}}|^2 + |v_{\boldsymbol{k}}|^2 = 1 \tag{2.47a}
$$

$$
\Rightarrow \hat{H}_{\mathrm{BCS}} - \mu\hat{N} = E_0 + \sum_{\boldsymbol{k}} \left(\hat{\gamma}^{\dagger}_{\boldsymbol{k},+}, \hat{\gamma}_{-\boldsymbol{k},-} \right) \begin{pmatrix} \xi_{\Delta,\boldsymbol{k}} & 0 \\ 0 & -\xi_{\Delta,\boldsymbol{k}} \end{pmatrix} \begin{pmatrix} \hat{\gamma}_{\boldsymbol{k},+} \\ \hat{\gamma}^{\dagger}_{-\boldsymbol{k},-} \end{pmatrix}, \tag{2.47b}
$$

with $\xi_{\Delta,\boldsymbol{k}} = \sqrt{\xi_{\boldsymbol{k}}^2 + \Delta^2}$. The fermionic Bogoliubov quasi-particles $\hat{\gamma}_{\boldsymbol{k},\pm}$ describe excitations on top of the ground-state energy E_0. The presence of the Rydberg potential $V_{\mathrm{R}}(r)$, Eq. (2.37), changes the dispersion relation $\xi_{\boldsymbol{k}}$ in the BCS Hamiltonian, Eq. (2.46). The single-particle Hamiltonians $\hat{h}_0 = \sum_{\boldsymbol{n}} |\boldsymbol{n}\rangle\langle\boldsymbol{n}|\varepsilon_{\boldsymbol{n}}$ are then replaced by $\hat{h}_{\mathrm{R}} = \sum_{\boldsymbol{\alpha}} |\boldsymbol{\alpha}\rangle\langle\boldsymbol{\alpha}|E_{\boldsymbol{\alpha}}$. As we are only interested in the sudden response after the Rydberg excitation, we do not take into account a change of the gap parameter Δ due to the Rydberg potential.

The eigenenergies and Bogoliubov excitations in terms of the basis states $|\boldsymbol{n}\rangle$, $|\boldsymbol{\alpha}\rangle$ written in angular momenta are then found by a diagonalization of the matrices

$$
\hat{h}_{\Delta,0} = \begin{pmatrix} \hat{h}_0 - \mu\hat{\mathbb{1}} & \Delta\hat{\mathbb{1}} \\ \Delta\hat{\mathbb{1}} & -\hat{h}_0 + \mu\hat{\mathbb{1}} \end{pmatrix}, \quad \hat{h}_{\Delta,\mathrm{R}} = \begin{pmatrix} \hat{h}_{\mathrm{R}} - \mu\hat{\mathbb{1}} & \Delta\hat{\mathbb{1}} \\ \Delta\hat{\mathbb{1}} & -\hat{h}_{\mathrm{R}} + \mu\hat{\mathbb{1}} \end{pmatrix}. \tag{2.48}
$$

The Ramsey signal $S(t) = \det(\hat{\mathbb{1}} - n_{\mathrm{F}}(\hat{h}_{\Delta,0}) + n_{\mathrm{F}}(\hat{h}_{\Delta,0})\mathrm{e}^{\mathrm{i}\hat{h}_{\Delta,0}t}\mathrm{e}^{-\mathrm{i}\hat{h}_{\Delta,\mathrm{R}}t})$, Eq. (2.23), is computed via the determinant of a 2×2 block matrix:

$$
\det \begin{pmatrix} M^{++} & M^{+-} \\ M^{-+} & M^{--} \end{pmatrix} = \det(M^{++}) \det(M^{--} - M^{-+}(M^{++})^{-1}M^{+-}), \tag{2.49}
$$

where all the matrix elements can be expressed in terms of the overlaps $\langle\boldsymbol{n}|\boldsymbol{\alpha}\rangle$. We leave the details in the mentioned article in preparation.

Recently, it was analyzed how a Rydberg atom influences the spatial dependence of the gap parameter and density when situated in a one-dimensional superfluid for a system size that scarcely exceeds the Rydberg atom [CMS24]. However, similarly to Sec. 2.3, we are interested what happens after a sudden excitation before the superfluid has been equilibrated with the Rydberg atom and, for this, we consider the full three-dimensional space and compute actual radio-frequency spectra.

Figure 2.8 illustrates the different processes we observe in our computed absorption spectra. Around the frequency $\omega \simeq \varepsilon_{\mathrm{RM}} + \Delta$, a single atom can be trapped in the outermost well of the Rydberg potential, Eq. (2.37). In contrast to the case of the Fermi polaron, a superfluid almost exclusively consists of weakly bound Cooper pairs so the energy of the gap Δ has to be additionally paid in order to form a dimer with the Rydberg impurity [cf. Fig. 2.8(a)]. Around the frequency $\omega \simeq 2\varepsilon_{\mathrm{RM}}$, we detect trimer states, i.e., two atoms from the superfluid form a molecule together with the Rydberg atom. Here, we observe two different configurations: Firstly, a whole Cooper pair is bound by the
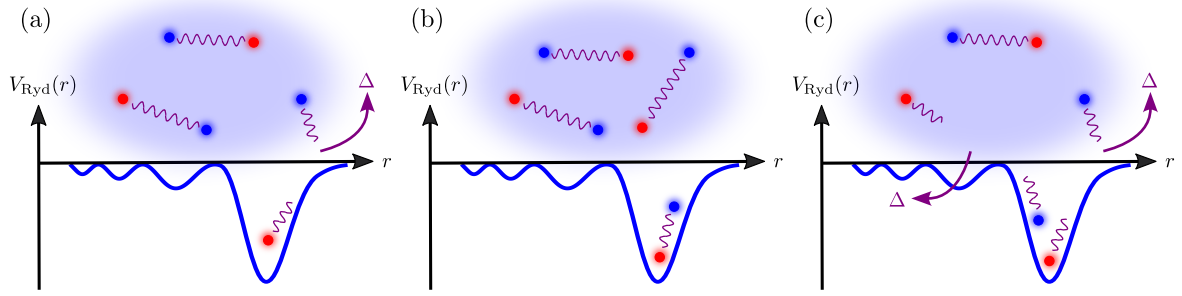
Figure 2.8.: Different processes that occur when a Rydberg atom is immersed in a BCS superfluid. The Rydberg potential $V_{\mathrm{Ryd}}(r)$, Eq. (2.37), is depicted by the blue curve, Cooper pairs by red and blue circles connected by a wiggly purple line. (a) A dimer is formed after breaking a Cooper pair by the energy cost of the gap parameter Δ. (b) A trimer is formed by binding a whole Cooper pair. (c) A trimer is formed by breaking two Cooper pairs with an energy cost of 2Δ.

Rydberg impurity [cf. Fig. 2.8(b)]. For this to happen, the size of the Cooper pair needs to be in accordance to the Rydberg radius. Secondly, two Cooper pairs can be broken by an additional energy cost of 2Δ and are bound to the Rydberg impurity [cf. Fig. 2.8(c)]. The discussed effects may as well involve different angular momentum states of the gas particles. Our computed absorption spectra thus serve as a fingerprint of the rich physics occurring in superfluids.

3. Effective bosons and the functional renormalization group

> *"While zoologists may have little need to talk to particle physicists, the right way to understand both the Higgs boson and the flocking of starlings is through the language of the renormalization group."*
>
> David Tong – Lectures on Statistical Field Theory

The functional renormalization group (fRG) is a versatile field-theoretical method to calculate correlation functions. The Wetterich equation is an exact equation for the generating functional of amputated vertex functions. Still, in almost all cases a certain truncation of the hierarchy of flow equations for multi-point correlation functions is required. The typical one-loop fRG approach provides two-point and four-point vertices, however, in an incomplete manner. To obtain these objects from total derivatives and thus without dependence on regulators, the multiloop extension of fRG has been developed. In this chapter, we derive how the idea of total derivatives in fRG can be transferred to three-point vertices as well. For this, we formulate fRG equations of three-point vertices arising from Hubbard–Stratonovich transformations. An alternative approach is the single-boson exchange (SBE) decomposition of the four-point vertex, for which we derive multiloop flow equations. In the end, we discuss how a regulator dependence of the bare interaction allows for even more flexibility in solving fRG equations for SBE vertices.

3.1. Review of the functional renormalization group

To begin, let us briefly provide the general framework for n-point correlation functions and vertices, a standard tool in quantum field theory [NO98].

The generic fermionic action S of a theory with a quartic interaction U reads

$$S[\bar{c}, c] = -\bar{c}_{1'}[G_0^{-1}]_{1'|1}c_1 - \tfrac{1}{4}U_{1'2'|12}\bar{c}_{1'}\bar{c}_{2'}c_2 c_1. \tag{3.1}$$

Here $\bar{c}_{1'}$ and c_1 are Grassmann fields (or for bosons, they are complex fields) whose indices $1', 2', 1, 2$ refer to arbitrary quantum numbers (e.g., frequencies, momenta, spin indices). We make use of Einstein's convention, i.e., doubled indices are implicitly summed over in Eq. (3.1). Due to the fermionic exchange statistics, the four-point vertex is antisymmetric

with respect to its first two or last two indices, i.e., it fulfills the crossing symmetries $U_{1'2'|12} = -U_{2'1'|12} = -U_{1'2'|21} = U_{2'1'|21}$. The microscopic action $S[\bar{c}, c]$ is contained in the functional integral of the partition function $Z = \int \mathcal{D}[\bar{c}, c]\,\mathrm{e}^{-S[\bar{c},c]}$ and thus serves as the backbone of the theoretical description for all physically measurable quantities. In the non-interacting limit, i.e., $U = 0$, the action is quadratic $S_0[\bar{c}, c] = S[\bar{c}, c]|_{U=0}$ and the partition function $Z_0 = Z|_{U=0}$ can be computed exactly as a functional Gaussian integral (cf. App. A).

In quantum field theory, n-point *correlation functions* are given by the functional integral

$$G^{(n)}_{1...n} = \langle c_n \cdots \bar{c}_2 \bar{c}_1 \rangle = \frac{1}{Z} \int \mathcal{D}[\bar{c}, c]\, c_n \cdots \bar{c}_2 \bar{c}_1 \mathrm{e}^{-S[\bar{c},c]}. \tag{3.2}$$

Alternatively, they can be obtained by functional derivatives after introducing source fields $\bar{j}, j$ into the partition function:

$$\mathcal{G}[\bar{j}, j] = \frac{1}{Z} \int \mathcal{D}[\bar{c}, c]\mathrm{e}^{-S[\bar{c},c]+\bar{c}_{1'}j_{1'}+\bar{j}_1 c_1} \Rightarrow G^{(n)}_{1...n} = \langle c_n \cdots \bar{c}_2 \bar{c}_1 \rangle = \frac{\delta^n \mathcal{G}[\bar{j}, j]}{\delta \bar{j}_n \cdots \delta j_2 \delta j_1}\bigg|_{\bar{j},j=0}. \tag{3.3}$$

In general, n-point correlation functions contain connected $\langle ... \rangle_{\mathrm{con}}$ and disconnected parts. The latter contain lower-order correlation functions only. By contrast, the connected terms can be generated by functional derivatives of the so-called *Schwinger functional* $W[\bar{j}, j]$, which is defined as

$$\mathrm{e}^{W[\bar{j},j]} = \frac{Z}{Z_0}\mathcal{G}[\bar{j}, j] \Rightarrow [G^{(n)}_{\mathrm{con}}]_{1...n} = \langle c_n \cdots \bar{c}_2 \bar{c}_1 \rangle_{\mathrm{con}} = \frac{\delta^n W[\bar{j}, j]}{\delta \bar{j}_n \cdots \delta j_2 \delta j_1}\bigg|_{\bar{j},j=0}. \tag{3.4}$$

It is more practical to represent connected correlation functions in terms of their amputated contributions that exclude external two-point propagators $G^{(2)}$. These amputated quantities are given by the n-point vertices $\Gamma^{(n)}$. To represent $\Gamma^{(n)}$ by functional derivatives, a Legendre transformation of the Schwinger functional $W[\bar{j}, j]$ with respect to the expectation values $\bar{\varphi}, \varphi$ in the presence of the source fields $\bar{j}, j$ is applied:

$$\bar{\varphi}_{1'} = \langle \bar{c}_{1'} \rangle_{\bar{j},j} = \frac{\int \mathcal{D}[\bar{c}, c]\bar{c}_{1'}\mathrm{e}^{-S[\bar{c},c]+\bar{c}_{2'}j_{2'}+\bar{j}_2 c_2}}{\int \mathcal{D}[\bar{c}, c]\mathrm{e}^{-S[\bar{c},c]+\bar{c}_{2'}j_{2'}+\bar{j}_2 c_2}}, \quad \varphi_1 = \langle c_1 \rangle_{\bar{j},j} = \frac{\int \mathcal{D}[\bar{c}, c]c_1\mathrm{e}^{-S[\bar{c},c]+\bar{c}_{2'}j_{2'}+\bar{j}_2 c_2}}{\int \mathcal{D}[\bar{c}, c]\mathrm{e}^{-S[\bar{c},c]+\bar{c}_{2'}j_{2'}+\bar{j}_2 c_2}} \tag{3.5a}$$

$$\Rightarrow S_{\mathrm{eff}}[\bar{\varphi}, \varphi] = \bar{j}_1[\bar{\varphi}, \varphi]\varphi_1 + \bar{\varphi}_{1'}j_{1'}[\bar{\varphi}, \varphi] - W[\bar{j}[\bar{\varphi}, \varphi], j[\bar{\varphi}, \varphi]] - S_0[\bar{\varphi}, \varphi]$$

$$\Rightarrow \Gamma^{(n)}_{1...n} = \frac{\delta^n S_{\mathrm{eff}}[\bar{\varphi}, \varphi]}{\delta \bar{\varphi}_n \cdots \delta \varphi_2 \delta \varphi_1}\bigg|_{\bar{\varphi},\varphi=0}. \tag{3.5b}$$

In the Legendre transform, the source fields $\bar{j}, j$ are written in terms of the fields $\bar{\varphi}, \varphi$.

The generating functional of the vertices $\Gamma^{(n)}$ is the *effective action* S_{eff}[1]. We here presented the building blocks of the so-called *one-particle irreducible* (1PI) formalism. Diagrams contained in the amputated vertices $\Gamma^{(n)}$ cannot be split by cutting a single propagator, in contrast to the connected correlation functions $G_{\text{con}}^{(n)}$. It is possible to extend this formalism to higher-point irreducible vertices by introducing higher-point source fields in the partition function. For example, the generating functional of two-particle irreducible (2PI) diagrams results from introducing new source field into the partition function that couple to two fields $\bar{c}$ and c (instead of $\bar{j}, j$ coupling to only one) [DM64, CJT74, Dup14, EKKH23].

In condensed matter physics, two-point and four-point correlation functions play a prominent role. That is why they deserve a special notation compared to $G^{(2)}$ and $\Gamma^{(4)}$ (including different sign conventions). The Green's function G is the fermionic propagator. It is related to the amputated *self-energy* Σ via the *Dyson equation*,

$$G_{1|1'} = -\langle c_1 \bar{c}_{1'} \rangle = [G_0]_{1|1'} + [G_0]_{1|2'} \Sigma_{2'|2} G_{2|1'},$$

$$1 \longleftarrow 1' \;=\; 1 \longleftarrow 1' \;+\; 1 \longleftarrow \overset{\Sigma}{\underset{2' \quad 2}{\bigcirc}} \longleftarrow 1' \,. \tag{3.6}$$

Here, the full Green's function G is depicted by a black line whereas its non-interacting counterpart G_0 is represented by a gray line. The diagram for the self-energy Σ is a gray circle.

The four-point vertex Γ describes renormalized interactions between two particles. It results from the connected and amputated part of the four-point correlation function $G^{(4)}$:

$$G^{(4)}_{12|1'2'} = \langle c_1 c_2 \bar{c}_{2'} \bar{c}_{1'} \rangle \equiv G_{1|1'} G_{2|2'} - G_{1|2'} G_{2|1'} + G_{1|3'} G_{2|4'} \Gamma_{3'4'|34} G_{3|1'} G_{4|2'},$$

$$\begin{array}{c} {}^{2'}\diagdown \quad \diagup^{2} \\ \boxed{G^{(4)}} \\ {}_{1}\diagup \quad \diagdown_{1'} \end{array} \;=\; \begin{array}{c} 2' \longrightarrow 2 \\ 1 \longleftarrow 1' \end{array} \;-\; \begin{array}{c} 2' \quad 2 \\ \downarrow \quad \uparrow \\ 1 \quad 1' \end{array} \;+\; \begin{array}{c} {}^{2'}\diagdown \;{}^{4}\; \boxed{\Gamma} \;{}^{4'}\; \diagup^{2} \\ {}_{1}\diagup\; {}_{3'}\quad{}_{3}\; \diagdown_{1'} \end{array} \,. \tag{3.7}$$

The *flying squirrel* diagram on the left-hand side clarifies that the four-point correlation function $G^{(4)}$ is an individual object whereas the vertex Γ on the right-hand side, indicated by a square, is multiplied by four propagator lines. Equation (3.7) is a special case of the so-called *tree expansion* (cf. Sec. 6.2.2 in Ref. [KBS10]), which relates n-point correlation functions to amputated ($m \leq n$)-point vertices.

---

[1]Note that we make use of the definition used in Ref. [KBS10] where the non-interacting term $S_0[\bar{\varphi}, \varphi]$ is subtracted in the definition of the effective action $S_{\text{eff}}[\bar{\varphi}, \varphi]$.

3.1.1. Functional renormalization group from the Wetterich equation

The functional renormalization group (fRG) is a powerful quantum field-theoretical method with numerous applications ranging from high-energy physics [FPR20] and quantum gravity [EGS09] to the fluid dynamics in flocks of birds [JL23]. For a more detailed introduction in the context of condensed matter systems, we recommend Refs. [KBS10, MSH+12, DCE+21].

In Wilson's renormalization group [Wil75, Sha94], high-energy modes (short length scales) are successively integrated out in the functional integral to obtain an effective theory at low energies (large length scales). In doing so, the coupling constants in the microscopic action S are replaced by renormalized couplings, which then depend on a cutoff scale Λ and fulfill differential equations, so-called *flow equations*. A fixed point analysis of the latter yields universal low-energy behavior of the respective physical system (see also Refs. [P5] and [P6]). In the *functional* renormalization group (fRG), this idea is extended by setting up flow equations for the whole correlation functions and not only for the scalar couplings as in Wilson's formulation. More precisely, a cutoff dependence on Λ is introduced in the non-interacting Green's function $G_0 \to G_0(\Lambda)$. At an initial ultraviolet scale $\Lambda = \Lambda_i$, quantum fluctuations are totally neglected $G_0(\Lambda_i) = 0$ yielding the bare interaction vertex $\Gamma(\Lambda_i) = U$. At a final infrared scale $\Lambda = \Lambda_f$, the complete dependencies are recovered yielding the full renormalized quantities $G_0(\Lambda_f) = G_0$ and $\Gamma(\Lambda_f) = \Gamma$. This way, frequency behavior of correlation functions can be predicted in a wider range.

The main result of fRG is the Wetterich equation [Wet93], which is an exact flow equation for the effective action S_{eff}, Eq. (3.5b). The cutoff dependence of the bare Green's function $G_0(\Lambda)$ is transferred to all vertex quantities. Using the more general notation introduced in Ref. [KBS10], where the action $S[\Psi]$ is defined in terms of general (bosonic or fermionic) fields Ψ [opposed to the fermionic fields $\bar{c}, c$ in Eq. (3.1)], yielding an effective action $S_{\text{eff}}[\Phi]$ in terms of the general mean fields Φ [opposed to $\bar{\varphi}, \varphi$ in Eq. (3.5b)], the Wetterich equation is given as (Eq. (7.51) in Ref. [KBS10])[2]

$$\partial_\Lambda S_{\text{eff},\Lambda}[\Phi] = \frac{1}{2} \text{tr} \left[(\partial_\Lambda G_{0,\Lambda}^{-1}) \left(\frac{\delta}{\delta\Phi} \otimes \frac{\delta}{\delta\Phi} S_{\text{eff},\Lambda}[\Phi] - \boldsymbol{\zeta} G_{0,\Lambda}^{-1} \right)^{-1} \right] + \partial_\Lambda \ln Z_{0,\Lambda}. \qquad (3.8)$$

The trace represents a summation over all degrees of freedom of the generalized fields Φ.

The Wetterich equation is just a representation of the numerically inaccessible func-

---

[2]In Ref. [KBS10], the bare action is given as $S_0[\Psi] = -\frac{1}{2}\Psi_\alpha [G_0^{-1}]_{\alpha,\beta}\Psi_\beta$ where the indices α, β also mark the particle type (boson vs. fermion). The sign factor $\boldsymbol{\zeta}$ reflects additional signs from exchanging fermionic fields $\boldsymbol{\zeta}_{\alpha\beta} = \zeta_\alpha \delta_{\alpha\beta}$ where $\zeta = \pm 1$ for bosons/fermions. The trace includes additional minus signs for fermions. Moreover, writing the double functional derivative $\delta^2/(\delta\Phi_\alpha \delta\Phi_\beta)$ as a tensor product reflects the fact that the quantity $\delta/\delta\Phi \otimes \delta/\delta\Phi \, S_{\text{eff},\Lambda}[\Phi]$ is a matrix-valued quantity with respect to α and β. Due to the revised definition of the effective action S_{eff} (see footnote 1), the regulator R_Λ does not appear explicitly in our formulation of the Wetterich equation and the additional term involving the cutoff-dependent bare partition function $Z_{0,\Lambda}$ needs to be accounted for.

tional integral and thus does not reduce the exponentially large Hilbert space. For numerical applications one writes both sides of the equation as an expansion of the n-point vertices $\Gamma^{(n)}$, which generates an infinite hierarchy of flow equations known as the *vertex expansion* [Mor94]. Below, we show the flow equations for the self-energy Σ, Eq. (3.6), and the four-point vertex Γ, Eq. (3.7), as they are obtained in the fermionic theory, Eq. (3.1):

$$\partial_\Lambda \Sigma_{1'|1} = -\Gamma_{1'2'|12} S_{2|2'},$$

(3.9a)
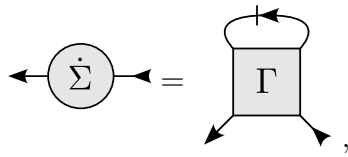
$$\partial_\Lambda \Gamma_{1'2'|12} = \Gamma_{1'4'|32}(G_{3|3'}S_{4|4'} + S_{3|3'}G_{4|4'})\Gamma_{3'2'|14} + \tfrac{1}{2}\Gamma_{1'2'|34}(G_{3|3'}S_{4|4'} + S_{3|3'}G_{4|4'})\Gamma_{3'4'|12}$$
$$- \Gamma_{1'3'|14}(G_{3|3'}S_{4|4'} + S_{3|3'}G_{4|4'})\Gamma_{4'2'|32} - \Gamma^{(6)}_{1'2'3'|123}S_{3|3'},$$
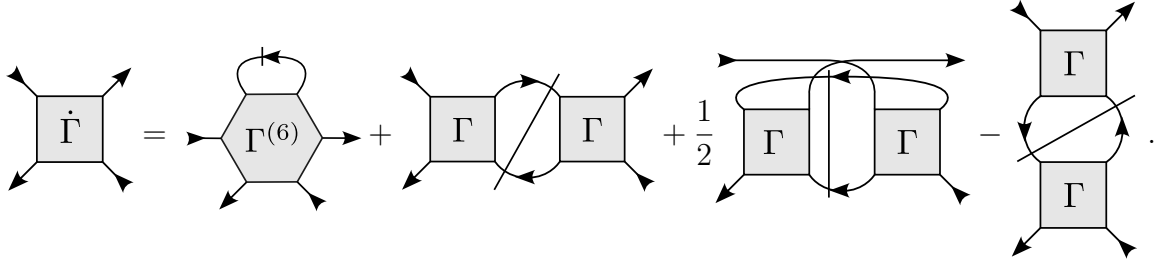
(3.9b)

Here, the single-scale propagator $S_{1|1'} = \partial_\Lambda|_{\dot{\Sigma}=0}G_{1|1'}$ (cf. Sec. 3.5.3) is depicted by crossed propagator lines and may not be confused with the fermionic action $S[\bar{c}, c]$, Eq. (3.1). Equations (3.9) cannot be solved exactly as they are part of an infinite hierarchy including flow equations for higher-point vertices $\dot{\Gamma}^{(n \geq 6)}$. For practical purposes, a truncation is often applied that neglects the six-point vertices $\Gamma^{(6)} \to 0$ and all higher contributions. This truncation is known as the *one-loop fRG* and can lead to uncontrolled results. In particular, the total derivatives on the right-hand sides of Eqs. (3.9) become incomplete, leading to results that depend on the regulator chosen.

3.1.2. Functional renormalization group from the parquet formalism

To circumvent the strong dependence on the regulator after introducing the one-loop truncation in the fRG vertex expansion, Fabian Kugler and Jan von Delft developed a completely different derivation of fRG flow equations [KD18b, KD18c, KD18d, Kug21]. The starting point of their consideration is the *parquet formalism*. In the late 1960s, the parquet formalism was motivated to sum up logarithmic divergent terms to all orders of perturbation theory [RGN69, NGR69]. In the 1990s, the parquet formalism was extended to contain full self-consistent vertex functions on the one- and two-particle

level [BW91, CB92, Bic04], which led to many numerical applications in recent years as a consequence of the rapid advancement in computational power [TFY+13, VST+15, LWP+16, LKPH19, ARR20, EHHK20, KPA+20]. We will elaborate more on the historical context in Chapter 5.

Essential to the parquet formalism is a decomposition of the full amputated four-point vertex Γ into contributions that are two-particle reducible. These diagrams fall apart after cutting two lines of Green's functions. Such a decomposition can be derived by functional identities [Kug21, EKKH23]. For the fermionic action, Eq. (3.1), there exist three channels of two-particle reducibility that are denoted as *antiparallel a*, *parallel p*, and *transversal t*. We write the parquet decomposition of the full vertex Γ as

$$\Gamma_{1'2'|12} = [\underbrace{I_a \circ \Pi_a \circ \Gamma}_{\gamma_a}]_{1'2'|12} + [\underbrace{I_p \circ \Pi_p \circ \Gamma}_{\gamma_p}]_{1'2'|12} + [\underbrace{I_t \circ \Pi_t \circ \Gamma}_{\gamma_t}]_{1'2'|12} + R_{1'2'|12},$$

(3.10)

Here, γ_r are the two-particle reducible vertices in the channels $r = a, p, t$ and $I_r = \Gamma - \gamma_r$ the respective two-particle irreducible vertices. The rest function R contains all contributions that are two-particle irreducible in all the three channels[3]. The *bubbles* Π_r are products of two Green's functions (cf. Eqs. (5) in Ref. [P1]),

$$[\Pi_a]_{34|3'4'} = G_{3|3'}G_{4|4'}, \quad [\Pi_p]_{34|3'4'} = \tfrac{1}{2}G_{3|3'}G_{4|4'}, \quad [\Pi_t]_{43|3'4'} = -G_{3|3'}G_{4|4'}. \quad (3.11)$$

The $\circ$ products, appearing in Eq. (3.10), include summations over all indices depending

---

[3]In the parquet literature, the full vertex Γ is often denoted by F, the two-particle reducible vertices γ_r by Φ_r, the irreducible vertices I_r by Γ_r and the rest function R by Λ [Bic04, HKT08]. We here follow the conventions used in the multiloop fRG literature [KD18b, KD18c, KD18d, Kug21]. Our three diagrammatic channels $r = a, p, t$ correspond to the crossed particle-hole $\overline{ph}$, the particle-particle pp and the particle-hole ph channel.

on the three channels (cf. Eqs. (6) in Ref. [P1]):

$$[A_a \circ B_a]_{12|34} = [A_a]_{16|54}[B_a]_{52|36}, \tag{3.12a}$$

$$[A_p \circ B_p]_{12|34} = [A_p]_{12|56}[B_p]_{56|34}, \tag{3.12b}$$

$$[A_t \circ B_t]_{12|34} = [A_t]_{62|54}[B_t]_{15|36}. \tag{3.12c}$$

These definitions are valid for arbitrary four-point objects, i.e., A_r and B_r represent different vertices Γ and bubbles Π_r. More details about these notations are discussed in Ref. [P1].

The two-particle reducible vertices γ_r in Eq. (3.10) fulfill the self-consistent *Bethe–Salpeter equations*,

$$\gamma_r = I_r \circ \Pi_r \circ \Gamma. \tag{3.13}$$

Solving Eq. (3.13) together with the Schwinger–Dyson equation for the self-energy (see Sec. 3.4.3) combined with a given input for the two-particle irreducible vertex R yields a solution, which is self-consistent on the one- and two-particle level and fulfills the crossing symmetries of the vertices [Bic04].

The idea of the new fRG approach [KD18b, KD18c, KD18d, Kug21] is to take the derivative ∂_Λ with respect to the scale parameter Λ on both sides of the Bethe–Salpeter equations (3.13) to obtain (using the short-hand notation $\dot{X} \equiv \partial_\Lambda X$)

$$\dot{\gamma}_r = \dot{I}_r \circ \Pi_r \circ \Gamma + I_r \circ \dot{\Pi}_r \circ \Gamma + I_r \circ \Pi_r \circ \underbrace{\dot{\Gamma}}_{\dot{I}_r + \dot{\gamma}_r}. \tag{3.14}$$

The dependence on $\dot{\gamma}_r$ at both sides of the equation is further rewritten by the inverted Bethe–Salpeter equations,

$$\Gamma = I_r + \Gamma \circ \Pi_r \circ I_r \Rightarrow (\mathbb{1}_r - I_r \circ \Pi_r)^{-1} \circ I_r = (\mathbb{1}_r + \Gamma \circ \Pi_r) \circ I_r. \tag{3.15}$$

Inserting Eq. (3.15) into Eq. (3.14) yields

$$\begin{aligned}
\dot{\gamma}_r &= (\mathbb{1}_r - I_r \circ \Pi_r)^{-1} \circ (\dot{I}_r \circ \Pi_r \circ \Gamma + I_r \circ \dot{\Pi}_r \circ \Gamma + I_r \circ \Pi_r \circ \dot{I}_r) \\
&= (\mathbb{1}_r + \Gamma \circ \Pi_r) \circ (\dot{I}_r \circ \Pi_r \circ \Gamma + I_r \circ \dot{\Pi}_r \circ \Gamma + I_r \circ \Pi_r \circ \dot{I}_r) \\
&= \dot{I}_r \circ \Pi_r \circ \Gamma + \Gamma \circ \Pi_r \circ \dot{I}_r \circ \Pi_r \circ \Gamma + \underbrace{(I_r + \Gamma \circ \Pi_r \circ I_r)}_{\Gamma} \circ (\dot{\Pi}_r \circ \Gamma + \Pi_r \circ \dot{I}_r), \quad (3.16)
\end{aligned}$$

and hence the *multiloop fRG equations*,

$$\dot{\gamma}_r = \Gamma \circ \dot{\Pi}_r \circ \Gamma + \dot{I}_r \circ \Pi_r \circ \Gamma + \Gamma \circ \Pi_r \circ \dot{I}_r \circ \Pi_r \circ \Gamma + \Gamma \circ \Pi_r \circ \dot{I}_r. \tag{3.17}$$

For $\dot{\gamma}_a$, the multiloop fRG equations can be expressed in graphical form as

$$(3.18)$$

The diagrams for $\dot{\gamma}_p$ and $\dot{\gamma}_t$ are drawn analogously [cf. Eq. (3.10)]. Intriguingly, the first term $\Gamma \circ \dot{\Pi}_r \circ \Gamma$ coincides with the term from the one-loop truncation of the vertex expansion of the Wetterich equation [cf. Eq. (3.9b)]. Consequently, the terms with $\dot{I}_r = \dot{\Gamma} - \dot{\gamma}_r$ on the left, at the center and on the right represent those contributions from the contraction of the six-point vertex that retain the self-consistency on the two-particle level provided in the parquet formalism. The flow equations (3.17) are an extension of the usual one-loop truncation of fRG and offer an alternative way of solving the parquet equations.

Note that the derivative of the bubble $\dot{\Pi}_r$ is a full derivative, i.e., it includes $\dot{G} = S + G\dot{\Sigma}G$ (see Sec. 3.5.3) [Kat04]. In the diagrams, this is represented by the doubly crossed line. The flow equations are thus total derivatives. This way, their solutions do not depend on the precise implementation of the cutoff dependence on Λ.

In Refs. [BPR11] and [BPR21], the parquet formalism was combined with the functional renormalization group for a ϕ^4 theory. In fact, Eq. (46) in Ref. [BPR21] is equivalent to the flow equation (3.17).

To solve the algebraic differential equations (3.17) for $\dot{\gamma}_r$, one typically employs a loop expansion. First of all, one assumes $\dot{R} = 0$ such that $\dot{I}_r = \sum_{\bar{r} \neq r} \dot{\gamma}_{\bar{r}}$. At the beginning, only the one-loop contribution $\dot{\gamma}_r^{(1)} = \Gamma \circ \dot{\Pi}_r \circ \Gamma$ is taken into account. This is inserted successively on the right-hand side yielding increasingly higher loop contributions $\dot{\gamma}_r^{(\ell)}$. Ideally, one repeats that iterative step until convergence in the loop order.

Over the last few years, the multiloop fRG was successfully applied in several condensed matter systems like quantum spin systems [TRK+20, KMI+22, RKM+22], the two-dimensional Hubbard model [THK+19, FHB+22, EHF+24] and the single-impurity Anderson model using the real-frequency Keldysh formalism [Wal21, GRW+24, RGW+24]. However, the tremendous effort raises the question if a solution of the flow equations (3.17) is really advantageous compared to the parquet formalism or if there are more direct alternatives to solve these algebraic differential equations without explicitly implementing the multiloop expansion, e.g., by gradient descent methods. In this dissertation, we put emphasis on efficient parametrizations of the four-point vertices Γ and γ_r to lower numerical costs. In doing so, we shed light on the relation between different fRG and self-consistent schemes. Nonetheless, we are not in a position to have the final say on the

usefulness of the multiloop fRG approach.

3.2. Hubbard–Stratonovich theory

In general, the four-point vertex Γ, Eq. (3.7), is a highly complicated object as it describes renormalized interactions between two fermions involving different values of frequencies, spin indices, momenta etc. (all incorporated in the generic labels $1', 2', 1, 2$). A common strategy in quantum field theory to reduce full fermionic interactions into simplified processes is the *Hubbard–Stratonovich transformation*. We here provide the overall concept of the Hubbard–Stratonovich theory to elucidate how it is related to the single-boson exchange (SBE) formalism in Sec. 3.4.1. The quartic interaction term $S_{\text{int}} = -\frac{1}{4} U_{1'2'|12} \bar{c}_{1'} \bar{c}_{2'} c_2 c_1$ in the fermionic action S, Eq. (3.1), is decoupled through auxiliary bosonic fields, which usually are related to order parameters in the system. We define the Hubbard–Stratonovich interaction,

$$S_{\text{HS}} = -\bar{\psi}_{3'} [W_{\psi,0}^{-1}]_{3'|3} \psi_3 - \tfrac{1}{2} \left([\bar{h}_{\psi,0}]_{1'23} \bar{c}_{1'} c_2 \psi_3 + [h_{\psi,0}]_{3'2'1} \bar{\psi}_{3'} \bar{c}_{2'} c_1 \right)$$
$$- \bar{\phi}_{3'} [W_{\phi,0}^{-1}]_{3'|3} \phi_3 - \tfrac{1}{2} \left([\bar{h}_{\phi,0}]_{1'2'3} \bar{c}_{1'} \bar{c}_{2'} \phi_3 + [h_{\phi,0}]_{3'12} \bar{\phi}_{3'} c_1 c_2 \right), \qquad (3.19)$$

with the two bosonic fields ψ and ϕ. Here, $\bar{\psi}, \psi$ are exchange bosons and $\bar{\phi}, \phi$ pairing bosons. The free propagators of the bosons are given by $W_{\psi,0}$ and $W_{\phi,0}$ whereas $\bar{h}_{\psi,0}, h_{\psi,0}, \bar{h}_{\phi,0}, h_{\phi,0}$ represent bare Yukawa couplings between one bosonic field and two fermionic fields[4]. The bosonic fields can be integrated out exactly by a functional Gaussian integral (cf. App. A), yielding the fermionic action $S = S_0 + S_{\text{int}}$, Eq. (3.1):

$$\frac{1}{Z_{\text{HS}}} \int \mathcal{D}[\bar{c}, c] \mathcal{D}[\bar{\psi}, \psi] \mathcal{D}[\bar{\phi}, \phi] e^{-S_0[\bar{c},c] - S_{\text{HS}}[\bar{c},c,\bar{\psi},\psi,\bar{\phi},\phi]} = \frac{1}{Z} \int \mathcal{D}[\bar{c}, c] e^{-S_0[\bar{c},c] - S_{\text{int}}[\bar{c},c]}. \quad (3.20)$$

In doing so, the bare interaction U appearing in S is identified with the quantities in the Hubbard–Stratonovich action S_{HS}:

$$U_{1'2'|12} = [\bar{h}_{\psi,0}]_{1'23} [W_{\psi,0}]_{3|3'} [h_{\phi,0}]_{3'2'1} + [\bar{h}_{\phi,0}]_{1'2'3} [W_{\phi,0}]_{3|3'} [h_{\phi,0}]_{3'12}. \qquad (3.21)$$

We define the bosonic Green's functions and self-energies in analogy to the fermionic Dyson equation (3.6):

$$[W_\psi]_{1|1'} = -\langle \psi_1 \bar{\psi}_{1'} \rangle = [W_{\psi,0}]_{1|1'} + [W_{\psi,0}]_{1|2'} [\Sigma_\psi]_{2'|2} [W_\psi]_{2|1'},$$

$$1 \rightsquigarrow\!\!\!\blacktriangleleft\!\!\rightsquigarrow 1' \;=\; 1 \rightsquigarrow\!\!\!\blacktriangleleft\!\!\rightsquigarrow 1' \;+\; 1 \rightsquigarrow\!\!\!\blacktriangleleft_{2'} \!\!\boxed{\Sigma_\psi}_{2} \!\!\blacktriangleright\!\!\rightsquigarrow 1' , \qquad (3.22a)$$

$$[W_\psi]_{1|1'} = -\langle \phi_1 \bar{\phi}_{1'} \rangle = [W_{\phi,0}]_{1|1'} + [W_{\phi,0}]_{1|2'} [\Sigma_\phi]_{2'|2} [W_\phi]_{2|1'},$$

---

[4]Note that the Yukawa couplings are antisymmetric with respect to their fermionic arguments, i.e., $[\bar{h}_{\phi,0}]_{1'2'3} = [\bar{h}_{\phi,0}]_{2'1'3}$ etc.

$$1 \mathrel{\leadsto\!\!\blacktriangleleft\!\!\leadsto} 1' \;=\; 1 \mathrel{\leadsto\!\!\blacktriangleleft\!\!\leadsto} 1' \;+\; 1 \mathrel{\leadsto\!\!\blacktriangleleft} {}_{2'}\!\left(\Sigma_\phi\right)_{2}\mathrel{\blacktriangleleft\!\!\leadsto} 1' \,. \tag{3.22b}$$

Diagrammatically, the Green's function of the exchange boson ψ is represented by a zig-zag line and that of the pairing boson ϕ by a wiggly line [KD18d].

Analogously to the four-point vertex Γ, which is defined through the connected four-point correlator $G^{(4)}$, Eq. (3.7), we define the full Yukawa couplings $\bar{h}_\psi, h_\psi, \bar{h}_\phi, h_\phi$ through the connected three-point correlators:

$$\langle c_1 \bar{c}_{2'} \bar{\psi}_{3'} \rangle_{\mathrm{con}} = G_{1|1'} G_{2|2'} [\bar{h}_\psi]_{1'23} [W_\psi]_{3|3'}, \qquad \langle \psi_3 c_2 \bar{c}_{1'} \rangle_{\mathrm{con}} = [W_\psi]_{3|3'} [h_\psi]_{3'2'1} G_{1|1'} G_{2|2'},$$

$$\tag{3.23a}$$

$$\langle c_1 c_2 \bar{\phi}_{3'} \rangle_{\mathrm{con}} = G_{1|1'} G_{2|2'} [\bar{h}_\phi]_{1'2'3} [W_\phi]_{3|3'}, \qquad \langle \phi_3 \bar{c}_{1'} \bar{c}_{2'} \rangle_{\mathrm{con}} = [W_\phi]_{3|3'} [h_\phi]_{3'12} G_{1|1'} G_{2|2'},$$

$$\tag{3.23b}$$

The three-point correlation functions are represented by triangular flying-squirrel diagrams while the three-point vertices are represented by usual triangles. Equations (3.23) naturally follow from the tree expansion (cf. Sec. 6.2.2 in Ref. [KBS10]).

In the following, we present Schwinger–Dyson equations, which relate the bosonic self-energies to the three-point vertices and the three-point vertices to four-point vertices. We will see that these Schwinger–Dyson equations have the same structure as the self-consistent equations for SBE vertices to be discussed in Sec. 3.3. For this, we introduce suitable bosonic source fields in the Hubbard–Stratonovich interaction:

$$S_{\mathrm{HS}} \mapsto S_{\mathrm{HS}}^{j} = S_{\mathrm{HS}} + \bar{j}_3^{\psi} \psi_3 + \bar{\psi}_{3'} j_{3'}^{\psi} + \bar{j}_3^{\phi} \phi_3 + \bar{\phi}_{3'} j_{3'}^{\phi}. \tag{3.24}$$

Schwinger–Dyson equations now follow from two steps (cf. Sec. 6.3.3 in Ref. [KBS10]): First, a shift in the fermionic and bosonic fields is performed, i.e., $c \mapsto c + \delta c$, $\psi \mapsto \psi + \delta\psi$, $\phi \mapsto \phi + \delta\phi$, and the generating functional $\mathcal{G}[\bar{j}, j]$, Eq. (3.3), is expanded to first order in these shifts. This adaption does not change $\mathcal{G}[\bar{j}, j]$ as $\mathcal{G}[\bar{j}, j]$ only depends on the source fields, not the original fields. In a second step, one takes derivatives with respect to the source fields $\bar{j}^{\psi}, j^{\psi}, \bar{j}^{\phi}, j^{\phi}$. More details are provided in App. C.1.

This procedure gives the following Schwinger–Dyson equations for the self-energies:

$$[\Sigma_\psi]_{1'|1} = [h_{\psi,0}]_{1'2'3} G_{2|2'} G_{3|3'} [\bar{h}_\psi]_{3'21} = \quad , \quad (3.25a)$$

$$[\Sigma_\phi]_{1'|1} = \tfrac{1}{2}[h_{\phi,0}]_{1'23} G_{2|2'} G_{3|3'} [\bar{h}_\phi]_{2'3'1} = \quad = \tfrac{1}{2} \quad , \quad (3.25b)$$

$$\Sigma_{1'|1} = -[\bar{h}_{\psi,0}]_{1'23} G_{2|2'} [W_\psi]_{3|3'} [h_\psi]_{3'2'1} - [\bar{h}_{\phi,0}]_{1'2'3} G_{2|2'} [W_\phi]_{2|2'} [h_\phi]_{3'12}$$

$$= \; 1' \;\leftarrow\; \Sigma \;\blacktriangleleft\; 1 \;=\; - \quad - \quad . \quad (3.25c)$$

Here, the bare three-point vertices are represented by white circles[5]. The Schwinger–Dyson equations for the three-point vertices read

$$[\bar{h}_\psi]_{1'23} = [\bar{h}_{\psi,0}]_{1'23} + I^\psi_{1'4'|52} G_{4|4'} G_{5|5'} [\bar{h}_{\psi,0}]_{5'43},$$

$$(3.26a)$$

$$[h_\psi]_{3'2'1} = [h_{\psi,0}]_{3'2'1} + [h_{\psi,0}]_{3'4'5} G_{4|4'} G_{5|5'} I^\psi_{5'2'|14},$$

$$(3.26b)$$

$$[\bar{h}_\phi]_{1'2'3} = [\bar{h}_{\phi,0}]_{1'2'3} + \tfrac{1}{2} I^\phi_{1'2'|54} G_{4|4'} G_{5|5'} [\bar{h}_{\phi,0}]_{5'4'3},$$

$$(3.26c)$$

$$[h_\phi]_{3'12} = [h_{\phi,0}]_{3'12} + \tfrac{1}{2}[h_{\phi,0}]_{3'54}G_{4|4'}G_{5|5'}I^\phi_{5'4'|12},$$

(3.26d)

Here, I^ψ and I^ϕ correspond to those parts of the fermionic four-point vertex Γ that are one-particle irreducible with respect to the bosonic propagators $W_{\psi,0}$ and $W_{\phi,0}$.

Let us finally comment on fRG within the Hubbard–Stratonovich theory. In general, flow equations for vertices are derived from a vertex expansion of the Wetterich equation Eq. (3.8). Due to the two functional derivatives on the right-hand side of Eq. (3.8), differentiated n-point vertices always depend on $(n+2)$-point vertices [cf. also Eqs. (3.9)]. In particular, the flow equations for the bosonic self-energies $\dot{\Sigma}_\psi$ and $\dot{\Sigma}_\phi$ involve bosonic four-point vertices describing the interaction of bosonic fields and the flow equations of the three-point vertices $\dot{\bar{h}}_\psi, \dot{h}_\psi, \dot{\bar{h}}_\phi, \dot{h}_\psi$ involve five-point vertices [KBS10]. It is clear that the hierarchy of flow equations cannot be closed for the Hubbard–Stratonovich theory. It has to be mentioned that interaction processes described by the four-point vertices of bosonic fields ψ and ϕ are not included in the usual parquet decomposition.

In order to arrive at closed flow equations yielding total differentials, we need to pursue another strategy than the vertex expansion of the Wetterich equation, similar to the multiloop extension, which was derived from the self-consistent Bethe–Salpeter equations [KD18c, KD18b, KD18d]. In our case, we use the recently introduced single-boson exchange decomposition [KV19, KVC19, KLR20, KVC+20, HLK21, HVB+21, KKH21, KK22] as a starting point for flow equations of bosonic propagators and three-point vertices, which is discussed in the following section.

3.3. Multiloop fRG equations in the SBE formalism

3.3.1. Overview

The four-point vertex Γ contains the relevant physics on the two-particle level. Computing this quantity exactly involving its full frequency and momentum dependence is highly demanding (see recent developments using the numerical renormalization group [KLD21, LKD21]). Satisfying energy conservation, Γ can be parametrized using three frequencies (in a fermionic system one typically uses one bosonic ω and two fermionic ν, ν'). Instead of saving the whole three-dimensional frequency dependence in a single gigantic data container, it has proven to be extremely useful to decompose the frequency dependence into classes that reflect the high-frequency asymptotic behavior [LWP+16, WLT+20, Wal21].

Thus, the two-particle reducible vertices γ_r, Eq. (3.13), are split into four parts:

$$\gamma_r(\omega, \nu, \nu') = \mathcal{K}_{1,r}(\omega) + \mathcal{K}_{2,r}(\omega, \nu) + \mathcal{K}_{2',r}(\omega, \nu') + \mathcal{K}_{3,r}(\omega, \nu, \nu'). \qquad (3.27)$$

Here, the first asymptotic class $\mathcal{K}_{1,r}$ arises from taking the limit $\lim_{|\nu|,|\nu'|\to\infty} \gamma_r$ and can be stored on a one-dimensional frequency grid while the second asymptotic classes $\mathcal{K}_{2,r}$ and $\mathcal{K}_{2',r}$ can be stored on two-dimensional frequency grids. They emerge in the limit of sending only one fermionic frequency $|\nu'|$ or $|\nu|$ to infinity. This decomposition saves a lot of numerical memory as characteristic features of γ_r are described by lower-dimensional frequency grids. It is hoped that the contribution of $\mathcal{K}_{3,r}$, which truly depends on three frequencies, has a smaller impact. Such a subordination of $\mathcal{K}_{3,r}$ is justified in the perturbative regime as terms contributing to $\mathcal{K}_{3,r}$ come at fourth order in the interaction $\mathcal{O}(U^4)$ while $\mathcal{K}_{2,r}$ and $\mathcal{K}_{2',r}$ come at third $\mathcal{O}(U^3)$ and $\mathcal{K}_{1,r}$ at second order $\mathcal{O}(U^2)$.

Over the years, there were several attempts to reduce the complexity of the vertex by introducing bilinear fermionic fields and interaction through exchange bosons similar to those appearing after a Hubbard–Stratonovich transformation [HS09, HGS12]. A quite powerful idea originates from Friedrich Krien and coworkers: the so-called *single-boson exchange decomposition* [KV19, KVC19, KLR20, KVC+20, HLK21, HVB+21, KKH21, KK22]. Here, the fermionic interactions of the four-point vertex are mediated by effective exchange bosons without explicitly introducing their bosonic fields. The theory remains completely fermionic as the bosonic interactions arise from a new criterion of sorting diagrams in perturbation theory, namely the reducibility with respect to the bare interaction U instead of the two-particle reducibility of parquet diagrams. The two-particle reducible vertices γ_r are thus divided into a U-irreducible part M_r, also referred to as the *multi-boson exchange (MBE) vertex*, and a U-reducible part $\nabla_r - U = \bar{\lambda}_r \bullet \eta_r \bullet \lambda_r - U$:

$$\gamma_r(\omega, \nu, \nu') = M_r(\omega, \nu, \nu') + \bar{\lambda}_r(\omega, \nu) \bullet \eta_r(\omega) \bullet \lambda_r(\omega, \nu') - U. \qquad (3.28)$$

The U-reducible part consists of a product of the *screened interaction* or *bosonic propagator* η_r depending on one frequency and the two *Hedin vertices* $\bar{\lambda}_r$ and λ_r [Hed65], which depend on one bosonic and one fermionic frequency each. Like the Yukawa couplings in the Hubbard–Stratonovich theory (cf. Sec. 3.2), they describe three-point interactions between one exchange boson and two fermions. The product $\bullet$ is defined in analogy to the product $\circ$, Eqs. (4.6), but a summation of frequency degrees of freedom is excluded. Practically, the product $\bar{\lambda}_r \bullet \eta_r \bullet \lambda_r$ contains a part of the third asymptotic class $\mathcal{K}_{3,r}$ and thus offers a more efficient way of saving the corresponding frequency dependence instead of using a huge three-dimensional frequency grid. The SBE decomposition, Eq. (3.28), is supposed to be advantageous compared to the decomposition in asymptotic classes, Eq. (3.27). This is because at criticality the respective susceptibility χ_r and thus η_r is increased, which is directly contained in $\mathcal{K}_{2,r}, \mathcal{K}_{2',r}$ and $\mathcal{K}_{3,r}$ diagrams, but only indirectly in $\bar{\lambda}_r, \lambda_r,$ and M_r diagrams.

U reducibility exists in the three diagrammatic channels $r = a, p, t$. The full four-point

vertex Γ is thus written as

$$\Gamma_{1'2'|12} = [\underbrace{\bar\lambda_a \bullet \eta_a \bullet \lambda_a}_{\nabla_a}]_{1'2'|12} + [\underbrace{\bar\lambda_p \bullet \eta_p \bullet \lambda_p}_{\nabla_p}]_{1'2'|12} + [\underbrace{\bar\lambda_t \bullet \eta_t \bullet \lambda_t}_{\nabla_t}]_{1'2'|12}$$
$$+ [I_U]_{1'2'|12} - 2U_{1'2'|12},$$

(3.29)

Diagrammatically, the bosonic propagator η_r is depicted by a wiggly line and the Hedin vertices $\bar\lambda_r$ and λ_r by triangles. The totally U-irreducible vertex I_U contains the multi-boson vertices M_r and the totally two-particle irreducible rest function $R - U$. As the U-reducible parts ∇_r themselves contain the bare vertex, a subtraction by $2U$ has to be performed to avoid overcounting.

In our paper [P1], we generalize the single-boson exchange formalism for the fermionic action, Eq. (3.1), with generic indices $1', 2', 1, 2$. In this framework, we derive self-consistent equations for the SBE constituents respecting the criterion of U reducibility. We derive multiloop fRG flow equations for the SBE vertices and clarify their relation to the asymptotic classes and three-point correlation functions.

In the main text of this dissertation, we refrain from using the symbol w_r for the bosonic propagator in order to avoid confusion with the bosonic frequency ω_r, and use the notation η_r instead. We also employ a more concise notation for the totally U-irreducible vertex, i.e., I_U instead of $\varphi^{U\mathrm{irr}}$ used in the paper.

Multiloop flow equations for single-boson exchange fRG

by

M. Gievers[1,2], E. Walter[1], A. Ge[1], J. von Delft[1], and F. B. Kugler[3]

[1]Arnold Sommerfeld Center for Theoretical Physics, Center for NanoScience, and

Munich Center for Quantum Science and Technology, Ludwig-Maximilians-Universität

München, 80333 Munich, Germany

[2]Max Planck Institute of Quantum Optics, 85748 Garching, Germany

[3]Department of Physics and Astronomy, Rutgers University, Piscataway, NJ 08854, USA

THE EUROPEAN
PHYSICAL JOURNAL B

Multiloop flow equations for single-boson exchange fRG

Marcel Gievers[1,2], Elias Walter[1], Anxiang Ge[1], Jan von Delft[1], and Fabian B. Kugler[3,a]

[1] Arnold Sommerfeld Center for Theoretical Physics, Center for NanoScience, and Munich Center for Quantum Science and Technology, Ludwig-Maximilians-Universität München, 80333 Munich, Germany
[2] Max Planck Institute of Quantum Optics, Hans-Kopfermann-Straße 1, 85748 Garching, Germany
[3] Department of Physics and Astronomy, Rutgers University, Piscataway, NJ 08854, USA

Abstract. The recently introduced single-boson exchange (SBE) decomposition of the four-point vertex of interacting fermionic many-body systems is a conceptually and computationally appealing parametrization of the vertex. It relies on the notion of reducibility of vertex diagrams with respect to the bare interaction U, instead of a classification based on two-particle reducibility within the widely used parquet decomposition. Here, we re-derive the SBE decomposition in a generalized framework (suitable for extensions to, e.g., inhomogeneous systems or real-frequency treatments) following from the parquet equations. We then derive multiloop functional renormalization group (mfRG) flow equations for the ingredients of this SBE decomposition, both in the parquet approximation, where the fully two-particle irreducible vertex is treated as an input, and in the more restrictive SBE approximation, where this role is taken by the fully U-irreducible vertex. Moreover, we give mfRG flow equations for the popular parametrization of the vertex in terms of asymptotic classes of the two-particle reducible vertices. Since the parquet and SBE decompositions are closely related, their mfRG flow equations are very similar in structure.

1 Introduction

The understanding of strongly correlated many-body systems like the two-dimensional Hubbard model remains an important challenge of contemporary condensed-matter physics [1]. For this, it is desirable to gain profound understanding of two-body interactions which are described by the full four-point vertex Γ.

A powerful technique for calculating the four-point vertex Γ is the functional renormalization group (fRG) [2,3]. There, a scale parameter Λ is introduced into the bare Green's function $G_0 \to G_0^\Lambda$ in such a way that for an initial value $\Lambda \to \Lambda_i$ the theory (specifically, the calculation of the self-energy Σ^Λ and the four-point vertex Γ^Λ) becomes solvable, and after successively integrating out higher energy modes $\Lambda \to \Lambda_f$, the fully renormalized objects Σ and Γ are obtained.

Traditionally, fRG is formulated as an infinite hierarchy of exact flow equations for n-point vertex functions. However, since already the six-point vertex is numerically intractable, truncations are needed. A frequently-used strategy employs a one-loop (1ℓ) truncation of the exact hierarchy of flow equations by completely neglecting six-point and higher vertices. This can be justified,

e.g., from a perturbative [2] or leading-log [4] perspective. Another truncation scheme is given by the multiloop fRG approach, mfRG, which includes all contributions of the six-point vertex to the flow of the four-point vertex and self-energy that can be computed with numerical costs proportional to the 1ℓ flow [5–7]. In doing so, it sums up all parquet diagrams, formally reconstructing the parquet approximation (PA) [8,9] if loop convergence is achieved. Converged multiloop results thus inherit all the properties of the PA. These include self-consistency at the one- and two-particle level (in that the PA is a solution of the self-consistent parquet equations [9]); the validity of one-particle conservation laws (but not of two-particle ones); and the independence of the final results on the choice of regulator (since the parquet equations and PA do not involve specifying any regulator). The mfRG approach was recently applied to the Hubbard model [10,11], Heisenberg models [12,13], and the Anderson impurity model [14].

A full treatment of the frequency and momentum dependence of the four-point vertex generally requires tremendous numerical resources. Hence, it is important to parametrize these dependencies in an efficient way, to reduce computational effort without losing information on important physical properties. One such scheme expresses the vertex as a sum of diagrammatic classes distinguished by their asymptotic frequency behavior [15,16]: Asymptotic classes which remain nonzero when one or two frequency arguments are sent to infinity do

---

Marcel Gievers, Elias Walter and Anxiang Ge contributed equally to this work.

[a] e-mail: kugler@physics.rutgers.edu (corresponding author)

not depend on these arguments, while the class depending on all three frequency arguments decays in each direction.

A related strategy is to express parts of the vertex through fermion bilinears that interact via exchange bosons [17,18]. Partial bosonization schemes, which approximate the vertex through one [19–21] or several boson-exchange channels [22–24], have been employed within the dual boson formalism, used in diagrammatic extensions of dynamical mean field theory (DMFT) aiming to include nonlocal correlations.

A decomposition of the full vertex into single-boson exchange (SBE) parts, involving functions of at most two frequencies, and residual parts depending on three frequencies was developed in Refs. [25–30]. The guiding principle of the SBE decomposition is reducibility in the bare interaction U [25]. This criterion distinguishes SBE contributions, that are U-reducible, from multiboson exchange and other contributions, that are not. The SBE *approximation* retains only the U-reducible part while neglecting all U-irreducible terms [26]. The SBE terms are expressible through bosonic fluctuations and their (Yukawa) couplings to fermions—the Hedin vertices—and thus have a transparent physical interpretation. Numerically, two- and three-point objects can be computed and stored more easily than a genuine four-point vertex.

Studies of the two-dimensional Hubbard model have shown that the SBE decomposition is a promising technique for computing the frequency and momentum dependences of the vertex [28–30]. In a 1ℓ fRG calculation, it was found that some of its essential features are already captured by its U-reducible parts, which are much easier to compute numerically than the U-irreducible ones [31]. Reference [31] also obtained results at strong interaction using DMF^{2}RG, a method that makes use of a DMFT vertex as the starting point for the fRG flow [32–34]. Here, a very interesting aspect of the SBE decomposition is that the SBE approximation (neglecting U-irreducible contributions) remains a meaningful approximation also in the strong-coupling regime [35], which is not the case for a similar approximation scheme based on the parametrization through asymptotic classes while using functions of at most two frequency arguments.

Given these encouraging developments, it is of interest to have a strategy for computing the ingredients of the SBE approach—the bosonic propagators, the Hedin vertices, and the remaining U-irreducible terms—not only in 1ℓ fRG [31] but also in mfRG. In this paper, we therefore derive multiloop flow equations for the SBE ingredients. To this end, we start from the parquet equations to derive a general form of the SBE decomposition where the structure of non-frequency arguments is not specified. We then derive multiloop flow equations for the SBE ingredients, and finally illustrate the relation of these objects to the parametrization of the vertex in terms of two-particle reducible asymptotic classes [16,31]. The numerical implementation of the resulting

SBE multiloop flow equations goes beyond the scope of this purely analytical paper and is left for the future.

The paper is organized as follows: In Sect. 2, we recapitulate the parquet equations, the corresponding mfRG flow equations, and the frequency parametrization of the four-point vertex adapted to each two-particle channel. In Sect. 3, we deduce the SBE decomposition from the parquet equations and derive multiloop flow equations for the SBE ingredients in two different ways. We also discuss the SBE approximation and its associated mfRG flow. In Sect. 4, we recall the definition of the asymptotic vertex classes and derive multiloop equations for these. We outline the relation between SBE ingredients and asymptotic classes and their respective mfRG equations. We conclude with a short outlook in Sect. 5. Appendices A and B illustrate the SBE ingredients and asymptotic vertex classes diagrammatically, while Appendix C describes the relation between our generalized notation of the SBE decomposition to that of the original papers. Finally, Appendices D and E give details on different definitions of correlators and susceptibilities and show their close relation to the SBE ingredients.

2 Recap of parquet and mfRG equations

The parquet equations and the associated multiloop fRG equations form the basis for the main outcomes of this paper. For ease of reference and use in future sections, we recapitulate the notational conventions and compactly summarize the main ingredients and results of the mfRG approach [5–7]. To make the presentation self-contained, we also recall from the literature the motivation for some of the definitions and conventions presented below.

2.1 Parquet equations

The action of a typical fermionic model reads

$$S = -\bar{c}_{1'}[G_0^{-1}]_{1'|1}c_1 - \tfrac{1}{4}U_{1'2'|12}\,\bar{c}_{1'}\bar{c}_{2'}c_2 c_1, \quad (1)$$

with the bare propagator G_0. The Grassmann fields c_i are labeled by a composite index i describing frequency and other quantum numbers, such as position or momentum, spin, etc. Throughout this paper, repeated i-indices are understood to be integrated over or summed over. Furthermore, U is the crossing symmetric bare interaction vertex, $U_{1'2'|12} = -U_{2'1'|12}$ (called Γ_0 in Refs. [6,7]). We assume it to be energy-conserving without further frequency dependence, as in any action derived directly from a time-independent Hamiltonian. Our expression for the action (1) and later definitions of correlation functions are given in the Matsubara formalism [36] and for fermionic fields. However, our analysis can easily be transcribed to the Keldysh formalism [37], and/or to bosonic fields, by suitably adapting the content of the index i on c_i and adjust-

ing some prefactors. Such changes do not modify the structure of the vertex decomposition and flow equations that are the focus of this paper.

The time-ordered one- and two-particle correlators, $G_{1|1'} = -\langle c_1 \bar{c}_{1'} \rangle$ and $G^{(4)}_{12|1'2'} = \langle c_1 c_2 \bar{c}_{2'} \bar{c}_{1'} \rangle$, can be expressed in standard fashion [3] through the self-energy and the four-point vertex,

$$\Sigma_{1'|1} = \;{}^{1'}\!\!\blacktriangleleft\!\!\bigcirc\!\!{\Sigma}\!\!\blacktriangleleft\!\!{}^{1} \;, \quad \Gamma_{1'2'|12} = \begin{array}{c} {}^{2}\searrow \quad \nearrow {}^{2'} \\ \boxed{\Gamma} \\ {}_{1'}\nearrow \quad \searrow{}_{1} \end{array}. \tag{2}$$

These contain all one-particle irreducible one- and two-particle vertex diagrams, respectively. Hence, these are (amputated connected) diagrams that cannot be split into two pieces by cutting a single bare propagator line.

The one-particle self-energy is related to the two-particle vertex via the Schwinger–Dyson equation (SDE) [9]. We do not discuss this equation much further because its treatment is similar for both vertex decompositions discussed below. On the two-particle level, the starting point of parquet approaches [9] is the parquet decomposition,

$$\Gamma = R + \gamma_a + \gamma_p + \gamma_t. \tag{3}$$

It states that the set of all vertex diagrams can be divided into four disjoint classes: the diagrams in γ_r, $r = a, p, t$, are two-particle reducible in channel r, i.e., they can be split into two parts by cutting two antiparallel (a), parallel (p), or transverse antiparallel (t) propagator lines, respectively. The diagrams in R do not fall apart by cutting two propagator lines and are thus fully two-particle irreducible. This classification is exact and unambiguous [16,38]. In the literature, the diagrammatic channels are also known as crossed particle–hole $(\overline{\text{ph}} \leftrightarrow a)$, particle–particle $(\text{pp} \leftrightarrow p)$, and particle–hole $(\text{ph} \leftrightarrow t)$ channel.

Since the four classes in the parquet decomposition are disjoint, one can decompose Γ w.r.t. its two-particle reducibility in one of the channels r, $\Gamma = I_r + \gamma_r$. Here, I_r comprises the sum of all diagrams irreducible in channel r and fulfills $I_r = R + \gamma_{\bar{r}}$ with $\gamma_{\bar{r}} = \sum_{r' \neq r} \gamma_{r'}$. The Bethe–Salpeter equations (BSEs) relate the reducible diagrams to the irreducible ones and can be summarized by

$$\gamma_r = I_r \circ \Pi_r \circ \Gamma = \Gamma \circ \Pi_r \circ I_r. \tag{4}$$

The Π_r *bubble*, defined as

$$\Pi_{a;34|3'4'} = G_{3|3'}G_{4|4'}, \tag{5a}$$

$$\Pi_{p;34|3'4'} = \tfrac{1}{2}G_{3|3'}G_{4|4'}, \tag{5b}$$

$$\Pi_{t;43|3'4'} = -G_{3|3'}G_{4|4'}, \tag{5c}$$

represents the corresponding propagator pair in channel r, see Fig. 1. (Note that $\Pi_{a;34|3'4'} = -\Pi_{t;43|3'4'}$
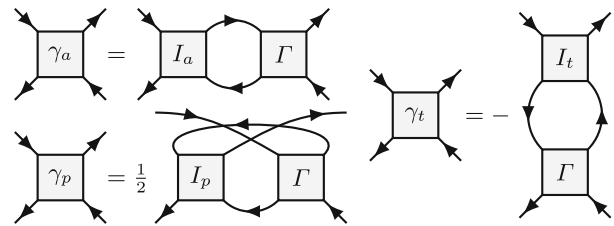
Fig. 1 Bethe–Salpeter equations in the antiparallel (a), parallel (p) and transverse (t) channels

is consistent with crossing symmetry.) The connector symbol $\circ$ denotes summation over internal frequencies and quantum numbers $(5, 6$ in Eqs. (6) below) and its definition depends on the channel $r \in \{a, p, t\}$: When connecting Π_r (or other four-leg objects labeled by r) to some vertex, it gives

$$a: \quad [A \circ B]_{12|34} = A_{16|54}B_{52|36}, \tag{6a}$$

$$p: \quad [A \circ B]_{12|34} = A_{12|56}B_{56|34}, \tag{6b}$$

$$t: \quad [A \circ B]_{12|34} = A_{62|54}B_{15|36}. \tag{6c}$$

By combining $\Gamma = I_r + \gamma_r$ with the BSEs (4), one can eliminate γ_r to get the "extended BSEs" [7] needed later:

$$\mathbb{1}_r + \Pi_r \circ \Gamma = (\mathbb{1}_r - \Pi_r \circ I_r)^{-1}, \tag{7a}$$

$$\mathbb{1}_r + \Gamma \circ \Pi_r = (\mathbb{1}_r - I_r \circ \Pi_r)^{-1}. \tag{7b}$$

Here, the channel-specific unit vertices $\mathbb{1}_r$, defined by the requirement $\Gamma = \mathbb{1}_r \circ \Gamma = \Gamma \circ \mathbb{1}_r$, are given by

$$\mathbb{1}_{a;12|34} = \delta_{13}\delta_{24}, \tag{8a}$$

$$\mathbb{1}_{p;12|34} = \tfrac{1}{2}(\delta_{13}\delta_{24} - \delta_{14}\delta_{23}), \tag{8b}$$

$$\mathbb{1}_{t;12|34} = \delta_{14}\delta_{23}. \tag{8c}$$

(For the p channel, the internal sum in $\mathbb{1}_p \circ \Gamma = \Gamma \circ \mathbb{1}_p$ runs over both outgoing (or ingoing) legs of Γ. Therefore, the crossing symmetry of the vertex, i.e., $\Gamma_{12|34} = -\Gamma_{21|34} = -\Gamma_{12|43}$, is transferred to $\mathbb{1}_p$, resulting in an expression more involved than for the other two channels.)

The combination of the Dyson equation $G = G_0(1 + \Sigma G)$, the SDE, the parquet decomposition (3), the three BSEs (4), and the definitions $I_r = \Gamma - \gamma_r$ constitutes the self-consistent *parquet equations*. The only truly independent object is the fully irreducible vertex R. If R is specified, everything else can be computed self-consistently via the parquet equations. However, R is the most complicated object: its diagrams contain several nested integrals/sums over internal arguments, whereas the integrals in reducible diagrams partially factorize. A common simplification, the *parquet approximation* (PA), replaces R by U, closing the set of parquet equations.

2.2 Parquet mfRG

The conventional mfRG flow equations can be derived from the parquet equations by introducing a regulator Λ into the bare propagator G_0, thus making all objects in the parquet equations Λ-dependent [7]. The fully irreducible vertex R is treated as an input and is thus assumed to be Λ-independent, $R^\Lambda \approx R$. For instance, this assumption arises both in the PA where $R \approx U$ or in the dynamical vertex approximation DΓA [39,40] where $R \approx R^{\mathrm{DMFT}}$ is taken from DMFT—here, we will not distinguish these cases explicitly. Taking the derivative of the SDE and the BSEs w.r.t. Λ then yields flow equations for Σ and Γ. Within the context of this paper, we will call this mfRG approach *parquet mfRG*, to distinguish it from an *SBE mfRG* approach to be discussed in Sect. 3.2.

When computing $\dot{\gamma}_r = \partial_\Lambda \gamma_r$ via the BSEs, one obtains terms including $\dot{I}_r = \sum_{r' \neq r} \dot{\gamma}_{r'}$. Thus, one has to iteratively insert the flow equation for γ_r into the equations of the other channels $r' \neq r$, yielding an infinite set of contributions of increasing *loop order*:

$$\dot{\Gamma} = \dot{\gamma}_a + \dot{\gamma}_p + \dot{\gamma}_t, \qquad \dot{\gamma}_r = \sum_{\ell=1}^{\infty} \dot{\gamma}_r^{(\ell)}. \tag{9}$$

The individual ℓ-loop contributions read [5,7]

$$\dot{\gamma}_r^{(1)} = \Gamma \circ \dot{\Pi}_r \circ \Gamma, \tag{10a}$$

$$\dot{\gamma}_r^{(2)} = \dot{\gamma}_{\bar{r}}^{(1)} \circ \Pi_r \circ \Gamma + \Gamma \circ \Pi_r \circ \dot{\gamma}_{\bar{r}}^{(1)} \tag{10b}$$

$$\dot{\gamma}_r^{(\ell+2)} = \dot{\gamma}_{\bar{r}}^{(\ell+1)} \circ \Pi_r \circ \Gamma + \Gamma \circ \Pi_r \circ \dot{\gamma}_{\bar{r}}^{(\ell)} \circ \Pi_r \circ \Gamma$$
$$+ \Gamma \circ \Pi_r \circ \dot{\gamma}_{\bar{r}}^{(\ell+1)}. \tag{10c}$$

where $\dot{\gamma}_{\bar{r}}^{(\ell)} = \sum_{r' \neq r} \dot{\gamma}_{r'}^{(\ell)}$ and Eq. (10c) applies for $\ell+2 \geq 3$. In general, all terms at loop order ℓ contain $\ell - 1$ factors of Π and one $\dot{\Pi}$ (i.e., ℓ loops, one of which is differentiated), connecting ℓ renormalized vertices Γ. We have $\dot{\Pi}_r \sim G\dot{G} + \dot{G}G$, where

$$\dot{G} = S + G \dot{\Sigma} G, \tag{11}$$

with the single-scale propagator $S = \dot{G}|_{\Sigma=\mathrm{const}}$. Figure 2 illustrates Eqs. (10) diagrammatically in the a channel.

The flow equation for the self-energy, derived in Ref. [7] by requiring Σ to satisfy the SDE throughout the flow, reads
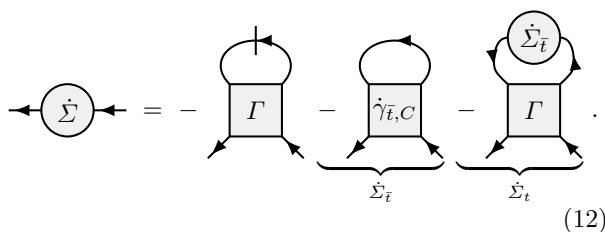
$$\tag{12}$$
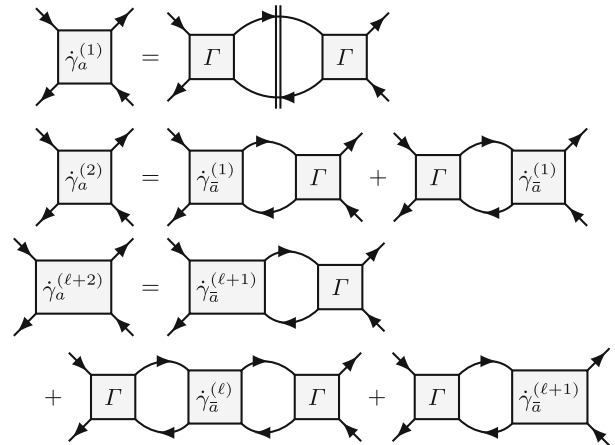
Fig. 2 Diagrammatic depiction of the mfRG flow equations (10) in the a channel. The double-dashed bubble $\dot{\Pi}_a$ represents a sum of two terms, $G\dot{G} + \dot{G}G$, where double-dashed propagators $\dot{G}$ are fully differentiated ones (cf. Eq. (11))

It has Γ and $\dot{\gamma}_{\bar{t},C} = \sum_\ell \Gamma \circ \Pi_r \circ \dot{\gamma}_{\bar{t}}^{(\ell)} \circ \Pi_r \circ \Gamma$ as input and holds irrespective of the choice of vertex parametrization. For this reason, we do not discuss the self-energy flow further in this paper, but it should of course be implemented for numerical work.

The 1ℓ contribution (10a) of the vertex flow, with the fully differentiated $\dot{G}$ replaced by the single-scale propagator S in $\dot{\Pi}_r$ is equivalent to the usual 1ℓ flow equation. Using $\dot{G}$ instead of S, as done in Eq. (10a), corresponds to the so-called Katanin substitution [41]: it contains the feedback of the differentiated self-energy into the vertex flow and already goes beyond the standard 1ℓ approximation. By adding higher-loop contributions until convergence is reached, one effectively solves the self-consistent parquet equations through an fRG flow. On the one hand, this ensures two-particle self-consistency and related properties mentioned in the introduction. On the other hand, it also provides a way of reaching a solution of the parquet equations by integrating differential equations. This may be numerically favorable compared to an iteration of the self-consistent equations. Particularly, when computing diagrammatic extensions of DMFT via DMF^{2}RG, one then needs only the *full* DMFT vertex as an input, and not the r-(ir)reducible ones entering the parquet equations. This is helpful in the Matsubara formalism, where the r-(ir)reducible vertices sometimes exhibit divergences [42–46], and even more so when aiming for real-frequency approaches [47,48].

2.3 Frequency parametrization

The four-point vertex Γ is a highly complicated object and must be parametrized efficiently. In this section, we summarize the frequency parametrization of the vertex adapted to the three diagrammatic channels.
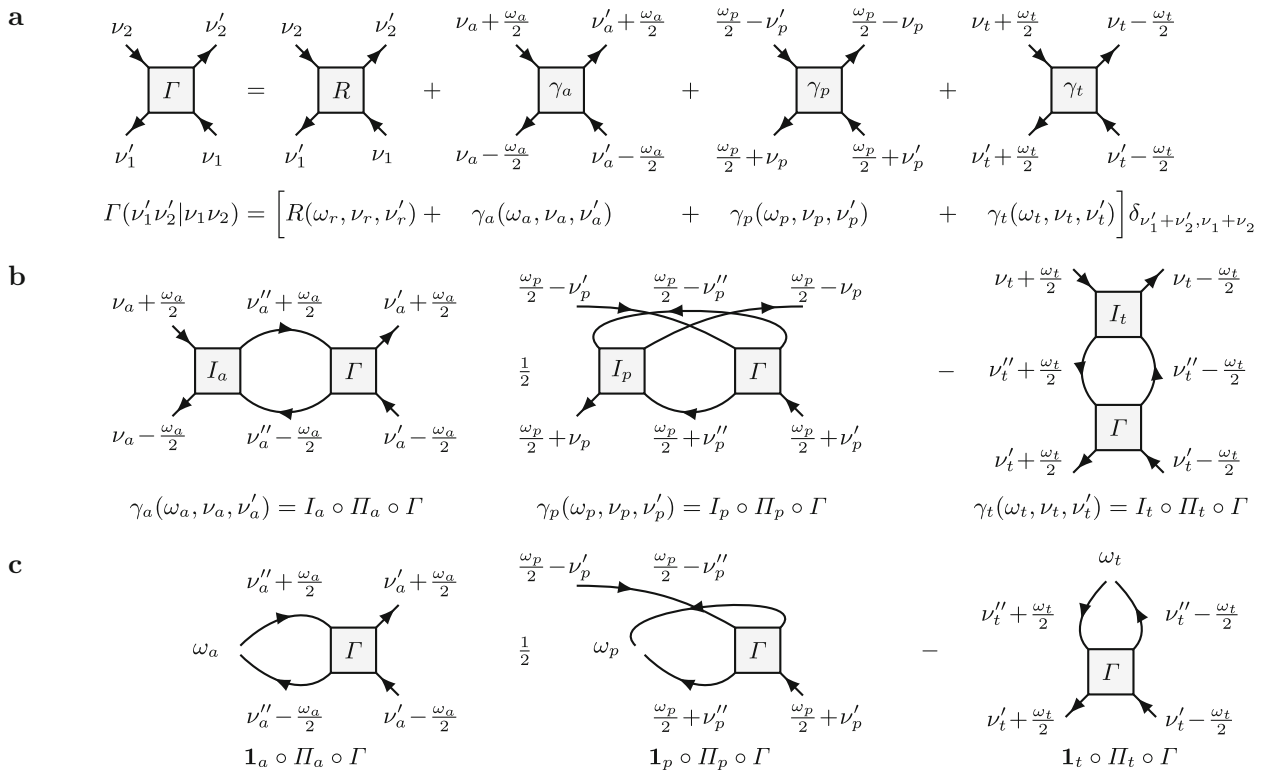
Fig. 3 Definition of the three channel-specific frequency parametrizations of the four-point vertex. **a** The vertex is nonzero only if the four fermionic frequencies satisfy $\nu_1' + \nu_2' = \nu_1 + \nu_2$. In that case, they can be expressed in three different ways through one bosonic transfer frequency, ω_r, and two fermionic frequencies, ν_r, ν_r'. Of course, each term can also be expressed through the frequencies $(\omega_r, \nu_r, \nu_r')$ of any of the three channels, as indicated here for R. **b** The choice of frequency arguments in each channel γ_a, γ_p, and γ_t is motivated by the structure of their BSEs (4). **c** Diagrammatic depiction of $\mathbf{1}_r \circ \Pi_r \circ \Gamma = \sum_{\nu_r''} \Pi_r \bullet \Gamma$ (Eqs. (22), third line), a four-leg object obtained by inserting $\mathbf{1}_r$ between U and Π_r (Eq. (21c)). The multiplication of $\mathbf{1}_r \circ$ onto $\Pi_r \circ \Gamma$ carries two instructions: draw Π_r such that the endpoints of the lines connected to $\mathbf{1}_r$ lie close together (awaiting being connected to U), and perform the sum over the fermionic frequency ν_r'' of Π_r

This parametrization is the building block for the SBE decomposition discussed in Sect. 3.

Focusing on the frequency dependence, we switch from the compact notation $\Gamma_{1'2'|12}$ to the more elaborate $\Gamma_{1'2'|12}(\nu_1'\nu_2'|\nu_1\nu_2)$, with frequency arguments written in brackets, and the subscripts now referring to non-frequency quantum numbers (position or momentum, spin, etc.). As mentioned earlier, we assume the bare vertex U to have the form

$$U_{1'2'|12}(\nu_1'\nu_2'|\nu_1\nu_2) = \delta_{\nu_1'+\nu_2',\nu_1+\nu_2} U_{1'2'|12}, \quad (13)$$

with $U_{1'2'|12}$ independent of frequency. If U is momentum-conserving without further momentum dependence, our treatment of frequency sums below may be extended to include momentum sums. To keep the discussion general, we refrain from elaborating this in detail. Note that, e.g., in the repulsive Hubbard model, our sign convention in Eq. (1) is such that $U^{\sigma\bar{\sigma}|\sigma\bar{\sigma}} = -U^{\bar{\sigma}\sigma|\sigma\bar{\sigma}} < 0$ (where, as usual, $\sigma \in \{\uparrow,\downarrow\}$, $\bar{\uparrow} = \downarrow$, $\bar{\downarrow} = \uparrow$).

Due to frequency conservation, one-particle correlators depend on only one frequency,

$$G_{1'1}(\nu_1',\nu_1) = \delta_{\nu_1',\nu_1} G_{1'1}(\nu_1). \quad (14)$$

Likewise, three frequencies are sufficient to parametrize the vertex. For each channel γ_r, we express the four fermionic frequencies $\nu_1', \nu_2', \nu_1, \nu_2$ at the vertex legs through a choice of three frequencies, a bosonic transfer frequency, ω_r, and two fermionic frequencies, ν_r and ν_r'. These are chosen differently for each channel (see Fig. 3a) and reflect its asymptotic behavior [16] as discussed in Sect. 4.1. We have

$$\gamma_{r;1'2'|12}(\nu_1'\nu_2'|\nu_1\nu_2) = \delta_{\nu_1'+\nu_2',\nu_1+\nu_2}\gamma_{r;1'2'|12}(\omega_r,\nu_r,\nu_r'), \quad (15)$$

with ω_r, ν_r, ν_r' related to ν_1', ν_1, ν_2 through

$$\begin{aligned}
\nu_1' &= \nu_a - \tfrac{\omega_a}{2} = \nu_p + \tfrac{\omega_p}{2} = \nu_t' + \tfrac{\omega_t}{2}, \\
\nu_1 &= \nu_a' - \tfrac{\omega_a}{2} = \nu_p' + \tfrac{\omega_p}{2} = \nu_t' - \tfrac{\omega_t}{2}, \\
\nu_2 &= \nu_a + \tfrac{\omega_a}{2} = -\nu_p' + \tfrac{\omega_p}{2} = \nu_t + \tfrac{\omega_t}{2}.
\end{aligned} \quad (16)$$

This parametrization symmetrically assigns $\pm\frac{\omega_r}{2}$ shifts to all external legs. (In the Matsubara formalism, the bosonic Matsubara frequency closest to $\pm\frac{\omega_r}{2}$ is chosen for the shift.) With these shifts, crossing symmetries ensure that prominent vertex peaks are centered around $\omega_r = 0$, which is convenient for numerical work. However, other conventions are of course possible, too.

Though the frequencies ω_r, ν_r, ν'_r are tailored to a specific channel γ_r, one may also use them to define the r parametrization of the full vertex, writing

$$\Gamma_{1'2'|12}(\nu'_1\nu'_2|\nu_1\nu_2) = \delta_{\nu'_1+\nu'_2,\nu_1+\nu_2}\Gamma_{1'2'|12}(\omega_r,\nu_r,\nu'_r). \tag{17}$$

Likewise, $R, \gamma_a, \gamma_p, \gamma_t$ can each be expressed as a δ symbol times a function of any of the variable sets $(\omega_r, \nu_r, \nu'_r)$. The r parametrization of $\Gamma \circ \Pi_r$ or $\Pi_r \circ \Gamma$ is obtained by inserting Eqs. (14) and (17) into Eqs. (6). The summations $\sum_{\nu_5\nu_6}$ over internal frequencies can be collapsed using frequency-conserving δ symbols, leading to

$$[\Gamma \circ \Pi_r](\omega_r, \nu_r, \nu''_r) = \Gamma(\omega_r, \nu_r, \nu''_r) \bullet \Pi(\omega_r, \nu''_r), \quad \text{(18a)}$$

$$[\Pi_r \circ \Gamma](\omega_r, \nu''_r, \nu'_r) = \Pi(\omega_r, \nu''_r) \bullet \Gamma(\omega_r, \nu''_r, \nu'_r), \quad \text{(18b)}$$

where the bubble factors $\Pi_r(\omega_r, \nu''_r)$ are given by

$$\Pi_{a;34|3'4'}(\omega_a, \nu''_a) = G_{3|3'}\big(\nu''_a - \tfrac{\omega_a}{2}\big)G_{4|4'}\big(\nu''_a + \tfrac{\omega_a}{2}\big), \quad \text{(19a)}$$

$$\Pi_{p;34|3'4'}(\omega_p, \nu''_p) = \tfrac{1}{2}G_{3|3'}\big(\tfrac{\omega_p}{2} + \nu''_p\big)G_{4|4'}\big(\tfrac{\omega_p}{2} - \nu''_p\big), \quad \text{(19b)}$$

$$\Pi_{t;43|3'4'}(\omega_t, \nu''_t) = -G_{3|3'}\big(\nu''_t - \tfrac{\omega_t}{2}\big)G_{4|4'}\big(\nu''_t + \tfrac{\omega_t}{2}\big). \quad \text{(19c)}$$

In Eqs. (18), the connector $\bullet$ by definition denotes an internal summation analogous to $\circ$, except that only non-frequency quantum numbers (position, spin, etc.) are summed over. Correspondingly, the bubble $\tilde{\Gamma} \circ \Pi_r \circ \Gamma$, involving two $\circ$ connectors, has the r parametrization

$$\begin{aligned}
&[\tilde{\Gamma} \circ \Pi_r \circ \Gamma](\omega_r, \nu_r, \nu'_r) \\
&= \sum_{\nu''_r} \tilde{\Gamma}(\omega_r, \nu_r, \nu''_r) \bullet \Pi_r(\omega_r, \nu''_r) \bullet \Gamma(\omega_r, \nu''_r, \nu'_r), \quad \text{(20)}
\end{aligned}$$

see Fig. 3b. Here, one frequency sum survives, running over the fermionic frequency ν''_r associated with Π_r.

For future reference, we define unit vertices for non-frequency quantum numbers, $\mathbf{1}_r$, by $\Gamma = \mathbf{1}_r \bullet \Gamma = \Gamma \bullet \mathbf{1}_r$. (For a bare vertex with momentum conservation and no further momentum dependence, one could include a momentum sum, $\sum_{k''_r}$, in Eq. (20) and exclude momentum indices from the $\bullet$ summation and $\mathbf{1}_r$.) The distinction between $\circ$, $\mathbb{1}$ and $\bullet$, $\mathbf{1}$, indicating if connectors and unit vertices include summations and δ symbols for frequency variables or not, will be needed for the SBE decomposition of Sect. 3. There, we will encounter bubbles involving one or two bare vertices, $U \circ \Pi_r \circ U$, $\tilde{\Gamma} \circ \Pi_r \circ U$, or $U \circ \Pi_r \circ \Gamma$. Expressing these in the form (20), the bare vertex U, since it is frequency independent, can be pulled out of the sum over ν''_r. To make

this explicit, we insert unit operators $\mathbf{1}_r$ next to U:

$$U \circ \Pi_r \circ U = U \bullet \mathbf{1}_r \circ \Pi_r \circ \mathbf{1}_r \bullet U, \quad \text{(21a)}$$

$$\tilde{\Gamma} \circ \Pi_r \circ U = \tilde{\Gamma} \circ \Pi_r \circ \mathbf{1}_r \bullet U, \quad \text{(21b)}$$

$$U \circ \Pi_r \circ \Gamma = U \bullet \mathbf{1}_r \circ \Pi_r \circ \Gamma. \quad \text{(21c)}$$

We suppressed frequency arguments for brevity, it being understood that equations linking Π_r and $\mathbf{1}_r$ use the r parametrization. Making the frequency sum involved in $\circ \Pi_r \circ$ explicit, we obtain four-leg objects,

$$\begin{aligned}
[\mathbf{1}_r \circ \Pi_r \circ \mathbf{1}_r](\omega_r) &= \sum_{\nu''_r} \Pi_r(\omega_r, \nu''_r), \\
[\tilde{\Gamma} \circ \Pi_r \circ \mathbf{1}_r](\omega_r, \nu_r) &= \sum_{\nu''_r} \tilde{\Gamma}(\omega_r, \nu_r, \nu''_r) \bullet \Pi_r(\omega_r, \nu''_r), \\
[\mathbf{1}_r \circ \Pi_r \circ \Gamma](\omega_r, \nu'_r) &= \sum_{\nu''_r} \Pi_r(\omega_r, \nu''_r) \bullet \Gamma(\omega_r, \nu''_r, \nu'_r)
\end{aligned}$$
$$\text{(22)}$$

that depend on only one or two frequency arguments (cf. Figure 3c) and are thus numerically cheaper than Γ. Note that, in general, $\mathbf{1}_r$ is not the unit operator w.r.t. the $\circ$ connector, i.e., $\mathbf{1}_r \circ \Gamma \neq \Gamma \neq \Gamma \circ \mathbf{1}_r$ since $\circ$ involves a frequency summation which does not affect $\mathbf{1}_r$.

3 SBE decomposition

We now turn to the SBE decomposition. It also yields an exact, unambiguous classification of vertex diagrams, now according to their U-reducibility in each channel. This notion of reducibility, introduced in Ref. [26], is very analogous to Π-reducibility, i.e., two-particle reducibility. A diagram is called U-reducible if it can be split into two parts by splitting apart a bare vertex U (in ways specified below) in either of the three channels. Otherwise, it is fully U-irreducible.

The SBE decomposition was originally formulated in terms of physical (charge, spin, and singlet pairing) channels which involve linear combinations of spin components. For our purposes, it is more convenient not to use such linear combinations (the relation between both formulations is given in Appendix C). Moreover, the original SBE papers considered models with translational invariance, with vertices labeled by three momentum variables. We here present a generalization of the SBE decomposition applicable to models without translational invariance, requiring four position or momentum labels. Starting from the BSEs, we use arguments inspired by Ref. [26] to arrive at a set of self-consistent equations for SBE ingredients which will also enable us to derive multiloop flow equations directly within this framework. In terms of notation, we follow Ref. [26] for the objects $\nabla_r, w_r, \bar{\lambda}_r, \lambda_r$—with φ^{irr} there denoted $\varphi^{U\text{irr}}$ here—while we follow Ref. [30] for M_r and T_r (the latter instead of φ_r from Ref. [26]).
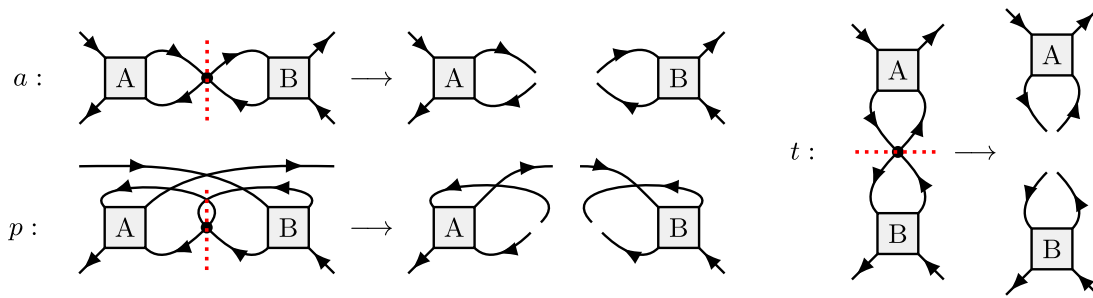
Fig. 4 Illustration of U-r-reducibility, analogous to Fig. 4 of [26]. A and B can be any vertex diagram or simply $\mathbb{1}_r$

3.1 Derivation of SBE decomposition from BSEs

As mentioned earlier, a vertex diagram is called two-particle reducible in a specified channel $r \in \{a, p, t\}$, or Π-r-reducible for short, if it can be split into two parts by cutting the two lines of a Π_r bubble (to be called *linking bubble*); if such a split is not possible, the diagram is Π-r-irreducible. The two-particle reducible vertex γ_r is the sum of all Π-r-reducible diagrams. Following Ref. [26], we now introduce a further channel-specific classification criterion. A Π-r-reducible diagram is called U-r-reducible if a linking bubble Π_r has two of its legs attached to the same bare vertex in the combination $U \circ \Pi_r$ or $\Pi_r \circ U$. Then, that bare vertex U, too, constitutes a link that, when "cut out", splits the diagram into two parts. (To visualize the meaning of "cutting out U" diagrammatically, one may replace U by $\mathbb{1}_r \bullet U \bullet \mathbb{1}_r$ and then remove U. This results in two pairs of legs ending close together, ready to be connected through reinsertion of U, see Figs. 3c and 4.) The lowest order U-r-reducible contribution to γ_r is $U \circ \Pi_r \circ U$. The lowest-order term of Γ, the bare vertex U (which is Π-r-irreducible), is viewed as U-r-reducible in all three channels, corresponding to the three possible ways of splitting its four legs into two pairs of two. All U-r-reducible diagrams describe "single-boson exchange" processes, in the sense that each link U connecting two otherwise separate parts of the diagram mediates a single bosonic transfer frequency, ω_r (as defined in Fig. 3), across that link, as will become explicit below.

All vertex diagrams that are not U-r-reducible are called U-r-irreducible. These comprise all multi-boson exchange (i.e., *not* single-boson exchange) diagrams from γ_r, and all Π-r-irreducible diagrams except the bare vertex (which is trivially U-r-reducible), i.e., all diagrams from $I_r - U = R - U + \sum_{r' \neq r} \gamma_{r'}$.

Next, we rewrite the parquet equations in terms of U-r-reducible and U-r-irreducible parts. We define ∇_r as the sum of all U-r-reducible diagrams, including (importantly) the bare vertex U, and M_r as the sum of all diagrams that are Π-r-reducible but U-r-irreducible, thus describing multi-boson exchange processes. Then, the Π-r-reducible vertex γ_r, which does not include U, fulfills

$$\gamma_r = \nabla_r - U + M_r. \tag{23}$$

Inserting Eq. (23) for γ_r into the parquet decomposition (3) yields

$$\Gamma = \varphi^{U\mathrm{irr}} + \sum_r \nabla_r - 2U, \tag{24a}$$
$$\varphi^{U\mathrm{irr}} = R - U + \sum_r M_r, \tag{24b}$$

where $\varphi^{U\mathrm{irr}}$ is the fully U-irreducible part of Γ. The U subtractions ensure that the bare vertex U, which is contained once in each ∇_r but not in $\varphi^{U\mathrm{irr}}$, is not over-counted. Some low-order diagrams of ∇_r, M_r, and R are shown in Fig. 5.

Just as γ_r, its parts ∇_r and M_r satisfy Bethe–Salpeter-type equations, which we derive next. Inserting Eq. (23) into the full vertex $\Gamma = I_r + \gamma_r$, we split it into a U-r-reducible part, ∇_r, and a U-r-irreducible remainder, T_r:

$$\Gamma = \nabla_r + T_r, \tag{25a}$$
$$T_r = I_r - U + M_r. \tag{25b}$$

The relation between the different decompositions of the full vertex implied by Eqs. (23)–(25) is illustrated in Fig. 6. Inserting Eqs. (23) and (25a) into either of the two forms of the BSEs (4) for γ_r, we obtain

$$\nabla_r - U + M_r = I_r \circ \Pi_r \circ \nabla_r + I_r \circ \Pi_r \circ T_r$$
$$= \nabla_r \circ \Pi_r \circ I_r + T_r \circ \Pi_r \circ I_r. \tag{26}$$

This single set of equations can be split into two separate ones, one for $\nabla_r - U$, the other for M_r, containing only U-r-reducible or only U-r-irreducible terms, respectively. The first terms on the right are clearly U-r-reducible, since they contain ∇_r. For the second terms on the right, we write I_r as the sum of U and $I_r - U$, yielding U-r-reducible and U-r-irreducible contributions, respectively. We thus obtain two separate sets of equations,
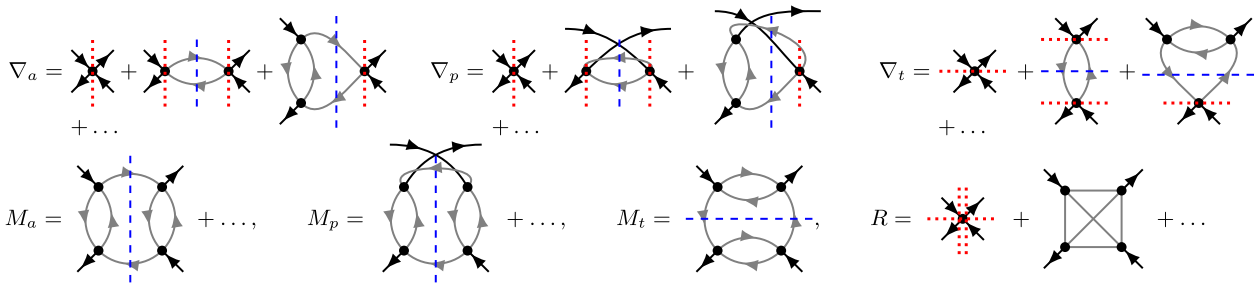
$$\nabla_r - U = I_r \circ \Pi_r \circ \nabla_r + U \circ \Pi_r \circ T_r$$
$$= \nabla_r \circ \Pi_r \circ I_r + T_r \circ \Pi_r \circ U, \tag{27}$$
$$M_r = (I_r - U) \circ \Pi_r \circ T_r$$
$$= T_r \circ \Pi_r \circ (I_r - U), \tag{28}$$

the latter of which corresponds to Eq. (17) in Ref. [30]. In Eqs. (27), we now bring all ∇_r contributions to the

Fig. 5 Low-order diagrams for ∇_r, M_r, and R, illustrating Π-r-reducibility (blue dashed lines) and U-r-reducibility (red dotted lines; their meaning is made explicit in Fig. 4). ∇_r contains all U-r-reducible diagrams; except for the bare vertex, they all are Π-r-reducible, too. M_a contains all diagrams that are Π-a- but not U-a-reducible. All diagrams in R are neither Π-r- nor U-r-reducible, except for the bare vertex, which is U-a-, U-p- and U-t-reducible (as indicated by three red dotted lines)
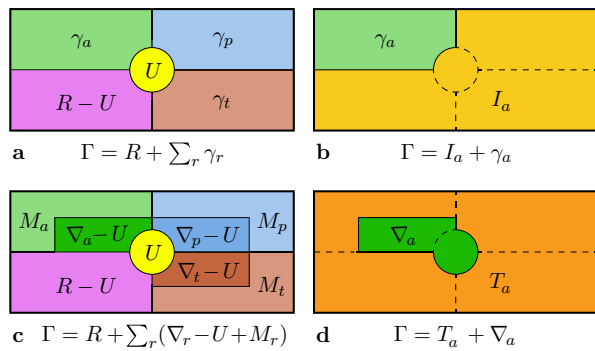
Fig. 6 Venn diagrams illustrating various ways of splitting the full vertex into distinct contributions. Panel **a** depicts the parquet decomposition (3), **b** the Π-a-reducible part γ_a and its complement I_a, **c** the SBE decomposition (24) (mimicking Fig. 6 of [26]), and **d** the U-a-reducible part ∇_a and its complement T_a. For $r = p, t$, the Π-r- and U-r-reducible parts and their complements can be depicted analogously

left,

$$(\mathbb{1}_r - I_r \circ \Pi_r) \circ \nabla_r = U \circ (\mathbb{1}_r + \Pi_r \circ T_r),$$
$$\nabla_r \circ (\mathbb{1}_r - \Pi_r \circ I_r) = (\mathbb{1}_r + T_r \circ \Pi_r) \circ U, \quad (29)$$

and solve for ∇_r by evoking the extended BSEs (7):

$$\nabla_r = (\mathbb{1}_r + \Gamma \circ \Pi_r) \circ U \circ (\mathbb{1}_r + \Pi_r \circ T_r)$$
$$= (\mathbb{1}_r + T_r \circ \Pi_r) \circ U \circ (\mathbb{1}_r + \Pi_r \circ \Gamma). \quad (30)$$

This directly exhibits the U-r-reducibility of ∇_r.

We now adopt the r parametrization and note a key structural feature of Eq. (30) for ∇_r: it contains a central bare vertex U, connected via $\circ \Pi_r \circ$ to either Γ or T_r or both. We may thus pull the frequency-independent U out of the frequency summations, so that $\circ \Pi_r \circ$ leads to $\bullet \mathbb{1}_r \circ \Pi_r \circ$ or $\circ \Pi_r \circ \mathbb{1}_r \bullet$, where the multiplication with $\mathbb{1}_r$ includes a sum over an internal fermionic frequency (recall Eqs. (21), (22) and Fig. 3).
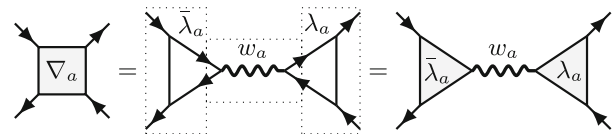
Fig. 7 Diagrammatic depiction of Eq. (33) (exemplified for the a channel), expressing the U-r-reducible vertex $\nabla_r = \bar{\lambda}_r \bullet w_r \bullet \lambda_r$ through two Hedin vertices, $\bar{\lambda}_r$, λ_r, and a screened interaction, w_r. The dashed boxes emphasize that $\bar{\lambda}_r$, w_r, λ_r all have four fermionic legs; those of w_r and the outer legs of $\bar{\lambda}_r$ and λ_r are amputated. Still, w_r depends on just a single, bosonic frequency and can hence be interpreted as an effective bosonic interaction. Its four legs lie pairwise close together since each pair stems from a bare vertex (see Eq. (43) and Fig. 3c). The two inward-facing legs of both $\bar{\lambda}_r$ and λ_r, connecting to w_r, are therefore also drawn close together, whereas the outward-facing legs are not. To depict this asymmetry in a compact manner, triangles are used on the right. For explicit index summations for all three channels, see Fig. 12 in Appendix A

Thus, Eq. (30) leads to

$$\nabla_r = (\mathbb{1}_r + \Gamma \circ \Pi_r \circ \mathbb{1}_r) \bullet U \bullet (\mathbb{1}_r + \mathbb{1}_r \circ \Pi_r \circ T_r)$$
$$= (\mathbb{1}_r + T_r \circ \Pi_r \circ \mathbb{1}_r) \bullet U \bullet (\mathbb{1}_r + \mathbb{1}_r \circ \Pi_r \circ \Gamma). \quad (31)$$

In the first or second line, the expressions on the right or left of $\bullet U \bullet$, respectively, are U-r-irreducible. These factors are the so-called Hedin vertices [49] (cf. Ref. [30], Eq. (5)),

$$\bar{\lambda}_r(\omega_r, \nu_r) \equiv \mathbb{1}_r + [T_r \circ \Pi_r \circ \mathbb{1}_r](\omega_r, \nu_r), \quad (32a)$$
$$\lambda_r(\omega_r, \nu'_r) \equiv \mathbb{1}_r + [\mathbb{1}_r \circ \Pi_r \circ T_r](\omega_r, \nu'_r). \quad (32b)$$

In our notation, the Hedin vertices have four fermionic legs, but (importantly) depend on only two frequencies. Indeed, regarding their frequency dependence, they can be viewed as the U-irreducible, amputated parts of three-point response functions (see Appendix D and Ref. [26]). Then, Eqs. (32) have the structure of SDEs for a three-point vertex with a bare three-point vertex $\mathbb{1}_r$ (cf. Refs. [3,7]). Via the Hedin vertices, ∇_r factorizes
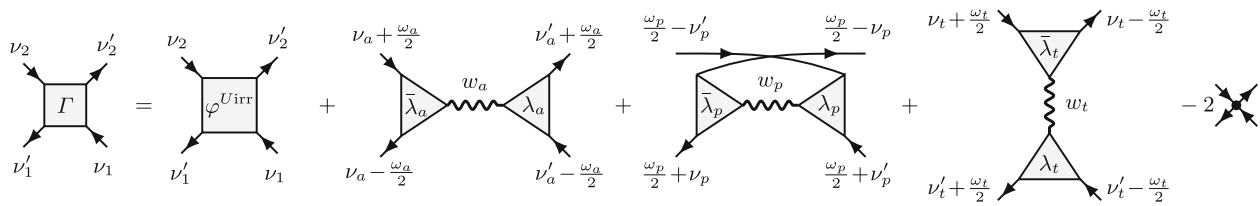
Fig. 8 SBE decomposition of the vertex Γ into U-r-irreducible and U-r-reducible contributions, with $r = a, p, t$. When connecting Hedin vertices to other objects, the two fermionic legs require a $\circ$ connector, the bosonic leg a $\bullet$ connector

into functions of at most two frequency arguments and is thus computationally cheaper than, e.g., γ_r. Following Refs. [26,30], we write

$$\nabla_r = \bar{\lambda}_r \bullet w_r \bullet \lambda_r, \tag{33}$$

where two U-r-irreducible Hedin vertices sandwich a U-r-reducible object, $w_r(\omega_r)$ (see Fig. 7). The object w_r depends only on the bosonic frequency ω_r and can be interpreted as a screened interaction. To find w_r explicitly, we first express Eq. (31) through Hedin vertices,

$$\begin{aligned}\nabla_r &= (\mathbf{1}_r + \Gamma \circ \Pi_r \circ \mathbf{1}_r) \bullet U \bullet \lambda_r \\ &= \bar{\lambda}_r \bullet U \bullet (\mathbf{1}_r + \mathbf{1}_r \circ \Pi_r \circ \Gamma). \end{aligned} \tag{34}$$

Then, $\Gamma = T_r + \nabla_r$ leads to implicit relations for ∇_r:

$$\begin{aligned}\nabla_r &= (\bar{\lambda}_r + \nabla_r \circ \Pi_r \circ \mathbf{1}_r) \bullet U \bullet \lambda_r \\ &= \bar{\lambda}_r \bullet U \bullet (\lambda_r + \mathbf{1}_r \circ \Pi_r \circ \nabla_r). \end{aligned} \tag{35}$$

Next, we insert Eq. (33) for ∇_r on both sides to obtain

$$\begin{aligned}\bar{\lambda}_r \bullet w_r \bullet \lambda_r &= \bar{\lambda}_r \bullet (U + w_r \bullet \lambda_r \circ \Pi_r \circ U) \bullet \lambda_r \\ &= \bar{\lambda}_r \bullet (U + U \circ \Pi_r \circ \bar{\lambda}_r \bullet w_r) \bullet \lambda_r. \end{aligned} \tag{36}$$

This implies that w_r satisfies a pair of Dyson equations,

$$\begin{aligned}w_r &= U + w_r \bullet \lambda_r \circ \Pi_r \circ U \\ &= U + U \circ \Pi_r \circ \bar{\lambda}_r \bullet w_r, \end{aligned} \tag{37}$$

which can be formally solved as

$$\begin{aligned}w_r &= U \bullet (\mathbf{1}_r - \lambda_r \circ \Pi_r \circ U)^{-1} \\ &= (\mathbf{1}_r - U \circ \Pi_r \circ \bar{\lambda}_r)^{-1} \bullet U. \end{aligned} \tag{38}$$

As desired, the screened interaction w_r is manifestly U-r-reducible, and depends on only a single, bosonic frequency, ω_r. To emphasize this fact, Eq. (38) can be written as

$$\begin{aligned}w_r &= U \bullet (\mathbf{1}_r - P_r \bullet U)^{-1} \\ &= (\mathbf{1}_r - U \bullet P_r)^{-1} \bullet U, \end{aligned} \tag{39}$$

where $P_r(\omega_r)$ is the polarization [30],

$$P_r = \lambda_r \circ \Pi_r \circ \mathbf{1}_r = \mathbf{1}_r \circ \Pi_r \circ \bar{\lambda}_r. \tag{40}$$

Regarding frequency dependencies, w_r can be viewed as a bosonic propagator and P_r as a corresponding self-energy; Eq. (40) then has the structure of a SDE for P_r involving the bare three-point vertex $\mathbf{1}_r$ [3,7].

Inserting Eq. (33) for ∇_r into Eq. (24a) for Γ, we arrive at the SBE decomposition of the full vertex of Ref. [26] in our generalized notation,

$$\Gamma = \varphi^{U\mathrm{irr}} + \sum_r \bar{\lambda}_r \bullet w_r \bullet \lambda_r - 2U, \tag{41a}$$

depicted diagrammatically in Fig. 8. For ease of reference, we gather all necessary relations for its ingredients:

$$w_r = U + U \bullet P_r \bullet w_r = U + w_r \bullet P_r \bullet U, \tag{41b}$$

$$P_r = \lambda_r \circ \Pi_r \circ \mathbf{1}_r = \mathbf{1}_r \circ \Pi_r \circ \bar{\lambda}_r, \tag{41c}$$

$$\bar{\lambda}_r = \mathbf{1}_r + T_r \circ \Pi_r \circ \mathbf{1}_r, \tag{41d}$$

$$\lambda_r = \mathbf{1}_r + \mathbf{1}_r \circ \Pi_r \circ T_r, \tag{41e}$$

$$T_r = \Gamma - \bar{\lambda}_r \bullet w_r \bullet \lambda_r, \tag{41f}$$

$$\varphi^{U\mathrm{irr}} = R - U + \sum_r M_r, \tag{41g}$$

$$M_r = (T_r - M_r) \circ \Pi_r \circ T_r = T_r \circ \Pi_r \circ (T_r - M_r). \tag{41h}$$

We collectively call Eqs. (41) the *SBE equations*. Together with the SDE for the self-energy and an input for the two-particle irreducible vertex R, the SBE equations are a self-consistent set of equations and thus fully define the four-point vertex Γ. They can either be solved self-consistently (as by Krien et al. in Refs. [27–30], where an analogous set of equations was set up), or via multiloop flow equations, derived in Sect. 3.2.

To conclude this section, let us point out the physical meaning of $\bar{\lambda}_r, w_r, \lambda_r$ by showing their relation to three-point vertices and susceptibilities. For this, a symmetric expression for w_r is needed, which can be obtained by comparing Eqs. (33) and (34) to deduce

$$\bar{\lambda}_r \bullet w_r = U + \Gamma \circ \Pi_r \circ U, \tag{42a}$$

$$w_r \bullet \lambda_r = U + U \circ \Pi_r \circ \Gamma, \tag{42b}$$

and inserting these into the Dyson equations (37):

$$w_r = U + U \circ \Pi_r \circ U + U \circ \Pi_r \circ \Gamma \circ \Pi_r \circ U. \quad (43)$$

Equations (42) and (43) can be expressed as

$$[\bar{\lambda}_r \bullet w_r](\omega_r, \nu_r) = \bar{\Gamma}_r^{(3)}(\omega_r, \nu_r) \bullet U, \quad (44a)$$

$$[w_r \bullet \lambda_r](\omega_r, \nu'_r) = U \bullet \Gamma_r^{(3)}(\omega_r, \nu'_r), \quad (44b)$$

$$w_r(\omega_r) = U + U \bullet \chi_r(\omega_r) \bullet U, \quad (44c)$$

where $\bar{\Gamma}_r^{(3)}$, $\Gamma_r^{(3)}$ represent full three-point vertices and χ_r susceptibilities, defined by

$$\bar{\Gamma}_r^{(3)}(\omega_r, \nu_r) = \mathbf{1}_r + [\Gamma \circ \Pi_r \circ \mathbf{1}_r](\omega, \nu_r), \quad (45a)$$

$$\Gamma_r^{(3)}(\omega_r, \nu'_r) = \mathbf{1}_r + [\mathbf{1}_r \circ \Pi_r \circ \Gamma](\omega_r, \nu'_r), \quad (45b)$$

$$\chi_r(\omega_r) = [\mathbf{1}_r \circ \Pi_r \circ \mathbf{1}_r](\omega_r)$$
$$+ [\mathbf{1}_r \circ \Pi_r \circ \Gamma \circ \Pi_r \circ \mathbf{1}_r](\omega_r). \quad (45c)$$

(The bare vertices were pulled out in front of the frequency sums, exploiting their frequency independence.) The relation of $\bar{\Gamma}_r^{(3)}$ and $\Gamma_r^{(3)}$ to three-point correlators and response functions is described in Appendix D; the relation of χ_r to physical susceptibilities for a local bare interaction U is discussed in Appendix E.

3.2 SBE mfRG from parquet mfRG

Having defined all the SBE ingredients, we are now ready to derive mfRG flow equations for them—the main goal of this work. Our strategy is to insert the SBE decomposition of Eqs. (23) and (24) into the parquet mfRG flow equations (10) for the Π-r-reducible vertices γ_r. An alternative derivation, starting directly from the SBE equations (41), is given in Sect. 3.3.

We begin by differentiating the decomposition of the Π_r-reducible vertex $\gamma_r = \bar{\lambda}_r \bullet w_r \bullet \lambda_r - U + M_r$ (Eq. (23)) w.r.t. the flow parameter. Since $\dot{U} = 0$ (the bare vertex does not depend on the regulator), we obtain

$$\dot{\gamma}_r = \dot{\bar{\lambda}}_r \bullet w_r \bullet \lambda_r + \bar{\lambda}_r \bullet \dot{w}_r \bullet \lambda_r + \bar{\lambda}_r \bullet w_r \bullet \dot{\lambda}_r + \dot{M}_r. \quad (46)$$

The loop expansion $\dot{\gamma}_r = \sum_\ell \dot{\gamma}_r^{(\ell)}$ implies similar expansions for $\dot{w}_r$, $\dot{\bar{\lambda}}_r$, $\dot{\lambda}_r$, and $\dot{M}_r$. Each term at a given loop order ℓ can be found from the mfRG flow (10) for $\dot{\gamma}_r^{(\ell)}$, by inserting the decomposition of the full vertex, $\Gamma = \bar{\lambda}_r \bullet w_r \bullet \lambda_r + T_r$ (Eq. (25a)) on the right of Eqs. (10).

The 1ℓ flow equation (10a) for $\dot{\gamma}_r^{(1)}$ has four contributions (shown diagrammatically for $\gamma_a^{(1)}$ in Fig. 9):

$$\dot{\gamma}_r^{(1)} = \left(\bar{\lambda}_r \bullet w_r \bullet \lambda_r + T_r\right) \circ \dot{\Pi}_r \circ \left(\bar{\lambda}_r \bullet w_r \bullet \lambda_r + T_r\right)$$
$$= T_r \circ \dot{\Pi}_r \circ \bar{\lambda}_r \bullet w_r \bullet \lambda_r$$
$$+ \bar{\lambda}_r \bullet w_r \bullet \lambda_r \circ \dot{\Pi}_r \circ \bar{\lambda}_r \bullet w_r \bullet \lambda_r$$
$$+ \bar{\lambda}_r \bullet w_r \bullet \lambda_r \circ \dot{\Pi}_r \circ T_r + T_r \circ \dot{\Pi}_r \circ T_r. \quad (47)$$

By matching terms in Eqs. (46) and (47) containing factors of $\bar{\lambda}_r$ and λ_r or not, we obtain the 1ℓ SBE flow:

$$\dot{w}_r^{(1)} = w_r \bullet \lambda_r \circ \dot{\Pi}_r \circ \bar{\lambda}_r \bullet w_r,$$
$$\dot{\bar{\lambda}}_r^{(1)} = T_r \circ \dot{\Pi}_r \circ \bar{\lambda}_r,$$
$$\dot{\lambda}_r^{(1)} = \lambda_r \circ \dot{\Pi}_r \circ T_r,$$
$$\dot{M}_r^{(1)} = T_r \circ \dot{\Pi}_r \circ T_r. \quad (48a)$$

This reproduces the 1ℓ SBE flow derived in Ref. [31] (their Eq. (18)). The higher loop terms can be found similarly from $\dot{\gamma}_r^{(2)}$ and $\dot{\gamma}_r^{(\ell+2)}$ of Eqs. (10b) and (10c). For each loop order ℓ, the $\dot{\gamma}_{\bar{r}}^{(\ell)}$ factors on the right side of these equations can be expressed through the already known flow of $\dot{w}_{r'}^{(\ell)}$, $\dot{\bar{\lambda}}_{r'}^{(\ell)}$ $\dot{\lambda}_{r'}^{(\ell)}$ and $\dot{M}_{r'}^{(\ell)}$. We obtain the flow equations ($\ell + 2 \geq 3$)

$$\dot{w}_r^{(2)} = 0,$$
$$\dot{\bar{\lambda}}_r^{(2)} = \dot{\gamma}_{\bar{r}}^{(1)} \circ \Pi_r \circ \bar{\lambda}_r,$$
$$\dot{\lambda}_r^{(2)} = \lambda_r \circ \Pi_r \circ \dot{\gamma}_{\bar{r}}^{(1)},$$
$$\dot{M}_r^{(2)} = \dot{\gamma}_{\bar{r}}^{(1)} \circ \Pi_r \circ T_r + T_r \circ \Pi_r \circ \dot{\gamma}_{\bar{r}}^{(1)}, \quad (48b)$$
$$\dot{w}_r^{(\ell+2)} = w_r \bullet \lambda_r \circ \Pi_r \circ \dot{\gamma}_{\bar{r}}^{(\ell)} \circ \Pi_r \circ \bar{\lambda}_r \bullet w_r,$$
$$\dot{\bar{\lambda}}_r^{(\ell+2)} = \dot{\gamma}_{\bar{r}}^{(\ell+1)} \circ \Pi_r \circ \bar{\lambda}_r + T_r \circ \Pi_r \circ \dot{\gamma}_{\bar{r}}^{(\ell)} \circ \Pi_r \circ \bar{\lambda}_r,$$
$$\dot{\lambda}_r^{(\ell+2)} = \lambda_r \circ \Pi_r \circ \dot{\gamma}_{\bar{r}}^{(\ell)} \circ \Pi_r \circ T_r + \lambda_r \circ \Pi_r \circ \dot{\gamma}_{\bar{r}}^{(\ell+1)},$$
$$\dot{M}_r^{(\ell+2)} = \dot{\gamma}_{\bar{r}}^{(\ell+1)} \circ \Pi_r \circ T_r + T_r \circ \Pi_r \circ \dot{\gamma}_{\bar{r}}^{(\ell)} \circ \Pi_r \circ T_r$$
$$+ T_r \circ \Pi_r \circ \dot{\gamma}_{\bar{r}}^{(\ell+1)}. \quad (48c)$$

Here, $\dot{\gamma}_{\bar{r}}^{(\ell)}$, required for the flow at loop orders $\ell + 1$ and $\ell + 2$, can directly be constructed from the SBE ingredients using Eq. (46). Similarly as in Eqs. (10), all terms at loop order ℓ contain $\ell - 1$ factors of Π and one $\dot{\Pi}$, now connecting the renormalized objects w_r, $\bar{\lambda}_r$, λ_r, T_r.

The SBE mfRG flow equations (48) are the most important result of this work. For the a channel, they are depicted diagrammatically in Fig. 10. Equations (48) can be condensed into more compact ones, giving the full flow (summed over all loop orders, $\dot{w}_r = \sum_{\ell \geq 1} \dot{w}_r^{(\ell)}$, etc.) of the SBE ingredients; see the next section. The multiloop flow equation for the self-energy [5,7] is given in Eq. (12).

3.3 SBE mfRG from SBE equations

In the previous section, we derived the SBE mfRG flow equations by inserting the SBE decomposition into the known parquet mfRG flow equations of the two-particle reducible vertices γ_r. They can also be derived without prior knowledge on the flow of γ_r, using the techniques of Ref. [7].

In the parquet setting of Ref. [7], one can view the Π-r-irreducible vertex I_r as the key ingredient for all equations related to channel r. In step (i), one uses I_r
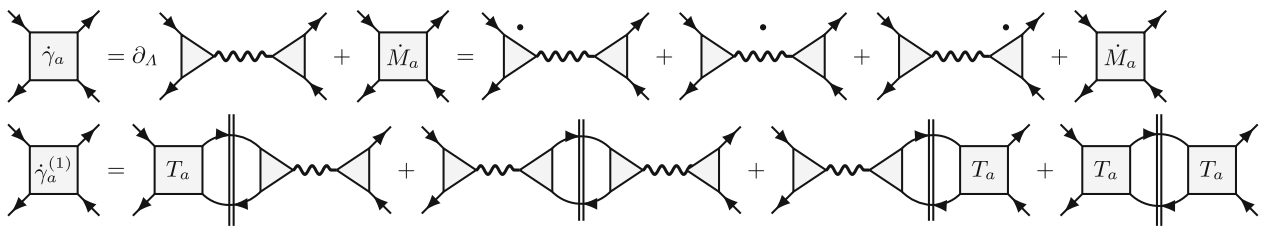
Fig. 9 SBE decomposition of the left and right sides of the 1ℓ flow equation (10a) (Fig. 2) in the a channel. The first line depicts Eq. (46), the second Eq. (47). Equating terms with matching structure yields Eq. (48a), depicted in Fig. 10, first line
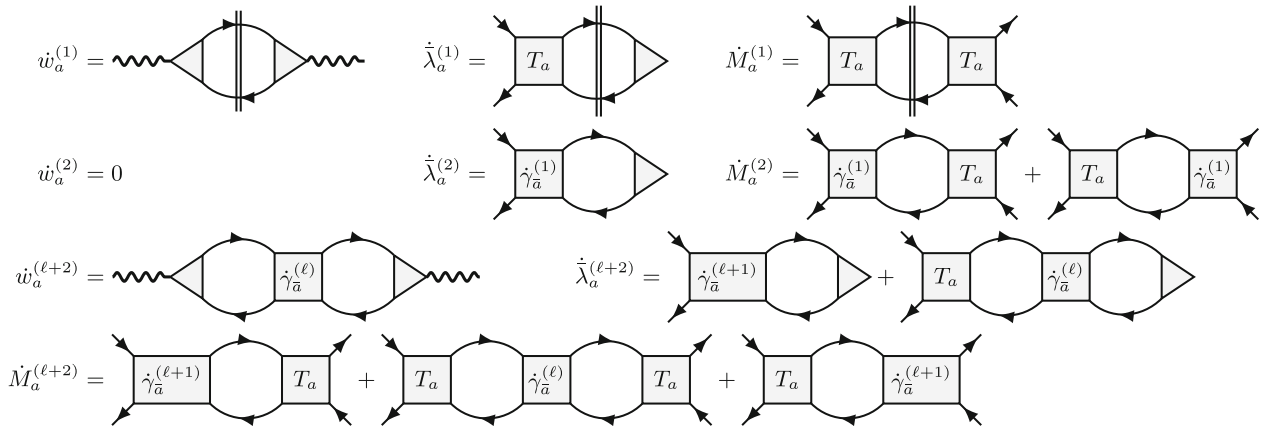
Fig. 10 Multiloop flow equations (48) for the ingredients of the SBE decomposition in the a channel

to generate γ_r and thus Γ through a BSE. Then, a post-processing of attaching and closing external legs yields (ii) (full) three-point vertices $\bar{\Gamma}_r^{(3)}$, $\Gamma_r^{(3)}$ and (iii) a susceptibility χ_r. The SBE setting can be understood in close analogy, with the only exception that one purposefully avoids generating U-r-reducible contributions, because these can (more efficiently) be constructed via $\nabla_r = \bar{\lambda}_r \bullet w_r \bullet \lambda_r$. To exclude U-r-reducible contributions, one uses in step (i) $I_r - U$ to generate M_r and thus T_r through a BSE. The same post-processing as before yields (ii) $\bar{\lambda}_r$, λ_r and then (iii) w_r or P_r.

Because of this structural analogy, the SBE mfRG flow equations can be derived in the exact same fashion as the parquet mfRG flow equation of Ref. [7]. One merely has to replace the variables according to the dictionary

$$I_r \to I_r - U, \quad \gamma_r \to M_r, \quad \Gamma \to T_r,$$
$$\bar{\Gamma}_r^{(3)} \to \bar{\lambda}_r, \qquad \Gamma_r^{(3)} \to \lambda_r, \quad \chi_r \to P_r. \quad (49)$$

For clarity, we now spell out the structural analogies between the original parquet formalism and its SBE version, presenting similarly-structured expressions in pairs of equations, (a) and (b). For both approaches, the full vertex can be decomposed in several ways:

$$\Gamma = R + \sum_r \gamma_r = I_r + \gamma_r, \quad (50a)$$

$$\Gamma = R + \sum_r M_r + \sum_r (\nabla_r - U) = T_r + \nabla_r. \quad (50b)$$

Here, γ_r and M_r satisfy analogous BSEs,

$$\gamma_r = I_r \circ \Pi_r \circ \Gamma, \quad (51a)$$
$$M_r = (I_r - U) \circ \Pi_r \circ T_r, \quad (51b)$$

where the objects on the left reappear on the right through

$$\Gamma = I_r + \gamma_r, \quad (52a)$$
$$T_r = (I_r - U) + M_r. \quad (52b)$$

Relations (51) and (52) are used for step (i). Differentiation of Eq. (51a) yields the mfRG flow of $\dot{\gamma}_r$ as in Eq. (10) and Fig. 2a of Ref. [7]. Here, we replace the variables as above and start by differentiating Eq. (51b):

$$\dot{M}_r = \dot{I}_r \circ \Pi_r \circ T_r + (I_r - U) \circ \dot{\Pi}_r \circ T_r$$
$$+ (I_r - U) \circ \Pi_r \circ \dot{I}_r + (I_r - U) \circ \Pi_r \circ \dot{M}_r$$
$$\Rightarrow \dot{M}_r = (\mathbb{1}_r - (I_r - U) \circ \Pi_r)^{-1} \circ \left[\dot{I}_r \circ \Pi_r \circ T_r \right.$$
$$\left. + (I_r - U) \circ \dot{\Pi}_r \circ T_r + (I_r - U) \circ \Pi_r \circ \dot{I}_r \right]. \quad (53)$$

For the first argument of Eq. (53), we used $\partial_\Lambda (I_r - U) = \dot{I}_r$, as $\dot{U} = 0$. Next, we use the extended BSE $\mathbb{1}_r + T_r \circ \Pi_r = (\mathbb{1}_r - (I_r - U) \circ \Pi_r)^{-1}$ for M_r, cf. Eqs. (7) and

(51). Recollecting the terms, we obtain the flow of $\dot{M}_r$ as

$$
\dot{M}_r = T_r \circ \dot{\Pi}_r \circ T_r + \dot{I}_r \circ \Pi_r \circ T_r \\
+ T_r \circ \Pi_r \circ \dot{I}_r \circ \Pi_r \circ T_r + T_r \circ \Pi_r \circ \dot{I}_r. \quad (54)
$$

A loop expansion with $\dot{I}_r = \dot{\gamma}_{\bar{r}} = \sum_\ell \dot{\gamma}_{\bar{r}}^{(\ell)}$ then yields our Eqs. (48) and Fig. 10.

For step (ii), we have the analogous relations

$$
\bar{\Gamma}_r^{(3)} = \mathbf{1}_r + \Gamma \circ \Pi_r \circ \mathbf{1}_r, \quad \Gamma_r^{(3)} = \mathbf{1}_r + \mathbf{1}_r \circ \Pi_r \circ \Gamma, \tag{55a}
$$

$$
\bar{\lambda}_r = \mathbf{1}_r + T_r \circ \Pi_r \circ \mathbf{1}_r, \quad \lambda_r = \mathbf{1}_r + \mathbf{1}_r \circ \Pi_r \circ T_r. \tag{55b}
$$

Differentiation of Eq. (55a) yields the mfRG flow of $\Gamma_r^{(3)}$ as in Eq. (42) and Fig. 7 of Ref. [7]. Here, we again replace the variables as above and differentiate Eq. (55b):

$$
\dot{\bar{\lambda}}_r = \dot{T}_r \circ \Pi_r \circ \mathbf{1}_r + T_r \circ \dot{\Pi}_r \circ \mathbf{1}_r, \\
\dot{\lambda}_r = \mathbf{1}_r \circ \dot{\Pi}_r \circ T_r + \mathbf{1}_r \circ \Pi_r \circ \dot{T}_r. \tag{56}
$$

As $\dot{T}_r = \dot{I}_r + \dot{M}_r$ (cf. Eq. (52b)), we insert the flow equation (54) for $\dot{M}_r$ into Eq. (56) and use again Eq. (55b) This yields the flow equations

$$
\dot{\bar{\lambda}}_r = T_r \circ \dot{\Pi}_r \circ \bar{\lambda}_r + \dot{I}_r \circ \Pi_r \circ \bar{\lambda}_r + T_r \circ \Pi_r \circ \dot{I}_r \circ \Pi_r \circ \bar{\lambda}_r, \\
\dot{\lambda}_r = \lambda_r \circ \dot{\Pi}_r \circ T_r + \lambda_r \circ \Pi_r \circ \dot{I}_r + \lambda_r \circ \Pi_r \circ \dot{I}_r \circ \Pi_r \circ T_r. \tag{57}
$$

Their loop expansion reproduces Eqs. (48) and Fig. 10.

Finally, in step (iii), we have the relations

$$
\chi_r = \Gamma_r^{(3)} \circ \Pi_r \circ \mathbf{1}_r = \mathbf{1}_r \circ \Pi_r \circ \bar{\Gamma}^{(3)}, \tag{58a}
$$

$$
P_r = \lambda_r \circ \Pi_r \circ \mathbf{1}_r = \mathbf{1}_r \circ \Pi_r \circ \bar{\lambda}_r. \tag{58b}
$$

Differentiation of Eq. (58a) yields the mfRG flow of χ_r as in Eq. (44) and Fig. 8 of Ref. [7]. Replacing the variables as above one more time, we differentiate Eq. (58b):

$$
\dot{P}_r = \mathbf{1}_r \circ \Pi_r \circ \dot{\bar{\lambda}}_r + \mathbf{1}_r \circ \dot{\Pi}_r \circ \bar{\lambda}_r. \tag{59}
$$

After inserting Eqs. (55b) and (57), we eventually obtain

$$
\dot{P}_r = \lambda_r \circ \left(\dot{\Pi}_r + \Pi_r \circ \dot{I}_r \circ \Pi_r \right) \circ \bar{\lambda}_r. \tag{60}
$$

The relation between $\dot{P}_r$ and $\dot{w}_r$ follows from the Dyson equation (41b) as

$$
\dot{w}_r = U \bullet \dot{P}_r \bullet w_r + U \bullet P_r \bullet \dot{w}_r. \tag{61}
$$

Solving this for $\dot{w}_r$ yields

$$
\dot{w}_r = (\mathbf{1}_r - U \bullet P_r)^{-1} \bullet U \bullet \dot{P}_r \bullet w_r = w_r \bullet \dot{P}_r \bullet w_r, \tag{62}
$$

having inserted the inverted Dyson equations (39). A loop expansion of Eq. (60) yields:

$$
\dot{P}_r^{(1)} = \lambda_r \circ \dot{\Pi}_r \circ \bar{\lambda}_r, \\
\dot{P}_r^{(2)} = 0, \\
\dot{P}_r^{(\ell+2)} = \lambda_r \circ \Pi_r \circ \dot{\gamma}_{\bar{r}}^{(\ell)} \circ \Pi_r \circ \bar{\lambda}_r. \tag{63}
$$

Inserting the loop expansion $\dot{P}_r^{(\ell)}$ into Eq. (62) for $\dot{w}_r$ yields the same flow equation for w_r as in our Eqs. (48) and Fig. 10.

Depending on the specific model, it can be more efficient to calculate the flow of the polarization, $\dot{P}_r$, by Eqs. (63) instead of the flow of the screened interaction, $\dot{w}_r$, by Eqs. (48). The screened interaction on the contrary can be obtained by the inverted Dyson Eqs. (39).

Altogether, Eqs. (54), (57), (60) and (62) (with T_r given by $\Gamma - \nabla_{\bar{r}}$, Eq. (50b)) build a system of closed fRG equations, as full derivatives of the SBE equations (41). Hence, combined with an appropriate self-energy flow (cf. Eq. (12) and Ref. [7]), they yield regulator-independent results. To integrate the flow equations in practice, one employs the mfRG loop expansions (48) and (63).

3.4 mfRG flow of the SBE approximation

To reduce numerical costs, it may sometimes be desirable to approximate the flow of the vertex treating only objects with less than all three frequency arguments. The simplest choice is to restrict the flow to functions depending on a single frequency. In the present context, this corresponds to keeping all objects except w_r constant. With $\dot{\bar{\lambda}}_r = 0 = \dot{\lambda}_r$, the flow of the polarization (59) is simply

$$
\dot{P}_r = \lambda_r \circ \dot{\Pi}_r \circ \mathbf{1}_r = \mathbf{1}_r \circ \dot{\Pi}_r \circ \bar{\lambda}_r. \tag{64}
$$

Hence, the flow equations of P_r and w_r completely decouple, and one effectively obtains a vertex consisting of three independent series of ladder diagrams. Nevertheless, such a flow may be helpful for code-developing purposes.

An approximation of the vertex with objects of at most two frequency arguments is given by the SBE approximation [26], which sets $\varphi^{U\mathrm{irr}} = 0$. More generally, one may also keep $\varphi^{U\mathrm{irr}} \neq 0$ constant during the flow, e.g., as obtained from DMFT (called SBE-DΓA in Ref. [26]). This was used in a 1ℓ implementation of DMF²RG in Ref. [31]. In the following, we will refer to the approximation of using a non-flowing U-irreducible part, $\dot{\varphi}^{U\mathrm{irr}} = 0$, as SBE approximation, regardless of whether $\varphi^{U\mathrm{irr}}$ is set to zero or not.

We now derive mfRG flow equations for the SBE approximation, so that $\dot{R} = 0$, as before, and furthermore $\dot{M}_r = 0$. For the most part, the SBE equations (41) remain unchanged. Only the BSE for M_r (41h) is not considered anymore, since now $\varphi^{U\text{irr}} = R - U + \sum_r M_r$ is used as an input. The corresponding flow equations can be obtained as in Sect. 3.3. The flow of the polarization, the screened interaction and the Hedin vertices, prior to any transformation, is still given by Eqs. (59), (62) and (56) (collected here for convenience)

$$\dot{P}_r = \mathbf{1}_r \circ \dot{\Pi}_r \circ \bar{\lambda}_r + \mathbf{1}_r \circ \Pi_r \circ \dot{\bar{\lambda}}_r$$
$$= \dot{\lambda}_r \circ \Pi_r \circ \mathbf{1}_r + \lambda_r \circ \dot{\Pi}_r \circ \mathbf{1}_r, \qquad (65\text{a})$$

$$\dot{w}_r = w_r \bullet \dot{P}_r \bullet w_r, \qquad (65\text{b})$$

$$\dot{\bar{\lambda}}_r = T_r \circ \dot{\Pi}_r \circ \mathbf{1}_r + \dot{T}_r \circ \Pi_r \circ \mathbf{1}_r, \qquad (65\text{c})$$

$$\dot{\lambda}_r = \mathbf{1}_r \circ \dot{\Pi}_r \circ T_r + \mathbf{1}_r \circ \Pi_r \circ \dot{T}_r. \qquad (65\text{d})$$

However, the flow of $T_r = I_r - U + M_r$ now has no $\dot{M}_r$ contribution. It is induced solely by $\dot{I}_r = \dot{\bar{\nabla}}_{\bar{r}}$, the flow of the U-reducible contributions from complementary channels,

$$\dot{T}_r = \dot{\bar{\nabla}}_{\bar{r}}, \qquad (65\text{e})$$

and thus is fully determined by $\dot{\bar{\lambda}}_{\bar{r}}$, $\dot{\lambda}_{\bar{r}}$ and $\dot{w}_{\bar{r}}$.

Equations (65) can be rewritten by inserting the flow of the higher-point objects into the lower-point objects:

$$\dot{\bar{\lambda}}_r = T_r \circ \dot{\Pi}_r \circ \mathbf{1}_r + \dot{\bar{\nabla}}_{\bar{r}} \circ \Pi_r \circ \mathbf{1}_r, \qquad (66\text{a})$$

$$\dot{\lambda}_r = \mathbf{1}_r \circ \dot{\Pi}_r \circ T_r + \mathbf{1}_r \circ \Pi_r \circ \dot{\bar{\nabla}}_{\bar{r}}, \qquad (66\text{b})$$

$$\dot{P}_r = \mathbf{1}_r \circ \dot{\Pi}_r \circ \bar{\lambda}_r + \mathbf{1}_r \circ \Pi_r \circ T_r \circ \dot{\Pi}_r \circ \mathbf{1}_r$$
$$\quad + \mathbf{1}_r \circ \Pi_r \circ \dot{\bar{\nabla}}_{\bar{r}} \circ \Pi_r \circ \mathbf{1}_r$$
$$= \mathbf{1}_r \circ \dot{\Pi}_r \circ \bar{\lambda}_r + \lambda_r \circ \dot{\Pi}_r \circ \mathbf{1}_r$$
$$\quad - \mathbf{1}_r \circ \dot{\Pi}_r \circ \mathbf{1}_r + \mathbf{1}_r \circ \Pi_r \circ \dot{\bar{\nabla}}_{\bar{r}} \circ \Pi_r \circ \mathbf{1}_r. \quad (66\text{c})$$

In the last line, we expressed $\mathbf{1}_r \circ \Pi_r \circ T_r$ in terms of the Hedin vertex $\lambda_r - \mathbf{1}_r$. Equations (66) are similar to the previous flow equations (57) and (60) of the more general case, but some occurrences of the Hedin vertices $\bar{\lambda}_r, \lambda_r$ on the right there are here replaced by their zeroth-order term $\mathbf{1}_r$. Evidently, the contributions needed to upgrade these $\mathbf{1}_r$ to $\bar{\lambda}_r, \lambda_r$ are omitted when setting $\dot{M}_r = 0$.

A loop expansion of the above equations then yields

$$\dot{P}_r^{(1)} = \mathbf{1}_r \circ \dot{\Pi}_r \circ \bar{\lambda}_r + \lambda_r \circ \dot{\Pi}_r \circ \mathbf{1}_r - \mathbf{1}_r \circ \dot{\Pi}_r \circ \mathbf{1}_r,$$
$$\dot{\bar{\lambda}}_r^{(1)} = T_r \circ \dot{\Pi}_r \circ \mathbf{1}_r,$$
$$\dot{\lambda}_r^{(1)} = \mathbf{1}_r \circ \dot{\Pi}_r \circ T_r, \qquad (67\text{a})$$
$$\dot{P}_r^{(2)} = 0,$$
$$\dot{\bar{\lambda}}_r^{(\ell+1)} = \dot{\bar{\nabla}}_{\bar{r}}^{(\ell)} \circ \Pi_r \circ \mathbf{1}_r,$$
$$\dot{\lambda}_r^{(\ell+1)} = \mathbf{1}_r \circ \Pi_r \circ \dot{\bar{\nabla}}_{\bar{r}}^{(\ell)}, \qquad (67\text{b})$$
$$\dot{P}_r^{(\ell+2)} = \mathbf{1}_r \circ \Pi_r \circ \dot{\bar{\nabla}}_{\bar{r}}^{(\ell)} \circ \Pi_r \circ \mathbf{1}_r,$$

$$\dot{w}_r^{(\ell)} = w_r \bullet \dot{P}_r^{(\ell)} \bullet w_r. \qquad (67\text{c})$$

Apart from the fact that $\dot{M}_r$ is not needed here, the other flow equations are also simpler than Eqs. (48) without $\dot{M}_r$, obtained from the full SBE equations. To be specific, Eqs. (48) contain $\bar{\lambda}_r$ or λ_r on the right of the flow equations for $\dot{\bar{\lambda}}_r^{(\ell)}$ or $\dot{\lambda}_r^{(\ell)}$, whereas the simplified Eqs. (67) contain $\mathbf{1}_r$ there, and, for $\ell \geq 2$, only one term where Eqs. (48) had two.

When using the above flow equations for the SBE approximation, the self-energy flow (12) should also be re-derived from either the SDE or the Hedin equation for Σ (e.g. Eq. (23) in Ref. [27]). Since the present paper focuses on vertex parametrizations, we leave a derivation of a suitably modified self-energy flow for future work. Here, it suffices to note that, when used together with such a modified self-energy flow, Eqs. (67) are again total derivatives of a closed set of equations. So, integrating the flow until loop convergence would yield the regulator-independent solution of the SBE approximation.

Transforming the self-consistent equations of the SBE approximation on the vertex level to an equivalent mfRG flow reveals its simplistic nature, with relations like $\dot{\lambda}_r^{(1)} = \mathbf{1}_r \bullet \dot{\Pi}_r \bullet T_r$, and demonstrates how fRG offers an intuitive way to go beyond that, using, e.g., $\dot{\lambda}_r^{(1)} = \lambda_r \bullet \dot{\Pi}_r \bullet T_r$ (still treating only functions of at most two frequencies). However, the latter flow would be regulator-dependent *per se*. It remains to be seen how severe the lack of regulator independence for this flow, as used, e.g., in Ref. [31], is.

The simplified schemes presented in this section [i.e., Eqs. (64) and (67)] are closed flow equations on the vertex level and thus offer an appealing way for approaching the full SBE mfRG equations (48). Thereby, SBE ingredients with more complicated frequency dependence can be taken into account successively during code development. To what extent they can succeed in actually capturing the essential physics of a given problem will have to be investigated on a case-by-case basis. Generally, we showed that mfRG offers a way to make the choice of a certain approximation regulator independent, either for the simplistic flow of the SBE approximation or for the full SBE mfRG flow reproducing the PA.

4 Asymptotic classes

In numerical implementations of parquet mfRG [10–14], it is useful to handle the numerical complexity of the vertex by decomposing it into asymptotic classes with well-defined high-frequency behaviors. It is convenient to compute the flow of these asymptotic classes using their own flow equations; here, we recapitulate their derivation. We also elucidate the close relation between vertex parametrizations using the parquet decomposition with asymptotic classes or the SBE decomposition, deriving explicit equations relating their ingredients.

These equations may facilitate the adaption of codes devised for parquet mfRG to SBE mfRG applications.

4.1 Definition of asymptotic classes

The parametrization of two-particle reducible vertices γ_r via asymptotic classes was introduced in Ref. [16] to conveniently express their high-frequency asymptotics through simpler objects with fewer frequency arguments. One makes the ansatz

$$
\begin{aligned}
&\gamma_r(\omega_r, \nu_r, \nu'_r) \\
&= \mathcal{K}_1^r(\omega_r) + \mathcal{K}_2^r(\omega_r, \nu_r) + \mathcal{K}_{2'}^r(\omega_r, \nu'_r) + \mathcal{K}_3^r(\omega_r, \nu_r, \nu'_r).
\end{aligned}
\tag{68}
$$

Here, $\mathcal{K}_1^r$ contains all diagrams having both ν_r legs connected to the same bare vertex and both ν'_r legs connected to another bare vertex. (For a diagrammatic depiction, see Appendix B, Fig. 14.) These diagrams are thus independent of ν_r, ν'_r and stay finite in the limit $|\nu_r| \to \infty$, $|\nu'_r| \to \infty$,

$$
\lim_{|\nu_r| \to \infty} \lim_{|\nu'_r| \to \infty} \gamma_r(\omega_r, \nu_r, \nu'_r) = \mathcal{K}_1^r(\omega_r). \tag{69a}
$$

$\mathcal{K}_2^r$ (or $\mathcal{K}_{2'}^r$) analogously contains the part of the vertex having both ν'_r (or ν_r) legs connected to the same bare vertex while the two ν_r (or ν'_r) legs are connected to different bare vertices. Hence, it is finite for $|\nu'_r| \to \infty$ (or $|\nu_r| \to \infty$) but vanishes for $|\nu_r| \to \infty$ (or $|\nu'_r| \to \infty$):

$$
\begin{aligned}
\lim_{|\nu'_r| \to \infty} \gamma_r(\omega_r, \nu_r, \nu'_r) &= \mathcal{K}_1^r(\omega_r) + \mathcal{K}_2^r(\omega_r, \nu_r), \\
\lim_{|\nu_r| \to \infty} \gamma_r(\omega_r, \nu_r, \nu'_r) &= \mathcal{K}_1^r(\omega_r) + \mathcal{K}_{2'}^r(\omega_r, \nu'_r).
\end{aligned}
\tag{69b}
$$

$\mathcal{K}_3^r$ exclusively contains diagrams having both ν_r legs connected to different bare vertices, and likewise for both ν'_r legs. Such diagrams depend on all three frequencies and thus decay if any of them is sent to infinity. When taking the above limits for bubbles involving channels r' different from r, we obtain zero,

$$
\lim_{|\nu_r| \to \infty} \gamma_{r' \neq r} = \lim_{|\nu'_r| \to \infty} \gamma_{r' \neq r} = 0, \tag{69c}
$$

as each $\Pi_{r'}$ in $\gamma_{r'}$ has a denominator containing $\omega_{r' \neq r}$, which is a linear combination of ω_r, ν_r and ν'_r.

Since R explicitly depends on all frequencies, it decays to the bare vertex U at high frequencies, and the asymptotic classes can be obtained by taking limits of the full vertex. Explicitly, $\mathcal{K}_1^r$ can be obtained from

$$
\lim_{|\nu_r| \to \infty} \lim_{|\nu'_r| \to \infty} \Gamma(\omega_r, \nu_r, \nu'_r) = U + \mathcal{K}_1^r(\omega_r), \tag{70a}
$$

taking the double limit in such a way that $\nu_r \pm \nu'_r$ is not constant, to ensure that all bosonic frequencies $|\omega_{r' \neq r}|$ go to ∞ [16]. Similarly, $\mathcal{K}_2^r$, $\mathcal{K}_{2'}^r$ can be obtained from

objects Γ_2^r, $\Gamma_{2'}^r$ defined via the limits

$$
\Gamma_2^r(\omega_r, \nu_r) = \lim_{|\nu'_r| \to \infty} \Gamma(\omega_r, \nu_r, \nu'_r) = U + \mathcal{K}_1^r + \mathcal{K}_2^r, \tag{70b}
$$

$$
\Gamma_{2'}^r(\omega_r, \nu'_r) = \lim_{|\nu_r| \to \infty} \Gamma(\omega_r, \nu_r, \nu'_r) = U + \mathcal{K}_1^r + \mathcal{K}_{2'}^r. \tag{70c}
$$

For each of the latter two limits, we denote the complementary part of the vertex (vanishing in said limit) by

$$
\bar{\Gamma}_2^r(\omega_r, \nu_r, \nu'_r) = \Gamma - \Gamma_2^r = \mathcal{K}_{2'}^r + \mathcal{K}_3^r + \gamma_{\bar{r}} + R - U, \tag{70d}
$$

$$
\bar{\Gamma}_{2'}^r(\omega_r, \nu_r, \nu'_r) = \Gamma - \Gamma_{2'}^r = \mathcal{K}_2^r + \mathcal{K}_3^r + \gamma_{\bar{r}} + R - U. \tag{70e}
$$

By taking suitable limits in the BSEs (4), the asymptotic classes can be expressed through the full vertex Γ and the bare interaction U [16]:

$$
\mathcal{K}_1^r(\omega_r) = U \circ (\Pi_r + \Pi_r \circ \Gamma \circ \Pi_r) \circ U, \tag{71a}
$$

$$
\mathcal{K}_2^r(\omega_r, \nu_r) = \Gamma \circ \Pi_r \circ U - \mathcal{K}_1^r, \tag{71b}
$$

$$
\mathcal{K}_{2'}^r(\omega_r, \nu'_r) = U \circ \Pi_r \circ \Gamma - \mathcal{K}_1^r. \tag{71c}
$$

Hence, they are directly related to the three-point vertices $\bar{\Gamma}_r^{(3)}$, $\Gamma_r^{(3)}$ and susceptibilities χ_r (cf. Eqs. (45) and Ref. [16]) as

$$
\chi_r(\omega_r) = U^{-1} \bullet \mathcal{K}_1^r(\omega_r) \bullet U^{-1}, \tag{72a}
$$

$$
\bar{\Gamma}_r^{(3)}(\omega_r, \nu_r) = [U + \mathcal{K}_1^r + \mathcal{K}_2^r](\omega_r, \nu_r) \bullet U^{-1}, \tag{72b}
$$

$$
\Gamma_r^{(3)}(\omega_r, \nu'_r) = U^{-1} \bullet [U + \mathcal{K}_1^r + \mathcal{K}_{2'}^r](\omega_r, \nu'_r). \tag{72c}
$$

$\mathcal{K}_1^r$ diagrams are therefore mediated by the bosonic fluctuations described by the susceptibility χ_r, whereas $\mathcal{K}_2^r$ and $\mathcal{K}_{2'}^r$ describe the coupling of fermions to these bosonic fluctuations via the three-point vertices $\bar{\Gamma}_r^{(3)}$ and $\Gamma_r^{(3)}$. This hints at the close relation between asymptotic classes and SBE components which is further discussed in Sec. 4.3.

4.2 mfRG equations for asymptotic classes

When the vertex is parametrized through its asymptotic classes, it is convenient to compute the latter directly during the flow, without numerically sending certain frequencies to infinity. This facilitates systematically adding or neglecting higher asymptotic classes. Therefore, we now derive explicit mfRG flow equations for the asymptotic classes, starting from the general multiloop flow equations (10), similar to the derivation of the mfRG flow equations for the SBE ingredients in Sect. 3.2. (For a diagrammatic derivation, see Refs. [50,51].)

The parametrization (68) of γ_r in terms of asymptotic classes holds analogously at each loop order,

$$
\dot{\gamma}_r^{(\ell)} = \dot{\mathcal{K}}_1^{r(\ell)} + \dot{\mathcal{K}}_2^{r(\ell)} + \dot{\mathcal{K}}_{2'}^{r(\ell)} + \dot{\mathcal{K}}_3^{r(\ell)}. \tag{73}
$$

Then, each summand can be obtained from Eqs. (10) for $\dot{\gamma}_r^{(\ell)}$ by taking suitable limits of the fermionic frequencies ν_r, ν_r', as specified in Eqs. (69). For example, consider a bubble of type $\Gamma \circ \dot{\Pi}_r \circ \tilde{\Gamma}$, in the r representation of Eq. (20). In the limit $|\nu_r| \to \infty$, the first vertex reduces to $\Gamma_{2'}^r$ (Eq. (70c)), while for $|\nu_r'| \to \infty$, the second vertex reduces to $\tilde{\Gamma}_2^r$ (Eq. (70b)). Using Eq. (20), we thus obtain

$$\lim_{|\nu_r| \to \infty} \Gamma \circ \dot{\Pi}_r \circ \tilde{\Gamma} = \Gamma_{2'}^r \circ \dot{\Pi}_r \circ \tilde{\Gamma}, \qquad (74a)$$

$$\lim_{|\nu_r'| \to \infty} \Gamma \circ \dot{\Pi}_r \circ \tilde{\Gamma} = \Gamma \circ \dot{\Pi}_r \circ \tilde{\Gamma}_2^r. \qquad (74b)$$

By contrast, when taking these limits for bubbles involving channels r' different from r, we obtain zero,

$$\lim_{|\nu_r| \to \infty} \Gamma \circ \dot{\Pi}_{r' \neq r} \circ \tilde{\Gamma} = 0, \quad \lim_{|\nu_r'| \to \infty} \Gamma \circ \dot{\Pi}_{r' \neq r} \circ \tilde{\Gamma} = 0, \qquad (74c)$$

by similar reasoning as that leading to Eq. (69c). In this manner, the 1ℓ flow equation (10a) for $\dot{\gamma}_r^{(1)}$ readily yields

$$\dot{\mathcal{K}}_1^{r\,(1)} = \Gamma_{2'}^r \circ \dot{\Pi}_r \circ \Gamma_2^r,$$
$$\dot{\mathcal{K}}_2^{r\,(1)} = \bar{\Gamma}_{2'}^r \circ \dot{\Pi}_r \circ \Gamma_2^r,$$
$$\dot{\mathcal{K}}_{2'}^{r\,(1)} = \Gamma_{2'}^r \circ \dot{\Pi}_r \circ \bar{\Gamma}_2^r,$$
$$\dot{\mathcal{K}}_3^{r\,(1)} = \bar{\Gamma}_{2'}^r \circ \dot{\Pi}_r \circ \bar{\Gamma}_2^r. \qquad (75a)$$

Similarly, the two-loop contribution $\dot{\gamma}_r^{(2)}$, Eq. (10b), yields

$$\dot{\mathcal{K}}_1^{r\,(2)} = 0,$$
$$\dot{\mathcal{K}}_2^{r\,(2)} = \dot{\gamma}_{\bar{r}}^{(1)} \circ \Pi_r \circ \Gamma_2^r,$$
$$\dot{\mathcal{K}}_{2'}^{r\,(2)} = \Gamma_{2'}^r \circ \Pi_r \circ \dot{\gamma}_{\bar{r}}^{(1)},$$
$$\dot{\mathcal{K}}_3^{r\,(2)} = \dot{\gamma}_{\bar{r}}^{(1)} \circ \Pi_r \circ \bar{\Gamma}_2^r + \bar{\Gamma}_{2'}^r \circ \Pi_r \circ \dot{\gamma}_{\bar{r}}^{(1)}. \quad (75b)$$

Due to Eq. (69c), $\dot{\mathcal{K}}_1^{r\,(2)}$ vanishes and $\dot{\mathcal{K}}_2^{r\,(2)}$ or $\dot{\mathcal{K}}_{2'}^{r\,(2)}$ contain no terms with $\dot{\gamma}_{\bar{r}}^{(1)}$ on their right or left sides, respectively. Finally, Eq. (10c) for $\dot{\gamma}_r^{(\ell+2)}$, with $\ell \geq 1$, yields

$$\dot{\mathcal{K}}_1^{r\,(\ell+2)} = \Gamma_{2'}^r \circ \Pi_r \circ \dot{\gamma}_{\bar{r}}^{(\ell)} \circ \Pi_r \circ \Gamma_2^r,$$
$$\dot{\mathcal{K}}_2^{r\,(\ell+2)} = \dot{\gamma}_{\bar{r}}^{(\ell+1)} \circ \Pi_r \circ \Gamma_2^r + \bar{\Gamma}_{2'}^r \circ \Pi_r \circ \dot{\gamma}_{\bar{r}}^{(\ell)} \circ \Pi_r \circ \Gamma_2^r,$$
$$\dot{\mathcal{K}}_{2'}^{r\,(\ell+2)} = \Gamma_{2'}^r \circ \Pi_r \circ \dot{\gamma}_{\bar{r}}^{(\ell)} \circ \Pi_r \circ \bar{\Gamma}_2^r + \Gamma_{2'}^r \circ \Pi_r \circ \dot{\gamma}_{\bar{r}}^{(\ell+1)},$$
$$\dot{\mathcal{K}}_3^{r\,(\ell+2)} = \dot{\gamma}_{\bar{r}}^{(\ell+1)} \circ \Pi_r \circ \bar{\Gamma}_2^r + \bar{\Gamma}_{2'}^r \circ \Pi_r \circ \dot{\gamma}_{\bar{r}}^{(\ell)} \circ \Pi_r \circ \bar{\Gamma}_2^r$$
$$+ \bar{\Gamma}_{2'}^r \circ \Pi_r \circ \dot{\gamma}_{\bar{r}}^{(\ell+1)}. \qquad (75c)$$

Here, $\dot{\mathcal{K}}_1^{r\,(\ell+2)} \neq 0$ since $\dot{\gamma}_{\bar{r}}^{(1)}$ appears in the middle in the central term of Eq. (10c); hence, Eq. (69c) does not apply.

Note that these equations can also be used in the context of DMF^{2}RG [32,33]. There, only the full vertex Γ is given as an input. While $\mathcal{K}_1^r$, $\mathcal{K}_2^r$ and $\mathcal{K}_{2'}^r$ can be deduced from Γ by sending certain frequencies to infinity (cf. Eqs. (70)) or using Eqs. (71), it is not possible to similarly extract $\mathcal{K}_3^r$ in a given channel as some frequency limit of the full vertex Γ. However, the classes $\mathcal{K}_3^r$ do not enter the right-hand sides of the flow equations (75) individually, but only the combination $R + \mathcal{K}_3 = R + \sum_r \mathcal{K}_3^r$. This is already clear from the general formulation of the mfRG flow equations (10). Consider, e.g., the 1ℓ contribution $\dot{\mathcal{K}}_2^{r\,(1)}$ of Eq. (75a). There, $\bar{\Gamma}_{2'}^r$ contains $R + \mathcal{K}_3 + \gamma_{\bar{r}} = R + \mathcal{K}_3 + \sum_{r' \neq r}(\mathcal{K}_1^{r'} + \mathcal{K}_2^{r'} + \mathcal{K}_{2'}^{r'})$, and hence only requires knowledge of the full $R + \mathcal{K}_3$. This holds equivalently for all insertions of the full vertex into flow equations at any loop order. Now, insertions of the *differentiated* vertex in loop order ℓ into the flow equations of order $\ell + 1$ and $\ell + 2$ *do* require a channel decomposition $\dot{\mathcal{K}}_3 = \sum_r \dot{\mathcal{K}}_3^r$. For example, the two-loop contribution $\dot{\mathcal{K}}_2^{r\,(2)}$ of Eq. (75b) contains $\dot{\gamma}_{\bar{r}}^{(1)}$, which, by Eq. (73), involves differentiated vertices $\dot{\mathcal{K}}_3^{r' \neq r\,(1)}$. These *are* available via Eq. (75a). Therefore, in the DMF^{2}RG context, one would start with $\mathcal{K}_1^r$, $\mathcal{K}_2^r$, $\mathcal{K}_{2'}^r$ and the full $R + \mathcal{K}_3$ from DMFT, compute the differentiated vertices $\dot{\mathcal{K}}_i^r$ independently (including $\dot{\mathcal{K}}_3^r$), successively insert them in higher loop orders, and eventually update $\mathcal{K}_3$ using $\dot{\mathcal{K}}_3 = \sum_{\ell,r} \dot{\mathcal{K}}_3^{r\,(\ell)}$ in each step of the flow (recall that R does not flow, $\dot{R} = 0$). The same reasoning also applies to the multi-boson terms M_r.

4.3 Relating SBE ingredients and asymptotic classes

The asymptotic classes and SBE ingredients are closely related [31]. This is not surprising as the properties of both follow from the assumption that the bare vertex contains no frequency dependence, except for frequency conservation. For convenience, we collect these relations below.

Comparison of Eqs. (43) and (71a) yields

$$w_r(\omega_r) = U + \mathcal{K}_1^r(\omega_r). \qquad (76)$$

Similarly, using Eqs. (42), (43), (71b), and (71c), we can write the products of Hedin vertices and the screened interaction as

$$\bar{\lambda}_r \bullet w_r = U + \Gamma \circ \Pi_r \circ U = U + \mathcal{K}_1^r + \mathcal{K}_2^r, \qquad (77a)$$
$$w_r \bullet \lambda_r = U + U \circ \Pi_r \circ \Gamma = U + \mathcal{K}_1^r + \mathcal{K}_{2'}^r. \qquad (77b)$$

We now insert Eq. (76) for $U + \mathcal{K}_1^r$ and solve for λ_r, $\bar{\lambda}_r$, formally defining w_r^{-1} through $w_r \bullet w_r^{-1} = w_r^{-1} \bullet w_r = \mathbf{1}_r$. Thus, we obtain

$$\bar{\lambda}_r = \mathbf{1}_r + \mathcal{K}_2^r \bullet w_r^{-1}, \quad \lambda_r = \mathbf{1}_r + w_r^{-1} \bullet \mathcal{K}_{2'}^r, \quad (78)$$

full vertex: $\qquad\qquad$ Γ

$$\boxed{\text{frequencies:}\quad 1\quad 2\quad 3}$$

parquet decomp.: $\qquad$ $R + \sum_r \gamma_r$

$\hookrightarrow$ asymp. classes: $\qquad$ $R + \sum_r \left[\underbrace{\mathcal{K}_1^r + \mathcal{K}_2^r + \mathcal{K}_{2'}^r + \mathcal{K}_3^r}\right]$

$\hookrightarrow$ U-r-reduc.: $\quad$ $\underbrace{R - U} + U + \sum_r \left[\overbrace{\bar{\lambda}_r \bullet w_r \bullet \lambda_r - U + M_r}\right]$

SBE decomp.: $\quad$ $\varphi^{U\mathrm{irr}} - 2U + \sum_r \bar{\lambda}_r \bullet w_r \bullet \lambda_r$
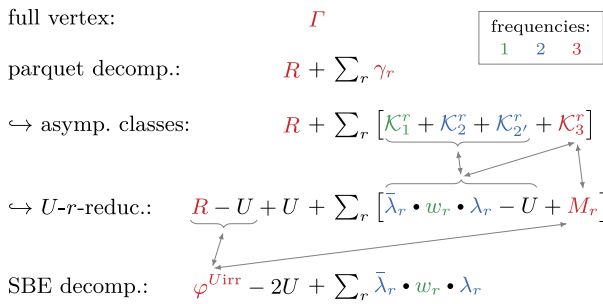
Fig. 11 Overview over vertex decompositions: The parquet decomposition (second line) can be grouped by asymptotic classes (third line) or U-r-reducibility (fourth line), highlighting the relation between these two notions. Arrows link terms that can be identified: $\mathcal{K}_3^r = M_r + \mathcal{K}_2^r \bullet w_r^{-1} \bullet \mathcal{K}_{2'}^r$ and $\mathcal{K}_1^r + \mathcal{K}_2^r + \mathcal{K}_{2'}^r + \mathcal{K}_2^r \bullet w_r^{-1} \bullet \mathcal{K}_{2'}^r = \bar{\lambda}_r \bullet w_r \bullet \lambda_r - U$ for the Π-r-reducible contributions, and $\varphi^{U\mathrm{irr}} = R - U + \sum_r M_r$ for the fully U-r-irreducible contributions. The colors indicate whether the objects depend on 1, 2, or 3 frequency arguments

which, when inserted into Eq. (33), yields

$$\nabla_r = \left(\mathbf{1}_r + \mathcal{K}_2^r \bullet w_r^{-1}\right) \bullet w_r \bullet \left(\mathbf{1}_r + w_r^{-1} \bullet \mathcal{K}_{2'}^r\right)$$
$$= U + \mathcal{K}_1^r + \mathcal{K}_2^r + \mathcal{K}_{2'}^r + \mathcal{K}_2^r \bullet w_r^{-1} \bullet \mathcal{K}_{2'}^r. \quad (79)$$

Depending on model details, it may happen that not all components of w_r^{-1} are uniquely defined. However, the right-hand sides of Eqs. (78)–(79) are unambiguous as the SBE ingredients are well defined through Eqs. (41).

Recalling that $\gamma_r = \nabla_r - U + M_r$, we conclude that

$$M_r = \mathcal{K}_3^r - \mathcal{K}_2^r \bullet w_r^{-1} \bullet \mathcal{K}_{2'}^r. \quad (80)$$

Hence, ∇_r contains a part of $\mathcal{K}_3^r$, namely $\mathcal{K}_2^r \bullet w_r^{-1} \bullet \mathcal{K}_{2'}^r$, which can be fully expressed through functions that each depend on at most two frequencies. M_r contains the remaining part of $\mathcal{K}_3^r$, which must be explicitly parametrized through three frequencies and thus is numerically most expensive. A recent study of the Hubbard model showed that $\sum_r M_r$ is strongly localized in frequency space, particularly in the strong-coupling regime [31]. This allows for a cheaper numerical treatment of the vertex part truly depending on three frequencies and constitutes the main computational advantage of the SBE decomposition.

Equations (76)–(79) fully express the SBE ingredients through asymptotic classes. Analogous results were obtained by similar arguments in Appendix A of Ref. [31]. Figure 11 summarizes the relation between the two vertex decompositions and their ingredients.

Conversely, the asymptotic classes can also be expressed fully through the SBE ingredients. Using Eqs. (23), (68), (76), and (78), one finds

$$\mathcal{K}_1^r = w_r - U \quad (81\mathrm{a})$$
$$\mathcal{K}_2^r = (\bar{\lambda}_r - \mathbf{1}_r) \bullet w_r, \quad (81\mathrm{b})$$
$$\mathcal{K}_{2'}^r = w_r \bullet (\lambda_r - \mathbf{1}_r), \quad (81\mathrm{c})$$

$$\mathcal{K}_3^r = M_r + (\bar{\lambda}_r - \mathbf{1}_r) \bullet w_r \bullet (\lambda_r - \mathbf{1}_r). \quad (81\mathrm{d})$$

Moreover, Eqs. (25a), (70b), (70c), and (77) imply

$$\Gamma_2^r = \bar{\lambda}_r \bullet w_r, \quad (82\mathrm{a})$$
$$\Gamma_{2'}^r = w_r \bullet \lambda_r, \quad (82\mathrm{b})$$
$$\bar{\Gamma}_2^r = \bar{\lambda}_r \bullet w_r \bullet (\lambda_r - \mathbf{1}_r) + T_r \quad (82\mathrm{c})$$
$$\bar{\Gamma}_{2'}^r = (\bar{\lambda}_r - \mathbf{1}_r) \bullet w_r \bullet \lambda_r + T_r. \quad (82\mathrm{d})$$

For the latter two equations, we used Eq. (25a) in the form $\Gamma = \bar{\lambda}_r \bullet w_r \bullet \lambda_r + T_r$. Equivalently, using the definitions of the Hedin vertices in Eqs. (32), we can express $\mathcal{K}_2^r$, $\mathcal{K}_3^r$, and Eqs. (82) as

$$\mathcal{K}_2^r = T_r \circ \Pi_r \circ w_r, \quad (83\mathrm{a})$$
$$\mathcal{K}_{2'}^r = w_r \circ \Pi_r \circ T_r, \quad (83\mathrm{b})$$
$$\mathcal{K}_3^r = M_r + T_r \circ \Pi_r \circ w_r \circ \Pi_r \circ T_r, \quad (83\mathrm{c})$$
$$\Gamma_2^r = w_r + T_r \circ \Pi_r \circ w_r, \quad (83\mathrm{d})$$
$$\Gamma_{2'}^r = w_r + w_r \circ \Pi_r \circ T_r, \quad (83\mathrm{e})$$
$$\bar{\Gamma}_2^r = T_r + w_r \circ \Pi_r \circ T_r + T_r \circ \Pi_r \circ w_r \circ \Pi_r \circ T_r, \quad (83\mathrm{f})$$
$$\bar{\Gamma}_{2'}^r = T_r + T_r \circ \Pi_r \circ w_r + T_r \circ \Pi_r \circ w_r \circ \Pi_r \circ T_r. \quad (83\mathrm{g})$$

Since the asymptotic classes and SBE ingredients are closely related, the same is true for their mfRG flow. Indeed, it is straightforward to derive the mfRG SBE flow equations (48) from the flow equations (75) for $\dot{\mathcal{K}}_i^{r\,(\ell)}$. We briefly indicate the strategy, without presenting all details.

We differentiate the equations (81) expressing $\mathcal{K}_i^r$ through SBE ingredients, and subsequently use Eqs. (32) to eliminate $\bar{\lambda}_r - \mathbf{1}_r$ and $\lambda_r - \mathbf{1}_r$. Thereby, we obtain

$$\dot{\mathcal{K}}_1^r = \dot{w}_r, \quad (84\mathrm{a})$$
$$\dot{\mathcal{K}}_2^r = \dot{\bar{\lambda}}_r \bullet w_r + T_r \circ \Pi_r \circ \dot{w}_r, \quad (84\mathrm{b})$$
$$\dot{\mathcal{K}}_{2'}^r = \dot{w}_r \circ \Pi_r \circ T_r + w_r \bullet \dot{\lambda}_r, \quad (84\mathrm{c})$$
$$\dot{\mathcal{K}}_3^r = \dot{\bar{\lambda}}_r \bullet w_r \circ \Pi_r \circ T_r + T_r \circ \Pi_r \circ \dot{w}_r \circ \Pi_r \circ T_r$$
$$+ T_r \circ \Pi_r \circ w_r \bullet \dot{\lambda}_r + \dot{M}_r. \quad (84\mathrm{d})$$

Now, we use Eqs. (75) to express the $\dot{\mathcal{K}}_i^{r\,(\ell)}$ on the left through Γ_2^r, $\Gamma_{2'}^r$, $\bar{\Gamma}_2^r$, $\bar{\Gamma}_{2'}^r$, and Eqs. (82) to express the latter through SBE ingredients. By matching terms on the left and right in each loop order, we obtain flow equations for $\dot{w}^{(\ell)}$, $\dot{\bar{\lambda}}_r^{(\ell)}$, $\dot{\lambda}_r^{(\ell)}$ and $\dot{M}_r^{(\ell)}$. For example, at 1ℓ order, Eqs. (75a) and (84a) for $\dot{\mathcal{K}}_1^{r\,(1)}$ yield

$$\dot{w}_r^{(1)} = \Gamma_{2'}^r \circ \dot{\Pi}_r \circ \Gamma_2^r = w_r \bullet \lambda_r \circ \dot{\Pi}_r \circ \bar{\lambda}_r \bullet w_r, \quad (85)$$

consistent with Eq. (48a). Similarly, for $\dot{\mathcal{K}}_2^{r\,(1)}$, we obtain

$$\dot{\bar{\lambda}}_r^{(1)} \bullet w_r + T_r \circ \Pi_r \circ \dot{w}_r^{(1)} = \bar{\Gamma}_{2'}^r \circ \dot{\Pi}_r \circ \Gamma_2^r$$
$$= T_r \circ \dot{\Pi}_r \circ \bar{\lambda}_r \bullet w_r + T_r \circ \Pi_r \circ w_r \bullet \lambda_r \circ \dot{\Pi}_r \circ \bar{\lambda}_r \bullet w_r. \quad (86)$$

The second terms on the left and right cancel due to Eq. (85). The remaining terms, right-multiplied by w_r^{-1}, yield $\dot{\bar{\lambda}}_r^{(1)} = T_r \circ \dot{\Pi}_r \circ \bar{\lambda}_r$, consistent with Eq. (48a). All of the equations (48) can be derived in this manner.

5 Conclusions and outlook

The SBE decomposition of the four-point vertex was originally introduced in Hubbard-like models respecting SU(2) spin symmetry and was written in terms of physical (e.g., spin and charge) channels [26]. Inspired by Refs. [25–30], we here formulated the SBE decomposition without specifying the structure of non-frequency arguments (such as position or momentum, spin, etc.) starting from the parquet equations for general fermionic models. The only restriction on the structure of the bare vertex U is that, apart from being frequency-conserving, it is otherwise constant in frequency. Our formulation can thus be used as a starting point for a rather general class of models. It can also be easily extended to the Keldysh formalism or to other types of particles such as bosons or real fermions.

In this generalized framework, we re-derived self-consistent equations for the ingredients of the SBE decomposition $\nabla_r = \bar{\lambda}_r \bullet w_r \bullet \lambda_r$, the so-called SBE equations, by separating the BSEs for the two-particle reducible vertices regarding their U-reducibility. The U-reducible ∇_r have a transparent interpretation through bosonic exchange fluctuations and Hedin vertices, describing the coupling of these bosonic fluctuations to fermions. As our main result, we derived multiloop flow equations for the SBE ingredients in two different ways: first by inserting the SBE decomposition into parquet mfRG and second by differentiating the SBE equations. Thereby, we presented the multiloop generalization of the 1ℓ SBE flow of Ref. [31]. In addition, we gave a detailed discussion of the relation between the SBE ingredients, M_r and $\nabla_r = \bar{\lambda}_r \bullet w_r \bullet \lambda_r$, and the asymptotic classes $\mathcal{K}_i^r$ of the two-particle reducible vertices. Finally, we also presented multiloop flow equations for the $\mathcal{K}_i^r$ and thus provided a unified formulation for the mfRG treatment of the parquet and the SBE vertex decompositions.

A numerical study of the SBE mfRG flow for relevant model systems, such as the single-impurity Anderson model or the Hubbard model, is left for future work. Below, we outline some open questions to be addressed.

The numerically most expensive SBE ingredient is the fully U-irreducible vertex $\varphi^{U\mathrm{irr}}$, involving the multiboson exchange terms M_r, because these all depend on three frequency arguments. One may hope that, for certain applications, it might suffice to neglect $\varphi^{U\mathrm{irr}}$ (as done in Ref. [35] for a DMFT treatment of the Hubbard model), or to treat it in a cheap fashion, e.g., by not keeping track of its full frequency dependence or by not letting it flow (cf. Ref. [31]). This spoils the parquet

two-particle self-consistency while retaining SBE self-consistency. It is an interesting open question which of the main qualitative features of the parquet solution, such as fulfillment of the Mermin–Wagner theorem [52], remain intact this way.

One formal feature, namely regulator independence, is maintained if multiloop flow equations in the SBE approximation are used. These equations are derived by setting $\varphi^{U\mathrm{irr}} = 0$ and $\dot{M}_r = 0$ from the beginning (Sect. 3.4) and are actually simpler than those obtained by setting $\dot{M}_r = 0$ in the full SBE mfRG flow. We left the derivation of a self-energy flow directly within the SBE approximation for future work. The combination of such a self-energy flow with the vertex flow of Sect. 3.4 would constitute the total derivative of the SBE approximation. Therefore, if loop convergence can be achieved when integrating these simplified flow equations, the results will be regulator independent, just as for the full SBE mfRG flow with $\varphi^{U\mathrm{irr}} = \sum_r M_r$ and $\dot{M}_r \neq 0$, reproducing the PA.

Even if it turns out that a full treatment of $\varphi^{U\mathrm{irr}}$ is required for capturing essential qualitative features of the vertex, this might still be numerically cheaper than a full treatment of $\mathcal{K}_3$. The reason is that each $\mathcal{K}_3^r$ contains a contribution, the $\mathcal{K}_2^r \bullet w_r^{-1} \bullet \mathcal{K}_{2'}^r$ term in Eq. (79), which is included not in M_r but in ∇_r, and parametrized through the numerically cheaper Hedin vertices and screened interactions, see Fig. 11. If these terms decay comparatively slowly with frequency, their treatment via the $\mathcal{K}_i^r$ decomposition would be numerically expensive, and the SBE decomposition could offer a numerically cheaper alternative. A systematic comparison of the numerical costs required to compute the multiloop flow of the two decompositions should thus be a main goal of future work.

Author contributions

M.G., E.W., A.G., and F.B.K. contributed to the derivation of the presented equations. All authors jointly prepared the manuscript.
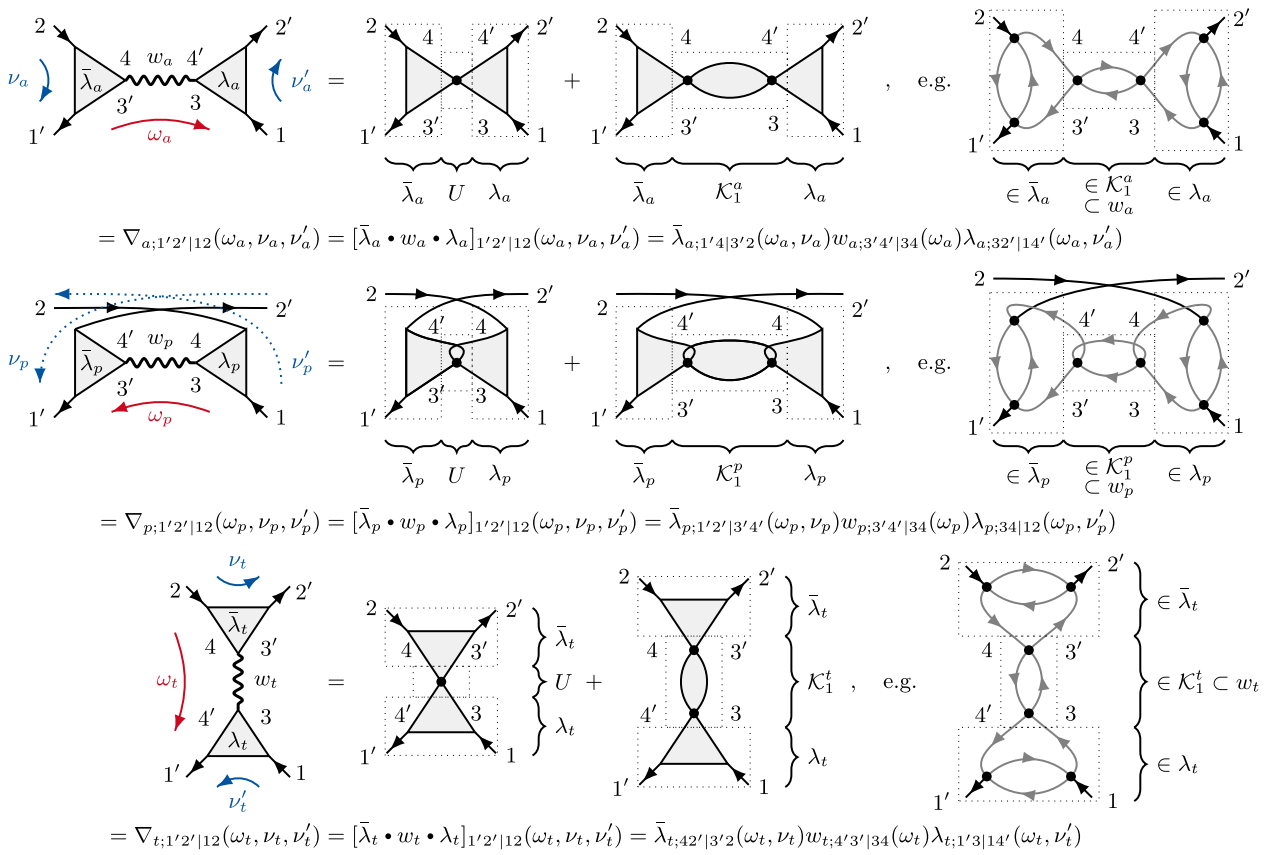
Fig. 12 Illustration of the structure of ∇_r using $w_r = U + \mathcal{K}_1^r$ (Eq. (76)), including an exemplary sixth-order diagram. While $\bar{\lambda}_r$, w_r, λ_r factorize w.r.t. their frequency dependence (since they are connected by bare vertices in ∇_r), they are viewed as four-point objects w.r.t. the other quantum numbers (the internal indices $3, 3', 4, 4'$ have to be summed over, cf. Eqs. (6))

A Diagrams of SBE ingredients

Figure 12 illustrates which parts of the U-r-reducible diagrams ∇_r belong to the Hedin vertices $\bar{\lambda}_r, \lambda_r$ and which parts belong to the screened interactions w_r (for exemplary low-order diagrams, see Fig. 5).

B Diagrams of asymptotic classes

We illustrate the channel-specific frequency parametrizations of the vertex (Fig. 3) in second-order perturbation theory in Fig. 13.

The bosonic frequency ω_r is transferred through the bubble in which each diagram is reducible, while the fermionic frequencies ν_r, ν_r' parametrize the frequency dependence on each side of the bubble. Evidently, the internal propagator lines only depend on the bosonic transfer frequency of the corresponding channel (and the internal integration frequency). The external fermionic frequency ν_r flows in and out at the same bare vertex, and so does ν_r' at another bare vertex, such that the value of each diagram is independent
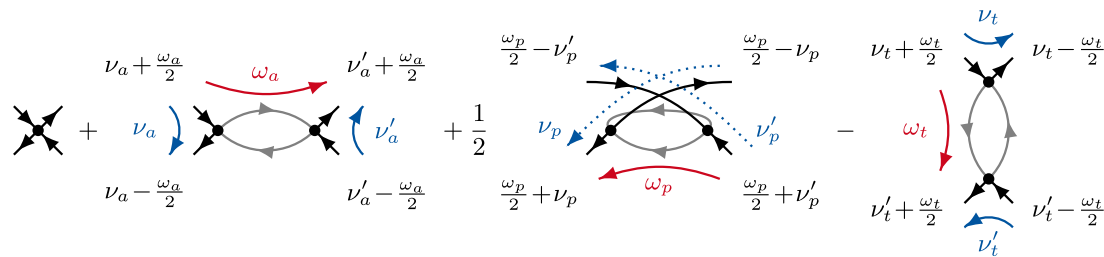
Fig. 13 Diagrams in second-order perturbation theory including the channel-specific frequency parametrization

$$\gamma_a(\omega_a, \nu_a, \nu'_a) = \mathcal{K}_1^a(\omega_a) + \mathcal{K}_2^a(\omega_a, \nu_a) + \mathcal{K}_{2'}^a(\omega_a, \nu'_a) + \mathcal{K}_3^a(\omega_a, \nu_a, \nu'_a),$$

$$\gamma_p(\omega_p, \nu_p, \nu'_p) = \mathcal{K}_1^p(\omega_p) + \mathcal{K}_2^p(\omega_p, \nu_p) + \mathcal{K}_{2'}^p(\omega_p, \nu'_p) + \mathcal{K}_3^p(\omega_p, \nu_p, \nu'_p),$$

$$\gamma_t(\omega_t, \nu_t, \nu'_t) = \mathcal{K}_1^t(\omega_t) + \mathcal{K}_2^t(\omega_t, \nu_t) + \mathcal{K}_{2'}^t(\omega_t, \nu'_t) + \mathcal{K}_3^t(\omega_t, \nu_t, \nu'_t).$$

Fig. 14 Illustration of the decomposition of the two-particle reducible vertices γ_r into asymptotic classes, $\mathcal{K}_1^r + \mathcal{K}_2^r + \mathcal{K}_{2'}^r + \mathcal{K}_3^r$

of ν_r, ν'_r. This notion can be generalized [16], leading to the decomposition of each Π-r-reducible vertex γ_r into four different asymptotic classes, $\mathcal{K}_1^r + \mathcal{K}_2^r + \mathcal{K}_{2'}^r + \mathcal{K}_3^r$, depicted diagrammatically in Fig. 14. A formal definition is given by Eqs. (69) in the main text.

C Relation to SBE in physical channels

The SBE decomposition was originally defined in terms of the charge, spin, and singlet pairing channels [26]. These involve specific linear combinations of the spin components, chosen to diagonalize the spin structure in the BSEs for SU(2)-symmetric systems [9]. Assuming SU(2) spin symmetry, we show below how these "physical" SBE channels are related to the "diagrammatic" SBE channels used in the main text.

By spin conservation, each incoming spin $\sigma \in \{\uparrow, \downarrow\}$ must also come out of a vertex. The nonzero components thus are

$$\Gamma^{\sigma\bar{\sigma}} = \Gamma^{\sigma\bar{\sigma}|\sigma\bar{\sigma}}, \quad \hat{\Gamma}^{\sigma\bar{\sigma}} = \Gamma^{\sigma\bar{\sigma}|\bar{\sigma}\sigma}, \quad \Gamma^{\sigma\sigma} = \Gamma^{\sigma\sigma|\sigma\sigma}. \quad (87)$$

Furthermore, crossing symmetry relates $\Gamma^{\uparrow\downarrow}$ and $\hat{\Gamma}^{\uparrow\downarrow}$, and SU(2) spin symmetry yields $\Gamma^{\sigma\sigma} = \Gamma^{\sigma\bar{\sigma}} + \hat{\Gamma}^{\sigma\bar{\sigma}}$ [53].

On the level of the full vertex, one defines the charge, spin, and singlet or triplet pairing channels as [9,38]

$$\Gamma^{\text{ch/sp}} = \Gamma^{\uparrow\uparrow} \pm \Gamma^{\uparrow\downarrow}, \quad \Gamma^{\text{tr/si}} = \Gamma^{\uparrow\downarrow} \pm \hat{\Gamma}^{\uparrow\downarrow}. \quad (88)$$

This notation carries over to all vertex objects like ∇_r^α, λ_r^α and w_r^α, with α denoting ch, sp, si, or tr.

The bare vertex has $U^{\uparrow\uparrow} = 0$ and $U^{\uparrow\downarrow} = -\hat{U}^{\uparrow\downarrow}$, so that

$$U^{\text{ch/sp}} = U^{\uparrow\uparrow} \pm U^{\uparrow\downarrow} = \pm U^{\uparrow\downarrow}, \quad (89a)$$

$$U^{\text{si}} = U^{\uparrow\downarrow} - \hat{U}^{\uparrow\downarrow} = 2U^{\uparrow\downarrow}. \quad (89b)$$

The bare interaction U^{tr} in the triplet pairing channel vanishes and does not give a U-reducible contribution [26].

We now show that, if the ingredients of the SBE decomposition Eq. (41a) are expressed through the physical charge and spin components (ch, sp) rather than the diagrammatic components ($\uparrow\uparrow$, $\uparrow\downarrow$) used here, one indeed obtains the original form of the SBE decomposition depicted in Fig. 1 of Ref. [26].

This is trivial to see for the fully U-irreducible part $\varphi^{U\mathrm{irr}}$ (analogous to Eq. (88)) and the bare vertex U (Eqs. (89)). It remains to show that for the U-r-reducible terms $\nabla_r = \bar{\lambda}_r \bullet w_r \bullet \lambda_r$, the components ∇_r^α have the form given in Fig. 1 of Ref. [26], with $\alpha = $ ch or sp.

We start with the t channel. Defining sign factors for charge and spin channels, $s^{\mathrm{ch}} = 1$ and $s^{\mathrm{sp}} = -1$, we have

$$
\begin{aligned}
\nabla_t^\alpha &= \nabla_t^{\uparrow\uparrow} + s^\alpha \nabla_t^{\uparrow\downarrow} \\
&= \bar{\lambda}_t^{\sigma\uparrow|\sigma\uparrow} w_t^{\sigma'\sigma|\sigma'\sigma} \lambda_t^{\uparrow\sigma'|\uparrow\sigma'} + s^\alpha \bar{\lambda}_t^{\sigma\downarrow|\sigma\downarrow} w_t^{\sigma'\sigma|\sigma'\sigma} \lambda_t^{\uparrow\sigma'|\uparrow\sigma'}.
\end{aligned}
\tag{90}
$$

Here, we sum as usual over spin indices σ, σ'. Making use of $w_t^{\uparrow\uparrow} = w_t^{\downarrow\downarrow}$, $w_t^{\downarrow\uparrow} = w_t^{\uparrow\downarrow}$, and similarly for $\bar{\lambda}_t$, λ_t, we can collect the summands as

$$
\begin{aligned}
\nabla_t^\alpha &= (\bar{\lambda}_t^{\uparrow\uparrow} + s^\alpha \bar{\lambda}_t^{\uparrow\downarrow})(w_t^{\uparrow\uparrow} + s^\alpha w_t^{\uparrow\downarrow})(\lambda_t^{\uparrow\uparrow} + s^\alpha \lambda_t^{\uparrow\downarrow}) \\
&= \bar{\lambda}_t^\alpha w_t^\alpha \lambda_t^\alpha,
\end{aligned}
\tag{91}
$$

which is equivalent to ∇^{ph} in Ref. [26]. (Note that in our convention of depicting diagrams, all diagrams are mirrored along the diagonal from the top left to bottom right (i.e., the bottom left and top right legs are exchanged) compared to the convention used in Ref. [26]: The ph ($\overline{\mathrm{ph}}$) channel corresponds to the t (a) channel.)

We continue with the a channel, which is related to the t channel by crossing symmetry,

$$
\hat{\Gamma}^{\uparrow\downarrow}(\omega_a, \nu_a, \nu_a') = -\Gamma^{\uparrow\downarrow}(\omega_t = \omega_a, \nu_t = \nu_a, \nu_t' = \nu_a').
\tag{92}
$$

The frequency arguments on the right are defined according to the t-channel conventions $(\omega_t, \nu_t, \nu_t')$, and then evaluated at the a-channel frequencies occurring on the left. In particular, we have (cf. Eq. (11) of Ref. [26])

$$
\begin{aligned}
&\Gamma^\alpha(\omega_a, \nu_a, \nu_a') \\
&= -\tfrac{1}{2}\left[\Gamma^{\mathrm{ch}} + (1 + 2s^\alpha)\Gamma^{\mathrm{sp}}\right](\omega_t = \omega_a, \nu_t = \nu_a, \nu_t' = \nu_a').
\end{aligned}
\tag{93}
$$

The U-a-reducible diagrams ∇_a can therefore be expressed through the U-t-reducible diagrams ∇_t:

$$
\begin{aligned}
&\nabla_a^\alpha(\omega_a, \nu_a, \nu_a') \\
&= -\tfrac{1}{2}\left[\bar{\lambda}_t^{\mathrm{ch}} w_t^{\mathrm{ch}} \lambda_t^{\mathrm{ch}} + (1 + 2s^\alpha)\bar{\lambda}_t^{\mathrm{sp}} w_t^{\mathrm{sp}} \lambda_t^{\mathrm{sp}}\right](\omega_a, \nu_a, \nu_a'),
\end{aligned}
\tag{94}
$$

reproducing $\nabla^{\overline{\mathrm{ph}}}$ in Ref. [26]. The frequency arguments on the right have the same meaning as in Eq. (92).

Last, we consider the p channel. With SU(2) symmetry, $\nabla_p^{\uparrow\uparrow} = \nabla_p^{\uparrow\downarrow} + \hat{\nabla}_p^{\uparrow\downarrow}$, we have

$$
\begin{aligned}
\nabla_p^\alpha &= \nabla_p^{\uparrow\uparrow} + s^\alpha \nabla_p^{\uparrow\downarrow} = \hat{\nabla}_p^{\uparrow\downarrow} + (1 + s^\alpha)\nabla_p^{\uparrow\downarrow} \\
&= \bar{\lambda}_p^{\uparrow\downarrow|\sigma\bar{\sigma}} w_p^{\sigma\bar{\sigma}|\sigma'\bar{\sigma}'} \lambda_p^{\sigma'\bar{\sigma}'|\uparrow\downarrow} \\
&\quad + (1 + s^\alpha)\bar{\lambda}_p^{\uparrow\downarrow|\sigma\bar{\sigma}} w_p^{\sigma\bar{\sigma}|\sigma'\bar{\sigma}'} \lambda_p^{\sigma'\bar{\sigma}'|\downarrow\uparrow}.
\end{aligned}
\tag{95}
$$

Note that the spins in the first and second pair of spin indices of w_p have to be opposite, $\sigma\bar{\sigma}$ and $\sigma'\bar{\sigma}'$, since they connect to the same bare vertex (cf. Fig. 12), and $U^{\sigma\sigma} = 0$. Furthermore, the crossing relation $U^{\uparrow\downarrow} = -\hat{U}^{\uparrow\downarrow}$ implies

$w_p^{\uparrow\downarrow} = -\hat{w}_p^{\uparrow\downarrow}$. By use of this, we can combine the terms in the spin sums as

$$
\begin{aligned}
\nabla_p^\alpha &= \tfrac{s^\alpha}{2}(\bar{\lambda}_p^{\uparrow\downarrow} - \hat{\bar{\lambda}}_p^{\uparrow\downarrow})(w_p^{\uparrow\downarrow} - \hat{w}_p^{\uparrow\downarrow})(\lambda_p^{\uparrow\downarrow} - \hat{\lambda}_p^{\uparrow\downarrow}) \\
&= \tfrac{s^\alpha}{2} \bar{\lambda}_p^{\mathrm{si}} w_p^{\mathrm{si}} \lambda_p^{\mathrm{si}},
\end{aligned}
\tag{96}
$$

which gives ∇^{pp} in Ref. [26].

In summary, we thus reproduce the decomposition of Ref. [26]:

$$
\Gamma^\alpha = \varphi^{U\mathrm{irr},\alpha} + \nabla_a^\alpha + \nabla_p^\alpha + \nabla_t^\alpha - 2U^\alpha,
\tag{97a}
$$

where the U-r-reducible parts are defined as

$$
\begin{aligned}
\nabla_a^\alpha(\omega_a, \nu_a, \nu_a') &= -\tfrac{1}{2}\nabla_t^{\mathrm{ch}}(\omega_a, \nu_a, \nu_a') \\
&\quad - (\tfrac{3}{2} - 2\delta_{\alpha,\mathrm{sp}})\nabla_t^{\mathrm{sp}}(\omega_a, \nu_a, \nu_a'),
\end{aligned}
\tag{97b}
$$

$$
\nabla_p^\alpha(\omega_p, \nu_p, \nu_p') = (\tfrac{1}{2} - \delta_{\alpha,\mathrm{sp}})[\bar{\lambda}_p^{\mathrm{si}} w_p^{\mathrm{si}} \lambda_p^{\mathrm{si}}](\omega_p, \nu_p, \nu_p'),
\tag{97c}
$$

$$
\nabla_t^\alpha(\omega_t, \nu_t, \nu_t') = [\bar{\lambda}_t^\alpha w_t^\alpha \lambda_t^\alpha](\omega_t, \nu_t, \nu_t').
\tag{97d}
$$

D Correlators and susceptibilities

Reference [26] established that the SBE ingredients $\bar{\lambda}_r$, w_r, λ_r are related to three-point correlators and generalized susceptibilities. For completeness, we illustrate here how these relations arise within the present framework. The starting point is the general relation between the four-point correlator $G^{(4)}$ and the four-point vertex Γ,

$$
\begin{aligned}
G_{12|1'2'}^{(4)} = \langle c_1 c_2 \bar{c}_{2'} \bar{c}_{1'}\rangle &= G_{1|1'}G_{2|2'} - G_{1|2'}G_{2|1'} \\
&\quad + G_{1|5'}G_{2|6'}\Gamma_{5'6'|56}G_{5|1'}G_{6|2'}.
\end{aligned}
\tag{98}
$$

By combining two fermionic fields, one obtains the bosonic exchange field ψ, the pairing field ϕ, and its conjugate $\bar{\phi}$,

$$
\psi_{12'}(\omega) = \sum_\nu c_1(\nu - \tfrac{\omega}{2})\bar{c}_{2'}(\nu + \tfrac{\omega}{2}) = \bar{\psi}_{2'1}(-\omega),
\tag{99a}
$$

$$
\phi_{12}(\omega) = \sum_\nu c_1(\tfrac{\omega}{2} + \nu)c_2(\tfrac{\omega}{2} - \nu),
\tag{99b}
$$

$$
\bar{\phi}_{1'2'}(\omega) = \sum_{\nu'} \bar{c}_{2'}(\tfrac{\omega}{2} - \nu')\bar{c}_{1'}(\tfrac{\omega}{2} + \nu').
\tag{99c}
$$

Three-point correlators and bosonic two-point correlators involving these fields can be obtained from $G^{(4)}$ by summing over the frequency $\nu_r^{(')}$ in the channel-specific parametrization (cf. Equation (17) and Fig. 3):

$$
\bar{G}_{r;12|1'2'}^{(3)}(\omega_r, \nu_r) = \sum_{\nu_r'} G_{12|1'2'}^{(4)}(\omega_r, \nu_r, \nu_r'),
\tag{100a}
$$

$$
G_{r;12|1'2'}^{(3)}(\omega_r, \nu_r') = \sum_{\nu_r} G_{12|1'2'}^{(4)}(\omega_r, \nu_r, \nu_r'),
\tag{100b}
$$

$$
D_{r;12|1'2'}(\omega_r) = \sum_{\nu_r, \nu_r'} G_{12|1'2'}^{(4)}(\omega_r, \nu_r, \nu_r').
\tag{100c}
$$

For example, in the p channel, we have

$$
\bar{G}_{p;12|1'2'}^{(3)} = \langle c_1 c_2 \bar{\phi}_{1'2'}\rangle, \quad D_{p;12|1'2'} = \langle \phi_{12}\bar{\phi}_{1'2'}\rangle.
\tag{101}
$$

The four-point correlator $G^{(4)}$ is closely related to the *generalized* susceptibilities $\chi_r^{(4)}$ [38]:

$$\chi^{(4)}_{a;12|1'2'}(\omega_a, \nu_a, \nu'_a)$$
$$= G^{(4)}_{12|1'2'}(\omega_a, \nu_a, \nu'_a) + \delta_{\omega_a,0} G_{1|2'}(\nu_a) G_{2|1'}(\nu'_a)$$
$$= \delta_{\nu_a \nu'_a} \Pi_{a;12|1'2'}(\omega_a, \nu_a) + [\Pi_a \circ \Gamma \circ \Pi_a]_{12|1'2'}(\omega_a, \nu_a, \nu'_a),$$
$$\text{(102a)}$$

$$\chi^{(4)}_{p;12|1'2'}(\omega_p, \nu_p, \nu'_p) = \tfrac{1}{4} G^{(4)}_{12|1'2'}(\omega_p, \nu_p, \nu'_p)$$
$$= \delta_{\nu_p \nu'_p} \tfrac{1}{2} \Pi_{p;12|1'2'}(\omega_p, \nu_p) - \delta_{\nu_p,-\nu'_p} \tfrac{1}{2} \Pi_{p;12|2'1'}(\omega_p, \nu_p)$$
$$+ [\Pi_p \circ \Gamma \circ \Pi_p]_{12|1'2'}(\omega_p, \nu_p, \nu'_p),$$
$$\text{(102b)}$$

$$\chi^{(4)}_{t;12|1'2'}(\omega_t, \nu_t, \nu'_t)$$
$$= G^{(4)}_{12|1'2'}(\omega_t, \nu_t, \nu'_t) - \delta_{\omega_t,0} G_{1|1'}(\nu'_t) G_{2|2'}(\nu_t)$$
$$= \delta_{\nu_t \nu'_t} \Pi_{t;12|1'2'}(\omega_t, \nu_t) + [\Pi_t \circ \Gamma \circ \Pi_t]_{12|1'2'}(\omega_t, \nu_t, \nu'_t).$$
$$\text{(102c)}$$

In analogy to Eqs. (100), we then obtain three-point functions $\bar{\chi}^{(3)}_r, \chi^{(3)}_r$ and physical susceptibilities χ_r by summing over frequencies:

$$\bar{\chi}^{(3)}_{r;12|1'2'}(\omega_r, \nu_r) = \sum_{\nu'_r} \chi^{(4)}_{r;12|1'2'}(\omega_r, \nu_r, \nu'_r), \qquad \text{(103a)}$$

$$\chi^{(3)}_{r;12|1'2'}(\omega_r, \nu'_r) = \sum_{\nu_r} \chi^{(4)}_{r;12|1'2'}(\omega_r, \nu_r, \nu'_r), \qquad \text{(103b)}$$

$$\chi_{r;12|1'2'}(\omega_r) = \sum_{\nu_r, \nu'_r} \chi^{(4)}_{r;12|1'2'}(\omega_r, \nu_r, \nu'_r). \qquad \text{(103c)}$$

The prefactor $\frac{1}{4}$ in Eq. (102b) ensures that the susceptibility χ_r in Eqs. (103c) is consistent with its counterpart in the main text (cf. Eq. (45c)).

To make a connection between $\bar{\chi}^{(3)}_r, \chi^{(3)}_r, \chi_r$ and SBE objects, we use Eqs. (102), multiply by the bare interaction U, and express the result in terms of the four-point vertex:

$$\bar{\chi}^{(3)}_r \bullet U = \Pi_r \circ (U + \Gamma \circ \Pi_r \circ U), \qquad \text{(104a)}$$

$$U \bullet \chi^{(3)}_r = (U + U \circ \Pi_r \circ \Gamma) \circ \Pi_r, \qquad \text{(104b)}$$

$$U \bullet \chi_r \bullet U = U \circ \Pi_r \circ U + U \circ \Pi_r \circ \Gamma \circ \Pi_r \circ U. \qquad \text{(104c)}$$

Finally, comparing these expressions to Eqs. (42)–(44) shows their relation to the SBE ingredients:

$$\bar{\chi}^{(3)}_r = \Pi_r \circ \bar{\lambda}_r \bullet w_r \bullet U^{-1} = \Pi_r \circ \bar{\Gamma}^{(3)}_r, \qquad \text{(105a)}$$

$$\chi^{(3)}_r = U^{-1} \bullet w_r \bullet \lambda_r \circ \Pi_r = \Gamma^{(3)}_r \circ \Pi_r, \qquad \text{(105b)}$$

$$\chi_r = U^{-1} \bullet (w_r - U) \bullet U^{-1}. \qquad \text{(105c)}$$

These relations are analogous to those given in Eqs. (6), (8) and (15) in Ref. [26]. Relations between the bosonic correlators $\bar{G}^{(3)}_r, G^{(3)}_r, D_r$ from Eqs. (100) and the SBE ingredients $\bar{\lambda}_r, w_r, \lambda_r$ are analogous up to disconnected terms and can be readily constructed from Eqs. (103), (102), and (105). For example, in the a channel, we have

$$\bar{G}^{(3)}_{a;12|1'2'}(\omega_a, \nu_a) = [\Pi_a \circ \bar{\lambda}_a \bullet w_a \bullet U^{-1}]_{12|1'2'}(\omega_a, \nu_a)$$
$$- \delta_{\omega_a,0} G_{1|2'}(\nu_a) \sum_{\nu'_a} G_{2|1'}(\nu'_a),$$

$$D_{a;12|1'2'}(\omega_a) = [U^{-1} \bullet (w_a - U) \bullet U^{-1}]_{12|12'}(\omega_a)$$
$$- \delta_{\omega_a,0} \sum_{\nu_a} G_{1|2'}(\nu_a) \sum_{\nu'_a} G_{2|1'}(\nu'_a).$$
$$\text{(106)}$$

E Susceptibilities for Hubbard interaction

The susceptibilities defined in Eq. (45c) and in Appendix D exhibit general dependencies w.r.t. their non-frequency indices $12|1'2'$. In the following, we show how they are related to physical charge, spin, and pairing susceptibilities. To this end, we focus on models with a local (momentum-independent) bare interaction, which has only spin degrees of freedom subject to the Pauli principle. In the a and t channel, Eq. (44c) with $\mathcal{K}^r_1 = w_r - U$ then reads

$$\mathcal{K}^{a;\sigma\sigma'|\sigma\sigma'}_1 = U^{\sigma\bar{\sigma}|\bar{\sigma}'\sigma'} \chi^{\bar{\sigma}'\bar{\sigma}|\bar{\sigma}'\bar{\sigma}}_a U^{\bar{\sigma}'\sigma'|\sigma\bar{\sigma}}, \quad \text{(107a)}$$

$$\mathcal{K}^{t;\sigma\sigma'|\sigma\sigma'}_1 = U^{\bar{\sigma}'\sigma'|\bar{\sigma}'\sigma'} \chi^{\bar{\sigma}'\bar{\sigma}|\bar{\sigma}\bar{\sigma}'}_t U^{\sigma\bar{\sigma}|\sigma\bar{\sigma}}. \quad \text{(107b)}$$

We further specify $U^{\sigma\bar{\sigma}|\bar{\sigma}'\sigma'} = u(\delta_{\sigma\sigma'} - \delta_{\sigma\bar{\sigma}'})$, with the (scalar) bare interaction strength u. With SU(2) symmetry, $\chi^{\sigma_1\sigma'_1|\sigma_2\sigma'_2}_r = \chi^{\bar{\sigma}_1\bar{\sigma}'_1|\bar{\sigma}_2\bar{\sigma}'_2}_r$, Eqs. (107) thus simplify to

$$\chi^{\sigma\sigma'|\sigma\sigma'}_{a/t} = \mathcal{K}^{a/t;\sigma\sigma'|\sigma\sigma'}_1 / u^2. \qquad \text{(108)}$$

In the p channel, we have

$$\mathcal{K}^{p;\sigma\sigma'|\sigma\sigma'}_1 = \sum_{\sigma_1\sigma_2} U^{\sigma\sigma'|\sigma_1\bar{\sigma}_1} \chi^{\sigma_1\bar{\sigma}_1|\sigma_2\bar{\sigma}_2}_p U^{\sigma_2\bar{\sigma}_2|\sigma\sigma'}$$
$$\text{(109a)}$$

$$= U^{\sigma\sigma'|\sigma\sigma'} \tilde{\chi}^{\sigma\sigma'|\sigma\sigma'}_p U^{\sigma\sigma'|\sigma\sigma'}. \qquad \text{(109b)}$$

Here, the second line (109b) follows from SU(2) and crossing symmetry. It employs

$$\tilde{\chi}_p(\omega_p) = [\mathbf{1}_p \circ \tilde{\Pi}_p \circ \mathbf{1}_p](\omega_p)$$
$$+ [\mathbf{1}_p \circ \tilde{\Pi}_p \circ \Gamma \circ \tilde{\Pi}_p \circ \mathbf{1}_p](\omega_p), \qquad \text{(110)}$$

where $\tilde{\Pi}_{p;34|3'4'} = G_{3|3'} G_{4|4'} = 2\Pi_{p;34|3'4'}$ does *not* include a prefactor $1/2$ (introduced in Eq. (5b) to avoid double counting within internal spin sums), since there are no spin sums in Eq. (109b). (This definition of the p susceptibility agrees with the related literature, e.g., Ref. [38].) With $U^{\sigma\sigma'|\sigma\sigma'} = -u\delta_{\sigma\bar{\sigma}'}$, we can write

$$\tilde{\chi}^{\sigma\sigma'|\sigma\sigma'}_p = \delta_{\sigma\bar{\sigma}'} \mathcal{K}^{p;\sigma\sigma'|\sigma\sigma'}_1 / u^2, \qquad \text{(111)}$$

in analogy to Eq. (108).

The relation between these "diagrammatic" susceptibilities χ_r and their "physical" counterparts can be made explicit by means of the bilinears

$$\rho_{\sigma\sigma'} = \bar{c}_\sigma c_{\sigma'}, \qquad \delta\rho_{\sigma\sigma'} = \rho_{\sigma\sigma'} - \langle\rho_{\sigma\sigma}\rangle\delta_{\sigma\sigma'} \quad \text{(112a)}$$

$$\rho^-_{\sigma\sigma'} = c_\sigma c_{\sigma'}, \qquad \rho^+_{\sigma\sigma'} = \bar{c}_{\sigma'}\bar{c}_\sigma. \quad \text{(112b)}$$

Then, we have in the imaginary-time domain

$$\chi^{\sigma\sigma'|\sigma\sigma'}_a(\tau) = -\langle\delta\rho_{\sigma'\sigma}(\tau)\delta\rho_{\sigma\sigma'}(0)\rangle, \qquad \text{(113a)}$$

$$\tilde{\chi}^{\sigma\sigma'|\sigma\sigma'}_p(\tau) = \langle\rho^-_{\sigma\sigma'}(\tau)\rho^+_{\sigma\sigma'}(0)\rangle, \qquad \text{(113b)}$$

$$\chi^{\sigma\sigma'|\sigma\sigma'}_t(\tau) = \langle\delta n_\sigma(\tau)\delta n_{\sigma'}(0)\rangle. \qquad \text{(113c)}$$

with $n_\sigma = \rho_{\sigma\sigma}$. Choosing the spin arguments as $\chi^{\uparrow\downarrow}_r = \chi^{\uparrow\downarrow|\uparrow\downarrow}_r$, we furthermore get

$$\chi_a^{\uparrow\downarrow}(\tau) = -\langle S_-(\tau)S_+\rangle, \qquad (114a)$$

$$\tilde{\chi}_p^{\uparrow\downarrow}(\tau) = \langle \Delta_{\mathrm{si}}(\tau)\Delta_{\mathrm{si}}^\dagger(0)\rangle, \qquad (114b)$$

$$\chi_t^{\uparrow\downarrow}(\tau) = \langle \delta n_\uparrow(\tau)\delta n_\downarrow(0)\rangle. \qquad (114c)$$

Hence, $\chi_a^{\uparrow\downarrow}$ describes spin fluctuations ($S_- = \bar{c}_\downarrow c_\uparrow$, $S_+ = \bar{c}_\uparrow c_\downarrow$) and $\tilde{\chi}_p^{\uparrow\downarrow}$ singlet pairing fluctuations ($\Delta_{\mathrm{si}} = c_\uparrow c_\downarrow$). By SU(2) spin symmetry, $\frac{1}{2}\chi_a^{\uparrow\downarrow}(\tau) = -\langle S_z(\tau)S_z\rangle$, with $S_z = \frac{1}{2}(n_\uparrow - n_\downarrow) = \frac{1}{2}(\delta n_\uparrow - \delta n_\downarrow)$. It then follows that

$$\begin{aligned}\chi_t^{\uparrow\downarrow}(\tau) - \tfrac{1}{2}\chi_a^{\uparrow\downarrow}(\tau) &= \tfrac{1}{2}(\langle \delta n_\uparrow(\tau)\delta n_\uparrow\rangle + \langle \delta n_\uparrow(\tau)\delta n_\downarrow\rangle) \\ &= \tfrac{1}{4}\langle \delta n(\tau)\delta n\rangle \end{aligned} \qquad (115)$$

describes charge fluctuations with $n = n_\uparrow + n_\downarrow$.

References

1. T. Schäfer, N. Wentzell, F. Šimkovic, Y.Y. He, C. Hille, M. Klett, C.J. Eckhardt, B. Arzhang, V. Harkov, F.M. Le Régent et al., Phys. Rev. X **11**, 011058 (2021)
2. W. Metzner, M. Salmhofer, C. Honerkamp, V. Meden, K. Schönhammer, Rev. Mod. Phys. **84**, 299 (2012)
3. P. Kopietz, L. Bartosch, F. Schütz, *Introduction to the Functional Renormalization Group*, vol. 798 (Springer, Berlin, 2010)
4. J. Diekmann, S.G. Jakobs, Phys. Rev. B **103**, 155156 (2021)
5. F.B. Kugler, J. von Delft, Phys. Rev. B **97** (2018)
6. F.B. Kugler, J. von Delft, Phys. Rev. Lett. **120** (2018)
7. F.B. Kugler, J. von Delft, New J. Phys. **20**, 123029 (2018)
8. B. Roulet, J. Gavoret, P. Nozières, Phys. Rev. **178**, 1072 (1969)
9. N.E. Bickers, in *in: Sénéchal D., Tremblay A.-M., Bourbonnais C. (eds), Theoretical Methods for Strongly Correlated Electrons, CRM Series in Mathematical Physics* (Springer, New York, 2004)
10. A. Tagliavini, C. Hille, F.B. Kugler, S. Andergassen, A. Toschi, C. Honerkamp, SciPost Phys. **6**, 9 (2019)
11. C. Hille, F.B. Kugler, C.J. Eckhardt, Y.Y. He, A. Kauch, C. Honerkamp, A. Toschi, S. Andergassen, Phys. Rev. Res. **2**, 033372 (2020)
12. J. Thoenniss, M.K. Ritter, F.B. Kugler, J. von Delft, M. Punk, arXiv:2011.01268 [cond-mat.str-el] (2020)
13. D. Kiese, T. Mueller, Y. Iqbal, R. Thomale, S. Trebst, Phys. Rev. Res. **4**, 023185 (2022)
14. P. Chalupa-Gantner, F.B. Kugler, C. Hille, J. von Delft, S. Andergassen, A. Toschi, Phys. Rev. Res. **4**, 023050 (2022)
15. G. Li, N. Wentzell, P. Pudleiner, P. Thunström, K. Held, Phys. Rev. B **93**, 165103 (2016)
16. N. Wentzell, G. Li, A. Tagliavini, C. Taranto, G. Rohringer, K. Held, A. Toschi, S. Andergassen, Phys. Rev. B **102**, 085106 (2020)
17. C. Husemann, M. Salmhofer, Phys. Rev. B **79**, 195125 (2009)
18. C. Husemann, K.U. Giering, M. Salmhofer, Phys. Rev. B **85**, 075121 (2012)
19. E.A. Stepanov, A. Huber, E.G.C.P. van Loon, A.I. Lichtenstein, M.I. Katsnelson, Phys. Rev. B **94**, 205110 (2016)
20. E.A. Stepanov, S. Brener, F. Krien, M. Harland, A.I. Lichtenstein, M.I. Katsnelson, Phys. Rev. Lett. **121**, 037204 (2018)
21. E.A. Stepanov, A. Huber, A.I. Lichtenstein, M.I. Katsnelson, Phys. Rev. B **99**, 115124 (2019)
22. E.A. Stepanov, V. Harkov, A.I. Lichtenstein, Phys. Rev. B **100**, 205115 (2019)
23. V. Harkov, M. Vandelli, S. Brener, A.I. Lichtenstein, E.A. Stepanov, Phys. Rev. B **103**, 245123 (2021)
24. E.A. Stepanov, Y. Nomura, A.I. Lichtenstein, S. Biermann, Phys. Rev. Lett. **127**, 207205 (2021)
25. F. Krien, Phys. Rev. B **99**, 235106 (2019)
26. F. Krien, A. Valli, M. Capone, Phys. Rev. B **100**, 155149 (2019)
27. F. Krien, A. Valli, Phys. Rev. B **100**, 245147 (2019)
28. F. Krien, A.I. Lichtenstein, G. Rohringer, Phys. Rev. B **102**, 235133 (2020)
29. F. Krien, A. Valli, P. Chalupa, M. Capone, A.I. Lichtenstein, A. Toschi, Phys. Rev. B **102**, 195131 (2020)
30. F. Krien, A. Kauch, K. Held, Phys. Rev. Res. **3**, 013149 (2021)
31. P.M. Bonetti, A. Toschi, C. Hille, S. Andergassen, D. Vilardi, Phys. Rev. Res. **4**, 013034 (2022)
32. C. Taranto, S. Andergassen, J. Bauer, K. Held, A. Katanin, W. Metzner, G. Rohringer, A. Toschi, Phys. Rev. Lett. **112**, 196402 (2014)
33. D. Vilardi, C. Taranto, W. Metzner, Phys. Rev. B **99**, 104501 (2019)
34. A.A. Katanin, Phys. Rev. B **99**, 115112 (2019)
35. V. Harkov, A.I. Lichtenstein, F. Krien, Phys. Rev. B **104**, 125141 (2021)
36. A. Altland, B.D. Simons, *Condensed Matter Field Theory* (Cambridge University Press, 2010)
37. A. Kamenev, *Field Theory of Non-equilibrium Systems* (Cambridge University Press, 2011)
38. G. Rohringer, A. Valli, A. Toschi, Phys. Rev. B **86**, 125114 (2012)
39. A. Toschi, A.A. Katanin, K. Held, Phys. Rev. B **75**, 045118 (2007)
40. K. Held, A.A. Katanin, A. Toschi, Prog. Theor. Phys. Supp. **176**, 117 (2008)
41. A.A. Katanin, Phys. Rev. B **70**, 115109 (2004)
42. T. Schäfer, G. Rohringer, O. Gunnarsson, S. Ciuchi, G. Sangiovanni, A. Toschi, Phys. Rev. Lett. **110**, 246405 (2013)
43. T. Schäfer, S. Ciuchi, M. Wallerberger, P. Thunström, O. Gunnarsson, G. Sangiovanni, G. Rohringer, A. Toschi, Phys. Rev. B **94**, 235108 (2016)
44. O. Gunnarsson, G. Rohringer, T. Schäfer, G. Sangiovanni, A. Toschi, Phys. Rev. Lett. **119**, 056402 (2017)
45. P. Chalupa, P. Gunacker, T. Schäfer, K. Held, A. Toschi, Phys. Rev. B **97**, 245136 (2018)
46. P. Thunström, O. Gunnarsson, S. Ciuchi, G. Rohringer, Phys. Rev. B **98**, 235107 (2018)
47. F.B. Kugler, S.S.B. Lee, J. von Delft, Phys. Rev. X **11**, 041006 (2021)
48. S.S.B. Lee, F.B. Kugler, J. von Delft, Phys. Rev. X **11**, 041007 (2021)
49. L. Hedin, Phys. Rev. **139**, A796 (1965)
50. E. Walter, Ph.D. thesis, Ludwig-Maximilians-Universität München (2021)
51. S. Aguirre Lamus, Master's thesis, Ludwig-Maximilians-Universität München (2020)
52. N.E. Bickers, D.J. Scalapino, Phys. Rev. B **46**, 8050 (1992)
53. G. Rohringer, Ph.D. thesis, TU Wien (2013)

3.4. Supplements to the SBE formalism

In this section, we provide some additional aspects of the SBE formalism that are not discussed in our paper [P1]. First of all, we clarify the relation between the SBE formalism and the Hubbard–Stratonovich theory discussed in Sec. 3.2. Subsequently, we show two different forms of SBE equations and describe how the self-energy is written in terms of the SBE vertices. The latter two steps are essential for the implementation of our SBE code, which is discussed in Chapter 4.

3.4.1. Connection to Hubbard–Stratonovich fields

The similarities of the SBE approach with other partial bosonization techniques using Hubbard–Stratonovich fields is undeniable [HS09, HGS12]. Indeed, the SBE equations (cf. Eqs. (41) in Ref. [P1]) themselves have the form of Schwinger–Dyson equations we encountered in Sec. 3.2. Here, we give a generalized identification of SBE vertices with the corresponding constituents from a Hubbard–Stratonovich theory compared to that given in App. B of Ref. [BTH$^+$22].

The SBE formalism is related to an unusual Hubbard–Stratonovich action where bosonic fields carry one bosonic frequency, but two general indices involving other quantum numbers like spin and momenta. We introduce the following Hubbard–Stratonovich action with frequency-independent bare bosonic propagators $W_{a,0}$ and $W_{p,0}$ and bare Yukawa couplings $\bar{h}_{a,0}$, $h_{a,0}$, $\bar{h}_{p,0}$, $h_{p,0}$ each involving four fermionic indices [cf. Eq. (3.19)]:

$$
\begin{aligned}
S_{\mathrm{HS}} = {} & \tfrac{2}{\beta} \sum_{\omega} \bar{\psi}_{1'2}(\omega)[W_{a,0}^{-1}]_{12|1'2'}\psi_{12'}(\omega) - \tfrac{1}{\beta} \sum_{\omega} \bar{\phi}_{1'2'}(\omega)[W_{p,0}^{-1}]_{12|1'2'}\phi_{12} \\
& - \tfrac{1}{\beta^2}\left[\sum_{\omega,\nu}[\bar{h}_{a,0}]_{1'2'|12}\bar{c}_{1'}(\nu)c_2(\nu+\omega)\psi_{12'}(\omega)+\sum_{\omega,\nu'}[h_{a,0}]_{1'2'|12}\bar{\psi}_{1'2}(\omega)\bar{c}_{2'}(\nu'+\omega)c_1(\nu')\right] \\
& - \tfrac{1}{2\beta^2}\left[\sum_{\omega,\nu}[\bar{h}_{p,0}]_{1'2'|12}\bar{c}_{1'}(-\nu)\bar{c}_{2'}(\nu+\omega)\phi_{12}(\omega)+\sum_{\omega,\nu'}[h_{p,0}]_{1'2'|12}\bar{\phi}_{1'2'}(\omega)c_2(\nu'+\omega)c_1(-\nu')\right] \\
& + \tfrac{1}{2}U_{1'2'|12}\tfrac{1}{\beta^3}\sum_{\omega,\nu,\nu'}\bar{c}_{1'}(\nu)\bar{c}_{2'}(\nu'+\omega)c_2(\nu+\omega)c_1(\nu'). \qquad (3.30)
\end{aligned}
$$

The last quartic term of fermionic actions is there to compensate terms in the following. When applying the Gaussian field integral back to the full fermionic theory [cf. Eq. (3.20)],

we receive the following interaction term in the fermionic action:

$$S_{\text{int}} = \tfrac{1}{2}\tfrac{1}{\beta^3}\sum_{\omega,\nu,\nu'}[\bar{h}_{a,0}]_{1'4'|32}[W_{a,0}]_{34|3'4'}[h_{a,0}]_{3'2'|14}\bar{c}_{1'}(\nu)c_2(\nu+\omega)\bar{c}_{2'}(\nu'+\omega)c_1(\nu')$$

$$- \tfrac{1}{4}\tfrac{1}{\beta^3}\sum_{\omega,\nu,\nu'}[\bar{h}_{p,0}]_{1'2'|34}[W_{p,0}]_{34|3'4'}[h_{p,0}]_{3'4'|12}\bar{c}_{1'}(-\nu)\bar{c}_2(\nu+\omega)c_{2'}(\nu'+\omega)c_1(-\nu')$$

$$+ \tfrac{1}{2}U_{1'2'|12}\tfrac{1}{\beta^3}\sum_{\omega,\nu,\nu'}\bar{c}_{1'}(\nu)\bar{c}_{2'}(\nu'+\omega)c_2(\nu+\omega)c_1(\nu'). \tag{3.31}$$

Further, we introduce the third diagrammatic channel, i.e., the transversal channel t, by subdividing the first term into two, exchanging the summation indices $1' \leftrightarrow 2'$ and using the following relations for the bare bosonic propagator and bare Yukawa couplings:

$$[W_{t,0}]_{34|3'4'} = -[W_{a,0}]_{43|3'4'}, \quad [\bar{h}_{t,0}]_{4'2'|32} = -[\bar{h}_{a,0}]_{2'4'|32}, \quad [h_{t,0}]_{1'3'|14} = -[h_{a,0}]_{3'1'|14}. \tag{3.32}$$

The summations in S_{int}, Eq. (3.31), are then identified with the channel-dependent products • (excluding frequency summations), Eqs. (4.6). By comparing with the original fermionic action S, Eq. (3.1), we deduce the following relation between the fermionic bare vertices U and the constituents of the Hubbard–Stratonovich theory:

$$3U = \bar{h}_{a,0} \bullet W_{a,0} \bullet h_{a,0} + \bar{h}_{p,0} \bullet W_{p,0} \bullet h_{p,0} + \bar{h}_{t,0} \bullet W_{t,0} \bullet h_{t,0}. \tag{3.33}$$

This identity is trivially fulfilled for $\bar{h}_{r,0} = \mathbf{1}_r = h_{r,0}$ and $W_{r,0} = U$. In that case, all the Hubbard–Stratonovich channels are treated on equal footing, i.e., $U = \bar{h}_{a,0} \bullet W_{a,0} \bullet h_{a,0} = \bar{h}_{p,0}\bullet W_{p,0}\bullet h_{p,0} = \bar{h}_{t,0}\bullet W_{t,0}\bullet h_{t,0}$. In general, different bosonic fields and Yukawa couplings in the Hubbard–Stratonovich action S_{HS}, Eq. (3.19), may lead to the same fermionic coupling. This phenomenon is related to the *Fierz ambiguity* [JW03, Bra12, KV19, KWK$^+$24].

The concept of U reducibility in channel r in the fermionic theory is attributed to the reducibility of a single bosonic propagator line $W_{r,0}$ in the Hubbard–Stratonovich theory. While the Schwinger–Dyson equations of the Hedin vertices, $\bar{\lambda}_r = \mathbf{1}_r + T_r \circ \Pi_r \circ \mathbf{1}_r$ and $\lambda_r = \mathbf{1}_r + \mathbf{1}_r \circ \Pi_r \circ T_r$ (cf. Eqs. (41d)–(41c) in Ref. [P1]), include the U-irreducible vertices T_r from the fermionic theory, the Schwinger–Dyson equations (3.26) of the three-point vertices, $\bar{h}_{\phi,\psi} = \bar{h}_{\phi,\psi,0} + I^{\psi,\phi} \circ \Pi_r \circ \bar{h}_{\phi,\psi,0}$ and $h_{\phi,\psi} = h_{\phi,\psi,0} + h_{\phi,\psi,0} \circ \Pi_r \circ I^{\psi,\phi}$, include the one-particle irreducible vertices $I^{\psi,\phi}$ from the Hubbard–Stratonovich theory. Similarly, the Schwinger–Dyson equations of the polarization P_r involve the Hedin vertices $\bar{\lambda}_r$, λ_r while that of the bosonic self-energies $\Sigma_{\phi,\psi}$ involve the three-point vertices $\bar{h}^{\psi,\phi}$, $h^{\psi,\phi}$. In this regard, the SBE formalism translates to a conventional Hubbard–Stratonovich theory. Only, it is a fully fermionic theory with the new concept of U reducibility in the diagrams of the four-point vertex Γ.

3.4.2. Left and right SBE equations

Let us comment on a fact that is usually swept under the carpet. The Bethe–Salpeter equations (3.13) come in two variants depending on the order of appearance of the irreducible vertex I_r and the full vertex Γ. Being aware of both variants provides more flexibility in the numerical computation of vertices and leads to a deeper understanding of the structure of parquet and fRG equations.

We mostly write down the *left* Bethe–Salpeter equations where the irreducible vertices I_r appear first:

$$
\begin{aligned}
\gamma_r = I_r \circ \Pi_r \circ \Gamma &= (U + T_r - M_r) \circ \Pi_r \circ (T_r + \nabla_r) \\
&= (T_r - M_r) \circ \Pi_r \circ T_r + U \circ \Pi_r \circ \Gamma + (T_r - M_r) \circ \Pi_r \circ \nabla_r \\
&= M_r + \eta_r \bullet \lambda_r - U + (T_r - M_r) \circ \Pi_r \circ \bar{\lambda}_r \bullet \eta_r \bullet \lambda_r \\
&= M_r + [\mathbf{1}_r + (T_r - M_r) \circ \Pi_r \circ \bar{\lambda}_r] \bullet \eta_r \bullet \lambda_r - U.
\end{aligned}
\tag{3.34}
$$

Here, we inserted relations from Ref. [P1]: $I_r = U + T_r - M_r$, Eq. (25b), $\Gamma = \nabla_r + T_r$, Eq. (25a), $M_r = (T_r - M_r) \circ \Pi_r \circ T_r$, Eq. (41h), $U \circ \Pi_r \circ \Gamma = \eta_r \bullet \lambda_r - U$, Eq. (42b), and $\nabla_r = \bar{\lambda}_r \bullet \eta_r \bullet \lambda_r$, Eq. (33). With $\gamma_r = M_r + \bar{\lambda}_r \bullet \eta_r \bullet \lambda_r - U$, Eq. (23) in Ref. [P1], we find an alternative version of the Schwinger–Dyson equation for the left Hedin vertex:

$$
\bar{\lambda}_r = \mathbf{1}_r + (T_r - M_r) \circ \Pi_r \circ \bar{\lambda}_r.
\tag{3.35}
$$

Analogously, there are *right* Bethe–Salpeter equations where the irreducible vertices I_r appear at the end:

$$
\begin{aligned}
\gamma_r = \Gamma \circ \Pi_r \circ I_r &= (T_r + \nabla_r) \circ \Pi_r \circ (U + T_r - M_r) \\
&= T_r \circ \Pi_r \circ (T_r - M_r) + \Gamma \circ \Pi_r \circ U + \nabla_r \circ \Pi_r \circ (T_r - M_r) \\
&= M_r + \bar{\lambda}_r \bullet \eta_r - U + \bar{\lambda}_r \bullet \eta_r \bullet \lambda_r \circ \Pi_r \circ (T_r - M_r) \\
&= M_r + \bar{\lambda}_r \bullet \eta_r \bullet [\mathbf{1}_r + \lambda_r \circ \Pi_r \circ (T_r - M_r)] - U,
\end{aligned}
\tag{3.36}
$$

obtained from the analogous expressions from Ref. [P1]: $M_r = T_r \circ \Pi_r \circ (T_r - M_r)$, Eq. (41h), and $\Gamma \circ \Pi_r \circ U = \bar{\lambda}_r \bullet \eta_r - U$, Eq. (42a). Similarly, we deduce the alternative *right* Schwinger–Dyson equation for the right Hedin vertex:

$$
\lambda_r = \mathbf{1}_r + \lambda_r \circ \Pi_r \circ (T_r - M_r).
\tag{3.37}
$$

To summarize, all SBE equations (41) in Ref. [P1] have a left and right version originating from the left and right version of the Bethe–Salpeter equations:

$$
\begin{aligned}
\gamma_r &= I_r \circ \Pi_r \circ \Gamma & &= \Gamma \circ \Pi_r \circ I_r, & (3.38\text{a}) \\
P_r &= \mathbf{1}_r \circ \Pi_r \circ \bar{\lambda}_r & &= \lambda_r \circ \Pi_r \circ \mathbf{1}_r, & (3.38\text{b}) \\
\tilde{\eta}_r &= U \bullet P_r \bullet \eta_r & &= \eta_r \bullet P_r \bullet U, & (3.38\text{c})
\end{aligned}
$$

Table 3.1.: This list shows which objects replace Γ, Π_r, and I_r in the left and right SBE equations (3.38b)–(3.38f) for $\tilde{\eta}_r, \bar{\tilde{\lambda}}_r, \tilde{\lambda}_r, M_r$ compared to the original left and right Bethe–Salpeter equation (3.38a) for γ_r.

γ_r	P_r	$\tilde{\eta}_r$	$\bar{\tilde{\lambda}}_r$	$\tilde{\lambda}_r$	M_r
Γ left	λ_r	η_r	T_r	λ_r	T_r
Γ right	$\bar{\lambda}_r$	η_r	$\bar{\lambda}_r$	T_r	T_r
Π_r	Π_r	P_r	Π_r	Π_r	Π_r
I_r left	$\mathbf{1}_r$	U	$T_r - M_r$	$\mathbf{1}_r$	$T_r - M_r$
I_r right	$\mathbf{1}_r$	U	$\mathbf{1}_r$	$T_r - M_r$	$T_r - M_r$

$$\bar{\tilde{\lambda}}_r = (T_r - M_r) \circ \Pi_r \circ \bar{\lambda}_r = T_r \circ \Pi_r \circ \mathbf{1}_r, \tag{3.38d}$$

$$\tilde{\lambda}_r = \mathbf{1}_r \circ \Pi_r \circ T_r \qquad\quad = \lambda_r \circ \Pi_r \circ (T_r - M_r), \tag{3.38e}$$

$$M_r = (T_r - M_r) \circ \Pi_r \circ T_r = T_r \circ \Pi_r \circ (T_r - M_r). \tag{3.38f}$$

Comparing these SBE equations with the original Bethe–Salpeter equation (3.38a) for γ_r, in every SBE equation, the full vertex Γ, the bubble Π_r, and the two-particle irreducible vertex I_r are replaced by other vertices, listed in Tab. 3.1. We here subtract the constant parts of the bosonic propagator $\tilde{\eta}_r = \eta_r - U$ and the Hedin vertices $\bar{\tilde{\lambda}}_r = \bar{\lambda}_r - \mathbf{1}_r$, $\tilde{\lambda}_r = \lambda_r - \mathbf{1}_r$. With Eqs. (3.38), the multiloop fRG flow equations for the SBE vertices, Eqs. (54), (56), (59), and (61) in Ref. [P1] follow directly from the structure of the multiloop fRG flow equation (3.17) for $\dot{\gamma}_r$ by replacing the vertices according to Tab. 3.1:

$$\dot{\gamma}_r = \Gamma \circ \dot{\Pi}_r \circ \Gamma + \dot{I}_r \circ \Pi_r \circ \Gamma + \Gamma \circ \Pi_r \circ \dot{I}_r \circ \Pi_r \circ \Gamma + \Gamma \circ \Pi_r \circ \dot{I}_r, \tag{3.39a}$$

$$\dot{P}_r = \lambda_r \circ \dot{\Pi}_r \circ \bar{\lambda}_r + \lambda_r \circ \Pi_r \circ \dot{I}_r \circ \Pi_r \circ \bar{\lambda}_r, \tag{3.39b}$$

$$\dot{\eta}_r = \eta_r \bullet \dot{P}_r \bullet \eta_r, \tag{3.39c}$$

$$\dot{\bar{\tilde{\lambda}}}_r = T_r \circ \dot{\Pi}_r \circ \bar{\lambda}_r + \dot{I}_r \circ \Pi_r \circ \bar{\lambda}_r + T_r \circ \Pi_r \circ \dot{I}_r \circ \Pi_r \circ \bar{\lambda}_r, \tag{3.39d}$$

$$\dot{\tilde{\lambda}}_r = \lambda_r \circ \dot{\Pi}_r \circ T_r + \lambda_r \circ \Pi_r \circ \dot{I}_r \circ \Pi_r \circ T_r + \lambda_r \circ \Pi_r \circ \dot{I}_r, \tag{3.39e}$$

$$\dot{M}_r = T_r \circ \dot{\Pi}_r \circ T_r + \dot{I}_r \circ \Pi_r \circ T_r + T_r \circ \Pi_r \circ \dot{I}_r \circ \Pi_r \circ T_r + T_r \circ \Pi_r \circ \dot{I}_r. \tag{3.39f}$$

We hereby use the quantities listed in Tab. 3.1 and their differentiated counterparts with $\dot{U} = 0$, $\dot{\mathbf{1}}_r = 0$, $\dot{T}_r - \dot{M}_r = \dot{I}_r$. The similarities between the self-consistent equations (3.38) and flow equations (3.39) help to structure their numerical implementation in a lucid way.

3.4.3. Self-energy in the SBE formalism

So far, we mainly considered the Bethe–Salpeter equations to compute two-particle reducible vertices γ_r and SBE vertices. As a further ingredient, we need to evaluate the fermionic self-energy Σ. In general, this is given by the Schwinger–Dyson equation:

$$\Sigma_{1'|1} = -U_{1'2'|12}G_{2|2'} - \tfrac{1}{2}U_{1'4'|32}G_{2|2'}G_{3|3'}G_{4|4'}\Gamma_{3'2'|14},$$
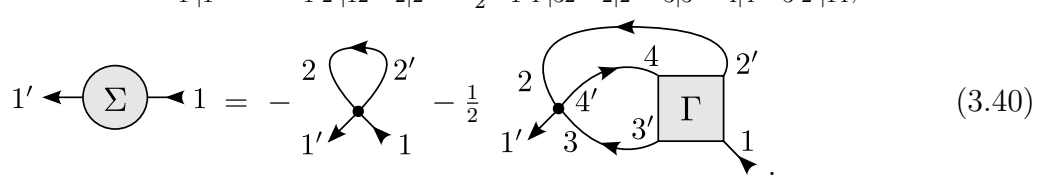
$$\tag{3.40}$$

The first term is the Hartree term Σ_{H} and just yields a constant shift of the self-energy. In the following, we will focus on the second term, $\tilde{\Sigma}(\nu) = \Sigma(\nu) - \Sigma_{\mathrm{H}}$, which vanishes for $|\nu| \to \infty$. We introduce the loop product as

$$[\Gamma \cdot G]_{1'|1} = \Gamma_{1'2'|12}G_{2|2'} = -\Gamma_{1'2'|21}G_{2|2'} = -[G \cdot \Gamma]_{1'|1},$$
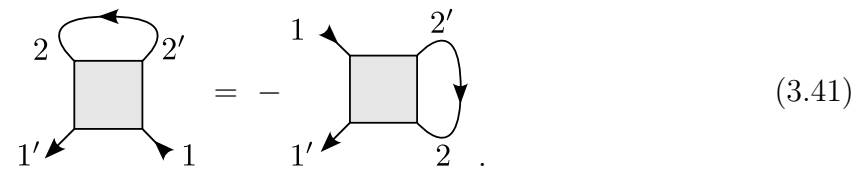
$$\tag{3.41}$$

We here have two versions of the product depending on the alignment of the vertex. To avoid an accumulation of symbols, we denote both products by $\cdot$. The order of the Green's function and the vertex clarifies then which loop product we refer to. In this notation, the Schwinger–Dyson equation (3.40) can be written as

$$\Sigma = -U \cdot G - \tfrac{1}{2}(U \circ \Pi_a \circ \Gamma) \cdot G \tag{3.42a}$$
$$= -U \cdot G - (U \circ \Pi_p \circ \Gamma) \cdot G \tag{3.42b}$$
$$= G \cdot U + \tfrac{1}{2}G \cdot (\Gamma \circ \Pi_t \circ U), \tag{3.42c}$$

expressed in the three diagrammatic channels $r = a, p, t$. Following Sec. 3.4.2, there exist also the complementary versions where the bare vertex appears on the other side of the bubble product:

$$\Sigma = -U \cdot G - \tfrac{1}{2}(\Gamma \circ \Pi_a \circ U) \cdot G \tag{3.43a}$$
$$= -U \cdot G - (\Gamma \circ \Pi_p \circ U) \cdot G \tag{3.43b}$$
$$= G \cdot U + \tfrac{1}{2}G \cdot (U \circ \Pi_t \circ \Gamma). \tag{3.43c}$$

The formulation in SBE vertices is rather straightforward after using $\bar{\lambda}_r \bullet \eta_r = U + \Gamma \circ \Pi_r \circ \Gamma$

and $\eta_r \bullet \lambda_r = U + U \circ \Pi_r \circ \Gamma$, Eq. (42) in Ref. [P1]:

$$\Sigma = -\tfrac{1}{2}U \cdot G - \tfrac{1}{2}(\eta_a \bullet \lambda_a) \cdot G = -\tfrac{1}{2}U \cdot G - \tfrac{1}{2}(\bar{\lambda}_a \bullet \eta_a) \cdot G \qquad (3.44\text{a})$$
$$= -(\eta_p \bullet \lambda_p) \cdot G \qquad\qquad = -(\bar{\lambda}_p \bullet \eta_p) \cdot G \qquad (3.44\text{b})$$
$$= \tfrac{1}{2}G \cdot U + \tfrac{1}{2}G \cdot (\eta_t \bullet \lambda_t) \quad = \tfrac{1}{2}G \cdot U + \tfrac{1}{2}G \cdot (\bar{\lambda}_t \bullet \eta_t). \qquad (3.44\text{c})$$

Here, the Hartree term Σ_H is partially absorbed in the second term. As the SBE vertices have a simpler frequency/momentum dependence, the formulation (3.44) can be computationally advantageous. As discussed in Sec. 4.5 and thus Ref. [P4], a truncation in the momentum dependence may spoil the numerical results depending on which channel is used in Eqs. (3.44).

There are multiple ways of formulating a flow equation for the self-energy [KD18d]. Differentiating Eqs. (3.44) on both sides with respect to a flow parameter Λ yields

$$\dot{\Sigma} = -(\dot{\eta}_p \bullet \lambda_p) \cdot G - (\eta_p \bullet \dot{\lambda}_p) \cdot G - (\eta_p \bullet \lambda_p) \cdot \dot{G}. \qquad (3.45)$$

This is an algebraic differential equation as $\dot{\eta}_p$, $\dot{\lambda}_p$ and $\dot{G}$ on the right-hand side depend on $\dot{\Sigma}$, too. In practice, many iterations over this equation are needed to get a converged value for $\dot{\Sigma}$ [HKE+20, HRHA20], also see Ref. [P4].

3.5. Interaction flow in the SBE formalism

The content of this section is part of the following paper in preparation:

Generalization of the fermionic functional renormalization group with interaction flows: Illustration with the single-boson exchange formalism

Aiman Al-Eryani, **Marcel Gievers**, Kilian Fraboulet

An advantage of fRG compared to self-consistent summations of the parquet or SBE equations is the flexibility in how the flow equations can be actually solved. In other words, with a cleverly chosen and physically well motivated regulator, one might access solutions in regimes were the convergence of the parquet equations is not possible anymore. This is indicated in Ref. [GRW+24] and by our discussion in Sec. 5.2.

In many-body systems with correlated fermions like the Hubbard model, effective interactions, mediated by bosonic fluctuations, play a dominant role. This is revealed by divergences in susceptibilities χ_r that appear during the fRG flow. In the SBE formalism, susceptibilities χ_r are directly connected to bosonic propagators η_r (cf. Eq. (105c) in Ref. [P1]). Thus, it is desirable to gain better control of the bosonic propagators η_r when

solving their flow equations. The non-interacting value of η_r is the bare interaction U so it might be expedient to introduce a regulator dependence in U itself.

Our approach is derived from a differentiation of the SBE equations and is similar to the derivation of the multiloop flow equations of parquet [KD18b, KD18c, KD18d] and SBE vertices [P1]. This way, it differs from previous formulations of flowing interactions. In Wetterich's fRG scheme (cf. Sec. 3.1), a multiplicative regulator in the bare Green's function $G_0(\Lambda) = \Lambda G_0$ can be absorbed in a regulator-dependent bare vertex $U(\Lambda)$ [HRAE04]. In contrast to this, we want to allow for more general cutoff dependencies in the bare interaction $U(\Lambda)$, independent of that applied to the Green's function $G_0(\Lambda)$. Furthermore, an interaction flow was formulated within the 2PI formalism [Dup14], which has been numerically implemented for benchmark models [RJM15, RMJ16] and more recently for the two-dimensional Hubbard model in combination with the dynamical mean-field theory (DMFT) [Kat19]. Yet, our emphasis is on the SBE vertices so we stay in the framework of the less demanding SBE formalism.

We introduce the scale dependence in the bare interaction $U \mapsto U(\Lambda)$ without specifying its precise form. For example, this can be realized by starting from the non-interacting theory $U(\Lambda_i) = 0$ and flowing to the full theory $U(\Lambda_f) = U$. Since in the fermionic action, Eq. (3.1), $U(\Lambda)$ couples to four fields whereas $G_0(\Lambda)$ only couples to two fields, the interaction flow implicitly relates two-point correlators to four-point correlators. An appealing realization of the Λ dependence in $U(\Lambda)$ could thus exploit Luttinger–Ward identities [KBC+10, Kri18]. We also allow for an additional regulator in the bare fermionic Green's function $G_0 \mapsto G_0(\Lambda)$, which gives us even more flexibility. However, it has to be mentioned that a combination of bosonic and fermionic regulators needs to be treated with care [FW09, FKW10, HJY24]. From now on, we do not explicitly write down the dependence on Λ anymore.

The derivation of the multiloop fRG equation for $\dot{\gamma}_r$ is identical to Eqs. (3.14)–(3.17). Consequently the dependence on the cutoff scheme does not appear explicitly in the flow equations for $\dot{\gamma}_r$, but $\dot{\Pi}_r$ and $\dot{I}_r$ implicitly depend on both $\dot{G}_0$ and $\dot{U}$.

In the following, we assume that the differentiated parquet approximation, i.e., the differentiated two-particle irreducible vertex, is only given by $\dot{R} = \dot{U}$. According to the definition of the irreducible vertices $I_r = R + \sum_{r' \neq r} \gamma_{r'}$, this implies that $\dot{I}_r$ in Eq. (3.17) satisfies:

$$\dot{I}_r = \sum_{r' \neq r} \dot{\gamma}_{r'} + \dot{U} \equiv \dot{\gamma}_{\bar{r}} + \dot{U}. \tag{3.46}$$

To solve for the self-consistency in $\dot{\gamma}_r$, Eq. (3.17) can be iteratively solved by inserting the loop expansion of γ_r in the form $\dot{\gamma}_r = \sum_{\ell=1}^{\infty} \dot{\gamma}_r^{(\ell)}$, or more specifically $\dot{I}_r = \sum_{r' \neq r} \sum_{\ell=1}^{\infty} \dot{\gamma}_{r'}^{(\ell)} +$

$\dot{U}$, into Eq. (3.17). Identifying the terms then yields the following multiloop equations:

$$\dot{\gamma}_r^{(1)} = \Gamma \circ \dot{\Pi}_r \circ \Gamma + \dot{U} \circ \Pi_r \circ \Gamma + \Gamma \circ \Pi_r \circ \dot{U} + \Gamma \circ \Pi_r \circ \dot{U} \circ \Pi_r \circ \Gamma, \tag{3.47a}$$

$$\dot{\gamma}_r^{(2)} = \dot{\gamma}_{\overline{r}}^{(1)} \circ \Pi_r \circ \Gamma + \Gamma \circ \Pi_r \circ \dot{\gamma}_{\overline{r}}^{(1)}, \tag{3.47b}$$

$$\dot{\gamma}_r^{(\ell \geq 3)} = \dot{\gamma}_{\overline{r}}^{(\ell-1)} \circ \Pi_r \circ \Gamma + \Gamma \circ \Pi_r \circ \dot{\gamma}_{\overline{r}}^{(\ell-2)} \circ \Pi_r \circ \Gamma + \Gamma \circ \Pi_r \circ \dot{\gamma}_{\overline{r}}^{(\ell+1)}, \tag{3.47c}$$

where $\dot{\gamma}_{\overline{r}}^{(\ell)} = \sum_{r' \neq r} \dot{\gamma}_{r'}^{(\ell)}$.

Compared to the conventional multiloop fRG equations [KD18b, KD18c, KD18d], only the one-loop equation (3.47a) contains additional terms, which explicitly depend on the differentiated bare interaction $\dot{U}$. In Sec. 3.5.3, we will combine the terms that explicitly depend on $\dot{U}$ into a bosonic single-scale propagator.

The flow equations for the SBE objects can be derived in two different ways: First, we derive them by differentiation of the SBE equations (3.38). Second, we insert the SBE decomposition of γ_r, Eq. (3.28), into its flow equation $\dot{\gamma}_r$, Eq. (3.17). Both derivations are analogous to those presented in Ref. [P1]. We see that the two different approaches are equivalent also when the terms generated by the cutoff dependence of the bare interaction $\dot{U} \neq 0$ are included.

3.5.1. Derivation from the SBE equation

Similar to the two-particle reducible vertex γ_r, the MBE vertices M_r fulfill Bethe–Salpeter equations [cf. Eq. (3.38f)]. Compared to the conventional Bethe–Salpeter equation (3.38a), γ_r is replaced by M_r, I_r is replaced by $T_r - M_r$ and Γ is replaced by T_r (cf. Tab. 3.1). From Eq. (3.17), we directly obtain the differentiated multi-boson exchange vertex:

$$\begin{aligned}\dot{M}_r &= T_r \circ \dot{\Pi}_r \circ T_r + (\dot{T}_r - \dot{M}_r) \circ \Pi_r \circ T_r + T_r \circ \Pi_r \circ (\dot{T}_r - \dot{M}_r) \circ \Pi_r \circ T_r \\ &\quad + T_r \circ \Pi_r \circ (\dot{T}_r - \dot{M}_r) \\ &= T_r \circ \dot{\Pi}_r \circ T_r + (\dot{I}_r - \dot{U}) \circ \Pi_r \circ T_r + T_r \circ \Pi_r \circ (\dot{I}_r - \dot{U}) \circ \Pi_r \circ T_r + T_r \circ \Pi_r \circ (\dot{I}_r - \dot{U}).\end{aligned} \tag{3.48}$$

In the last line we made the dependence on the $\dot{U}$ explicit by using $T_r - M_r = I_r - U$, Eq. (52b) in Ref. [P1].

The Hedin vertices $\bar{\lambda}_r$ and λ_r fulfill Schwinger–Dyson equations (3.38d)–(3.38e), which in the following are differentiated as well. Here, we use the differentiated form of

$T_r - M_r = I_r - U$, Eq. (52b) in Ref. [P1], and insert Eq. (3.48) for $\dot{M}_r$:

$$
\begin{aligned}
\dot{\bar{\lambda}}_r &= \dot{T}_r \circ \Pi_r \circ \mathbf{1}_r + T_r \circ \dot{\Pi}_r \circ \mathbf{1}_r \\
&= (\dot{I}_r - \dot{U}) \circ \Pi_r \circ \mathbf{1}_r + T_r \circ \dot{\Pi}_r \circ T_r \circ \Pi_r \circ \mathbf{1}_r + (\dot{I}_r - \dot{U}) \circ \Pi_r \circ T_r \circ \Pi_r \circ \mathbf{1}_r \\
&\quad + T_r \circ \Pi_r \circ (\dot{I}_r - \dot{U}) \circ \Pi_r \circ T_r \circ \Pi_r \circ \mathbf{1}_r + T_r \circ \Pi_r \circ (\dot{I}_r - \dot{U}) \circ \Pi_r \circ \mathbf{1}_r + T_r \circ \dot{\Pi}_r \circ \mathbf{1}_r \\
&= T_r \circ \dot{\Pi}_r \circ \bar{\lambda}_r + (\dot{I}_r - \dot{U}) \circ \Pi_r \circ \bar{\lambda}_r + T_r \circ \Pi_r \circ (\dot{I}_r - \dot{U}) \circ \Pi_r \circ \bar{\lambda}_r, \quad (3.49a) \\
\dot{\lambda}_r &= \mathbf{1}_r \circ \dot{\Pi}_r \circ T_r + \mathbf{1}_r \circ \Pi_r \circ \dot{T}_r \\
&= \mathbf{1}_r \circ \dot{\Pi}_r \circ T_r + \mathbf{1}_r \circ \Pi_r \circ (\dot{I}_r - \dot{U}) + \mathbf{1}_r \circ \Pi_r \circ T_r \circ \dot{\Pi}_r \circ T_r + \mathbf{1}_r \circ \Pi_r \circ (\dot{I}_r - \dot{U}) \circ \Pi_r \circ T_r \\
&\quad + \mathbf{1}_r \circ \Pi_r \circ T_r \circ \Pi_r \circ (\dot{I}_r - \dot{U}) \circ \Pi_r \circ T_r + \mathbf{1}_r \circ \Pi_r \circ T_r \circ \Pi_r \circ (\dot{I}_r - \dot{U}) \\
&= \lambda_r \circ \dot{\Pi}_r \circ T_r + \lambda_r \circ \Pi_r \circ (\dot{I}_r - \dot{U}) + \lambda_r \circ \Pi_r \circ (\dot{I}_r - \dot{U}) \circ \Pi_r \circ T_r. \quad (3.49b)
\end{aligned}
$$

The bosonic self-energy P_r fulfills the Schwinger–Dyson equation (3.38b), which is differentiated as

$$
\begin{aligned}
\dot{P}_r &= \mathbf{1}_r \circ \dot{\Pi}_r \circ \bar{\lambda}_r + \mathbf{1}_r \circ \Pi_r \circ \dot{\bar{\lambda}}_r \\
&= \mathbf{1}_r \circ \dot{\Pi}_r \circ \bar{\lambda}_r + \mathbf{1}_r \circ \Pi_r \circ T_r \circ \dot{\Pi}_r \circ \bar{\lambda}_r + \mathbf{1}_r \circ \Pi_r \circ (\dot{I}_r - \dot{U}) \circ \Pi_r \circ \bar{\lambda}_r \\
&\quad + \mathbf{1}_r \circ \Pi_r \circ T_r \circ \Pi_r \circ (\dot{I}_r - \dot{U}) \circ \Pi_r \circ \bar{\lambda}_r \\
&= \lambda_r \circ \dot{\Pi}_r \circ \bar{\lambda}_r + \lambda_r \circ \Pi_r \circ (\dot{I}_r - \dot{U}) \circ \Pi_r \circ \bar{\lambda}_r. \quad (3.50)
\end{aligned}
$$

Here we inserted Eqs. (3.49) and Eq. (3.38d).

Finally, we give a differentiated version of the bosonic Dyson equation (3.38c):

$$
\dot{\eta}_r = \dot{U} + \dot{U} \bullet P_r \bullet \eta_r + U \bullet \dot{P}_r \bullet \eta_r + U \bullet P_r \bullet \dot{\eta}_r. \quad (3.51)
$$

The differentiated object, here $\dot{\eta}_r$, appears on both sides of the equation. To obviate this, we use the inverted bosonic Dyson equation:

$$
\eta_r = U + U \bullet P_r \bullet \eta_r \Rightarrow U \bullet (\mathbf{1}_r - U \bullet P_r)^{-1} = U \bullet (\mathbf{1}_r + \eta_r \bullet P_r). \quad (3.52)
$$

With this, Eq. (3.51) reads

$$
\begin{aligned}
\dot{\eta}_r &= (\mathbf{1}_r - U \bullet P_r)^{-1} \bullet \left[\dot{U} \bullet (\mathbf{1}_r + P_r \bullet \eta_r) + U \bullet \dot{P}_r \bullet \eta_r \right] \\
&= (\mathbf{1}_r + \eta_r \circ P_r) \bullet \left[\dot{U} \bullet (\mathbf{1}_r + P_r \bullet \eta_r) + U \bullet \dot{P}_r \bullet \eta_r \right] \\
&= (\mathbf{1}_r + \eta_r \circ P_r) \bullet \dot{U} \bullet (\mathbf{1}_r + P_r \bullet \eta_r) + \eta_r \bullet \dot{P}_r \bullet \eta_r. \quad (3.53)
\end{aligned}
$$

Inserting $\dot{P}_r$, Eq. (3.50), into Eq. (3.53) yields

$$
\eta_r \bullet \dot{P}_r \bullet \eta_r = \eta_r \circ \lambda_r \circ \dot{\Pi}_r \circ \bar{\lambda}_r \bullet \eta_r + \eta_r \bullet \lambda_r \circ \Pi_r \circ (\dot{I}_r - \dot{U}) \circ \Pi_r \circ \bar{\lambda}_r \bullet \eta_r. \quad (3.54)
$$

In Sec. 3.5.3, we elaborate that the first term, which depends explicitly on $\dot{U}$ can be understood as a bosonic single-scale propagator while the second term serves as a Katanin correction [Kat04] to the differentiated bosonic propagator $\dot{\eta}_r$.

While the differentiated parquet equations (3.17) do not explicitly depend on $\dot{U}$, the differentiated SBE equations Eqs. (3.48)–(3.53) are explicitly modified by $\dot{U}$.

3.5.2. Derivation from the parquet multiloop fRG equations

Besides starting from the SBE equations (3.38), discussed in the previous section, we can derive the flow equations for SBE vertices from the parquet multiloop fRG equations (3.17). As shown in Ref. [P1], these two different derivations lead to identical flow equations for the bosonic propagators η_r, Hedin vertices $\bar{\lambda}_r, \lambda_r$, and MBE vertices M_r in the context of the conventional flow scheme (where the flow parameter is only introduced via $G_0 \mapsto G_0(\Lambda)$). We will see that this equivalence also holds in the framework of the interaction flow.

We consider first the SBE decomposition of γ_r, Eq. (3.28), and differentiate it with respect to the flow parameter Λ. Within the interaction flow $\dot{U} \neq 0$, this yields

$$\dot{\gamma}_r = \dot{\bar{\lambda}}_r \bullet \eta_r \bullet \lambda_r + \bar{\lambda}_r \bullet \dot{\eta}_r \bullet \lambda_r + \bar{\lambda}_r \bullet \eta_r \bullet \dot{\lambda}_r + \dot{M}_r - \dot{U}. \tag{3.55}$$

We then exploit the parquet multiloop fRG equations as follows: we start from Eq. (3.17) and then introduce $\dot{U}$ at the expense of $\dot{I}_r$ using Eq. (3.46). This translates into

$$\dot{\gamma}_r = \Gamma \circ \dot{\Pi}_r \circ \Gamma + \dot{\gamma}_{\bar{r}} \circ \Pi_r \circ \Gamma + \Gamma \circ \Pi_r \circ \dot{\gamma}_{\bar{r}} + \Gamma \circ \Pi_r \circ \dot{\gamma}_{\bar{r}} \circ \Pi_r \circ \Gamma$$
$$+ \dot{U} \circ \Pi_r \circ \Gamma + \Gamma \circ \Pi_r \circ \dot{U} + \Gamma \circ \Pi_r \circ \dot{U} \circ \Pi_r \circ \Gamma. \tag{3.56}$$

We then replace Γ in the latter result by SBE vertices with the relation $\Gamma = \nabla_r + T_r$:

$$\dot{\gamma}_r = \left(\bar{\lambda}_r \bullet \eta_r \bullet \lambda_r + T_r \right) \circ \dot{\Pi}_r \circ \left(\bar{\lambda}_r \bullet \eta_r \bullet \lambda_r + T_r \right)$$
$$+ \dot{\gamma}_{\bar{r}} \circ \Pi_r \circ \left(\bar{\lambda}_r \bullet \eta_r \bullet \lambda_r + T_r \right)$$
$$+ \left(\bar{\lambda}_r \bullet \eta_r \bullet \lambda_r + T_r \right) \circ \Pi_r \circ \dot{\gamma}_{\bar{r}}$$
$$+ \left(\bar{\lambda}_r \bullet \eta_r \bullet \lambda_r + T_r \right) \circ \Pi_r \circ \dot{\gamma}_{\bar{r}} \circ \Pi_r \circ \left(\bar{\lambda}_r \bullet \eta_r \bullet \lambda_r + T_r \right)$$
$$+ \dot{U} \circ \Pi_r \circ \left(\bar{\lambda}_r \bullet \eta_r \bullet \lambda_r + T_r \right)$$
$$+ \left(\bar{\lambda}_r \bullet \eta_r \bullet \lambda_r + T_r \right) \circ \Pi_r \circ \dot{U}$$
$$+ \left(\bar{\lambda}_r \bullet \eta_r \bullet \lambda_r + T_r \right) \circ \Pi_r \circ \dot{U} \circ \Pi_r \circ \left(\bar{\lambda}_r \bullet \eta_r \bullet \lambda_r + T_r \right). \tag{3.57}$$

To identify the individual contributions to the flow equations, we have to further manipulate the last three terms, which explicitly depend on $\dot{U}$. Here, we make use of the fact that $\dot{U}$ does not depend on frequency (momenta) and their summation can be excluded

according to

$$\dot{U} \circ \Pi_r \circ \Gamma = \dot{U} \bullet (\mathbf{1}_r \circ \Pi_r \circ \Gamma), \quad \Gamma \circ \Pi_r \circ \dot{U} = (\Gamma \circ \Pi_r \circ \mathbf{1}_r) \bullet \dot{U}. \tag{3.58}$$

With this and by using the SBE equations (3.38), the first term yields

$$\begin{aligned} \dot{U} \circ \Pi_r \circ \left(\bar{\lambda}_r \bullet \eta_r \bullet \lambda_r + T_r \right) &= \dot{U} \bullet (\mathbf{1}_r \circ \Pi_r \circ \bar{\lambda}_r \bullet \eta_r \bullet \lambda_r + \mathbf{1}_r \circ \Pi_r \circ T_r) \\ &= \dot{U} \bullet (P_r \bullet \eta_r \bullet \lambda_r + \lambda_r - \mathbf{1}_r) \\ &= \dot{U} \bullet (\mathbf{1}_r + P_r \bullet \eta_r) \bullet \lambda_r - \dot{U}. \end{aligned} \tag{3.59}$$

The analogous calculation for the second term yields

$$\begin{aligned} \left(\bar{\lambda}_r \bullet \eta_r \bullet \lambda_r + T_r \right) \circ \Pi_r \circ \dot{U} &= \left(\bar{\lambda}_r \bullet \eta_r \bullet \lambda_r \circ \Pi_r \circ \mathbf{1}_r + T_r \circ \Pi_r \circ \mathbf{1}_r \right) \bullet \dot{U} \\ &= (\bar{\lambda}_r \bullet \eta_r \bullet P_r + \bar{\lambda}_r - \mathbf{1}_r) \bullet \dot{U} \\ &= \bar{\lambda}_r \bullet (\mathbf{1}_r + \eta_r \bullet P_r) \bullet \dot{U} - \dot{U}, \end{aligned} \tag{3.60}$$

and for the third term

$$\begin{aligned} &\left(\bar{\lambda}_r \bullet \eta_r \bullet \lambda_r + T_r \right) \circ \Pi_r \circ \dot{U} \circ \Pi_r \circ \left(\bar{\lambda}_r \bullet \eta_r \bullet \lambda_r + T_r \right) \\ &= (\bar{\lambda}_r \bullet \eta_r \bullet \lambda_r \circ \Pi_r \circ \mathbf{1}_r + T_r \circ \Pi_r \circ \mathbf{1}_r) \bullet \dot{U} \bullet (\mathbf{1}_r \circ \Pi_r \circ \bar{\lambda}_r \bullet \eta_r \bullet \lambda_r + \mathbf{1}_r \circ \Pi_r \circ T_r) \\ &= (\bar{\lambda}_r \bullet \eta_r \bullet P_r + \bar{\lambda}_r - \mathbf{1}_r) \bullet \dot{U} \bullet (P_r \bullet \eta_r \bullet \lambda_r + \lambda_r - \mathbf{1}_r) \\ &= \bar{\lambda}_r \bullet (\mathbf{1}_r + \eta_r \circ P_r) \bullet \dot{U} \bullet (\mathbf{1}_r + P_r \bullet \eta_r) \bullet \lambda_r \\ &\quad - \bar{\lambda}_r \bullet (\mathbf{1}_r + \eta_r \bullet P_r) \bullet \dot{U} - \dot{U} \bullet (\mathbf{1}_r + P_r \bullet \eta_r) + \dot{U}. \end{aligned} \tag{3.61}$$

Summing over the three terms, Eqs. (3.59)–(3.61) yield

$$\begin{aligned} &\dot{U} \circ \Pi_r \circ \Gamma + \Gamma \circ \Pi_r \circ \dot{U} + \Gamma \circ \Pi_r \circ \dot{U} \circ \Pi_r \circ \Gamma \\ &= \bar{\lambda}_r \bullet (\mathbf{1}_r + \eta_r \circ P_r) \bullet \dot{U} \bullet (\mathbf{1}_r + P_r \bullet \eta_r) \bullet \lambda_r - \dot{U}. \end{aligned} \tag{3.62}$$

We conclude that only the differentiated bosonic propagator $\dot{\eta}_r$ carries the modifications due to terms including $\dot{U}$ in the parquet multiloop fRG equations.

Inserting Eq. (3.62) into Eq. (3.57) gives

$$
\begin{aligned}
\dot{\gamma}_r =\ & (T_r \circ \dot{\Pi}_r \circ \bar{\lambda}_r + \dot{\gamma}_{\bar{r}} \circ \Pi_r \circ \bar{\lambda}_r + T_r \circ \Pi_r \circ \dot{\gamma}_{\bar{r}} \circ \Pi_r \circ \bar{\lambda}_r) \bullet \eta_r \bullet \lambda_r \\
&+ \bar{\lambda}_r \bullet (\eta_r \bullet \lambda_r \circ \dot{\Pi}_r \circ \bar{\lambda}_r \bullet \eta_r + \eta_r \bullet \lambda_r \circ \Pi_r \circ \dot{\gamma}_{\bar{r}} \circ \Pi_r \circ \bar{\lambda}_r \bullet \eta_r) \bullet \lambda_r \\
&+ \bar{\lambda}_r \bullet (\mathbf{1}_r + \eta_r \circ P_r) \bullet \dot{U} \bullet (\mathbf{1}_r + P_r \bullet \eta_r) \bullet \lambda_r \\
&+ \bar{\lambda}_r \bullet \eta_r \bullet (\lambda_r \circ \dot{\Pi}_r \circ T_r + \lambda_r \circ \Pi_r \circ \dot{\gamma}_{\bar{r}} + \lambda_r \circ \Pi_r \circ \dot{\gamma}_{\bar{r}} \circ \Pi_r \circ T_r) \\
&+ T \circ \dot{\Pi}_r \circ T + \dot{\gamma}_{\bar{r}} \circ \Pi_r \circ T_r + T_r \circ \Pi_r \circ \dot{\gamma}_{\bar{r}} + T_r \circ \Pi_r \circ \dot{\gamma}_{\bar{r}} \circ \Pi_r \circ T_r \\
&- \dot{U}.
\end{aligned}
\tag{3.63}
$$

Comparing the terms with Eq. (3.55), one can read off the flow equations (3.48)–(3.54) for the SBE vertices. So the two derivations are consistent.

3.5.3. Single-scale propagators

One of the main advantages of a cutoff dependence in the bare interaction, i.e., $\dot{U} \neq 0$ is the additional degree of freedom to solve the fRG equations along the flow. Here we show that the cutoff dependence $\dot{U} \neq 0$ has a direct impact on the bosonic propagator and thus serves as a regulation tool of bosonic fluctuations.

Let us first recall the flow equation for the full propagator G. When taking the derivative of the fermionic Dyson equation,

$$
G = G_0 + G_0 \Sigma G = G_0 + G \Sigma G_0 \Rightarrow G^{-1} = G_0^{-1} - \Sigma,
\tag{3.64}
$$

two terms appear:

$$
\dot{G} = -G \, (\partial_\Lambda G_0^{-1} - \dot{\Sigma}) \, G = -G \, (\partial_\Lambda G_0^{-1}) \, G + G \, \dot{\Sigma} \, G.
\tag{3.65}
$$

The first term is known as the *single-scale propagator*,

$$
S = \partial_\Lambda|_{\dot{\Sigma}=0} G = -G \, (\partial_\Lambda G_0^{-1}) \, G = G \, G_0^{-1} \, \dot{G}_0 \, G_0^{-1} \, G = (1 + G \, \Sigma) \, \dot{G}_0 \, (1 + \Sigma \, G),
\tag{3.66}
$$

and does not involve a differentiation of the self-energy $\dot{\Sigma}$. The above relation shows that the single-scale propagator S is only finite if there is a cutoff dependence of the bare Green's function, i.e., $\dot{G}_0 \neq 0 \Rightarrow S \neq 0$ (strictly speaking $G_0^{-1} \neq 0$ is required, too). In the case of a pure U flow, the whole cutoff dependence on three Green's function is induced by the second term involving $\dot{\Sigma}$. That is why the inclusion of the second term in Eq. (3.65), also known as *Katanin substitution* [Kat04], is crucial for a more direct influence of the U flow.

The bosonic propagator η_r fulfills the bosonic Dyson equation (cf. Eq. (41b) in Ref. [P1]) with its bare counterpart U and the polarization P_r as its corresponding bosonic self-energy. The resulting flow equation is analogous to that of the fermionic propagator in

Eq. (3.65):

$$\eta_r = U + U \bullet P_r \bullet \eta_r = U + P_r \bullet \eta_r \Rightarrow \eta_r^{-1} = U^{-1} - P_r, \tag{3.67a}$$

$$\Rightarrow \dot{\eta}_r = -\eta_r \bullet (\partial_\Lambda U^{-1} - \dot{P}_r) \bullet \eta_r = -\eta_r \bullet (\partial_\Lambda U^{-1}) \bullet \eta_r + \eta_r \bullet \dot{P}_r \bullet \eta_r. \tag{3.67b}$$

In analogy to the fermionic case [cf. Eq. (3.66)], we define the bosonic single-scale propagator S_{η_r} and identify it with the first term in Eqs. (3.53) and (3.67b):

$$
\begin{aligned}
S_{\eta_r} &= \partial_\Lambda|_{\dot{P}_r=0}\eta_r = -\eta_r \bullet \partial_\Lambda(U^{-1}) \bullet \eta_r = \eta_r \bullet U^{-1} \bullet \dot{U} \bullet U^{-1} \bullet \eta_r \\
&= (\mathbf{1}_r + \eta_r \bullet P_r) \bullet \dot{U} \bullet (\mathbf{1}_r + P_r \bullet \eta_r).
\end{aligned}
\tag{3.68}
$$

In particular, we conclude that the bosonic single-scale propagator S_{η_r} only exists if $\dot{U} \neq 0$. In that sense the flow equations of the fermionic and bosonic propagators $\dot{G}$, Eq. (3.65), and $\dot{\eta}_r$, Eq. (3.67b), are complementary. Their single-scale propagators are directly influenced by $\dot{G}_0$ and $\dot{U}$, respectively, while the Katanin substitutions, involving $\dot{\Sigma}$ and $\dot{P}_r$, take along a dependence on both cutoff scales.

Surprisingly, the bosonic single-scale propagator S_{η_r} captures all terms contained in $\dot{\gamma}_r$, Eq. (3.56), that explicitly depend on $\dot{U}$. From Eq. (3.62), we conclude the following relation:

$$\dot{U} \circ \Pi_r \circ \Gamma + \Gamma \circ \Pi_r \circ \dot{U} + \Gamma \circ \Pi_r \circ \dot{U} \circ \Pi_r \circ \Gamma = \bar{\lambda}_r \bullet S_{\eta_r} \bullet \lambda_r - \dot{U}. \tag{3.69}$$

Since all changes of the conventional flow equations can be incorporated through the single-scale propagator, this allows a minimal change in numerical implementations.

As mentioned below Eq. (3.66), an inclusion of the self-energy flow $\dot{\Sigma}$ is crucial, especially in a frame where only U depends on the regulator, i.e., $\dot{G}_0 = 0$. In our numerical treatment, the self-energy flow is computed via the differentiated Schwinger–Dyson equation (3.45) using SBE vertices.

4. SBE formalism for two particle types

"Software and cathedrals are much the same – first we build them, then we pray."
Samuel T. Redwine, Jr. – 4th International Software Process Workshop (1988)

In the previous chapter, the single-boson exchange (SBE) formalism was derived for generic fermionic models with a quartic interaction. Here, we specify the formalism for Hubbard-like models with two distinct particle types. In contrast to many other applications, we do not impose SU(2) spin symmetry here. We present the structure of our code for solving the SBE equations and fRG flow using imaginary frequencies in the Matsubara formalism. A nice benchmark model is a single-site Hubbard model, the so-called *Hubbard atom*, in a magnetic field and at arbitrary filling. We provide analytical formulas for the individual SBE vertices belonging to the generalized Hubbard atom. In the end, we include an application of the two-dimensional Hubbard model, where it is shown that a truncation in the momenta may spoil the results for the self-energy computed in the SBE formalism.

4.1. Correlation functions and vertices

This section deals with a specific case of the SBE formalism introduced in Sec. 3.3 where the indices of the vertex $\Gamma_{1'2'|12}$ only refer to two particle types denoted by $\uparrow$ and $\downarrow$. We discuss the structure of the SBE equations and show how symmetries reduce the numerical effort to compute the SBE vertices.

4.1.1. Basic definitions

In the correlation functions and vertices presented in Chapter 3, the indices $1', 2', 1, 2$ are kept general, i.e., they include frequencies, spin indices, momenta and other variables. In the following, we focus on the frequency dependence. As discussed in Sec. 3.3, we assume a bare vertex $U_{1'2'|12}$ that does not explicitly depend on frequencies apart from respecting frequency conservation (cf. Eq. (15) in Ref. [P1]). The four-point vertex can thus be parametrized using one bosonic frequency ω and two fermionic frequencies ν, ν' in the three diagrammatic channels of two-particle reducibility. In this chapter, we use
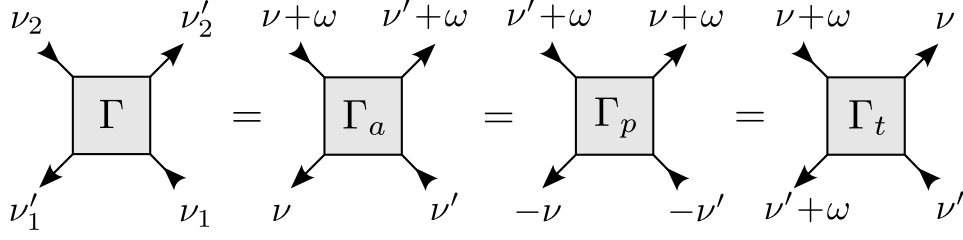
Figure 4.1.: Frequency conventions for the four-point vertex Γ in the respective channels of two-particle reducibility.

the following conventions:

$$\Gamma_a(\omega, \nu, \nu') = \Gamma(\nu, \nu' + \omega | \nu', \nu + \omega), \tag{4.1a}$$
$$\Gamma_p(\omega, \nu, \nu') = \Gamma(-\nu, \omega + \nu | -\nu', \omega + \nu'), \tag{4.1b}$$
$$\Gamma_t(\omega, \nu, \nu') = \Gamma(\omega + \nu', \nu | \nu', \omega + \nu), \tag{4.1c}$$

which are depicted in Fig. 4.1. For transforming from one channel to the other, one has to apply the following linear combinations:

$$\begin{pmatrix} \omega_a \\ \nu_a \\ \nu'_a \end{pmatrix} = \begin{pmatrix} 1 & 1 & 1 \\ 0 & -1 & 0 \\ 0 & 0 & -1 \end{pmatrix} \begin{pmatrix} \omega_p \\ \nu_p \\ \nu'_p \end{pmatrix}, \quad \begin{pmatrix} \omega_a \\ \nu_a \\ \nu'_a \end{pmatrix} = \begin{pmatrix} 0 & 1 & -1 \\ 1 & 0 & 1 \\ 0 & 0 & 1 \end{pmatrix} \begin{pmatrix} \omega_t \\ \nu_t \\ \nu'_t \end{pmatrix}, \tag{4.2a}$$

$$\begin{pmatrix} \omega_p \\ \nu_p \\ \nu'_p \end{pmatrix} = \begin{pmatrix} 1 & 1 & 1 \\ 0 & -1 & 0 \\ 0 & 0 & -1 \end{pmatrix} \begin{pmatrix} \omega_a \\ \nu_a \\ \nu'_a \end{pmatrix}, \quad \begin{pmatrix} \omega_p \\ \nu_p \\ \nu'_p \end{pmatrix} = \begin{pmatrix} 1 & 1 & 1 \\ -1 & 0 & -1 \\ 0 & 0 & -1 \end{pmatrix} \begin{pmatrix} \omega_t \\ \nu_t \\ \nu'_t \end{pmatrix}, \tag{4.2b}$$

$$\begin{pmatrix} \omega_t \\ \nu_t \\ \nu'_t \end{pmatrix} = \begin{pmatrix} 0 & 1 & -1 \\ 1 & 0 & 1 \\ 0 & 0 & 1 \end{pmatrix} \begin{pmatrix} \omega_a \\ \nu_a \\ \nu'_a \end{pmatrix}, \quad \begin{pmatrix} \omega_t \\ \nu_t \\ \nu'_t \end{pmatrix} = \begin{pmatrix} 0 & -1 & 1 \\ 1 & 1 & 0 \\ 0 & 0 & -1 \end{pmatrix} \begin{pmatrix} \omega_p \\ \nu_p \\ \nu'_p \end{pmatrix}. \tag{4.2c}$$

To save space, we usually do not carry the channel index r along all the frequency arguments. As done in Eqs. (4.1), the channel r of the frequency parametrization can be marked by an index of the vertex Γ_r, which for the full vertex Γ does *not* indicate any two-particle reducibility. Moreover, we may use square brackets around the vertices to indicate that the frequency arguments are transformed from one channel to the other. For example, a vertex originally given in the parametrization of the a channel converted into the p channel can be denoted as

$$[\Gamma_a]_p(\omega_p = \omega_a + \nu_a + \nu'_a, \nu_p = -\nu_a, \nu'_p = -\nu'_a) \text{ or simply } [\Gamma_a]_p(\omega + \nu + \nu', -\nu, -\nu'). \tag{4.3}$$

The transformation from channel r to channel r', Eqs. (4.2), can be written in an even shorter way by using the notation $\boldsymbol{\nu}_{r'}(\boldsymbol{\nu}_r)$. (We denote the triplet of frequencies by a
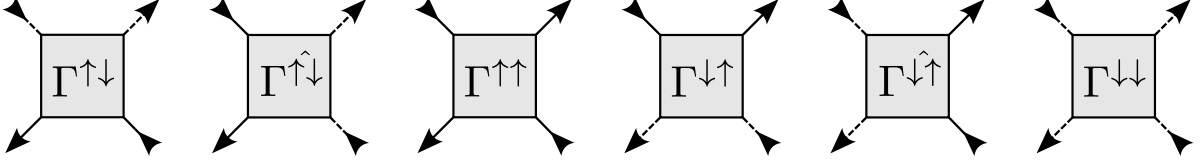
Figure 4.2.: Spin components of the four-point vertex Γ. The $\uparrow$ component is represented by a solid leg and the $\downarrow$ component by a dashed leg.

bold symbol $\boldsymbol{\nu}_r = (\omega_r, \nu_r, \nu_r')$.) In the example of Eq. (4.3), we thus consider $\Gamma(\boldsymbol{\nu}_p(\boldsymbol{\nu}_a))$.

Let us now specify the spin structure of the vertex functions. We consider models of two distinct particle types denoted by $\uparrow, \downarrow$ and also referred to as *spin components*. We consider the case where the generic action, Eq. (3.1), is replaced by the following form:

$$S = -\tfrac{1}{\beta} \sum_\nu \bar{c}^\uparrow(\nu)[G_0^\uparrow(\nu)]^{-1} c^\uparrow(\nu) - \tfrac{1}{\beta} \sum_\nu \bar{c}^\downarrow(\nu)[G_0^\downarrow(\nu)]^{-1} c^\downarrow(\nu)$$

$$- U^{\uparrow\downarrow} \tfrac{1}{\beta^3} \sum_{\omega,\nu,\nu'} \bar{c}^\uparrow(\nu)\bar{c}^\downarrow(\nu+\omega)c^\downarrow(\nu'+\omega)c^\uparrow(\nu'). \tag{4.4}$$

This action does not allow spin flips of single particles so the propagators are diagonal with respect to their spin components, i.e., $\langle c^\uparrow(\nu)\bar{c}^\downarrow(\nu)\rangle = 0 = \langle c^\downarrow(\nu)\bar{c}^\uparrow(\nu)\rangle$. For the four-point vertex Γ, there are in general six different spin components:

$$\Gamma^{\uparrow\downarrow} = \Gamma_{\uparrow\downarrow|\uparrow\downarrow}, \quad \Gamma^{\hat{\uparrow}\downarrow} = \Gamma_{\uparrow\downarrow|\downarrow\uparrow}, \quad \Gamma^{\uparrow\uparrow} = \Gamma_{\uparrow\uparrow|\uparrow\uparrow}, \tag{4.5}$$

and the components $\Gamma^{\downarrow\uparrow}$, $\Gamma^{\hat{\downarrow}\uparrow}$, $\Gamma^{\downarrow\downarrow}$ that are obtained by exchanging $\uparrow$ with $\downarrow$. The corresponding diagrams are shown in Fig. 4.2. Note that by definition $\Gamma^{\hat{\uparrow}\uparrow} = \Gamma^{\uparrow\uparrow}$ and $\Gamma^{\hat{\downarrow}\downarrow} = \Gamma^{\downarrow\downarrow}$.

The Bethe–Salpeter equations (3.10) involve summations over different indices of four-point objects, which differ for the three diagrammatic channels $r = a, p, t$. For a more compact notation of these summations, we introduced channel-specific products, which we denote by the symbol $\circ$ (cf. Eqs. (4.6) and Eqs. (6) in Ref. [P1]). For the respective spin components, Eq. (4.5), the products of a four-point object A_r with another four-point object B_r are given by

$$[A_a \circ B_a]^{\uparrow\downarrow} = A_a^{\uparrow\downarrow} B_a^{\uparrow\downarrow}, \;\; [A_a \circ B_a]^{\uparrow\uparrow} = A_a^{\uparrow\uparrow} B_a^{\uparrow\uparrow} + A_a^{\hat{\uparrow}\downarrow} B_a^{\hat{\downarrow}\uparrow}, \;\; [A_a \circ B_a]^{\hat{\uparrow}\downarrow} = A_a^{\uparrow\uparrow} B_a^{\hat{\uparrow}\downarrow} + A_a^{\hat{\uparrow}\downarrow} B_a^{\downarrow\downarrow},$$
$$\tag{4.6a}$$

$$[A_p \circ B_p]^{\uparrow\uparrow} = A_p^{\uparrow\uparrow} B_p^{\uparrow\uparrow}, \;\; [A_p \circ B_p]^{\hat{\uparrow}\downarrow} = A_p^{\uparrow\downarrow} B_p^{\hat{\uparrow}\downarrow} + A_p^{\hat{\uparrow}\downarrow} B_p^{\downarrow\uparrow}, \;\; [A_p \circ B_p]^{\uparrow\downarrow} = A_p^{\uparrow\downarrow} B_p^{\uparrow\downarrow} + A_p^{\hat{\uparrow}\downarrow} B_p^{\hat{\downarrow}\uparrow},$$
$$\tag{4.6b}$$

$$[A_t \circ B_t]^{\hat{\uparrow}\downarrow} = A_t^{\hat{\uparrow}\downarrow} B_t^{\hat{\uparrow}\downarrow}, \;\; [A_t \circ B_t]^{\uparrow\downarrow} = A_t^{\uparrow\downarrow} B_t^{\uparrow\uparrow} + A_t^{\downarrow\downarrow} B_t^{\uparrow\downarrow}, \;\; [A_t \circ B_t]^{\uparrow\uparrow} = A_t^{\uparrow\uparrow} B_t^{\uparrow\uparrow} + A_t^{\downarrow\uparrow} B_t^{\uparrow\downarrow},$$
$$\tag{4.6c}$$

and respectively for the remaining components by exchanging $\uparrow \leftrightarrow \downarrow$. Equations (4.6) suggest that each diagrammatic channel has diagonal spin components ($\uparrow\downarrow$ and $\downarrow\uparrow$ for a, $\uparrow\uparrow$ and $\downarrow\downarrow$ for p, $\hat{\uparrow}\hat{\downarrow}$ and $\hat{\downarrow}\hat{\uparrow}$ for t) and non-diagonal spin components. For a more compact notation, we arrange the spin components of a four-point object A_r in 4×4 matrices according to the diagrammatic channels:

$$A_a = \begin{bmatrix} A_a^{\uparrow\downarrow} & 0 & 0 & 0 \\ 0 & A_a^{\downarrow\uparrow} & 0 & 0 \\ 0 & 0 & A_a^{\uparrow\uparrow} & A_a^{\hat{\uparrow}\hat{\downarrow}} \\ 0 & 0 & A_a^{\hat{\downarrow}\hat{\uparrow}} & A_a^{\downarrow\downarrow} \end{bmatrix}, \quad A_p = \begin{bmatrix} A_p^{\uparrow\uparrow} & 0 & 0 & 0 \\ 0 & A_p^{\downarrow\downarrow} & 0 & 0 \\ 0 & 0 & A_p^{\uparrow\downarrow} & A_p^{\hat{\uparrow}\hat{\downarrow}} \\ 0 & 0 & A_p^{\hat{\downarrow}\hat{\uparrow}} & A_p^{\downarrow\uparrow} \end{bmatrix}, \quad A_t = \begin{bmatrix} A_t^{\hat{\uparrow}\hat{\downarrow}} & 0 & 0 & 0 \\ 0 & A_t^{\hat{\downarrow}\hat{\uparrow}} & 0 & 0 \\ 0 & 0 & A_t^{\uparrow\uparrow} & A_t^{\downarrow\uparrow} \\ 0 & 0 & A_t^{\uparrow\downarrow} & A_t^{\downarrow\downarrow} \end{bmatrix}.$$
$$(4.7)$$

This way, the effect of the $\circ$ product [cf. Eqs. (4.6)] is just obtained by simple matrix multiplication over these 4×4 matrices. Due to fermionic crossing symmetries, i.e., $U_{1'2'|12} = -U_{2'1'|12} = -U_{1'2'|21}$, there is only one independent spin component of the bare vertex, namely $U^{\uparrow\downarrow}$, which appears in the action, Eq. (4.4). Hence, the corresponding 4×4 matrices have a simpler structure:

$$U_a = U^{\uparrow\downarrow} \begin{bmatrix} 1 & 0 & 0 & 0 \\ 0 & 1 & 0 & 0 \\ 0 & 0 & 0 & -1 \\ 0 & 0 & -1 & 0 \end{bmatrix}, \quad U_p = U^{\uparrow\downarrow} \begin{bmatrix} 0 & 0 & 0 & 0 \\ 0 & 0 & 0 & 0 \\ 0 & 0 & 1 & -1 \\ 0 & 0 & -1 & 1 \end{bmatrix}, \quad U_t = U^{\uparrow\downarrow} \begin{bmatrix} -1 & 0 & 0 & 0 \\ 0 & -1 & 0 & 0 \\ 0 & 0 & 0 & 1 \\ 0 & 0 & 1 & 0 \end{bmatrix}.$$
$$(4.8)$$

Besides vertices, Bethe–Salpeter equations contain the bubbles Π_r as products of two Green's functions. With respect to their spin components, their general form (3.11) is reduced to

$$\Pi_a^{\uparrow\downarrow}(\omega, \nu'') = G^{\uparrow}(\nu'') G^{\downarrow}(\nu'' + \omega), \tag{4.9a}$$

$$\Pi_p^{\uparrow\downarrow}(\omega, \nu'') = \tfrac{1}{2} G^{\uparrow}(-\nu'') G^{\downarrow}(\nu'' + \omega), \tag{4.9b}$$

$$\Pi_t^{\hat{\uparrow}\hat{\downarrow}}(\omega, \nu'') = -G^{\downarrow}(\nu'') G^{\uparrow}(\nu'' + \omega). \tag{4.9c}$$

Since the propagators do not change the spin flavor, some components of the bubbles vanish, i.e., $\Pi_a^{\hat{\uparrow}\hat{\downarrow}} = 0 = \Pi_p^{\hat{\uparrow}\hat{\downarrow}} = \Pi_t^{\uparrow\downarrow}$, so in their matrix representation they are all diagonal:

$$\Pi_a = \begin{bmatrix} \Pi_a^{\uparrow\downarrow} & 0 & 0 & 0 \\ 0 & \Pi_a^{\downarrow\uparrow} & 0 & 0 \\ 0 & 0 & \Pi_a^{\uparrow\uparrow} & 0 \\ 0 & 0 & 0 & \Pi_a^{\downarrow\downarrow} \end{bmatrix}, \quad \Pi_p = \begin{bmatrix} \Pi_p^{\uparrow\uparrow} & 0 & 0 & 0 \\ 0 & \Pi_p^{\downarrow\downarrow} & 0 & 0 \\ 0 & 0 & \Pi_p^{\uparrow\downarrow} & 0 \\ 0 & 0 & 0 & \Pi_p^{\downarrow\uparrow} \end{bmatrix}, \quad \Pi_t = \begin{bmatrix} \Pi_t^{\hat{\uparrow}\hat{\downarrow}} & 0 & 0 & 0 \\ 0 & \Pi_t^{\hat{\downarrow}\hat{\uparrow}} & 0 & 0 \\ 0 & 0 & \Pi_t^{\uparrow\uparrow} & 0 \\ 0 & 0 & 0 & \Pi_t^{\downarrow\downarrow} \end{bmatrix}.$$
$$(4.10)$$

This simplifies the identification of the spin components in the Bethe–Salpeter equations (3.13), $\gamma_r = I_r \circ \Pi_r \circ \Gamma$:

$$\gamma_a^{\uparrow\downarrow} = I_a^{\uparrow\downarrow}\Pi_a^{\uparrow\downarrow}\Gamma^{\uparrow\downarrow}, \quad \begin{bmatrix} \gamma_a^{\uparrow\uparrow} & \gamma_a^{\hat{\uparrow}\downarrow} \\ \gamma_a^{\hat{\downarrow}\uparrow} & \gamma_a^{\downarrow\downarrow} \end{bmatrix} = \begin{bmatrix} I_a^{\uparrow\uparrow} & I_a^{\hat{\uparrow}\downarrow} \\ I_a^{\hat{\downarrow}\uparrow} & I_a^{\downarrow\downarrow} \end{bmatrix} \begin{bmatrix} \Pi_a^{\uparrow\uparrow} & 0 \\ 0 & \Pi_a^{\downarrow\downarrow} \end{bmatrix} \begin{bmatrix} \Gamma^{\uparrow\uparrow} & \Gamma^{\hat{\uparrow}\downarrow} \\ \Gamma^{\hat{\downarrow}\uparrow} & \Gamma^{\downarrow\downarrow} \end{bmatrix}, \tag{4.11a}$$

$$\gamma_p^{\uparrow\uparrow} = I_p^{\uparrow\uparrow}\Pi_p^{\uparrow\uparrow}\Gamma^{\uparrow\uparrow}, \quad \begin{bmatrix} \gamma_p^{\uparrow\downarrow} & \gamma_p^{\hat{\uparrow}\downarrow} \\ \gamma_p^{\hat{\downarrow}\uparrow} & \gamma_p^{\downarrow\uparrow} \end{bmatrix} = \begin{bmatrix} I_p^{\uparrow\downarrow} & I_p^{\hat{\uparrow}\downarrow} \\ I_p^{\hat{\downarrow}\uparrow} & I_p^{\downarrow\uparrow} \end{bmatrix} \begin{bmatrix} \Pi_p^{\uparrow\downarrow} & 0 \\ 0 & \Pi_p^{\downarrow\uparrow} \end{bmatrix} \begin{bmatrix} \Gamma^{\uparrow\downarrow} & \Gamma^{\hat{\uparrow}\downarrow} \\ \Gamma^{\hat{\downarrow}\uparrow} & \Gamma^{\downarrow\uparrow} \end{bmatrix}, \tag{4.11b}$$

$$\gamma_t^{\hat{\uparrow}\downarrow} = I_t^{\hat{\uparrow}\downarrow}\Pi_t^{\hat{\uparrow}\downarrow}\Gamma^{\hat{\uparrow}\downarrow}, \quad \begin{bmatrix} \gamma_t^{\uparrow\uparrow} & \gamma_t^{\downarrow\uparrow} \\ \gamma_t^{\uparrow\downarrow} & \gamma_t^{\downarrow\downarrow} \end{bmatrix} = \begin{bmatrix} I_t^{\uparrow\uparrow} & I_t^{\downarrow\uparrow} \\ I_t^{\uparrow\downarrow} & I_t^{\downarrow\downarrow} \end{bmatrix} \begin{bmatrix} \Pi_t^{\uparrow\uparrow} & 0 \\ 0 & \Pi_t^{\downarrow\downarrow} \end{bmatrix} \begin{bmatrix} \Gamma^{\uparrow\uparrow} & \Gamma^{\downarrow\uparrow} \\ \Gamma^{\uparrow\downarrow} & \Gamma^{\downarrow\downarrow} \end{bmatrix}. \tag{4.11c}$$

Using the frequency conventions from Eqs. (4.1), the Bethe–Salpeter equations (3.13) include the following frequency summations (cf. Eq (20) in Ref. [P1]):

$$\gamma_r(\omega, \nu, \nu') = \tfrac{1}{\beta} \sum_{\nu''} I_r(\omega, \nu, \nu'') \bullet \Pi_r(\omega, \nu'') \bullet \Gamma_r(\omega, \nu'', \nu'). \tag{4.12}$$

As in Ref. [P1], the • product only refers to the summation over spin indices, *not* frequency arguments (or momenta).

In the following, we give the spin structure of the *single-boson exchange* (SBE) vertices, which are defined by the so-called *SBE equations* (cf. Eqs. (41) in Ref. [P1]).

We start with the *multi-boson exchange* (MBE) vertices $M_r(\omega, \nu, \nu')$ that are U irreducible, but two-particle reducible. They strictly depend on three frequencies and are therefore the most expensive objects to compute numerically. The MBE vertices fulfill Bethe–Salpeter equations whose spin structure is the same as in Eqs. (4.11). We therefore just write their frequency summation analogous to Eq. (4.12) (cf. Eq. (41h) in Ref. [P1]):

$$M_r(\omega, \nu, \nu') = \tfrac{1}{\beta} \sum_{\nu''} [T_r(\omega, \nu, \nu'') - M_r(\omega, \nu, \nu'')] \bullet \Pi_r(\omega, \nu'') \bullet T_r(\omega, \nu'', \nu'). \tag{4.13}$$

Here, T_r contains the parts of the full vertex that are U irreducible in channel r. We postpone their definition to the end of this section [cf. Eq. (4.24)].

As a second ingredient, we have the *Hedin vertices* $\bar{\lambda}_r(\omega, \nu)$ and $\lambda_r(\omega, \nu')$ that describe interactions between one exchange boson and two fermions. They depend on one bosonic and one fermionic frequency and are computed by Schwinger–Dyson equations involving the U-irreducible vertices $T_r(\omega, \nu, \nu')$. In the following, we subdivide them into an asymptotically decaying part $\tilde{\bar{\lambda}}_r(\omega, \nu) = \bar{\lambda}_r(\omega, \nu) - \mathbf{1}_r$, $\tilde{\lambda}_r(\omega, \nu') = \lambda_r(\omega, \nu') - \mathbf{1}_r$ and into the constant part $\mathbf{1}_r$. The latter is the identity operator with respect to the • product in channel r (cf. App. C.2). In the notation of 4×4 matrices, Eqs. (4.7), $\mathbf{1}_r$ is simply given by identity matrices. By this consideration, the Hedin vertices have the following

asymptotic values for $|\omega| \to \infty$ (cf. Eqs. (41d)–(41e) in Ref. [P1]):

$$\lambda_a^{\uparrow\downarrow}, \lambda_a^{\uparrow\uparrow} \to 1, \quad \lambda_a^{\hat{\uparrow}\downarrow} \to 0, \quad \lambda_p^{\uparrow\uparrow}, \lambda_p^{\uparrow\downarrow} \to 1, \quad \lambda_p^{\hat{\uparrow}\downarrow} \to 0, \quad \lambda_t^{\hat{\uparrow}\downarrow}, \lambda_t^{\uparrow\uparrow} \to 1, \quad \lambda_t^{\uparrow\downarrow} \to 0. \quad (4.14)$$

The same is valid for $\bar{\lambda}_r$ and the flipped spin components ($\uparrow \leftrightarrow \downarrow$). The spin structure of the Schwinger–Dyson equations for the (asymptotically vanishing parts of the) Hedin vertices is given as

$$\tilde{\tilde{\lambda}}_a^{\uparrow\downarrow} = T_a^{\uparrow\downarrow}\Pi_a^{\uparrow\downarrow}, \quad \begin{bmatrix} \tilde{\tilde{\lambda}}_a^{\uparrow\uparrow} & \tilde{\tilde{\lambda}}_a^{\hat{\uparrow}\downarrow} \\ \tilde{\tilde{\lambda}}_a^{\hat{\downarrow}\uparrow} & \tilde{\tilde{\lambda}}_a^{\downarrow\downarrow} \end{bmatrix} = \begin{bmatrix} T_a^{\uparrow\uparrow} & T_a^{\hat{\uparrow}\downarrow} \\ T_a^{\hat{\downarrow}\uparrow} & T_a^{\downarrow\downarrow} \end{bmatrix} \begin{bmatrix} \Pi_a^{\uparrow\uparrow} & 0 \\ 0 & \Pi_a^{\downarrow\downarrow} \end{bmatrix} = \begin{bmatrix} T_a^{\uparrow\uparrow}\Pi_a^{\uparrow\uparrow} & T_a^{\hat{\uparrow}\downarrow}\Pi_a^{\downarrow\downarrow} \\ T_a^{\hat{\downarrow}\uparrow}\Pi_a^{\uparrow\uparrow} & T_a^{\downarrow\downarrow}\Pi_a^{\downarrow\downarrow} \end{bmatrix}, \quad (4.15a)$$

$$\tilde{\tilde{\lambda}}_p^{\uparrow\uparrow} = T_p^{\uparrow\uparrow}\Pi_p^{\uparrow\uparrow}, \quad \begin{bmatrix} \tilde{\tilde{\lambda}}_p^{\uparrow\downarrow} & \tilde{\tilde{\lambda}}_p^{\hat{\uparrow}\downarrow} \\ \tilde{\tilde{\lambda}}_p^{\hat{\downarrow}\uparrow} & \tilde{\tilde{\lambda}}_p^{\downarrow\uparrow} \end{bmatrix} = \begin{bmatrix} T_p^{\uparrow\downarrow} & T_p^{\hat{\uparrow}\downarrow} \\ T_p^{\hat{\downarrow}\uparrow} & T_p^{\downarrow\uparrow} \end{bmatrix} \begin{bmatrix} \Pi_p^{\uparrow\downarrow} & 0 \\ 0 & \Pi_p^{\downarrow\uparrow} \end{bmatrix} = \begin{bmatrix} T_p^{\uparrow\downarrow}\Pi_p^{\uparrow\downarrow} & T_p^{\hat{\uparrow}\downarrow}\Pi_p^{\downarrow\uparrow} \\ T_p^{\hat{\downarrow}\uparrow}\Pi_p^{\uparrow\downarrow} & T_p^{\downarrow\uparrow}\Pi_p^{\downarrow\uparrow} \end{bmatrix}, \quad (4.15b)$$

$$\tilde{\tilde{\lambda}}_t^{\hat{\uparrow}\downarrow} = T_t^{\hat{\uparrow}\downarrow}\Pi_t^{\hat{\uparrow}\downarrow}, \quad \begin{bmatrix} \tilde{\tilde{\lambda}}_t^{\uparrow\uparrow} & \tilde{\tilde{\lambda}}_t^{\downarrow\uparrow} \\ \tilde{\tilde{\lambda}}_t^{\uparrow\downarrow} & \tilde{\tilde{\lambda}}_t^{\downarrow\downarrow} \end{bmatrix} = \begin{bmatrix} T_t^{\uparrow\uparrow} & T_t^{\downarrow\uparrow} \\ T_t^{\uparrow\downarrow} & T_t^{\downarrow\downarrow} \end{bmatrix} \begin{bmatrix} \Pi_t^{\uparrow\uparrow} & 0 \\ 0 & \Pi_t^{\downarrow\downarrow} \end{bmatrix} = \begin{bmatrix} T_t^{\uparrow\uparrow}\Pi_t^{\uparrow\uparrow} & T_t^{\downarrow\uparrow}\Pi_t^{\downarrow\downarrow} \\ T_t^{\uparrow\downarrow}\Pi_t^{\uparrow\uparrow} & T_t^{\downarrow\downarrow}\Pi_t^{\downarrow\downarrow} \end{bmatrix}, \quad (4.15c)$$

$$\tilde{\lambda}_a^{\uparrow\downarrow} = \Pi_a^{\uparrow\downarrow}T_a^{\uparrow\downarrow}, \quad \begin{bmatrix} \tilde{\lambda}_a^{\uparrow\uparrow} & \tilde{\lambda}_a^{\hat{\uparrow}\downarrow} \\ \tilde{\lambda}_a^{\hat{\downarrow}\uparrow} & \tilde{\lambda}_a^{\downarrow\downarrow} \end{bmatrix} = \begin{bmatrix} \Pi_a^{\uparrow\uparrow} & 0 \\ 0 & \Pi_a^{\downarrow\downarrow} \end{bmatrix} \begin{bmatrix} T_a^{\uparrow\uparrow} & T_a^{\hat{\uparrow}\downarrow} \\ T_a^{\hat{\downarrow}\uparrow} & T_a^{\downarrow\downarrow} \end{bmatrix} = \begin{bmatrix} \Pi_a^{\uparrow\uparrow}T_a^{\uparrow\uparrow} & \Pi_a^{\uparrow\uparrow}T_a^{\hat{\uparrow}\downarrow} \\ \Pi_a^{\downarrow\downarrow}T_a^{\hat{\downarrow}\uparrow} & \Pi_a^{\downarrow\downarrow}T_a^{\downarrow\downarrow} \end{bmatrix}, \quad (4.16a)$$

$$\tilde{\lambda}_p^{\uparrow\uparrow} = \Pi_p^{\uparrow\uparrow}T_p^{\uparrow\uparrow}, \quad \begin{bmatrix} \tilde{\lambda}_p^{\uparrow\downarrow} & \tilde{\lambda}_p^{\hat{\uparrow}\downarrow} \\ \tilde{\lambda}_p^{\hat{\downarrow}\uparrow} & \tilde{\lambda}_p^{\downarrow\uparrow} \end{bmatrix} = \begin{bmatrix} \Pi_p^{\uparrow\downarrow} & 0 \\ 0 & \Pi_p^{\downarrow\uparrow} \end{bmatrix} \begin{bmatrix} T_p^{\uparrow\downarrow} & T_p^{\hat{\uparrow}\downarrow} \\ T_p^{\hat{\downarrow}\uparrow} & T_p^{\downarrow\uparrow} \end{bmatrix} = \begin{bmatrix} \Pi_p^{\uparrow\downarrow}T_p^{\uparrow\downarrow} & \Pi_p^{\uparrow\downarrow}T_p^{\hat{\uparrow}\downarrow} \\ \Pi_p^{\downarrow\uparrow}T_p^{\hat{\downarrow}\uparrow} & \Pi_p^{\downarrow\uparrow}T_p^{\downarrow\uparrow} \end{bmatrix}, \quad (4.16b)$$

$$\tilde{\lambda}_t^{\hat{\uparrow}\downarrow} = \Pi_t^{\hat{\uparrow}\downarrow}T_t^{\hat{\uparrow}\downarrow}, \quad \begin{bmatrix} \tilde{\lambda}_t^{\uparrow\uparrow} & \tilde{\lambda}_t^{\downarrow\uparrow} \\ \tilde{\lambda}_t^{\uparrow\downarrow} & \tilde{\lambda}_t^{\downarrow\downarrow} \end{bmatrix} = \begin{bmatrix} \Pi_t^{\uparrow\uparrow} & 0 \\ 0 & \Pi_t^{\downarrow\downarrow} \end{bmatrix} \begin{bmatrix} T_t^{\uparrow\uparrow} & T_t^{\downarrow\uparrow} \\ T_t^{\uparrow\downarrow} & T_t^{\downarrow\downarrow} \end{bmatrix} = \begin{bmatrix} \Pi_t^{\uparrow\uparrow}T_t^{\uparrow\uparrow} & \Pi_t^{\uparrow\uparrow}T_t^{\downarrow\uparrow} \\ \Pi_t^{\downarrow\downarrow}T_t^{\uparrow\downarrow} & \Pi_t^{\downarrow\downarrow}T_t^{\downarrow\downarrow} \end{bmatrix}. \quad (4.16c)$$

On the other hand, the frequency summations involved in these Schwinger–Dyson equations are given by

$$\tilde{\tilde{\lambda}}_r(\omega, \nu) = \tfrac{1}{\beta} \sum_{\nu''} T_r(\omega, \nu, \nu'') \bullet \Pi_r(\omega, \nu''), \quad (4.17a)$$

$$\tilde{\lambda}_r(\omega, \nu') = \tfrac{1}{\beta} \sum_{\nu''} \Pi_r(\omega, \nu'') \bullet T_r(\omega, \nu'', \nu'). \quad (4.17b)$$

Finally, we have the *bosonic propagators* $\eta_r(\omega)$ describing the exchange bosons of the three diagrammatic channels. The bosonic propagators depend on one bosonic frequency ω. For practical reasons, we separate it into a part $\tilde{\eta}_r(\omega) = \eta_r(\omega) - U$ that vanishes for $|\omega| \to \infty$ and the constant contribution given by the bare interaction vertex U. The

bosonic propagators fulfill the following Dyson equations (cf. Eq. (41b) in Ref. [P1]):

$$\tilde{\eta}_a^{\uparrow\downarrow} = U^{\uparrow\downarrow} P_a^{\uparrow\downarrow} \eta_a^{\uparrow\downarrow}, \quad \begin{bmatrix} \tilde{\eta}_a^{\uparrow\uparrow} & \tilde{\eta}_a^{\uparrow\hat{\downarrow}} \\ \tilde{\eta}_a^{\downarrow\hat{\uparrow}} & \tilde{\eta}_a^{\downarrow\downarrow} \end{bmatrix} = \begin{bmatrix} 0 & -U^{\uparrow\downarrow} \\ -U^{\uparrow\downarrow} & 0 \end{bmatrix} \begin{bmatrix} P_a^{\uparrow\uparrow} & P_a^{\uparrow\hat{\downarrow}} \\ P_a^{\downarrow\hat{\uparrow}} & P_a^{\downarrow\downarrow} \end{bmatrix} \begin{bmatrix} \eta_a^{\uparrow\uparrow} & \eta_a^{\uparrow\hat{\downarrow}} \\ \eta_a^{\downarrow\hat{\uparrow}} & \eta_a^{\downarrow\downarrow} \end{bmatrix}, \qquad (4.18a)$$

$$\tilde{\eta}_p^{\uparrow\uparrow} = 0, \quad \begin{bmatrix} \tilde{\eta}_p^{\uparrow\downarrow} & \tilde{\eta}_p^{\uparrow\hat{\downarrow}} \\ \tilde{\eta}_p^{\downarrow\hat{\uparrow}} & \tilde{\eta}_p^{\downarrow\uparrow} \end{bmatrix} = \begin{bmatrix} U^{\uparrow\downarrow} & -U^{\uparrow\downarrow} \\ -U^{\uparrow\downarrow} & U^{\uparrow\downarrow} \end{bmatrix} \begin{bmatrix} P_p^{\uparrow\downarrow} & P_p^{\uparrow\hat{\downarrow}} \\ P_p^{\downarrow\hat{\uparrow}} & P_p^{\downarrow\uparrow} \end{bmatrix} \begin{bmatrix} \eta_p^{\uparrow\downarrow} & \eta_p^{\uparrow\hat{\downarrow}} \\ \eta_p^{\downarrow\hat{\uparrow}} & \eta_p^{\downarrow\uparrow} \end{bmatrix}, \qquad (4.18b)$$

$$\tilde{\eta}_t^{\uparrow\hat{\downarrow}} = U^{\uparrow\hat{\downarrow}} P_t^{\uparrow\hat{\downarrow}} \eta_t^{\uparrow\hat{\downarrow}}, \quad \begin{bmatrix} \tilde{\eta}_t^{\uparrow\uparrow} & \tilde{\eta}_t^{\downarrow\uparrow} \\ \tilde{\eta}_t^{\uparrow\downarrow} & \tilde{\eta}_t^{\downarrow\downarrow} \end{bmatrix} = \begin{bmatrix} 0 & U^{\uparrow\downarrow} \\ U^{\uparrow\downarrow} & 0 \end{bmatrix} \begin{bmatrix} P_t^{\uparrow\uparrow} & P_t^{\downarrow\uparrow} \\ P_t^{\uparrow\downarrow} & P_t^{\downarrow\downarrow} \end{bmatrix} \begin{bmatrix} \eta_t^{\uparrow\uparrow} & \eta_t^{\downarrow\uparrow} \\ \eta_t^{\uparrow\downarrow} & \eta_t^{\downarrow\downarrow} \end{bmatrix}. \qquad (4.18c)$$

Here, we make use of the *polarization* P_r, which takes the role of a bosonic self-energy. Equations (4.18) do not involve any summation over frequencies:

$$\tilde{\eta}_r(\omega) = U \bullet P_r(\omega) \bullet \eta_r(\omega). \qquad (4.19)$$

The bosonic self-energy $P_r(\omega)$ is obtained by Schwinger–Dyson equations involving the Hedin vertices (cf. Eq. (41c) in Ref. [P1]). Their spin components yield

$$P_a^{\uparrow\downarrow} = \Pi_a^{\uparrow\downarrow} \bar{\lambda}_a^{\uparrow\downarrow} = \lambda_a^{\uparrow\downarrow} \Pi_a^{\uparrow\downarrow}, \quad \begin{bmatrix} P_a^{\uparrow\uparrow} & P_a^{\uparrow\hat{\downarrow}} \\ P_a^{\downarrow\hat{\uparrow}} & P_a^{\downarrow\downarrow} \end{bmatrix} = \begin{bmatrix} \Pi_a^{\uparrow\uparrow} & 0 \\ 0 & \Pi_a^{\downarrow\downarrow} \end{bmatrix} \begin{bmatrix} \bar{\lambda}_a^{\uparrow\uparrow} & \bar{\lambda}_a^{\uparrow\hat{\downarrow}} \\ \bar{\lambda}_a^{\downarrow\hat{\uparrow}} & \bar{\lambda}_a^{\downarrow\downarrow} \end{bmatrix} = \begin{bmatrix} \Pi_a^{\uparrow\uparrow}\bar{\lambda}_a^{\uparrow\uparrow} & \Pi_a^{\uparrow\uparrow}\bar{\lambda}_a^{\uparrow\hat{\downarrow}} \\ \Pi_a^{\downarrow\downarrow}\bar{\lambda}_a^{\downarrow\hat{\uparrow}} & \Pi_a^{\downarrow\downarrow}\bar{\lambda}_a^{\downarrow\downarrow} \end{bmatrix}$$

$$= \begin{bmatrix} \lambda_a^{\uparrow\uparrow} & \lambda_a^{\uparrow\hat{\downarrow}} \\ \lambda_a^{\downarrow\hat{\uparrow}} & \lambda_a^{\downarrow\downarrow} \end{bmatrix} \begin{bmatrix} \Pi_a^{\uparrow\uparrow} & 0 \\ 0 & \Pi_a^{\downarrow\downarrow} \end{bmatrix} = \begin{bmatrix} \lambda_a^{\uparrow\uparrow}\Pi_a^{\uparrow\uparrow} & \lambda_a^{\uparrow\hat{\downarrow}}\Pi_a^{\downarrow\downarrow} \\ \lambda_a^{\downarrow\hat{\uparrow}}\Pi_a^{\uparrow\uparrow} & \lambda_a^{\downarrow\downarrow}\Pi_a^{\downarrow\downarrow} \end{bmatrix}, \qquad (4.20a)$$

$$P_p^{\uparrow\uparrow} = \Pi_p^{\uparrow\uparrow} \bar{\lambda}_p^{\uparrow\uparrow} = \lambda_p^{\uparrow\uparrow} \Pi_p^{\uparrow\uparrow}, \quad \begin{bmatrix} P_p^{\uparrow\downarrow} & P_p^{\uparrow\hat{\downarrow}} \\ P_p^{\downarrow\hat{\uparrow}} & P_p^{\downarrow\uparrow} \end{bmatrix} = \begin{bmatrix} \Pi_p^{\uparrow\downarrow} & 0 \\ 0 & \Pi_p^{\downarrow\uparrow} \end{bmatrix} \begin{bmatrix} \bar{\lambda}_p^{\uparrow\downarrow} & \bar{\lambda}_p^{\uparrow\hat{\downarrow}} \\ \bar{\lambda}_p^{\downarrow\hat{\uparrow}} & \bar{\lambda}_p^{\downarrow\uparrow} \end{bmatrix} = \begin{bmatrix} \Pi_p^{\uparrow\downarrow}\bar{\lambda}_p^{\uparrow\downarrow} & \Pi_p^{\uparrow\downarrow}\bar{\lambda}_p^{\uparrow\hat{\downarrow}} \\ \Pi_p^{\downarrow\uparrow}\bar{\lambda}_p^{\downarrow\hat{\uparrow}} & \Pi_p^{\downarrow\uparrow}\bar{\lambda}_p^{\downarrow\uparrow} \end{bmatrix}$$

$$= \begin{bmatrix} \lambda_p^{\uparrow\downarrow} & \lambda_p^{\uparrow\hat{\downarrow}} \\ \lambda_p^{\downarrow\hat{\uparrow}} & \lambda_p^{\downarrow\uparrow} \end{bmatrix} \begin{bmatrix} \Pi_p^{\uparrow\downarrow} & 0 \\ 0 & \Pi_p^{\downarrow\uparrow} \end{bmatrix} = \begin{bmatrix} \lambda_p^{\uparrow\downarrow}\Pi_p^{\uparrow\downarrow} & \lambda_p^{\uparrow\hat{\downarrow}}\Pi_p^{\downarrow\uparrow} \\ \lambda_p^{\downarrow\hat{\uparrow}}\Pi_p^{\uparrow\downarrow} & \lambda_p^{\downarrow\uparrow}\Pi_p^{\downarrow\uparrow} \end{bmatrix}, \qquad (4.20b)$$

$$P_t^{\uparrow\hat{\downarrow}} = \Pi_t^{\uparrow\hat{\downarrow}} \bar{\lambda}_t^{\uparrow\hat{\downarrow}} = \lambda_t^{\uparrow\hat{\downarrow}} \Pi_t^{\uparrow\hat{\downarrow}}, \quad \begin{bmatrix} P_t^{\uparrow\uparrow} & P_t^{\downarrow\uparrow} \\ P_t^{\uparrow\downarrow} & P_t^{\downarrow\downarrow} \end{bmatrix} = \begin{bmatrix} \Pi_t^{\uparrow\uparrow} & 0 \\ 0 & \Pi_t^{\downarrow\downarrow} \end{bmatrix} \begin{bmatrix} \bar{\lambda}_t^{\uparrow\uparrow} & \bar{\lambda}_t^{\downarrow\uparrow} \\ \bar{\lambda}_t^{\uparrow\downarrow} & \bar{\lambda}_t^{\downarrow\downarrow} \end{bmatrix} = \begin{bmatrix} \Pi_t^{\uparrow\uparrow}\bar{\lambda}_t^{\uparrow\uparrow} & \Pi_t^{\uparrow\uparrow}\bar{\lambda}_t^{\downarrow\uparrow} \\ \Pi_t^{\downarrow\downarrow}\bar{\lambda}_t^{\uparrow\downarrow} & \Pi_t^{\downarrow\downarrow}\bar{\lambda}_t^{\downarrow\downarrow} \end{bmatrix}$$

$$= \begin{bmatrix} \lambda_t^{\uparrow\uparrow} & \lambda_t^{\downarrow\uparrow} \\ \lambda_t^{\uparrow\downarrow} & \lambda_t^{\downarrow\downarrow} \end{bmatrix} \begin{bmatrix} \Pi_t^{\uparrow\uparrow} & 0 \\ 0 & \Pi_t^{\downarrow\downarrow} \end{bmatrix} = \begin{bmatrix} \lambda_t^{\uparrow\uparrow}\Pi_t^{\uparrow\uparrow} & \lambda_t^{\downarrow\uparrow}\Pi_t^{\downarrow\downarrow} \\ \lambda_t^{\uparrow\downarrow}\Pi_t^{\uparrow\uparrow} & \lambda_t^{\downarrow\downarrow}\Pi_t^{\downarrow\downarrow} \end{bmatrix}. \qquad (4.20c)$$

These involve the following frequency summations:

$$P_r(\omega) = \tfrac{1}{\beta} \sum_{\nu''} \Pi_r(\omega, \nu'') \bullet \bar{\lambda}_r(\omega, \nu'') = \tfrac{1}{\beta} \sum_{\nu''} \lambda_r(\omega, \nu'') \bullet \Pi_r(\omega, \nu''). \qquad (4.21)$$

The product of two Hedin vertices $\bar{\lambda}_r, \lambda_r$ with one bosonic propagator η_r in the middle gives the U-reducible contribution ∇_r of the full vertex Γ in a specific channel r. The spin components are computed as

$$\nabla_a^{\uparrow\downarrow} = \bar{\lambda}_a^{\uparrow\downarrow}\eta_a^{\uparrow\downarrow}\lambda_a^{\uparrow\downarrow}, \quad \begin{bmatrix} \nabla_a^{\uparrow\uparrow} & \nabla_a^{\hat{\uparrow\downarrow}} \\ \nabla_a^{\hat{\downarrow\uparrow}} & \nabla_a^{\downarrow\downarrow} \end{bmatrix} = \begin{bmatrix} \bar{\lambda}_a^{\uparrow\uparrow} & \bar{\lambda}_a^{\hat{\uparrow\downarrow}} \\ \bar{\lambda}_a^{\hat{\downarrow\uparrow}} & \bar{\lambda}_a^{\downarrow\downarrow} \end{bmatrix} \begin{bmatrix} \eta_a^{\uparrow\uparrow} & \eta_a^{\hat{\uparrow\downarrow}} \\ \eta_a^{\hat{\downarrow\uparrow}} & \eta_a^{\downarrow\downarrow} \end{bmatrix} \begin{bmatrix} \lambda_a^{\uparrow\uparrow} & \lambda_a^{\hat{\uparrow\downarrow}} \\ \lambda_a^{\hat{\downarrow\uparrow}} & \lambda_a^{\downarrow\downarrow} \end{bmatrix}, \tag{4.22a}$$

$$\nabla_p^{\uparrow\uparrow} = 0, \quad \begin{bmatrix} \nabla_p^{\uparrow\downarrow} & \nabla_p^{\hat{\uparrow\downarrow}} \\ \nabla_p^{\hat{\downarrow\uparrow}} & \nabla_p^{\downarrow\uparrow} \end{bmatrix} = \begin{bmatrix} \bar{\lambda}_p^{\uparrow\downarrow} & \bar{\lambda}_p^{\hat{\uparrow\downarrow}} \\ \bar{\lambda}_p^{\hat{\downarrow\uparrow}} & \bar{\lambda}_p^{\downarrow\uparrow} \end{bmatrix} \begin{bmatrix} \eta_p^{\uparrow\downarrow} & \eta_p^{\hat{\uparrow\downarrow}} \\ \eta_p^{\hat{\downarrow\uparrow}} & \eta_p^{\downarrow\uparrow} \end{bmatrix} \begin{bmatrix} \lambda_p^{\uparrow\downarrow} & \lambda_p^{\hat{\uparrow\downarrow}} \\ \lambda_p^{\hat{\downarrow\uparrow}} & \lambda_p^{\downarrow\uparrow} \end{bmatrix}, \tag{4.22b}$$

$$\nabla_t^{\hat{\uparrow\downarrow}} = \bar{\lambda}_t^{\hat{\uparrow\downarrow}}\eta_t^{\hat{\uparrow\downarrow}}\lambda_t^{\hat{\uparrow\downarrow}}, \quad \begin{bmatrix} \nabla_t^{\uparrow\uparrow} & \nabla_t^{\downarrow\uparrow} \\ \nabla_t^{\uparrow\downarrow} & \nabla_t^{\downarrow\downarrow} \end{bmatrix} = \begin{bmatrix} \bar{\lambda}_t^{\uparrow\uparrow} & \bar{\lambda}_t^{\downarrow\uparrow} \\ \bar{\lambda}_t^{\uparrow\downarrow} & \bar{\lambda}_t^{\downarrow\downarrow} \end{bmatrix} \begin{bmatrix} \eta_t^{\uparrow\uparrow} & \eta_t^{\downarrow\uparrow} \\ \eta_t^{\uparrow\downarrow} & \eta_t^{\downarrow\downarrow} \end{bmatrix} \begin{bmatrix} \lambda_t^{\uparrow\uparrow} & \lambda_t^{\downarrow\uparrow} \\ \lambda_t^{\uparrow\downarrow} & \lambda_t^{\downarrow\downarrow} \end{bmatrix}. \tag{4.22c}$$

Importantly, the computation of ∇_r does not involve any frequency summation:

$$\nabla_r(\omega, \nu, \nu') = \bar{\lambda}_r(\omega, \nu) \bullet \eta_r(\omega) \bullet \lambda_r(\omega, \nu'). \tag{4.23}$$

From this, we can compute the U-irreducible vertices T_r with respect to the channel r, which are given as (cf. Eq. (41f) in Ref. [P1])

$$T_r(\omega, \nu, \nu') = \Gamma_r(\omega, \nu, \nu') - \nabla_r(\omega, \nu, \nu')$$
$$= \tilde{R}_r(\omega, \nu, \nu') + \sum_{r'=a,p,t} M_{r'}(\boldsymbol{\nu}_{r'}(\boldsymbol{\nu}_r)) + \sum_{r'\neq r} \nabla_{r'}(\boldsymbol{\nu}_{r'}(\boldsymbol{\nu}_r)) - 2U. \tag{4.24}$$

Here we use the notation for frequency transformations introduced after Eqs. (4.2). $\tilde{R} = R - U$ is the rest function of the full vertex, which is neither two-particle reducible nor U reducible (in the parquet approximation, we set $\tilde{R} = 0$). The subtraction of $2U$ ensures that T_r itself does not contain any constant bare vertex U since T_r is U irreducible.

4.1.2. Symmetries

The equations discussed in the previous section can be simplified and shortened by the usage of symmetries, which reduces numerical costs tremendously. In particular, the parquet and SBE vertices satisfy crossing symmetries and the physical applications we consider additionally fulfill time-reversal symmetry.

Crossing symmetries

The indistinguishability of fermions combined with Pauli's exclusion principle leads to the so-called *crossing symmetries* of the vertices. In its most general form, we have

$$\Gamma_{1'2'|12} = -\Gamma_{2'1'|12} = -\Gamma_{1'2'|21} = \Gamma_{2'1'|21}. \tag{4.25}$$

Now, we apply the frequency parametrization, Eqs. (4.1), and the spin components, Eqs. (4.5), introduced in the previous section. The crossing symmetries, Eqs. (4.25), then take the following form:

$$\Gamma_a^{\uparrow\downarrow}(\omega,\nu,\nu') = -\Gamma_t^{\downarrow\hat{\uparrow}}(\omega,\nu,\nu') \qquad = \Gamma_a^{\downarrow\uparrow}(-\omega,\nu'+\omega,\nu+\omega) \quad = -\Gamma_t^{\hat{\uparrow}\downarrow}(-\omega,\nu'+\omega,\nu+\omega),$$
(4.26a)

$$\Gamma_p^{\uparrow\downarrow}(\omega,\nu,\nu') = -\Gamma_p^{\hat{\uparrow}\downarrow}(\omega,\nu,-\nu'-\omega) = \Gamma_p^{\downarrow\uparrow}(\omega,-\nu-\omega,-\nu'-\omega) = -\Gamma_p^{\downarrow\hat{\uparrow}}(\omega,-\nu-\omega,\nu'),$$
(4.26b)

$$\Gamma_t^{\uparrow\downarrow}(\omega,\nu,\nu') = -\Gamma_a^{\downarrow\hat{\uparrow}}(\omega,\nu,\nu') \qquad = \Gamma_t^{\downarrow\uparrow}(-\omega,\nu'+\omega,\nu+\omega) \quad = -\Gamma_a^{\hat{\uparrow}\downarrow}(-\omega,\nu'+\omega,\nu+\omega).$$
(4.26c)

The symmetries for $\Gamma^{\uparrow\uparrow}$ and $\Gamma^{\downarrow\downarrow}$ trivially follow from these. The crossing symmetries, Eqs. (4.26), are valid for all four-point vertices, which depend on three frequencies. We conclude that crossing symmetries relate the a- and t-reducible diagrams to each other such that for numerical computations we can fully drop the computation of one of them (in our case: the t channel). Moreover, p-reducible diagrams are related to themselves. The simplifications evoked by that are discussed in the following.

From the definitions of the bubbles Π_r, Eqs. (4.9), we can set up analogous symmetry relations:

$$\Pi_a^{\uparrow\downarrow}(\omega,\nu'') = -\Pi_t^{\downarrow\hat{\uparrow}}(\omega,\nu'') = \Pi_a^{\downarrow\uparrow}(-\omega,\nu''+\omega) = -\Pi_t^{\hat{\uparrow}\downarrow}(-\omega,\nu''+\omega), \qquad (4.27a)$$

$$\Pi_p^{\uparrow\downarrow}(\omega,\nu'') = \Pi_p^{\downarrow\uparrow}(\omega,-\nu''-\omega). \qquad (4.27b)$$

We call these the crossing symmetries of the bubbles.

With the crossing symmetries of four-point vertices, Eqs. (4.26), and the bubbles, Eqs. (4.27), the spin structure of the Bethe–Salpeter equation in the p channel, Eq. (4.11b), can be written as

$$\frac{1}{\beta}\sum_{\nu''} I_p^{\uparrow\hat{\downarrow}}(\omega,\nu,\nu'')\Pi_p^{\downarrow\hat{\uparrow}}(\omega,\nu'')\Gamma_p^{\downarrow\hat{\uparrow}}(\omega,\nu'',\nu')$$

$$= \frac{1}{\beta}\sum_{\nu''} I_p^{\uparrow\downarrow}(\omega,\nu,-\nu''-\omega)\Pi_p^{\uparrow\downarrow}(\omega,-\nu''-\omega)\Gamma_p^{\uparrow\downarrow}(\omega,-\nu''-\omega,\nu')$$

$$= \frac{1}{\beta}\sum_{\nu''} I_p^{\uparrow\downarrow}(\omega,\nu,\nu'')\Pi_p^{\uparrow\downarrow}(\omega,\nu'')\Gamma_p^{\uparrow\downarrow}(\omega,\nu'',\nu'), \qquad (4.28)$$

such that the matrix form in the p channel is superfluous:

$$\gamma_p^{\uparrow\downarrow} = I_p^{\uparrow\downarrow}\Pi_p^{\uparrow\downarrow}\Gamma_p^{\uparrow\downarrow} + I_p^{\uparrow\hat{\downarrow}}\Pi_p^{\downarrow\hat{\uparrow}}\Gamma_p^{\downarrow\hat{\uparrow}} = I_p^{\uparrow\downarrow}2\Pi_p^{\uparrow\downarrow}\Gamma_p^{\uparrow\downarrow}, \qquad (4.29a)$$

$$\gamma_p^{\uparrow\hat{\downarrow}} = I_p^{\uparrow\downarrow}\Pi_p^{\uparrow\downarrow}\Gamma_p^{\uparrow\hat{\downarrow}} + I_p^{\uparrow\hat{\downarrow}}\Pi_p^{\downarrow\hat{\uparrow}}\Gamma_p^{\downarrow\uparrow} = I_p^{\uparrow\downarrow}2\Pi_p^{\uparrow\downarrow}\Gamma_p^{\uparrow\hat{\downarrow}}. \qquad (4.29b)$$

Combining the crossing symmetries of the U-irreducible vertices $T_r(\omega,\nu,\nu')$, Eqs. (4.26),

with those belonging to the bubbles $\Pi_r(\omega, \nu)$, Eqs. (4.27), we deduce crossing symmetries for the Hedin vertices $\bar{\lambda}_r$ and λ_r. In particular, for the p channel, we deduce

$$
\begin{aligned}
\tilde{\bar{\lambda}}_p^{\uparrow\uparrow}(\omega, \nu'') &= \sum_{\nu''} T_p^{\uparrow\uparrow}(\omega, \nu, \nu'') \Pi_p^{\uparrow\uparrow}(\omega, \nu'') = -\sum_{\nu''} T_p^{\uparrow\uparrow}(\omega, \nu, -\nu'' - \omega) \Pi_p^{\uparrow\uparrow}(\omega, -\nu'' - \omega) \\
&= -\sum_{\nu''} T_p^{\uparrow\uparrow}(\omega, \nu, \nu'') \Pi_p^{\uparrow\uparrow}(\omega, \nu'') = -\tilde{\bar{\lambda}}_p^{\uparrow\uparrow}(\omega, \nu'') \Rightarrow \tilde{\bar{\lambda}}_p^{\uparrow\uparrow}(\omega, \nu'') = 0, \quad (4.30a)
\end{aligned}
$$

$$
\begin{aligned}
\tilde{\bar{\lambda}}_p^{\uparrow\hat{\downarrow}}(\omega, \nu) &= \sum_{\nu''} T_p^{\uparrow\hat{\downarrow}}(\omega, \nu, \nu'') \Pi_p^{\downarrow\uparrow}(\omega, \nu'') = -\sum_{\nu''} T_p^{\uparrow\downarrow}(\omega, \nu, -\nu'' - \omega) \Pi_p^{\uparrow\downarrow}(\omega, -\nu'' - \omega) \\
&= -\sum_{\nu''} T_p^{\uparrow\downarrow}(\omega, \nu, \nu'') \Pi_p^{\uparrow\downarrow}(\omega, \nu'') = -\tilde{\bar{\lambda}}_p^{\uparrow\downarrow}(\omega, \nu). \quad (4.30b)
\end{aligned}
$$

In the last step, we shifted the frequencies ν'' that are being summed over. By similar arguments, we obtain the following crossing symmetries:

$$
\begin{aligned}
\lambda_a^{\uparrow\downarrow}(\omega, \nu') &= & \lambda_t^{\downarrow\hat{\uparrow}}(\omega, \nu') &= \bar{\lambda}_a^{\downarrow\uparrow}(-\omega, \nu' + \omega) = & \bar{\lambda}_t^{\uparrow\hat{\downarrow}}(-\omega, \nu' + \omega), \quad (4.31a) \\
\bar{\lambda}_a^{\uparrow\downarrow}(\omega, \nu') &= & \bar{\lambda}_t^{\downarrow\hat{\uparrow}}(\omega, \nu) &= \lambda_a^{\downarrow\uparrow}(-\omega, \nu + \omega) = & \lambda_t^{\uparrow\hat{\downarrow}}(-\omega, \nu + \omega), \quad (4.31b) \\
\tilde{\lambda}_p^{\uparrow\downarrow}(\omega, \nu') &= & -\tilde{\lambda}_p^{\downarrow\hat{\uparrow}}(\omega, \nu') &= \tilde{\lambda}_p^{\downarrow\uparrow}(\omega, -\nu' - \omega) = & -\tilde{\lambda}_p^{\uparrow\hat{\downarrow}}(\omega, -\nu' - \omega), \quad (4.31c) \\
\tilde{\bar{\lambda}}_p^{\uparrow\downarrow}(\omega, \nu) &= -\tilde{\bar{\lambda}}_p^{\downarrow\hat{\uparrow}}(\omega, -\nu - \omega) &= \tilde{\bar{\lambda}}_p^{\downarrow\uparrow}(\omega, -\nu - \omega) &= & -\tilde{\bar{\lambda}}_p^{\uparrow\hat{\downarrow}}(\omega, \nu), \quad (4.31d) \\
\bar{\lambda}_t^{\uparrow\downarrow}(\omega, \nu) &= & \bar{\lambda}_a^{\downarrow\hat{\uparrow}}(\omega, \nu) &= \lambda_a^{\uparrow\hat{\downarrow}}(-\omega, \omega + \nu) = & \lambda_t^{\downarrow\uparrow}(-\omega, \omega + \nu), \quad (4.31e) \\
\lambda_t^{\uparrow\downarrow}(\omega, \nu') &= & \lambda_a^{\downarrow\hat{\uparrow}}(\omega, \nu') &= \bar{\lambda}_a^{\uparrow\hat{\downarrow}}(-\omega, \omega + \nu') = & \bar{\lambda}_t^{\downarrow\uparrow}(-\omega, \omega + \nu'). \quad (4.31f)
\end{aligned}
$$

We conclude that there are only two independent components left for the Hedin vertices $\bar{\lambda}_p$ and λ_p, respectively. Their matrix structure is thus simplified as

$$
\tilde{\bar{\lambda}}_p^{\uparrow\uparrow} = 0 = \tilde{\lambda}_p^{\uparrow\uparrow}, \quad
\begin{bmatrix} \tilde{\bar{\lambda}}_p^{\uparrow\downarrow} & \tilde{\bar{\lambda}}_p^{\uparrow\hat{\downarrow}} \\ \tilde{\bar{\lambda}}_p^{\downarrow\hat{\uparrow}} & \tilde{\bar{\lambda}}_p^{\downarrow\uparrow} \end{bmatrix} =
\begin{bmatrix} \tilde{\bar{\lambda}}_p^{\uparrow\downarrow} & -\tilde{\bar{\lambda}}_p^{\uparrow\downarrow} \\ -\tilde{\bar{\lambda}}_p^{\downarrow\uparrow} & \tilde{\bar{\lambda}}_p^{\downarrow\uparrow} \end{bmatrix}, \quad
\begin{bmatrix} \tilde{\lambda}_p^{\uparrow\downarrow} & \tilde{\lambda}_p^{\uparrow\hat{\downarrow}} \\ \tilde{\lambda}_p^{\downarrow\hat{\uparrow}} & \tilde{\lambda}_p^{\downarrow\uparrow} \end{bmatrix} =
\begin{bmatrix} \tilde{\lambda}_p^{\uparrow\downarrow} & -\tilde{\lambda}_p^{\downarrow\uparrow} \\ -\tilde{\lambda}_p^{\uparrow\downarrow} & \tilde{\lambda}_p^{\downarrow\uparrow} \end{bmatrix}. \quad (4.32)
$$

To obtain the full Hedin vertices $\bar{\lambda}_r = \mathbf{1}_r + \tilde{\bar{\lambda}}_r$ and $\lambda_r = \mathbf{1}_r + \tilde{\lambda}_r$, there appear additional constants depending on the spin components [cf. Eq. (4.14)]. Note that the matrices in Eq. (4.32) are not invertible anymore. The consequences of that are discussed below.

Equipped with the crossing symmetries for the Hedin vertices, Eqs. (4.31), we deduce the symmetry relations for the bosonic self-energy P_r. In the p channel, we have the following relation by using $\bar{\lambda}_p^{\uparrow\hat{\downarrow}} = \tilde{\bar{\lambda}}_p^{\uparrow\hat{\downarrow}} = -\tilde{\bar{\lambda}}_p^{\uparrow\downarrow} = 1 - \bar{\lambda}_p^{\uparrow\downarrow}$ and $\lambda_p^{\uparrow\hat{\downarrow}} = \tilde{\lambda}_p^{\uparrow\hat{\downarrow}} = -\tilde{\lambda}_p^{\downarrow\uparrow} = 1 - \lambda_p^{\downarrow\uparrow}$:

$$
\begin{aligned}
P_p^{\uparrow\hat{\downarrow}}(\omega) &= \tfrac{1}{\beta} \sum_{\nu''} \Pi_p^{\uparrow\downarrow}(\omega, \nu'') \bar{\lambda}_p^{\uparrow\hat{\downarrow}}(\omega, \nu'') = \tfrac{1}{\beta} \sum_{\nu''} \Pi_p^{\uparrow\downarrow}(\omega, \nu'') \left[1 - \bar{\lambda}_p^{\uparrow\downarrow}(\omega, \nu'') \right] \\
&= \tfrac{1}{\beta} \sum_{\nu''} \Pi_p^{\uparrow\downarrow}(\omega, \nu'') - P_p^{\uparrow\downarrow}(\omega) \quad (4.33a)
\end{aligned}
$$

$$= \tfrac{1}{\beta} \sum_{\nu''} \lambda_p^{\uparrow\hat{\downarrow}}(\omega,\nu'') \Pi_p^{\downarrow\uparrow}(\omega,\nu'') = \tfrac{1}{\beta} \sum_{\nu''} \left[1 - \lambda_p^{\downarrow\uparrow}(\omega,\nu'') \right] \Pi_p^{\downarrow\uparrow}(\omega,\nu'')$$

$$= \tfrac{1}{\beta} \sum_{\nu''} \Pi_p^{\downarrow\uparrow}(\omega,\nu'') - P_p^{\downarrow\uparrow}(\omega). \tag{4.33b}$$

With the crossing symmetries of the bubbles, Eqs. (4.27), we further have $\tfrac{1}{\beta}\sum_{\nu''}\Pi_p^{\downarrow\uparrow}(\omega,\nu'')$ $= \tfrac{1}{\beta}\sum_{\nu''}\Pi_p^{\uparrow\downarrow}(\omega,\nu'')$. Hence, all the components of the bosonic self-energies in the p channel are related to each other. To simplify the treatment of P_p and to get rid of the explicit summations over bubbles, we can express P_p by a single component, defined as

$$\tilde{P}_p^{\uparrow\downarrow}(\omega) \equiv P_p^{\uparrow\downarrow}(\omega) - P_p^{\hat{\downarrow}\uparrow}(\omega) = 2P_p^{\uparrow\downarrow}(\omega) - \tfrac{1}{\beta}\sum_{\nu''}\Pi_p^{\uparrow\downarrow}(\omega,\nu'')$$

$$= \tfrac{1}{\beta}\sum_{\nu''} \left[2\lambda_p^{\uparrow\downarrow}(\omega,\nu'') - 1 \right] \Pi_p^{\uparrow\downarrow}(\omega,\nu'')$$

$$= \tfrac{1}{\beta}\sum_{\nu''} \left[2\lambda_p^{\downarrow\uparrow}(\omega,-\nu''-\omega) - 1 \right] \Pi_p^{\downarrow\uparrow}(\omega,-\nu''-\omega)$$

$$= \tfrac{1}{\beta}\sum_{\nu''} \left[2\lambda_p^{\downarrow\uparrow}(\omega,\nu'') - 1 \right] \Pi_p^{\downarrow\uparrow}(\omega,\nu'') = P_p^{\downarrow\uparrow}(\omega) - P_p^{\uparrow\hat{\downarrow}}(\omega). \tag{4.34}$$

In this calculation, we made use of the spin structures for P_p, Eqs. (4.20), as well as the crossing symmetries for Π_p, Eqs. (4.27). Similarly, we define $\tilde{P}_p^{\uparrow\hat{\downarrow}} = 2(P_p^{\uparrow\hat{\downarrow}} - P_p^{\downarrow\uparrow})$, $\tilde{P}_p^{\downarrow\uparrow} = 2(P_p^{\downarrow\uparrow} - P_p^{\uparrow\hat{\downarrow}})$ and $\tilde{P}_p^{\hat{\downarrow}\uparrow} = 2(P_p^{\hat{\downarrow}\uparrow} - P_p^{\uparrow\downarrow})$. In total, the crossing symmetries for the bosonic self-energy are

$$P_a^{\uparrow\downarrow}(\omega) = -P_t^{\hat{\downarrow}\uparrow}(\omega) = P_a^{\downarrow\uparrow}(-\omega) = -P_t^{\uparrow\hat{\downarrow}}(-\omega), \tag{4.35a}$$

$$\tilde{P}_p^{\uparrow\downarrow}(\omega) = -\tilde{P}_p^{\hat{\downarrow}\uparrow}(\omega) = \tilde{P}_p^{\downarrow\uparrow}(\omega) \quad = -\tilde{P}_p^{\uparrow\hat{\downarrow}}(\omega), \tag{4.35b}$$

$$P_t^{\uparrow\downarrow}(\omega) = -P_a^{\hat{\downarrow}\uparrow}(\omega) = P_t^{\downarrow\uparrow}(-\omega) = -P_a^{\uparrow\hat{\downarrow}}(-\omega). \tag{4.35c}$$

Arranging $\tilde{P}_p$ in matrix form also yields a non-invertible matrix.

The parts $\tilde{\eta}_r(\omega) = \eta_r(\omega) - U$ from the bosonic propagators that vanish in the limit $|\omega| \to \infty$ actually coincide with the first asymptotic class $\tilde{\eta}_r(\omega) = \mathcal{K}_{1,r}(\omega) = \lim_{|\nu|,|\nu'|\to\infty}\gamma_r(\omega,\nu,\nu')$. Crossing symmetries for the bosonic propagators can thus be simply obtained by dropping the arguments of the fermionic frequencies ν, ν' in Eqs. (4.26):

$$\eta_a^{\uparrow\downarrow}(\omega) = -\eta_t^{\hat{\downarrow}\uparrow}(\omega) = \eta_a^{\downarrow\uparrow}(-\omega) = -\eta_t^{\uparrow\hat{\downarrow}}(-\omega), \tag{4.36a}$$

$$\eta_p^{\uparrow\downarrow}(\omega) = -\eta_p^{\hat{\downarrow}\uparrow}(\omega) = \eta_p^{\downarrow\uparrow}(\omega) \quad = -\eta_p^{\uparrow\hat{\downarrow}}(\omega), \tag{4.36b}$$

$$\eta_t^{\uparrow\downarrow}(\omega) = -\eta_a^{\hat{\downarrow}\uparrow}(\omega) = \eta_t^{\downarrow\uparrow}(-\omega) = -\eta_a^{\uparrow\hat{\downarrow}}(-\omega). \tag{4.36c}$$

In particular, Eq. (4.36b) implies that there exists only one independent component

of the bosonic propagator in the p channel. Equations (4.36) are in fact equivalent to the crossing symmetries of P_r, Eqs. (4.35). Similar as for the Hedin vertices $\tilde{\bar{\lambda}}_p$, $\bar{\lambda}_p$ [cf. Eq. (4.32)] and the bosonic self-energy $\tilde{P}_p$ [cf. Eq. (4.35b)], the 4×4 matrix for η_p is not invertible, either.

Let us consider the matrix form of $\tilde{\eta}_p$, Eq. (4.18b):

$$
\tilde{\eta}_p^{\uparrow\downarrow}
\begin{bmatrix} 1 & -1 \\ -1 & 1 \end{bmatrix}
= U^{\uparrow\downarrow}
\begin{bmatrix} 1 & -1 \\ -1 & 1 \end{bmatrix}
\begin{bmatrix} P_p^{\uparrow\downarrow} & P_p^{\hat{\uparrow}\downarrow} \\ P_p^{\downarrow\hat{\uparrow}} & P_p^{\downarrow\downarrow} \end{bmatrix}
\eta_p^{\uparrow\downarrow}
\begin{bmatrix} 1 & -1 \\ -1 & 1 \end{bmatrix}
$$

$$
= U^{\uparrow\downarrow}
\begin{bmatrix} P_p^{\uparrow\downarrow} - P_p^{\downarrow\hat{\uparrow}} & P_p^{\hat{\uparrow}\downarrow} - P_p^{\downarrow\downarrow} \\ P_p^{\downarrow\hat{\uparrow}} - P_p^{\uparrow\downarrow} & P_p^{\downarrow\downarrow} - P_p^{\hat{\uparrow}\downarrow} \end{bmatrix}
\eta_p^{\uparrow\downarrow}
\begin{bmatrix} 1 & -1 \\ -1 & 1 \end{bmatrix}
$$

$$
= U^{\uparrow\downarrow}\tilde{P}_p^{\uparrow\downarrow}
\begin{bmatrix} 1 & -1 \\ -1 & 1 \end{bmatrix}
\eta_p^{\uparrow\downarrow}
\begin{bmatrix} 1 & -1 \\ -1 & 1 \end{bmatrix}
= U^{\uparrow\downarrow}2\tilde{P}_p^{\uparrow\downarrow}\eta_p^{\uparrow\downarrow}
\begin{bmatrix} 1 & -1 \\ -1 & 1 \end{bmatrix}. \tag{4.37}
$$

Although the 2×2 matrix on both sides of the equation is not invertible, every spin component has its unambiguous form. The bosonic propagator η_p is either multiplied by one-dimensional objects of the same structure, i.e., U_p and $\tilde{P}_p$, or two-dimensional objects, $\bar{\lambda}_p$ and λ_p, with the structure given in Eqs. (4.32). We consider the matrix products,

$$
\begin{bmatrix} 1 & -1 \\ -1 & 1 \end{bmatrix}
\begin{bmatrix} 1 & -1 \\ -1 & 1 \end{bmatrix}
= 2
\begin{bmatrix} 1 & -1 \\ -1 & 1 \end{bmatrix}, \tag{4.38}
$$

$$
\begin{bmatrix} A & -A \\ -B & B \end{bmatrix}
\begin{bmatrix} 1 & -1 \\ -1 & 1 \end{bmatrix}
= 2
\begin{bmatrix} A & -A \\ -B & B \end{bmatrix}, \qquad
\begin{bmatrix} 1 & -1 \\ -1 & 1 \end{bmatrix}
\begin{bmatrix} A & -B \\ -A & B \end{bmatrix}
= 2
\begin{bmatrix} A & -B \\ -A & B \end{bmatrix},
$$

and conclude that the products $\tilde{\bar{\lambda}}_p \bullet \eta_p$ and $\eta_p \bullet \tilde{\lambda}_p$ keep the matrix structure of the two-dimensional objects, $\tilde{\bar{\lambda}}_p$ and $\tilde{\lambda}_p$,

$$
\begin{bmatrix} [\tilde{\bar{\lambda}}_p \bullet \eta_p]^{\uparrow\downarrow} & [\tilde{\bar{\lambda}}_p \bullet \eta_p]^{\hat{\uparrow}\downarrow} \\ [\tilde{\bar{\lambda}}_p \bullet \eta_p]^{\downarrow\hat{\uparrow}} & [\tilde{\bar{\lambda}}_p \bullet \eta_p]^{\downarrow\uparrow} \end{bmatrix}
=
\begin{bmatrix} \tilde{\bar{\lambda}}_p^{\uparrow\downarrow} & -\tilde{\bar{\lambda}}_p^{\uparrow\downarrow} \\ -\tilde{\bar{\lambda}}_p^{\downarrow\uparrow} & \tilde{\bar{\lambda}}_p^{\downarrow\uparrow} \end{bmatrix}
2\eta_p^{\uparrow\downarrow}, \tag{4.39a}
$$

$$
\begin{bmatrix} [\eta_p \bullet \tilde{\lambda}_p]^{\uparrow\downarrow} & [\eta_p \bullet \tilde{\lambda}_p]^{\hat{\uparrow}\downarrow} \\ [\eta_p \bullet \tilde{\lambda}_p]^{\downarrow\hat{\uparrow}} & [\eta_p \bullet \tilde{\lambda}_p]^{\downarrow\uparrow} \end{bmatrix}
= 2\eta_p^{\uparrow\downarrow}
\begin{bmatrix} \tilde{\lambda}_p^{\uparrow\downarrow} & -\tilde{\lambda}_p^{\downarrow\uparrow} \\ -\tilde{\lambda}_p^{\uparrow\downarrow} & \tilde{\lambda}_p^{\downarrow\uparrow} \end{bmatrix}. \tag{4.39b}
$$

The effect of the multiplication with η_p can thus be reversed by dividing the products $\tilde{\bar{\lambda}}_p \bullet \eta_p$ and $\eta_p \bullet \tilde{\lambda}_p$ by $1/(2\eta_p^{\uparrow\downarrow})$. The appearance of η_r^{-1} in Eqs. (78)–(80) in Ref. [P1] and the usage of the 4×4 matrices, Eqs. (4.8), is therefore no matter of concern as long as one takes care of the above relations in the p channel (see also App. C.4).

Similar to the Bethe–Salpeter equations in the p channel, Eqs. (4.29), the product for the U-reducible vertex $\nabla_p = \bar{\lambda}_p \bullet \eta_p \bullet \lambda_p$ is simplified according to the reduced dependence

of η_p, $\bar{\lambda}_p$, and λ_p:

$$\nabla_p^{\uparrow\downarrow} = (2\bar{\lambda}_p^{\uparrow\downarrow} - 1)\eta_p^{\uparrow\downarrow}(2\lambda_p^{\uparrow\downarrow} - 1), \quad \nabla_p^{\hat{\uparrow\downarrow}} = (2\bar{\lambda}_p^{\uparrow\downarrow} - 1)\eta_p^{\uparrow\downarrow}(2\lambda_p^{\hat{\uparrow\downarrow}} - 1). \tag{4.40}$$

In our numerical computations, we therefore save and compute the Hedin vertices always in the combinations $2\bar{\lambda}_p^{\uparrow\downarrow} - 1$ and $2\lambda_p^{\uparrow\downarrow} - 1$. Their constant parts are given as

$$2\lambda_p^{\uparrow\downarrow} - 1 = 2\tilde{\lambda}_p^{\uparrow\downarrow} + 1, \quad 2\lambda_p^{\hat{\uparrow\downarrow}} - 1 = 2\tilde{\lambda}_p^{\hat{\uparrow\downarrow}} - 1. \tag{4.41}$$

With the crossing symmetries, the objects in the t channel can be completely expressed through the objects in the a channel. Further, they simplify the expressions in the p channel significantly such that the matrix formulation becomes superfluous there.

Complex-conjugation symmetry

The symmetry of complex conjugation originates from the relation $\langle \hat{c}_1 \cdots \hat{c}_n \rangle^* = \langle \hat{c}_n^\dagger \cdots \hat{c}_1^\dagger \rangle$ with fermionic operators $\hat{c}_1, ..., \hat{c}_n$ (cf. Sec. 2.2.1.3 in Ref. [Roh13]). For the one- and two-particle correlation functions, this translates to

$$[G_{1|1'}(\nu)]^* = G_{1'|1}(-\nu), \quad [G_{12|1'2'}^{(4)}(\nu_1, \nu_2, \nu_{1'}, \nu_{2'})]^* = G_{1'2'|12}^{(4)}(-\nu_{1'}, -\nu_{2'}, -\nu_1, -\nu_2). \tag{4.42}$$

Since the vertex Γ fulfills the same symmetries as the correlation function $G^{(4)}$, we deduce the following symmetry relations using the frequency conventions, Eqs. (4.1):

$$[\Gamma_a^{\uparrow\downarrow}(\omega, \nu, \nu')]^* = \Gamma_a^{\uparrow\downarrow}(-\omega, -\nu', -\nu), \qquad [\Gamma_a^{\hat{\uparrow\downarrow}}(\omega, \nu, \nu')]^* = \Gamma_a^{\hat{\downarrow\uparrow}}(-\omega, -\nu', -\nu), \tag{4.43a}$$

$$[\Gamma_p^{\uparrow\downarrow}(\omega, \nu, \nu')]^* = \Gamma_p^{\uparrow\downarrow}(-\omega, -\nu', -\nu), \qquad [\Gamma_p^{\hat{\uparrow\downarrow}}(\omega, \nu, \nu')]^* = \Gamma_p^{\hat{\downarrow\uparrow}}(-\omega, -\nu', -\nu), \tag{4.43b}$$

$$[\Gamma_t^{\uparrow\downarrow}(\omega, \nu, \nu')]^* = \Gamma_t^{\uparrow\downarrow}(\omega, -\nu-\omega, -\nu'-\omega), \quad [\Gamma_t^{\hat{\uparrow\downarrow}}(\omega, \nu, \nu')]^* = \Gamma_t^{\hat{\downarrow\uparrow}}(\omega, -\nu-\omega, -\nu'-\omega). \tag{4.43c}$$

By analogous considerations as for the crossing symmetries, we deduce the following relations for the SBE vertices:

$$\eta_a^{\hat{\uparrow\downarrow}}(\omega) = [\eta_a^{\hat{\downarrow\uparrow}}(-\omega)]^*, \qquad \eta_p^{\hat{\uparrow\downarrow}}(\omega) = [\eta_p^{\hat{\downarrow\uparrow}}(-\omega)]^*, \tag{4.44a}$$

$$\bar{\lambda}_a^{\uparrow\downarrow}(\omega, \nu) = [\lambda_a^{\uparrow\downarrow}(-\omega, -\nu)]^*, \quad \bar{\lambda}_a^{\hat{\uparrow\downarrow}}(\omega, \nu) = [\lambda_a^{\hat{\downarrow\uparrow}}(-\omega, -\nu)]^*, \tag{4.44b}$$

$$\bar{\lambda}_p^{\uparrow\downarrow}(\omega, \nu) = [\lambda_p^{\uparrow\downarrow}(-\omega, -\nu)]^*, \quad \bar{\lambda}_p^{\hat{\uparrow\downarrow}}(\omega, \nu) = [\lambda_p^{\hat{\downarrow\uparrow}}(-\omega, -\nu)]^*. \tag{4.44c}$$

Especially, these symmetry relations combine the Hedin vertices $\bar{\lambda}_r$ and λ_r with each other and reduce the frequency values needed for numerical computations.

Time-reversal symmetry

The system we are considering is time-reversal symmetric, i.e., the action, Eq. (4.4), is not supposed to change under a sign change of momenta, angular momenta or a magnetic field. This can be adjusted by the dependencies of the bare Green's functions $G_0^{\uparrow,\downarrow}$ and the bare interaction $U^{\uparrow\downarrow}$. Even the Hamiltonian of the generalized Hubbard atom, Eq. (4.86), is time-reversal symmetric despite the magnetic field h. This is because the magnetic field there is only pointing in z direction. While for non-relativistic quantum mechanics time reversion is implemented by complex conjugation of its wavefunctions, the time reversal symmetry of correlation functions in imaginary time is revealed by the fact that the latter are purely real (cf. Sec. 2.2.2.3 in Ref. [Roh13]):

$$[G^{(4)}_{12|1'2'}(\tau_1, \tau_2, \tau_{1'}, \tau_{2'})]^* = G^{(4)}_{12|1'2'}(\tau_1, \tau_2, \tau_{1'}, \tau_{2'}). \tag{4.45}$$

This implies the following for the correlation function expressed in Matsubara frequencies:

$$[G^{(4)}_{12|1'2'}(\nu_1, \nu_2, \nu_{1'}, \nu_{2'})]^* = G^{(4)}_{12|1'2'}(-\nu_1, -\nu_2, -\nu_{1'}, -\nu_{2'}). \tag{4.46}$$

This symmetry carries over to all vertices, including SBE vertices:

$$\Gamma^{ij}_r(\omega, \nu, \nu') = [\Gamma^{ij}_r(-\omega, -\nu, -\nu')]^*, \tag{4.47a}$$

$$\eta^{ij}_r(\omega) = [\eta^{ij}_r(-\omega)]^*, \qquad P^{ij}_r(\omega) = [P^{ij}_r(-\omega)]^*, \tag{4.47b}$$

$$\bar{\lambda}^{ij}_r(\omega, \nu) = [\bar{\lambda}^{ij}_r(-\omega, -\nu')]^*, \qquad \lambda^{ij}_r(\omega, \nu') = [\lambda^{ij}_r(-\omega, -\nu')]^*. \tag{4.47c}$$

In particular, the combination of complex conjugation and time-reversal symmetry yields

$$\Gamma^{\uparrow\downarrow}_a(\omega, \nu, \nu') = \Gamma^{\uparrow\downarrow}_a(\omega, \nu', \nu), \qquad \Gamma^{\hat{\uparrow}\downarrow}_a(\omega, \nu, \nu') = \Gamma^{\hat{\downarrow}\uparrow}_a(\omega, \nu', \nu), \tag{4.48a}$$

$$\Gamma^{\uparrow\downarrow}_p(\omega, \nu, \nu') = \Gamma^{\uparrow\downarrow}_p(\omega, \nu', \nu), \qquad \Gamma^{\hat{\uparrow}\downarrow}_p(\omega, \nu, \nu') = \Gamma^{\hat{\downarrow}\uparrow}_p(\omega, \nu', \nu), \tag{4.48b}$$

$$\Gamma^{\uparrow\downarrow}_t(\omega, \nu, \nu') = \Gamma^{\uparrow\downarrow}_t(-\omega, \nu+\omega, \nu'+\omega), \quad \Gamma^{\hat{\uparrow}\downarrow}_t(\omega, \nu, \nu') = \Gamma^{\hat{\downarrow}\uparrow}_t(-\omega, \nu+\omega, \nu'+\omega), \tag{4.48c}$$

$$\bar{\lambda}^{\uparrow\downarrow}_a(\omega, \nu) = \lambda^{\uparrow\downarrow}_a(\omega, \nu), \quad \bar{\lambda}^{\hat{\uparrow}\downarrow}_a(\omega, \nu) = \lambda^{\hat{\downarrow}\uparrow}_a(\omega, \nu), \tag{4.49a}$$

$$\bar{\lambda}^{\uparrow\downarrow}_p(\omega, \nu) = \lambda^{\uparrow\downarrow}_p(\omega, \nu), \quad \bar{\lambda}^{\hat{\uparrow}\downarrow}_p(\omega, \nu) = \lambda^{\hat{\downarrow}\uparrow}_p(\omega, \nu). \tag{4.49b}$$

By time-translation symmetry, not only the frequency space, where vertex objects are stored, is reduced significantly. The combination of complex-conjugation and time-reversal symmetry also leads to an identification of the left and right Hedin vertices $\bar{\lambda}_r$ and λ_r.

4.1.3. Spin components of the self-energy

In Sec. 3.4.3, we showed how the self-energy can be generally computed in terms of the SBE vertices. Thereby we introduced the loop products, Eq. (3.41), written as $\cdot$, to denote the loop contraction appearing in the Schwinger–Dyson equation (3.40) for the self-energy. As in the previous sections, we focus here on the spin structure. The spin structure of the loop products is given by

$$[\Gamma \cdot G]^\uparrow = \Gamma^{\uparrow\uparrow} G^\uparrow + \Gamma^{\uparrow\downarrow} G^\downarrow, \quad [G \cdot \Gamma]^\uparrow = G^\uparrow \Gamma^{\uparrow\uparrow} + G^\downarrow \Gamma^{\hat{\uparrow}\downarrow}. \tag{4.50}$$

These involve the following summations over frequencies:

$$[\Gamma \cdot G](\nu) = \tfrac{1}{\beta} \sum_{\nu''} \Gamma_t(0, \nu'', \nu) \cdot G(\nu''), \quad [G \cdot \Gamma](\nu) = \tfrac{1}{\beta} \sum_{\nu''} \Gamma_a(0, \nu, \nu'') \cdot G(\nu''). \tag{4.51}$$

By exchanging two legs in the vertices inside the Schwinger–Dyson equation, we deduce the following identities:

$$[U^{\hat{\uparrow}\downarrow}\Pi_a^{\downarrow\downarrow}\Gamma^{\hat{\downarrow}\uparrow}]G^\uparrow = \quad\quad\quad = \quad\quad\quad = [U^{\uparrow\downarrow}\Pi_a^{\uparrow\downarrow}\Gamma^{\uparrow\downarrow}]G^\downarrow, \tag{4.52a}$$

$$G^\uparrow[\Gamma^{\downarrow\uparrow}\Pi_t^{\downarrow\downarrow}U^{\uparrow\downarrow}] = \quad\quad\quad = \quad\quad\quad = G^\downarrow[\Gamma^{\hat{\uparrow}\downarrow}\Pi_t^{\hat{\uparrow}\downarrow}U^{\hat{\uparrow}\downarrow}]. \tag{4.52b}$$

Similarly to Fig. 4.2, the $\uparrow$ component is denoted by a solid line whereas the $\downarrow$ component is denoted by a dashed line.

Consequently, the frequency-dependent part of the self-energy, $\tilde{\Sigma} = \Sigma - \Sigma_\mathrm{H}$, can be expressed in all three diagrammatic channels as a single combination of spin components:

$$\tilde{\Sigma}^\uparrow = -\frac{1}{2}\left([U \circ \Pi_a \circ \Gamma]^{\uparrow\uparrow} G^\uparrow + [U \circ \Pi_a \circ \Gamma]^{\uparrow\downarrow} G^\downarrow\right) = -\frac{1}{2}\left([U^{\hat{\uparrow}\downarrow}\Pi_a^{\downarrow\downarrow}\Gamma^{\hat{\downarrow}\uparrow}]G^\uparrow + [U^{\uparrow\downarrow}\Pi_a^{\uparrow\downarrow}\Gamma^{\uparrow\downarrow}]G^\downarrow\right)$$

$$= -[U^{\uparrow\downarrow}\Pi_a^{\uparrow\downarrow}\Gamma^{\uparrow\downarrow}]G^\downarrow \tag{4.53a}$$

$$= -\left([U \circ \Pi_p \circ \Gamma]^{\uparrow\uparrow} G^\uparrow + [U \circ \Pi_p \circ \Gamma]^{\uparrow\downarrow} G^\downarrow\right) = -[U^{\uparrow\downarrow}2\Pi_p^{\uparrow\downarrow}\Gamma^{\uparrow\downarrow}]G^\downarrow \tag{4.53b}$$

$$= \frac{1}{2}\left(G^\uparrow[\Gamma \circ \Pi_t \circ U]^{\uparrow\uparrow} + G^\downarrow[\Gamma \circ \Pi_t \circ U]^{\hat{\uparrow}\downarrow}\right) = \frac{1}{2}\left(G^\uparrow[\Gamma^{\downarrow\uparrow}\Pi_t^{\downarrow\downarrow}U^{\uparrow\downarrow}] + G^\downarrow[\Gamma^{\hat{\uparrow}\downarrow}\Pi_t^{\hat{\uparrow}\downarrow}U^{\hat{\uparrow}\downarrow}]\right)$$

$$= G^\downarrow[\Gamma^{\hat{\uparrow}\downarrow}\Pi_t^{\hat{\uparrow}\downarrow}U^{\hat{\uparrow}\downarrow}]. \tag{4.53c}$$

Here, we used the Bethe–Salpeter equations (4.11), which are simplified for $U \circ \Pi_r \circ \Gamma$ as $U^{\uparrow\uparrow} = 0 = U^{\downarrow\downarrow}$.

For writing these terms in SBE vertices, we use $\eta_r \bullet \lambda_r = U + U \circ \Pi_r \circ \Gamma$ and $\bar{\lambda}_r \bullet \eta_r = U + \Gamma \circ \Pi_r \circ U$, Eq. (42) in Ref. [P1]:

$$U^{\uparrow\downarrow}\Pi_a^{\uparrow\downarrow}\Gamma^{\uparrow\downarrow} = [U \circ \Pi_a \circ \Gamma]^{\uparrow\downarrow} = [\eta_a \bullet \lambda_a - U]^{\uparrow\downarrow} = \eta_a^{\uparrow\downarrow}\lambda_a^{\uparrow\downarrow} - U^{\uparrow\downarrow}, \tag{4.54}$$

$$U^{\uparrow\downarrow}2\Pi_p^{\uparrow\downarrow}\Gamma^{\uparrow\downarrow} = [U \circ \Pi_p \circ \Gamma]^{\uparrow\downarrow} = [\eta_p \bullet \lambda_p - U]^{\uparrow\downarrow} = \eta_p^{\uparrow\downarrow}(2\lambda_p^{\uparrow\downarrow} - 1) - U^{\uparrow\downarrow}, \tag{4.55}$$

$$\Gamma^{\hat{\uparrow\downarrow}}\Pi_t^{\hat{\uparrow\downarrow}}U^{\hat{\uparrow\downarrow}} = [\Gamma \circ \Pi_t \circ U]^{\hat{\uparrow\downarrow}} = [\bar{\lambda}_t \bullet \eta_t - U]^{\hat{\uparrow\downarrow}} = \bar{\lambda}_t^{\hat{\uparrow\downarrow}}\eta_t^{\hat{\uparrow\downarrow}} - U^{\hat{\uparrow\downarrow}}. \tag{4.56}$$

Combining everything yields the expressions of the Schwinger–Dyson equations in SBE vertices using the three diagrammatic channels:

$$\tilde{\Sigma}^{\uparrow}(\nu) = -\tfrac{1}{\beta}\sum_{\nu''}\left[\eta_a^{\uparrow\downarrow}(\nu'' - \nu)\lambda_a^{\uparrow\downarrow}(\nu'' - \nu, \nu) - U^{\uparrow\downarrow}\right]G^{\downarrow}(\nu'') \tag{4.57a}$$

$$= -\tfrac{1}{\beta}\sum_{\nu''}\left[\eta_p^{\uparrow\downarrow}(\nu + \nu'')(2\lambda_p^{\uparrow\downarrow}(\nu + \nu', -\nu) - 1) - U^{\uparrow\downarrow}\right]G^{\downarrow}(\nu'') \tag{4.57b}$$

$$= \tfrac{1}{\beta}\sum_{\nu''}\left[\bar{\lambda}_t^{\hat{\uparrow\downarrow}}(\nu - \nu'', \nu'')\eta_t^{\hat{\uparrow\downarrow}}(\nu - \nu'') - U^{\hat{\uparrow\downarrow}}\right]G^{\downarrow}(\nu''). \tag{4.57c}$$

This is the specification of Eqs. (3.44) using the spin components $\uparrow$ and $\downarrow$.

For the models we consider, the Dyson equation (3.6) for the Green's function G does not involve any summation over spin components or frequencies:

$$G^{\uparrow}(\nu) = \left[1/[G_0^{\uparrow}(\nu)] - \Sigma_{\mathrm{H}}^{\uparrow} - \tilde{\Sigma}^{\uparrow}(\nu)\right]^{-1}. \tag{4.58}$$

Let us finally discuss how to solve for the Hartree term $\Sigma_{\mathrm{H}} = -U \cdot G$ appearing in the Schwinger–Dyson equation (3.40). The Green's function has the asymptotic form $G \sim 1/(\mathrm{i}\nu) + \mathcal{O}(\nu^{-2})$ and is therefore not converging fast enough for a summation over all Matsubara frequencies. However, there is an infinitesimal time shift due to the functional integral, i.e., $G(\nu) \to \mathrm{e}^{\mathrm{i}\nu 0^+}G(\nu)$ [AS10]. The sum over fermionic Matsubara frequencies for the asymptotic part is obtained by the following identity:

$$\tfrac{1}{\beta}\sum_{\nu}\frac{\mathrm{e}^{\mathrm{i}\nu 0^+}}{\mathrm{i}\nu - \xi} = n_{\mathrm{F}}(\xi) \quad \Rightarrow \tfrac{1}{\beta}\sum_{\nu}\frac{1}{\mathrm{i}\nu}\mathrm{e}^{\mathrm{i}\nu 0^+} = n_{\mathrm{F}}(0) = \frac{1}{2}. \tag{4.59}$$

Consequently the correct Hartree term is extracted as follows:

$$
\begin{aligned}
\frac{1}{\beta} \sum_{\nu} \mathrm{e}^{i\nu 0^+} G(\nu) &\approx \frac{1}{\beta} \sum_{\nu} \left[G(\nu) - \frac{1}{i\nu} + \frac{1}{i\nu} \mathrm{e}^{i\nu 0^+} \right] \\
&= \frac{1}{\beta} \sum_{\nu} \left[G(\nu) - \frac{1}{i\nu} \right] + \frac{1}{\beta} \sum_{\nu} \frac{1}{i\nu} \mathrm{e}^{i\nu 0^+} = \frac{1}{\beta} \sum_{\nu>0} \left[G(\nu) + G(-\nu) \right] + \frac{1}{2}.
\end{aligned}
\tag{4.60}
$$

Here, the first term is converging fast enough and can thus be calculated numerically in a finite frequency box whereas the second term gives the correction due to the infinitesimal time shift and always needs to be included in the Hartree term.

Explicitly, the Hartree term is then computed by the following relation:

$$
\Sigma_{\mathrm{H}}^{\uparrow} = -U^{\uparrow\downarrow} \left(\frac{1}{2\beta} \sum_{\nu} \left[G^{\downarrow}(\nu) + G^{\downarrow}(-\nu) \right] + \frac{1}{2} \right).
\tag{4.61}
$$

As the right-hand side contains $\Sigma_{\mathrm{H}}^{\downarrow}$ through $G^{\downarrow} = (1/G_0^{\downarrow} - \Sigma_{\mathrm{H}}^{\downarrow} - \tilde{\Sigma}^{\downarrow})^{-1}$ [cf. Eq. (4.58)], the equations for the Hartree terms $\Sigma_{\mathrm{H}}^{\uparrow}$ and $\Sigma_{\mathrm{H}}^{\downarrow}$ are self-consistent and need to be computed iteratively until convergence is reached.

4.2. Structure of the code

4.2.1. Implementation of the SBE equations

After we have introduced all vertex objects of the SBE formalism as well as their symmetries and defining equations, we describe how we implement their numerical computation in a code using the `Julia` programming language. At the moment, our code allows a self-consistent solution of the SBE equations as well as a solution of the one-loop fRG equations. The code is limited to the finite-temperature Matsubara formalism since it uses dense grids over Matsubara frequencies. It treats fermionic models with two particle types given by the action, Eq. (4.4). In particular, we have included three different models: (i) the single-impurity Anderson model (SIAM), (ii) the Hubbard atom (HA) (both for generic fillings and with the possibility of a magnetic field in z direction) and (iii) Fermi polarons formed by immobile impurities, which includes the model for the X-ray edge singularity (XES). With this, vertices in the code do not need to obey SU(2) spin symmetry. As a severe limitation, however, our implementation does not include a momentum dependence.

We make use of the recently developed library `MatsubaraFunctions.jl` by Dominik Kiese [KGR+24]. This allows a convenient treatment of data containers for n-particle correlation functions with values on Matsubara frequency grids. More explicitly, data for $G^{(n)}_{i_1,...,i_{2n}}(\nu_1, ..., \nu_{2n})$, Eq. (3.2), are generated where ν are fermionic $\nu \in (2\mathbb{Z} + 1)\pi T$ or

Table 4.1.: Overview of the quantities used in the code with the corresponding spin components and numbers of frequency grid points. The quantities $G_0, \Sigma_{\mathrm{H}}^{\mathrm{corr}}, \Pi_r^{\mathrm{corr}}, U, \mathbf{1}_r, R$ are precalculated and not updated. The asymptotic corrections $\Sigma_{\mathrm{H}}^{\mathrm{corr}}, \Pi_r^{\mathrm{corr}}$ are defined in Eqs. (4.63). $G, \Sigma_{\mathrm{H}}, \tilde{\Sigma}, \tilde{\eta}_r, P_r, \tilde{\bar{\lambda}}_r, \tilde{\lambda}_r, M_r$ are members of the state Ψ and updated during the computation. Π_r, T_r^L, T_r^R are included in the ΠT buffer. The two versions T_r^L and T_r^R of U-irreducible vertices are clarified in Eqs. (4.66). This is updated during the computation, but not saved in the end. For the numbers of frequency points, we usually take $N_\nu^G = 64N$, $N_\nu^\Sigma = N_\omega^P = 32N$, $N_\omega^\lambda = 16N$, $N_\nu^\lambda = 12N$, $N_\omega^M = 8N$, $N_\nu^M = 6$ and $N_\nu^T = N_\nu^\Pi = N_\omega^P + N_\omega^\lambda + N_\nu^\lambda$, where N is a reference number.

quantity	spin components	# grid points	contained in
G_0	$\uparrow, \downarrow$	N_ν^G	Ψ, precalc.
$\Sigma_{\mathrm{H}}^{\mathrm{corr}}$	$\uparrow, \downarrow$	1	Ψ, precalc.
Π_r^{corr}	$\uparrow\downarrow, \uparrow\uparrow, \downarrow\uparrow, \downarrow\downarrow$	N_ω^P	Ψ, precalc.
$U, \mathbf{1}_r$	$\uparrow\downarrow, \hat{\uparrow}\downarrow, \uparrow\uparrow, \downarrow\uparrow, \hat{\downarrow}\uparrow, \downarrow\downarrow$	1	Ψ, precalc.
$\tilde{R}$	$\hat{\uparrow}\downarrow, \uparrow\uparrow, \downarrow\uparrow, \hat{\downarrow}\uparrow, \downarrow\downarrow$	$N_\omega^R \times N_\nu^R \times N_\nu^R$	Ψ, precalc.
G	$\uparrow, \downarrow$	N_ν^G	Ψ
Σ_{H}	$\uparrow, \downarrow$	1	Ψ
$\tilde{\Sigma}$	$\uparrow, \downarrow$	N_ν^Σ	Ψ
$\tilde{\eta}_r, P_r$	$\uparrow\downarrow, \hat{\uparrow}\downarrow, \uparrow\uparrow, \downarrow\uparrow, \hat{\downarrow}\uparrow, \downarrow\downarrow$	N_ω^P	Ψ
$\tilde{\bar{\lambda}}_r, \tilde{\lambda}_r$	$\uparrow\downarrow, \hat{\uparrow}\downarrow, \uparrow\uparrow, \downarrow\uparrow, \hat{\downarrow}\uparrow, \downarrow\downarrow$	$N_\omega^\lambda \times N_\nu^\lambda$	Ψ
M_r	$\uparrow\downarrow, \hat{\uparrow}\downarrow, \uparrow\uparrow, \downarrow\uparrow, \hat{\downarrow}\uparrow, \downarrow\downarrow$	$N_\omega^M \times N_\nu^M \times N_\nu^M$	Ψ
Π_r	$\uparrow\downarrow, \uparrow\uparrow, \downarrow\uparrow, \downarrow\downarrow$	$N_\omega^P \times N_\nu^\Pi$	ΠT buffer
T_r^L	$\uparrow\downarrow, \hat{\uparrow}\downarrow, \uparrow\uparrow, \downarrow\uparrow, \hat{\downarrow}\uparrow, \downarrow\downarrow$	$N_\omega^\lambda \times N_\nu^\lambda \times N_\nu^T$	ΠT buffer
T_r^R	$\uparrow\downarrow, \hat{\uparrow}\downarrow, \uparrow\uparrow, \downarrow\uparrow, \hat{\downarrow}\uparrow, \downarrow\downarrow$	$N_\omega^\lambda \times N_\nu^T \times N_\nu^\lambda$	ΠT buffer

bosonic Matsubara frequencies $\nu = 2\pi\mathbb{Z}T$, respectively. The additional indices $i_1, ..., i_{2n}$ contributing to the data containers are, in our case, used for the spin components of the vertices. Hereby, the Green's function G and the self-energy Σ take two different values $i = \uparrow, \downarrow$ and the SBE vertices six $i = \uparrow\downarrow, \hat{\uparrow}\downarrow, \uparrow\uparrow, \downarrow\uparrow, \hat{\downarrow}\uparrow, \downarrow\downarrow$. (The bubbles Π_r take four different values as they are diagonal matrices [cf. Eq. (4.10)].) All the data containers appearing in the code with their respective spin structure and size of frequency boxes are listed in Tab. 4.1. We are discussing the individual objects in the following.

The code is written in such a way that the explicit dependence on the physical parameters and models is only contained in precalculated quantities. Thus, the values for the bare Green's function G_0 as well as the bare interaction U are determined once at
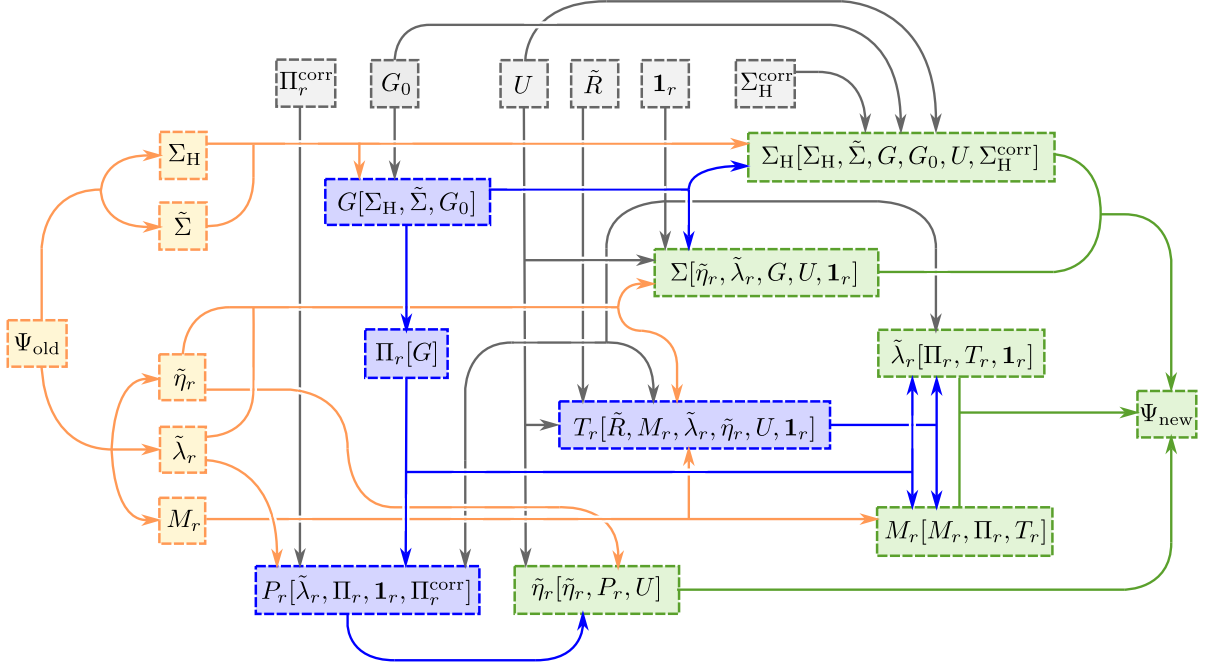
Figure 4.3.: Schematic overview of the parquet iteration: The prior state Ψ_{old} contains the quantities $\Sigma_{\text{H}}, \tilde{\Sigma}, \tilde{\eta}_r, \tilde{\lambda}_r, M_r$ from the previous parquet step (orange). Together with the constant values $\Gamma_0, G_0, R, \mathbf{1}_r, \Pi_r^{\text{corr}}, \Sigma_{\text{H}}^{\text{corr}}$ (gray) they serve as an input for the calculation of the auxiliary quantities G, Π_r, P_r, T_r (blue). Finally, the updated versions of the quantities $\Sigma_{\text{H}}, \tilde{\Sigma}, \tilde{\eta}_r, \tilde{\lambda}_r, M_r$ are calculated by the SBE equations and saved in a new state Ψ_{new} (green).

the beginning:

$$\text{SIAM:} \quad G_0(\nu) = [i\nu + i\,\text{sgn}(\nu)\Delta - \varepsilon_d]^{-1}, \tag{4.62a}$$

$$\text{HA:} \quad G_0^{\uparrow}(\nu) = [i\nu + \mu + h]^{-1}, \qquad G_0^{\downarrow}(\nu) = [i\nu + \mu - h]^{-1} \tag{4.62b}$$

$$\text{XES:} \quad G_0^d(\nu) = [i\nu - \xi_d]^{-1}, \qquad G_0^c(\nu) = -2i\,\rho\,\arctan(\xi_0/\nu). \tag{4.62c}$$

The parameters for the single-impurity Anderson model (SIAM) are discussed in Refs. [Wal21, GRW+24], for the Hubbard atom (HA) in Sec. 4.4, and for the X-ray edge singularity model (XES) in Sec. 5.1. Once the data containers of G_0 and U are filled, the remaining parts of the code are independent of the physical model and thus kept general.

As suggested in Ref. [KD18b] and done in other parquet and fRG solvers [TRK+20, Wal21, RKM+22, GRW+24, RGW+24], we organize all the data buffers for vertices in a state Ψ, which in our case includes $G, \Sigma_{\text{H}}, \tilde{\Sigma}, P_r, \tilde{\eta}_r, \tilde{\bar{\eta}}_r, \tilde{\lambda}_r, M_r$. In a parquet iteration, we compute new vertices contained in Ψ_{new} from the old vertices contained in Ψ_{old}.

We decided to compute and store the data for the bubbles Π_r and U-irreducible vertices T_r once for each parquet step. Thus, individual data are not computed multiple times "on

the fly". This way, we save runtime, but on the other hand sacrifice memory as very large data containers are needed for Π_r and T_r to effectively use all the information contained in the SBE vertices. We arrange Π_r and T_r together in an additional structure, which we call ΠT buffer. During a parquet iteration, Π_r and T_r are computed from the old vertices contained in Ψ_{old}, from which the new vertices in Ψ_{new} are determined (cf. Fig. 4.3). At this point, the old values of Π_r and T_r are just overwritten. Hence, we do not need to distinguish between old and new values of those and save some memory.

Table 4.1 gives an overview on the quantities computed in the code. It provides the corresponding spin components and numbers of frequencies in the grids, as well as the information how they are organized. Figure 4.3 illustrates how a parquet iteration is executed. We will explain more details in the following paragraphs.

The bottleneck of our code is the usage of dense grids of Matsubara frequencies within a finite frequency box. Up to an upper Matsubara frequency $|\nu| < \nu_{\text{max}}$, we compute and sum over data evaluated at every single Matsubara frequency. Values at frequencies out of the boxes are not taken into account explicitly. Since Green's functions asymptotically decay as $G \sim 1/(i\nu)$, at large enough frequencies $|\nu| > \nu_{\text{max}}$, the contribution of higher-order diagrams becomes small. For a more accurate treatment of frequency asymptotics, we approximate the high frequencies values in the sum over the bubbles Π_r (contained in the computation of P_r, Eq. (4.21), through $\bar{\lambda}_r$ and λ_r) and the sum over the Green's function G [contained in the the computation of Σ_{H}, Eq. (4.61)] by one-dimensional integrals over bare Green's functions:

$$\frac{1}{\beta} \sum_{\nu''} \Pi_r^{ij}(\omega, \nu'') \approx \frac{1}{\beta} \sum_{|\nu''| < \nu_{\text{max}}} \Pi_r^{ij}(\omega, \nu'') + \frac{\beta}{2\pi} \int_{|\nu''| > \nu_{\text{max}}} d\nu'' \, \Pi_{r,0}^{ij}(\omega, \nu''), \tag{4.63a}$$

$$\frac{1}{\beta} \sum_{\nu''} G^i(\nu'') \approx \frac{1}{\beta} \sum_{|\nu''| < \nu_{\text{max}}} G^i(\nu'') + \frac{\beta}{2\pi} \int_{|\nu''| > \nu_{\text{max}}} d\nu'' \, G_0^i(\nu''). \tag{4.63b}$$

We denote the latter integrals by $[\Pi_r^{\text{corr}}]^{ij}(\omega)$ and $\Sigma_{\text{H}}^{\text{corr}}$. They only need to be computed once at the beginning and are included in the state Ψ (cf. Tab. 4.1 and Fig. 4.3). Depending on the model, we have exact analytical expressions for the integrals or compute them numerically by standard routines.

As explained in Sec. 4.1.2, we fully drop the computation of the t channel as it is fully reproduced from the a channel by crossing symmetry. More explicitly, Eqs. (4.26) imply the following expressions for the two-particle reducible vertex components in the t channel ($\gamma_t = \nabla_t + M_t - U$):

$$\gamma_t^{\uparrow\downarrow}(\omega, \nu, \nu') = -\gamma_a^{\hat{\downarrow}\uparrow}(\omega, \nu, \nu'), \quad \gamma_t^{\hat{\uparrow}\downarrow}(\omega, \nu, \nu') = -\gamma_a^{\downarrow\uparrow}(\omega, \nu, \nu'). \tag{4.64}$$

Our code allows for an optional inclusion of the two-particle irreducible vertex $\tilde{R} = R - U$ as an additional input to compute vertices beyond the parquet approximation. (This is useful for the benchmarks of the Hubbard atom (cf. Sec. 4.4) where $I_U = \tilde{R} + \sum_r M_r$

is known exactly.) $\tilde{R}$ is represented in the frequency parametrization of the t channel, Eqs. (4.1c). The computation of the U-irreducible vertices T_r, Eq. (4.24), is then explicitly performed as

$$T_a(\boldsymbol{\nu}_a) = \tilde{R}(\boldsymbol{\nu}_t(\boldsymbol{\nu}_a)) + M_a(\boldsymbol{\nu}_a) + M_p(\boldsymbol{\nu}_p(\boldsymbol{\nu}_a)) - \hat{M}_a(\boldsymbol{\nu}_t(\boldsymbol{\nu}_a))$$
$$+ \nabla_p(\boldsymbol{\nu}_p(\boldsymbol{\nu}_a)) - \hat{\nabla}_a(\boldsymbol{\nu}_t(\boldsymbol{\nu}_a)) - 2U, \tag{4.65a}$$
$$T_p(\boldsymbol{\nu}_p) = \tilde{R}(\boldsymbol{\nu}_t(\boldsymbol{\nu}_p)) + M_a(\boldsymbol{\nu}_a(\boldsymbol{\nu}_p)) + M_p(\boldsymbol{\nu}_p) - \hat{M}_a(\boldsymbol{\nu}_t(\boldsymbol{\nu}_p))$$
$$+ \nabla_a(\boldsymbol{\nu}_a(\boldsymbol{\nu}_p)) - \hat{\nabla}_a(\boldsymbol{\nu}_t(\boldsymbol{\nu}_p)) - 2U. \tag{4.65b}$$

To save space, we denote the frequency transformation from channel r' to r as $\boldsymbol{\nu}_r(\boldsymbol{\nu}_{r'})$ [cf. the explanation after Eq. (4.3)]. Further, the usage of the crossed vertices, Eq. (4.64), is indicated by a hat, i.e., $[\hat{\nabla}_a]^{\uparrow\downarrow} = \nabla_a^{\hat{\downarrow}\uparrow}$ and $[\hat{\nabla}_a]^{\hat{\uparrow}\downarrow} = \nabla_a^{\downarrow\uparrow}$, to include the t-reducible vertices [cf. Eq. (4.64)]. In our code, the components of the U-reducible vertices $\nabla_r = \bar{\lambda}_r \bullet \eta_r \bullet \lambda_r$ are not computed and stored explicitly, but their components are calculated on the fly according to Eqs. (4.22)–(4.23) when computing the U-irreducible vertices T_r via Eqs. (4.65).

To avoid gigantic data containers with high-frequency values never used, we save the data for the U-irreducible vertices, Eqs. (4.65), in two versions: T_r^L and T_r^R. T_r^L contains more values for the second fermionic frequency ν' and is used when the bubble in a summation appears left of it while T_r^R contains more values for the first fermionic frequency ν and is used in the other cases (cf. Tab. 4.1). Explicitly, we have:

$$\tilde{\bar{\lambda}}_r(\omega, \nu) = \tfrac{1}{\beta} \sum_{\nu''} T_r^L(\omega, \nu, \nu'') \bullet \Pi_r(\omega, \nu''), \quad \tilde{\lambda}_r(\omega, \nu') = \tfrac{1}{\beta} \sum_{\nu''} \Pi_r(\omega, \nu'') \bullet T_r^R(\omega, \nu'', \nu'),$$
$$\tag{4.66a}$$

$$M_r(\omega, \nu, \nu') = \tfrac{1}{\beta} \sum_{\nu''} T_r^L(\omega, \nu, \nu'') \bullet \Pi_r(\omega, \nu'') \bullet T_r^R(\omega, \nu'', \nu')$$
$$- \tfrac{1}{2\beta} \sum_{\nu''} \left[M_r(\omega, \nu, \nu'') \bullet \Pi_r(\omega, \nu'') \bullet T_r^R(\omega, \nu'', \nu') \right.$$
$$\left. + T_r^L(\omega, \nu, \nu'') \bullet \Pi_r(\omega, \nu'') \bullet M_r(\omega, \nu'', \nu') \right]. \tag{4.66b}$$

Note that for the MBE vertices we use a symmetrized version of the Bethe–Salpeter equations [cf. Sec. 3.4.2]. The combination of complex-conjugation and time-reversal symmetry, Eqs. (4.48), relates T_r^L with T_r^R. So whenever we want to exploit all the symmetry relations, we can spare ourselves to compute the two versions of U-irreducible vertices and Hedin vertices.

After we have discussed the relations for the individual vertices, we can now combine everything as illustrated in Fig. 4.3. One parquet iteration from Ψ_{old} to Ψ_{new} consists of the following steps (cf. Fig. 4.3):

1. The values for G_0, U, $\mathbf{1}_r$, $\tilde{R}$, Π_H^{corr}, and Σ_H^{corr} are not changed (gray boxes in Fig. 4.3).

2. Updated data for the Green's functions $G[\Sigma_H, \tilde{\Sigma}, G_0]$ [Dyson equation (4.58)], the bubbles $\Pi_r[G]$, Eqs. (4.9), the bosonic self-energy $P_r[\bar{\lambda}_r, \Pi_r, \mathbf{1}_r, \Pi_r^{\text{corr}}]$ [Schwinger–Dyson equations (4.20)–(4.21)], and the U-irreducible vertices $T_r[\tilde{R}, M_r, \bar{\lambda}_r, \tilde{\eta}_r, U, \mathbf{1}_r]$, Eqs. (4.65), (blue boxes in Fig. 4.3) are computed from the vertices of the old state Ψ_{old} (orange boxes in Fig. 4.3).

3. Updated data for the Hartree term $\Sigma_H[\Sigma_H, \tilde{\Sigma}, G, G_0, U, \Sigma_H^{\text{corr}}]$, Eq. (4.61), the self-energy $\tilde{\Sigma}[\tilde{\eta}_r, \tilde{\lambda}_r, G, U, \mathbf{1}_r]$ [Schwinger–Dyson equations (4.57)], the bosonic propagators $\tilde{\eta}_r[\tilde{\eta}_r, P_r, U]$ [Dyson equations (4.18)–(4.19)], the Hedin vertices $\tilde{\lambda}_r[\Pi_r, T_r, \mathbf{1}_r]$ [Schwinger–Dyson equations (4.15)–(4.17)], and the MBE vertices $M_r[M_r, \Pi_r, T_r]$ [Bethe–Salpeter equations (4.13)] (green boxes in Fig. 4.3) are computed from the vertices of the old state Ψ_{old} (orange boxes in Fig. 4.3) and the vertices computed in step 2 (blue boxes in Fig. 4.3).

4. The old state Ψ_{old} is overwritten by the new state Ψ_{new} and the algorithm is repeated until a convergence criterion is fulfilled. If Anderson acceleration is used (see below), the algorithm handles the overwriting and convergence criterion implicitly.

To reach better convergence, we make use of Anderson's acceleration algorithm [And65, Kel22] as implemented in the standard library `NLsolve.jl`. While solving the self-consistent equations, the new state Ψ_{new} is mixed with older configurations Ψ_{old} in such a way that the convergence rate is accelerated and less parquet iterations have to be executed. In that case, Ψ_{old} is not completely overwritten by Ψ_{new} in step 4, but a couple of old configurations Ψ_{old} exist from which Ψ_{new} is determined.

4.2.2. Implementation of the functional renormalization group

For the sake of completeness, let us include some more details on our implementation of the fRG equations using the SBE formulation. So far, we have only implemented the one-loop fRG equations (including the Katanin substitution) in terms of the SBE vertices using both a regulator dependence in the Green's functions $G_0(\Lambda)$ and the bare interaction $U(\Lambda)$ (cf. Sec. 3.5). Basically, the code structure of our fRG solver is analogous to that of our parquet solver (due to the analogies discussed in Sec. 3.4.2). The state Ψ inherits the dependence on the scale parameter Λ. While the parquet iteration involves an update from Ψ_{old} to Ψ_{new}, we now use the state Ψ and its differentiated version $\dot{\Psi}$ to implement the fRG equations $\dot{\Psi} = f[\Psi]$ [KD18b]. This huge set of differential equations for every frequency data point is solved by the standard library `DifferentialEquations.jl` using a Runge–Kutta algorithm of order 5(4) by Tsitouras [Tsi11].

There are a few adaptions compared to the parquet solver. The differentiated quantities $\dot{G}, \dot{\tilde{\Sigma}}, \dot{\tilde{\eta}}_r, \dot{P}_r, \dot{\tilde{\lambda}}_r, \dot{\lambda}_r, \dot{M}_r$ are computed via their flow equations (3.48)–(3.53). Their data containers are treated in the same way as their undifferentiated counterparts (cf. Tab. 4.1)

and are contained in the differentiated state $\dot{\Psi}$. The bare Green's function $G_0(\Lambda)$ and the bare interaction $U(\Lambda)$ are not constant anymore, but they have to be updated for every single value of Λ. Besides them, we include data containers for the fermionic single-scale propagator $S(\Lambda)$, the differentiated bare interaction $\dot{U}(\Lambda)$, and the bosonic single-scale propagator $S_{\eta_r}(\Lambda) = \eta_r \bullet U^{-1} \bullet \dot{U} \bullet U^{-1} \bullet \eta_r$, Eq. (3.68). The spin structure of the latter is provided in App. C.3.

For the self-energy, we either use the standard one-loop flow equation $\dot{\Sigma} = -\Gamma \cdot S = -[T_r + \bar{\lambda}_r \bullet \eta_r \bullet \lambda_r] \cdot S$ [cf. Eq. (3.9a)] or the differentiated Schwinger–Dyson equation (3.45). There, the single-scale propagators can be extended using the Katanin substitution $\dot{G} = S + G\dot{\Sigma}G$, Eq. (3.65).

Results obtained from our fRG solver in the context of the Fermi-edge singularity appearing in X-ray absorption spectra are discussed in Sec. 5.2.

4.3. Correlation functions and the SBE formalism

Two-point and four-point correlation functions are the backbone for a theoretical description of numerous physical system. As a completion of Sec. 4.1, let us elaborate how the SBE vertices $\eta_r, \bar{\lambda}_r, \lambda_r, M_r$ can be determined from correlation functions and susceptibilities. This matter is discussed in App. D of Ref. [P1] for generic systems, here, however, we use a slightly different frequency parametrization of the vertices (cf. Fig. 4.1) and specify to the case of two distinct particle types $\uparrow, \downarrow$ introduced in Eq. (4.4).

Using the Matsubara formalism and following the notation of Refs. [Roh13, KGR$^+$24], we define generic n-point correlation functions in terms of the fermionic or bosonic annihilation and creation operators $\hat{a}_i$ as

$$G_{i_1 i_2}(\tau_1, \tau_2) = -\langle \mathcal{T} \hat{a}_{i_1}(\tau_1) \hat{a}_{i_2}(\tau_2) \rangle , \tag{4.67a}$$

$$G^{(n)}_{i_1 i_2 \dots i_n}(\tau_1, \tau_2, \dots, \tau_n) = \langle \mathcal{T} \hat{a}_{i_1}(\tau_1) \hat{a}_{i_2}(\tau_2) \cdots \hat{a}_{i_n}(\tau_n) \rangle , \tag{4.67b}$$

which are consistent with the field-theoretical conventions in Eqs. (3.6) and (3.2). The expectation values are taken in the grand canonical ensemble $\langle ... \rangle = \mathrm{tr}(\mathrm{e}^{-\beta(\hat{H} - \mu\hat{N})}...)/Z$ with the grand canonical partition function $Z = \mathrm{tr}\,\mathrm{e}^{-\beta(\hat{H} - \mu\hat{N})}$. Furthermore, $\mathcal{T}$ is the imaginary time-ordering operator and the imaginary time evolution of the operators $\hat{a}_i$ is given by

$$\hat{a}_i(\tau) = \mathrm{e}^{\tau(\hat{H} - \mu\hat{N})} \hat{a}_i \mathrm{e}^{-\tau(\hat{H} - \mu\hat{N})}. \tag{4.68}$$

Depending on whether $\hat{a}_i$ is a creation $\hat{c}_i^\dagger$ or annihilation operator $\hat{c}_i$, the Fourier transforms

to Matsubara frequencies ν are given by

$$\hat{c}_i(\tau) = \tfrac{1}{\beta}\sum_\nu \hat{c}_i(\nu)\mathrm{e}^{-\mathrm{i}\nu\tau}, \quad \hat{c}^\dagger(\tau) = \tfrac{1}{\beta}\sum_\nu \hat{c}_i^\dagger(\nu)\mathrm{e}^{\mathrm{i}\nu\tau}, \tag{4.69a}$$

$$\hat{c}_i(\nu) = \int_0^\beta \mathrm{d}\tau\,\hat{c}_i(\tau)\mathrm{e}^{\mathrm{i}\nu\tau}, \quad \hat{c}_i^\dagger(\nu) = \int_0^\beta \mathrm{d}\tau\,\hat{c}_i^\dagger(\tau)\mathrm{e}^{-\mathrm{i}\nu\tau}. \tag{4.69b}$$

Here, the Matsubara frequencies are fermionic $\nu \in (2\mathbb{Z}+1)\pi T$ or bosonic $\nu \in 2\mathbb{Z}\,\pi T$ depending on whether $\hat{c}_i^\dagger$ and $\hat{c}_i$ are fermionic or bosonic.

With these definitions, the fermionic propagator $G_{1|1'}$, Eq. (3.6), is written as

$$G_{1|1'}(\nu_1,\nu_{1'}) = -\left\langle c_1(\nu_1)\bar{c}_{1'}(\nu_{1'})\right\rangle = -\int_0^\beta \mathrm{d}\tau_1 \int_0^\beta \mathrm{d}\tau_{1'}\,\mathrm{e}^{\mathrm{i}\nu_1\tau_1 - \mathrm{i}\nu_{1'}\tau_{1'}}\left\langle \mathcal{T}\hat{c}_1(\tau_1)\hat{c}_{1'}^\dagger(\tau_{1'})\right\rangle, \tag{4.70}$$

and is consequently directly related to $G_{11'}(\tau_1,\tau_{1'})$. Similarly, the four-point correlation function $G^{(4)}_{12|1'2'}$, Eq. (3.7), is related to $G_{122'1'}(\tau_1,\tau_2,\tau_{2'},\tau_{1'})$:

$$G^{(4)}_{12|1'2'}(\nu_1,\nu_2,\nu_{1'},\nu_{2'}) = \left\langle c_1(\nu_1)c_2(\nu_2)\bar{c}_{2'}(\nu_{2'})\bar{c}_{1'}(\nu_{1'})\right\rangle$$
$$= \int_0^\beta \mathrm{d}\tau_1 \int_0^\beta \mathrm{d}\tau_2 \int_0^\beta \mathrm{d}\tau_{2'} \int_0^\beta \mathrm{d}\tau_{1'}\,\mathrm{e}^{\mathrm{i}\nu_1\tau_1 + \mathrm{i}\nu_2\tau_2 - \mathrm{i}\nu_{2'}\tau_{2'} - \mathrm{i}\nu_{1'}\tau_{1'}}\left\langle \mathcal{T}\hat{c}_1(\tau_1)\hat{c}_2(\tau_2)\hat{c}_{2'}^\dagger(\tau_{2'})\hat{c}_{1'}^\dagger(\tau_{1'})\right\rangle. \tag{4.71}$$

So the field-theoretical correlation functions involving Grassmann/complex fields $\bar{c}_i, c_i$ [see also Eq. (3.2)] with imaginary frequencies are obtained via Fourier transformation from the imaginary-time correlation functions involving fermionic/bosonic operators $\hat{c}_i^\dagger, \hat{c}_i$.

Following the frequency parametrization introduced in Fig. 4.1 and Eqs. (4.1), we define four-point correlation functions $G_r^{(4)}$, Eq. (3.7), in the three diagrammatic channels:

$$G^{(4)}_{a;12|1'2'}(\omega,\nu,\nu') = \left\langle c_1(\nu)c_2(\nu'+\omega)\bar{c}_{2'}(\nu+\omega)\bar{c}_{1'}(\nu')\right\rangle, \tag{4.72a}$$

$$G^{(4)}_{p;12|1'2'}(\omega,\nu,\nu') = \left\langle c_1(-\nu)c_2(\nu+\omega)\bar{c}_{2'}(\nu'+\omega)\bar{c}_{1'}(-\nu')\right\rangle, \tag{4.72b}$$

$$G^{(4)}_{t;12|1'2'}(\omega,\nu,\nu') = \left\langle c_1(\nu'+\omega)c_2(\nu)\bar{c}_{2'}(\nu+\omega)\bar{c}_{1'}(\nu')\right\rangle. \tag{4.72c}$$

We introduce bosonic fields ψ and ϕ via frequency summations over the fermionic fields $\bar{c}$ and c:

$$\psi_{12'}(\omega) = \tfrac{1}{\beta}\sum_\nu c_1(\nu)\bar{c}_{2'}(\nu+\omega) = \bar{\psi}_{2'1}(-\omega), \tag{4.73a}$$

$$\phi_{12}(\omega) = \tfrac{1}{\beta}\sum_\nu c_1(-\nu)c_2(\nu+\omega), \qquad \bar{\phi}_{1'2'}(\omega) = \tfrac{1}{\beta}\sum_{\nu'} \bar{c}_{2'}(\nu'+\omega)\bar{c}_{1'}(-\nu'). \tag{4.73b}$$

These are defined in such a way that they are the Fourier-transformed coupled operators evaluated at equal imaginary time:

$$\psi_{12'}(\omega) = \tfrac{1}{\beta} \sum_{\nu} \int_0^{\beta} \mathrm{d}\tau_1 \int_0^{\beta} \mathrm{d}\tau_2 \, \mathrm{e}^{\mathrm{i}\nu\tau_1 - \mathrm{i}(\omega+\nu)\tau_2} c_1(\tau_1) \bar{c}_{2'}(\tau_2) = \int_0^{\beta} \mathrm{d}\tau \, \mathrm{e}^{-\mathrm{i}\omega\tau} c_1(\tau) \bar{c}_{2'}(\tau),$$

(4.74a)

$$\phi_{12}(\omega) = \tfrac{1}{\beta} \sum_{\nu} \int_0^{\beta} \mathrm{d}\tau_1 \int_0^{\beta} \mathrm{d}\tau_2 \, \mathrm{e}^{-\mathrm{i}\nu\tau_1 + \mathrm{i}(\omega+\nu)\tau_2} c_1(\tau_1) c_2(\tau_2) = \int_0^{\beta} \mathrm{d}\tau \, \mathrm{e}^{\mathrm{i}\omega\tau} c_1(\tau) c_2(\tau),$$

(4.74b)

$$\bar{\phi}_{1'2'}(\omega) = \tfrac{1}{\beta} \sum_{\nu} \int_0^{\beta} \mathrm{d}\tau_1 \int_0^{\beta} \mathrm{d}\tau_2 \, \mathrm{e}^{-\mathrm{i}(\omega+\nu')\tau_1 + \mathrm{i}\nu'\tau_2} \bar{c}_{1'}(\tau_1) \bar{c}_{2'}(\tau_2) = \int_0^{\beta} \mathrm{d}\tau \, \mathrm{e}^{-\mathrm{i}\omega\tau} \bar{c}_{2'}(\tau) \bar{c}_{1'}(\tau).$$

(4.74c)

Consequently, the bosonic fields $\psi_{12'}(\omega), \phi_{12}(\omega), \bar{\phi}_{1'2'}(\omega)$, Eqs. (4.73), are underlain by time-evolved [cf. Eq. (4.68)] bosonic operators

$$\hat{\psi}_{12'} = \hat{c}_1 \hat{c}_{2'}^{\dagger}, \quad \hat{\phi}_{12} = \hat{c}_1 \hat{c}_2, \quad \hat{\phi}_{1'2'}^{\dagger} = \hat{c}_{2'}^{\dagger} \hat{c}_{1'}^{\dagger}.$$

(4.75)

Including the bosonic fields, we introduce three-point $\bar{G}_r^{(3)}, G_r^{(3)}$ and two-point correlation functions D_r in the three diagrammatic channels r:

$$\bar{G}_{a;12|1'2'}^{(3)}(\omega, \nu) = -\left\langle c_1(\nu) \bar{c}_{2'}(\nu + \omega) \bar{\psi}_{1'2}(\omega) \right\rangle,$$

(4.76a)

$$G_{a;12|1'2'}^{(3)}(\omega, \nu') = -\left\langle \psi_{12'}(\omega) c_2(\nu' + \omega) \bar{c}_{1'}(\nu') \right\rangle,$$

(4.76b)

$$D_{a;12|1'2'}(\omega) = -\left\langle \psi_{12'}(\omega) \bar{\psi}_{1'2}(\omega) \right\rangle,$$

(4.76c)

$$\bar{G}_{p;12|1'2'}^{(3)}(\omega, \nu) = \left\langle c_1(-\nu) c_2(\omega + \nu) \bar{\phi}_{1'2'}(\omega) \right\rangle,$$

(4.76d)

$$G_{p;12|1'2'}^{(3)}(\omega, \nu') = \left\langle \phi_{12}(\omega) \bar{c}_{2'}(\omega + \nu') \bar{c}_{1'}(-\nu') \right\rangle,$$

(4.76e)

$$D_{p;12|1'2'}(\omega, \nu') = \left\langle \phi_{12}(\omega) \bar{\phi}_{1'2'}(\omega) \right\rangle,$$

(4.76f)

$$\bar{G}_{t;12|1'2'}^{(3)}(\omega, \nu) = \left\langle c_2(\nu) \bar{c}_{2'}(\omega + \nu) \bar{\psi}_{1'1}(\omega) \right\rangle,$$

(4.76g)

$$G_{t;12|1'2'}^{(3)}(\omega, \nu') = \left\langle \psi_{22'}(\omega) c_1(\omega + \nu') \bar{c}_{1'}(\nu') \right\rangle,$$

(4.76h)

$$D_{t;12|1'2'}(\omega) = \left\langle \psi_{22'}(\omega) \bar{\psi}_{1'1}(\omega) \right\rangle.$$

(4.76i)

Importantly, all these definitions refer to the generic n-point functions, Eqs. (4.67), using arguments that are analogous to Eqs. (4.70)–(4.71). With the definition of the bosonic fields, Eqs. (4.73), we express Eqs. (4.76) in terms of $G_r^{(4)}$, Eqs. (4.72):

$$\bar{G}_{r;12|1'2'}^{(3)}(\omega, \nu) = \tfrac{1}{\beta} \sum_{\nu'} G_{r;12|1'2'}^{(4)}(\omega, \nu, \nu'),$$

(4.77a)

$$G^{(3)}_{r;12|1'2'}(\omega, \nu') = \tfrac{1}{\beta} \sum_\nu G^{(4)}_{r;12|1'2'}(\omega, \nu, \nu'), \tag{4.77b}$$

$$D_{r;12|1'2'}(\omega) = \tfrac{1}{\beta^2} \sum_{\nu,\nu'} G^{(4)}_{r;12|1'2'}(\omega, \nu, \nu'). \tag{4.77c}$$

For a more physical description, we relate the correlation functions to *generalized susceptibilities* [Roh13]. These are response functions to physical excitations and defined by subtracting disconnected parts from the four-point correlation functions $G^{(4)}_r$, Eqs. (4.72):

$$\chi^{(4)}_{a;12|1'2'}(\omega, \nu, \nu') = G^{(4)}_{a;12|1'2'}(\omega, \nu, \nu') + \delta_\omega G_{1|2'}(\nu) G_{2|1'}(\nu'), \tag{4.78a}$$

$$\chi^{(4)}_{p;12|1'2'}(\omega, \nu, \nu') = \tfrac{1}{4} G^{(4)}_{p;12|1'2'}(\omega, \nu, \nu'), \tag{4.78b}$$

$$\chi^{(4)}_{t;12|1'2'}(\omega, \nu, \nu') = G^{(4)}_{t;12|1'2'}(\omega, \nu, \nu') - \delta_\omega G_{1|1'}(\nu') G_{2|2'}(\nu). \tag{4.78c}$$

Similar to the three-point $\bar{G}^{(3)}_r, G^{(3)}_r$ and two-point correlation functions D_r, we introduce three-point $\bar{\chi}^{(3)}_r, \chi^{(3)}_r$ and physical susceptibilities χ_r by frequency summations over $\chi^{(4)}_r$, Eqs. (4.78):

$$\bar{\chi}^{(3)}_{r;12|1'2'}(\omega, \nu) = \tfrac{1}{\beta} \sum_{\nu'} \chi^{(4)}_{r;12|1'2'}(\omega, \nu, \nu'), \tag{4.79a}$$

$$\chi^{(3)}_{r;12|1'2'}(\omega, \nu') = \tfrac{1}{\beta} \sum_{\nu} \chi^{(4)}_{r;12|1'2'}(\omega, \nu, \nu'), \tag{4.79b}$$

$$\chi_{r;12|1'2'}(\omega) = \tfrac{1}{\beta^2} \sum_{\nu,\nu'} \chi^{(4)}_{r;12|1'2'}(\omega, \nu, \nu'). \tag{4.79c}$$

Via Eqs. (4.77) and (4.78), we can express these in terms of the three-point and two-point correlation functions:

$$\bar{\chi}^{(3)}_{a;12|1'2'}(\omega, \nu) = \bar{G}^{(3)}_{a;12|1'2'}(\omega, \nu) + \delta_\omega G_{1|2'}(\nu) \tfrac{1}{\beta} \sum_{\nu'} G_{2|1'}(\nu'), \tag{4.80a}$$

$$\chi^{(3)}_{a;12|1'2'}(\omega, \nu') = G^{(3)}_{a;12|1'2'}(\omega, \nu') + \delta_\omega \tfrac{1}{\beta} \sum_{\nu} G_{1|2'}(\nu) G_{2|1'}(\nu'), \tag{4.80b}$$

$$\chi_{a;12|1'2'}(\omega) = D_{a;12|1'2'}(\omega) + \tfrac{1}{\beta^2} \sum_{\nu,\nu'} G_{1|2'}(\nu) G_{2|1'}(\nu'), \tag{4.80c}$$

$$\bar{\chi}^{(3)}_{p;12|1'2'}(\omega, \nu) = \tfrac{1}{4} \bar{G}^{(3)}_{p;12|1'2'}(\omega, \nu), \tag{4.80d}$$

$$\chi^{(3)}_{p;12|1'2'}(\omega, \nu') = \tfrac{1}{4} G^{(3)}_{p;12|1'2'}(\omega, \nu), \tag{4.80e}$$

$$\chi_{p;12|1'2'}(\omega, \nu') = \tfrac{1}{4} D_{p;12|1'2'}(\omega, \nu, \nu'), \tag{4.80f}$$

$$\bar{\chi}^{(3)}_{t;12|1'2'}(\omega, \nu) = \bar{G}^{(3)}_{t;12|1'2'}(\omega, \nu) - \delta_\omega \tfrac{1}{\beta} \sum_{\nu'} G_{1|1'}(\nu') G_{2|2'}(\nu), \tag{4.80g}$$

$$\chi^{(3)}_{t;12|1'2'}(\omega, \nu') = G^{(3)}_{t;12|1'2'}(\omega, \nu') - \delta_\omega G_{1|1'}(\nu') \tfrac{1}{\beta} \sum_\nu G_{2|2'}(\nu), \qquad (4.80\text{h})$$

$$\chi_{t;12|1'2'}(\omega) = D_{t;12|1'2'}(\omega) + \tfrac{1}{\beta^2} \sum_{\nu,\nu'} G_{1|1'}(\nu') G_{2|2'}(\nu). \qquad (4.80\text{i})$$

Also here, disconnected parts are adequately subtracted. The sums over the Green's functions are given by the density, i.e., the zero-time correlation functions:

$$\tfrac{1}{\beta} \sum_\nu G_{1|1'}(\nu) = -\tfrac{1}{\beta} \sum_\nu \langle c_1(\nu)\bar{c}_{1'}(\nu) \rangle = -\langle c_1(\tau = 0)\bar{c}_{1'}(\tau = 0) \rangle = \langle \bar{c}_{1'} c_1 \rangle = \langle \hat{c}^\dagger_{1'}, \hat{c}_1 \rangle. \tag{4.81}$$

To relate the correlation functions and susceptibilities with the SBE vertices, we make use of a modified version of Eqs. (105) from Ref. [P1][1]:

$$\Pi_r \bullet \bar{\lambda}_r \bullet \eta_r = \bar{\chi}^{(3)}_r \bullet U, \qquad (4.82\text{a})$$

$$\eta_r \bullet \lambda_r \bullet \Pi_r = U \bullet \chi^{(3)}_r, \qquad (4.82\text{b})$$

$$\tilde{\eta}_r = \eta_r - U = U \bullet \chi_r \bullet U. \qquad (4.82\text{c})$$

With $U^{\hat{\uparrow}\downarrow} = -U^{\uparrow\downarrow}$ and $U^{\uparrow\uparrow} = 0$ [cf. Eq. (4.8)], Eqs. (4.82) the spin components for the bosonic propagator are obtained as

$$\tilde{\eta}^{\uparrow\downarrow}_a = [U^{\uparrow\downarrow}]^2 \chi^{\uparrow\downarrow}_a, \quad \tilde{\eta}^{\hat{\uparrow}\downarrow}_a = [U^{\uparrow\downarrow}]^2 \chi^{\hat{\uparrow}\downarrow}_a, \quad \tilde{\eta}^{\uparrow\uparrow}_a = [U^{\uparrow\downarrow}]^2 \chi^{\downarrow\downarrow}_a, \qquad (4.83\text{a})$$

$$\tilde{\eta}^{\uparrow\downarrow}_p = 4[U^{\uparrow\downarrow}]^2 \chi^{\uparrow\downarrow}_p, \quad \tilde{\eta}^{\hat{\uparrow}\downarrow}_p = -4[U^{\uparrow\downarrow}]^2 \chi^{\uparrow\downarrow}_p, \quad \tilde{\eta}^{\uparrow\uparrow}_p = 0, \qquad (4.83\text{b})$$

$$\tilde{\eta}^{\uparrow\downarrow}_t = [U^{\uparrow\downarrow}]^2 \chi^{\uparrow\downarrow}_t, \quad \tilde{\eta}^{\hat{\uparrow}\downarrow}_t = [U^{\uparrow\downarrow}]^2 \chi^{\hat{\uparrow}\downarrow}_t, \quad \tilde{\eta}^{\uparrow\uparrow}_t = [U^{\uparrow\downarrow}]^2 \chi^{\downarrow\downarrow}_t. \qquad (4.83\text{c})$$

Further, the Hedin vertices $\bar{\lambda}_r$ and λ_r are obtained from Eqs. (4.82a)–(4.82b) as

$$\bar{\lambda}^{\uparrow\downarrow}_a = \frac{U^{\uparrow\downarrow}[\bar{\chi}^{(3)}_a]^{\uparrow\downarrow}}{\eta^{\uparrow\downarrow}_a \Pi^{\uparrow\downarrow}_a}, \ \bar{\lambda}^{\uparrow\uparrow}_a = \frac{U^{\uparrow\downarrow}}{\Pi^{\uparrow\uparrow}_a} \frac{[\bar{\chi}^{(3)}_a]^{\hat{\uparrow}\downarrow} \eta^{\downarrow\downarrow}_a - [\bar{\chi}^{(3)}_a]^{\uparrow\uparrow} \eta^{\hat{\uparrow}\downarrow}_a}{\eta^{\hat{\uparrow}\downarrow}_a \eta^{\hat{\uparrow}\downarrow}_a - \eta^{\downarrow\downarrow}_a \eta^{\uparrow\uparrow}_a}, \ \bar{\lambda}^{\hat{\uparrow}\downarrow}_a = \frac{-U^{\uparrow\downarrow}}{\Pi^{\uparrow\uparrow}_a} \frac{[\bar{\chi}^{(3)}_a]^{\hat{\uparrow}\downarrow} \eta^{\hat{\uparrow}\downarrow}_a - [\bar{\chi}^{(3)}_a]^{\uparrow\uparrow} \eta^{\uparrow\uparrow}_a}{\eta^{\hat{\uparrow}\downarrow}_a \eta^{\hat{\uparrow}\downarrow}_a - \eta^{\downarrow\downarrow}_a \eta^{\uparrow\uparrow}_a},$$
$$(4.84\text{a})$$

$$\bar{\lambda}^{\uparrow\uparrow}_p = 1, \qquad \bar{\lambda}^{\uparrow\downarrow}_p = \frac{1}{2} + \frac{U^{\uparrow\downarrow}[\bar{\chi}^{(3)}_p]^{\uparrow\downarrow}}{\eta^{\uparrow\downarrow}_p \Pi^{\uparrow\downarrow}_p}, \qquad \bar{\lambda}^{\hat{\uparrow}\downarrow}_p = \frac{1}{2} - \frac{U^{\uparrow\downarrow}[\bar{\chi}^{(3)}_p]^{\uparrow\downarrow}}{\eta^{\uparrow\downarrow}_p \Pi^{\uparrow\downarrow}_p}, \qquad (4.84\text{b})$$

$$\bar{\lambda}^{\hat{\uparrow}\downarrow}_t = \frac{U^{\hat{\uparrow}\downarrow}[\bar{\chi}^{(3)}_t]^{\hat{\uparrow}\downarrow}}{\eta^{\hat{\uparrow}\downarrow}_t \Pi^{\hat{\uparrow}\downarrow}_t}, \ \bar{\lambda}^{\uparrow\uparrow}_t = \frac{U^{\hat{\uparrow}\downarrow}}{\Pi^{\uparrow\uparrow}_t} \frac{[\bar{\chi}^{(3)}_t]^{\downarrow\uparrow} \eta^{\downarrow\downarrow}_t - [\bar{\chi}^{(3)}_t]^{\uparrow\uparrow} \eta^{\uparrow\downarrow}_t}{\eta^{\downarrow\uparrow}_t \eta^{\uparrow\downarrow}_t - \eta^{\downarrow\downarrow}_t \eta^{\uparrow\uparrow}_t}, \ \bar{\lambda}^{\uparrow\downarrow}_t = \frac{-U^{\hat{\uparrow}\downarrow}}{\Pi^{\downarrow\downarrow}_t} \frac{[\bar{\chi}^{(3)}_t]^{\uparrow\uparrow} \eta^{\uparrow\downarrow}_t - [\bar{\chi}^{(3)}_t]^{\downarrow\downarrow} \eta^{\downarrow\downarrow}_t}{\eta^{\downarrow\uparrow}_t \eta^{\uparrow\downarrow}_t - \eta^{\downarrow\downarrow}_t \eta^{\uparrow\uparrow}_t},$$
$$(4.84\text{c})$$

---

[1]Following Eqs. (18) in Ref. [P1], the relations including Π_r and $\bar{\lambda}_r, \lambda_r$, Eqs. (4.82a)–(4.82b), do not involve any summation over frequencies, but the corresponding bubbles, Eqs. (4.9), are just multiplied so we use $\bullet$ instead of $\circ$.

$$\lambda_a^{\uparrow\downarrow} = \frac{U^{\uparrow\downarrow}[\chi_a^{(3)}]^{\uparrow\downarrow}}{\eta_a^{\uparrow\downarrow}\Pi_a^{\uparrow\downarrow}}, \quad \lambda_a^{\uparrow\uparrow} = \frac{U^{\uparrow\downarrow}}{\Pi_a^{\uparrow\uparrow}} \frac{[\chi_a^{(3)}]^{\downarrow\hat{\uparrow}}\eta_a^{\downarrow\downarrow} - [\chi_a^{(3)}]^{\uparrow\uparrow}\eta_a^{\downarrow\hat{\uparrow}}}{\eta_a^{\downarrow\hat{\uparrow}}\eta_a^{\hat{\downarrow}\uparrow} - \eta_a^{\downarrow\downarrow}\eta_a^{\uparrow\uparrow}}, \quad \lambda_a^{\hat{\uparrow}\downarrow} = \frac{-U^{\uparrow\downarrow}}{\Pi_a^{\downarrow\downarrow}} \frac{[\chi_a^{(3)}]^{\hat{\uparrow}\downarrow}\eta_a^{\hat{\downarrow}\uparrow} - [\chi_a^{(3)}]^{\downarrow\downarrow}\eta_a^{\downarrow\downarrow}}{\eta_a^{\downarrow\hat{\uparrow}}\eta_a^{\hat{\downarrow}\uparrow} - \eta_a^{\downarrow\downarrow}\eta_a^{\uparrow\uparrow}},$$

$$(4.85a)$$

$$\lambda_p^{\uparrow\uparrow} = 1, \qquad \lambda_p^{\uparrow\downarrow} = \frac{1}{2} + \frac{U^{\uparrow\downarrow}[\chi_p^{(3)}]^{\uparrow\downarrow}}{\eta_p^{\uparrow\downarrow}\Pi_p^{\uparrow\downarrow}}, \qquad \lambda_p^{\hat{\uparrow}\downarrow} = \frac{1}{2} - \frac{U^{\uparrow\downarrow}[\chi_p^{(3)}]^{\downarrow\uparrow}}{\eta_p^{\uparrow\downarrow}\Pi_p^{\downarrow\uparrow}}, \qquad (4.85b)$$

$$\lambda_t^{\hat{\uparrow}\downarrow} = \frac{U^{\hat{\uparrow}\downarrow}[\chi_t^{(3)}]^{\hat{\uparrow}\downarrow}}{\eta_t^{\hat{\uparrow}\downarrow}\Pi_t^{\hat{\uparrow}\downarrow}}, \quad \lambda_t^{\uparrow\uparrow} = \frac{U^{\hat{\uparrow}\downarrow}}{\Pi_t^{\uparrow\uparrow}} \frac{[\chi_t^{(3)}]^{\uparrow\downarrow}\eta_t^{\downarrow\downarrow} - [\chi_t^{(3)}]^{\uparrow\uparrow}\eta_t^{\downarrow\uparrow}}{\eta_t^{\downarrow\uparrow}\eta_t^{\downarrow\uparrow} - \eta_t^{\downarrow\downarrow}\eta_t^{\uparrow\uparrow}}, \quad \lambda_t^{\uparrow\downarrow} = \frac{-U^{\hat{\uparrow}\downarrow}}{\Pi_t^{\uparrow\uparrow}} \frac{[\chi_t^{(3)}]^{\uparrow\uparrow}\eta_t^{\uparrow\uparrow} - [\chi_t^{(3)}]^{\uparrow\downarrow}\eta_t^{\uparrow\downarrow}}{\eta_t^{\downarrow\uparrow}\eta_t^{\downarrow\uparrow} - \eta_t^{\downarrow\downarrow}\eta_t^{\uparrow\uparrow}}.$$

$$(4.85c)$$

If we know the two-point D_r and three-point correlation functions $\bar{G}_r^{(3)}, G_r^{(3)}$, Eqs. (4.76), for a generic model with two particle types $\uparrow, \downarrow$ with a constant bare interaction $U^{\uparrow\downarrow}$ satisfying the action, Eq. (4.4), Eqs. (4.83)–(4.85) allow to determine the SBE vertices $\eta_r, \bar{\lambda}_r, \lambda_r$ by using the susceptibilities $\chi_r, \bar{\chi}_r^{(3)}, \chi_r^{(3)}$, Eqs. (4.4). Note that apart from the summation over the simple Green's function, Eq. (4.81), all the expressions do not involve any further frequency summation, but are algebraic combinations of the individual correlation functions. These steps are essential for obtaining the exact formulas of the single-site Hubbard model, which is discussed in the following section.

4.4. Hubbard atom in a magnetic field

Simple limiting cases along with an exact solution are essential for testing elaborate methods like the parquet formalism and the fRG. Over the years, the single-site Hubbard model, known as the *Hubbard atom*, has been proven to be a very useful benchmark for diagrammatic approaches [PST00, Roh13, TGCR18, SCC$^+$20, HSS23, Roh23, ERST24, RRS$^+$24]. The Hubbard atom is exactly solvable and corresponding correlation functions

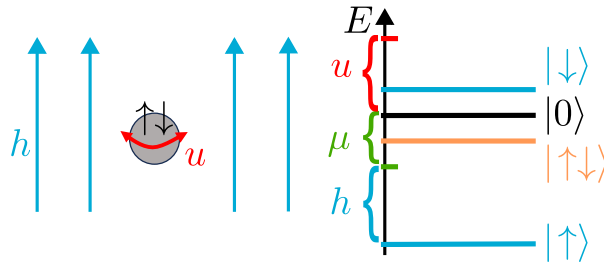Figure 4.4.: Sketch of the single-site Hubbard model, the so-called Hubbard atom, in a magnetic field h with repulsive on-site interaction u [cf. the Hamiltonian, Eq. (4.86)]. On the right, the energies E of the four different eigenstates $|\downarrow\rangle$, $|0\rangle$, $|\uparrow\downarrow\rangle$ and $|\uparrow\rangle$ are illustrated in terms of the system parameters u, μ, and h.

of arbitrary order can be computed analytically. Despite its rather simple spectrum, it provides many features of the strong-coupling limit of the Hubbard model. Moreover, corresponding correlation functions and vertices exhibit a rich complexity. They contain vertex divergences, which emerge in the parquet decomposition, and help to analyze them more thoroughly [TGCR18, SCC$^+$20, ERST24]. In this section, we present exact formulas of the SBE vertices for the Hubbard atom in the presence of a magnetic field and away from half filling and thus extend previous works. Such a computation is essential to test our code where $SU(2)$ spin symmetry is not satisfied.

The grand-canonical Hamiltonian of the Hubbard atom in a magnetic field h reads

$$\hat{\Xi} = \hat{H} - \mu\hat{N} = -\mu(\hat{c}_\uparrow^\dagger \hat{c}_\uparrow + \hat{c}_\downarrow^\dagger \hat{c}_\downarrow) - h(\hat{c}_\uparrow^\dagger \hat{c}_\uparrow - \hat{c}_\downarrow^\dagger \hat{c}_\downarrow) + u\,\hat{c}_\uparrow^\dagger \hat{c}_\downarrow^\dagger \hat{c}_\downarrow \hat{c}_\uparrow, \tag{4.86}$$

with the fermionic operators $\hat{c}_i^\dagger, \hat{c}_i$ fulfilling the anticommutation relations $\{\hat{c}_i, \hat{c}_j^\dagger\} = \delta_{ij}$ $(i, j = \uparrow, \downarrow)$. As we consider a single Hubbard site, the hopping parameter t from the Hubbard model is obviously absent. Note that, here, u refers to the Hubbard interaction and may not be confused with the bare interaction vertex U. A comparison to the action S, Eq. (4.4), yields $U^{\uparrow\downarrow} = -u$. We want to emphasize that h only refers to a magnetic field in z direction and thus does not spoil time-inversion symmetry (cf. Sec. 4.1.2).

The model has four eigenstates corresponding to the possible occupancies of the single site. These are given by

$$\hat{\Xi}|0\rangle = 0|0\rangle, \quad \hat{\Xi}|\uparrow\rangle = (-\mu - h)|\uparrow\rangle, \quad \hat{\Xi}|\downarrow\rangle = (-\mu + h)|\downarrow\rangle, \quad \hat{\Xi}|\uparrow\downarrow\rangle = (u - 2\mu)|\uparrow\downarrow\rangle, \tag{4.87}$$

where $\hat{c}_{\uparrow,\downarrow}|0\rangle$, $|\uparrow\rangle = \hat{c}_\uparrow^\dagger|0\rangle$, $|\downarrow\rangle = \hat{c}_\downarrow^\dagger|0\rangle$ and $|\uparrow\downarrow\rangle = \hat{c}_\uparrow^\dagger \hat{c}_\downarrow^\dagger|0\rangle$. Thus, the Hilbert state is only four dimensional. Note that for the simpler case of half filling $\mu = u/2$ and with zero magnetic field $h = 0$, the eigenstates are degenerate. The model is depicted in Fig. 4.4. The single Hubbard site (gray circle) can host a spin-up and spin-down electron (black arrows) interacting repulsively via u (red arrow). The Hubbard site is located in a magnetic field h (blue arrows) pointing in the z direction. The respective energies of the eigenstates, Eq. (4.87), are illustrated on the right. With the eigenstates, Eq. (4.87), the grand-canonical partition function Z and the density matrix $\hat{\rho}$ are evaluated as

$$Z = \operatorname{tr} e^{-\beta\hat{\Xi}} = 1 + e^{\beta(\mu+h)} + e^{\beta(\mu-h)} + e^{\beta(2\mu-u)}, \tag{4.88a}$$

$$\hat{\rho} = \tfrac{1}{Z}\left(|0\rangle\langle 0| + e^{\beta(\mu+h)}|\uparrow\rangle\langle\uparrow| + e^{\beta(\mu-h)}|\downarrow\rangle\langle\downarrow| + e^{\beta(2\mu-u)}|\uparrow\downarrow\rangle\langle\uparrow\downarrow|\right). \tag{4.88b}$$

Consequently, the densities of the $\uparrow$ and $\downarrow$ electron are given by

$$n_+ = \langle\hat{c}_\uparrow^\dagger \hat{c}_\uparrow\rangle = \tfrac{1}{Z}\left(e^{\beta(\mu+h)} + e^{\beta(2\mu-u)}\right), \quad n_- = \langle\hat{c}_\downarrow^\dagger \hat{c}_\downarrow\rangle = \tfrac{1}{Z}\left(e^{\beta(\mu-h)} + e^{\beta(2\mu-u)}\right), \tag{4.89}$$

where the expectation values are defined as $\langle...\rangle = \operatorname{tr}(\hat{\rho}\,...)/Z$. It is clear that the densities coincide for $h = 0$ and a spin flip $\uparrow\leftrightarrow\downarrow$ can be compensated by a sign change in the

magnetic field $h \to -h$. We deduce the following relations:

$$1 - n_\pm = \tfrac{1}{Z}(1 + e^{\beta(\mu \mp h)}), \tag{4.90a}$$

$$n_- - n_+ = \tfrac{1}{Z}(e^{\beta(\mu-h)} - e^{\beta(\mu+h)}), \tag{4.90b}$$

$$n_+ + n_- - 1 = \tfrac{1}{Z}(e^{\beta(2\mu-u)} - 1). \tag{4.90c}$$

Importantly, $n_- - n_+$ vanishes for a zero magnetic field $h \to 0$ and $n_+ + n_- - 1$ for half filling $\mu \to u/2$.

As we have access to the four eigenenergies and eigenstates, the correlation functions $G^{(n)}_{i_1 \dots i_n}$, Eqs. (4.70)–(4.71), can be computed exactly by using the spectral representation [KLD21, HSS23]. The correlation functions are expressed as a summation over suitable matrices and kernel functions. In the following, we provide the exact correlation functions, which are determined from the spectral representation using a `Mathematica` notebook.

The bare and full Green's functions are given as (cf. Eq. (B4) in Ref. [PST00])

$$G_0^{\uparrow/\downarrow}(\nu) = \frac{1}{\mathrm{i}\nu + \mu \pm h} = \frac{1}{x_\pm(\nu)}, \quad G^{\uparrow/\downarrow}(\nu) = \frac{1 - n_\mp}{x_\pm(\nu)} + \frac{n_\mp}{y_\pm(\nu)} = \frac{y_\pm(\nu) + un_\mp}{x_\pm(\nu)y_\pm(\nu)}, \tag{4.91}$$

where we use the abbreviations

$$x_\pm(\nu) = \mathrm{i}\nu + \mu \pm h, \quad y_\pm(\nu) = \mathrm{i}\nu + \mu \pm h - u. \tag{4.92}$$

In Eq. (4.91), $\uparrow$ refers to the upper sign for x, y, n and $\downarrow$ to the lower one. We deduce the following expression for the self-energies:

$$\Sigma^{\uparrow/\downarrow}(\nu) = \frac{1}{G_0^{\uparrow/\downarrow}} - \frac{1}{G^{\uparrow/\downarrow}} = \frac{x_\pm(\nu)un_\mp}{y_\pm(\nu) + un_\mp}. \tag{4.93}$$

From this, the Hartree term results as $\Sigma_{\mathrm{H}}^{\uparrow/\downarrow} = \lim_{\nu \to \infty} \Sigma^{\uparrow/\downarrow}(\nu) = un_\mp$.

In consideration of the crossing symmetries (cf. Sec. 4.1.2), there are four independent components of the bosonic propagators $\tilde{\eta}_r$:

$$\tilde{\eta}_a^{\uparrow\downarrow}(\omega) = \frac{u^2}{2h - \mathrm{i}\omega}(n_- - n_+), \tag{4.94a}$$

$$\tilde{\eta}_a^{\hat{\uparrow}\downarrow}(\omega) = \frac{u^2\beta\delta_\omega}{Z^2}(e^{2\beta\mu} - e^{\beta(2\mu-u)}), \tag{4.94b}$$

$$\tilde{\eta}_a^{\uparrow\uparrow}(\omega) = u^2\beta\delta_\omega(n_- - 1)n_-, \tag{4.94c}$$

$$\tilde{\eta}_p^{\uparrow\downarrow}(\omega) = \frac{u^2}{u - 2\mu - \mathrm{i}\omega}(1 - n_+ - n_-). \tag{4.94d}$$

As discussed before, the spin-flipped components are received by a sign change of the

magnetic field, e.g., $\tilde{\eta}_a^{\downarrow\uparrow} = \tilde{\eta}_a^{\uparrow\downarrow}\big|_{h\to -h}$. According to Eqs. (4.90), one might naïvely guess that $\tilde{\eta}_a^{\uparrow\downarrow}$ vanishes for zero magnetic field and $\tilde{\eta}_p^{\uparrow\downarrow}$ for half filling. However, one has to be careful about the denominators $2h - i\omega$ and $u - 2\mu - i\omega$ when $\omega = 0$. With the expansions of Eqs. (4.90) around $h = 0$ and $\mu = u/2$,

$$n_- - n_+ = -\frac{2\beta e^{\beta\mu}}{Z|_{h\to 0}}h + \mathcal{O}(h^3), \tag{4.95a}$$

$$n_+ + n_- - 1 = \frac{\beta}{Z|_{\mu\to u/2}}(2\mu - u) + \mathcal{O}[(2\mu - u)^3], \tag{4.95b}$$

we obtain the following limits:

$$\lim_{h\to 0}\tilde{\eta}_a^{\uparrow\downarrow}(\omega) = -\frac{u^2\beta\delta_\omega}{Z|_{h\to 0}}e^{\beta\mu}, \quad \lim_{\mu\to u/2}\tilde{\eta}_p^{\uparrow\downarrow}(\omega) = \frac{u^2\beta\delta_\omega}{Z|_{\mu\to u/2}}. \tag{4.96}$$

After exploiting the symmetry relations (cf. Sec. 4.1.2), there are four independent Hedin vertices $\bar{\lambda}_a^{\uparrow\downarrow}, \bar{\lambda}_a^{\hat{\uparrow}\downarrow}, \bar{\lambda}_a^{\uparrow\uparrow}, \bar{\lambda}_p^{\uparrow\downarrow}$, which are determined from the three-point susceptibilities $\bar{\chi}_r^{(3)}$, Eqs. (4.80):

$$[\bar{\chi}_a^{(3)}]^{\uparrow\downarrow}(\omega, \nu) = \Pi_a^{\uparrow\downarrow}(\omega, \nu) + \frac{u^2(e^{\beta(2\mu-u)} - e^{2\beta\mu})}{Z^2 x_+(\nu)y_+(\nu)x_-(\omega+\nu)y_-(\omega+\nu)}$$
$$+ \frac{1}{Z}\frac{u}{2h - i\omega}\left[\frac{e^{\beta(\mu+h)}}{x_+(\nu)y_-(\omega+\nu)} - \frac{e^{\beta(\mu-h)}}{y_+(\nu)x_-(\omega+\nu)}\right], \tag{4.97a}$$

$$[\bar{\chi}_a^{(3)}]^{\hat{\uparrow}\downarrow}(\omega, \nu) = \frac{u\beta\delta_\omega}{x_+(\nu)y_+(\nu)}(n_- - 1)n_-, \tag{4.97b}$$

$$[\bar{\chi}_a^{(3)}]^{\uparrow\uparrow}(\omega, \nu) = \Pi_a^{\uparrow\uparrow}(\omega, \nu) + \frac{u^2(1 - n_-)n_-}{x_+(\nu)y_+(\nu)x_+(\omega+\nu)y_+(\omega+\nu)}$$
$$+ \frac{u\beta\delta_\omega}{Z^2 x_+(\nu)y_+(\nu)}(e^{2\beta\mu} - e^{\beta(2\mu-u)}), \tag{4.97c}$$

$$[\bar{\chi}_p^{(3)}]^{\uparrow\downarrow}(\omega, \nu) = \tfrac{1}{2}\Pi_p^{\uparrow\downarrow}(\omega, \nu) + \frac{u^2(e^{\beta(2\mu-u)} - e^{2\beta\mu})}{4Z^2 x_+(-\nu)y_+(-\nu)x_-(\omega+\nu)y_-(\omega+\nu)} \tag{4.97d}$$
$$+ \frac{1}{4Z}\frac{u}{u - 2\mu - i\omega}\left[\frac{e^{\beta(2\mu-u)}}{y_+(-\nu)y_-(\omega+\nu)} - \frac{1}{x_+(-\nu)x_-(\omega+\nu)}\right].$$

Since the three-point susceptibilities $\bar{\chi}_r^{(3)}, \chi_r^{(3)}$ fulfill the same symmetries as the Hedin vertices $\bar{\lambda}_r, \lambda_r$, the components for the other susceptibility $\chi_r^{(3)}$ can be deduced from the

components of $\bar{\chi}_r^{(3)}$ [cf. Eqs. (4.49)]:

$$[\chi_a^{(3)}]^{\uparrow\downarrow}(\omega, \nu') = [\bar{\chi}_a^{(3)}]^{\uparrow\downarrow}(\omega, \nu'), \quad [\chi_a^{(3)}]^{\hat{\uparrow}\downarrow}(\omega, \nu') = [\bar{\chi}_a^{(3)}]^{\downarrow\uparrow}(\omega, \nu'), \tag{4.98a}$$

$$[\chi_a^{(3)}]^{\uparrow\uparrow}(\omega, \nu') = [\bar{\chi}_a^{(3)}]^{\uparrow\uparrow}(\omega, \nu'), \quad [\chi_p^{(3)}]^{\uparrow\downarrow}(\omega, \nu') = [\bar{\chi}_p^{(3)}]^{\uparrow\downarrow}(\omega, \nu'). \tag{4.98b}$$

Similarly to Eq. (4.96), the limits of zero magnetic field and half filling are non-trivial for the $\uparrow\downarrow$ component in the a and p channels. Additional Kronecker delta symbols δ_ω are generated since $2h - \mathrm{i}\omega$ and $u - 2\mu - \mathrm{i}\omega$ appear in the denominator of some terms. The Hedin vertices are calculated according to Eqs. (4.84)–(4.85), which is not explicitly shown here since the expressions are lengthy.

The connected parts of the four-point correlation functions $G^{(4)}$, Eqs. (3.7), are given by[2]

$$[G_{\mathrm{con}}^{(4)}]^{\uparrow\downarrow}(\nu_1, \nu_2, \nu_4, \nu_3) = \langle c_\uparrow(\nu_1) c_\downarrow(\nu_2) \bar{c}_\downarrow(\nu_3) \bar{c}_\uparrow(\nu_4) \rangle - \beta \delta_{\nu_1 \nu_4} G^\uparrow(\nu_1) G^\downarrow(\nu_2)$$

$$= \frac{u^2}{Z^2} \beta \delta_{\nu_2 \nu_3} \frac{\mathrm{e}^{\beta(2\mu - u)} - \mathrm{e}^{2\beta\mu}}{x_+(\nu_1) y_+(\nu_1) x_-(\nu_2) y_-(\nu_2)} \tag{4.99a}$$

$$+ \frac{u}{Z} \frac{1}{\mathrm{i}(\nu_1 + \nu_2) + 2\mu - u} \left[\frac{\mathrm{e}^{\beta(2\mu - u)}(2u - 2\mu - \mathrm{i}(\nu_1 + \nu_2))}{y_+(\nu_1) y_-(\nu_2) y_-(\nu_3) y_+(\nu_4)} - \frac{2\mu + \mathrm{i}(\nu_1 + \nu_2)}{x_+(\nu_1) x_-(\nu_2) x_-(\nu_3) x_+(\nu_4)} \right]$$

$$+ \frac{u}{Z} \frac{1}{\mathrm{i}(\nu_3 - \nu_1) - 2h} \left[\frac{\mathrm{e}^{\beta(\mu + h)}(2h + u - \mathrm{i}(\nu_3 - \nu_1))}{x_+(\nu_1) y_-(\nu_2) y_-(\nu_3) x_+(\nu_4)} + \frac{\mathrm{e}^{\beta(\mu - h)}(2h - u - \mathrm{i}(\nu_3 - \nu_1))}{y_+(\nu_1) x_-(\nu_2) x_-(\nu_3) y_+(\nu_4)} \right],$$

$$[G_{\mathrm{con}}^{(4)}]^{\hat{\uparrow}\downarrow}(\nu_1, \nu_2, \nu_4, \nu_3) = \langle c_\uparrow(\nu_1) c_\downarrow(\nu_2) \bar{c}_\uparrow(\nu_3) \bar{c}_\downarrow(\nu_4) \rangle + \beta \delta_{\nu_1 \nu_3} G^\uparrow(\nu_1) G^\downarrow(\nu_2)$$

$$= -[G_{\mathrm{con}}^{(4)}]^{\uparrow\downarrow}(\nu_1, \nu_2, \nu_3, \nu_4), \tag{4.99b}$$

$$[G_{\mathrm{con}}^{(4)}]^{\uparrow\uparrow}(\nu_1, \nu_2, \nu_4, \nu_3) = \langle c_\uparrow(\nu_1) c_\uparrow(\nu_2) \bar{c}_\uparrow(\nu_3) \bar{c}_\uparrow(\nu_4) \rangle + \beta(\delta_{\nu_1 \nu_3} - \delta_{\nu_1 \nu_4}) G^\uparrow(\nu_1) G^\uparrow(\nu_2)$$

$$= \beta u^2 (\delta_{\nu_2 \nu_3} - \delta_{\nu_1 \nu_3}) \frac{n_-(1 - n_-)}{x_+(\nu_1) y_+(\nu_1) x_+(\nu_2) y_+(\nu_2)}. \tag{4.99c}$$

A specification to the channel-dependent frequency parametrization [cf. Fig. 4.1 and Eqs. (4.72)] is straightforward by substituting the frequencies with ω, ν, ν' accordingly. In the limit of half-filling $\mu \to U/2$ a term including $\delta_{\nu_1 + \nu_2}$ is generated for $[G_{\mathrm{con}}^{(4)}]^{\uparrow\downarrow}$ and $[G_{\mathrm{con}}^{(4)}]^{\hat{\uparrow}\downarrow}$. Similarly, in the limit of zero magnetic field $h \to 0$ a term including $\delta_{\nu_1 \nu_3}$ occurs (cf. App. C.5).

According to Eqs. (3.7), the four-point vertices $\Gamma^{\uparrow\downarrow}, \Gamma^{\hat{\uparrow}\downarrow}, \Gamma^{\uparrow\uparrow}$ result from the connected four-point correlation functions $G_{\mathrm{con}}^{(4)}$, Eqs. (4.99), by dividing the terms by the corresponding product of four Green's functions. Only for the $\uparrow\uparrow$ component such an expression is

---

[2]Tremblay's correlation function $G_{\downarrow\uparrow,\downarrow\uparrow}^{\mathrm{IIc}}(\nu_1, \nu_2, (\nu_4), \nu_3)$ [PST00] coincides with our $[G_{\mathrm{con}}^{(4)}]^{\downarrow\uparrow}(\nu_1, \nu_2, \nu_4, \nu_3)$ and Rohringer's correlation function $G_{2,\uparrow\downarrow}(\nu, \nu + \omega, \nu' + \omega)$ [Roh13] corresponds to our $-G_t^{\uparrow\downarrow}(\omega, \nu', \nu)$, Eq. (4.72c), for the SU(2)-symmetric case. This is due to slightly different conventions used in these references.

relatively compact:

$$\Gamma^{\uparrow\uparrow}(\nu_1, \nu_2, \nu_4, \nu_3) = \frac{[G_{\mathrm{con}}^{(4)}]^{\uparrow\uparrow}(\nu_1, \nu_2, \nu_4, \nu_3)}{G^{\uparrow}(\nu_1)G^{\uparrow}(\nu_2)G^{\uparrow}(\nu_3)G^{\uparrow}(\nu_4)}$$

$$= \beta u^2 (\delta_{\nu_2\nu_3} - \delta_{\nu_1\nu_3})\frac{n_-(1-n_-)x_+(\nu_1)y_+(\nu_1)x_+(\nu_2)y_+(\nu_2)}{(y_+(\nu_1) + un_-)^2(y_+(\nu_2) + un_-)^2}. \quad (4.100)$$

The other components are obtained analogously.

To conclude, we found exact expressions for the SBE vertices, which provides a significant benchmark for our numerical implementations (cf. Sec. 4.3). More explicitly, we have closed forms of the fermionic propagators G, Eq. (4.91), the self-energies Σ, Eq. (4.93), the bosonic propagators η_r, Eqs. (4.94), the three-point susceptibilities $\bar{\chi}_r^{(3)}$, Eqs. (4.97), and the connected four-point correlation functions $G_{\mathrm{con}}^{(4)}$, Eqs. (4.99). Expressions for the Hedin vertices $\bar{\lambda}_r, \lambda_r$ and the full vertices Γ as well as the U-reducible vertices $\nabla_r = \bar{\lambda}_r \bullet \eta_r \bullet \lambda_r$ and U-irreducible vertices $T_r = \Gamma - \nabla_r$ are obtained from those by algebraic relations (cf. Secs. 4.1 and 4.3). However, a decomposition with respect to two-particle reducibility, i.e., the original parquet decomposition, would require an inversion of the Bethe–Salpeter equations (4.12), which is challenging and goes beyond our analysis. For the simpler case of the Hubbard atom without a magnetic field and at half filling, it is possible to find closed expressions for the two-particle reducible γ_r and irreducible vertices I_r using special matrix identities [TGCR18]. This method has not yet been conducted in the more general case considered here [cf. Eqs. (4.86)]. In other words, we cannot provide closed expressions for the MBE vertices M_r and therefore not for γ_r, either. Finally, we want to mention that we gave all our expressions in terms of the spin components $\uparrow\downarrow, \hat{\uparrow}\downarrow, \uparrow\uparrow$. It is possible to diagonalize these into physically more intuitive components [ERST24].

Figures 4.5–4.9 show the frequency dependencies of the vertex functions. The one-dimensional quantities $G^{\uparrow/\downarrow}(\nu)$, Eq. (4.91), $\tilde{\Sigma}^{\uparrow/\downarrow}(\nu)$, Eq. (4.93), and $\tilde{\eta}_r(\omega)$, Eqs. (4.94), are presented in Figs. 4.5 and 4.6. The differences between the individual spin components become obvious. Figure 4.7 shows the spin components of the two-dimensional Hedin vertices $\tilde{\lambda}_r(\omega, \nu')$, which are obtained from the susceptibilities $\bar{\chi}_r^{(3)}(\omega, \nu')$, Eqs. (4.97), using Eqs. (4.85). The main features only appear in the vicinity of the axes and diagonals, i.e., near $\omega = 0$, $\nu' = \pm\pi T$, $\nu' = \pm\omega \pm \pi T$. The same is valid for the totally U-irreducible vertex I_U shown in Fig. 4.8 and the channel-specific U-irreducible vertices T_r shown in Fig. 4.9. As discussed in Sec. 4.2, we decided to save the data for T_r in huge container to reduce computation time. The downside of this strategy is that the data containers for T_r need a lot of memory. It is discouraging that especially those vertices exhibit a rather simple structure. We hope that compressing methods such as the quantics tensor cross interpolation [RFW+24, FRJ+24, RRS+24] may offer a better alternative of saving higher-dimensional vertex functions in the future.

In App. C.5, we briefly relate our expressions (4.93)–(4.100) to the symmetric Hubbard
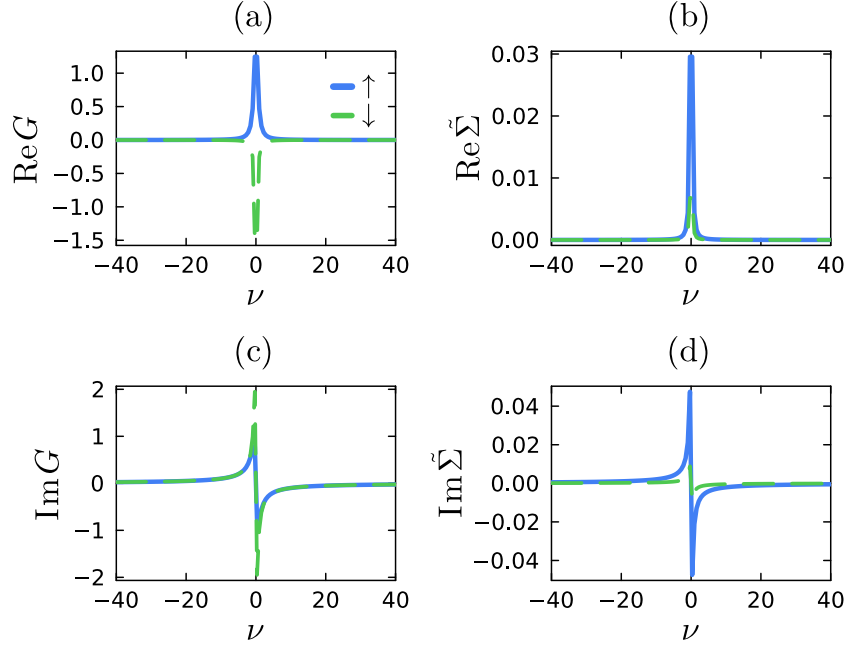
Figure 4.5.: Spin components of the Green's function G and self-energy $\tilde{\Sigma}$, belonging to the Hubbard atom with $T = 0.1$, $u = 0.5$, $\mu = 0.45$ and $h = 0.2$. The Hartree terms are given as $\Sigma_H^\uparrow \simeq 0.046$ and $\Sigma_H^\downarrow \simeq 0.491$.

atom at half filling $\mu = u/2$ and without a magnetic field $h = 0$, which is widely discussed in the literature [Roh13, TGCR18, SCC$^+$20, HSS23, Roh23, RRS$^+$24]. In that special case, the system obeys the SU(2) spin symmetry, which yields a single spin component for the Green's function $G^\uparrow = G^\downarrow$ and greatly simplifies the structure of the four-point vertex:

$$\Gamma^{\uparrow\downarrow} = \Gamma^{\downarrow\uparrow}, \quad \Gamma^{\uparrow\hat{\downarrow}} = \Gamma^{\downarrow\hat{\uparrow}}, \quad \Gamma^{\uparrow\uparrow} = \Gamma^{\downarrow\downarrow}, \quad \Gamma^{\uparrow\uparrow} = \Gamma^{\uparrow\downarrow} + \Gamma^{\uparrow\hat{\downarrow}}. \tag{4.101}$$

Consequently, it is more suitable to work in so-called *physical channels*. Following App. E in Ref. [P1], we define the *charge* ch, *spin* sp, *triplet* tr, and *singlet* sp channel as linear combinations over the spin components $\uparrow\downarrow, \uparrow\hat{\downarrow}, \uparrow\uparrow$:

$$\Gamma^{\text{ch/sp}} = \Gamma_t^{\uparrow\uparrow} \pm \Gamma_t^{\uparrow\downarrow}, \quad \Gamma^{\text{tr/si}} = \Gamma_p^{\uparrow\downarrow} \pm \Gamma_p^{\uparrow\hat{\downarrow}}. \tag{4.102}$$

These relations hold for all vertices appearing in the SBE formalism. The SBE equations obtain a diagonal form when written in these spin components (cf. App. C.5). Since the vertex functions of the general Hubbard atom contain denominators such as $u - 2\mu - i\omega$ and $h - i\omega$, one has to be careful while taking the limits $\mu \to u/2$ and $h \to 0$ [cf. Eq. (4.96)].
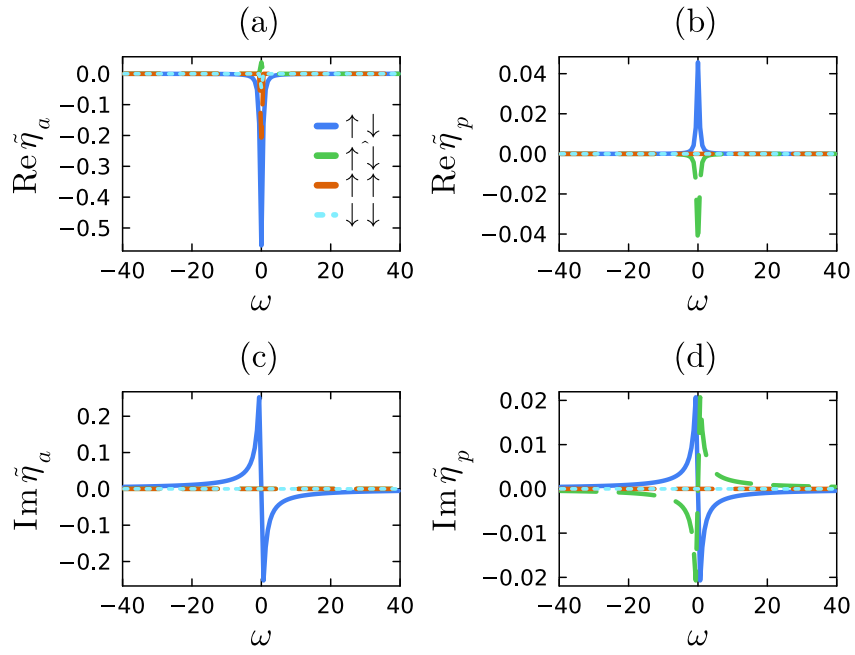
Figure 4.6.: Spin components of the bosonic propagators $\tilde{\eta}_a$ and $\tilde{\eta}_p$, belonging to the Hubbard atom with $T = 0.1$, $u = 0.5$, $\mu = 0.45$ and $h = 0.2$.
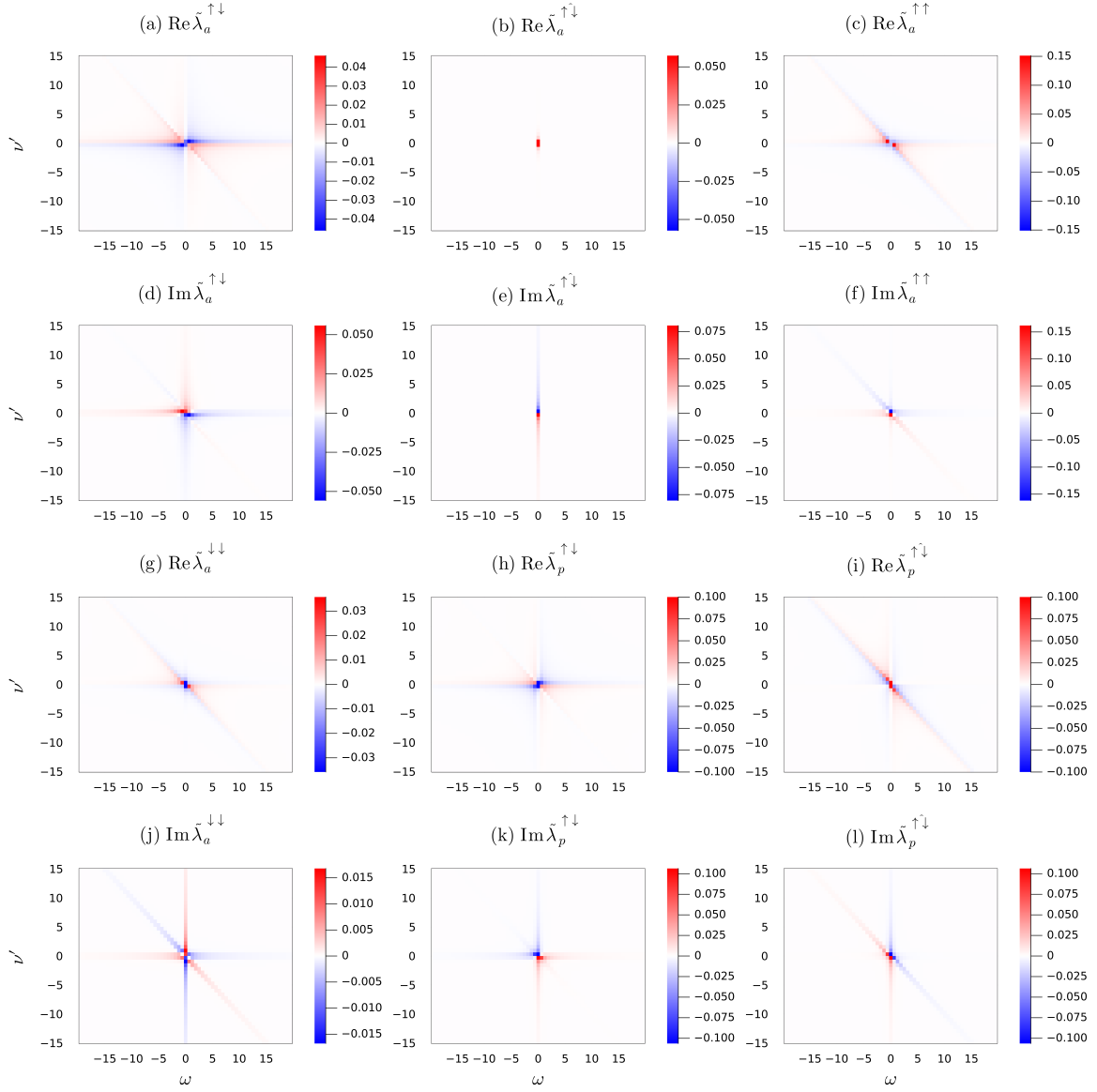
Figure 4.7.: Spin components of the two-dimensional Hedin vertices $\widetilde{\lambda}_a$ and $\widetilde{\lambda}_p$, belonging to the Hubbard atom with $T = 0.1$, $u = 0.5$, $\mu = 0.45$ and $h = 0.2$.
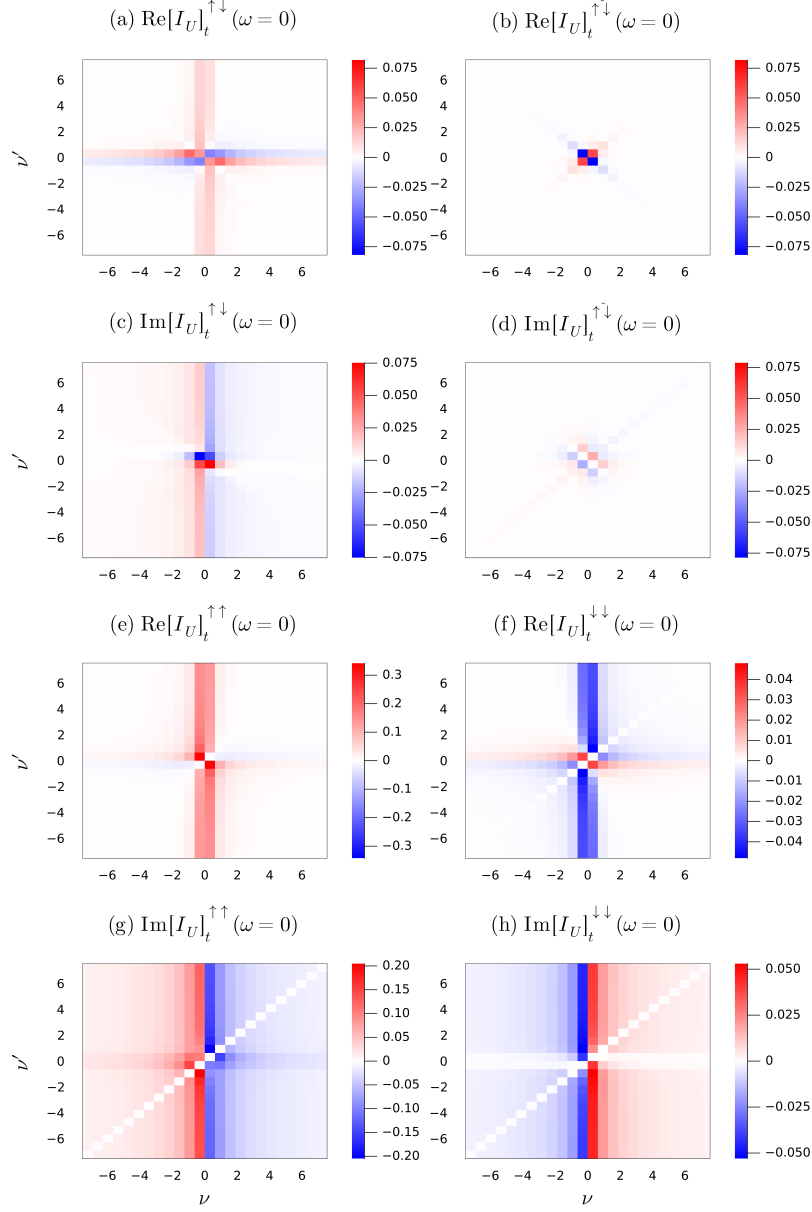
Figure 4.8.: Spin components of the U-irreducible rest function $I_U = \Gamma - \sum_r \bar{\lambda}_r \bullet \eta_r \bullet \lambda_r + 2U$, parametrized in the t channel and evaluated at bosonic frequency $\omega = 0$, belonging to the Hubbard atom with $T = 0.1$, $u = 0.5$, $\mu = 0.45$ and $h = 0.2$.
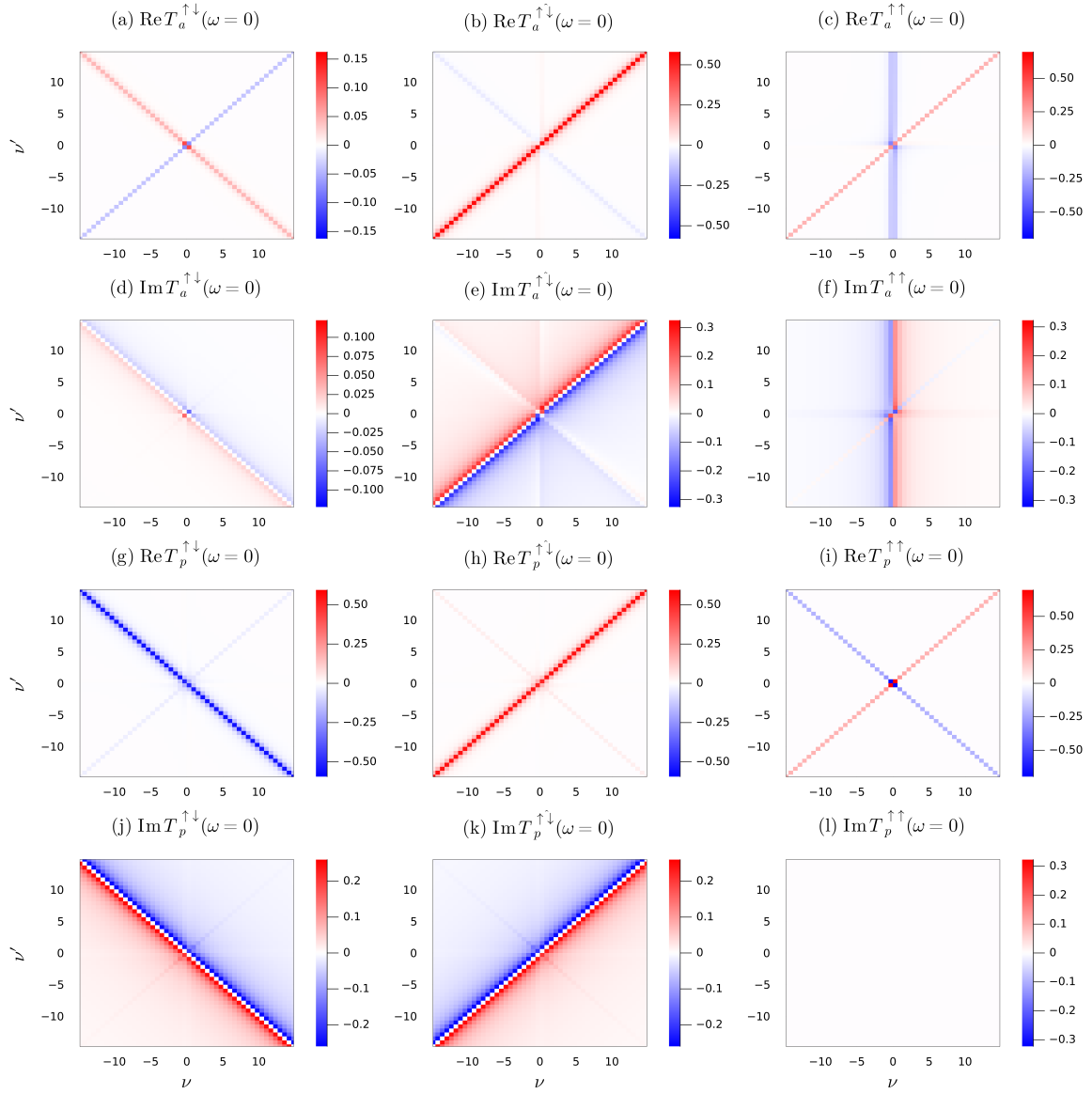
Figure 4.9.: Spin components of the U-irreducible vertices T_a and T_p evaluated at bosonic frequency $\omega = 0$, belonging to the Hubbard atom with $T = 0.1$, $u = 0.5$, $\mu = 0.45$ and $h = 0.2$.

4.5. Application: SBE fRG for the Hubbard model

4.5.1. Overview

In the previous sections, we have provided many details about the SBE formalism for systems with a Hubbard-like interaction U and two particle types $\uparrow$ and $\downarrow$. In particular, we discussed the spin structure of the self-consistent SBE equations and the symmetry relations satisfied by the SBE vertices. We presented our code to solve the SBE equations, which we successfully benchmarked with the exact formulas of a single Hubbard site at arbitrary filling and in an external magnetic field in z direction.

In the paper below, we demonstrate that our formalism is suited for more relevant models, explicitly the two-dimensional Hubbard model, which is one of the most important models in solid-state physics as its extensions might explain high-temperature superconductivity in cuprates [SWS$^+$21]. Basically, the single Hubbard site, Eq. (4.86), is extended by lattice indices i, j for the fermionic operators $\hat{c}_i^\dagger, \hat{c}_i$ and hopping parameters t_{ij} between two sites $i \leftrightarrow j$ (mostly, only up to next-nearest neighbor hopping is taken into account). The Hamiltonian of the Hubbard model reads

$$\hat{H} = -\sum_{i,j,\sigma} t_{ij} \left(\hat{c}_{i,\sigma}^\dagger \hat{c}_{j,\sigma} + \hat{c}_{j,\sigma}^\dagger \hat{c}_{i,\sigma} \right) + U \sum_i \hat{n}_{i,\uparrow} \hat{n}_{i,\downarrow}, \tag{4.103}$$

where $\sigma = \uparrow, \downarrow$ and $\hat{n}_{i,\sigma} = \hat{c}_{i,\sigma}^\dagger \hat{c}_{i,\sigma}$. The additional difficulty is that the Hubbard model involves a momentum dependence of the operators $\hat{c}_{\boldsymbol{k}}^\dagger, \hat{c}_{\boldsymbol{k}}$, which is transferred to all the vertex functions.

A numerical integration over the two-dimensional momenta in the whole first Brillouin zone is almost intractable. That is why the momentum-dependent four-point vertex $\Gamma(\boldsymbol{q}, \boldsymbol{k}, \boldsymbol{k}')$ is expanded in form factors $f_l(\boldsymbol{k})$, which respect symmetries of the lattice:

$$\Gamma(\boldsymbol{q}, \boldsymbol{k}, \boldsymbol{k}') = \sum_{l,l'} f_l^*(\boldsymbol{k}) \Gamma_{l,l'}(\boldsymbol{q}) f_{l'}(\boldsymbol{k}'), \quad \sum_l f_l^*(\boldsymbol{k}) f_l(\boldsymbol{k}') = \delta_{\boldsymbol{k}, \boldsymbol{k}'}. \tag{4.104}$$

If chosen appropriately, one aims to describe the relevant physics with only a few form factors such that the above summations can be truncated, which tremendously lowers the numerical costs. So called *truncated unity* solvers were originally and successfully applied in fRG approaches [HS09, LPR$^+$17] and more recently used in the parquet formalism [ESEH18, EHHK20].

In the work below, special emphasis is put on the computation of the self-energy in the SBE formulation (cf. Secs. 3.4.3 and 4.1.3). Using our numerical code presented in Sec. 4.2, we saw that the Schwinger–Dyson equation (4.57) in terms of the SBE vertices yields the same results for the different diagrammatic channels $r = a, p, t$. The investigations below, which include momentum variables, however, show that the truncated unity approach in the momentum summations may spoil the results for the self-energy and vertex quantities.

There, the final results for the self-energy differ depending on which channels are used in the differentiated Schwinger–Dyson equation.

The paper [P4] uses slightly different notations. The diagrammatic channels a, p, t are denoted as $\overline{ph}, pp, ph$, the full vertex Γ as V, and the bosonic propagator η_r as w_r. The physical channels $\mathrm{ch}, \mathrm{sp}, \mathrm{si}, \mathrm{tr}$, Eq. (4.102), used in the SU(2)-symmetric case are denoted as $\mathrm{C}, \mathrm{M}, \mathrm{s}, \mathrm{t}$.

Single-boson exchange formulation of the Schwinger–Dyson equation and its application to the functional renormalization group

by

M. Patricolo[1,2,3], M. Gievers[4,5], K. Fraboulet[1,6], A. Al-Eryani[7], S. Heinzelmann[6],

P. M. Bonetti[3,8], A. Toschi[2], D. Vilardi[3], and S. Andergassen[1,2]

[1] Institute of Information Systems Engineering, Vienna University of Technology, Vienna, Austria

[2] Institute for Solid State Physics, Vienna University of Technology, Vienna, Austria

[3] Max Planck Institute for Solid State Research, Heisenbergstrasse 1, Stuttgart, Germany

[4] Arnold Sommerfeld Center for Theoretical Physics, Center for NanoScience, and Munich Center for Quantum Science and Technology, Ludwig-Maximilians-Universität München, München, Germany

[5] Max Planck Institute of Quantum Optics, Garching, Germany

[6] Institute for Theoretical Physics and Center for Quantum Science, Universität Tübingen, Tübingen, Germany

[7] Institute for Theoretical Physics III, Ruhr-University Bochum, 44801 Bochum, Germany

[8] Department of Physics, Harvard University, Cambridge MA 02138, USA

Single-boson exchange formulation of the Schwinger-Dyson equation and its application to the functional renormalization group

Miriam Patricolo[1,2,3★], Marcel Gievers[4,5], Kilian Fraboulet[1,6],
Aiman Al-Eryani[7], Sarah Heinzelmann[6], Pietro M. Bonetti[3,8],
Alessandro Toschi[2], Demetrio Vilardi[3] and Sabine Andergassen[1,2]

1 Institute of Information Systems Engineering,
Vienna University of Technology, Vienna, Austria
2 Institute for Solid State Physics, Vienna University of Technology, Vienna, Austria
3 Max Planck Institute for Solid State Research, Heisenbergstrasse 1, Stuttgart, Germany
4 Arnold Sommerfeld Center for Theoretical Physics, Center for NanoScience,
and Munich Center for Quantum Science and Technology,
Ludwig-Maximilians-Universität München, München, Germany
5 Max Planck Institute of Quantum Optics, Garching, Germany
6 Institute for Theoretical Physics and Center for Quantum Science,
Universität Tübingen, Tübingen, Germany
7 Theoretical Physics III, Ruhr-University Bochum, 44801 Bochum, Germany
8 Department of Physics, Harvard University, Cambridge MA 02138, USA

★ miriam.patricolo@tuwien.ac.at

Abstract

We extend the recently introduced single-boson exchange formulation to the computation of the self-energy from the Schwinger–Dyson equation (SDE). In particular, we derive its expression both in diagrammatic and in physical channels. The simple form of the single-boson exchange SDE, involving only the bosonic propagator and the fermion-boson vertex, but not the rest function, allows for an efficient numerical implementation. We furthermore discuss its implications in a truncated unity solver, where a restricted number of form factors introduces an information loss in the projection of the momentum dependence that in general affects the equivalence between the different channel representations. In the application to the functional renormalization group, we find that the convergence in the number of form factors depends on the channel representation of the SDE. For the two-dimensional Hubbard model at weak coupling, the pseudogap opening driven by antiferromagnetic fluctuations is captured already by a single (s-wave) form factor in the magnetic channel representation, differently to the density and superconducting channels.

Contents

1   Introduction

The recently introduced single-boson exchange decomposition [1] provides a valuable tool in the quantum field-theoretic treatment of quantum many-body systems [2–12]. It features a physically intuitive and also computationally efficient description of the relevant fluctuations in terms of processes involving the exchange of a single boson, describing a collective excitation, and a residual part containing the multiboson processes. The effective bosonic interaction is represented by bosonic propagators and fermion-boson couplings also referred to as Yukawa couplings or Hedin vertices [13] determined from the vertex asymptotics, in analogy to the construction of the kernel functions defining the high-frequency asymptotics [14].

At weak coupling, this effective bosonic interaction yields quantitatively accurate results, while the multiboson contributions are irrelevant and can be neglected [15], allowing for a substantial reduction of the computational complexity of the vertex function: Since the multiboson processes are the only ones to depend on three independent momentum and frequency variables, neglecting them drastically reduces the computational complexity of the problem. In contrast, the bosonic propagators and fermion-boson couplings depend on one and two independent arguments, respectively, and therefore their numerical treatment including the full momentum and frequency dependence is much less demanding.

At strong coupling, the advantages of the single-boson exchange formalism are particularly prominent in the non-perturbative regime of intermediate to strong electron-electron interaction. In fact, these interaction values lead to multiple divergences in the two-particle irreducible vertex functions [16–30], which makes the applicability of conventional Bethe–Salpeter equations and/or parquet formalism [31,32] beyond the weak-coupling regime rather problematic. In the single-boson exchange formulation of the diagrammatics, instead, the corresponding irreducible vertex functions are defined in a different way: They are obtained from

the difference between the full vertex and the single-boson exchange diagrams, each of which is composed of diagrams that correspond to physical correlators up to an amputation of the external legs. Beyond providing a much more transparent link to the underlying physics than the parquet formalism, no diagrammatic element of the single-boson exchange decompositions of the vertex function displays [1, 2] the non-perturbative divergencies which plague their parquet counterparts.

We here provide a unified framework for the consistent derivation of the Schwinger–Dyson equation (SDE) for the self-energy in the single-boson exchange formulation. Its simpler form involves only the bosonic propagator and the fermion-boson vertex in a single channel and not the rest function. Moreover, the expression for the SDE derived within the single-boson exchange formalism has a one-loop structure, making its evaluation easier than the standard textbook expression. Notably, the possibility of using different but equivalent self-energy formulations in the various channels does not depend on a specific choice of the Fierz decoupling parameter, which is related to the Fierz ambiguity [33]. Moreover, the change of representation of the Schwinger–Dyson equation in the resulting triangular form is particularly useful for the postprocessing tool of the fluctuation diagnostic, which enables the quantification of the different fluctuation contributions. Specifically, this approach avoids the need for partial summations required in earlier methods [34–38]. On a more practical perspective, we also discuss the relevant implications for truncated unity (TU) solvers [4, 39–44], where the information loss in the form-factor projection of the momentum dependence generally affects the equivalence between the different channel representations. Specifically, we apply the single-boson exchange expression for the SDE to the functional renormalization group (fRG) [45, 46] and demonstrate that the self-energy flow determined by its derivative [47] captures the pseudogap opening in the two-dimensional (2D) Hubbard model at weak coupling. However, the different channel representations of the SDE converge differently in the number of form factors. The antiferromagnetic fluctuations dominating at half filling are best described in the magnetic channel in which the onset of the pseudogap opening is captured by using only the s-wave form factor.

The paper is structured as follows: we first introduce the formalism in Section 2. Specifically, the presented matrix representation of the spin structure allows for a compact notation to efficiently sum over the involved variables and indices, the technical details are reported in Appendix A. After a brief review of the single-boson exchange representation, we derive the form of the SDE as the main result of the present work. In Section 3, we showcase the application to the fRG. We present results for the 2D Hubbard model at weak coupling and discuss the implications arising in the implementation with TU solvers. Finally, we provide a summary of our findings and conclusions in Section 4.

2 Single-boson exchange formulation of the SDE

2.1 Conventional SDE and matrix formalism

Before reviewing the single-boson exchange representation, we present the formalism [9] applicable to any lattice fermion system with the classical action of the form

$$S[\bar{c}, c] = -\bar{c}_{1'} G^{-1}_{0;1'|1} c_1 - \frac{1}{4} U_{1'2'|12} \bar{c}_{1'} \bar{c}_{2'} c_2 c_1 \,. \tag{1}$$

The numbers $1', 2', 1, 2$ labelling the Grassmann fields c_i represent generic indices, which enclose spin components, momenta, and Matsubara frequencies. For these, we use Einstein's convention, i.e., repeated indices are summed over. Furthermore, G_0 denotes the bare propagator and U the crossing-symmetric [31, 32] bare interaction vertex $U_{1'2'|12} = -U_{2'1'|12} = -U_{1'2'|21}$.

We assume energy conservation and translational invariance resulting in momentum and frequency conservation.

The conventional form of the SDE for the self-energy is the main subject of the present work and reads [31, 32]

$$\Sigma_{1'|1} = -U_{1'2'|12}G_{2|2'} - \frac{1}{2}U_{1'3'|42}G_{2|2'}G_{3|3'}G_{4|4'}V_{4'2'|13} \, . \tag{2}$$

Here, V is the full four-point interaction vertex. Equation (2) represents the starting point for the derivation of its single-boson exchange formulation, as presented in the next sections. The products of the Green's functions define the bubbles in a given channel

$$\Pi_{ph;12|34} = -G_{2|3}G_{1|4} \, , \qquad \Pi_{\overline{ph};12|34} = G_{1|3}G_{2|4} \, , \qquad \Pi_{pp;12|34} = \frac{1}{2}G_{1|3}G_{2|4} \, . \tag{3}$$

With these definitions, Eq. (2) can be rewritten as

$$
\begin{aligned}
\Sigma_{1'|1} &= -U_{1'2'|12}G_{2|2'} + \frac{1}{2}G_{4|4'}U_{1'3'|42}\Pi_{ph;32|2'3'}V_{4'2'|13} \\
&= -U_{1'2'|12}G_{2|2'} + \frac{1}{2}G_{4|4'}U_{3'1'|24}\big[\Pi_{ph} \circ V\big]_{4'2|13'} \\
&= U_{2'1'|12}G_{2|2'} + \frac{1}{2}G_{4|4'}\big[U \circ \Pi_{ph} \circ V\big]_{4'1'|14} \, ,
\end{aligned}
\tag{4}
$$

in the ph channel. Omitting the indices, yields the compact form

$$\Sigma = G \cdot \left(U + \frac{1}{2}\big[U \circ \Pi_{ph} \circ V\big]\right) \, , \tag{5}$$

where we introduced the ∘ product indicating the summation over spin indices, momenta, and frequencies [9, 48]. The channel-dependent product of four-point functions A and B is defined by

$$
\begin{aligned}
ph \quad &: \quad [A \circ B]_{12|34} = A_{62|54}B_{15|36} \, , & \tag{6a} \\
\overline{ph} \quad &: \quad [A \circ B]_{12|34} = A_{16|54}B_{52|36} \, , & \tag{6b} \\
pp \quad &: \quad [A \circ B]_{12|34} = A_{12|56}B_{56|34} \, . & \tag{6c}
\end{aligned}
$$

Note that the product can be represented by matrices, see Appendix A for details. We furthermore used the product involving a (two-point) Green's function G defined by

$$[A \cdot G]_{1'|1} = A_{1'2'|12}G_{2|2'} = -G_{2|2'}A_{2'1'|12} = -[G \cdot A]_{1'|1} \, . \tag{7}$$

For the definition of the loop product ·, the order of G and A is decisive since we absorb a minus sign originating from the crossing symmetry of the vertex A. Analogously, we can rewrite the second term on the right-hand side of Eq. (2) in the other diagrammatic channels. We obtain

$$
\begin{aligned}
U_{1'3'|42}G_{2|2'}G_{3|3'}G_{4|4'}V_{4'2'|13} &= G_{2|2'}U_{1'3'|42}\Pi_{\overline{ph};34|3'4'}V_{4'2'|13} \\
&= G_{2|2'}\big[U \circ \Pi_{\overline{ph}} \circ V\big]_{1'2'|12} \, ,
\end{aligned}
\tag{8}
$$

for the $\overline{ph}$ channel and

$$
\begin{aligned}
U_{1'3'|42}G_{2|2'}G_{3|3'}G_{4|4'}V_{4'2'|13} &= U_{1'3'|42}G_{3|3'}2\Pi_{pp;24|2'4'}V_{4'2'|13} \\
&= G_{3|3'}\big[U \circ 2\Pi_{pp} \circ V\big]_{1'3'|13} \, ,
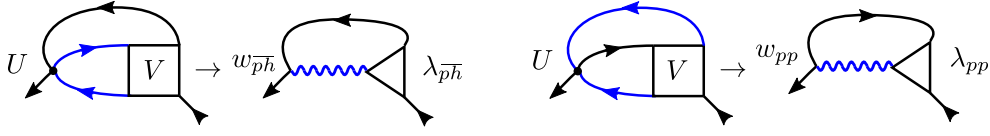\end{aligned}
\tag{9}
$$

Figure 1: Diagrammatic representation of the SDE for the self-energy: We show the diagram in the conventional form and the corresponding respresentation in single-boson exchange formalism in the $\overline{ph}$ and pp channel (without the Hartree term).

for the pp channel. Thus, Eq. (5) can be expressed equivalently as

$$\Sigma = -\left(U + \frac{1}{2}[U \circ \Pi_{\overline{ph}} \circ V] \right) \cdot G \tag{10a}$$

$$= -\left(U + [U \circ \Pi_{pp} \circ V] \right) \cdot G, \tag{10b}$$

see Fig. 1 for their diagrammatic representation. We note that the sign change in the Hartree term is due to the reverted order of the product, see also Eq. (7). Equations (5) and (10) are the starting point for the derivation of the SDE in the single-boson exchange representation.

2.2 Single-boson exchange representation

The single-boson exchange decomposition of the two-particle vertex is based on an alternative notion of reducibility, known as U reducibility, where U is the bare interaction [1]. The concept builds on the observation of the primary bosonic dependence of diagrams and their interpretation as exchange of a single boson. Diagrams falling into this category are termed U-reducible as they can be divided into two parts by cutting a bare interaction. Conversely, diagrams that cannot be divided this way are termed U irreducible. Similarly to the two-particle reducibility underlying the classification of diagrams in the parquet formalism [31, 32], the U-reducible diagrams can be further categorized on whether the two lines connected to the bare interaction are particle-particle (pp), particle-hole (ph), or particle-hole crossed ($\overline{ph}$) lines. Note that a U-reducible diagram is also two-particle reducible, with the exception of the bare interaction itself, which is considered U-reducible in all three channels.

Exploiting momentum and frequency conservation for one-particle correlators, such as the Green's function, gives

$$G_{\sigma_{1'}|\sigma_1}(k_{1'}|k_1) = \delta_{\sigma_{1'}|\sigma_1}\delta_{\mathbf{k}_{1'},\mathbf{k}_1}\delta_{\nu_{1'},\nu_1}G_{\sigma_{1'},\sigma_1}(k_1). \tag{11}$$

For two-particle objects, such as the full two-particle vertex, we have

$$V_{\sigma_{1'}\sigma_{2'}|\sigma_1\sigma_2}(k_{1'},k_{2'}|k_1,k_2) = \delta_{\mathbf{k}_{1'}+\mathbf{k}_{2'},\mathbf{k}_1+\mathbf{k}_2}\delta_{\nu_{1'}+\nu_{2'},\nu_1+\nu_2}V_{\sigma_{1'}\sigma_{2'}|\sigma_1\sigma_2}(Q_r,k_r,k_r'), \tag{12}$$

where the channel r defines the bosonic $Q_r = (\mathbf{Q}_r, \Omega_r)$ and fermionic arguments $k_r = (\mathbf{k}_r, \nu_r)$ and $k_r' = (\mathbf{k}_r', \nu_r')$, see also Fig. 7 in Appendix A for the definitions of k_r and Q_r in the respective channels r.

Specifically, the latter applies also for the bare interaction vertex $U_{\sigma_{1'}\sigma_{2'}|\sigma_1\sigma_2}(k_{1'},k_{2'}|k_1,k_2)$. Through Eqs. (11)–(12), one-particle objects only depend on one momentum and frequency variable, while two-particle objects in general depend on three.

The sum of all U-reducible diagrams in a given channel $r = pp, ph, \overline{ph}$ including the bare interaction is given by

$$\nabla_r = \bar{\lambda}_r \bullet w_r \bullet \lambda_r, \tag{13}$$

where the $\bullet$ product indicates the summation over spin indices only (with the same definition as in Eqs. (6), but excluding the summation over momenta and frequencies). It represents the

exchange of a single bosonic propagator w_r between two fermion-boson couplings λ_r and $\bar{\lambda}_r$. Diagrams that are two-particle reducible, but U irreducible with respect to the channel r do not fall into this category. They are collected in the rest function M_r containing the multiboson exchange processes (see Fig. 1 in [10] and Fig. 5 in [9] as examples). In the notation introduced above, both λ_r and w_r are four-point objects with respect to the spin indices. For the reduced frequency and momentum dependence of the single-boson exchange vertices, it is essential that the bare interaction U does not depend on frequencies and momenta. In particular, this is the case for an instantaneous local U. Explicitly, the bosonic propagator $w_r = w_r(Q_r)$ then depends on a single bosonic argument and $\lambda_r = \lambda_r(Q_r, k_r)$ on both a bosonic and a fermionic argument in the presence of momentum and frequency conservation.

In the following, we will exploit the relation [9]:

$$w_r \bullet \lambda_r = U + U \circ \Pi_r \circ V \tag{14}$$

($\bar{\lambda}_r \bullet w_r = U + V \circ \Pi_r \circ U$ respectively), which is crucial in the derivation of the SDE in single-boson exchange representation. This relation applies for local interactions, while the generalization to non-local interactions is briefly discussed in Appendix B.

2.3 Derivation in diagrammatic channels

We first determine the SDE for the self-energy in diagrammatic channels. In the single-boson exchange formulation, its form turns out to be particularly simple and hence more advantageous for the numerical implementation.

For the spin $\uparrow$ component (the $\downarrow$ component is obtained straightforwardly by inverting the spin indices), Eqs. (5) and (10) for the different channels read

$$\Sigma^\uparrow = G^\downarrow \cdot U^{\widehat{\downarrow\uparrow}} + \frac{1}{2} G^\uparrow \cdot \left[U \circ \Pi_{ph} \circ V \right]^{\uparrow\uparrow} + \frac{1}{2} G^\downarrow \cdot \left[U \circ \Pi_{ph} \circ V \right]^{\widehat{\downarrow\uparrow}}, \tag{15a}$$

$$\Sigma^\uparrow = -U^{\uparrow\downarrow} \cdot G^\downarrow - \frac{1}{2} [U \circ \Pi_{\overline{ph}} \circ V]^{\uparrow\uparrow} \cdot G^\uparrow - \frac{1}{2} [U \circ \Pi_{\overline{ph}} \circ V]^{\uparrow\downarrow} \cdot G^\downarrow, \tag{15b}$$

$$\Sigma^\uparrow = -U^{\uparrow\downarrow} \cdot G^\downarrow - [U \circ \Pi_{pp} \circ V]^{\uparrow\uparrow} \cdot G^\uparrow - [U \circ \Pi_{pp} \circ V]^{\uparrow\downarrow} \cdot G^\downarrow, \tag{15c}$$

where we used $U^{\uparrow\uparrow} = 0$ for local interactions and introduced the short-hand notation

$$\Sigma^\sigma = \Sigma^{\sigma|\sigma}, \qquad U^{\sigma\sigma} = U^{\sigma\sigma|\sigma\sigma}, \qquad U^{\sigma\bar{\sigma}} = U^{\sigma\bar{\sigma}|\sigma\bar{\sigma}}, \qquad U^{\widehat{\sigma\bar{\sigma}}} = U^{\sigma\bar{\sigma}|\bar{\sigma}\sigma}, \tag{16}$$

with $\sigma = \uparrow / \downarrow$ and $\bar{\uparrow} = \downarrow$, $\bar{\downarrow} = \uparrow$. We here assume only U(1) symmetry in order to account for a magnetic field. We will restrict ourselves to the SU(2) symmetric case for the derivation in physical channels in Sec. 2.4, where we exploit $\Sigma^\uparrow = \Sigma^\downarrow$, $G^\uparrow = G^\downarrow$, $V^{\uparrow\uparrow} = V^{\uparrow\downarrow} + V^{\widehat{\uparrow\downarrow}}$ and $V^{\uparrow\downarrow} = V^{\downarrow\uparrow}$ [31,32]. In Eqs. (15), only the spin indices are reported explicitly, whereas the full momentum and frequency dependence is determined below. As a general rule, the sum in the products includes all indices except for the specified ones (in this case, the spin indices have already been summed over). In the following, we first focus on the ph channel and then extend our results to the $\overline{ph}$ and pp channels. The summation over the spin indices in Eq. (15a) yields

$$\Sigma^\uparrow = G^\downarrow \cdot U^{\widehat{\downarrow\uparrow}} + G^\downarrow \cdot U^{\widehat{\downarrow\uparrow}} \circ \Pi_{ph}^{\widehat{\downarrow\uparrow}} \circ V^{\widehat{\downarrow\uparrow}}, \tag{17}$$

where we used that $\Pi_{ph}^{\uparrow\downarrow} = 0$ due to the matrix structure and

$$G^\uparrow \cdot U^{\downarrow\uparrow} \circ \Pi_{ph}^{\downarrow\downarrow} \circ V^{\uparrow\downarrow} = G^\downarrow \cdot U^{\widehat{\downarrow\uparrow}} \circ \Pi_{ph}^{\widehat{\downarrow\uparrow}} \circ V^{\widehat{\downarrow\uparrow}}, \tag{18}$$

as a consequence of crossing symmetry. The latter is obtained by applying the relation (A.3) discussed in Appendix A to both the bare interaction U and the full vertex V.

We now express our findings in the single-boson exchange formalism. Using the relation outlined in Eq. (14), we can express the product $U^{\downarrow\uparrow} \circ \Pi_{ph}^{\downarrow\uparrow} \circ V^{\downarrow\uparrow}$ in Eq. (17) as

$$\left[U \circ \Pi_{ph} \circ V \right]^{\widehat{\downarrow\uparrow}} = \left[w_{ph} \bullet \lambda_{ph} - U \right]^{\widehat{\downarrow\uparrow}} . \tag{19}$$

Performing the spin summations yields

$$\Sigma^{\uparrow} = G^{\downarrow} \cdot (w_{ph}^{\widehat{\downarrow\uparrow}} \lambda_{ph}^{\widehat{\downarrow\uparrow}}) , \tag{20}$$

for the self-energy in the ph channel. We note that in contrast to Eq. (17), the Hartree term does not explicitly appear anymore, since it is absorbed in the translation to the single-boson exchange representation through w_{ph} and λ_{ph} by (19).

Analogous steps allow us to rewrite Eqs. (15b) and (15c) for the $\overline{ph}$ and the pp channel, respectively

$$\Sigma^{\uparrow} = -(w_{\overline{ph}}^{\uparrow\downarrow} \lambda_{\overline{ph}}^{\uparrow\downarrow}) \cdot G^{\downarrow} , \tag{21a}$$

$$\Sigma^{\uparrow} = -[w_{pp}^{\uparrow\downarrow}(2\lambda_{pp}^{\uparrow\downarrow} - 1)] \cdot G^{\downarrow} , \tag{21b}$$

where we used the relations $w_{pp}^{\widehat{\uparrow\downarrow}} = -w_{pp}^{\uparrow\downarrow}$ and $\lambda_{pp}^{\widehat{\downarrow\uparrow}} = 1 - \lambda_{pp}^{\uparrow\downarrow}$.

We note that the SDE in single-boson exchange representation can also be obtained by directly applying Eqs. (14) to Eqs. (5) and (10), yielding

$$\Sigma = -(w_r \bullet \lambda_r) \cdot G . \tag{22}$$

The corresponding diagrammatic representations are shown in Fig. 1 for the $\overline{ph}$ and pp channel representations (21). For the pp channel, the product $w_{pp} \bullet \lambda_{pp}$ is determined by

$$\begin{bmatrix} [w_{pp} \bullet \lambda_{pp}]^{\uparrow\downarrow} & [w_{pp} \bullet \lambda_{pp}]^{\widehat{\uparrow\downarrow}} \\ [w_{pp} \bullet \lambda_{pp}]^{\widehat{\downarrow\uparrow}} & [w_{pp} \bullet \lambda_{pp}]^{\downarrow\uparrow} \end{bmatrix} = w_{pp}^{\uparrow\downarrow} \begin{bmatrix} 1 & -1 \\ -1 & 1 \end{bmatrix} \begin{bmatrix} \lambda_{pp}^{\uparrow\downarrow} & -(\lambda_{pp}^{\uparrow\downarrow} - 1) \\ -(\lambda_{pp}^{\uparrow\downarrow} - 1) & \lambda_{pp}^{\downarrow\uparrow} \end{bmatrix}$$

$$= w_{pp}^{\uparrow\downarrow} \begin{bmatrix} (2\lambda_{pp}^{\uparrow\downarrow} - 1) & -(2\lambda_{pp}^{\downarrow\uparrow} - 1) \\ -(2\lambda_{pp}^{\uparrow\downarrow} - 1) & (2\lambda_{pp}^{\downarrow\uparrow} - 1) \end{bmatrix} , \tag{23}$$

where the simple forms of the matrices result from crossing symmetry, see Appendix A. Specifying the spin component, the self-energy can be read off as

$$\Sigma^{\uparrow} = -[w_{pp}^{\uparrow\downarrow}(2\lambda_{pp}^{\uparrow\downarrow} - 1)] \cdot G^{\downarrow} . \tag{24}$$

However, for the ph and $\overline{ph}$ channels the corresponding matrices have a more complex form and crossing symmetry can only be used at the level of Eqs. (15a) and (15b) to simplify the spin summations. We now provide the momentum and frequency dependence of the SDE for the self-energy in diagrammatic channels. Applying the momentum and frequency conventions, we determine the explicit forms of Eqs. (20) and (21) to be

$$\Sigma^{\uparrow}(\mathbf{k}; \nu) = \sum_{\mathbf{Q}, \Omega} w_{ph}^{\widehat{\downarrow\uparrow}}(\mathbf{Q}; \Omega) \lambda_{ph}^{\widehat{\downarrow\uparrow}}\left(\mathbf{Q}, \mathbf{k} - \mathbf{Q}; \Omega, \nu - \left[\frac{\Omega}{2} \right] \right) G^{\downarrow}(\mathbf{k} - \mathbf{Q}; \nu - \Omega) , \tag{25a}$$

$$\Sigma^{\uparrow}(\mathbf{k}; \nu) = -\sum_{\mathbf{Q}, \Omega} w_{\overline{ph}}^{\uparrow\downarrow}(\mathbf{Q}; \Omega) \lambda_{\overline{ph}}^{\uparrow\downarrow}\left(\mathbf{Q}, \mathbf{k} - \mathbf{Q}; \Omega, \nu - \left[\frac{\Omega}{2} \right] \right) G^{\downarrow}(\mathbf{k} - \mathbf{Q}; \nu - \Omega) , \tag{25b}$$

$$\Sigma^{\uparrow}(\mathbf{k}; \nu) = -\sum_{\mathbf{Q}, \Omega} w_{pp}^{\uparrow\downarrow}(\mathbf{Q}; \Omega) \left[2\lambda_{pp}^{\uparrow\downarrow}\left(\mathbf{Q}, \mathbf{Q} - \mathbf{k}; \Omega, \left[\frac{\Omega}{2} \right] - \nu \right) - 1 \right] G^{\downarrow}(\mathbf{Q} - \mathbf{k}; \Omega - \nu) , \tag{25c}$$

where the symbol $\lceil \cdots \rceil \left(\lfloor \cdots \rfloor \right)$ rounds its argument up (down) to the nearest bosonic Matsubara frequency. The corresponding equations for $\Sigma^{\downarrow}$ are obtained by reversing the spin indices. For the details on the derivation, we refer to Appendix C. Without any approximation, the three expressions of the SDE in single-boson exchange representation, Eqs. (25), are equivalent: the bosonic propagator and fermion-boson coupling from any single channel allows to reconstruct all self-energy diagrams. However, TU solvers expanding the fermionic momentum dependence in a finite number of form factors generally lead to different results for the various channels, as will be discussed below.

2.4 Derivation in physical channels

In this section, we translate the simple form of the SDE in single-boson exchange representation derived in diagrammatic channels to physical ones,[1] i.e., the magnetic, density, and superconducting channels, in which the single-boson exchange decomposition has been originally introduced [1]. These channels involve specific linear combinations of the spin components, designed to diagonalize the spin structure in the Bethe-Salpeter equations for systems with SU(2) symmetry [31, 32]. This offers interpretative advantages as it allows for a direct physical identification of the collective degrees of freedom at play.

Restricting ourselves to SU(2)-symmetric systems, in the shorthand notation introduced above, the six spin components of the full vertex reduce to $V^{\uparrow\downarrow}$, $V^{\widehat{\uparrow\downarrow}}$, $V^{\uparrow\uparrow}$, equivalent to $V^{\downarrow\uparrow}$, $V^{\widehat{\downarrow\uparrow}}$, and $V^{\downarrow\downarrow}$ respectively. Similarly, for the spin components of the self-energy and the Green's function holds $\Sigma^{\uparrow} = \Sigma^{\downarrow}$ and $G^{\uparrow} = G^{\downarrow}$. Furthermore, we have $V^{\uparrow\uparrow} = V^{\uparrow\downarrow} + V^{\widehat{\uparrow\downarrow}}$, as it follows from the definitions in Eqs. (16). We define the density, magnetic, and the superconducting channels as [49]

$$V^{\mathrm{M}} = V_{ph}^{\uparrow\uparrow} - V_{ph}^{\uparrow\downarrow} = -V_{\underline{ph}}^{\uparrow\downarrow}, \tag{26a}$$

$$V^{\mathrm{D}} = V_{ph}^{\uparrow\uparrow} + V_{ph}^{\uparrow\downarrow} = 2V_{ph}^{\uparrow\downarrow} - V_{\underline{ph}}^{\uparrow\downarrow}, \tag{26b}$$

$$V^{\mathrm{SC}} = V_{pp}^{\uparrow\downarrow}. \tag{26c}$$

The bosonic propagators w in physical channels are determined by analogous relations. The same applies for the fermion-boson couplings λ except for its expression in the superconducting channel, see below. Their inversion yields

$$w_{ph}^{\widehat{\uparrow\downarrow}} = w^{\mathrm{M}}, \qquad w_{ph}^{\uparrow\uparrow} = \frac{w^{\mathrm{M}} + w^{\mathrm{D}}}{2}, \qquad w_{ph}^{\uparrow\downarrow} = \frac{w^{\mathrm{D}} - w^{\mathrm{M}}}{2}, \qquad w_{pp}^{\uparrow\downarrow} = w^{\mathrm{SC}}, \tag{27a}$$

$$\lambda_{ph}^{\widehat{\uparrow\downarrow}} = \lambda^{\mathrm{M}}, \qquad \lambda_{ph}^{\uparrow\uparrow} = \frac{\lambda^{\mathrm{M}} + \lambda^{\mathrm{D}}}{2}, \qquad \lambda_{ph}^{\uparrow\downarrow} = \frac{\lambda^{\mathrm{D}} - \lambda^{\mathrm{M}}}{2}, \qquad \lambda_{pp}^{\uparrow\downarrow} = \frac{\lambda^{\mathrm{SC}} + 1}{2}, \tag{27b}$$

where we used the $\widehat{\uparrow\downarrow}$ component for the magnetic channel. We note that indeed $w_r^{\widehat{\uparrow\downarrow}} = w_r^{\uparrow\uparrow} - w_r^{\uparrow\downarrow}$. For the details on the superconducting fermion-boson coupling $\lambda^{\mathrm{SC}} = 2\lambda_{pp}^{\uparrow\downarrow} - 1$ differing from the corresponding one for the bosonic propagator, we refer to Appendix A. It is worth noting that the *pp* channel allows to define both the singlet and triplet pairing channels

$$V^{\mathrm{s}} = V_{pp}^{\uparrow\downarrow} - V_{pp}^{\widehat{\uparrow\downarrow}}, \qquad V^{\mathrm{t}} = V_{pp}^{\uparrow\downarrow} + V_{pp}^{\widehat{\uparrow\downarrow}}. \tag{28}$$

Thus, the definition of the SC channel is consistent with

$$V^{\mathrm{SC}} = \frac{V^{\mathrm{s}} + V^{\mathrm{t}}}{2}. \tag{29}$$

---

[1]Ref. [9] illustrates the relationship between these "physical" and the "diagrammatic" channels assuming SU(2) spin symmetry.

Equations (28) hold also for the bosonic propagators w^s, w^t and for the fermion-boson couplings λ^s, λ^t. The relation to the above expression for λ^{SC} is obtained by considering $\lambda^{\uparrow\uparrow}_{pp} = 1$, see Appendix A. The singlet channel then reads

$$\lambda^s = \lambda^{\uparrow\downarrow}_{pp} - \lambda^{\widehat{\uparrow\downarrow}}_{pp} = \lambda^{\uparrow\downarrow}_{pp} - \lambda^{\uparrow\uparrow}_{pp} + \lambda^{\uparrow\downarrow}_{pp} = 2\lambda^{\uparrow\downarrow}_{pp} - 1\,, \tag{30}$$

which encodes the superconducting channel, while $\lambda^t = \lambda^{\uparrow\downarrow}_{pp} + \lambda^{\widehat{\uparrow\downarrow}}_{pp} = 1$.

Using the relations in Eqs. (27), both the ph and $\overline{ph}$ formulations of the self-energy in Eqs. (20) and (21a) translate to

$$\Sigma = G \cdot (w^M \lambda^M)\,. \tag{31}$$

For the superconducting channel, Eq. (21b) yields

$$\Sigma = -(w^{SC} \lambda^{SC}) \cdot G\,. \tag{32}$$

In order to derive the density channel formulation, we have to start from the general form (15a). In the single-boson exchange formulation, it reads

$$\Sigma^\uparrow = \frac{1}{2} G^\downarrow \cdot U^{\widehat{\downarrow\uparrow}} + \frac{1}{2} G^\uparrow \cdot (w^{\uparrow\uparrow}_{ph} \lambda^{\uparrow\uparrow}_{ph} + w^{\downarrow\uparrow}_{ph} \lambda^{\uparrow\downarrow}_{ph}) + \frac{1}{2} G^\downarrow \cdot (w^{\widehat{\downarrow\uparrow}}_{ph} \lambda^{\widehat{\downarrow\uparrow}}_{ph})\,, \tag{33}$$

where we used Eq. (14). In presence of SU(2) symmetry, this translates to

$$\Sigma = \frac{3}{4} G \cdot (w^M \lambda^M) + \frac{1}{4} G \cdot (w^D \lambda^D) - \frac{1}{2} G \cdot U^D\,, \tag{34}$$

where we introduced $U^D = U^{\uparrow\downarrow}$ consistently with the density component of the bare vertex in Eqs. (26). The comparison with Eq. (31) then leads to

$$\Sigma = G \cdot (w^D \lambda^D) - 2G \cdot U^D\,. \tag{35}$$

This shows that the general form of Eq. (15a) is essential to derive the SDE in all three channels.

The explicit momentum and frequency dependence of the SDE in physical channels can be determined along the same lines as for the diagrammatic channels (for the details on the derivation see Appendix C) and reads

$$\Sigma(\mathbf{k}; \nu) = \sum_{\mathbf{Q},\Omega} w^M(\mathbf{Q}; \Omega) \lambda^M\left(\mathbf{Q}, \mathbf{k} - \mathbf{Q}; \Omega, \nu - \left\lceil \frac{\Omega}{2} \right\rceil\right) G(\mathbf{k} - \mathbf{Q}; \nu - \Omega)\,, \tag{36a}$$

$$\Sigma(\mathbf{k}; \nu) = \sum_{\mathbf{Q},\Omega} \left[w^D(\mathbf{Q}; \Omega) \lambda^D\left(\mathbf{Q}, \mathbf{k} - \mathbf{Q}; \Omega, \nu - \left\lceil \frac{\Omega}{2} \right\rceil\right) - 2U^D(\mathbf{Q}, \mathbf{k}; \Omega, \nu) \right] G(\mathbf{k} - \mathbf{Q}; \nu - \Omega)\,, \tag{36b}$$

$$\Sigma(\mathbf{k}; \nu) = -\sum_{\mathbf{Q},\Omega} w^{SC}(\mathbf{Q}; \Omega) \lambda^{SC}\left(\mathbf{Q}, \mathbf{Q} - \mathbf{k}; \Omega, \left\lceil \frac{\Omega}{2} \right\rceil - \nu\right) G(\mathbf{Q} - \mathbf{k}; \Omega - \nu)\,, \tag{36c}$$

where $U^D(\mathbf{Q}, \mathbf{k}; \Omega, \nu) \equiv U^D(k - Q, k|k, k - Q)$. Together with the forms in diagrammatic channels (25), the above equations represent the main result of the present paper.

2.5 Expansion in form factors

We now address the possible problems associated with TU solvers that use a truncated form-factor expansion for the fermionic momenta, as the TU fRG [39, 40, 43] and the TU parquet equations [4, 44].

"Truncated unity" refers to the insertion of the unity

$$\mathbb{1} = \int d\mathbf{p}' \delta(\mathbf{p} - \mathbf{p}') = \int d\mathbf{p}' \sum_m f_m^*(\mathbf{p}) f_m(\mathbf{p}')\,,$$
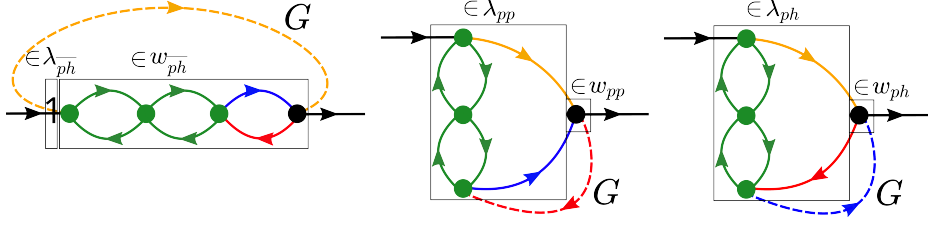
Figure 2: The same self-energy diagram drawn as $\lambda_{\overline{ph}} w_{\overline{ph}} G$ (left), as $\lambda_{pp} w_{pp} G$ (center), and as $\lambda_{ph} w_{ph} G$ (on the right). The dashed line indicates the closing Green's function. Using only an s-wave form factor is exact for the computation via $\lambda_{\overline{ph}} w_{\overline{ph}} G$, but not for $\lambda_{pp/ph} w_{pp/ph} G$, due to the information loss induced by the form-factor projections.

and the subsequent truncation to only few form factors in practical applications. For this, we rewrite the above SDE in diagrammatic channels, Eqs. (25), in form-factor notation (analogous arguments hold for the physical channels)

$$\Sigma^{\uparrow}(\mathbf{k}; \nu) = \sum_{\mathbf{Q},\Omega} G^{\downarrow}(\mathbf{k}-\mathbf{Q}; \nu-\Omega) w_{\overline{ph}}^{\widehat{\uparrow\downarrow}}(\mathbf{Q};\Omega) \left[\sum_m f_m(\mathbf{k}-\mathbf{Q}) \lambda_{\overline{ph};m}^{\widehat{\uparrow\downarrow}}\left(\mathbf{Q};\Omega, \nu-\left[\frac{\Omega}{2}\right]\right) \right], \tag{37a}$$

$$\Sigma^{\uparrow}(\mathbf{k}; \nu) = -\sum_{\mathbf{Q},\Omega} G^{\downarrow}(\mathbf{k}-\mathbf{Q}; \nu-\Omega) w_{\overline{ph}}^{\uparrow\downarrow}(\mathbf{Q};\Omega) \left[\sum_m f_m(\mathbf{k}-\mathbf{Q}) \lambda_{\overline{ph};m}^{\uparrow\downarrow}\left(\mathbf{Q};\Omega, \nu-\left[\frac{\Omega}{2}\right]\right) \right], \tag{37b}$$

$$\Sigma^{\uparrow}(\mathbf{k}; \nu) = -\sum_{\mathbf{Q},\Omega} G^{\downarrow}(\mathbf{Q}-\mathbf{k};\Omega-\nu) w_{pp}^{\uparrow\downarrow}(\mathbf{Q};\Omega) \left[2\sum_m f_m(\mathbf{Q}-\mathbf{k}) \lambda_{pp;m}^{\uparrow\downarrow}\left(\mathbf{Q};\Omega, \left[\frac{\Omega}{2}\right]-\nu\right)-1 \right], \tag{37c}$$

where $\{f_m(\mathbf{k})\}_{m=0}^{\infty}$ is a set of form factors defined on the Brillouin zone. The range of their real space representation is determined by the bond length. If the results are converged in the number of form factors, all three single-boson exchange expressions of the SDE (37) yield the same result. This is in general not the case if only a small number is considered. In fact, the restriction to a small number of form factors leads in general to a violation of the crossing symmetry [44]. In particular, a truncation in the form factors fully includes the diagrams reducible in the corresponding channel (any r-reducible diagram in the formulation including λ_r), but only partially those reducible in the other channels. This is exemplified in Fig. 2: using only an s-wave form factor; i.e., restricting to $f_0(\mathbf{k}) = 1$, the diagram shown in the figure is computed exactly in the $\overline{ph}$ formulation of the SDE. Indeed, the argument of the bosonic propagator w, being entirely bosonic, is not affected by the s-wave form-factor truncation. However, the same diagram is not accounted for correctly in its formulation, since $\lambda_{ph/pp}$ depends also on a fermionic argument which is not captured by the constant s-wave form factor. We note that all ladder diagrams formulated in the corresponding channel are treated exactly (see left diagram of Fig. 2 as an example), only the corrections from the other channels to these ladders are affected by the truncation in the number of considered form factors.

To summarize, some diagrams are not treated optimally in the single-boson exchange SDE with respect to a truncation in form factors. In this case, the computation of the self-energy generally depends on the choice of the channel, as will be shown in the application to the 2D Hubbard model presented in the next section. Specifically, when the fermionic momentum dependence is expanded in form factors, the crossing symmetry between the particle-hole channels is broken [12, 44].

3 Application to the fRG: The pseudogap opening in the 2D Hubbard model

We now apply the SDE in the single-boson exchange representation to the fRG [45, 46]. We focus on the pseudogap opening in the 2D Hubbard model at weak coupling,[2] where fore-front algorithmic advancements brought the fRG to a quantitatively reliable level [51, 52]. In particular, the multiloop extension [53, 54] allows one to recover the parquet approximation [31, 55, 56]. In this scheme, the self-energy flow is determined by the derivative of the SDE. In the implementation based on the parquet decomposition, the use of the SDE has been shown to be crucial for detecting the pseudogap opening. [47]. Here, we employ the single-boson exchange formulation of the SDE derived above, extending the single-boson exchange formulation of the fRG [10, 15, 57] to the computation of the self-energy.

For the Hubbard model [58] with nearest-neighbor hopping amplitude t, chemical potential μ, and local Coulomb repulsion U, the classical action is of the form (1), with

$$U_{\sigma_{1'}\sigma_{2'}|\sigma_1\sigma_2}(k_{1'},k_{2'}|k_1,k_2) = -U\delta(k_{1'}+k_{2'}-k_1-k_2)(\delta_{\sigma_{1'},\sigma_1}\delta_{\sigma_{2'},\sigma_2} - \delta_{\sigma_{1'},\sigma_2}\delta_{\sigma_{2'},\sigma_1})$$
$$\times (1 - \delta_{\sigma_1,\sigma_2}), \tag{38}$$

and the bare propagator given by

$$G^{-1}_{0,\sigma_{1'}|\sigma_1}(k_{1'}|k_1) = (i\nu_1 - \epsilon_{\mathbf{k}_1} + \mu)\delta(k_{1'}-k_1), \tag{39}$$

where the dispersion relation reads $\epsilon_{\mathbf{k}} = -2t[\cos(k_x) + \cos(k_y)]$. Throughout our analysis, we consider $t \equiv 1$ as energy unit and focus on $|U| = 2$ and half filling with $\langle \hat{n} \rangle = 1$. Using the T flow [59], allows us to track the temperature evolution of the pseudogap opening along the renormalization-group flow. The flow equations for the bosonic propagator, the fermion-boson coupling, and the rest function are reported in Appendix D. The self-energy flow is determined from the derivative of the SDE (31), (32), and (34). For the magnetic channel formulation, Eq. (31) leads to

$$\dot{\Sigma} = \dot{G} \cdot (w^{\mathrm{M}}\lambda^{\mathrm{M}}) + G \cdot (\dot{w}^{\mathrm{M}}\lambda^{\mathrm{M}}) + G \cdot (w^{\mathrm{M}}\dot{\lambda}^{\mathrm{M}}). \tag{40}$$

The momentum and frequency dependencies are obtained by following the explicit form (37a). The corresponding expressions for the D and SC channels can be derived analogously. We note that the derivative of the self-energy appearing in the Katanin correction for $\dot{G}$ on the right-hand side is replaced by the conventional 1ℓ flow. In order to account for the full feedback, the equation should be iterated until convergence. Since this results only in quantitative corrections [52], we neglect the iterations here.

We here perform a two-loop (2ℓ) computation[3] that neglects the flow of the U-irreducible rest functions (in the considered parameter regime its effects are very small [15]). Specifically, we use $n = 8$ positive fermionic and $2n$ bosonic frequencies for the parametrization of the fermion-boson coupling and rest function, whereas for the bosonic propagators we use $64n$ positive bosonic frequencies. For the self-energy, we use $10n$ positive fermionic frequencies, and for the bubble integrand we use $64n$ positive bosonic and $64n$ positive fermionic frequencies. The fermionic momentum dependence of the fermion-boson coupling is accounted for by a form-factor expansion, where we consider only the local s-wave contribution since at half filling the physics is dominated by antiferromagnetic fluctuations. For the transfer momentum parametrization, in addition to 16×16 momentum patches distributed on an equally spaced grid in the Brillouin zone, we take into account a finer grid around the antiferromagnetic peak

---

[2]See Ref. [50] for a review.

[3]Differently to the conventional 1ℓ scheme, the 2ℓ truncation is exact to third order in U with corrections of $\mathcal{O}(U^4)$. For the details on the implementation in the single-boson exchange formulation, we refer to Ref. [60].
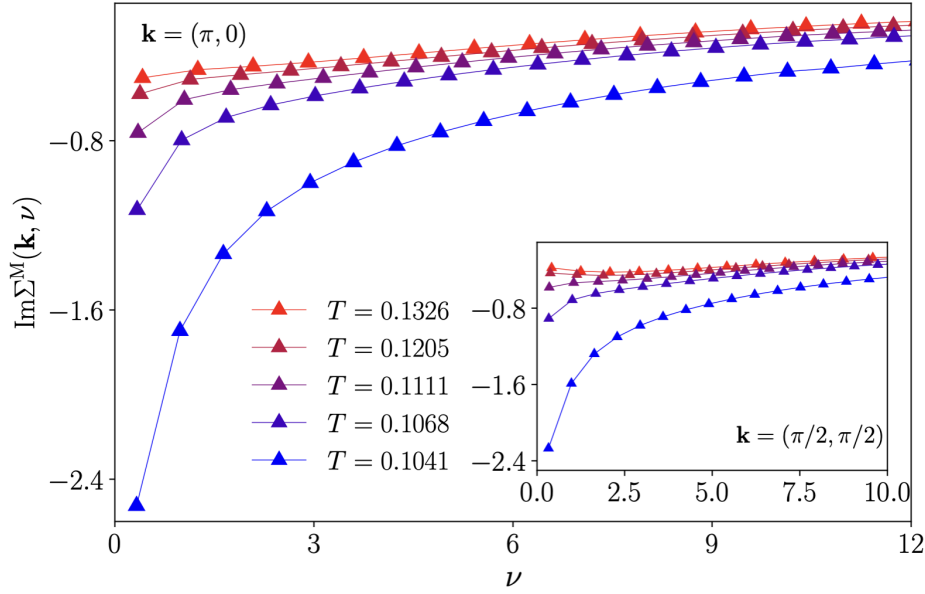
Figure 3: Imaginary part of the self-energy as a function of Matsubara frequencies at half filling ($\mu = 0$), $U = 2$, and various temperatures, as determined by its expression in the magnetic channel (36a). At the antinodal point $\mathbf{k} = (\pi, 0)$ displayed in the main panel, the pseudogap opens at higher temperatures as compared to the nodal point $\mathbf{k} = (\pi/2, \pi/2)$, see inset.

at $\mathbf{k} = (\pi, \pi)$ and the superconducting peak at $\mathbf{k} = (0, 0)$. The bubble transfer momentum dependence is calculated on a much denser grid of 80×80 momentum patches, see Ref. [57] for the details.

We here focus on the analysis in Matsubara frequencies. A non-Fermi-liquid behavior can be signaled by deviations of the quasiparticle weight

$$Z(\mathbf{k}) = \left(1 - \frac{\partial \operatorname{Re}\Sigma(\nu, \mathbf{k})}{\partial \nu}\bigg|_{\nu \to 0}\right)^{-1} < 1, \tag{41}$$

where ν is a real frequency. In the limit of low temperatures, $\partial_\nu \operatorname{Re}\Sigma(\nu, \mathbf{k})|_{\nu \to 0}$ can be translated to Matsubara frequencies. The gap opening can then be observed directly in the imaginary part of the self-energy bending towards negative large values. In contrast, the Fermi-liquid regime is always characterized by a bending towards small values. In Figs. 3 and 4 we present the fRG results obtained for the different channel representations of the SDE. Due to their equivalence, these are expected to yield the same result. In the TU-fRG, however, the pseudogap opening is only observed in the magnetic channel representation and not in the density or superconducting one. As we will discuss below, this is a consequence of the reduced number of form factors and their convergence, which is different in the three channel representations. We first focus on the magnetic (or $\overline{ph}$) channel data shown in Fig. 3. At low temperatures, we observe an insulating behavior initially at the antinodal point $\mathbf{k} = (0, \pi)$. At the nodal point $\mathbf{k} = (\pi/2, \pi/2)$, the gap opening occurs at lower temperatures. These findings agree with the results obtained with the parquet formulation [47]. The results for the density and superconducting channel representation of the SDE are reported in Fig. 4. We find equal self-energies in the superconducting and density formulations, in agreement to the expectation based on $\mathrm{SU}_P(2)$-symmetry on the square lattice at half-filling. Differently from the magnetic channel, these representations fail to capture the pseudogap opening even at the antinodal point, where it should be more pronounced. Note also the different scales with respect to Fig. 3. This behavior can be
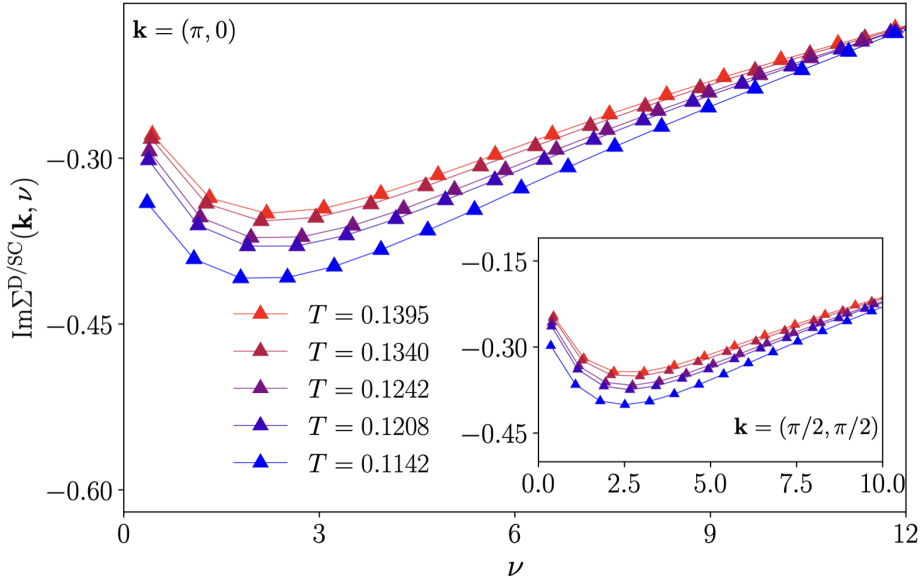
Figure 4: Same as Fig. 3, but determined by the density and superconducting channel using Eqs. (36b) and (36c). It can be clearly seen that these representations fail to capture the pseudogap opening both at the antinodal and the nodal point. Note also the different scales with respect to Fig. 3.

understood in the light of the discussion in Section 2.5: The magnetic fluctuations driving the pseudogap opening are not translated efficiently to the subleading channels in the TU fRG and the flow diverges before the onset of the pseudogap opening develops. As a consequence, the self-energy retains a Fermi-liquid nature for all values of the temperature in our analysis. We note that the pseudo-critical transition temperature in the density and superconducting channel representations appears to be higher than for magnetic one. This is due to the information loss induced by the form-factor projections which reduces the screening of the strong antiferromagnetic fluctuations at half filling. In particular, the two channel representations appear to be affected in the same way, see also Fig. 2. At finite doping, we expect the same qualitative behavior since the pseudogap opening is driven by antiferromagnetic fluctuations also in this case [61, 62].

We finally note that the dependence on the different representations is due to the different convergence in the number of form factors. In the magnetic channel, the pseudogap opening is captured already by the single *s*-wave form factor considered here, while in the density and superconducting ones it is insufficient. This problem can be circumvented by using the parquet-based formulation of the SDE. The latter does not induce a bias between the different physical channels and captures the pseudogap opening within the *s*-wave truncation [47]. In this formulation, replacing the two-particle vertex by its single-boson exchange representation, the SDE includes also multiboson contributions [63].

We note that the self-energy is independent of the sign of U [64]. Moreover, at half filling, the Shiba transformation [65] maps the attractive ($U < 0$) to the repulsive Hubbard model. Specifically, the *s*-wave superconducting fluctuations at $\mathbf{Q} = (0,0)$ and the density fluctuations at $\mathbf{Q} = (\pi, \pi)$ in the attractive model correspond to the antiferromagnetic spin components in the repulsive model. Consequently, as expected, for the attractive Hubbard, we obtain the same results, but with exchanged channels: the dominant density and superconducting fluctuations drive the pseudogap opening observed in the corresponding channel representations, while no pseudogap opening is detected in the magnetic channel representation. At half filling,
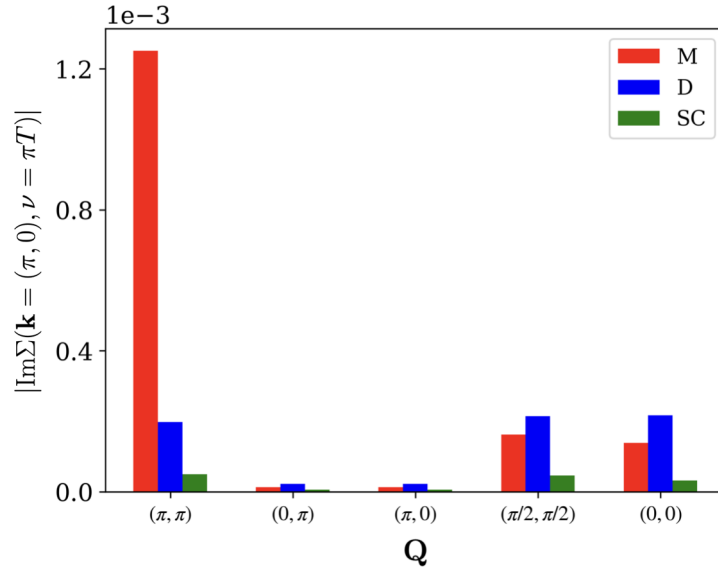
Figure 5: Fluctuation diagnostics of the imaginary part of the self-energy at the antinodal point, for the repulsive Hubbard model at half filling, $U = 2$ and $T = 0.13$. The histogram bars display the contributions of the different bosonic momenta $Q = (\mathbf{Q}, \Omega = 0)$ in the magnetic (red), density (blue) and superconducting (green) representations. The pronounced red bar at $\mathbf{Q} = (\pi, \pi)$ clearly shows the dominant contributions of the antiferromagnetic spin fluctuations.

the results obtained from the density and superconducting channel representations for the attractive model coincide with the ones determined by the magnetic channel in the repulsive model and the magnetic channel representation results for the attractive model with the ones determined by the density and superconducting channels in the repulsive model. Also in this case, the channels controlling the physical behavior yield the correct description.

A more detailed understanding can be obtained by applying the fluctuation diagnostics approach [34–38] to analyze the main collective mode contributions to the self-energy in both the repulsive and attractive cases. We recall that the single-boson exchange SDE for the self-energy in the different channels, Eqs. (36), includes – by construction – an integral over processes in which the Green's function is renormalized by a momentum and frequency dependent boson as well as by a fermion-boson coupling. Although, in general, all momenta and frequencies will contribute, in the representation reflecting the physically relevant fluctuations, specific momenta and frequencies will dominate the contributions to the integral. In the framework of the fluctuation diagnostics, this indicates that a boson of the corresponding channel can be deemed primarily responsible for the self-energy/spectral feature under investigation. For our analysis of the pseudogap opening, following Refs. [34, 38] we focus on the first Matsubara frequency at the antinodal point $\mathbf{k} = (0, \pi)$. The corresponding fluctuation diagnostics results for the formulation of the self-energy in the magnetic, density, and superconducting channel are reported in Fig. 5 for the repulsive Hubbard model. In particular, we visualize the integrands of Eqs. (36) as a function of the bosonic transfer momentum $\mathbf{Q}$ (and $\Omega = 0$), since this vector defines the transfer momentum of the corresponding collective modes. Then, a dominant contribution appearing as a peak in the integrand of the magnetic or charge representation of the self-energy at $\mathbf{Q} = (\pi, \pi)$ can be attributed to antiferromagnetic or charge density wave fluctuations respectively, while a peak in the superconducting representation of the SDE at $\mathbf{Q} = (0, 0)$ hints at strong pairing fluctuations. The data in Fig. 5 shed light on the underlying physics of the pseudogap observed in the fRG data: In the magnetic representa-
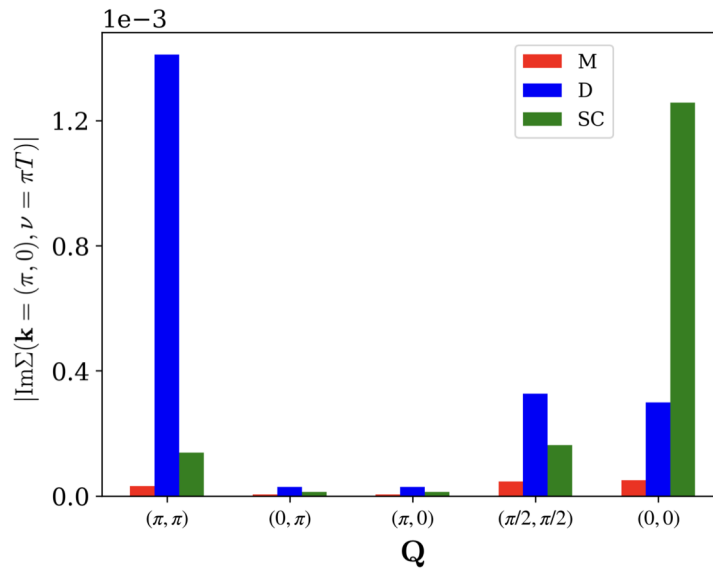
Figure 6: Same as Fig. 5, but for the attractive Hubbard model ($U = -2$). In this case, the density and superconducting fluctuations at $\mathbf{Q} = (\pi, \pi)$ and respectively $\mathbf{Q} = (0, 0)$ dominate.

tion, the dominant contribution at $\mathbf{Q} = (\pi, \pi)$ reflects the strong influence of antiferromagnetic fluctuations, while the density and superconducting representations yield an essentially featureless momentum distribution, not presenting significant contributions to the self-energy for any specific momentum vector.

Reversing the sign of the interaction U in our model, we carry out an analogous analysis to characterize the physics underlying the pseudogap opening in the attractive Hubbard model. Here, the fluctuation diagnostics identifies charge density wave and s-wave pairing fluctuations as key players, see Fig. 6. The results show significant contributions at $\mathbf{Q} = (\pi, \pi)$ in the density representation and at $\mathbf{Q} = (0, 0)$ in the superconducting one. At the same time, now the magnetic representation does not display any pronounced momentum-selective behavior. We note that the displayed results include only the $\Omega = 0$ evaluation of the integrand, from which the degeneracy of the density and superconducting contributions can not be directly inferred (the same applies to Fig. 5).

4 Conclusions and outlook

We derived the expression for the Schwinger–Dyson equation (SDE) for the self-energy in the single-boson exchange formulation. The employed formalism makes use of matrices to encode the spin structure and allows for a compact representation of the SDE. The resulting equation exhibits a simple form involving only the bosonic propagator and the fermion-boson vertex (and not the rest function). Moreover, the single-boson exchange SDE is a one-loop equation, in contrast to the two-loop nature of its conventional expression. As a result of the symmetry of the systems (e.g. SU(2), U(1), ...) our SDE expression can be recast in several, formally equivalent representations, which essentially corresponds to the physical scattering channels of the system.

However, such a formal equivalence is generally broken if truncated-unity (TU) approximations are included in the algorithm used for the calculations (e.g., for parquet and fRG implementations using a restricted number of form factors). In particular, the information loss introduced by the projection of the momentum dependence directly affects specific channel representations of the SDE and may be reflected in an unphysical dependence on the chosen SDE form. In the specific case of the fRG presented in this work, we analyzed the pseudogap opening in the 2D Hubbard model at half filling. We found that the self-energy flow yields the expected behavior already by the *s*-wave form factor in the magnetic channel representation. In contrast, the convergence in the number of form factors in the density and superconducting channel representation is slower. For these, an *s*-wave computation does not provide an accurate description of the antiferromagnetic fluctuations dominating the physics.

As an outlook, the extension to non-local interactions, only briefly alluded to here, represents an important step / plays an important role also in the generalization of the fluctuations diagnostics [34, 37, 66] as a versatile post-processing tool to quantify the contributions of the different scattering processes. Concerning the fRG implementation, further developments include the extension to the strong coupling regime by the combination with the dynamical mean-field theory (DMFT) [67, 68] in the so-called DMF^{2}RG [10, 14, 69, 70].

Acknowledgments

A   Details on the formalism

In this appendix, we present the notation to handle the spin and momentum/frequency structure of the single-boson exchange vertices introduced in Ref. [9] and discussed in more detail in Ref. [71].

A.1   Matrix representation of the spin structure

The summation over spin indices for products of four-point objects such as Π and V or any other object with the same index structure can be carried out efficiently by storing their spin components in 4×4 matrices. The summation over spin indices is then carried out by performing standard matrix products. Assuming that $A = \Pi$, V, etc., the matrices in the different diagrammatic channels read

$$
A_{ph} = \begin{bmatrix} A_{ph}^{\widehat{\uparrow\downarrow}} & 0 & 0 & 0 \\ 0 & A_{ph}^{\widehat{\downarrow\uparrow}} & 0 & 0 \\ 0 & 0 & A_{ph}^{\uparrow\uparrow} & A_{ph}^{\downarrow\uparrow} \\ 0 & 0 & A_{ph}^{\uparrow\downarrow} & A_{ph}^{\downarrow\downarrow} \end{bmatrix}, \quad
A_{\overline{ph}} = \begin{bmatrix} A_{\overline{ph}}^{\uparrow\downarrow} & 0 & 0 & 0 \\ 0 & A_{\overline{ph}}^{\downarrow\uparrow} & 0 & 0 \\ 0 & 0 & A_{\overline{ph}}^{\uparrow\uparrow} & A_{\overline{ph}}^{\widehat{\uparrow\downarrow}} \\ 0 & 0 & A_{\overline{ph}}^{\widehat{\downarrow\uparrow}} & A_{\overline{ph}}^{\downarrow\downarrow} \end{bmatrix}, \quad
A_{pp} = \begin{bmatrix} A_{pp}^{\uparrow\uparrow} & 0 & 0 & 0 \\ 0 & A_{pp}^{\downarrow\downarrow} & 0 & 0 \\ 0 & 0 & A_{pp}^{\uparrow\downarrow} & A_{pp}^{\widehat{\uparrow\downarrow}} \\ 0 & 0 & A_{pp}^{\downarrow\uparrow} & A_{pp}^{\widehat{\downarrow\uparrow}} \end{bmatrix}.
$$
(A.1a)

Following the definition of the bubble products in Eqs. (6), the products involving these objects are obtained through usual matrix multiplications. There is always a "natural" spin component where the multiplication has a diagonal structure, i.e., $A_{ph}^{\widehat{\uparrow\downarrow}}$, $A_{\overline{ph}}^{\uparrow\downarrow}$ and $A_{pp}^{\uparrow\uparrow}$ (and $A_{ph}^{\widehat{\downarrow\uparrow}}$, $A_{\overline{ph}}^{\downarrow\uparrow}$, $A_{pp}^{\downarrow\downarrow}$). For the other spin components, the multiplication is non-diagonal. Explicitly:

$$
[A_{ph} \circ B_{ph}]^{\widehat{\uparrow\downarrow}} = A_{ph}^{\widehat{\uparrow\downarrow}} \circ B_{ph}^{\widehat{\uparrow\downarrow}}, \qquad [A_{ph} \circ B_{ph}]^{\widehat{\downarrow\uparrow}} = A_{ph}^{\widehat{\downarrow\uparrow}} \circ B_{ph}^{\widehat{\downarrow\uparrow}},
$$
$$
\begin{bmatrix} [A_{ph} \circ B_{ph}]^{\uparrow\uparrow} & [A_{ph} \circ B_{ph}]^{\downarrow\uparrow} \\ [A_{ph} \circ B_{ph}]^{\uparrow\downarrow} & [A_{ph} \circ B_{ph}]^{\downarrow\downarrow} \end{bmatrix} = \begin{bmatrix} A_{ph}^{\uparrow\uparrow} & A_{ph}^{\downarrow\uparrow} \\ A_{ph}^{\uparrow\downarrow} & A_{ph}^{\downarrow\downarrow} \end{bmatrix} \circ \begin{bmatrix} B_{ph}^{\uparrow\uparrow} & B_{ph}^{\downarrow\uparrow} \\ B_{ph}^{\uparrow\downarrow} & B_{ph}^{\downarrow\downarrow} \end{bmatrix},
$$
(A.2a)

$$
[A_{\overline{ph}} \circ B_{\overline{ph}}]^{\uparrow\downarrow} = A_{\overline{ph}}^{\uparrow\downarrow} \circ B_{\overline{ph}}^{\uparrow\downarrow}, \qquad [A_{\overline{ph}} \circ B_{\overline{ph}}]^{\downarrow\uparrow} = A_{\overline{ph}}^{\downarrow\uparrow} \circ B_{\overline{ph}}^{\downarrow\uparrow},
$$
$$
\begin{bmatrix} [A_{\overline{ph}} \circ B_{\overline{ph}}]^{\uparrow\uparrow} & [A_{\overline{ph}} \circ B_{\overline{ph}}]^{\widehat{\uparrow\downarrow}} \\ [A_{\overline{ph}} \circ B_{\overline{ph}}]^{\widehat{\downarrow\uparrow}} & [A_{\overline{ph}} \circ B_{\overline{ph}}]^{\downarrow\downarrow} \end{bmatrix} = \begin{bmatrix} A_{\overline{ph}}^{\uparrow\uparrow} & A_{\overline{ph}}^{\widehat{\uparrow\downarrow}} \\ A_{\overline{ph}}^{\widehat{\downarrow\uparrow}} & A_{\overline{ph}}^{\downarrow\downarrow} \end{bmatrix} \circ \begin{bmatrix} B_{\overline{ph}}^{\uparrow\uparrow} & B_{\overline{ph}}^{\widehat{\uparrow\downarrow}} \\ B_{\overline{ph}}^{\widehat{\downarrow\uparrow}} & B_{\overline{ph}}^{\downarrow\downarrow} \end{bmatrix},
$$
(A.2b)

$$
[A_{pp} \circ B_{pp}]^{\uparrow\uparrow} = A_{ph}^{\uparrow\uparrow} \circ B_{ph}^{\uparrow\uparrow}, \qquad [A_{pp} \circ B_{pp}]^{\downarrow\downarrow} = A_{pp}^{\downarrow\downarrow} \circ B_{pp}^{\downarrow\downarrow},
$$
$$
\begin{bmatrix} [A_{pp} \circ B_{pp}]^{\uparrow\downarrow} & [A_{pp} \circ B_{pp}]^{\widehat{\uparrow\downarrow}} \\ [A_{pp} \circ B_{pp}]^{\widehat{\downarrow\uparrow}} & [A_{pp} \circ B_{pp}]^{\downarrow\uparrow} \end{bmatrix} = \begin{bmatrix} A_{pp}^{\uparrow\downarrow} & A_{pp}^{\widehat{\uparrow\downarrow}} \\ A_{pp}^{\downarrow\uparrow} & A_{pp}^{\widehat{\downarrow\uparrow}} \end{bmatrix} \circ \begin{bmatrix} B_{pp}^{\uparrow\downarrow} & B_{pp}^{\widehat{\uparrow\downarrow}} \\ B_{pp}^{\downarrow\uparrow} & B_{pp}^{\widehat{\downarrow\uparrow}} \end{bmatrix}.
$$
(A.2c)

Note that the products of U-reducible vertices $\bar{\lambda}_r \bullet w_r$ and $w_r \bullet \lambda_r$ exactly follow that structure. Also the spin structure of the triple products $V \circ \Pi_r \circ U$ and $U \circ \Pi_r \circ V$ are obtained by applying the matrix products twice. We also stress that, as in the main text, the involved summations over frequencies and momenta are not accounted for and still have to be considered.

Making use of channel-dependent momentum/frequency parametrization (cf. Fig. 7) and of the crossing symmetries

$$
V_{12|34} = -V_{21|34} = -V_{12|43} = V_{21|43},
$$
(A.3)

one can deduce the following relations for the vertex:

$$
\begin{aligned}
V_{ph}^{\uparrow\downarrow}(Q_{ph}, k_{ph}, k'_{ph}) &= -V_{\overline{ph}}^{\widehat{\uparrow\downarrow}}(-\mathbf{Q}_{ph}, \mathbf{Q}_{ph} + \mathbf{k}'_{ph}, \mathbf{Q}_{ph} + \mathbf{k}_{ph}, -\Omega_{ph}, \nu'_{ph}, \nu_{ph}) \\
&= -V_{\overline{ph}}^{\widehat{\downarrow\uparrow}}(\mathbf{Q}_{ph}, \mathbf{k}_{ph}, \mathbf{k}'_{ph}, \Omega_{ph}, \nu_{ph}, \nu'_{ph}) \\
&= V_{ph}^{\downarrow\uparrow}(-\mathbf{Q}_{ph}, \mathbf{Q}_{ph} + \mathbf{k}'_{ph}, \mathbf{Q}_{ph} + \mathbf{k}_{ph}, -\Omega_{ph}, \nu'_{ph}, \nu_{ph}),
\end{aligned}
$$
(A.4a)

$$V_{\overline{ph}}^{\uparrow\downarrow}(Q_{\overline{ph}}, k_{\overline{ph}}, k'_{\overline{ph}}) = -V_{\overline{ph}}^{\widehat{\uparrow\downarrow}}(-\mathbf{Q}_{\overline{ph}}, \mathbf{Q}_{\overline{ph}} + \mathbf{k}'_{\overline{ph}}, \mathbf{Q}_{\overline{ph}} + \mathbf{k}_{\overline{ph}}, -\Omega_{\overline{ph}}, \nu'_{\overline{ph}}, \nu_{\overline{ph}})$$

$$= -V_{\overline{ph}}^{\widehat{\downarrow\uparrow}}(\mathbf{Q}_{\overline{ph}}, \mathbf{k}_{\overline{ph}}, \mathbf{k}'_{\overline{ph}}, \Omega_{\overline{ph}}, \nu_{\overline{ph}}, \nu'_{\overline{ph}})$$

$$= V_{\overline{ph}}^{\downarrow\uparrow}(-\mathbf{Q}_{\overline{ph}}, \mathbf{Q}_{\overline{ph}} + \mathbf{k}'_{\overline{ph}}, \mathbf{Q}_{\overline{ph}} + \mathbf{k}_{\overline{ph}}, -\Omega_{\overline{ph}}, \nu'_{\overline{ph}}, \nu_{\overline{ph}}), \tag{A.4b}$$

$$V_{pp}^{\uparrow\downarrow}(Q_{pp}, k_{pp}, k'_{pp}) = -V_{pp}^{\widehat{\uparrow\downarrow}}(\mathbf{Q}_{pp}, \mathbf{Q}_{pp} - \mathbf{k}_{pp}, \mathbf{k}'_{pp}, \Omega_{pp}, -\nu_{pp} + \delta\Omega_{pp}, \nu'_{pp})$$

$$= -V_{pp}^{\widehat{\downarrow\uparrow}}(\mathbf{Q}_{pp}, \mathbf{k}_{pp}, \mathbf{Q}_{pp} - \mathbf{k}'_{pp}, \Omega_{pp}, \nu_{pp}, -\nu'_{pp} + \delta\Omega_{pp})$$

$$= V_{pp}^{\downarrow\uparrow}(\mathbf{Q}_{pp}, \mathbf{Q}_{pp} - \mathbf{k}_{pp}, \mathbf{Q}_{pp} - \mathbf{k}'_{pp}, \Omega_{pp}, -\nu_{pp} + \delta\Omega_{pp}, -\nu'_{pp} + \delta\Omega_{pp}), \tag{A.4c}$$

where $Q_r = (\mathbf{Q}_r, \Omega_r)$, $k_r = (\mathbf{k}_r, \nu_r)$ and $k'_r = (\mathbf{k}'_r, \nu'_r)$ are the bosonic and fermionic quadrivectors. For convenience, we also defined $\delta\Omega_r = \lceil\frac{\Omega_r}{2}\rceil - \lfloor\frac{\Omega_r}{2}\rfloor$. Note that, since we use symmetrized frequencies, the aforementioned objects depend on Ω_r through the terms $\lceil\frac{\Omega_r}{2}\rceil$ and $\lfloor\frac{\Omega_r}{2}\rfloor$, as illustrated in Fig. 7. Therefore, when the frequency changes sign ($\Omega_r \to -\Omega_r$), the following identities are used:

$$\left\lceil -\frac{\Omega_r}{2} \right\rceil = -\left\lfloor \frac{\Omega_r}{2} \right\rfloor, \qquad \left\lfloor -\frac{\Omega_r}{2} \right\rfloor = -\left\lceil \frac{\Omega_r}{2} \right\rceil. \tag{A.5}$$

The crossing symmetries for the bubble operators are deduced in a similar manner:

$$\Pi_{ph}^{\widehat{\uparrow\downarrow}}(\mathbf{Q}_{ph}, \mathbf{k}_{ph}, \Omega_{ph}, \nu_{ph}) = \Pi_{ph}^{\widehat{\downarrow\uparrow}}(-\mathbf{Q}_{ph}, \mathbf{Q}_{ph} + \mathbf{k}_{ph}, -\Omega_{ph}, \nu_{ph}), \tag{A.6a}$$

$$\Pi_{\overline{ph}}^{\uparrow\downarrow}(\mathbf{Q}_{\overline{ph}}, \mathbf{k}_{\overline{ph}}, \Omega_{\overline{ph}}, \nu_{\overline{ph}}) = \Pi_{\overline{ph}}^{\downarrow\uparrow}(-\mathbf{Q}_{\overline{ph}}, \mathbf{Q}_{\overline{ph}} + \mathbf{k}_{\overline{ph}}, -\Omega_{\overline{ph}}, \nu_{\overline{ph}}), \tag{A.6b}$$

$$\Pi_{pp}^{\uparrow\downarrow}(\mathbf{Q}_{pp}, \mathbf{k}_{pp}, \Omega_{pp}, \nu_{pp}) = \Pi_{pp}^{\downarrow\uparrow}(\mathbf{Q}_{pp}, \mathbf{Q}_{pp} - \mathbf{k}_{pp}, \Omega_{pp}, \delta\Omega_{pp} - \nu_{pp}). \tag{A.6c}$$

In the matrix space for spin indices, the bubble operators are all diagonal. In particular, this means that the following components vanish:

$$\Pi_{ph}^{\uparrow\downarrow} = \Pi_{ph}^{\downarrow\uparrow} = 0, \qquad \Pi_{\overline{ph}}^{\widehat{\uparrow\downarrow}} = \Pi_{\overline{ph}}^{\widehat{\downarrow\uparrow}} = 0, \qquad \Pi_{pp}^{\widehat{\uparrow\downarrow}} = \Pi_{pp}^{\widehat{\downarrow\uparrow}} = 0. \tag{A.7}$$
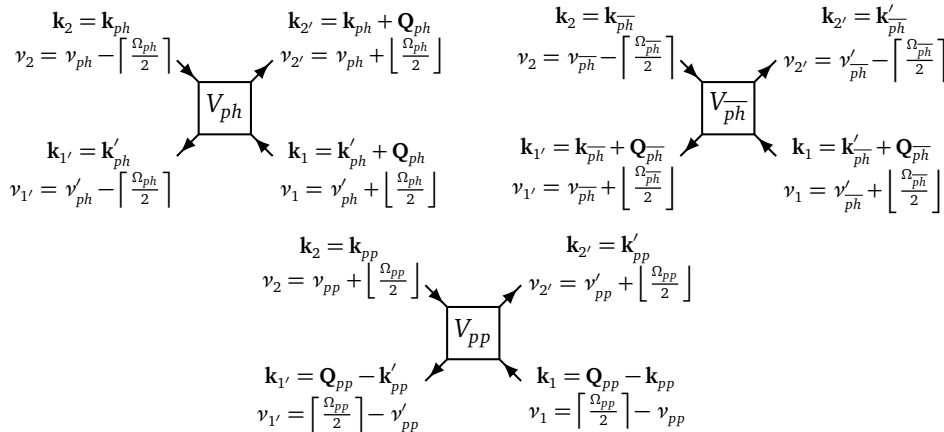

Figure 7: Momentum and frequency conventions for the two-particle vertex in the different channel notations, where $\lceil\cdots\rceil$ ($\lfloor\cdots\rfloor$) rounds the argument up (down) to the nearest bosonic Matsubara frequency. We use a symmetrized notation for the frequencies, which is more convenient for the numerical implementation.

Note that for an SU(2)-symmetric system, the non-vanishing components of the matrices $\mathbf{\Pi}_r$ are all equivalent, since $G^\uparrow = G^\downarrow$. Thus, to define the bubbles in physical channels, it is sufficient to consider the matrix elements of $\Pi_{\overline{ph}}$ for defining Π^M, the matrix elements of Π_{ph} for Π^D and the elements of Π_{pp} for Π^{SC}.

We here provide the explicit form for the objects used in the main part of the paper. Recalling the definition of the fermion-boson couplings $\lambda_r = 1_r + 1_r \circ \Pi_r \circ \mathcal{I}_r$ [9], where $\mathcal{I}_r$ is the U-irreducible vertex in channel r, it is possible to explicitly derive their matrix structure. To simplify the exposition, we will provide the matrix form of the objects $\widetilde{\lambda}_r = \lambda_r - 1_r$, as the corresponding λ_r can be easily determined from these. In particular, they read

$$\widetilde{\lambda}_{ph}^{\widehat{\uparrow\downarrow}} = \Pi_{ph}^{\widehat{\uparrow\downarrow}} \circ \mathcal{I}_{ph}^{\widehat{\uparrow\downarrow}},$$

$$\begin{bmatrix} \widetilde{\lambda}_{ph}^{\uparrow\uparrow} & \widetilde{\lambda}_{ph}^{\downarrow\uparrow} \\ \widetilde{\lambda}_{ph}^{\uparrow\downarrow} & \widetilde{\lambda}_{ph}^{\downarrow\downarrow} \end{bmatrix} = \begin{bmatrix} \Pi_{ph}^{\uparrow\uparrow} & 0 \\ 0 & \Pi_{ph}^{\downarrow\downarrow} \end{bmatrix} \circ \begin{bmatrix} \mathcal{I}_{ph}^{\uparrow\uparrow} & \mathcal{I}_{ph}^{\downarrow\uparrow} \\ \mathcal{I}_{ph}^{\uparrow\downarrow} & \mathcal{I}_{ph}^{\downarrow\downarrow} \end{bmatrix} = \begin{bmatrix} \Pi_{ph}^{\uparrow\uparrow} \circ \mathcal{I}_{ph}^{\uparrow\uparrow} & \Pi_{ph}^{\uparrow\uparrow} \circ \mathcal{I}_{ph}^{\downarrow\uparrow} \\ \Pi_{ph}^{\downarrow\downarrow} \circ \mathcal{I}_{ph}^{\uparrow\downarrow} & \Pi_{ph}^{\downarrow\downarrow} \circ \mathcal{I}_{ph}^{\downarrow\downarrow} \end{bmatrix}, \tag{A.8a}$$

$$\widetilde{\lambda}_{\overline{ph}}^{\uparrow\downarrow} = \Pi_{\overline{ph}}^{\uparrow\downarrow} \circ \mathcal{I}_{\overline{ph}}^{\uparrow\downarrow},$$

$$\begin{bmatrix} \widetilde{\lambda}_{\overline{ph}}^{\uparrow\uparrow} & \widetilde{\lambda}_{\overline{ph}}^{\widehat{\uparrow\downarrow}} \\ \widetilde{\lambda}_{\overline{ph}}^{\widehat{\downarrow\uparrow}} & \widetilde{\lambda}_{\overline{ph}}^{\downarrow\downarrow} \end{bmatrix} = \begin{bmatrix} \Pi_{\overline{ph}}^{\uparrow\uparrow} & 0 \\ 0 & \Pi_{\overline{ph}}^{\downarrow\downarrow} \end{bmatrix} \circ \begin{bmatrix} \mathcal{I}_{\overline{ph}}^{\uparrow\uparrow} & \mathcal{I}_{\overline{ph}}^{\widehat{\uparrow\downarrow}} \\ \mathcal{I}_{\overline{ph}}^{\widehat{\downarrow\uparrow}} & \mathcal{I}_{\overline{ph}}^{\downarrow\downarrow} \end{bmatrix} = \begin{bmatrix} \Pi_{\overline{ph}}^{\uparrow\uparrow} \circ \mathcal{I}_{\overline{ph}}^{\uparrow\uparrow} & \Pi_{\overline{ph}}^{\uparrow\uparrow} \circ \mathcal{I}_{\overline{ph}}^{\widehat{\uparrow\downarrow}} \\ \Pi_{\overline{ph}}^{\downarrow\downarrow} \circ \mathcal{I}_{\overline{ph}}^{\widehat{\downarrow\uparrow}} & \Pi_{\overline{ph}}^{\downarrow\downarrow} \circ \mathcal{I}_{\overline{ph}}^{\downarrow\downarrow} \end{bmatrix}, \tag{A.8b}$$

$$\widetilde{\lambda}_{pp}^{\uparrow\uparrow} = 0,$$

$$\begin{bmatrix} \widetilde{\lambda}_{pp}^{\uparrow\downarrow} & \widetilde{\lambda}_{pp}^{\widehat{\uparrow\downarrow}} \\ \widetilde{\lambda}_{pp}^{\widehat{\downarrow\uparrow}} & \widetilde{\lambda}_{pp}^{\downarrow\uparrow} \end{bmatrix} = \begin{bmatrix} \Pi_{pp}^{\uparrow\downarrow} & 0 \\ 0 & \Pi_{pp}^{\downarrow\uparrow} \end{bmatrix} \circ \begin{bmatrix} \mathcal{I}_{pp}^{\uparrow\downarrow} & \mathcal{I}_{pp}^{\widehat{\uparrow\downarrow}} \\ \mathcal{I}_{pp}^{\widehat{\downarrow\uparrow}} & \mathcal{I}_{pp}^{\downarrow\uparrow} \end{bmatrix} = \begin{bmatrix} \Pi_{pp}^{\uparrow\downarrow} \circ \mathcal{I}_{pp}^{\uparrow\downarrow} & \Pi_{pp}^{\uparrow\downarrow} \circ \mathcal{I}_{pp}^{\widehat{\uparrow\downarrow}} \\ \Pi_{pp}^{\downarrow\uparrow} \circ \mathcal{I}_{pp}^{\widehat{\downarrow\uparrow}} & \Pi_{pp}^{\downarrow\uparrow} \circ \mathcal{I}_{pp}^{\downarrow\uparrow} \end{bmatrix}. \tag{A.8c}$$

The expressions for the other fermion-boson vertex $\bar{\lambda}_r$ are obtained by inverting the order in the multiplication. For the bosonic propagators, only the pp channel presents a different form:

$$w_{pp} = w_{pp}^{\uparrow\downarrow} \begin{bmatrix} 0 & 0 & 0 & 0 \\ 0 & 0 & 0 & 0 \\ 0 & 0 & 1 & -1 \\ 0 & 0 & -1 & 1 \end{bmatrix}. \tag{A.9}$$

As before, this can be derived by exploiting the matrix multiplications involved, recalling the definitions $w_r = U + w_r \bullet P_r \bullet U$, where $P_r = \lambda_r \circ \Pi_r \circ 1_r$ [9]. As the bosonic propagator can be represented as $w_r(Q_r) = U + \lim_{|k_r|,|k'_r| \to \infty} V(Q_r, k_r, k'_r)$ [9], the bosonic propagator satisfies the following crossing symmetry based relations: for the pp channel

$$w_{pp}^{\uparrow\downarrow}(Q_{pp}) = -w_{pp}^{\widehat{\uparrow\downarrow}}(Q_{pp}) = -w_{pp}^{\widehat{\downarrow\uparrow}}(Q_{pp}) = w_{pp}^{\downarrow\uparrow}(Q_{pp}), \qquad w_{pp}^{\uparrow\uparrow}(Q_{pp}) = w_{pp}^{\downarrow\downarrow}(Q_{pp}) = 0, \tag{A.10}$$

an similarly in the ph and in the $\overline{ph}$ channels

$$w_{ph}^{\uparrow\downarrow}(Q_{ph}) = -w_{ph}^{\widehat{\downarrow\uparrow}}(Q_{ph}) = w_{ph}^{\downarrow\uparrow}(-Q_{ph}) = -w_{ph}^{\widehat{\downarrow\uparrow}}(-Q_{ph}), \tag{A.11a}$$

$$w_{\overline{ph}}^{\uparrow\downarrow}(Q_{\overline{ph}}) = -w_{\overline{ph}}^{\widehat{\downarrow\uparrow}}(Q_{\overline{ph}}) = w_{\overline{ph}}^{\downarrow\uparrow}(-Q_{\overline{ph}}) = -w_{ph}^{\widehat{\uparrow\downarrow}}(-Q_{\overline{ph}}), \tag{A.11b}$$

$$w_{\overline{ph}}^{\uparrow\uparrow/\downarrow\downarrow}(Q_{\overline{ph}}) = -w_{ph}^{\uparrow\uparrow/\downarrow\downarrow}(Q_{\overline{ph}}) = w_{\overline{ph}}^{\uparrow\uparrow/\downarrow\downarrow}(-Q_{\overline{ph}}) = -w_{ph}^{\uparrow\uparrow/\downarrow\downarrow}(-Q_{\overline{ph}}). \tag{A.11c}$$

Moreover, using the definition of the fermion-boson vertex $\bar{\lambda}_r = \mathbf{1}_r + \mathcal{I}_r \circ \Pi_r \circ \mathbf{1}_r$, we find the crossing symmetry for the pp channel

$$\lambda_{pp}^{\widehat{\downarrow\uparrow}}(Q_{pp}, k_{pp}) = \sum_{k''} \Pi_{pp}^{\downarrow\uparrow}(Q_{pp}, k'') \mathcal{I}_{pp}^{\widehat{\downarrow\uparrow}}(Q_{pp}, k_{pp}, k'')$$

$$= -\sum_{k''} \Pi_{pp}^{\uparrow\downarrow}(Q_{pp}, k'') \mathcal{I}_{pp}^{\uparrow\downarrow}(Q_{pp}, k_{pp}, k'') = 1 - \lambda_{pp}^{\uparrow\downarrow}(Q_{pp}, k_{pp}). \tag{A.12}$$

Analogously, for the ph and the $\overline{ph}$ channels, we obtain

$$\lambda_{ph}^{\uparrow\downarrow}(Q_{ph}, k_{ph}) = \lambda_{\overline{ph}}^{\widehat{\downarrow\uparrow}}(Q_{ph}, k_{ph}), \tag{A.13a}$$

$$\lambda_{\overline{ph}}^{\uparrow\downarrow}(Q_{ph}, k_{ph}) = \lambda_{ph}^{\widehat{\downarrow\uparrow}}(Q_{\overline{ph}}, k_{\overline{ph}}), \tag{A.13b}$$

$$\lambda_{\overline{ph}}^{\uparrow\uparrow/\downarrow\downarrow}(Q_{\overline{ph}}, k_{\overline{ph}}) = \lambda_{ph}^{\uparrow\uparrow/\downarrow\downarrow}(Q_{\overline{ph}}, k_{\overline{ph}}). \tag{A.13c}$$

Note that following the crossing-symmetry related Eqs. (A.10) and (A.12) in the pp channel, the matrix representations of w_{pp}, $\bar{\lambda}_{pp}$ and λ_{pp} are well defined even though some 4×4 matrices are not invertible in the space of all spin components [71].

A.2 Momentum and frequency conventions

This section aims to report important relations to extract the momentum and frequency dependence (according to our conventions defined by Fig. 7) for the results obtained with the formalism outlined in the main text.

To begin with, we focus on the first version of the loop product, Eq. (7), involved in various forms of the SDE encountered in this paper

$$[A \cdot G]_{1'|1} = A_{1'2'|12} G_{2|2'} = \sum_{k_2, k_{2'}} A_{\sigma_{1'}\sigma_{2'}|\sigma_1\sigma_2}(k_{1'}, k_{2'}|k_1, k_2) G_{\sigma_2|\sigma_{2'}}(k_2|k_{2'}). \tag{A.14}$$

Assuming translational invariance and energy conservation, we have

$$A_{\sigma_{1'}\sigma_{2'}|\sigma_1\sigma_2}(k_{1'}, k_{2'}|k_1, k_2) = \delta_{k_{1'}+k_{2'}, k_1+k_2} A_{\sigma_{1'}\sigma_{2'}|\sigma_1\sigma_2}(k_{1'} = k_1 + k_2 - k_{2'}, k_{2'}|k_1, k_2), \tag{A.15a}$$

$$G_{\sigma_2|\sigma_{2'}}(k_2|k_{2'}) = \delta_{k_2, k_{2'}} G_{\sigma_2|\sigma_{2'}}(k_2). \tag{A.15b}$$

Inserting Eqs. (A.15) into (A.14) yields

$$[A \cdot G]_{1'|1} = \sum_{k_2} A_{\sigma_{1'}\sigma_{2'}|\sigma_1\sigma_2}(k_1, k_2|k_1, k_2) G_{\sigma_2|\sigma_{2'}}(k_2). \tag{A.16}$$

In other words, we see that translational invariance and momentum conservation induce that the vertex A inside the loop product $A \cdot G$ comes with $k_{1'} = k_1$ and $k_{2'} = k_2$. As can be understood from Fig. 7, the condition $k_{1'} = k_1$ imposes that $Q_{ph} = 0$, which makes the ph convention particularly convenient to parametrize the momentum and frequency dependence of $A_{\sigma_{1'}\sigma_{2'}|\sigma_1\sigma_2}(k_1, k_2|k_1, k_2)$.

We thus set $A_{\sigma_{1'}\sigma_{2'}|\sigma_1\sigma_2}(k_1, k_2|k_1, k_2) = A_{\sigma_{1'}\sigma_{2'}|\sigma_1\sigma_2}(Q_{ph} = 0, k_{ph} = k_2, k'_{ph} = k_1)$, which enables us to rewrite the equation above as

$$[A \cdot G]_{1'|1} = \sum_{k_{ph}} A_{\sigma_{1'}\sigma_{2'}|\sigma_1\sigma_2}(Q_{ph} = 0, k_{ph}, k'_{ph}) G_{\sigma_2|\sigma_{2'}}(k_{ph}). \tag{A.17}$$

Alternatively, one can also use the crossing symmetry of A to rewrite Eq. (A.14) as

$$[A \cdot G]_{1'|1} = A_{2'1'|21} G_{2|2'}. \tag{A.18}$$

This has the effect of exchanging the roles of k_{ph} and k'_{ph} in Eq. (A.17) and therefore yields

$$[A \cdot G]_{1'|1} = \sum_{k'_{ph}} A_{\sigma_{2'}\sigma_{1'}|\sigma_2\sigma_1}(Q_{ph} = 0, k_{ph}, k'_{ph}) G_{\sigma_2|\sigma_{2'}}(k'_{ph}). \tag{A.19}$$

We now turn to the second version of the loop product, Eq. (7), which plays a key role in the SDE formulation. Specifically, from Eq. (20), it is clear that in the *ph* channel formulation we consider

$$[G \cdot A]_{1'|1} = G_{2|2'}A_{2'1'|12} = \sum_{k_2,k_{2'}} G_{\sigma_2|\sigma_{2'}}(k_2|k_{2'})A_{\sigma_{2'}\sigma_{1'}|\sigma_1\sigma_2}(k_{2'},k_{1'}|k_1,k_2). \tag{A.20}$$

Translational invariance and energy conservation implies

$$[A \cdot G]_{1'|1} = \sum_{k_2} G_{\sigma_2|\sigma_{2'}}(k_2)A_{\sigma_{2'}\sigma_{1'}|\sigma_1\sigma_2}(k_2,k_1|k_1,k_2). \tag{A.21}$$

As before, the loop product imposes that $k_{1'} = k_1$ and $k_{2'} = k_2$ for A. As a consequence, we conclude this time that the use of the $\overline{ph}$ convention to parametrize the momentum and frequency dependence of $A_{\sigma_{2'}\sigma_{1'}|\sigma_1\sigma_2}(k_2,k_1|k_1,k_2)$ is the most convenient choice, yielding

$$[A \cdot G]_{1'|1} = \sum_{k_{\overline{ph}}} G_{\sigma_2|\sigma_{2'}}(k_{\overline{ph}})A_{\sigma_{2'}\sigma_{1'}|\sigma_1\sigma_2}(Q_{\overline{ph}} = 0, k_{\overline{ph}}, k'_{\overline{ph}}). \tag{A.22}$$

As above, the crossing symmetry of A allows us to write equivalently

$$[A \cdot G]_{1'|1} = \sum_{k'_{\overline{ph}}} G_{\sigma_2|\sigma_{2'}}(k'_{\overline{ph}})A_{\sigma_{1'}\sigma_{2'}|\sigma_1\sigma_2}(Q_{\overline{ph}} = 0, k_{\overline{ph}}, k'_{\overline{ph}}). \tag{A.23}$$

As a next step, we focus on relations that enable us to derive the flow equations for the bosonic propagators, the fermion-boson couplings and for the rest functions in Appendix D. In other words, we show that the following relations hold for the $\overline{ph}$ channel

$$\left[A \circ \Pi_{\overline{ph}}\right](Q_{\overline{ph}}, k_{\overline{ph}}, k'_{\overline{ph}}) = A(Q_{\overline{ph}}, k_{\overline{ph}}, k'_{\overline{ph}}) \bullet \Pi_{\overline{ph}}(Q_{\overline{ph}}, k'_{\overline{ph}}), \tag{A.24a}$$

$$\left[A \circ \Pi_{\overline{ph}} \circ B\right](Q_{\overline{ph}}, k_{\overline{ph}}, k'_{\overline{ph}}) = \sum_{k''_{\overline{ph}}} A(Q_{\overline{ph}}, k_{\overline{ph}}, k''_{\overline{ph}}) \bullet \Pi_{\overline{ph}}(Q_{\overline{ph}}, k''_{\overline{ph}}) \bullet B(Q_{\overline{ph}}, k''_{\overline{ph}}, k'_{\overline{ph}}), \tag{A.24b}$$

and similarly for the $\overline{ph}$ and pp channel

$$\left[A \circ \Pi_{ph}\right](Q_{ph}, k_{ph}, k'_{ph}) = A(Q_{ph}, k_{ph}, k'_{ph}) \bullet \Pi_{ph}(Q_{ph}, k'_{ph}), \tag{A.25a}$$

$$\left[A \circ \Pi_{ph} \circ B\right](Q_{ph}, k_{ph}, k'_{ph}) = \sum_{k''_{ph}} A(Q_{ph}, k_{ph}, k''_{ph}) \bullet \Pi_{ph}(Q_{ph}, k''_{ph}) \bullet B(Q_{ph}, k''_{ph}, k'_{ph}), \tag{A.25b}$$

and respectively

$$\left[A \circ \Pi_{pp}\right](Q_{pp}, k_{pp}, k'_{pp}) = A(Q_{pp}, k_{pp}, k'_{pp}) \bullet \Pi_{pp}(Q_{pp}, k_{pp}), \tag{A.26a}$$

$$\left[A \circ \Pi_{pp} \circ B\right](Q_{pp}, k_{pp}, k'_{pp}) = \sum_{k''_{pp}} A(Q_{pp}, k''_{pp}, k'_{pp}) \bullet \Pi_{pp}(Q_{pp}, k''_{pp}) \bullet B(Q_{pp}, k_{pp}, k''_{pp}). \tag{A.26b}$$

Here, A and B are generic two-particle objects. For the derivation of these equations, we first consider products of the form

$$\left[A \circ \Pi_{\overline{ph}}\right]_{12|34} = A_{16|54}\Pi_{\overline{ph};52|36} = \sum_{k_5,k_6} A_{\sigma_1\sigma_6|\sigma_5\sigma_4}(k_1,k_6|k_5,k_4)\Pi_{\overline{ph};\sigma_5\sigma_2|\sigma_3\sigma_6}(k_5,k_2|k_3,k_6), \tag{A.27}$$

from Eq. (A.24a), where we restrict ourselves to the $\overline{ph}$ channel for simplicity. Using

$$A_{\sigma_1\sigma_6|\sigma_5\sigma_4}(k_1,k_6|k_5,k_4) = \delta_{k_1+k_6,k_5+k_4}A_{\sigma_1\sigma_6|\sigma_5\sigma_4}\left(Q_{\overline{ph}}, k_{\overline{ph}}, k^{(1)}_{\overline{ph}}\right), \tag{A.28}$$

and the channel-dependent bubble

$$\Pi_{\overline{ph};\sigma_5\sigma_2|\sigma_3\sigma_6}(k_5,k_2|k_3,k_6) = \delta_{k_5,k_3}\delta_{k_2,k_6}G_{\sigma_5|\sigma_3}(k_3)G_{\sigma_2|\sigma_6}(k_2)\,, \tag{A.29}$$

we obtain

$$\left[A\circ\Pi_{\overline{ph}}\right]_{12|34} = \delta_{k_1+k_2,k_3+k_4}A_{\sigma_1\sigma_6|\sigma_5\sigma_4}\left(Q_{\overline{ph}},k_{\overline{ph}},k_{\overline{ph}}^{(1)}\right)G_{\sigma_5|\sigma_3}(k_3)G_{\sigma_2|\sigma_6}(k_2)\,, \tag{A.30}$$

where the parametrization in terms of $Q_{\overline{ph}}$, $k_{\overline{ph}}$, and $k_{\overline{ph}}^{(1)}$ of the two-particle vertex follows the conventions specified in Fig. 7, with

$$\begin{cases} k_1 = \left(\mathbf{k}_{\overline{ph}}+\mathbf{Q}_{\overline{ph}}, v_{\overline{ph}}+\left\lfloor\frac{\Omega_{\overline{ph}}}{2}\right\rfloor\right)\,, \\ k_6 = \left(\mathbf{k}_{\overline{ph}}^{(1)}, v_{\overline{ph}}^{(1)}-\left\lceil\frac{\Omega_{\overline{ph}}}{2}\right\rceil\right)\,, \\ k_5 = \left(\mathbf{k}_{\overline{ph}}^{(1)}+\mathbf{Q}_{\overline{ph}}, v_{\overline{ph}}^{(1)}+\left\lfloor\frac{\Omega_{\overline{ph}}}{2}\right\rfloor\right)\,, \\ k_4 = \left(\mathbf{k}_{\overline{ph}}, v_{\overline{ph}}-\left\lceil\frac{\Omega_{\overline{ph}}}{2}\right\rceil\right)\,. \end{cases} \tag{A.31}$$

At the same time, it holds

$$\begin{aligned} \left[A\circ\Pi_{\overline{ph}}\right]_{12|34} &= \left[A\circ\Pi_{\overline{ph}}\right]_{\sigma_1\sigma_2|\sigma_3\sigma_4}(k_1,k_2|k_3,k_4) \\ &= \delta_{k_1+k_2,k_3+k_4}\left[A\circ\Pi_{\overline{ph}}\right]_{\sigma_1\sigma_2|\sigma_3\sigma_4}\left(Q_{\overline{ph}}^{(1)},k_{\overline{ph}}^{(2)},k_{\overline{ph}}^{(3)}\right)\,, \end{aligned} \tag{A.32}$$

where

$$\begin{cases} k_1 = \left(\mathbf{k}_{\overline{ph}}^{(2)}+\mathbf{Q}_{\overline{ph}}^{(1)}, v_{\overline{ph}}^{(2)}+\left\lfloor\frac{\Omega_{\overline{ph}}^{(1)}}{2}\right\rfloor\right)\,, \\ k_2 = \left(\mathbf{k}_{\overline{ph}}^{(3)}, v_{\overline{ph}}^{(3)}-\left\lceil\frac{\Omega_{\overline{ph}}^{(1)}}{2}\right\rceil\right)\,, \\ k_3 = \left(\mathbf{k}_{\overline{ph}}^{(3)}+\mathbf{Q}_{\overline{ph}}^{(1)}, v_{\overline{ph}}^{(3)}+\left\lfloor\frac{\Omega_{\overline{ph}}^{(1)}}{2}\right\rfloor\right)\,, \\ k_4 = \left(\mathbf{k}_{\overline{ph}}^{(2)}, v_{\overline{ph}}^{(2)}-\left\lceil\frac{\Omega_{\overline{ph}}^{(1)}}{2}\right\rceil\right)\,. \end{cases} \tag{A.33}$$

We find

$$\left[A\circ\Pi_{\overline{ph}}\right]_{\sigma_1\sigma_2|\sigma_3\sigma_4}\left(Q_{\overline{ph}},k_{\overline{ph}},k_{\overline{ph}}^{(1)}\right) = A_{\sigma_1\sigma_6|\sigma_5\sigma_4}\left(Q_{\overline{ph}},k_{\overline{ph}},k_{\overline{ph}}^{(1)}\right)\Pi_{\overline{ph};\sigma_5\sigma_2|\sigma_3\sigma_6}\left(Q_{\overline{ph}},k_{\overline{ph}}^{(1)}\right)\,, \tag{A.34}$$

as stated in Eq. (A.24a), where

$$\Pi_{\overline{ph};\sigma_1\sigma_2|\sigma_3\sigma_4}\left(Q_{\overline{ph}},k_{\overline{ph}}^{(1)}\right) = G_{\sigma_1|\sigma_3}\left(\mathbf{k}_{\overline{ph}}^{(1)}+\mathbf{Q}_{\overline{ph}}, v_{\overline{ph}}^{(1)}+\left\lfloor\frac{\Omega_{\overline{ph}}}{2}\right\rfloor\right)G_{\sigma_2|\sigma_4}\left(\mathbf{k}_{\overline{ph}}^{(1)}, v_{\overline{ph}}^{(1)}-\left\lceil\frac{\Omega_{\overline{ph}}}{2}\right\rceil\right)\,. \tag{A.35}$$

Analogously, the above relation can be easily extended to the $\overline{ph}$ and pp channel.

We also consider products involving an additional B as in Eq. (A.24b). Starting from

$$\begin{aligned} \left[A\circ\Pi_{\overline{ph}}\circ B\right]_{12|34} &= \left[A\circ\Pi_{\overline{ph}}\right]_{16|54}B_{52|36} \\ &= \sum_{k_5,k_6}\left[A\circ\Pi_{\overline{ph}}\right]_{\sigma_1\sigma_6|\sigma_5\sigma_4}(k_1,k_6|k_5,k_4)B_{\sigma_5\sigma_2|\sigma_3\sigma_6}(k_5,k_2|k_3,k_6)\,, \end{aligned} \tag{A.36}$$

we set

$$
\begin{cases}
k_1 = \left(\mathbf{k}_{\overline{ph}} + \mathbf{Q}_{\overline{ph}}, \nu_{\overline{ph}} + \left\lfloor \frac{\Omega_{\overline{ph}}}{2} \right\rfloor\right), \\[2mm]
k_6 = \left(\mathbf{k}_{ph}^{(1)}, \nu_{ph}^{(1)} - \left\lceil \frac{\Omega_{\overline{ph}}}{2} \right\rceil\right), \\[2mm]
k_5 = \left(\mathbf{k}_{ph}^{(1)} + \mathbf{Q}_{\overline{ph}}, \nu_{ph}^{(1)} + \left\lfloor \frac{\Omega_{\overline{ph}}}{2} \right\rfloor\right), \\[2mm]
k_4 = \left(\mathbf{k}_{\overline{ph}}, \nu_{\overline{ph}} - \left\lceil \frac{\Omega_{\overline{ph}}}{2} \right\rceil\right),
\end{cases}
\qquad
\begin{cases}
k_5 = \left(\mathbf{k}_{ph}^{(2)} + \mathbf{Q}_{ph}^{(1)}, \nu_{ph}^{(2)} + \left\lfloor \frac{\Omega_{ph}^{(1)}}{2} \right\rfloor\right), \\[2mm]
k_2 = \left(\mathbf{k}_{ph}^{(3)}, \nu_{ph}^{(3)} - \left\lceil \frac{\Omega_{ph}^{(1)}}{2} \right\rceil\right), \\[2mm]
k_3 = \left(\mathbf{k}_{ph}^{(3)} + \mathbf{Q}_{ph}^{(1)}, \nu_{ph}^{(3)} + \left\lfloor \frac{\Omega_{ph}^{(1)}}{2} \right\rfloor\right), \\[2mm]
k_6 = \left(\mathbf{k}_{ph}^{(2)}, \nu_{ph}^{(2)} - \left\lceil \frac{\Omega_{ph}^{(1)}}{2} \right\rceil\right).
\end{cases}
\tag{A.37}
$$

With these specifications, we obtain

$$
\left[A \circ \Pi_{\overline{ph}} \circ B\right]_{12|34} = \delta_{k_2 - k_3, k_1 - k_4} \sum_{k_5} \left[A \circ \Pi_{\overline{ph}}\right]_{\sigma_1 \sigma_6 | \sigma_5 \sigma_4} \left(Q_{\overline{ph}}, k_{\overline{ph}}, k_{ph}^{(1)}\right)
$$
$$
\times B_{\sigma_5 \sigma_2 | \sigma_3 \sigma_6}\left(Q_{\overline{ph}}, k_{ph}^{(1)}, k_{ph}^{(3)}\right).
\tag{A.38}
$$

In addition, we employ the relation

$$
\left[A \circ \Pi_{\overline{ph}} \circ B\right]_{12|34} = \delta_{k_1 + k_2, k_3 + k_4} \left[A \circ \Pi_{\overline{ph}} \circ B\right]_{\sigma_1 \sigma_2 | \sigma_3 \sigma_4}\left(Q_{ph}^{(2)}, k_{ph}^{(4)}, k_{ph}^{(5)}\right),
\tag{A.39}
$$

with

$$
\begin{cases}
k_1 = \left(\mathbf{k}_{ph}^{(4)} + \mathbf{Q}_{ph}^{(2)}, \nu_{ph}^{(4)} + \left\lfloor \frac{\Omega_{ph}^{(2)}}{2} \right\rfloor\right), \\[3mm]
k_2 = \left(\mathbf{k}_{ph}^{(5)}, \nu_{ph}^{(5)} - \left\lceil \frac{\Omega_{ph}^{(2)}}{2} \right\rceil\right), \\[3mm]
k_3 = \left(\mathbf{k}_{ph}^{(5)} + \mathbf{Q}_{ph}^{(2)}, \nu_{ph}^{(5)} + \left\lfloor \frac{\Omega_{ph}^{(2)}}{2} \right\rfloor\right), \\[3mm]
k_4 = \left(\mathbf{k}_{ph}^{(4)}, \nu_{ph}^{(4)} - \left\lceil \frac{\Omega_{ph}^{(2)}}{2} \right\rceil\right).
\end{cases}
\tag{A.40}
$$

Thus, we infer

$$
\left[A \circ \Pi_{\overline{ph}} \circ B\right]_{12|34} = \delta_{k_1 + k_2, k_3 + k_4} \left[A \circ \Pi_{\overline{ph}} \circ B\right]_{\sigma_1 \sigma_2 | \sigma_3 \sigma_4}\left(Q_{\overline{ph}}, k_{\overline{ph}}, k_{ph}^{(3)}\right).
\tag{A.41}
$$

Comparing Eqs. (A.38) and (A.41) yields the anticipated result, i.e., Eq. (A.24b). This is evident by relabelling $k_{\overline{ph}}^{(1)}$ by $k_{\overline{ph}}^{(2)}$ and $k_{\overline{ph}}^{(3)}$ by $k_{ph}^{(1)}$

$$
\left[A \circ \Pi_{\overline{ph}} \circ B\right]_{\sigma_1 \sigma_2 | \sigma_3 \sigma_4}\left(Q_{\overline{ph}}, k_{\overline{ph}}, k_{ph}^{(1)}\right) = \sum_{k_{ph}^{(2)}} \left[A \circ \Pi_{\overline{ph}}\right]_{\sigma_1 \sigma_6 | \sigma_5 \sigma_4}\left(Q_{\overline{ph}}, k_{\overline{ph}}, k_{ph}^{(2)}\right)
$$
$$
\times B_{\sigma_1 \sigma_2 | \sigma_3 \sigma_6}\left(Q, k_{ph}^{(2)}, k_{ph}^{(1)}\right).
\tag{A.42}
$$

B Extension to non-local interactions

In the presence of non-local bare interactions of the generic form $U = U(Q_r, k_r, k_r')$, a naive application of the single-boson exchange decomposition based on the classification of diagrams

in terms of U reducibility yields bosonic propagators $w_r(Q_r, k_r, k'_r)$ and fermion-boson couplings $\lambda_r(Q_r, k_r, k'_r)$ with the full momentum and frequency dependence, spoiling its original idea.

For the extended Hubbard model with an additional nearest-neighbor interaction, this can be overcome by considering a generalized single-boson exchange formulation [57], where the notion of bare interaction reducibility is replaced by a $\mathcal{B}$ reducibility: the bare interaction in each channel is split according to

$$U_r(Q_r, k_r, k'_r) = \mathcal{B}_r(Q_r) + \mathcal{F}_r(Q_r, k_r, k'_r), \tag{B.1}$$

where $\mathcal{B}_r$ depends exclusively on the bosonic momentum and frequency in channel r, while $\mathcal{F}_r$ carries the dependence on the fermionic arguments. The bosonic propagator $w_r^{(\mathcal{B})}(Q_r)$ and the fermion-boson coupling $\lambda_r^{(\mathcal{B})}(Q_r, k_r)$ then retain their reduced momentum and frequency dependence characteristic of the single-boson exchange formulation[4] (we here introduced an additional superscript to disambiguate them from the w_r and λ_r for local interactions referred to in the main text). However, the relation (14) does not hold anymore in this case

$$w_r^{(\mathcal{B})} \bullet \lambda_r^{(\mathcal{B})} \neq U_r + U_r \circ \Pi_r \circ V_r. \tag{B.2}$$

For the generalized single-boson exchange formulation we have instead

$$w_r^{(\mathcal{B})} \bullet \lambda_r^{(\mathcal{B})} = \mathcal{B}_r + \mathcal{B}_r \circ \Pi_r \circ V_r. \tag{B.3}$$

As a consequence, the SDE will not reduce to the form derived for local interactions. In particular, inserting Eq. (B.1) in the conventional form of the SDE leads to an additional term of the form $\mathcal{F}_r \circ \Pi_r \circ V_r$ that cannot be absorbed in a product of $w_r^{(\mathcal{B})}$ and $\lambda_r^{(\mathcal{B})}$. However, if $\mathcal{F}_r \circ \Pi_r \circ V_r = 0$, the results of the main text still apply. In fact, this applies for the extended Hubbard model in the s-wave truncation [57].

C Momentum and frequency dependence of the SDE

We here outline the derivation of the SDE in the form of Eqs. (25) with the explicit momentum and frequency dependence. Starting from Eqs. (21) derived in the main text, Eq. (A.17) introduced in Appendix A.2 allows us to rewrite the SDE as

$$\Sigma_{\sigma_{1'}|\sigma_1}(k'_{ph}) = \sum_{k_{ph}} A_{\sigma_{1'}\sigma_{2'}|\sigma_1\sigma_2}(Q_{ph} = 0, k_{ph}, k'_{ph}) G_{\sigma_2|\sigma_{2'}}(k_{ph}). \tag{C.1}$$

Specifically, we focus on the $\overline{ph}$ channel formulation first. In order to directly compare to Eq. (21a), where the spin components for the various terms contributing to the SDE are already fixed, we rewrite Eq. (C.1) for $\sigma_{1'} = \sigma_1 = \uparrow$ and $\sigma_{2'} = \sigma_2 = \downarrow$, namely

$$\Sigma^{\uparrow}(k'_{ph}) = \sum_{k_{ph}} A_{\uparrow\downarrow}(Q_{ph} = 0, k_{ph}, k'_{ph}) G^{\downarrow}(k_{ph}), \tag{C.2}$$

where we also used the shorthand notation (16) to express $\Sigma^{\uparrow|\uparrow} = \Sigma^{\uparrow}$, $A_{\uparrow\downarrow|\uparrow\downarrow} = A_{\uparrow\downarrow}$, and $G_{\downarrow|\downarrow} = G^{\downarrow}$. We stress that Eq. (C.2) does not involve any summation over spin indices, like Eqs. (21). We can thus write Eq. (21a) in the form (C.2) by setting

$$A_{\uparrow\downarrow}(Q_{ph} = 0, k_{ph}, k'_{ph}) = \left[-w_{\overline{ph}}^{\uparrow\downarrow}(Q_{\overline{ph}}) \lambda_{\overline{ph}}^{\uparrow\downarrow}(Q_{\overline{ph}}, k'_{\overline{ph}}) \right](Q_{ph} = 0, k_{ph}, k'_{ph}). \tag{C.3}$$

---

[4]Note that in Ref. [9], w_r and λ_r are defined by separating the U-reducible parts of the full vertex V, regardless of the momentum dependence of U. In contrast, $w_r^{(\mathcal{B})}$ and $\lambda_r^{(\mathcal{B})}$ are defined with respect to $\mathcal{B}$ reducibility with a reduced momentum and frequency dependence. In this sense they represent a generalization of w_r and λ_r for non-local interactions.

In order to determine the momentum and frequency dependence of $w^{\uparrow\downarrow}_{\underline{ph}}$ and $\lambda^{\uparrow\downarrow}_{\underline{ph}}$, we translate $Q_{\overline{ph}}$ and $k'_{\underline{ph}}$ into the ph notation with $Q_{ph} = 0$ by using the following relations from Fig. 7

$$Q_{\overline{ph}} = (\mathbf{Q}_{\overline{ph}}, \Omega_{\overline{ph}}) \underset{Q_{ph}=0}{=} (\mathbf{k}'_{ph} - \mathbf{k}_{ph}, \nu'_{ph} - \nu_{ph}), \qquad \text{(C.4a)}$$

$$k'_{\underline{ph}} = (\mathbf{k}'_{\underline{ph}}, \nu'_{\underline{ph}}) \underset{Q_{ph}=0}{=} \left(\mathbf{k}_{ph}, \left\lceil \frac{\nu_{ph} + \nu'_{ph}}{2} \right\rceil_{\text{ferm}} \right), \qquad \text{(C.4b)}$$

where we introduced the notation $\lceil ... \rceil_{\text{ferm}}$ $\left(\lfloor ... \rfloor_{\text{ferm}} \right)$ which rounds its argument up (down) to the nearest *fermionic* Matsubara frequency. This differs from the symbols $\lceil ... \rceil$ and $\lfloor ... \rfloor$ used previously to round up or down to the nearest *bosonic* Matsubara frequency. For clarity, these symbols will be replaced by $\lceil ... \rceil_{\text{bos}}$ and $\lfloor ... \rfloor_{\text{bos}}$ respectively in the following. Hence, we can rewrite Eq. (C.3) as

$$A_{\uparrow\downarrow}(Q_{ph} = 0, k_{ph}, k'_{ph}) = -w^{\uparrow\downarrow}_{\underline{ph}}(\mathbf{k}'_{ph} - \mathbf{k}_{ph}; \nu'_{ph} - \nu_{ph})$$

$$\times \lambda^{\uparrow\downarrow}_{\underline{ph}} \left(\mathbf{k}'_{ph} - \mathbf{k}_{ph}, \mathbf{k}_{ph}; \nu'_{ph} - \nu_{ph}, \left\lceil \frac{\nu_{ph} + \nu'_{ph}}{2} \right\rceil_{\text{ferm}} \right). \qquad \text{(C.5)}$$

The self-energy, Eq. (C.2), then reads

$$\Sigma^{\uparrow}(\mathbf{k}; \nu) = -\sum_{\mathbf{k}', \nu'} w^{\uparrow\downarrow}_{\underline{ph}}(\mathbf{k} - \mathbf{k}'; \nu - \nu') \lambda^{\uparrow\downarrow}_{\underline{ph}} \left(\mathbf{k} - \mathbf{k}', \mathbf{k}'; \nu - \nu', \left\lceil \frac{\nu + \nu'}{2} \right\rceil_{\text{ferm}} \right) G^{\downarrow}(\mathbf{k}'; \nu'), \qquad \text{(C.6)}$$

where the momentum and frequency indices have been relabeled. Setting $\mathbf{Q} = \mathbf{k} - \mathbf{k}'$ and $\Omega = \nu - \nu'$, the fermionic frequency argument of λ^{M} can be expressed as

$$\left\lceil \frac{\nu + \nu'}{2} \right\rceil_{\text{ferm}} = \left\lceil \frac{2\nu - \Omega}{2} \right\rceil_{\text{ferm}} = \nu - \left\lceil \frac{\Omega}{2} \right\rceil_{\text{bos}}. \qquad \text{(C.7)}$$

With this, the right-hand side of Eq. (C.6) can be rewritten as a sum over the bosonic arguments $\mathbf{Q}$ and Ω by

$$\Sigma^{\uparrow}(\mathbf{k}; \nu) = -\sum_{\mathbf{Q}, \Omega} w^{\uparrow\downarrow}_{\underline{ph}}(\mathbf{Q}; \Omega) \lambda^{\uparrow\downarrow}_{\underline{ph}} \left(\mathbf{Q}, \mathbf{k} - \mathbf{Q}; \Omega, \nu - \left\lceil \frac{\Omega}{2} \right\rceil_{\text{bos}} \right) G^{\downarrow}(\mathbf{k} - \mathbf{Q}; \nu - \Omega). \qquad \text{(C.8)}$$

As explained in Appendix A.2, one can also use crossing symmetry to obtain Eq. (A.19), for which the starting point of our derivation is

$$\Sigma^{\uparrow}(k_{ph}) = \sum_{k'_{ph}} A_{\uparrow\downarrow}(Q_{ph} = 0, k_{ph}, k'_{ph}) G^{\downarrow}(k'_{ph}), \qquad \text{(C.9)}$$

instead of Eq. (C.2). This modifies the arguments in Eq. (C.8) which are substituted by

$$\Sigma^{\uparrow}(\mathbf{k}; \nu) = -\sum_{\mathbf{Q}, \Omega} w^{\uparrow\downarrow}_{\underline{ph}}(\mathbf{Q}; \Omega) \lambda^{\uparrow\downarrow}_{\underline{ph}} \left(\mathbf{Q}, \mathbf{k}; \Omega, \nu + \left\lceil \frac{\Omega}{2} \right\rceil_{\text{bos}} \right) G^{\downarrow}(\mathbf{k} + \mathbf{Q}; \nu + \Omega). \qquad \text{(C.10)}$$

We note that Eqs. (C.8) and (C.10) are fully equivalent since they are only related by crossing symmetry.

A similar result can be derived for the ph channel formulation by starting from Eqs. (20) and (A.22). From their comparison we infer

$$\Sigma^{\uparrow}(k'_{\underline{ph}}) = \sum_{k_{\overline{ph}}} G^{\downarrow}(k_{\overline{ph}}) A_{\downarrow\uparrow}(Q_{\overline{ph}} = 0, k_{\overline{ph}}, k'_{\underline{ph}}). \qquad \text{(C.11)}$$

Thus, we identify

$$A_{\widehat{\downarrow\uparrow}}(Q_{\overline{ph}} = 0, k_{\overline{ph}}, k'_{\overline{ph}}) = \left[w_{ph}^{\widehat{\downarrow\uparrow}}(Q_{ph}) \lambda_{ph}^{\widehat{\downarrow\uparrow}}(Q_{ph}, k'_{ph}) \right](Q_{\overline{ph}} = 0, k_{\overline{ph}}, k'_{\overline{ph}}). \tag{C.12}$$

Following the same steps as above, and applying crossing symmetry, we obtain two different, yet equivalent expressions in the *ph* channel

$$\Sigma^{\uparrow}(\mathbf{k}; \nu) = \sum_{\mathbf{Q},\Omega} w_{ph}^{\widehat{\downarrow\uparrow}}(\mathbf{Q}; \Omega) \lambda_{ph}^{\widehat{\downarrow\uparrow}}\left(\mathbf{Q}, \mathbf{k} - \mathbf{Q}; \Omega, \nu - \left\lceil \frac{\Omega}{2} \right\rceil_{\text{bos}} \right) G^{\downarrow}(\mathbf{k} - \mathbf{Q}; \nu - \Omega), \tag{C.13a}$$

$$\Sigma^{\uparrow}(\mathbf{k}; \nu) = \sum_{\mathbf{Q},\Omega} w_{ph}^{\widehat{\downarrow\uparrow}}(\mathbf{Q}; \Omega) \lambda_{ph}^{\widehat{\downarrow\uparrow}}\left(\mathbf{Q}, \mathbf{k}; \Omega, \nu + \left\lceil \frac{\Omega}{2} \right\rceil_{\text{bos}} \right) G^{\downarrow}(\mathbf{k} + \mathbf{Q}; \nu + \Omega). \tag{C.13b}$$

The derivation in the superconducting channel is similar. In this case, we use the translation from the *pp* to the *ph* notation. Alternatively, it is also possible to start from Eq. (C.2), with

$$A_{\uparrow\downarrow}(Q_{ph} = 0, k_{ph}, k'_{ph}) = \left[-w_{pp}^{\uparrow\downarrow}(Q_{pp})\left(2\lambda_{pp}^{\uparrow\downarrow}(Q_{pp}, k'_{pp}) - 1 \right) \right](Q_{ph} = 0, k_{ph}, k'_{ph}). \tag{C.14}$$

From Fig. 7 we infer

$$Q_{pp} = (\mathbf{Q}_{pp}, \Omega_{pp}) \underset{Q_{ph} = 0}{=} (\mathbf{k}_{ph} + \mathbf{k}'_{ph}, \nu_{ph} + \nu'_{ph}), \tag{C.15a}$$

$$k'_{pp} = (\mathbf{k}'_{pp}, \nu'_{pp}) \underset{Q_{ph} = 0}{=} \left(\mathbf{k}_{ph}, \left\lceil \frac{\nu_{ph} - \nu'_{ph}}{2} \right\rceil_{\text{ferm}} \right), \tag{C.15b}$$

leading to

$$\Sigma^{\uparrow}(\mathbf{k}; \nu) = -\sum_{\mathbf{k}', \nu'} w_{pp}^{\uparrow\downarrow}(\mathbf{k} + \mathbf{k}'; \nu + \nu') \left(2\lambda_{pp}^{\uparrow\downarrow}\left(\mathbf{k} + \mathbf{k}', \mathbf{k}'; \nu + \nu', \left\lceil \frac{\nu' - \nu}{2} \right\rceil_{\text{ferm}} \right) - 1 \right) G^{\downarrow}(\mathbf{k}'; \nu'). \tag{C.16}$$

By introducing the bosonic arguments $\mathbf{Q} = \mathbf{k} + \mathbf{k}'$ and $\Omega = \nu + \nu'$, this can be rewritten as

$$\Sigma^{\uparrow}(\mathbf{k}; \nu) = -\sum_{\mathbf{Q},\Omega} w_{pp}^{\uparrow\downarrow}(\mathbf{Q}; \Omega) \left(2\lambda_{pp}^{\uparrow\downarrow}\left(\mathbf{Q}, \mathbf{Q} - \mathbf{k}; \Omega, \left\lceil \frac{\Omega}{2} \right\rceil_{\text{bos}} - \nu \right) - 1 \right) G^{\downarrow}(\mathbf{Q} - \mathbf{k}; \Omega - \nu). \tag{C.17}$$

As before, crossing symmetry can be used to determine the equivalent expression

$$\Sigma^{\uparrow}(\mathbf{k}; \nu) = -\sum_{\mathbf{Q},\Omega} w_{pp}^{\uparrow\downarrow}(\mathbf{Q}; \Omega) \left(2\lambda_{pp}^{\uparrow\downarrow}\left(\mathbf{Q}, \mathbf{k}; \Omega, \nu - \left\lceil \frac{\Omega}{2} \right\rceil_{\text{bos}} \right) - 1 \right) G^{\downarrow}(\mathbf{Q} - \mathbf{k}; \Omega - \nu). \tag{C.18}$$

We now outline the derivation within the physical channel formulations, as presented in Eq. (36) in the main text, showing how it follows straightforwardly from the above lines assuming SU(2) symmetry. First, we focus on the magnetic channel formulation. In Eq. (C.3), we can identify

$$A_{\uparrow\downarrow} = -w_{\overline{ph}}^{\uparrow\downarrow}(Q_{\overline{ph}})\lambda_{\overline{ph}}^{\uparrow\downarrow}(Q_{\overline{ph}}, k'_{\overline{ph}}) = w^{\text{M}}(Q_{\overline{ph}})\lambda^{\text{M}}(Q_{\overline{ph}}, k'_{\overline{ph}}). \tag{C.19}$$

Thus, following the same steps that led us to recover the final forms in Eqs. (C.8) and (C.10), we can derive the two equivalent magnetic channel formulations, which are related by crossing symmetry. With the explicit momentum and frequency dependencies, they read

$$\Sigma(\mathbf{k}; \nu) = \sum_{\mathbf{Q},\Omega} w^{\text{M}}(\mathbf{Q}; \Omega)\lambda^{\text{M}}\left(\mathbf{Q}, \mathbf{k} - \mathbf{Q}; \Omega, \nu - \left\lceil \frac{\Omega}{2} \right\rceil_{\text{bos}} \right) G(\mathbf{k} - \mathbf{Q}; \nu - \Omega) \tag{C.20a}$$

$$= \sum_{\mathbf{Q},\Omega} w^{\text{M}}(\mathbf{Q}; \Omega)\lambda^{\text{M}}\left(\mathbf{Q}, \mathbf{k}; \Omega, \nu + \left\lceil \frac{\Omega}{2} \right\rceil_{\text{bos}} \right) G(\mathbf{k} + \mathbf{Q}; \nu + \Omega). \tag{C.20b}$$

The same reasoning applies for the density channel formulation for which we also use the translation from the $\overline{ph}$ to the ph parametrization to obtain the explicit form of the self-energy. Similarly, crossing symmetry yields two different, but equivalent expressions

$$\Sigma(\mathbf{k}; \nu) = \sum_{\mathbf{Q},\Omega} \left[w^{\mathrm{D}}(\mathbf{Q};\Omega) \lambda^{\mathrm{D}}\left(\mathbf{Q}, \mathbf{k}-\mathbf{Q};\Omega, \nu - \left\lceil \frac{\Omega}{2} \right\rceil_{\mathrm{bos}} \right) - 2U^{\mathrm{D}}(\mathbf{Q},\mathbf{k};\Omega,\nu) \right] G(\mathbf{k}-\mathbf{Q}; \nu - \Omega), \quad \text{(C.21a)}$$

$$\Sigma(\mathbf{k}; \nu) = \sum_{\mathbf{Q},\Omega} \left[w^{\mathrm{D}}(\mathbf{Q};\Omega) \lambda^{\mathrm{D}}\left(\mathbf{Q}, \mathbf{k};\Omega, \nu + \left\lceil \frac{\Omega}{2} \right\rceil_{\mathrm{bos}} \right) - 2U^{\mathrm{D}}(\mathbf{Q},\mathbf{k};\Omega,\nu) \right] G(\mathbf{k}+\mathbf{Q}; \nu + \Omega). \quad \text{(C.21b)}$$

For the superconducting channel, the key point is the identification of

$$A_{\uparrow\downarrow} = -w_{pp}^{\uparrow\downarrow}(Q_{pp})\left(2\lambda_{pp}^{\uparrow\downarrow}(Q_{pp}, k'_{pp}) - 1 \right) = -w^{\mathrm{SC}}(Q_{pp})\lambda^{\mathrm{SC}}(Q_{pp}, k'_{pp}) \quad \text{(C.22)}$$

in Eq. (C.14). Analogously to the derivation of Eqs.(C.17) and (C.18), we obtain the two crossing symmetry-related equivalent formulations

$$\Sigma(\mathbf{k}; \nu) = -\sum_{\mathbf{Q},\Omega} w^{\mathrm{SC}}(\mathbf{Q};\Omega) \lambda^{\mathrm{SC}}\left(\mathbf{Q}, \mathbf{Q}-\mathbf{k};\Omega, \left\lceil \frac{\Omega}{2} \right\rceil_{\mathrm{bos}} - \nu \right) G(\mathbf{Q}-\mathbf{k};\Omega - \nu) \quad \text{(C.23a)}$$

$$= -\sum_{\mathbf{Q},\Omega} w^{\mathrm{SC}}(\mathbf{Q};\Omega) \lambda^{\mathrm{SC}}\left(\mathbf{Q}, \mathbf{k};\Omega, \nu - \left\lceil \frac{\Omega}{2} \right\rceil_{\mathrm{bos}} \right) G(\mathbf{Q}-\mathbf{k};\Omega - \nu). \quad \text{(C.23b)}$$

D   Single-boson exchange flow equations

In this section, we report the (1ℓ) fRG equations for the bosonic propagators, the fermion-boson couplings, and the rest functions (the flow equation for the self-energy is obtained from the derivative of the SDE). In diagrammatic channels [9, 10, 15], they read

$$\dot{w}_r = w_r \bullet \lambda_r \circ \dot{\Pi}_r \circ \lambda_r \bullet w_r, \quad \text{(D.1a)}$$

$$\dot{\lambda}_r = \lambda_r \circ \dot{\Pi}_r \circ \mathcal{I}_r, \quad \text{(D.1b)}$$

$$\dot{M}_r = \mathcal{I}_r \circ \dot{\Pi}_r \circ \mathcal{I}_r, \quad \text{(D.1c)}$$

where $\mathcal{I}_r$ is the U irreducible vertex in channel r.

In physical channels, the explicit form for the magnetic channel is[5]

$$\dot{w}^{\mathrm{M}}(Q) = -\dot{w}_{ph}^{\uparrow\downarrow}(Q) = -\left[w^{\mathrm{M}}(Q) \right]^2 \sum_k \lambda^{\mathrm{M}}(Q,k) \dot{\Pi}^{\mathrm{M}}(Q,k) \lambda^{\mathrm{M}}(Q,k), \quad \text{(D.2a)}$$

$$\dot{\lambda}^{\mathrm{M}}(Q,k) = \dot{\lambda}_{ph}^{\uparrow\downarrow} = -\sum_{k'} \lambda^{\mathrm{M}}(Q,k') \dot{\Pi}^{\mathrm{M}}(Q,k') \mathcal{I}^{\mathrm{M}}(Q,k',k), \quad \text{(D.2b)}$$

$$\dot{M}^{\mathrm{M}}(Q,k,k') = -\dot{M}_{ph}^{\uparrow\downarrow}(Q,k,k') = -\sum_{k''} \mathcal{I}^{\mathrm{M}}(Q,k,k'') \dot{\Pi}^{\mathrm{M}}(Q,k'') \mathcal{I}^{\mathrm{M}}(Q,k'',k'). \quad \text{(D.2c)}$$

Analogously, for the density channel we have

$$\dot{w}^{\mathrm{D}}(Q) = \dot{w}_{ph}^{\uparrow\uparrow}(Q) + \dot{w}_{ph}^{\uparrow\downarrow}(Q) = \left[w^{\mathrm{D}}(Q) \right]^2 \sum_k \lambda^{\mathrm{D}}(Q,k) \dot{\Pi}^{\mathrm{D}}(Q,k) \lambda^{\mathrm{D}}(Q,k), \quad \text{(D.3a)}$$

$$\dot{\lambda}^{\mathrm{D}}(Q,k) = \dot{\lambda}_{ph}^{\uparrow\uparrow}(Q,k) + \dot{\lambda}_{ph}^{\uparrow\downarrow}(Q,k) = \sum_{k'} \lambda^{\mathrm{D}}(Q,k') \dot{\Pi}^{\mathrm{D}}(Q,k') \mathcal{I}^{\mathrm{D}}(Q,k',k), \quad \text{(D.3b)}$$

$$\dot{M}^{\mathrm{D}}(Q,k,k') = \dot{M}_{ph}^{\uparrow\uparrow}(Q,k,k') + \dot{M}_{ph}^{\uparrow\downarrow}(Q,k,k') = \sum_{k''} \mathcal{I}^{\mathrm{D}}(Q,k,k'') \dot{\Pi}^{\mathrm{D}}(Q,k'') \mathcal{I}^{\mathrm{D}}(Q,k'',k'), \quad \text{(D.3c)}$$

---

[5]For completeness, we here report also the flow equation for the rest function, despite it is neglected in the numerical results discussed in Section 3.

and for the superconducting channel

$$\dot{w}^{SC}(Q) = \dot{w}_{pp}^{\uparrow\downarrow}(Q) - \dot{w}_{pp}^{\widehat{\uparrow\downarrow}}(Q) = \left[w^{SC}(Q)\right]^2 \sum_k \lambda^{SC}(Q,k)\dot{\Pi}^{SC}(Q,k)\lambda^{SC}(Q,k), \qquad \text{(D.4a)}$$

$$\dot{\lambda}^{SC}(Q,k) = \dot{\lambda}_{pp}^{\uparrow\downarrow}(Q,k) - \dot{\lambda}_{pp}^{\widehat{\uparrow\downarrow}}(Q,k) = \sum_{k'} \lambda^{SC}(Q,k')\dot{\Pi}^{SC}(Q,k')\mathcal{I}^{SC}(Q,k,k'), \qquad \text{(D.4b)}$$

$$\dot{M}^{SC}(Q,k,k') = \dot{M}_{pp}^{\uparrow\downarrow}(Q,k,k') - \dot{M}_{pp}^{\widehat{\uparrow\downarrow}}(Q,k,k') = \sum_{k''} \mathcal{I}^{SC}(Q,k'',k')\dot{\Pi}^{SC}(Q,k'')\mathcal{I}^{SC}(Q,k,k''),$$
$$\text{(D.4c)}$$

where we used the corresponding definitions in the physical channels for the bubbles, Eq. (3), as well as the considerations provided in Appendix A.

As an example, we illustrate how the flow equation for the bosonic propagator in the magnetic channel is obtained from Eq. (D.1a) through the use of Eq. (6b)

$$\dot{w}^M = -\dot{w}_{\overline{ph}}^{\uparrow\downarrow} = -\left[w_{\overline{ph}} \bullet \lambda_{\overline{ph}} \circ \dot{\Pi}_{\overline{ph}} \circ \lambda_{\overline{ph}} \bullet w_{\overline{ph}}\right]^{\uparrow\downarrow}$$
$$= -\left[w_{\overline{ph}}^{\uparrow\downarrow}\right]^2 \left[\lambda_{\overline{ph}} \circ \dot{\Pi}_{\overline{ph}} \circ \lambda_{\overline{ph}}\right]^{\uparrow\downarrow}$$
$$= -\left[w_{\overline{ph}}^{\uparrow\downarrow}\right]^2 \lambda_{\overline{ph}}^{\uparrow\downarrow} \circ \dot{\Pi}_{\overline{ph}}^{\uparrow\downarrow} \circ \lambda_{\overline{ph}}^{\uparrow\downarrow}. \qquad \text{(D.5)}$$

Up to now we focused on the spin structure, the momentum and frequency dependence as well as the respective summations still have to be considered. While for the $\circ$ product we can use Eq. (A.24b), the $\bullet$ multiplication with the bosonic propagator involves only the summation over spin indices. With the translation to the magnetic channel, Eq. (27), we thus recover Eq. (D.2a).

The derivation of the flow equations for the fermion-boson coupling (D.2b) and the rest function (D.2c) is straightforward, since these correspond to the $\uparrow\downarrow$ spin component of the products in Eqs. (D.1b) and (D.1c) which are diagonal in the $\overline{ph}$ channel. The flow equations in the density and superconducting channels are obtained along the same lines. This applies also to the derivation of the momentum and frequency dependence of the multiloop equations, i.e., where Eqs. (D.1) are replaced by Eqs. (48) of Ref. [9].

References

[1] F. Krien, A. Valli and M. Capone, *Single-boson exchange decomposition of the vertex function*, Phys. Rev. B **100**, 155149 (2019), doi:10.1103/PhysRevB.100.155149.

[2] F. Krien, A. I. Lichtenstein and G. Rohringer, *Fluctuation diagnostic of the nodal/antinodal dichotomy in the Hubbard model at weak coupling: A parquet dual fermion approach*, Phys. Rev. B **102**, 235133 (2020), doi:10.1103/physrevb.102.235133.

[3] T. Denz, M. Mitter, J. M. Pawlowski, C. Wetterich and M. Yamada, *Partial bosonization for the two-dimensional Hubbard model*, Phys. Rev. B **101**, 155115 (2020), doi:10.1103/PhysRevB.101.155115.

[4] F. Krien, A. Valli, P. Chalupa, M. Capone, A. I. Lichtenstein and A. Toschi, *Boson-exchange parquet solver for dual fermions*, Phys. Rev. B **102**, 195131 (2020), doi:10.1103/PhysRevB.102.195131.

[5] F. Krien, P. Worm, P. Chalupa-Gantner, A. Toschi and K. Held, *Explaining the pseudogap through damping and antidamping on the Fermi surface by imaginary spin scattering*, Commun. Phys. **5**, 336 (2022), doi:10.1038/s42005-022-01117-5.

[6] F. Krien, A. Kauch and K. Held, *Tiling with triangles: Parquet and $GW\gamma$ methods unified*, Phys. Rev. Res. **3**, 013149 (2021), doi:10.1103/PhysRevResearch.3.013149.

[7] V. Harkov, A. I. Lichtenstein and F. Krien, *Parametrizations of local vertex corrections from weak to strong coupling: Importance of the Hedin three-leg vertex*, Phys. Rev. B **104**, 125141 (2021), doi:10.1103/PhysRevB.104.125141.

[8] F. Krien and A. Kauch, *The plain and simple parquet approximation: Single-and multi-boson exchange in the two-dimensional Hubbard model*, Eur. Phys. J. B **95**, 69 (2022), doi:10.1140/epjb/s10051-022-00329-6.

[9] M. Gievers, E. Walter, A. Ge, J. von Delft and F. B. Kugler, *Multiloop flow equations for single-boson exchange fRG*, Eur. Phys. J. B **95**, 108 (2022), doi:10.1140/epjb/s10051-022-00353-6.

[10] P. M. Bonetti, A. Toschi, C. Hille, S. Andergassen and D. Vilardi, *Single-boson exchange representation of the functional renormalization group for strongly interacting many-electron systems*, Phys. Rev. Res. **4**, 013034 (2022), doi:10.1103/PhysRevResearch.4.013034.

[11] S. Adler, F. Krien, P. Chalupa-Gantner, G. Sangiovanni and A. Toschi, *Non-perturbative intertwining between spin and charge correlations: A "smoking gun" single-boson-exchange result*, SciPost Phys. **16**, 054 (2024), doi:10.21468/SciPostPhys.16.2.054.

[12] D. Kiese, N. Wentzell, I. Krivenko, O. Parcollet, K. Held and F. Krien, *Embedded multi-boson exchange: A step beyond quantum cluster theories*, Phys. Rev. Res. **6**, 043159 (2024), doi:10.1103/PhysRevResearch.6.043159.

[13] M. V. Sadovskii, *Diagrammatics*, World Scientific, Singapore, ISBN 9789811212208 (2019), doi:10.1142/11605.

[14] N. Wentzell, G. Li, A. Tagliavini, C. Taranto, G. Rohringer, K. Held, A. Toschi and S. Andergassen, *High-frequency asymptotics of the vertex function: Diagrammatic parametrization and algorithmic implementation*, Phys. Rev. B **102**, 085106 (2020), doi:10.1103/PhysRevB.102.085106.

[15] K. Fraboulet, S. Heinzelmann, P. M. Bonetti, A. Al-Eryani, D. Vilardi, A. Toschi and S. Andergassen, *Single-boson exchange functional renormalization group application to the two-dimensional Hubbard model at weak coupling*, Eur. Phys. J. B **95**, 202 (2022), doi:10.1140/epjb/s10051-022-00438-2.

[16] T. Schäfer, G. Rohringer, O. Gunnarsson, S. Ciuchi, G. Sangiovanni and A. Toschi, *Divergent precursors of the Mott-Hubbard transition at the two-particle level*, Phys. Rev. Lett. **110**, 246405 (2013), doi:10.1103/PhysRevLett.110.246405.

[17] V. Janiš and V. Pokorný, *Critical metal-insulator transition and divergence in a two-particle irreducible vertex in disordered and interacting electron systems*, Phys. Rev. B **90**, 045143 (2014), doi:10.1103/PhysRevB.90.045143.

[18] O. Gunnarsson, T. Schäfer, J. P. F. LeBlanc, J. Merino, G. Sangiovanni, G. Rohringer and A. Toschi, *Parquet decomposition calculations of the electronic self-energy*, Phys. Rev. B **93**, 245102 (2016), doi:10.1103/PhysRevB.93.245102.

[19] T. Schäfer, A. Toschi and K. Held, *Dynamical vertex approximation for the two-dimensional Hubbard model*, J. Magn. Magn. Mater. **400**, 107 (2016), doi:10.1016/j.jmmm.2015.07.103.

[20] T. Ribic, G. Rohringer and K. Held, *Nonlocal correlations and spectral properties of the Falicov-Kimball model*, Phys. Rev. B **93**, 195105 (2016), doi:10.1103/PhysRevB.93.195105.

[21] O. Gunnarsson, G. Rohringer, T. Schäfer, G. Sangiovanni and A. Toschi, *Breakdown of traditional many-body theories for correlated electrons*, Phys. Rev. Lett. **119**, 056402 (2017), doi:10.1103/PhysRevLett.119.056402.

[22] J. Vučičević, N. Wentzell, M. Ferrero and O. Parcollet, *Practical consequences of the Luttinger-Ward functional multivaluedness for cluster DMFT methods*, Phys. Rev. B **97**, 125141 (2018), doi:10.1103/PhysRevB.97.125141.

[23] P. Chalupa, P. Gunacker, T. Schäfer, K. Held and A. Toschi, *Divergences of the irreducible vertex functions in correlated metallic systems: Insights from the Anderson impurity model*, Phys. Rev. B **97**, 245136 (2018), doi:10.1103/PhysRevB.97.245136.

[24] P. Thunström, O. Gunnarsson, S. Ciuchi and G. Rohringer, *Analytical investigation of singularities in two-particle irreducible vertex functions of the Hubbard atom*, Phys. Rev. B **98**, 235107 (2018), doi:10.1103/PhysRevB.98.235107.

[25] D. Springer, P. Chalupa, S. Ciuchi, G. Sangiovanni and A. Toschi, *Interplay between local response and vertex divergences in many-fermion systems with on-site attraction*, Phys. Rev. B **101**, 155148 (2020), doi:10.1103/PhysRevB.101.155148.

[26] C. Melnick and G. Kotliar, *Fermi-liquid theory and divergences of the two-particle irreducible vertex in the periodic Anderson lattice*, Phys. Rev. B **101**, 165105 (2020), doi:10.1103/PhysRevB.101.165105.

[27] M. Reitner, P. Chalupa, L. Del Re, D. Springer, S. Ciuchi, G. Sangiovanni and A. Toschi, *Attractive effect of a strong electronic repulsion: The physics of vertex divergences*, Phys. Rev. Lett. **125**, 196403 (2020), doi:10.1103/PhysRevLett.125.196403.

[28] P. Chalupa, T. Schäfer, M. Reitner, D. Springer, S. Andergassen and A. Toschi, *Fingerprints of the local moment formation and its Kondo screening in the generalized susceptibilities of many-electron problems*, Phys. Rev. Lett. **126**, 056403 (2021), doi:10.1103/PhysRevLett.126.056403.

[29] T. B. Mazitov and A. A. Katanin, *Effect of local magnetic moments on spectral properties and resistivity near interaction- and doping-induced Mott transitions*, Phys. Rev. B **106**, 205148 (2022), doi:10.1103/PhysRevB.106.205148.

[30] M. Pelz, S. Adler, M. Reitner and A. Toschi, *Highly nonperturbative nature of the Mott metal-insulator transition: Two-particle vertex divergences in the coexistence region*, Phys. Rev. B **108**, 155101 (2023), doi:10.1103/PhysRevB.108.155101.

[31] N. E. Bickers, *Self-consistent many-body theory for condensed matter systems*, in *Theoretical methods for strongly correlated electrons*, Springer, New York, USA, ISBN 9780387008950 (2004), doi:10.1007/0-387-21717-7_6.

[32] G. Rohringer, A. Valli and A. Toschi, *Local electronic correlation at the two-particle level*, Phys. Rev. B **86**, 125114 (2012), doi:10.1103/PhysRevB.86.125114.

[33] F. Krien and A. Valli, *Parquetlike equations for the Hedin three-leg vertex*, Phys. Rev. B **100**, 245147 (2019), doi:10.1103/physrevb.100.245147.

[34] O. Gunnarsson, T. Schäfer, J. P. F. LeBlanc, E. Gull, J. Merino, G. Sangio-vanni, G. Rohringer and A. Toschi, *Fluctuation diagnostics of the electron self-energy: Origin of the pseudogap physics*, Phys. Rev. Lett. **114**, 236402 (2015), doi:10.1103/PhysRevLett.114.236402.

[35] W. Wu, M. Ferrero, A. Georges and E. Kozik, *Controlling Feynman diagrammatic expansions: Physical nature of the pseudogap in the two-dimensional Hubbard model*, Phys. Rev. B **96**, 041105 (2017), doi:10.1103/PhysRevB.96.041105.

[36] G. Rohringer, *Spectra of correlated many-electron systems: From a one- to a two-particle description*, J. Electron Spectrosc. Relat. Phenom. **241**, 146804 (2020), doi:10.1016/j.elspec.2018.11.003.

[37] T. Schäfer and A. Toschi, *How to read between the lines of electronic spectra: The diagnostics of fluctuations in strongly correlated electron systems*, J. Phys.: Condens. Matter **33**, 214001 (2021), doi:10.1088/1361-648x/abeb44.

[38] X. Dong, L. Del Re, A. Toschi and E. Gull, *Mechanism of superconductivity in the Hubbard model at intermediate interaction strength*, Proc. Natl. Acad. Sci. **119**, e2205048119 (2022), doi:10.1073/pnas.2205048119.

[39] C. Husemann and M. Salmhofer, *Efficient parametrization of the vertex function, Ω scheme, and the t, t' Hubbard model at van Hove filling*, Phys. Rev. B **79**, 195125 (2009), doi:10.1103/PhysRevB.79.195125.

[40] W.-S. Wang, Y.-Y. Xiang, Q.-H. Wang, F. Wang, F. Yang and D.-H. Lee, *Functional renormalization group and variational Monte Carlo studies of the electronic instabilities in graphene near $\frac{1}{4}$ doping*, Phys. Rev. B **85**, 035414 (2012), doi:10.1103/PhysRevB.85.035414.

[41] F. Bauer, J. Heyder and J. von Delft, *Functional renormalization group approach for inhomogeneous interacting Fermi systems*, Phys. Rev. B **89**, 045128 (2014), doi:10.1103/PhysRevB.89.045128.

[42] L. Weidinger, F. Bauer and J. von Delft, *Functional renormalization group approach for inhomogeneous one-dimensional Fermi systems with finite-ranged interactions*, Phys. Rev. B **95**, 035122 (2017), doi:10.1103/PhysRevB.95.035122.

[43] J. Lichtenstein, D. Sánchez de la Peña, D. Rohe, E. Di Napoli, C. Honerkamp and S. A. Maier, *High-performance functional renormalization group calculations for interacting fermions*, Comput. Phys. Commun. **213**, 100 (2017), doi:10.1016/j.cpc.2016.12.013.

[44] C. J. Eckhardt, C. Honerkamp, K. Held and A. Kauch, *Truncated unity parquet solver*, Phys. Rev. B **101**, 155104 (2020), doi:10.1103/PhysRevB.101.155104.

[45] W. Metzner, M. Salmhofer, C. Honerkamp, V. Meden and K. Schönhammer, *Functional renormalization group approach to correlated fermion systems*, Rev. Mod. Phys. **84**, 299 (2012), doi:10.1103/RevModPhys.84.299.

[46] N. Dupuis, L. Canet, A. Eichhorn, W. Metzner, J. M. Pawlowski, M. Tissier and N. Wschebor, *The nonperturbative functional renormalization group and its applications*, Phys. Rep. **910**, 1 (2021), doi:10.1016/j.physrep.2021.01.001.

[47] C. Hille, D. Rohe, C. Honerkamp and S. Andergassen, *Pseudogap opening in the two-dimensional Hubbard model: A functional renormalization group analysis*, Phys. Rev. Res. **2**, 033068 (2020), doi:10.1103/PhysRevResearch.2.033068.

[48] F. B. Kugler and J. von Delft, *Derivation of exact flow equations from the self-consistent parquet relations*, New J. Phys. **20**, 123029 (2018), doi:10.1088/1367-2630/aaf65f.

[49] C. U. Hille, *The role of the self-energy in the functional renormalization group description of interacting Fermi systems*, PhD thesis, Universität Tübingen, Tübingen, Germany (2020), doi:10.15496/publikation-46212.

[50] T. Schäfer et al., *Tracking the footprints of spin fluctuations: A multimethod, multimessenger study of the two-dimensional Hubbard model*, Phys. Rev. X **11**, 011058 (2021), doi:10.1103/PhysRevX.11.011058.

[51] A. Tagliavini, C. Hille, F. Kugler, S. Andergassen, A. Toschi and C. Honerkamp, *Multiloop functional renormalization group for the two-dimensional Hubbard model: Loop convergence of the response functions*, SciPost Phys. **6**, 009 (2019), doi:10.21468/SciPostPhys.6.1.009.

[52] C. Hille, F. B. Kugler, C. J. Eckhardt, Y.-Y. He, A. Kauch, C. Honerkamp, A. Toschi and S. Andergassen, *Quantitative functional renormalization group description of the two-dimensional Hubbard model*, Phys. Rev. Res. **2**, 033372 (2020), doi:10.1103/PhysRevResearch.2.033372.

[53] F. B. Kugler and J. von Delft, *Multiloop functional renormalization group that sums up all parquet diagrams*, Phys. Rev. Lett. **120**, 057403 (2018), doi:10.1103/PhysRevLett.120.057403.

[54] F. B. Kugler and J. von Delft, *Multiloop functional renormalization group for general models*, Phys. Rev. B **97**, 035162 (2018), doi:10.1103/PhysRevB.97.035162.

[55] G. Li, A. Kauch, P. Pudleiner and K. Held, *The victory project v1.0: An efficient parquet equations solver*, Comput. Phys. Commun. **241**, 146 (2019), doi:10.1016/j.cpc.2019.03.008.

[56] A. Kauch, F. Hörbinger, M. Kitatani, G. Li and K. Held, *Interplay between magnetic and superconducting fluctuations in the doped 2d Hubbard model*, (arXiv preprint) doi:10.48550/arXiv.1901.09743.

[57] A. Al-Eryani, S. Heinzelmann, K. Fraboulet, F. Krien and S. Andergassen, *Screening and effective RPA-like charge susceptibility in the extended Hubbard model*, (arXiv preprint) doi:10.48550/arXiv.2412.07323.

[58] M. Qin, T. Schäfer, S. Andergassen, P. Corboz and E. Gull, *The Hubbard model: A computational perspective*, Annu. Rev. Condens. Matter Phys. **13**, 275 (2022), doi:10.1146/annurev-conmatphys-090921-033948.

[59] C. Honerkamp and M. Salmhofer, *Temperature-flow renormalization group and the competition between superconductivity and ferromagnetism*, Phys. Rev. B **64**, 184516 (2001), doi:10.1103/PhysRevB.64.184516.

[60] K. Fraboulet, A. Al-Eryani, S. Heinzelmann and S. Andergassen, *Multiloop extension of the single-boson exchange functional renormalization group and application to the two-dimensional Hubbard model*, in preparation.

[61] H. Braun, S. Heinzelmann, F. Krien and S. Andergassen, *Functional renormalization group analysis of the pseudogap opening in the two-dimensional Hubbard model at finite doping*, in preparation.

[62] D. Vilardi, P. M. Bonetti and W. Metzner, *Dynamical functional renormalization group computation of order parameters and critical temperatures in the two-dimensional Hubbard model*, Phys. Rev. B **102**, 245128 (2020), doi:10.1103/PhysRevB.102.245128.

[63] S. Heinzelmann, *The single-boson exchange formalism and its application to the functional renormalization group*, PhD thesis, Universität Tübingen, Tübingen, Germany (2023).

[64] L. Del Re, M. Capone and A. Toschi, *Dynamical vertex approximation for the attractive Hubbard model*, Phys. Rev. B **99**, 045137 (2019), doi:10.1103/PhysRevB.99.045137.

[65] H. Shiba and P. A. Pincus, *Thermodynamic properties of the one-dimensional half-filled-band Hubbard model*, Phys. Rev. B **5**, 1966 (1972), doi:10.1103/PhysRevB.5.1966.

[66] Y. Yu, S. Iskakov, E. Gull, K. Held and F. Krien, *Unambiguous fluctuation decomposition of the self-energy: Pseudogap physics beyond spin fluctuations*, Phys. Rev. Lett. **132**, 216501 (2024), doi:10.1103/PhysRevLett.132.216501.

[67] W. Metzner and D. Vollhardt, *Correlated lattice fermions in $d = \infty$ dimensions*, Phys. Rev. Lett. **62**, 324 (1989), doi:10.1103/PhysRevLett.62.324.

[68] A. Georges, G. Kotliar, W. Krauth and M. J. Rozenberg, *Dynamical mean-field theory of strongly correlated fermion systems and the limit of infinite dimensions*, Rev. Mod. Phys. **68**, 13 (1996), doi:10.1103/RevModPhys.68.13.

[69] C. Taranto, S. Andergassen, J. Bauer, K. Held, A. Katanin, W. Metzner, G. Rohringer and A. Toschi, *From infinite to two dimensions through the functional renormalization group*, Phys. Rev. Lett. **112**, 196402 (2014), doi:10.1103/PhysRevLett.112.196402.

[70] D. Vilardi, C. Taranto and W. Metzner, *Antiferromagnetic and d-wave pairing correlations in the strongly interacting two-dimensional Hubbard model from the functional renormalization group*, Phys. Rev. B **99**, 104501 (2019), doi:10.1103/PhysRevB.99.104501.

[71] M. Gievers, *Functional approaches to Fermi polarons in cold atomic gases and solid state systems*, PhD thesis, Ludwig-Maximilians-Universität, Munich, Germany (2025).

5. Logarithmic divergences in diagrammatic approaches

"So, to make our calculations we make these diagrams, write down what they correspond to mathematically, and add the amplitudes – a straightforward, 'cookbook' process."

Richard P. Feynman about his diagrams[1]

Using the single-boson exchange (SBE) decomposition of the four-point vertex is numerically advantageous since essential features can be described by vertices with a simpler frequency dependence. Still, the role of multi-boson exchange (MBE) contributions has to be clarified. In this chapter, we examine a paradigmatic model with a logarithmically divergent perturbation series: the Fermi-edge singularity model to describe X-ray absorption in metals. Although this model can be exactly solved by simpler methods, historically it was important for the development of the parquet formalism, which obtains all leading logarithmic terms of arbitrary orders in a perturbative expansion of the interaction. We investigate the model in the SBE formalism and also include next-to-leading logarithmic terms self-consistently. Unfortunately, we find that MBE vertices are essential already at leading logarithmic order. Finally, we establish the connection to a Fermi polaron formed by an immobile impurity.

5.1. X-ray edge singularity problem

5.1.1. Overview

Power laws occur in numerous areas of physics. An expansion with respect to their exponents automatically yields logarithmic terms, which, close to some critical value, can generate divergences. Here, we systematically analyze how the parquet formalism can be used to sum up all leading and next-to-leading logarithms in a perturbative series to predict power-law behavior. For this, we examine the analytical behavior of Feynman diagrams in perturbation theory and combine that with the numerical computation of the full interaction vertex using various self-consistent summations.

The physical model we consider was introduced by Nozières and coworkers in the late 1960s to describe the Fermi-edge singularity occurring in X-ray absorption spectra [RGN69,

---

[1]From Chapter 3 of his book "QED: The strange theory of light and matter" (1985).

NGR69, ND69]. Being a prominent model in theoretical condensed matter physics, it has an exact solution, but is notoriously hard to solve via diagrammatic techniques. It made significant contribution to the development of the parquet formalism. More recently, an fRG study of the same model was pivotal for the initiation of the multiloop-fRG approach [KD18a, KD18c].

The model is characterized by a deep flat band, which can host a core electron of energy $\varepsilon_d < 0$, represented by the fermionic operators $\hat{d}^\dagger$, $\hat{d}$. Moreover, there is a Fermi sea of conduction electrons $\hat{c}_{\boldsymbol{k}}^\dagger$, $\hat{c}_{\boldsymbol{k}}$ with a dispersion relation $\varepsilon_{\boldsymbol{k}}$. When the core electron is excited to the conduction band due to X-ray absorption, the conduction electrons interact attractively with the remaining local hole (see Fig. 1 in Ref. [P3] for a schematic overview). The Hamiltonian,

$$\hat{H} = \varepsilon_d \hat{d}^\dagger \hat{d} + \sum_{\boldsymbol{k}} \varepsilon_{\boldsymbol{k}} \hat{c}_{\boldsymbol{k}}^\dagger c_{\boldsymbol{k}} - \frac{U}{V} \sum_{\boldsymbol{k},\boldsymbol{k}'} \hat{d} \hat{d}^\dagger \hat{c}_{\boldsymbol{k}}^\dagger \hat{c}_{\boldsymbol{k}'}, \qquad (5.1)$$

is basically identical to the Hamiltonian, Eq. (2.16), discussed in the context of the FDA (cf. Sec. 2.2). The occupation of an impurity atom in an atomic Fermi gas corresponds to the creation of a local hole in the electron gas of a metal. In other words, after the excitation of the core electron, the Fermi gas of conduction electrons forms a Fermi polaron in the limit of a single immobile impurity. This is why a detailed study of the model is reasonable before tackling the complete Fermi polaron Hamiltonian, Eq. (2.13), using our diagrammatic methods.

As the interaction term appearing in the Hamiltonian, Eq. (5.1), is local and the impurity is immobile, the Hamiltonian corresponding to the subspace of conduction electrons is quadratic [cf. discussion after Eq. (2.16)]. Moreover, in a perturbative treatment, the momenta $\boldsymbol{k}$ and $\boldsymbol{k}'$ of the conduction electrons are completely decoupled since the bare interaction U does not carry any momentum argument. As long as we consider only momentum-summed observables, they can be computed diagrammatically without the need for momentum summations over vertices. By using the local Green's function G^c of the conduction electrons,

$$G^c(\nu) = -\frac{1}{V} \sum_{\boldsymbol{k}} \langle c_{\boldsymbol{k}}(\nu) \bar{c}_{\boldsymbol{k}}(\nu) \rangle = \frac{1}{V} \sum_{\boldsymbol{k}} \frac{1}{\mathrm{i}\nu - \varepsilon_{\boldsymbol{k}} - \mu} = \int \mathrm{d}\varepsilon \, \frac{\rho(\varepsilon)}{\mathrm{i}\nu - \varepsilon - \mu}, \qquad (5.2)$$

with the density of states $\rho(\varepsilon) = 1/V \sum_{\boldsymbol{k}} \delta(\varepsilon - \varepsilon_{\boldsymbol{k}})$, we can express all the relevant quantities in terms of their frequencies and do not need to include momentum variables in our numerical computations. This procedure corresponds to integrating out all non-local conduction electrons in the action.

In our analysis, the main attention is on the description of characteristic power laws appearing in the particle-hole susceptibility χ^{dc} and the Green's function G^d of the core electron, known as the *Fermi-edge singularity* and *Anderson's orthogonality catastrophe*. (The components of vertex functions are here denoted by d and c instead

of $\uparrow$ and $\downarrow$, which were used in Chapter 4.) The FDA (cf. Sec. 2.2) offers a numerically exact way of computing these power laws in the absorption spectra. In a perturbative series, by contrast, power laws become noticeable via logarithmic singularities. It is hard to obtain the correct power-law behavior beyond the leading-logarithmic terms in a diagrammatic approach. In our paper [P3], we show that the parquet formalism, including all diagrammatic channels $r = a, p, t$ and the self-energy Σ, offers a way of including not only leading logarithmic terms, but also next-to-leading logarithmic terms in a controlled manner. In addition, we point out the importance of the MBE vertices M_r, which already contribute to the leading logarithm. We can thus conclude that considering the Fermi polaron problem in the SBE approximation (i.e., $M_r \to 0$) does not provide a correct description of Anderson's orthogonality catastrophe.

As the main part of the paper [P3] only concerns the single vertex component Γ^{dc}, we use a slightly different notation for drawing diagrams and denoting vertex components compared to the notation used in Chapter 4. For readers who first want to familiarize themselves with this notation, we recommend reading App. F.1 beforehand. While our numerical code (cf. Sec. 4.2) uses the frequency conventions presented in Eqs. (4.1) and Fig. 4.1, the paper uses conventions described in Eqs. (C1) and Fig. 15. To translate between vertices computed in the one convention and shown in the paper, we use the following identities:

$$\Gamma_a^{\mathrm{paper}}(\omega, \nu, \nu') = \Gamma_a^{\mathrm{code}}(\omega, \nu + \omega, \nu' + \omega), \tag{5.3a}$$

$$\Gamma_p^{\mathrm{paper}}(\omega, \nu, \nu') = \Gamma_p^{\mathrm{code}}(-\omega, -\nu - \omega, -\nu' - \omega), \tag{5.3b}$$

$$\Gamma_t^{\mathrm{paper}}(\omega, \nu, \nu') = \Gamma_t^{\mathrm{code}}(\omega, \nu + \omega, \nu' + \omega). \tag{5.3c}$$

Subleading logarithmic behavior in the parquet formalism

by

M. Gievers[1,2], R. Schmidt[3], J. von Delft[1], and F. B. Kugler[4]

[1]Arnold Sommerfeld Center for Theoretical Physics, Center for NanoScience, and
Munich Center for Quantum Science and Technology, Ludwig-Maximilians-Universität
München, 80333 Munich, Germany

[2]Max Planck Institute of Quantum Optics, 85748 Garching, Germany

[3]Institut für Theoretische Physik, Universität Heidelberg, 69120 Heidelberg, Germany

[4]Center for Computational Quantum Physics, Flatiron Institute, 162 5th Avenue, New
York, New York 10010, USA

Subleading logarithmic behavior in the parquet formalism

Marcel Gievers[1,2] Richard Schmidt[3] Jan von Delft[1] and Fabian B. Kugler[4]

[1]*Arnold Sommerfeld Center for Theoretical Physics, Center for NanoScience, and Munich Center for Quantum Science and Technology,
Ludwig-Maximilians-Universität München, 80333 Munich, Germany*
[2]*Max Planck Institute of Quantum Optics, Hans-Kopfermann-Straße 1, 85748 Garching, Germany*
[3]*Institut für Theoretische Physik, Universität Heidelberg, 69120 Heidelberg, Germany*
[4]*Center for Computational Quantum Physics, Flatiron Institute, 162 5th Avenue, New York, New York 10010, USA*

The Fermi-edge singularity in x-ray absorption spectra of metals is a paradigmatic case of a logarithmically divergent perturbation series. Prior work has thoroughly analyzed the leading logarithmic terms. Here, we investigate the perturbation theory beyond leading logarithms and formulate self-consistent equations to incorporate all leading and next-to-leading logarithmic terms. This parquet solution of the Fermi-edge singularity goes beyond the previous first-order parquet solution and sheds new light on the parquet formalism regarding logarithmic behavior. We present numerical results in the Matsubara formalism and discuss the characteristic power laws. We also show that, within the single-boson exchange framework, multi-boson exchange diagrams are needed already at the leading logarithmic level.

I. INTRODUCTION

Perturbative expansions are ubiquitous in theoretical physics, and logarithmic divergences therein often lead to power laws in observables. In the 1960s, several works developed self-consistent methods to sum up the leading logarithmic terms from Feynman diagrams of all orders. Among other systems, these techniques were successfully applied to meson scattering [1], the Kondo model [2], the one-dimensional interacting Fermi gas [3,4], and the Fermi-edge singularity in x-ray absorption in metals [5,6]. These self-consistent summations take into account two diagrammatic channels, but exclude self-energy corrections. Following Ref. [5], we refer to them as the *first-order parquet* approach.

Presently, the Hubbard model is one of the most studied many-body problems of condensed matter physics [7,8]. To capture the interplay of its competing fluctuations, another type of self-consistent summation of diagrams was developed, which we here call *full parquet* approach. It involves the self-energy and the effective interactions in all three channels of two-particle reducibility [9–12]. As the perturbative series of the Hubbard model does not exhibit logarithmic divergences, such a treatment was not motivated by logarithmic terms but by the fulfillment of crossing symmetry and self-consistency on the one- and two-particle level [12,13]. With increasing computational power, the numerical solution of the parquet equations has nowadays become a viable tool [14–20].

In this work, we examine what the transition from the first-order to the full parquet approach entails for logarithmically divergent problems. To this end, we revisit the Fermi-edge singularity, which was recently revived as an inspiring workhorse to better understand diagrammatic techniques [21–25]. Although it can be solved in a one-particle scheme [26,27], a precise analysis in perturbation theory remains challenging. It was shown that the leading logarithmic behavior can be obtained using the one-loop functional renormalization group [24,25], while the full summation of all parquet diagrams is only recovered in a multiloop expansion [23,28,29].

Remarkably, we find that a well-defined subset of diagrams from the full parquet solution offers a convenient way to not only capture the leading logarithmic singularity, but also the next-to-leading contributions. Hence, we close the gap between the traditional summation of leading logarithms (first-order parquet) and the one- and two-particle self-consistent summation (full parquet), giving new insights into the structure of logarithmically divergent perturbation theories. The power-law exponent of the particle-hole susceptibility obtained from our approach is closer to the exact result than that obtained from previous diagrammatic analyses respecting only the leading logarithmic contributions. Our analysis beyond the leading logarithms is possible (despite the concerns of Ref. [6]) as our numerical results include the full dependence of individual diagrams beyond logarithmic accuracy. Moreover, we briefly explain that the self-energy diagrams needed to capture Anderson's orthogonality catastrophe [30] go beyond the present approach.

Treating the full frequency dependence of the effective interaction requires huge numerical effort. In recent years, there were several attempts to make use of frequency asymptotics to lower the numerical costs [31]. One of them is the decomposition of the full interaction vertex into bosonic exchange
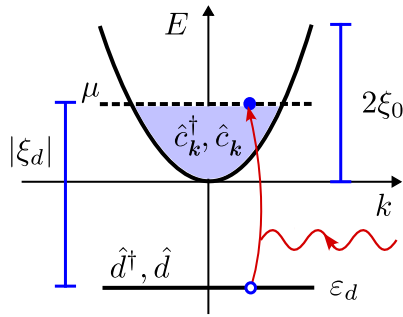
FIG. 1. Illustration of the model defined by Eq. (1). The conduction band with quadratic dispersion relation and finite bandwidth $2\xi_0$ hosts electrons $\hat{c}_k^\dagger, \hat{c}_k$. The deep core level at energy ε_d hosts a single electron $\hat{d}^\dagger, \hat{d}$, which gets excited to the Fermi level by absorbing a photon.

processes, the so-called *single-boson exchange* [32–43] as well as the remaining and numerically most expensive *multi-boson exchange* terms. We show that multi-boson exchange terms are essential already at the leading logarithmic level; neglecting them is thus not justified in the present case.

The rest of our paper is organized as follows. Section II serves as a reminder of the model and the diagrammatic approach. In Sec. III, we discuss the lowest terms in perturbation theory. In Sec. IV, we explain our self-consistent summation scheme and show the corresponding numerical results. We conclude in Sec. V.

II. MODEL AND METHOD

The model for the Fermi-edge singularity of x-ray absorption in metals was introduced in the late 1960s [5,6,26,44,45]. It is visualized in Fig. 1. A conduction band with quadratic dispersion relation $\varepsilon_k = k^2/(2m)$ hosts electrons represented by creation and annihilation operators $\hat{c}_k^\dagger, \hat{c}_k$. In addition, there is a deep, localized core level at energy $\varepsilon_d < 0$, which hosts a single $\hat{d}^\dagger, \hat{d}$ electron. Spin indices for the electrons are omitted since the spin degeneracy only results in a doubled density of states [1]. An empty core level corresponds to the presence of a core hole, with an effective attraction of strength $U > 0$ to the conduction electrons. The Hamiltonian reads

$$\hat{H} = \sum_k \varepsilon_k \hat{c}_k^\dagger \hat{c}_k + \varepsilon_d \hat{d}^\dagger \hat{d} - \frac{U}{V} \sum_{k,k'} \hat{c}_k^\dagger \hat{c}_{k'} \hat{d} \hat{d}^\dagger. \qquad (1)$$

We assume a finite bandwidth $2\xi_0$ of the conduction band and set the chemical potential to half the bandwidth, i.e., $\mu = \xi_0$. Absorption of a photon of frequency $\omega \simeq -\xi_d = \mu - \varepsilon_d$ excites the core electron to a state near the Fermi level. Due to the sharp Fermi edge, a singularity arises in absorption and emission spectra.

---

[1]This is justified since, as in the original model [26], we ignore exchange processes, in which the deep hole and one conduction electron reverse their spins.

We are interested in two quantities. First, we analyze the particle-hole susceptibility,

$$X(t) = -i\frac{1}{V} \sum_{k,k'} \langle \mathcal{T}\hat{d}^\dagger(t)\hat{c}_k(t)\hat{c}_{k'}^\dagger \hat{d}\rangle, \qquad (2)$$

where $\mathcal{T}$ is the time-ordering operator. $X(t)$ is the response function to the photo-excitation of a conduction-particle and core-hole pair. Its imaginary part in frequency space corresponds to the x-ray transition rate [5,6,25]. Second, we investigate the propagator of the d electron,

$$G(t) = -i\langle \mathcal{T}\hat{d}(t)\hat{d}^\dagger\rangle, \qquad (3)$$

which encodes single-particle excitations. The expectation values in Eqs. (2) and (3) are taken with respect to the ground state $|\Psi_0\rangle$. For large enough $|\xi_d|$, the ground state is given by the occupied core level and the Fermi sea of conduction electrons in the sense of Fermi-liquid theory. Consequently, at zero temperature $T = 0$ (and more generally for $T \ll |\xi_d|$), $X(t)$ is purely retarded while $G(t)$ is purely advanced, as follows from the effect of the time-ordering operators $\mathcal{T}$ in Eqs. (2)–(3). In Appendix A, we provide numerically exact solutions of the two quantities using the functional determinant approach [46–48].

The fact that $G(t)$ is purely advanced has important consequences. It implies that there are no self-energy contributions to the c electrons beyond the Hartree term. Since there is precisely one local d level, this Hartree term reads $U/V f(\xi_d)$, with the Fermi–Dirac distribution function $f(\varepsilon) = 1/(1 + e^{\beta \varepsilon})$, where $\beta = 1/T$. Now, bringing the Hamiltonian, Eq. (1), into normal order, we get an additional term $-U/V$. This term and the c-electron Hartree self-energy cancel exactly at $T = 0$. We may thus suppress these $\sim U$ single-particle terms altogether, thereby effectively working with Hartree-dressed propagators for the c electrons [24,25].

In Matsubara field theory, the expectation value $\langle \dots \rangle = \frac{1}{Z}\text{tr}(e^{-\beta(\hat{H}-\mu\hat{N})} \dots)$ (with $Z = \text{tr}\, e^{-\beta(\hat{H}-\mu\hat{N})}$) can be written as a functional integral involving the action

$$S = -\frac{1}{\beta}\sum_{\nu,k} \bar{c}_{k,\nu}(i\nu - \xi_k)c_{k,\nu} - \frac{1}{\beta}\sum_\nu \bar{d}_\nu(i\nu - \xi_d)d_\nu$$

$$+ \frac{U}{V}\frac{1}{\beta^3}\sum_{\omega,\nu,\nu',k,k'} \bar{d}_\nu \bar{c}_{k,\nu'+\omega}c_{k',\nu+\omega}d_{\nu'}. \qquad (4)$$

Here, $\xi_k = \varepsilon_k - \mu$, $\xi_d = \varepsilon_d - \mu$, and the fields depend on the fermionic (bosonic) Matsubara frequencies ν (ω). Evidently, only the c electron at the core hole, $\frac{1}{\sqrt{V}}\sum_k c_{k,\nu}$, referred to as the *local* c electron, interacts with the d hole. We may thus integrate out all c electrons that are not located at the core hole.

In the following, we assume a constant local density of states of the conduction electrons

$$\rho(\varepsilon) = \frac{1}{V}\sum_k \delta(\varepsilon - \varepsilon_k) = \rho\,\Theta(2\xi_0 - \varepsilon)\Theta(\varepsilon). \qquad (5)$$

This holds in two dimension, and in three dimensions, it is an approximation motivated by the dominance of effects near the Fermi level. We can hence rescale the local c electrons by $\sqrt{\rho}$

to avoid trivial factors of ρ. Thereby, we obtain the action

$$S = -\frac{1}{\beta}\sum_\nu \bar{c}_\nu g_\nu^{-1} c_\nu - \frac{1}{\beta}\sum_\nu \bar{d}_\nu (i\nu - \xi_d) d_\nu$$
$$+ u\frac{1}{\beta^3}\sum_{\omega,\nu,\nu'} \bar{c}_{\nu'+\omega} c_{\nu+\omega} \bar{d}_\nu d_{\nu'} \tag{6}$$

with the dimensionless interaction $u = \rho U$ and the dimensionless local c propagator $g_\nu = -\frac{1}{\rho V}\sum_{\boldsymbol{k}}\langle c_{\boldsymbol{k},\nu}\bar{c}_{\boldsymbol{k},\nu}\rangle$. At half filling, $\mu = \xi_0$, the latter is given by

$$g_\nu = \int_0^{2\xi_0}\frac{d\varepsilon}{i\nu - \varepsilon + \xi_0} = -2i\arctan\frac{\xi_0}{\nu} = g_\nu^{\text{sm}}. \tag{7}$$

We refer to this as the *smooth* propagator. Previous diagrammatic works [5,6,21,23–25,28] approximated it by

$$g_\nu^{\text{sh}} = -i\pi\,\text{sgn}(\nu)\Theta(\xi_0 - |\nu|), \tag{8}$$

its *sharp* form. This expression is convenient for analytical calculations of the power law around $\omega \simeq |\xi_d|$. However, it is problematic for self-consistent numerical computations, as it violates basic properties, such as the $\sim 1/(i\nu)$ decay for large $|\nu|$. Indeed, for our calculations beyond logarithmic accuracy, it is crucial to use g^{sm} instead of g^{sh}. Note that we also obtain a dimensionless susceptibility in terms of the rescaled local c fields,

$$\chi(\omega) = X(\omega)/\rho. \tag{9}$$

Seminal works from the 1960s showed that χ and G exhibit characteristic power laws close to the threshold ω_0 (cf. Eq. (66) in Ref. [26] and Refs. [5,6,30,44]):

$$\chi(\omega + i0^+) \simeq \frac{1}{\alpha_X}\left[1 - \left(\frac{\omega + i0^+ - \omega_0}{-\xi_0}\right)^{-\alpha_X}\right], \tag{10a}$$

$$G(\nu - i0^+) \simeq \frac{1}{\nu - i0^+ + \omega_0}\left(\frac{\nu - i0^+ + \omega_0}{\xi_0}\right)^{\alpha_G}. \tag{10b}$$

Here, the power law of χ characterizes the x-ray edge singularity, while that of G is related to Anderson's orthogonality catastrophe. Note that Eqs. (10) are given in real frequencies, in contrast to all the other expressions in this paper. The power-law exponents $\alpha_X = 2\delta/\pi - (\delta/\pi)^2$ and $\alpha_G = (\delta/\pi)^2$ depend on the s-wave scattering phase shift δ evaluated at the Fermi surface. For the present model [cf. Eq. (5)], this is related to the interaction strength via $\delta = \arctan(\pi u)$. We have verified the power laws in Eqs. (10) with our numerically exact data using the functional determinant approach (cf. Appendix A).

The threshold frequency ω_0 depends sensitively on how the UV cutoff ξ_0 is implemented in the model [5,6]. As discussed later, our diagrammatic analysis allows for computing ω_0 independently from all other quantities (cf. Sec. III E and Appendix A 2). For now, we set ω_0 to its bare value $\omega_0 \to -\xi_d$. In the final results, $-\xi_d$ can be replaced by ω_0.

Expanding the power-law expressions, Eqs. (10), in u reveals the logarithmic divergences. For small u, we can approximate $\delta/\pi = u + \mathcal{O}(u^3)$ (cf. Appendix B). The resulting

form for χ in imaginary frequencies is

$$\chi(i\omega) \simeq \frac{1}{2u - u^2}\left[1 - \left(\frac{i\omega + \xi_d}{-\xi_0}\right)^{-2u+u^2}\right]$$

$$\equiv \frac{1}{2u - u^2}\left[1 - e^{(-2u+u^2)L}\right]$$

$$= L - uL^2 + u^2\left[\tfrac{2}{3}L^3 + \tfrac{1}{2}L^2\right] - u^3\left[\tfrac{1}{3}L^4 + \tfrac{2}{3}L^3\right]$$

$$+ u^4\left[\tfrac{2}{15}L^5 + \tfrac{1}{2}L^4 + \tfrac{1}{6}L^3\right] + \mathcal{O}(u^5). \tag{11}$$

Here, we introduced the logarithmic factor

$$L(\omega) = \ln\frac{i\omega + \xi_d}{-\xi_0}. \tag{12}$$

Taking only the highest power of L in each order of u yields the leading logarithmic result, where $2u - u^2$ is replaced by $2u$ (cf. Eq. (42) in Ref. [5] and Eq. (57) in Ref. [6]).

Analogously, G in imaginary frequencies has an expansion in terms of $\bar{L}(\nu) = L(-\nu) = \ln[(i\nu - \xi_d)/\xi_0]$:

$$G(i\nu) \simeq \frac{1}{i\nu - \xi_d}\left(\frac{i\nu - \xi_d}{\xi_0}\right)^{u^2} \equiv \frac{1}{i\nu - \xi_d}e^{u^2\bar{L}}$$

$$= \frac{1}{i\nu - \xi_d}\left[1 + u^2\bar{L} + \tfrac{1}{2}u^4\bar{L}^2 + \mathcal{O}(u^6)\right]. \tag{13}$$

In this work, we will show that a suitable summation of parquet diagrams not only contains the leading logarithmic result of χ, but also the second-highest power of L at each order of u in Eq. (11). Taking into account even lower powers of L would require diagrams beyond the parquet approximation. Differently from χ, the expansion of G, Eq. (13), is in terms of $u^2\bar{L}$. So, with higher orders of u, the difference in the powers of u and of $\bar{L}$ increases. Hence, a perturbative analysis of G (and thus the overlap related to Anderson's orthogonality catastrophe [30]) would require going beyond leading/subleading logarithms and beyond the parquet approximation (cf. Appendix E).

Numerical parameters

For all our plots, we fix the dimensionless interaction strength to $u = 0.28$, if not stated otherwise. The analytical results are presented for $T = 0$, where $\frac{1}{\beta}\sum_\nu \to \int_{-\infty}^{\infty}\frac{d\nu}{2\pi} \equiv \int_\nu$. There, we mostly use g_ν^{sh}, Eq. (8), as we focus on the behavior near the threshold, $|i\omega + \xi_d| \ll \xi_0$. The numerical results are obtained for a finite temperature $T/\xi_0 = 0.002$ and a discrete grid of Matsubara frequencies. For numerically determined perturbative results, we compare both propagator choices g_ν in Eqs. (7) and (8). Details of the implementation are given in Appendix G.

The remaining parameter is the excitation energy ξ_d. Physically, one imagines $\varepsilon_d < 0$ and $\xi_d \ll -T$, so that $f(\xi_d) \simeq 1$, corresponding to an occupied core level. In our diagrammatic approach, we have already used $f(\xi_d) \simeq 1$ by canceling the term U/V from normal-ordering with the c-electron Hartree self-energy equal to $U/V f(\xi_d)$. Consequently, there are no more c Hartree diagrams (involving a closed d line) in the expansion, and the d-level occupation is never actually probed.

Instead, there is a single d line threading through all diagrams of $\chi(i\omega)$, and one may choose to keep the external frequency argument paired with ξ_d, e.g., in the form $i\omega + \xi_d$ (cf. Sec. III E). As a result, ξ_d can be shifted to any (negative) value [24,25].

Here, we use $\xi_d/\xi_0 = -0.01$. The reason is that, in the Matsubara formalism, ξ_d broadens the characteristic features of the correlation functions χ and G, and, to reduce the effects of such a broadening, we use small $|\xi_d| \ll \xi_0$. Additionally, this corresponds to larger values of $\ln(-\xi_d/\xi_0)$, which is beneficial to clearly separate logarithmic terms of different powers at small frequencies in the perturbative expansions, Eqs. (11)–(13). However, we keep $|\xi_d| > \pi T$ so that features below ξ_d (the lowest nonthermal energy scale) are resolved by the Matsubara grid. After analytical continuation, the parameter ξ_d eventually only shifts the threshold frequency ω_0 and is irrelevant for the analysis of the power-law behavior.

III. PERTURBATION THEORY

To get an intuition about typical diagrammatic contributions to the infrared divergence to subleading accuracy, we analyze Feynman diagrams at low orders. We start with the well-known leading logarithmic terms in the particle-hole susceptibility. Next, we discuss subleading terms in the self-energy and the vertex. Finally, we consider a multi-boson exchange diagram and present a rule to generally assess the logarithmic behavior in the present model. The logarithmic behavior of the diagrams in Secs. III A–III C was already discussed in Refs. [5,6]. We here extend their analysis by giving numerical results along with some exact analytical results [Eqs. (16) and (21)] as well as a general rule for extracting the logarithmic behavior.

A. Leading logarithmic diagrams

Utilizing a similar notation and diagrammatic representation as in Refs. [23,28,29,43], the particle-hole susceptibility is given by

$$\chi(\omega) = \quad + \quad$$
$$= \int_\nu \Pi^a_{\omega,\nu} + \int_{\nu,\nu'} \Pi^a_{\omega,\nu} \Gamma^a_{\omega,\nu,\nu'} \Pi^a_{\omega,\nu'}. \quad (14)$$

Here, Γ refers to the full four-point vertex. By energy conversation, it depends on only three frequencies (cf. Appendix C). The index a in Γ^a signifies that its frequencies are parametrized with respect to the a channel (a stands for *antiparallel* and p, used below, for *parallel*). The bubbles $\Pi^r_{\omega,\nu}$ are products of Green's functions,

$$\Pi^a_{\omega,\nu} = G_{\nu-\omega} g_\nu, \quad \Pi^p_{\omega,\nu} = G_{\nu-\omega} g_{-\nu} = -\Pi^a_{\omega,\nu}, \quad (15)$$

having used $g_{-\nu} = -g_\nu$ in the last step. Diagrammatically, G is represented by a dashed line and g by a solid line. The vertex Γ is denoted by a gray circle, its lowest-order contribution $\Gamma^{(1)} = -u$ by a black dot (cf. Fig. 2).
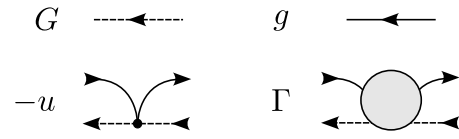
FIG. 2. Diagrammatic representation of the d propagator G and the c propagator g as well as the bare vertex $\Gamma^{(1)} = -u$ and the full vertex Γ.

The lowest-order term of the susceptibility $\chi^{(0)}$ is an integrated a bubble:

$$\chi^{(0)}(\omega) = \quad = - \quad$$
$$= \int_\nu \Pi^a_{\omega,\nu} = \ln \frac{i\omega + \xi_d}{i\omega + \xi_d - \xi_0} \simeq L(\omega). \quad (16)$$

The first expression is the exact result [cf. Eq. (D8)] with $g^{\rm sm}$, Eq. (7). The second gives the logarithmic behavior, Eq. (12), near the threshold (indicated by the symbol "$\simeq$"), which is also obtained with $g^{\rm sh}$ (cf. Eqs. (D10)–(D12) and Refs. [5,22–25,44]). Indeed, the approximation is justified for $|i\omega + \xi_d| \ll \xi_0$, which, after analytic continuation $i\omega \to \omega + i0^+$, corresponds to frequencies close to the absorption threshold $-\xi_d = |\xi_d|$.

Figure 3(a) shows the frequency dependence of $\chi^{(0)}$, Eq. (16). The result from the smooth propagator $g^{\rm sm}$ is the exact result at $u = 0$ and is seen to obey $\mathrm{Re}\,\chi^{(0)} < 0$. As expected, the numerical data obtained from $g^{\rm sm}$ at finite temperature (blue dots) lie on top of the analytical exact result
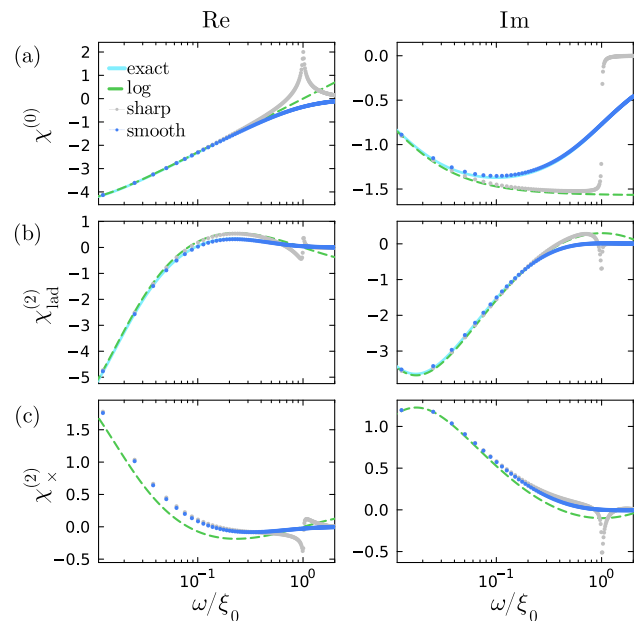
FIG. 3. (a) Zeroth-order diagram $\chi^{(0)} \simeq L$, Eq. (16), (b) second-order ladder diagram $\chi^{(2)}_{\rm lad} \simeq u^2 L^3$, Eq. (18), and (c) second-order cross diagram $\chi^{(2)}_\times \simeq -\frac{1}{3} u^2 L^3$, Eq. (19), comparing numerical results with smooth $g^{\rm sm}$ (blue dots) and sharp $g^{\rm sh}$ (gray dots) to the analytical logarithmic form (green, dashed) and the exact result (light blue, solid).

at $T = 0$ (light blue line). Furthermore, we note that (i) the numerical result with the sharp propagator g^{sh}, Eq. (8), (gray dots) yields artifacts around $\omega \simeq \pm \xi_0$ and violates $\mathrm{Re}\, \chi^{(0)} < 0$; (ii) the (approximate) analytical result $L(\omega)$ violates $\mathrm{Re}\, \chi^{(0)} < 0$ as well as $\lim_{|\omega| \to 0} \chi^{(0)} \to 0$.

The simplest diagrams of the vertex Γ are ladder diagrams, which are products of $\chi^{(0)}$. We consider ladder diagrams in the antiparallel (γ^a) and parallel (γ^p) channels, built from the antiparallel (Π^a) and parallel (Π^p) bubble, respectively. Their nth-order contributions are (the external legs are amputated):

$$[\gamma^a_{\mathrm{lad}}]^{(n \geq 2)}_\omega = \quad \text{[diagram]}$$

$$= (-u)^n \left[\int_\nu \Pi^a_{\omega, \nu} \right]^{n-1} \simeq (-u)^n [L(\omega)]^{n-1}, \tag{17a}$$

$$[\gamma^p_{\mathrm{lad}}]^{(n \geq 2)}_\omega = \quad \text{[diagram]}$$

$$= (-u)^n \left[\int_\nu \Pi^p_{\omega, \nu} \right]^{n-1} \simeq (-u)^n [-L(\omega)]^{n-1}. \tag{17b}$$

The ladder diagrams of χ have two more integrated bubbles, and their logarithmic behavior is thus

$$\chi^{(n)}_{\mathrm{lad}}(\omega) = \quad \text{[diagram]}$$

$$= \int_{\nu, \nu'} \Pi^a_{\omega, \nu} [\gamma^a_{\mathrm{lad}}]^{(n)}_\omega \Pi^a_{\omega, \nu'} \simeq (-u)^n [L(\omega)]^{n+1}. \tag{18}$$

Figure 3(b) shows the frequency dependence of the second-order ladder diagram $\chi^{(2)}_{\mathrm{lad}}$, Eq. (18). Similarly as in Fig. 3(a), one notices artifacts at $\omega \simeq \xi_0$ in the numerical solution with g^{sh} as well as spurious high-frequency behavior in this solution and the analytical result. While the full susceptibility obeys $\mathrm{Re}\, \chi < 0$, for a single diagrammatic contribution, $\mathrm{Re}\, \chi^{(2)}_{\mathrm{lad}} < 0$ need not hold.

The so-called *crossed diagram* is the first nonladder diagram which contributes to the leading logarithm of the susceptibility. It is obtained by integrating $[\gamma^p]^{(2)}$ with two a bubbles (see Appendix D 1 for details):

$$\chi^{(2)}_\times(\omega) = \quad \text{[diagram]}$$

$$= \int_{\nu, \nu'} \Pi^a_{\omega, \nu} [\gamma^p]^{(2)}_{\omega - \nu - \nu'} \Pi^a_{\omega, \nu'} \simeq -\tfrac{1}{3} u^2 L^3(\omega). \tag{19}$$

Figure 3(c) shows the numerical result for $\chi^{(2)}_\times(\omega)$. The opposite sign compared to $\chi^{(0)}$ and $\chi^{(2)}_{\mathrm{lad}}$ shows that the crossed diagram counteracts the growth of the full result.

Generally, susceptibility diagrams proportional to $u^n L^{n+1}$ are referred to as *leading log*. Summing up only ladder diagrams yields the random phase approximation (RPA), resulting in an unphysical bound state [44]. It was shown that, for a complete summation of leading-log diagrams, one has to take into account the interplay between the a and p channels.

This is referred to as the first-order parquet approach [5,6] because it takes only the highest power of logarithms in each order of the power-law expansion, Eq. (11). In a more general perturbative treatment, diagrams proportional to lower orders of L show up, i.e., $u^n L^{n+1-p}$ with $n + 1 > p > 0$. In this work, we will go beyond Ref. [5] by including all diagrams with $p = 1$, which we denote as *subleading log*.

B. Self-energy

To include subleading-log contributions, we next consider the impact of the d-electron self-energy [6], which was neglected in most previous diagrammatic analyses [5,21–25,44]. The d Hartree self-energy shifts the threshold frequency by $u\xi_0$ [cf. Eq. (D19)]. The second-order diagram $\Sigma^{(2)}$ is the first to exhibit (subleading) logarithmic behavior. Its general expression,

$$\Sigma^{(2)}_\nu = \quad - \quad \text{[diagram]}$$

$$= -u^2 \int_{\omega, \nu'} G_{\nu - \omega} g_{\nu' - \omega} g_{\nu'}, \tag{20}$$

is evaluated to (cf. Appendix D 2):

$$\frac{1}{u^2} \Sigma^{(2)}_\nu = i\tilde{\nu} \ln \frac{i\tilde{\nu}}{i\tilde{\nu} + \xi_0} + (i\tilde{\nu} + 2\xi_0) \ln \frac{i\tilde{\nu} + 2\xi_0}{i\tilde{\nu} + \xi_0} \tag{21a}$$

$$\simeq i\tilde{\nu} \ln \frac{i\tilde{\nu}}{\xi_0} + 2\xi_0 \ln 2, \tag{21b}$$

where $i\tilde{\nu} = i\nu - \xi_d$. The first summand gives the logarithmic behavior $(i\nu - \xi_d)L(-\nu)$ that contributes to the shape of the x-ray edge singularity and was given in previous studies (cf. line after Eq. (13) in Ref. [6]). The second, proportional to ξ_0 is constant and thus merely shifts the threshold frequency, just like the Hartree term $u\xi_0$ mentioned before.

As discussed in Sec. II A, we want to exclude shifts of the threshold frequency since they blur the singular frequency dependence. The easiest way to do so is to generally subtract the zero-frequency part [6]. In the Matsubara formalism, this amounts to replacing Σ_ν by

$$\Delta \Sigma_\nu = \Sigma_\nu - \mathrm{Re}\, \Sigma_{\nu = 0}, \tag{22}$$

as $\mathrm{Im}\, \Sigma_\nu$ is antisymmetric and thus vanishes at zero frequency. (In practice, we approximate $\mathrm{Re}\, \Sigma_{\nu=0}$ by $\mathrm{Re}\, \Sigma_{\nu=\pi T}$.) However, the (imaginary-frequency) logarithmic terms of the self-energy also have a finite contribution at $\nu = 0$, which we do not want to subtract. Indeed, the first term in Eq. (21b) evaluates to $-\xi_d L(0)$ at zero frequency. If the latter contribution to the shift is added back, we obtain

$$\Delta \tilde{\Sigma}_\nu = \Delta \Sigma_\nu - u^2 \xi_d L(0). \tag{23}$$

Figure 4(a) shows our numerical results for the self-energy. The finite-T results using g^{sm} [blue dots in Fig. 4(a)] lie on top of the $T = 0$ exact result, Eq. (21a) [light blue line in Fig. 4(a)]. We see that using g^{sh}, Eq. (8), violates causality, i.e., leads to $\mathrm{Im}\, \Sigma^{(2)} > 0$ for $\nu > 0$ [gray dots in Fig. 4(a)], whereas the result from g^{sm}, Eq. (7), naturally obeys this property [blue dots in Fig. 4(a)]. At low frequencies, the results from g^{sm} agree well with the analytic logarithmic behavior
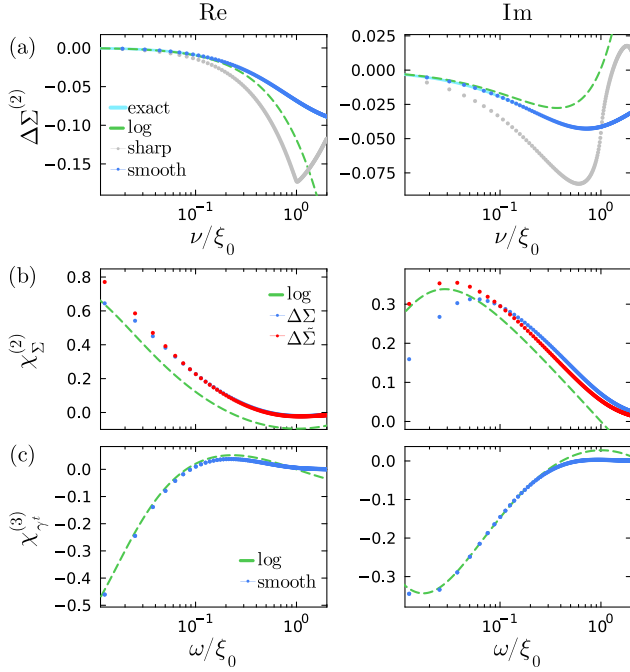
FIG. 4. (a) Second-order self-energy $\Sigma^{(2)} \simeq u^2 \mathrm{i}\bar{\nu}\bar{L}$, Eq. (20), where the zero-frequency value is subtracted, i.e., $\Delta\Sigma_\nu^{(2)} = \Sigma_\nu^{(2)} - \mathrm{Re}\,\Sigma_{\nu=0}^{(2)}$ [cf. Eq. (22)]. (b) The corresponding susceptibility $\chi_\Sigma^{(2)} \simeq \frac{1}{2}u^2 L^2$, Eq. (24). Here, we only use the numerical results computed with the smooth propagator g^{sm}, first with the self-energy difference $\Delta\Sigma_\nu^{(2)}$ (blue dots) and then with $\Delta\tilde{\Sigma}^{(2)}$, Eq. (23), including the logarithmic part at $\nu = 0$ (red dots). (c) Third-order diagram $\chi_{\gamma^t}^{(3)} \simeq \frac{1}{3}u^3 L^3$, Eq. (25), originating from the t-reducible vertex $[\gamma^t]^{(3)}$.

$u^2(\mathrm{i}\nu - \xi_d)L(-\nu)$ (green), which however bends over to unphysical results with $\mathrm{Im}\,\Sigma^{(2)} > 0$ already for $\nu/\xi_0 \gtrsim 0.5$.

One directly sees that the corresponding second-order term of the d propagator $G^{(2)} = G^{(0)}\Sigma^{(2)}G^{(0)} = u^2 L(-\nu)/(\mathrm{i}\nu - \xi_d)$ matches the perturbative series, Eq. (13). To find the corresponding subleading-log term for χ, we insert $G^{(2)}$ into the integrated bubble, Eq. (16):

$$
\chi_\Sigma^{(2)}(\omega) = \quad - \quad \text{}
$$
$$
= \int_\nu [\Pi^a]_{\omega,\nu}^{(0)} \Sigma_{\nu-\omega}^{(2)} G_{\nu-\omega}^{(0)} \simeq \tfrac{1}{2}u^2 L^2(\omega). \tag{24}
$$

The same logarithmic term appears in the perturbative series of the power law, Eq. (11), which was evaluated at the bare threshold frequency $\omega_0 = -\xi_d$. Hence, the logarithmic term $u^2(\mathrm{i}\nu - \xi_d)L(-\nu)$ of $\Sigma^{(2)}$, Eq. (20), does indeed not change the threshold frequency [while the full expression, Eq. (21), does].

The numerical results for $\chi_\Sigma^{(2)}$ are first computed with $\Delta\Sigma^{(2)}$, Eq. (22) [blue dots in Fig. 4(b)]. To minimize the effect of the threshold shift when computing $\chi_\Sigma^{(2)}$, we use $\Delta\tilde{\Sigma}^{(2)}$, Eq. (23), which adds back the logarithmic contribution $-u^2\xi_d L(0)$. Primarily, this brings the imaginary part of the data closer to the analytical result [red dots in Fig. 4(b)].

This strategy to compensate shifts of the threshold is further discussed in Sec. III E.

At third order, there are two diagrams contributing to the self-energy, which cancel each other as $[\gamma_{\mathrm{lad}}^a]_\omega^{(3)} = [\gamma_{\mathrm{lad}}^p]_{-\omega}^{(3)}$ [cf. Eq. (D27)]. This observation matches with the exact power law of the d propagator, which only scales with u^2 [cf. Eq. (13)].

C. t-reducible diagram

Generally, there is a third type of two-particle reducibility, namely in the *transversal* channel (or short t channel). Its first contribution occurs at third order and reads (cf. Eq. (15) in Ref. [6] and Appendix D 3 for details)

$$
[\gamma^t]_{\omega,\nu'}^{(3)} = \quad - \quad \text{}
$$
$$
= u^3 \int_{\nu_1,\nu_2} G_{\nu_1} G_{\nu_1-\omega} g_{\nu_2} g_{\nu_1+\nu_2-\nu'} \tag{25}
$$
$$
= \frac{u}{\mathrm{i}\omega}\left(\Sigma_{\nu'}^{(2)} - \Sigma_{\nu'-\omega}^{(2)}\right).
$$

The expression in terms of the self-energy $\Sigma^{(2)}$ is exact and does not depend on the form of g. Indeed, it is a perturbative implementation of the $U(1)$ Ward identity (cf. Appendix D 4). Evidently, the logarithmic behavior of the self-energy and the t-reducible diagram are related [6]. Note that, to save space and to emphasize the advanced property of the d electron by a straight dashed line, we refrain from drawing the bubble of two d propagators vertically, which originally motivates the term *transversal* [23,29,43].

The resulting third-order term for χ is (see Appendix D 3 for details):

$$
\chi_{\gamma^t}^{(3)}(\omega) = \quad - \quad \text{}
$$
$$
= \int_{\nu,\nu'} \Pi_{\omega,\nu}^a [\gamma^t]_{\nu-\nu',\nu-\omega}^{(3)} \Pi_{\omega,\nu'}^a \simeq \tfrac{1}{3}u^3 L^3(\omega). \tag{26}
$$

Figure 4(c) shows that our numerical data are close to this subleading-log behavior. Together with the two terms of third order coming from $\Sigma^{(2)}$,

$$
\chi_\Sigma^{(2)}(-u)\chi^{(0)} + \chi^{(0)}(-u)\chi_\Sigma^{(2)}
$$
$$
= \quad - \quad \text{}
$$
$$
- \quad \text{} \tag{27}
$$
$$
\simeq 2 \times \tfrac{1}{2}u^2 L^2 \times (-u) \times L = -u^3 L^3,
$$

we hence arrive at the correct subleading-log contribution to third order, namely $-\tfrac{2}{3}u^3 L^3$ [cf. Eq. (11)].

D. Multi-boson exchange diagram

Multi-boson exchange (MBE) diagrams are two-particle reducible in a specific channel, i.e., their diagrams fall apart
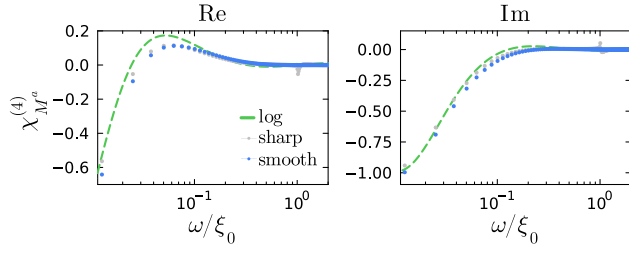
FIG. 5. Susceptibility contribution from the MBE diagram $[M^a]^{(4)}$. We compare the results computed with g^{sm} (blue dots) and g^{sh} (gray dots) to the analytically determined logarithmic behavior $\frac{2}{15}u^4L^5$, Eq. (29) (green, dashed).

FIG. 6. Demonstration that the single dashed line of d propagators in diagrams implies that $\Sigma = \Sigma(i\nu - \xi_d)$ and $\chi = \chi(i\omega + \xi_d)$. (a) Fourth-order diagram to Σ containing the t-reducible diagram $[\gamma^t]^{(3)}$. (b) Fourth-order diagram to χ containing the envelope diagram $R_{\boxtimes}^{(4)}$. The external frequencies ν and ω are contained in d propagators, the frequencies $\nu_1, \ldots, \nu_5$ are integrated over.

when cutting two propagator lines. However, they are not U reducible, which means that their diagrams do not fall apart by removing one dot of a bare vertex [43]. Numerically, they are the most expensive objects to compute as they inherently depend on three frequency arguments. Thus computational resources can be saved if their impact on physical quantities is low compared to other diagrams.

To analyze the relevance of MBE diagrams, we analytically check how the first multi-boson diagram $[M^a]^{(4)}$, occurring at fourth order,

$$[M^a]^{(4)}_{\omega,\nu,\nu'} = \qquad\qquad\qquad\qquad$$
$$= \int_{\nu''} [\gamma^p]^{(2)}_{\omega-\nu-\nu''} \Pi^a_{\omega,\nu''} [\gamma^p]^{(2)}_{\omega-\nu''-\nu'}, \qquad (28)$$

affects χ. We find (see Appendix D 5 for details)

$$\chi^{(4)}_{M^a}(\omega) = \qquad\qquad\qquad\qquad$$
$$= \int_{\nu,\nu'} \Pi^a_{\omega,\nu} [M^a]^{(4)}_{\omega,\nu,\nu'} \Pi^a_{\omega,\nu'} \simeq \frac{2}{15} u^4 L^5(\omega), \qquad (29)$$

which is leading log. Figure 5 confirms this behavior in finite-T numerical results. Hence, omitting MBE diagrams leads to an incomplete summation of diagrams already at leading-log order. We thus include MBE diagrams in the self-consist schemes presented in Sec. IV. As seen there, neglecting them changes the results drastically at intermediate values of u.

E. Comment on the threshold frequency ω_0

Since we have numerical access to the full frequency dependence of individual diagrams, we can make a statement about the position of the threshold frequency, in contrast to previous diagrammatic analyses [5,6,21–25]. Generally, the threshold frequency $-\xi_d$ is shifted to a value ω_0 which depends on the interaction u. A large value of ω_0 blurs the characteristic features of imaginary-frequency data near $\omega = 0$. For our numerical results presented in Sec. IV B, we thus needed a strategy to compensate this effect, which is discussed in the following.

As mentioned in Sec. II A, our treatment of the c Hartree self-energy and the advanced property of the d propagator G imply that there are no closed d loops in the diagrammatic

expansion. In other words, all nonvanishing diagrams must contain a single line of d propagators. Hereby, it is always possible to find a frequency parametrization such that the external frequencies ω in χ and ν in Σ are only contained in the d propagators. (For four-point vertices, the according external frequencies are discussed in Appendix C.)

To demonstrate that this argument also holds for diagrams which are neither a- nor p-reducible, we show a self-energy diagram containing the third-order vertex $[\gamma^t]^{(3)}$ and a susceptibility diagram containing the fourth-order two-particle irreducible vertex $R_{\boxtimes}^{(4)}$ in Fig. 6. Here, we explicitly write the frequency arguments on every single propagator and conclude that the susceptibility χ is a function of $i\omega + \xi_d$ and the self-energy Σ of $i\nu - \xi_d$. Thus, after analytical continuation to real frequencies, the effect of different values of ξ_d can be recovered by corresponding shifts of the external frequencies.[2]

The threshold frequency ω_0 appears likewise in the power laws of χ and G [cf. Eqs. (10)]. These forms demonstrate that, near the threshold, χ is described by a function of $i\omega - \omega_0$ and Σ by a function of $i\nu + \omega_0$, suggesting that ω_0 merely renormalizes its noninteracting correspondent $-\xi_d$. The threshold is fully determined by the self-energy as, after analytical continuation, i.e., $i\nu \to \nu - i0^+$, the expression from the Dyson equation $1/(i\nu - \xi_d - \Sigma_\nu)$ becomes singular at $\nu = -\omega_0$.

Our perturbative analysis shows that the self-energy consists both of terms which do not affect the threshold-frequency and terms which renormalize it. In second order [cf. Eq. (21)], the logarithmic term $u^2(i\nu - \xi_d)L(-\nu)$ does not change the threshold, since it appears in the power law expansion with an unrenormalized threshold $\omega_0 = -\xi_d$ [cf. Eq. (13)], while the term $u^2 2\xi_0 \ln 2$, proportional to the UV cutoff ξ_0, does [cf. Eqs. (A19) and (B3)]. Without knowing the analytical results, this separation of terms in the self-energy cannot be extended straightforwardly to higher orders in perturbation theory.

Similar to the second-order term, we suspect that more generally the dependence on the threshold frequency is mainly governed by a constant shift in the self-energy. So, to leave the threshold frequency unrenormalized in numerical com-

---

[2]In shifting ξ_d, we assume that no nonanalyticities of χ in $i\omega + \xi_d$ or of Σ in $i\nu - \xi_d$ are crossed. Indeed, we have not detected such nonanalyticities in the analytical expressions from perturbation theory and our numerical data.

FIG. 7. Step-wise procedure to deduce the logarithmic behavior of diagrams, exemplified for (a) $\chi_\Sigma^{(2)} \sim u^2 L^2$, Eq. (24), and (b) a fourth-order two-particle irreducible diagram, $R_{\boxtimes}^{(4)} \sim u^4 L$. We successively integrate loops involving d and c lines; the lines being integrated at a given step are marked green.

putations of more general diagrams, we subtract the value $\mathrm{Re}\,\Sigma_{\nu=0}$ from the numerically computed self-energy Σ_ν [cf. Eq. (22)]. (The smallest imaginary Matsubara frequency $i\pi T$ is the closest value to the real threshold frequency $-\omega_0$.) Still, we have to recover those terms at $\nu = 0$ that do not renormalize the threshold frequency. The only expression we know analytically is that of second order, so we add $-u^2 \xi_d L(0)$ [cf. Eq. (23)], as done for $\chi_\Sigma^{(2)}$ [cf. red dots in Fig. 4(b)].

Although this strategy does not guarantee a full elimination of the threshold renormalization in our numerical computations, it does allow us to deduce reasonable values for the threshold frequency from the numerically determined subleading-log self-energy (cf. Appendix A 2, in particular Fig. 14).
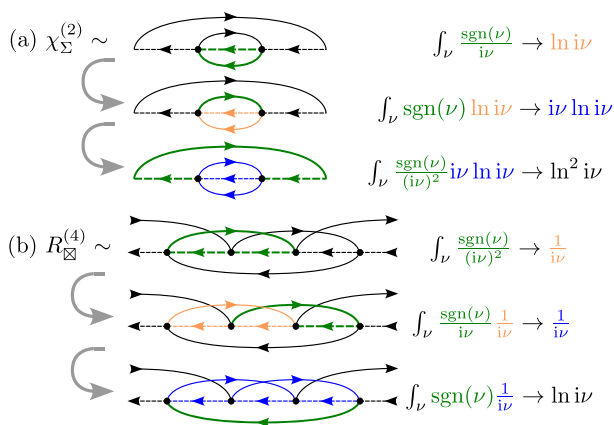
F. Logarithmic behavior in general diagrams

We show how to quickly deduce the leading power of the logarithm L in the singular behavior of any diagram involving d and c propagators (see also Appendix E of Ref. [6]). Close to the threshold, the bare d propagator behaves as $G_\nu \sim 1/(i\nu)$, while the local c propagator obeys $g_\nu \sim \mathrm{sgn}(\nu)$ at small frequencies [cf. Eq. (8)]. We estimate the leading logarithm by successively integrating over closed loops.

Take, e.g., the susceptibility diagram $\chi_\Sigma^{(2)}$, Eq. (24), shown in Fig. 7(a). An integration over the inner dc bubble yields a logarithm $\int_\nu \mathrm{sgn}(\nu)/(i\nu) \sim \ln i\nu$. The subsequent integral, involving the second c propagator, does not raise the power of the logarithm, $\int_\nu \mathrm{sgn}(\nu) \ln i\nu \sim i\nu \ln i\nu$. The final integral, involving two d propagators and one c propagator, in turn raises its power, $\int_\nu \mathrm{sgn}(\nu) \ln i\nu/(i\nu) \sim \ln^2 i\nu$. This matches Eq. (24).

More generally, any integrated dc bubble yields a logarithm, $\int_\nu \mathrm{sgn}(\nu)/(i\nu) \sim \ln i\nu$ [cf. Eq. (16)]. If every subsequent loops contains another d line, each integral increases the power of the logarithm according to $\int_\nu \mathrm{sgn}(\nu) \ln^n i\nu/(i\nu) \sim \ln^{n+1} i\nu$ [cf. Eq. (D1)]. This is precisely what happens for the leading-log diagrams. By contrast, if a loop at a later stage does not contain a further d line, then the power of the

logarithm is not raised, $\int_\nu \ln^n i\nu \sim i\nu \ln^n i\nu$ [cf. Eqs. (D2)–(D3)]. Now, if the first loop in a vertex diagram has more d lines than c lines, this does not generate logarithmic behavior, as $\int_\nu \mathrm{sgn}(\nu)/(i\nu)^m \sim 1/(i\nu)^{m-1}$. Such an imbalance of dashed and solid lines within integration loops yields subleading diagrams. Indeed, many more loops with c lines are required until the power of the logarithm is raised. Since, $\int_\nu \mathrm{sgn}(\nu) \ln^n i\nu/(i\nu)^m \sim \ln^n i\nu/(i\nu)^{m-1}$ [cf. Eqs. (D4)–(D5)], the first $(m - 1)$ subsequent integrals with c lines reduce the power m that originates from the d propagators, before further integrals can eventually raise the power n of the logarithm.

This reasoning also applies to diagrams which are two-particle irreducible in all three channel (*totally irreducible diagrams*). These go beyond the full parquet approach. The lowest-order vertex diagram of that type occurs at fourth order and is often called *envelope* diagram $R_{\boxtimes}^{(4)}$ (cf. Fig. 5 in Ref. [6]). In Fig. 7(b), we show that its logarithmic behavior can be estimated as $u^4 L$. With two more dc bubbles, the corresponding susceptibility is $\chi_{R_{\boxtimes}}^{(4)} = \int \Pi^a R_{\boxtimes}^{(4)} \Pi^a \sim u^4 L^3$, which has two powers of L less compared to the leading logarithm $\chi_{\mathrm{lead}}^{(n)} \sim u^n L^{n+1}$ and is thus beyond our subleading approximation $\chi_{\mathrm{sub}}^{(n)} \sim u^n L^n$. (Actually, there are two envelope diagrams at fourth order, whose leading contributions cancel by symmetry (cf. footnote 10 in Ref. [6]).) Further totally irreducible diagrams like the fifth-order "sealed" envelope diagram $R_{\boxtimes}^{(5)} \sim u^5 L \Rightarrow \chi_{\boxtimes}^{(5)} \sim u^5 L^3$ have even fewer powers of L.

The strategy presented above allows us to estimate the logarithmic behavior, but of course does not yield the correct prefactor and does not account for possible cancellations of diagrams. Nevertheless, it is essential for the next step. To obtain the power-law behavior of χ up to a certain accuracy, one has to perform a self-consistent summation, which takes into account all diagrams with the corresponding power of logarithms. With the presented strategy, we can classify all parts of the parquet formalism by their dominant logarithmic behavior.

IV. SELF-CONSISTENT SUMMATION

In this section, we extend the self-consistent summation of all leading-log diagrams of Ref. [5] (*first-order parquet* approach) toward the *full parquet* approach, widely used to describe physics related to the Hubbard model [9–12]. We show that, in this way, we can additionally include all subleading-log diagrams in a systematic manner.

A. Parquet approach

In Sec. III, we introduced various quantities which appear in a diagrammatic description of the model's characteristic power laws, Eqs. (10). The perturbative expansion of the susceptibility χ, Eq. (14), involves terms scaling as $\chi^{(n)} \sim u^n L^{n+1-p}$, where $p = 0$ encompasses the leading-log terms, while $p = 1$ accounts for the subleading-log ones [L is defined in Eq. (12)]. The full four-point vertex Γ has an expansion $\Gamma^{(n)} \sim u^n L^{n-1-p}$ and is decomposed into two-particle reducible vertices γ^r in the channels $r = a, p, t$ and a totally irreducible part R. (Note that what Refs. [5,6] call R corre-
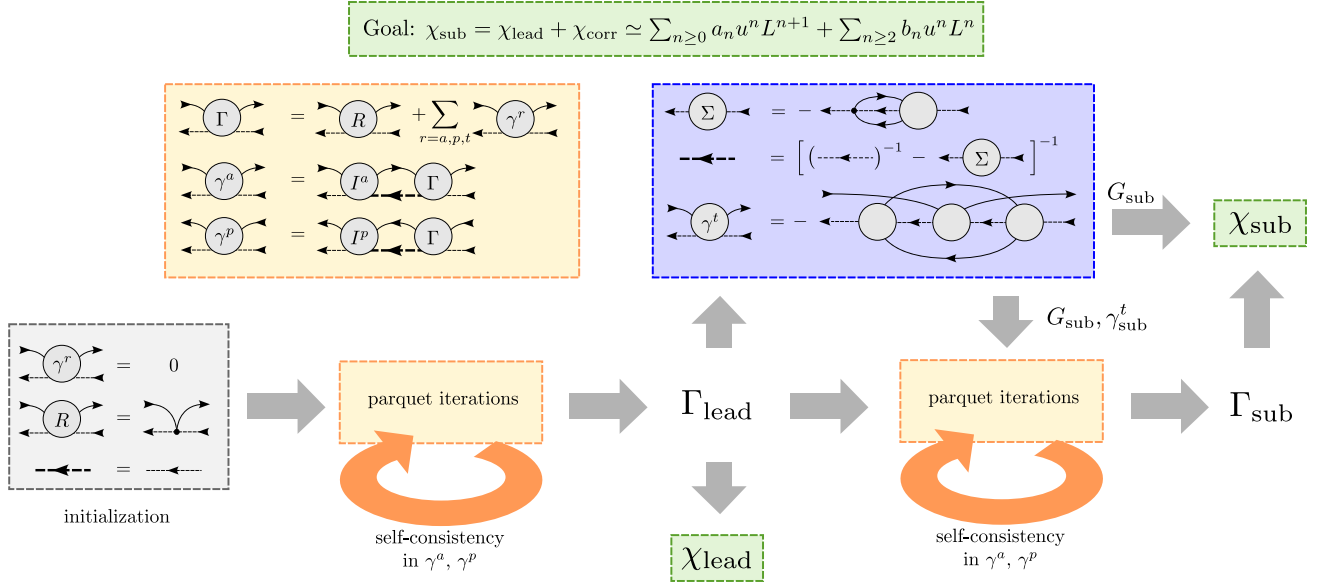
FIG. 8. Overview of the computed quantities and used self-consistency schemes: the parquet iteration (yellow box) involves the Bethe–Salpeter equations (30) and (36). First, these are solved self-consistently (initialized using the gray box) without Σ and γ^t and give the vertex Γ_{lead} to leading-log accuracy. This output is used to compute Σ, Eq. (32), and γ^t, Eq. (34) (blue box). These results in turn serve as an input to a second self-consistency loop, which yields Γ up to subleading-log accuracy.

sponds to $\gamma^t + R$ for us.) We argued that the lowest-order contributions of γ^a and γ^p are leading log while those of γ^t are subleading log and those of R are subsubleading log. Finally, the self-energy Σ has an expansion $\Sigma^{(n)} \sim u^n i\tilde{\nu} \bar{L}^{n-1-p}$ and yields subleading-log contributions to χ. An overview of how the different objects are computed self-consistently is given in Fig. 8. Its details are explained throughout this section.

All leading-log diagrams can be summed within a parquet approach containing only the a- and p-reducible vertices $\gamma^{r=a,p}$ [5]. These fulfill Bethe–Salpeter equations involving the full vertex Γ and the a- and p-irreducible vertices $I^{r=a,p}$. Since no fully irreducible diagram contributes to the leading-log behavior except for the bare vertex $\Gamma^{(1)} = -u$, we set $R = -u$ (often called *parquet approximation*). The relevant equations are (cf. yellow box in Fig. 8):

$$\Gamma^r_{\omega,\nu,\nu'} = -u + \gamma^r_{\omega,\nu,\nu'} + \gamma^{\bar{r}}_{\omega-\nu-\nu',-\nu',-\nu}, \tag{30a}$$

$$\gamma^r_{\omega,\nu,\nu'} = \int_{\nu''} I^r_{\omega,\nu,\nu''} \Pi^r_{\omega,\nu''} \Gamma^r_{\omega,\nu'',\nu'}, \tag{30b}$$

$$I^r_{\omega,\nu,\nu'} = \Gamma^r_{\omega,\nu,\nu'} - \gamma^r_{\omega,\nu,\nu'}, \tag{30c}$$

$$\tag{30d}$$

Here, we use the channel indices $r = a, p$ and $\bar{r} = p, a$ and the bubbles $\Pi^r_{\omega,\nu}$, Eq. (15). The frequency arguments follow from the parametrization of the vertex, Appendix C.

Equations (30) must be solved self-consistently. In this process, one can apply the reasoning from Sec. III F to show that two leading-log vertices $\Gamma^{(n_{i=1,2})}_{\text{lead}} \sim u^{n_i} L^{n_i-1}$ in the Bethe–Salpeter equation (30b) yield again a leading-log vertex:

$$\int_\nu \Gamma^{(n_1)}_{\text{lead}} \Pi^r \Gamma^{(n_2)}_{\text{lead}} \sim \int_\nu u^{n_1} L^{n_1-1} \frac{\text{sgn}(\nu)}{i\nu} u^{n_2} L^{n_2-1}$$
$$\sim u^{n_1+n_2} L^{n_1+n_2-1} = \Gamma^{(n_1+n_2)}_{\text{lead}}. \tag{31}$$

In Sec. III, we showed that the self-energy Σ and the t-reducible vertex γ^t contribute to the subleading logarithm. We calculate Σ from the Schwinger–Dyson equation. The (d-electron) Hartree term $u\xi_0$ yields a frequency-independent shift of the threshold frequency and is therefore irrelevant for the power-law exponent. Beyond the Hartree term, we have (cf. blue box in Fig. 8)

$$= u \int_{\nu_1,\nu_2} \Pi^a_{\nu_1-\nu,\nu_2} g_{\nu_1} \Gamma^a_{\nu_1-\nu,\nu_2,\nu_1} \tag{32}$$

$$= u \int_{\nu_1,\nu_2} \Pi^p_{\nu_1-\nu,\nu_2} g_{-\nu_1} \Gamma^p_{\nu_1-\nu,\nu_2,\nu_1}.$$

Reference [6] argued against using the Schwinger–Dyson equation (32) as their analytic evaluation was limited to logarithmic accuracy of individual diagrams. By contrast, our numerics produce the full frequency dependence of vertex functions, allowing us to straightforwardly use Eq. (32).

Following Sec. III F, inserting a leading-log vertex $\Gamma^{(n)}_{\text{lead}} \sim u^n L^{n-1}$ into the Schwinger–Dyson equation (32) yields a

subleading-log self-energy:

$$
\int_{\nu_1,\nu_2} u \Pi^r g \Gamma_{\text{lead}}^{(n)} \sim \int_{\nu_1,\nu_2} u \frac{\text{sgn}(\nu_2)}{i\nu_2} \text{sgn}(\nu_1) u^n L^{n-1}
$$
$$
\sim \int_\nu u \, \text{sgn}(\nu) u^n L^n \sim u^{n+1} i\nu L^n = \Sigma_{\text{sub}}^{(n+1)}.
$$
(33)

Here, we first integrated over the dc bubble and then over the last c propagator. It follows that self-energy corrections yield subleading-log contributions to χ. Furthermore, inserting Σ again into the d propagator or inserting a subleading-log vertex $\Gamma^{(n)} \sim u^n L^{n-2}$ into Eq. (32) would go beyond our approximation.

To include the t-reducible vertex γ^t, we use the subleading-log expression at third order, $[\gamma^t]^{(3)}$ in Eq. (25), and replace all bare vertices $\Gamma^{(1)} = -u$ by full vertices Γ. As we show in Appendix F 2, this ansatz takes into account all subleading-l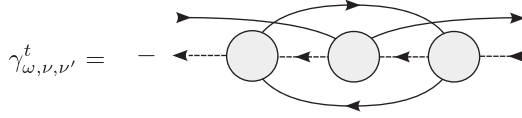og contributions starting from the most general parquet approach. The resulting expression for γ^t (corresponding to Fig. 4(b) in Ref. [6]) is (cf. blue box in Fig. 8):

$$
= -\int_{\nu_1,\nu_2} \Gamma_{\omega,\nu,\nu_1}^t G_{\nu_1-\omega} G_{\nu_1} \Gamma_{\nu_2-\nu_1,\nu'-\nu_1+\nu_2,\nu_2}^a
$$
$$
\times g_{\nu_2-\nu_1+\nu'} g_{\nu_2} \Gamma_{\omega-\nu_1+\nu_2,\nu_2,\nu'+\nu_2-\nu_1}^a.
$$
(34)

If all vertices in Eq. (34) are leading log, i.e., $\Gamma_{\text{lead}}^{(n_{i=1,2,3})} \sim u^{n_i} L^{n_i-1}$, integrating first over the loop including the c propagators and then over the loop with the two d propagators yields

$$
\int_{\nu_1,\nu_2} \Gamma_{\text{lead}}^{(n_1)} GG \Gamma_{\text{lead}}^{(n_2)} gg \Gamma_{\text{lead}}^{(n_3)}
$$
$$
\sim \int_{\nu_1} \Gamma_{\text{lead}}^{(n_1)} GG \int_{\nu_2} u^{n_2} L^{n_2-1} \text{sgn}^2(\nu_2) u^{n_3} L^{n_3-1}
$$
$$
\sim \int_\nu u^{n_1} L^{n_1-1} \frac{1}{(i\nu)^2} u^{n_2+n_3} i\nu L^{n_2+n_3-2}
$$
$$
\sim u^{n_1+n_2+n_3} L^{n_1+n_2+n_3-2} = \Gamma_{\text{sub}}^{n_1+n_2+n_3},
$$
(35)

which is subleading log. Including the self-energy in the d propagators or subleading-log vertices in Eq. (34) would go beyond the subleading approximation. In the expansion of the susceptibility Eq. (11), such terms would contribute similarly as the totally irreducible diagrams R.

From the logarithmic behavior in Eqs. (33) and (35), we conclude that the leading contributions to the self-energy $\Sigma \sim u^n i\tilde{\nu} \bar{L}^{n-1}$ and the t-reducible vertex $\gamma^t \sim u^n L^{n-2}$ are already fully recovered by inserting the leading-log vertex $\Gamma_{\text{lead}} \sim u^n L^{n-1}$ into Eqs. (32) and (34). Our strategy (depicted in Fig. 8) is thus to first compute the leading-log vertex Γ by iteratively solving Eqs. (30). In the next step, Σ and γ^t are determined from Eqs. (32) and (34). These then form an

input to a second iterative solution of the parquet equations, but now the d lines are dressed through the Dyson equation $G_\nu = (1/G_\nu^{(0)} - \Sigma_\nu)^{-1}$ and the full vertex Γ includes γ^t from Eq. (34):

$$
\Gamma_{\omega,\nu,\nu'}^a = -u + \gamma_{\omega,\nu,\nu'}^a + \gamma_{\omega-\nu-\nu',-\nu',-\nu}^p + \gamma_{\nu-\nu',\nu,\nu-\omega}^t, \quad (36a)
$$
$$
\Gamma_{\omega,\nu,\nu'}^p = -u + \gamma_{\omega,\nu,\nu'}^p + \gamma_{\omega-\nu-\nu',-\nu',-\nu}^a + \gamma_{\nu-\nu',-\nu',\nu-\omega}^t.
$$
(36b)

Thereby, Eqs. (36) replace Eq. (30a). Finally, with the inclusion of Σ and γ^t, we obtain γ^a and γ^p self-consistently up to subleading-log order and may altogether compute χ up to subleading-log order.

We note that further iterations over Eqs. (32) and (34) would yield subsubleading-log diagrams, but not in a complete and systematic manner since totally irreducible diagrams like the envelope diagram [cf. Fig. 7(b)] would not be taken into account. Moreover, also the t-reducible vertex from the full parquet solution includes further subsubleading contributions, as discussed in Appendix F 2, which exceed the scope of this work.

B. Numerical results

In this section, we present our numerical results obtained from the self-consistency schemes discussed in Sec. IV A and compare them to the analytical power law in Eq. (10a). Although, strictly speaking, these power laws hold very close to the threshold frequency and at $T = 0$, they adequately describe the physical results in a much wider range (cf. Appendix A and also Ref. [48]). In our numerical implementations, the frequency dependence of the vertex is handled by a decomposition into single- and multi-boson exchange vertices [32–43] using the recently developed Julia library `MatsubaraFunctions.jl` [49]; further details are given in Appendix G.

To start with, Fig. 9 shows how χ depends on imaginary frequencies at fixed u. We compare the result of the leading-log scheme (blue dots), Eqs. (30), and the subleading-log scheme (red dots), Eqs. (36), to the power law (10a) with exponents $\alpha_X = 2u$ (leading log, green), $\alpha_X = 2u - u^2$ (subleading log, pink) and $\alpha_X = 2\delta/\pi - (\delta/\pi)^2$ (exact, light blue). The analytical power laws describe the behavior at small frequencies, but of course do not capture the correct large-frequency behavior, including $\lim_{\omega\to\infty} \chi(i\omega) = 0$. For the present choice of parameters, the results from our subleading-log parquet scheme are closest to the exact power law (red dots match light blue curve) while those from the leading-log parquet scheme are closest to the subleading-log power law (blue dots lie near pink curve). However, this strongly depends on the value of ξ_d, as elaborated below.

To get an overview on the results for different parameters and obtained from the various self-consistent methods, we present χ at zero Matsubara frequency as a function of u in Fig. 10. Here, we compare again our numerical results with the power law, Eq. (10a), including different exponents α_X. The power law with $\alpha_X = \delta/\pi - (\delta/\pi)^2$ matches the numerically exact results from the functional determinant approach, when evaluated at $\omega_0 + \xi_d$ (cf. Appendix A). We draw the following conclusions from Fig. 10.
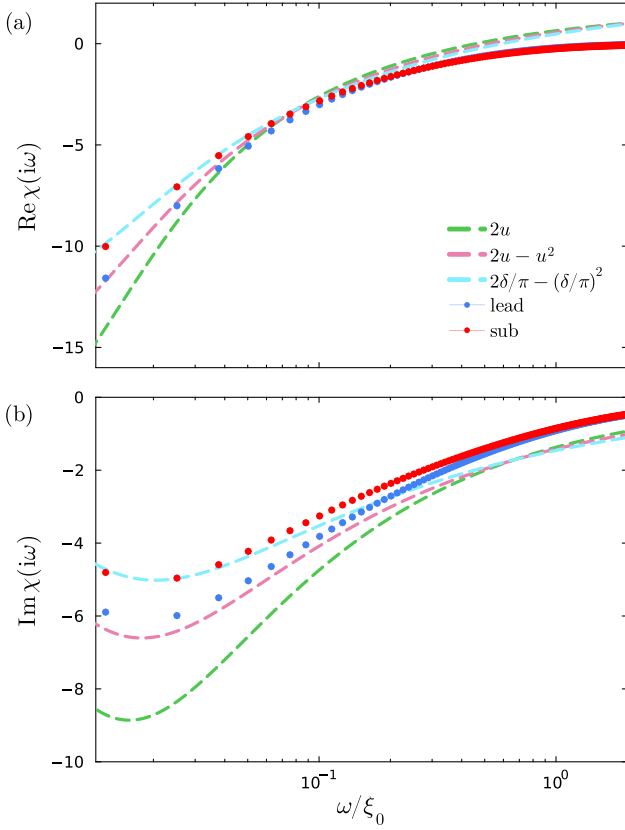
FIG. 9. Frequency dependence of χ from self-consistent summations with g^{sm} at $u = 0.28$, $T/\xi_0 = 0.002$, and $\xi_d/\xi_0 = -0.01$. We compare numerical results from the leading-log scheme (blue dots) and subleading-log scheme (red dots) to the analytical power law (10a) with exponents $\alpha_X = 2u$ (leading log, green), $\alpha_X = 2u - u^2$ (subleading log, pink), and $\alpha_X = 2\delta/\pi - (\delta/\pi)^2$ (exact, light blue).

FIG. 10. Interaction dependence of $\chi(i\omega = 0)$ from self-consistent summations at $T/\xi_0 = 0.002$ and different choices of ξ_d/ξ_0. We compare results from the leading-log scheme, Eqs. (30), in the SBE approximation with g^{sm} (light green dots) and including MBE diagrams with g^{sm} (blue dots) and g^{sh} (purple dots), as well as from the subleading scheme, Eqs. (32)–(36), with g^{sm} including MBE diagrams (red dots). The numerical results are compared to the analytical power laws for leading-log $\alpha_X = 2u$ (green, dashed), subleading-log $\alpha_X = 2u - u^2$ (pink, dashed), and exact exponent $\alpha_X = \delta/\pi - (\delta/\pi)^2$ (light blue, dashed).

Dropping multi-boson exchange diagrams, which is known as the *single-boson exchange approximation* [41–43], clearly fails already at intermediate values of the interaction (cf. light green dots in Fig. 10). We anticipated that from our perturbative analysis since multi-boson diagrams contribute to leading-log diagrams and are therefore essential to obtain a power law at all (cf. Sec. III D).

The leading-log parquet solution using the sharp c propagator g^{sh}, Eq. (8), (cf. purple dots in Fig. 10) bends down from the leading-log power law (green) at intermediate values of the interaction, similarly as in previous studies (see Fig. 4(c) in Ref. [23]). This might originate from the artifacts around $|\omega| \simeq \xi_0$, encountered already in Sec. III.

Our main focus is on the results of the leading-log [Eqs. (30), blue dots in Fig. 10] and subleading-log parquet schemes [Eqs. (36), red dots], both using the exact propagator g^{sm}, Eq. (7). The results start to deviate from one another and from the power-law curves with $\alpha_X = 2u$ (green) and $\alpha_X = 2u - u^2$ (pink), respectively, already at intermediate values of $u \gtrsim 0.2$. The results from the subleading-log parquet scheme are systematically improved in powers of the logarithmic factor $\ln(-\xi_d/\xi_0)$ [cf. Eq. (12)] in the region where the expansion of the power law in u, Eq. (11), is valid.

The value of $\chi(i\omega = 0)$ is strongly affected by the parameter ξ_d/ξ_0. At larger values of $|\xi_d|/\xi_0$, where different powers of the logarithm are hardly distinguishable, the results move down in magnitude [cf. Fig. 10(b)]. The resulting apparent agreement between the self-consistent calculation to leading- and subleading-log accuracy with the power-law curves $\alpha_X = 2u - u^2$ (pink) and $\alpha_X = 2\delta/\pi - (\delta/\pi)^2$ (light blue), respectively, is likely coincidental.

Smaller values of $|\xi_d|/\xi_0$ [larger values of $\ln(-\xi_d/\xi_0)$] yield a clearer separation between different powers of the logarithm. For $\xi_d/\xi_0 = -0.005$ [cf. Fig. 10(c)], the numerical results come much closer to the expected behavior: the leading-log parquet results (blue dots) follow the $2u$ power law (green) and the subleading-log parquet (red dots) results the $2u - u^2$ power law (pink) up to $u \approx 0.2$. The value $\ln(-\xi_d/\xi_0) \approx -5.3$ is still relatively small. However, reducing $|\xi_d|/\xi_0$ further goes beyond our current numerical limitations, since this would require lower T and thus more frequencies to resolve the vertex functions. It also becomes harder to converge the parquet equations at small $|\xi_d|/\xi_0$ and at large u (hence, we computed less data points in that regime).

Ideally, one would like to analyze the numerical results in real frequencies. To this end, we use analytical
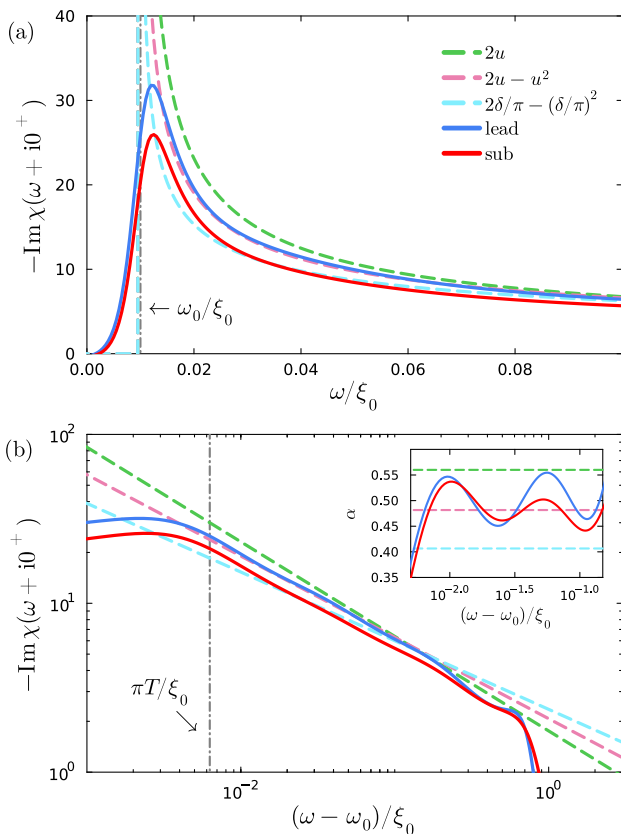
FIG. 11. Absorption spectrum $-\mathrm{Im}\,\chi(\omega + i0^+)$ obtained by analytical continuation of the imaginary-frequency data at $T/\xi_0 = 0.002$, $\xi_d/\xi_0 = -0.01$, and $u = 0.28$. We compare data from the leading-log (blue) and subleading-log scheme (red) to the respective analytical power laws. The upper plot has linear scales; here, the vertical dash-dotted line marks the threshold frequency $\omega_0 = -\xi_0$. The lower plot has logarithmic scales and frequencies shifted by ω_0; here, the vertical line marks the lowest fermionic Matsubara frequency πT to indicate where T cuts off the logarithmic behavior. The inset shows the negative logarithmic derivative.

continuation via the recently developed minimal pole representation [50,51]. Here, the susceptibilities are analytically continued as sums over a small number of complex poles, i.e., $\chi(z) = \sum_i A_i/(z - x_i)$, $x_i \in \mathbb{C}$, by use of Prony's approximation method. The results, shown in Fig. 11, agree with the previous statements [cf. Figs. 9 and 10(a)]: for these parameters ($\xi_d/\xi_0 = -0.01$ and $u = 0.28$), the leading-log (blue dots) and subleading-log (red dots) numerical results are close to the curves of the analytical subleading-log (pink) and exact (light blue) power laws, respectively. As one would expect, the singularity at the threshold is cut off by T at the corresponding energy scale πT [cf. Fig. 11(b)]. The analytical continuation also confirms that correcting the self-energy by $\Sigma_\nu \to \Delta \tilde{\Sigma}_\nu$, Eq. (23), does not lead to a detectable renormalization of the threshold frequency $\omega_0 = -\xi_d$ [cf. Fig. 11(a)]. For a more rigorous analysis of the power law, one can extract the power-law exponents from the logarithmic derivative (see Appendix H for details). The result, shown in the inset of Fig. 11(b), exhibits strong oscillations somewhat

centered around the subleading-log exponent $\alpha = 2u - u^2$ (dashed pink). We attribute the oscillations to the fact that the analytically continued data stem from only a small number of complex poles [50,51].

V. CONCLUSION

In this work, we elucidated a conceptual aspect of a diagrammatic technique widely used in condensed-matter physics and beyond, the parquet formalism. The parquet formalism is well known for providing a way to sum all leading-log diagrams in a logarithmically divergent perturbation theory. On the example of the x-ray edge singularity, we showed that the parquet formalism actually allows for capturing all next-to-leading-log diagrams, too. To this end, one extends the first-order parquet approach [5], which involves only two two-particle channels and no self-energy, to the full parquet approach [9], often used for Hubbard-like models, involving all three two-particle channels and the self-energy determined from the Schwinger–Dyson equation.

We first examined the problem at low orders in perturbation theory. Thereby, we also provided exact results for the bare particle-hole susceptibility and the second-order self-energy, which to our knowledge had not been given before. We illustrated the vertex and self-energy contributions and formulated a general recipe for deducing the highest logarithmic power in a given diagram. This allowed us to formulate a self-consistent scheme, within the full parquet approach mentioned above, summing all leading- and subleading-log diagrams.

For all our results, we presented numerical data obtained in the finite-temperature Matsubara formalism. In doing so, we use the exact expressions for the bare propagators and resolve the full frequency dependence of any diagram, including four-point vertices, thus going beyond logarithmic accuracy used in previous works [5,6,21–25]. Our implementation exploits the recently introduced single- and multi-boson exchange decomposition, for which we showed that multi-boson exchange diagrams contribute already at the leading-log level.

In future work, our code could be used to treat other models with two distinct particle types. Examples are Fermi polarons with heavy impurities [48,52,53] or Hubbard-like models without SU(2) spin symmetry. It would be interesting to lift the flat-band approximation of the d electron, which however requires including momenta, significantly raising computational costs.

On the technical level, it would be desirable to numerically resolve the power laws in an even cleaner fashion. One direction in this pursuit would be to lower the temperature T/ξ_0 and the excitation energy $|\xi_d|/\xi_0$. In the current implementation, using dense grids, this is not feasible since the memory scales as $(T/\xi_0)^{-3}$. However, techniques for using sparse grids or compression have recently been suggested [54–60]. Another direction is to directly work in real frequencies, thus circumventing the analytical continuation. The model can be numerically implemented using the zero-temperature formalism [24]. Beyond that, recent work has shown the viability of working in the Keldysh formalism with full frequency resolution of four-point functions [61–65].

APPENDIX A: FUNCTIONAL DETERMINANT APPROACH

In this Appendix, we discuss how we obtain numerically exact results for the particle-hole susceptibility $X(t)$, Eq. (2), and the d propagator $G(t)$, Eq. (3), using the functional determinant approach [46–48].

1. Exact computation of the spectra

For large enough $|\varepsilon_d|$, the ground state is given by the occupied core level, $|1\rangle = \hat{d}^\dagger|0\rangle$, and the Fermi sea of conduction electrons $|\text{FS}\rangle$ in the sense of Fermi-liquid theory, i.e., $|\Psi_0\rangle = |1\rangle \otimes |\text{FS}\rangle$ [25]. Generally, the core level is either empty or occupied, so the full Hamiltonian, Eq. (1), can be brought into a form $\hat{H} = |0\rangle\langle 0| \otimes \hat{H}_1 + |1\rangle\langle 1| \otimes (\hat{H}_0 + \varepsilon_d \hat{\mathbb{1}})$, where $\hat{H}_0$ and $\hat{H}_1$ only act on the subspace of the conduction electrons:

$$\hat{H}_0 = \sum_{\boldsymbol{k}} \varepsilon_{\boldsymbol{k}} \hat{c}_{\boldsymbol{k}}^\dagger \hat{c}_{\boldsymbol{k}}, \quad \hat{H}_1 = \sum_{\boldsymbol{k},\boldsymbol{k}'} \left(\varepsilon_{\boldsymbol{k}} \delta_{\boldsymbol{k}\boldsymbol{k}'} - \frac{U}{V} \right) \hat{c}_{\boldsymbol{k}}^\dagger \hat{c}_{\boldsymbol{k}'}. \quad (A1)$$

Since these are quadratic, the system is exactly solvable. The time evolution of the many-body state with an empty $|0\rangle$ or occupied $|1\rangle$ core level is then determined by

$$e^{-i\hat{\Xi}t}(|0\rangle \otimes |\Psi\rangle) = |0\rangle \otimes e^{-i(\hat{H}_1 - \mu\hat{N}_0)t}|\Psi\rangle, \quad (A2a)$$

$$e^{-i\hat{\Xi}t}(|1\rangle \otimes |\Psi\rangle) = e^{-i(\varepsilon_d - \mu)t}|1\rangle \otimes e^{-i(\hat{H}_0 - \mu\hat{N}_0)t}|\Psi\rangle. \quad (A2b)$$

Here, we use the number operator of the conduction electrons $\hat{N}_0 = \sum_{\boldsymbol{k}} \hat{c}_{\boldsymbol{k}}^\dagger \hat{c}_{\boldsymbol{k}}$ and $\hat{\Xi} = \hat{H} - \mu\hat{N}$, with the total number operator $\hat{N} = \hat{N}_0 + \hat{d}^\dagger \hat{d}$.

As mentioned in the main text, we use the ground state $|\Psi_0\rangle = |1\rangle \otimes |\text{FS}\rangle$ as reference state for the expectation value. The time-ordering operator $\mathcal{T}$ generates two terms. In the expressions for $X(t)$ and $G(t)$, however, only one remains according to the occupancy of the d electron.

Inserting the time evolution $\hat{d}^{(\dagger)}(t) = e^{i\hat{\Xi}t}\hat{d}^{(\dagger)}e^{-i\hat{\Xi}t}$ into the definition of $G(t)$, Eq. (3), yields

$$\begin{aligned} G(t) &= i\,\Theta(-t)(\langle 1| \otimes \langle \text{FS}|\hat{d}^\dagger e^{i\hat{\Xi}t}\hat{d}e^{-i\hat{\Xi}t}(|1\rangle \otimes |\text{FS}\rangle)) \\ &= i\,\Theta(-t)(\langle 0| \otimes \langle \text{FS}|e^{i(\hat{H}_1 - \mu\hat{N}_0)t}) \\ &\quad \times (e^{-(i\varepsilon_d - \mu)t}|0\rangle \otimes e^{-i(\hat{H}_0 - \mu\hat{N}_0)t}|\text{FS}\rangle)), \quad (A3) \end{aligned}$$

which, after evaluating the effect of the d electron, gives

$$G(t) = i\Theta(-t)e^{-i\xi_d t} \langle \text{FS}|e^{i\hat{H}_1 t}e^{-i\hat{H}_0 t}|\text{FS}\rangle. \quad (A4)$$

Note that the terms including the number operators $\hat{N}_0$ cancel each other by conservation of particle number, i.e., $[\hat{H}_{0,1}, \hat{N}_0] = 0$. With $|\text{FS}\rangle\langle \text{FS}| = e^{-\beta(\hat{H}_0 - \mu\hat{N}_0)}/Z_0$, where $Z_0 = \text{tr}\,e^{-\beta(\hat{H}_0 - \mu\hat{N}_0)}$, the expectation value is expressed as a trace:

$$G(t) = i\Theta(-t)e^{-i(\varepsilon_d - \mu)t}\frac{1}{Z_0}\text{tr}\left[e^{-\beta(\hat{H}_0 - \mu\hat{N}_0)}e^{i\hat{H}_1 t}e^{-i\hat{H}_0 t}\right]. \quad (A5)$$

As the Hamiltonians are bilinear $\hat{H}_{0,1} = \sum_{\boldsymbol{k},\boldsymbol{k}'}[\hat{h}_{0,1}]_{\boldsymbol{k}\boldsymbol{k}'}\hat{c}_{\boldsymbol{k}}^\dagger\hat{c}_{\boldsymbol{k}'}$, we use Klich's formula [47,48] to express the many-particle trace as a determinant over single-particle operators $\hat{h}_{0,1}$:

$$\text{tr}\left[e^{-\beta(\hat{H}_0 - \mu\hat{N}_0)}e^{i\hat{H}_1 t}e^{-i\hat{H}_0 t}\right] = \det\left[\hat{\mathbb{1}} + e^{-\beta(\hat{h}_0 - \mu)}e^{i\hat{h}_1 t}e^{-i\hat{h}_0 t}\right]. \quad (A6)$$

Due to the fermionic properties, the Green's function is finally written in terms of the Fermi-Dirac distribution:

$$G(t) = i\Theta(-t)e^{-i(\varepsilon_d - \mu)t}\det\left[\hat{\mathbb{1}} - f(\hat{h}_0) + f(\hat{h}_0)e^{i\hat{h}_1 t}e^{-i\hat{h}_0 t}\right]. \quad (A7)$$

In frequency space, the expression for the advanced Green's function is obtained from fast Fourier transformation $G(\nu) = \int_t e^{i\nu t}G(t)$ after exact diagonalization of the single-particle Hamiltonians $[\hat{h}_1]_{\boldsymbol{k}\boldsymbol{k}'} = \varepsilon_{\boldsymbol{k}}\delta_{\boldsymbol{k}\boldsymbol{k}'} - U/V$ (for details, see Supplemental Material of Ref. [53]).

The susceptibility, Eq. (2), is computed in a similar fashion. Due to the occupancy of the d electron, here only the retarded term of the time ordering survives:

$$\begin{aligned} X(t) &= -i\,\Theta(t)\frac{1}{V}\sum_{\boldsymbol{k},\boldsymbol{k}'}(\langle 1| \otimes \langle \text{FS}|)e^{i\hat{\Xi}t}\hat{d}^\dagger e^{-i\hat{\Xi}t} \\ &\quad \times e^{i\hat{\Xi}t}\hat{c}_{\boldsymbol{k}}e^{-i\hat{\Xi}t}\hat{c}_{\boldsymbol{k}'}^\dagger\hat{d}(|1\rangle \otimes |\text{FS}\rangle), \quad (A8) \end{aligned}$$

which according to the time evolutions, Eq. (A2), yields

$$\begin{aligned} X(t) &= -i\,\Theta(t)\frac{1}{V}\sum_{\boldsymbol{k},\boldsymbol{k}'}(\langle 0|e^{i(\varepsilon_d - \mu)t} \otimes \langle \text{FS}|e^{i(\hat{H}_0 - \mu\hat{N}_0)t}\hat{c}_{\boldsymbol{k}}) \\ &\quad \times (|0\rangle \otimes e^{-i(\hat{H}_1 - \mu\hat{N}_0)t}\hat{c}_{\boldsymbol{k}'}^\dagger|\text{FS}\rangle). \quad (A9) \end{aligned}$$

Again, the d degree of freedom is evaluated straightforwardly. By particle-number conservation, we can write $e^{-i\mu\hat{N}_0 t}\hat{c}_{\boldsymbol{k}}e^{i\mu\hat{N}_0 t} = e^{i\mu t}\hat{c}_{\boldsymbol{k}}$, so the terms with the chemical potentials cancel, and we get the following expression:

$$X(t) = -i\Theta(t)e^{i\varepsilon_d t}\frac{1}{V}\sum_{\boldsymbol{k},\boldsymbol{k}'}\langle \text{FS}|e^{i\hat{H}_0 t}\hat{c}_{\boldsymbol{k}}e^{-i\hat{H}_1 t}\hat{c}_{\boldsymbol{k}'}^\dagger|\text{FS}\rangle. \quad (A10)$$

By using $[\hat{H}_1, \hat{c}_{\boldsymbol{k}}] = \sum_{\boldsymbol{k}'}[\hat{h}_1]_{\boldsymbol{k}\boldsymbol{k}'}\hat{c}_{\boldsymbol{k}'}$ with the single-particle operator $\hat{h}_1$, we can write

$$\hat{c}_{\boldsymbol{k}}\mathrm{e}^{-\mathrm{i}\hat{H}_1 t} = \mathrm{e}^{-\mathrm{i}\hat{H}_1 t}\sum_{\boldsymbol{k}'}[\mathrm{e}^{-\mathrm{i}\hat{h}_1 t}]_{\boldsymbol{k}\boldsymbol{k}'}\hat{c}_{\boldsymbol{k}'}. \qquad (A11)$$

The term including the single-particle operator $\hat{h}_1$ can be pulled out of the expectation value and the susceptibility yields

$$X(t) = -\mathrm{i}\Theta(t)\mathrm{e}^{\mathrm{i}\varepsilon_d t}\frac{1}{V}\sum_{\boldsymbol{k},\boldsymbol{k}',\boldsymbol{k}''}[\mathrm{e}^{-\mathrm{i}\hat{h}_1 t}]_{\boldsymbol{k}\boldsymbol{k}''}\langle\mathrm{FS}|\mathrm{e}^{\mathrm{i}\hat{H}_0 t}\mathrm{e}^{-\mathrm{i}\hat{H}_1 t}\hat{c}_{\boldsymbol{k}''}\hat{c}_{\boldsymbol{k}'}^{\dagger}|\mathrm{FS}\rangle. \qquad (A12)$$

Applying the anticommutation relation $\hat{c}_{\boldsymbol{k}''}\hat{c}_{\boldsymbol{k}'}^{\dagger} = \delta_{\boldsymbol{k}'\boldsymbol{k}''} - \hat{c}_{\boldsymbol{k}'}^{\dagger}\hat{c}_{\boldsymbol{k}''}$ generates two terms. The first term is analogous to the d propagator. In the second term,

$$\langle\mathrm{FS}|\mathrm{e}^{\mathrm{i}\hat{H}_0 t}\mathrm{e}^{-\mathrm{i}\hat{H}_1 t}\hat{c}_{\boldsymbol{k}'}^{\dagger}\hat{c}_{\boldsymbol{k}''}|\mathrm{FS}\rangle$$
$$= \frac{1}{Z_0}\mathrm{tr}\big[\mathrm{e}^{-\beta(\hat{H}_0-\mu\hat{N}_0)}\mathrm{e}^{\mathrm{i}\hat{H}_0 t}\mathrm{e}^{-\mathrm{i}\hat{H}_1 t}\hat{c}_{\boldsymbol{k}'}^{\dagger}\hat{c}_{\boldsymbol{k}''}\big], \qquad (A13)$$

the density operator can be treated as a derivative of a bilinear operator:

$$\hat{c}_{\boldsymbol{k}'}^{\dagger}\hat{c}_{\boldsymbol{k}''} = \frac{\mathrm{d}}{\mathrm{d}a}\mathrm{e}^{a\hat{c}_{\boldsymbol{k}'}^{\dagger}\hat{c}_{\boldsymbol{k}''}}\bigg|_{a=0} \equiv \frac{\mathrm{d}}{\mathrm{d}a}\mathrm{e}^{a\sum_{q,q'}[\hat{A}_{\boldsymbol{k}'\boldsymbol{k}''}]_{qq'}\hat{c}_q^{\dagger}\hat{c}_{q'}}\bigg|_{a=0}. \qquad (A14)$$

Here, the single-particle operator $\hat{A}_{\boldsymbol{k}'\boldsymbol{k}''}$ just picks the mode with the corresponding momenta. Consequently, Klich's formula is applicable:

$$\langle\mathrm{FS}|\mathrm{e}^{\mathrm{i}\hat{H}_0 t}\mathrm{e}^{-\mathrm{i}\hat{H}_1 t}\hat{c}_{\boldsymbol{k}'}^{\dagger}\hat{c}_{\boldsymbol{k}''}|\mathrm{FS}\rangle$$
$$= \frac{\mathrm{d}}{\mathrm{d}a}\det\big[\hat{\mathbb{1}} - f(\hat{h}_0) + f(\hat{h}_0)\mathrm{e}^{\mathrm{i}\hat{h}_0 t}\mathrm{e}^{-\mathrm{i}\hat{h}_1 t}\mathrm{e}^{a\hat{A}_{\boldsymbol{k}'\boldsymbol{k}''}}\big]\bigg|_{a=0}. \qquad (A15)$$

Let us define $B(t) = \hat{\mathbb{1}} - f(\hat{h}_0) + f(\hat{h}_0)\mathrm{e}^{\mathrm{i}\hat{h}_0 t}\mathrm{e}^{-\mathrm{i}\hat{h}_1 t}$. Using Jacobi's formula for the derivative of a determinant,

$$\frac{\mathrm{d}}{\mathrm{d}a}\det A(a) = \det A(a)\,\mathrm{tr}\bigg(A^{-1}(a)\frac{\mathrm{d}A(a)}{\mathrm{d}a}\bigg), \qquad (A16)$$

yields

$$\langle\mathrm{FS}|\mathrm{e}^{\mathrm{i}\hat{H}_0 t}\mathrm{e}^{-\mathrm{i}\hat{H}_1 t}\hat{c}_{\boldsymbol{k}''}^{\dagger}\hat{c}_{\boldsymbol{k}'}|\mathrm{FS}\rangle$$
$$= \det B(t)\,\mathrm{tr}\big[B^{-1}(t)f(\hat{h}_0)\mathrm{e}^{\mathrm{i}\hat{h}_0 t}\mathrm{e}^{-\mathrm{i}\hat{h}_1 t}\hat{A}_{\boldsymbol{k}'\boldsymbol{k}''}\big]$$
$$= \det B(t)\big[B^{-1}(t)f(\hat{h}_0)\mathrm{e}^{\mathrm{i}\hat{h}_0 t}\mathrm{e}^{-\mathrm{i}\hat{h}_1 t}\big]_{\boldsymbol{k}''\boldsymbol{k}'}. \qquad (A17)$$

In the last line, we used the property of $\hat{A}_{\boldsymbol{k}'\boldsymbol{k}''}$. It picks up only one mode and thus gives only one matrix element in the trace, i.e., $\mathrm{tr}(MA_{\boldsymbol{k}'\boldsymbol{k}''}) = M_{\boldsymbol{k}''\boldsymbol{k}'}$. Combining everything, we get the final form for the susceptibility, Eq. (A12):

$$X(t) = -\mathrm{i}\Theta(t)\mathrm{e}^{\mathrm{i}\varepsilon_d t}\det B(t)$$
$$\times \frac{1}{V}\sum_{\boldsymbol{k},\boldsymbol{k}''}\big[\mathrm{e}^{-\mathrm{i}\hat{h}_1 t}(\hat{\mathbb{1}} - B^{-1}(t)f(\hat{h}_0)\mathrm{e}^{\mathrm{i}\hat{h}_0 t}\mathrm{e}^{-\mathrm{i}\hat{h}_1 t})\big]_{\boldsymbol{k}\boldsymbol{k}''}$$
$$= -\mathrm{i}\Theta(t)\mathrm{e}^{\mathrm{i}\varepsilon_d t}\det B(t)$$
$$\times \frac{1}{V}\sum_{\boldsymbol{k},\boldsymbol{k}''}\big[\mathrm{e}^{-\mathrm{i}\hat{h}_1 t}B^{-1}(t)(\hat{\mathbb{1}} - f(\hat{h}_0))\big]_{\boldsymbol{k}\boldsymbol{k}''}. \qquad (A18)$$
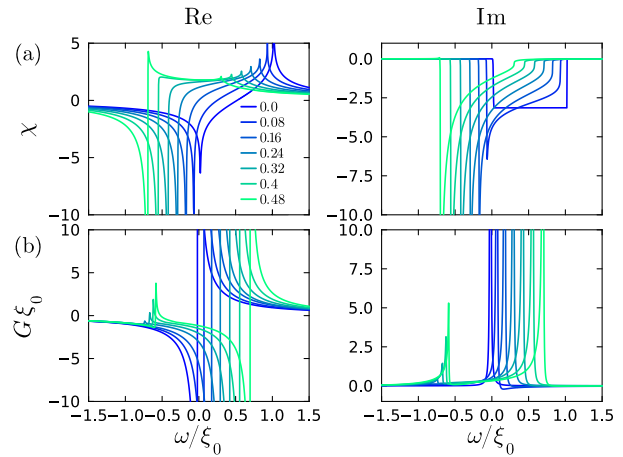
FIG. 12. Results for the (a) the particle-hole susceptibility $\chi(\omega) = X(\omega)/\rho$ and (b) the d propagator $G(\nu)$ from the functional determinant approach for $T/\xi_0 = 0.002$, $\xi_d = -0.02$, $n_{\max} = 1000$, and different values of u (marked by different colors).

Also here, the retarded correspondent is obtained via Fourier transformation $X(\omega) = \int_t \mathrm{e}^{\mathrm{i}\omega t}X(t)$.

Equations (A7) and (A18) are computed by exact diagonalization of the single-particle matrix $[\hat{h}_1]_{\boldsymbol{k}\boldsymbol{k}'} = \varepsilon\delta_{\boldsymbol{k}\boldsymbol{k}'} - U/V$. To be more precise, we discretize the single-particle states with noninteracting energies $\varepsilon_n = 2\xi_0 n/n_{\max}$ where the number of states is given by $n_{\max} = \lfloor 2\xi_0\rho V\rfloor$ [25]. This way, we simulate a constant density of states ρ for a finite volume V [cf. Eq. (5)]. We observe convergence of our data with respect to the finite size at high enough volumes, i.e., $n_{\max} \gtrsim 1000$.

The finite size, however, discretizes the energy spectrum $\delta\varepsilon = 2\xi_0/n_{\max}$, so we limit our Fourier integral up to time scales $t_{\max} = \pi/\delta\varepsilon \simeq \pi\rho V$. Furthermore, we broaden the frequency-dependent data by applying an exponential decay $\mathrm{e}^{\pm 2t/t_{\max}}$ in the Fourier transform. Here $+$ is used in the exponent for the advanced Green's function $G(t)$, Eq. (A7), and $-$ for the retarded susceptibility $X(t)$, Eq. (A18).

We present our numerically exact data from the functional determinant approach in Fig. 12. The Fermi edge as well as the corresponding power laws are visible in both quantities. Note that the singularities are cut due to finite-size effects and the regularization we implement in the Fourier transforms. The additional peaks at negative frequencies in G for large enough interactions u [cf. Fig. 12(b)] mark the additional bound states [44]. Close to the threshold frequency ω_0, we can confirm that the analytical power-law behavior Eq. (10a) is well described by the functional determinant approach (cf. Fig. 13).

2. Numerical results of the threshold

From the positions corresponding to the x-ray edge singularity in Im χ [cf. Fig. 12(a)] and the peak due to Anderson's orthogonality catastrophe in Im G [cf. Fig. 12(b)], we extract the values for the threshold frequency ω_0 (i.e., for χ the peaks are located at ω_0 and for G at $-\omega_0$). Figure 14 shows that the data for ω_0 obtained from χ and G lie on top (blue and light blue data points).
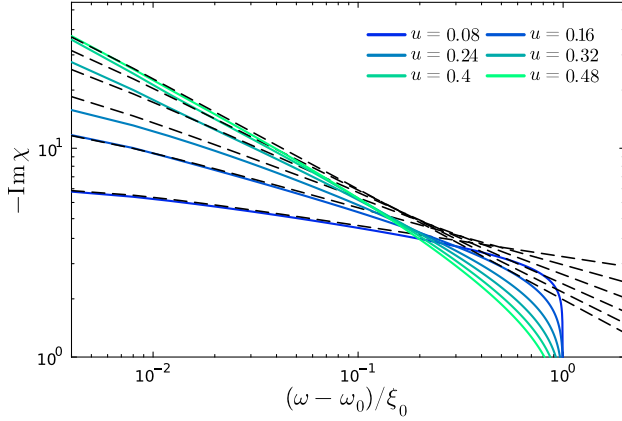
FIG. 13. Susceptibility from the functional determinant approach with parameters as in Fig. 12 compared to the analytical power-law behavior Eq. (10a) (black dashed lines).

Furthermore, we compare these numerically exact data to the values form the diagrammatic approaches. First of all, we have the form in second-order perturbation theory,

$$\omega_0 = -\xi_d - u\xi_0 - u^2 \, 2\xi_0 \ln 2 + \mathcal{O}(u^3), \quad (A19)$$

which describes the behavior quite accurately up to intermediate values $u \lesssim 0.3$ (cf. green dashed line in Fig. 14).

Moreover, Fig. 14 also serves as a check that our empirical strategy for an adjustment of the renormalized threshold frequency in the parquet formalism (cf. Sec. III E) is quite accurate. To this end, we determine values for the threshold as

$$\omega_0 = -\xi_d - u\xi_0 - [\Sigma_{\text{sub}}]_{\text{i}\nu=0} - u^2\xi_d L(0). \quad (A20)$$

Here, Σ_{sub} is the imaginary-frequency self-energy obtained by an insertion of the leading-log vertex Γ_{lead}, Eqs. (30), into the Schwinger–Dyson equation (32). The terms, which do not affect the threshold frequency are hereby compensated
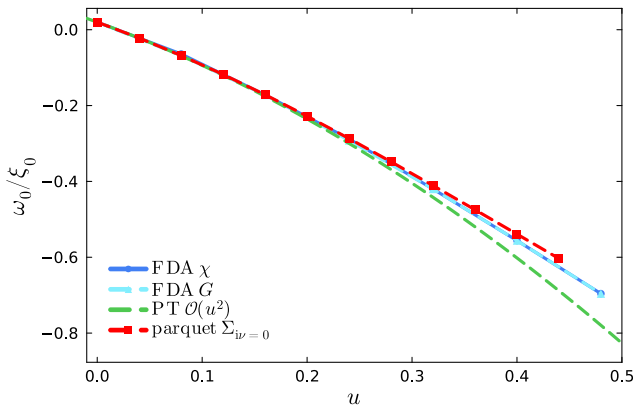
FIG. 14. Threshold frequencies ω_0 obtained from the functional determinant approach for χ (blue) and G (light blue) (cf. Fig. 12) compared to the values obtained from second-order perturbation theory, Eq. (A19), (green, dashed) and the subleading-log self-energy $\Sigma_{\text{i}\nu=0}$ at zero imaginary frequency (red squares) [cf. Eq. (A20)]. The data are evaluated at $T/\xi_0 = 0.002$ and $\xi_d/\xi_0 = -0.02$.

perturbatively, by adding the second-order logarithmic term $-u^2\xi_d L(0)$ [cf. Eq. (21)]. The data points extracted from Eq. (A20) (red squares in Fig. 14) are closer to the actual values (blue) than the prediction from second-order perturbation theory (green dashed line).

In a general treatment, the threshold frequency $\tilde{\omega}_0$ predicted by parquet results differs from the actual value ω_0. To compare the power-law behavior predicted by parquet data with that predicted by the functional determinant approach, we need to adjust the threshold frequencies accordingly. Analytical continuation of parquet data to real frequencies provides a behavior $\chi^R(\omega) = \chi(\omega + \text{i}0^+) \sim (\omega + \text{i}0^+ - \tilde{\omega}_0)^{-\alpha_X}$ near the presumed threshold $\tilde{\omega}_0$ [cf. Eq. (10a)]. The value at zero Matsubara frequency $\chi_{\text{parq}}(\text{i}\omega = 0) \sim (-\tilde{\omega}_0)^{-\alpha_X}$ is approximately reproduced by the exact data at a shifted frequency $\chi^R(\omega = \omega_0 - \tilde{\omega}_0)$. Following this reasoning, the data $\chi_{\text{parq}}(\text{i}\omega = 0)$ presented in Fig. 10 that are computed with $\tilde{\omega}_0 \simeq -\xi_d$ (cf. Sec. III E) correspond to the values $\chi_{\text{FDA}}(\omega = \omega_0 + \xi_d)$ in Fig. 12.

APPENDIX B: FURTHER POWER-LAW EXPANSIONS

For completeness, let us give the Taylor expansion of Eqs. (10) using the full exponents depending on the phase shift $\delta = \arctan(\pi u)$:

$$\begin{aligned}
\chi(\text{i}\omega) = {}& L - uL^2 + u^2\left[\tfrac{2}{3}L^3 + \tfrac{1}{2}L^2\right] \\
& - u^3\left[\tfrac{1}{3}L^4 + \tfrac{2}{3}L^3 - \tfrac{1}{3}\pi^2 L^2\right] \\
& + u^4\left[\tfrac{2}{15}L^5 + \tfrac{1}{2}L^4 + \left(\tfrac{1}{6} - \tfrac{4}{9}\pi^2\right)L^3 - \tfrac{1}{3}\pi^2 L^2\right] \\
& + \mathcal{O}(u^5), \quad (\text{B1a})
\end{aligned}$$

$$G(\text{i}\nu) = \frac{1}{\text{i}\nu - \xi_d}\left[1 + u^2\bar{L} + u^4\left(\tfrac{1}{2}\bar{L}^2 - \tfrac{2}{3}\pi^2\bar{L}\right) + \mathcal{O}(u^6)\right]. \quad (\text{B1b})$$

As $2\delta/\pi - (\delta/\pi)^2 = 2u - u^2 - 2\pi^2 u^3/3 + \mathcal{O}(u^4)$, the leading- and subleading-log terms in χ are not changed compared to Eqs. (11). Only the subsubleading terms are changed by the addends including π. Similarly, in the expansion of G, the highest power of logarithms at each order remains unchanged compared to Eq. (13), since $(\delta/\pi)^2 = u^2 - 2\pi^2 u^4/3 + \mathcal{O}(u^6)$.

It is worth to mention that the power law for the self-energy Σ is completely analogous to that of the Green's function G. Applying the Dyson equation to Eq. (10b) yields

$$\Sigma(\nu - \text{i}0^+) = (\nu - \text{i}0^+ + \omega_0)\left[1 - \left(\frac{\nu - \text{i}0^+ + \omega_0}{\xi_0}\right)^{-\alpha_G}\right]. \quad (\text{B2})$$

Let us come back to the subleading-log power law $\alpha_X = 2u - u^2$. Strictly speaking, the threshold frequency in the exact power law, Eq. (10a), also depends on the interaction, i.e., $\omega_0 = \omega_0(u) = -\xi_d + \mathcal{O}(u)$. This causes additional terms in

the Taylor series of Eq. (11) (recall $i\tilde{\omega} = i\omega + \xi_d$):

$$
\chi(i\omega) = \frac{1}{2u - u^2}\left[1 - \left(\frac{i\omega - \omega_0(u)}{-\xi_0}\right)^{-2u + u^2}\right]
$$

$$
= L - u\left[L^2 + \frac{\omega_0'(0)}{i\tilde{\omega}}\right] + u^2\left[\tfrac{2}{3}L^3 + \tfrac{1}{2}L^2\right]
$$

$$
+ u^2\left[2L\frac{\omega_0'(0)}{i\tilde{\omega}} - \frac{1}{2}\frac{[\omega_0'(0)]^2}{(i\tilde{\omega})^2} - \frac{1}{2}\frac{\omega_0''(0)}{i\tilde{\omega}}\right]. \quad \text{(B3)}
$$

The terms involving $\omega_0'(0) = -\xi_0$ originate from the d Hartree self-energy $\Sigma_H = u\xi_0$, Eq. (D19). [(i) $-u\,\omega_0'(0)/(i\tilde{\omega})$ is generated by a bubble including one d Hartree term, (ii) $2u^2 L\,\omega_0'(0)/(i\tilde{\omega})$ is generated by two connected bubbles where one includes a d Hartree term, (iii) $-\frac{1}{2}u^2[\omega_0'(0)]^2/(i\tilde{\omega})^2$ is generated by one bubble including two d Hartree terms.] Further, $\omega_0''(0)$ comes from the frequency-independent part of $\Sigma^{(2)}$, Eq. (21b), inserted into $\chi_\Sigma^{(2)}$, Eq. (24). We thus identify $\omega_0''(0) = -4\xi_0 \ln 2$, which corresponds to Eq. (A19).

This interpretation is confirmed in the expansion of the self-energy $\Sigma = [G_0]^{-1} - G^{-1}$ with G given by an extended form of Eq. (13) (recall $i\tilde{\nu} = i\nu - \xi_d$):

$$
\Sigma(i\nu) = \frac{1}{G_0(i\nu)} - \frac{1}{G(i\nu)}
$$

$$
= i\tilde{\nu} - (i\nu + \omega_0(u))\left(\frac{i\nu + \omega_0(u)}{\xi_0}\right)^{-u^2}
$$

$$
= -u\,\omega_0'(0) + u^2\left[i\tilde{\nu}\bar{L} - \tfrac{1}{2}\omega_0''(0)\right] + \mathcal{O}(u^3). \quad \text{(B4)}
$$

Clearly, the first term corresponds to the d Hartree self-energy, Eq. (D19), and the second term coincides with $\Sigma^{(2)}$, Eq. (21b).

APPENDIX C: FREQUENCY PARAMETRIZATION OF THE VERTEX

As a four-leg object, in general, the full vertex has four entries each depending on a frequency and particle type (c vs d). Our analysis in the main text is conducted exclusively in one realization of particle types with four distinguishable legs: one ingoing and outgoing d leg and one ingoing and outgoing c leg. We denote the four entries of the four-point vertex $\Gamma_{1'2'|12}$ where $1'$ refers to outgoing d, $2'$ outgoing c, 1 ingoing d and 2 outgoing c. By energy conservation, Γ only depends on three frequencies [43]. In this work, we use the following conventions:

$$
\Gamma^a_{\omega,\nu,\nu'} = \Gamma_{\nu-\omega,\nu'|\nu'-\omega,\nu}, \quad \text{(C1a)}
$$

$$
\Gamma^p_{\omega,\nu,\nu'} = \Gamma_{\nu-\omega,-\nu|\nu'-\omega,-\nu'}, \quad \text{(C1b)}
$$

$$
\Gamma^t_{\omega,\nu,\nu'} = \Gamma_{\nu',\nu-\omega|\nu'-\omega,\nu}. \quad \text{(C1c)}
$$

These are illustrated in Fig. 15. Note that in contrast to γ^r and I^r, the channel index r in Γ^r does not indicate any reducibility property but just marks the channel taken for the frequency dependence. Due to Eqs. (C1), the Bethe–Salpeter equations are performed using the following summation/integration

$$
\int_{\nu''} \Gamma^r_{\omega,\nu,\nu''} \Pi^r_{\omega,\nu''} \tilde{\Gamma}^r_{\omega,\nu'',\nu'}. \quad \text{(C2)}
$$
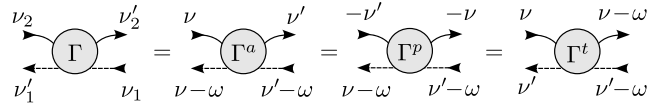
FIG. 15. Channel-specific frequency conventions of the four-point vertices Γ.

If the vertices Γ or $\tilde{\Gamma}$ are replaced by r'-reducible vertices, one has to transform the arguments from channel r to r' according to the parametrization Eq. (C1). The transformations are given by the following linear maps:

$$
\begin{pmatrix}\omega\\\nu\\\nu'\end{pmatrix}^a = \begin{pmatrix}1&-1&-1\\0&0&-1\\0&-1&0\end{pmatrix}\begin{pmatrix}\omega\\\nu\\\nu'\end{pmatrix}^p \qquad \begin{pmatrix}0&1&-1\\0&1&0\\-1&1&0\end{pmatrix}\begin{pmatrix}\omega\\\nu\\\nu'\end{pmatrix}^t,
$$
(C3a)

$$
\begin{pmatrix}\omega\\\nu\\\nu'\end{pmatrix}^p = \begin{pmatrix}1&-1&-1\\0&0&-1\\0&-1&0\end{pmatrix}\begin{pmatrix}\omega\\\nu\\\nu'\end{pmatrix}^a \qquad \begin{pmatrix}1&-1&-1\\1&-1&0\\0&-1&0\end{pmatrix}\begin{pmatrix}\omega\\\nu\\\nu'\end{pmatrix}^t,
$$
(C3b)

$$
\begin{pmatrix}\omega\\\nu\\\nu'\end{pmatrix}^t = \begin{pmatrix}0&1&-1\\0&1&0\\-1&1&0\end{pmatrix}\begin{pmatrix}\omega\\\nu\\\nu'\end{pmatrix}^a \qquad \begin{pmatrix}0&1&-1\\0&0&-1\\-1&1&0\end{pmatrix}\begin{pmatrix}\omega\\\nu\\\nu'\end{pmatrix}^p.
$$
(C3c)

APPENDIX D: DETAILS OF THE PERTURBATION SERIES

Individual diagrams in perturbation theory are obtained from successive integration over logarithmic terms. In the following, we give the most important integral expressions.

The integral over a logarithm to some power n multiplied with the d propagator $G \sim 1/(i\nu)$ raises the power of the logarithm according to

$$
\int_a^b d\nu\, \frac{1}{i\nu + i\omega} \ln^n \frac{i\nu + i\omega}{\xi_0} = \left[\frac{-i}{n+1} \ln^{n+1} \frac{i\nu + i\omega}{\xi_0}\right]_a^b, \quad \text{(D1)}
$$

where $n \in \mathbb{N}_0$.

The power of the logarithm is not raised when there is no additional d propagator. This becomes obvious from the simple integral

$$
\int_a^b d\nu\, \ln \frac{i\nu + i\omega}{\xi_0} = \left[(\nu + \omega)\ln \frac{i\nu + i\omega}{\xi_0} - \nu\right]_a^b, \quad \text{(D2)}
$$

which inductively can be generalized to higher powers of the logarithm

$$
\int_a^b d\nu\, \ln^n \frac{i\nu + i\omega}{\xi_0} = \left[(\nu + \omega)\ln^n \frac{i\nu + i\omega}{\xi_0}\right]_a^b
$$

$$
- n \int_a^b d\nu\, \ln^{n-1} \frac{i\nu + i\omega}{\xi_0}. \quad \text{(D3)}
$$

Furthermore, if there are multiple d propagators combined with a logarithm, the power of the logarithm is also not raised.

This is shown by

$$\int_a^b d\nu \frac{1}{(i\nu + i\omega)^n} \ln \frac{i\nu + i\omega}{\xi_0}$$
$$= \left[\frac{i}{n-1} \frac{1}{(i\nu + i\omega)^{n-1}} \left(\ln \frac{i\nu + i\omega}{\xi_0} + \frac{1}{n-1} \right) \right]_a^b, \quad (D4)$$

where $n > 1$. For higher powers of the logarithm $m > 1$, this has the following recursive generalization:

$$\int_a^b d\nu \frac{1}{(i\nu + i\omega)^n} \ln^m \frac{i\nu + i\omega}{\xi_0}$$
$$= \left[\frac{i}{n-1} \frac{1}{(i\nu + i\omega)^{n-1}} \right.$$
$$\times \left. \left(\ln^m \frac{i\nu + i\omega}{\xi_0} + \frac{1}{n-1} \ln^{m-1} \frac{i\nu + i\omega}{\xi_0} \right) \right]_a^b$$
$$+ \frac{m-1}{n-1} \int_a^b d\nu \frac{1}{(i\nu + i\omega)^n}$$
$$\times \left(\ln^{m-1} \frac{i\nu + i\omega}{\xi_0} + \frac{1}{n-1} \ln^{m-2} \frac{i\nu + i\omega}{\xi_0} \right). \quad (D5)$$

1. Leading-log diagrams

The integral over the bare bubble, Eq. (16), including the smooth propagator $g^{\rm sm}$, Eq. (7), is exactly solvable for $T = 0$. For this, we keep the original energy integral, which comes from the density of states, Eq. (5) (we use $i\tilde\omega = i\omega + \xi_d$):

$$\int_\nu \Pi^a_{\omega,\nu} = \int_\nu G_{\omega-\nu} g^{\rm sm}_\nu = \int_{-\infty}^\infty \frac{d\nu}{2\pi} \frac{1}{i\nu - i\tilde\omega} \int_{-\xi_0}^{\xi_0} \frac{d\xi}{i\nu - \xi}. \quad (D6)$$

First, the ν integral is solved via the residue theorem

$$\int_{-\infty}^\infty \frac{d\nu}{2\pi} \frac{1}{i\nu - i\tilde\omega} \frac{1}{i\nu - \xi} = \frac{\Theta(\xi)}{-\xi + i\tilde\omega}. \quad (D7)$$

Next, the ξ integral gives the logarithmic behavior:

$$\int_\nu \Pi^a_{\omega,\nu} = - \int_0^{\xi_0} \frac{d\xi}{\xi - i\tilde\omega} = \ln \frac{i\tilde\omega}{i\tilde\omega - \xi_0}. \quad (D8)$$

We are interested in the power-law behavior near the threshold frequency $\omega \simeq -\xi_d$. So, after analytic continuation, i.e., $i\omega \to \omega + i0^+$, $|\tilde\omega| \ll \xi_0$, and we may use [cf. Eq. (16)] [5,6],

$$\ln \frac{i\tilde\omega}{i\tilde\omega - \xi_0} = \ln \frac{i\tilde\omega}{-\xi_0} + \mathcal{O}\left(\frac{i\tilde\omega}{-\xi_0} \right). \quad (D9)$$

For general diagrams, the exact treatment of $g^{\rm sm}$ becomes difficult. Therefore we now use the approximation $g^{\rm sh}$, Eq. (8), which holds close to the threshold frequency.

We first compute a general integral over a product of the bubble Π^a, involving the sharp Green's function $g^{\rm sh}$ Eq. (8),

and an arbitrary function $f(\nu)$:

$$\int_\nu \Pi^a_{\omega,\nu} f(\nu) = -\frac{i}{2} \int_{-\xi_0}^{\xi_0} d\nu \frac{{\rm sgn}(\nu)}{i\nu - i\tilde\omega} f(\nu)$$
$$= -\frac{i}{2} \int_0^{\xi_0} d\nu \sum_{\sigma=\pm} \frac{f(\sigma\nu)}{i\nu - \sigma i\tilde\omega}. \quad (D10)$$

Setting $f(\nu) = 1$, we find the integrated bubble

$$\chi^{(0)}(\omega) = \int_\nu \Pi^a_{\omega,\nu} = \frac{1}{2} \sum_{\sigma=\pm} \ln \frac{i\tilde\omega}{i\tilde\omega - \sigma i\xi_0}. \quad (D11)$$

This resembles the exact result, Eq. (D8), yet the usage of $g^{\rm sh}$ generates some artifacts at the UV cutoff $|\omega| \simeq \xi_0$. Using $\ln i + \ln -i = 0$, we may rewrite this as

$$\chi^{(0)}(\omega) = \frac{1}{2} \sum_{\sigma=\pm} \ln \frac{i\tilde\omega}{\sigma\tilde\omega - \xi_0} = \ln \frac{i\tilde\omega}{-\xi_0} - \frac{1}{2} \sum_{\sigma=\pm} \ln \left(1 + \frac{\tilde\omega}{\xi_0} \right)$$
$$= \ln \frac{i\tilde\omega}{-\xi_0} + \mathcal{O}\left[\left(\frac{\tilde\omega}{\xi_0} \right)^2 \right], \quad (D12)$$

consistent with Eq. (D9), Eq. (16) in the main text and Eq. (16) in Ref. [5].

Logarithms with more complicated arguments are simplified up to logarithmic accuracy in order to apply the integral Eq. (D1):

$$\ln \frac{i\nu + i\nu' + i\tilde\omega}{-\xi_0} \simeq \Theta(|\nu| - |\nu'|) \ln \frac{i\nu + i\tilde\omega}{-\xi_0}$$
$$+ \Theta(|\nu'| - |\nu|) \ln \frac{i\nu' + i\tilde\omega}{-\xi_0}, \quad (D13)$$

which was first used before Eq. (29) in Ref. [5].

Turning to the crossed diagram Eq. (19), the integral over ν' is solved by inserting $[\gamma^p]^{(2)} = -u^2 L$ into Eq. (D10):

$$\int_{\nu'} [\gamma^p]^{(2)}_{\omega-\nu-\nu'} \Pi^a_{\omega,\nu'}$$
$$= \frac{iu^2}{2} \sum_{\sigma'} \int_0^{\xi_0} d\nu' \frac{1}{i\nu' - \sigma' i\tilde\omega} \ln \frac{i\nu' + \sigma' i\nu - \sigma' i\tilde\omega}{\sigma' \xi_0}. \quad (D14)$$

Via Eqs. (D1) and (D13), the integral is evaluated as

$$\int_0^{\xi_0} d\nu' \frac{1}{i\nu' - \sigma' i\tilde\omega} \ln \frac{i\nu' + i\sigma'\nu - i\sigma'\omega}{\sigma'\xi_0}$$
$$\simeq \int_0^{|\nu|} d\nu' \frac{1}{i\nu' - \sigma' i\tilde\omega} \ln \frac{i\sigma'\nu - i\sigma'\omega}{\sigma'\xi_0}$$
$$+ \int_{|\nu|}^{\xi_0} d\nu' \frac{1}{i\nu' - \sigma' i\tilde\omega} \ln \frac{i\nu' - i\sigma'\omega}{\sigma'\xi_0}$$
$$= -i \ln \frac{i\nu - i\tilde\omega}{\xi_0} \ln \frac{i|\nu| - \sigma' i\tilde\omega}{-\sigma' i\tilde\omega} - \frac{i}{2} \ln^2 \frac{i\nu' - i\sigma'\omega}{\sigma'\xi_0} \Big|_{|\nu|}^{\xi_0}. \quad (D15)$$

We write the result as

$$i \ln \frac{i\nu - i\tilde\omega}{\xi_0} \left[\ln \frac{-i\tilde\omega}{\xi_0} - \ln \frac{i|\nu| - \sigma' i\tilde\omega}{\sigma'\xi_0} \right] + \frac{i}{2} \ln^2 \frac{i|\nu| - i\sigma'\tilde\omega}{\sigma'\xi_0}, \quad (D16)$$

where, in the second term, we neglected terms arising from the upper limit $\nu' = \xi_0$ as up to logarithmic accuracy we can set $|\mathrm{i}\xi_0 - \mathrm{i}\sigma'\tilde{\omega}| \simeq \xi_0$. Eventually, we combine the terms in Eq. (D16) by neglecting differences in the signs, as this is also correct up to logarithmic accuracy:

$$\left| \ln \frac{-\mathrm{i}\nu + \mathrm{i}\tilde{\omega}}{\xi_0} - \ln \frac{\mathrm{i}\nu + \mathrm{i}\tilde{\omega}}{\xi_0} \right| \simeq \left| \ln \frac{-\mathrm{i}\nu + \mathrm{i}\tilde{\omega}}{\mathrm{i}\nu + \mathrm{i}\tilde{\omega}} \right| \ll \left| \ln \frac{\mathrm{i}\nu + \mathrm{i}\tilde{\omega}}{\xi_0} \right|. \tag{D17}$$

This way, we obtain

$$\int_{\nu'} [\gamma^p]^{(2)}_{\omega-\nu-\nu'} \Pi^a_{\omega,\nu'}$$
$$\simeq u^2 \left[\frac{1}{2} \ln^2 \frac{\mathrm{i}\nu - \mathrm{i}\tilde{\omega}}{\xi_0} - \ln \frac{\mathrm{i}\nu - \mathrm{i}\tilde{\omega}}{\xi_0} \ln \frac{-\mathrm{i}\tilde{\omega}}{\xi_0} \right]. \tag{D18}$$

The integration over the second frequency ν in the crossed diagram, Eq. (19), is then performed straightforwardly by Eq. (D1) and yields the logarithmic behavior $-\frac{1}{3} u^2 L^3$ given in the main text.

2. Self-energy

The first-order Hartree diagram for the d electron Σ can be calculated exactly using g^{sm}:

$$\Sigma^{(1)}_{\mathrm{H}} = u \int_{\nu} g^{\mathrm{sm}}_{\nu} \mathrm{e}^{\mathrm{i}\nu 0^+} = u \int_{-\xi_0}^{\xi_0} \mathrm{d}\xi \int_{-\infty}^{\infty} \frac{\mathrm{d}\nu}{2\pi} \frac{\mathrm{e}^{\mathrm{i}\nu 0^+}}{\mathrm{i}\nu - \xi}$$
$$= u \int_{-\xi_0}^{\xi_0} \mathrm{d}\xi \, \Theta(-\xi) = u\xi_0. \tag{D19}$$

Also the self-energy to second order, Eq. (20), can be integrated exactly using g^{sm}, Eq. (7) (recall $\mathrm{i}\tilde{\nu} = \mathrm{i}\nu - \xi_d$):

$$\frac{1}{u^2} \Sigma^{(2)}_{\nu} = -\int_{-\infty}^{\infty} \frac{\mathrm{d}\omega}{2\pi} \frac{1}{\mathrm{i}\tilde{\nu} - \mathrm{i}\omega} \int_{-\infty}^{\infty} \frac{\mathrm{d}\nu'}{2\pi}$$
$$\times \int_{-\xi_0}^{\xi_0} \frac{\mathrm{d}\xi_1}{\mathrm{i}\nu' - \mathrm{i}\omega - \xi_1} \int_{-\xi_0}^{\xi_0} \frac{\mathrm{d}\xi_2}{\mathrm{i}\nu' - \xi_2}. \tag{D20}$$

The integrals over ω and ν are performed by the residue theorem, and we are left with

$$\frac{1}{u^2} \Sigma^{(2)}_{\nu} = \int_{-\xi_0}^{\xi_0} \mathrm{d}\xi_1 \int_{-\xi_0}^{\xi_0} \mathrm{d}\xi_2 \frac{\Theta(\xi_1)\Theta(-\xi_2)}{\xi_1 - \xi_2 + \mathrm{i}\tilde{\nu}}$$
$$= \mathrm{i}\tilde{\nu} \ln \frac{\mathrm{i}\tilde{\nu}}{\mathrm{i}\tilde{\nu} + \xi_0} + (\mathrm{i}\tilde{\nu} + 2\xi_0) \ln \frac{\mathrm{i}\tilde{\nu} + 2\xi_0}{\mathrm{i}\tilde{\nu} + \xi_0}. \tag{D21}$$

The leading behavior [cf. Eq. (21b)] is extracted as

$$\frac{1}{u^2} \Sigma^{(2)}_{\nu} = \mathrm{i}\tilde{\nu} \left(\ln \frac{\mathrm{i}\tilde{\nu}}{\xi_0} + \ln 2 - 1 \right) + 2\xi_0 \ln 2 + \mathcal{O}\left(\frac{(\mathrm{i}\tilde{\nu})^2}{\xi_0} \right). \tag{D22}$$

Setting $\mathrm{i}\tilde{\nu} = 0 \Rightarrow \mathrm{i}\nu = \xi_d$ in Eq. (D22) yields the term $u^2 2\xi_0 \ln 2$, which appears in the expansions Eqs. (B3)–(B4) as threshold renormalization.

We now turn back to the approximated version using g^{sh}, Eq. (8). Let us start by first integrating the bubble $\int \Pi^a \simeq L$, Eq. (16), inside Eq. (20) for the self-energy $\Sigma^{(2)}$. Using the following integral expression including g^{sh}, Eq. (8), and an

arbitrary function $f(\nu)$:

$$\int_{\nu} f(\nu) g_{\nu} = -\frac{\mathrm{i}}{2} \sum_{\sigma=\pm} \sigma \int_0^{\xi_0} \mathrm{d}\nu \, f(\sigma\nu), \tag{D23}$$

the self-energy term yields

$$\frac{1}{u^2} \Sigma^{(2)}_{\nu} = -\int_{\nu',\nu''} \Pi^a_{\nu'-\nu,\nu''} g_{\nu'} \simeq -\int_{\nu'} \ln \frac{\mathrm{i}\nu' - \mathrm{i}\tilde{\nu}}{-\xi_0} g_{\nu'}$$
$$= \frac{\mathrm{i}}{2} \sum_{\sigma'} \sigma' \int_0^{\xi_0} \mathrm{d}\nu' \ln \frac{\sigma'\mathrm{i}\nu' - \mathrm{i}\tilde{\nu}}{-\xi_0}, \tag{D24}$$

which is solved by Eq. (D2). So, we obtain

$$\frac{1}{u^2} \Sigma^{(2)}_{\nu} = \frac{\mathrm{i}}{2} \sum_{\sigma'} \sigma' \left[(\xi_0 - \sigma'\tilde{\nu}) \ln \frac{\mathrm{i}\xi_0 - \sigma'\mathrm{i}\tilde{\nu}}{-\sigma'\xi_0} - \xi_0 \right.$$
$$\left. + \sigma'\tilde{\nu} \ln \frac{\mathrm{i}\tilde{\nu}}{-\xi_0} \right]. \tag{D25}$$

To extract the logarithmic behavior in the first term, we approximate $\xi_0 - \sigma'\tilde{\nu} \simeq \xi_0$ such that the sum over σ' yields $-\xi_0 \ln(\mathrm{i}) + \xi_0 \ln(-\mathrm{i}) = -\mathrm{i}\pi\xi_0$. Together with the other terms, we obtain $u^2(\mathrm{i}\tilde{\nu}\bar{L} + \pi\xi_0/2)$. Here, the first term yields the correct logarithmic behavior given in the main text [cf. Eq. (21b)], but the constant term beyond logarithmic accuracy is incorrect compared to the exact result, Eq. (D21). We conclude that using g^{sh} instead of g^{sm} causes inconsistencies. That is why, in our numerical evaluation, we refrain from using g^{sh}.

The logarithmic behavior of the corresponding susceptibility, Eq. (24), is calculated by Eqs. (D10) (recall $\mathrm{i}\tilde{\omega} = \mathrm{i}\omega + \xi_d$):

$$\chi^{(2)}_{\Sigma}(\omega) = \int_{\nu} \Pi^a_{\omega,\nu} u^2 (\mathrm{i}\nu - \mathrm{i}\tilde{\omega}) \ln \frac{-\mathrm{i}\nu + \mathrm{i}\tilde{\omega}}{-\xi_0} \frac{1}{\mathrm{i}\nu - \mathrm{i}\tilde{\omega}}$$
$$= -u^2 \frac{\mathrm{i}}{2} \int_0^{\xi_0} \mathrm{d}\nu \sum_{\sigma} \frac{1}{\mathrm{i}\nu - \sigma\mathrm{i}\tilde{\omega}} \ln \frac{\mathrm{i}\nu - \sigma\mathrm{i}\tilde{\omega}}{\sigma\xi_0}. \tag{D26}$$

The expression is directly applicable to Eq. (D1) and yields the subleading-log term $\frac{1}{2} u^2 L^2$ [cf. Eq. (24)].

Let us briefly comment how the self-energy diagrams of third order cancel each other. In the Schwinger–Dyson equation (32), one can replace Γ by the second-order diagrams $\gamma_a^{(2)}$ and $\gamma_p^{(2)}$. This yields the following expression for the self-energy:

$$\Sigma^{(3)}_{\nu} = -\;\text{<diagram>}\;-\;\text{<diagram>}$$
$$= -\int_{\nu''} \left([\gamma^a_{\mathrm{lad}}]^{(3)}_{\nu''-\nu} g_{\nu''} + [\gamma^p_{\mathrm{lad}}]^{(3)}_{\nu''-\nu} g_{-\nu''} \right) = 0. \tag{D27}$$

The terms cancel each other as $[\gamma^a_{\mathrm{lad}}]^{(3)}_{\omega} = [\gamma^p_{\mathrm{lad}}]^{(3)}_{\omega}$ [cf. Eqs. (17)] and $g_{-\nu''} = -g_{\nu''}$.

3. t-reducible diagram

The t-reducible diagram $[\gamma_t]^{(3)}$, Eq. (25), contains the integrated bubble of two conduction-electron propagators, $\int_{\nu_2} g_{\nu_2-(\nu'-\nu_1)} g_{\nu_2}$ similar to the self-energy $\Sigma^{(2)}$. We expand the product $G_{\nu_1-\omega} G_{\nu_1}$ into partial fractions (recall

$i\tilde{\nu} = i\nu - \xi_d$ and $i\tilde{\omega} = i\omega + \xi_d$):

$$G_{\nu_1 - \omega} G_{\nu_1} = \frac{1}{i\tilde{\nu}_1 - i\omega} \frac{1}{i\tilde{\nu}_1} = \frac{1}{i\omega} \left[\frac{1}{i\tilde{\nu}_1 - i\omega} - \frac{1}{i\tilde{\nu}_1} \right]$$
$$= \frac{1}{i\omega} \left[G_{\nu_1 - \omega} - G_{\nu_1} \right], \qquad (D28)$$

and then we manipulate Eq. (25) as

$$[\gamma^t]^{(3)}_{\omega, \nu'} = \frac{u^3}{i\omega} \int_{\nu_1, \nu_2} [G_{\nu_1 - \omega} - G_{\nu_1}] g_{\nu_1 + \nu_2 - \nu'} g_{\nu_2}. \qquad (D29)$$

By substituting $\nu_1 \to \nu' - \omega'$ and $\nu_2 \to \nu''$, we identify terms from the self-energy $\Sigma^{(2)}$ Eq. (20):

$$[\gamma^t]^{(3)}_{\omega, \nu'} = -\frac{u}{i\omega} (-u^2) \int_{\nu', \omega'} [G_{\nu' - \omega - \omega'} - G_{\nu' - \omega'}] g_{\nu'' - \omega'} g_{\nu''}, \qquad (D30)$$

which yields the final expression, Eq. (25), given in the main text.

Inserting the logarithmic terms for the self-energies, Eq. (21), yields

$$[\gamma^t]^{(3)}_{\omega, \nu'} = \frac{u^3}{i\omega} \left[i\tilde{\nu}' \ln \frac{i\tilde{\nu}'}{\xi_0} - (i\tilde{\nu}' - i\omega) \ln \frac{i\tilde{\nu}' - i\omega}{\xi_0} \right]. \qquad (D31)$$

In numerical calculations, a discontinuity appears at $\omega = 0$, which reflects that the analytical behavior is critical there. Actually, the limit $\lim_{\omega \to 0} [\gamma^t]^{(3)}_{\omega, \nu} u^3 L(-\nu') + \mathcal{O}(1)$ is well behaved. To regularize our numerical results, we linearly interpolate $\gamma^t_{\omega, \nu}$ at $\omega = 0$ using the values for the first bosonic Matsubara frequencies $\omega = \pm \pi T$.

Finally, we derive the corresponding third-order term for the susceptibility, Eq. (26). First, we use Eq. (D10) and get

$$\chi^{(3)}_{\gamma^t}(\omega) = -\frac{1}{4} \sum_{\sigma, \sigma'} \int_0^{\xi_0} d\nu \int_0^{\xi_0} d\nu' \frac{\sigma}{\sigma i\nu - i\tilde{\omega}} \frac{\sigma'}{\sigma' i\nu' - i\tilde{\omega}}$$
$$\times [\gamma^t]^{(3)}_{\sigma \nu - \sigma' \nu', \sigma \nu - \omega}$$
$$\simeq \frac{u^3}{4} \sum_{\sigma, \sigma'} \int_0^{\xi_0} d\nu \int_0^{\xi_0} d\nu'$$
$$\times \left[\frac{\sigma \sigma'}{\sigma' i\nu' - i\tilde{\omega}} \frac{1}{i\sigma \nu - \sigma' i\nu'} \ln \frac{i\nu - \sigma i\tilde{\omega}}{\sigma \xi_0} \right.$$
$$\left. - \frac{\sigma \sigma'}{\sigma i\nu - i\tilde{\omega}} \frac{1}{\sigma i\nu - \sigma' i\nu'} \ln \frac{i\nu' - \sigma' i\tilde{\omega}}{\sigma' \xi_0} \right]. \qquad (D32)$$

By exchanging the integration and summation variables $\nu \leftrightarrow \nu'$ and $\sigma \leftrightarrow \sigma'$, the two terms are the same. The integral over ν' can be performed by use of

$$\int_a^b d\nu \frac{1}{(i\nu + i\nu_1)(i\nu + i\nu_2)}$$
$$= \frac{-i}{i\nu_1 - i\nu_2} [-\ln(\nu + \nu_1) + \ln(\nu + \nu_2)]_a^b$$
$$= \frac{-i}{i\nu_1 - i\nu_2} \left[-\ln \frac{i\nu + i\nu_1}{\xi_0} + \ln \frac{i\nu + i\nu_2}{\xi_0} \right]_a^b, \qquad (D33)$$

which is a special case of a product of d propagators (including different frequencies $\nu + \nu_i$) without a logarithmic term:

$$\int_a^b d\nu \prod_{i=1}^n \frac{1}{i\nu + i\nu_i} = \left[i(-1)^n \sum_{i=1}^n \ln \frac{i\nu + i\nu_i}{\xi_0} \prod_{j \neq i} \frac{1}{i\nu_j - i\nu_i} \right]_a^b. \qquad (D34)$$

We have

$$\int_0^{\xi_0} d\nu' \frac{-1}{(i\nu' - \sigma' i\tilde{\omega})(i\nu' - \sigma \sigma' i\nu)}$$
$$\simeq \frac{i\sigma'}{i\tilde{\omega} - \sigma i\nu} \left[\ln \frac{i\tilde{\omega}}{-\xi_0} - \ln \frac{i\nu}{\sigma \xi_0} \right], \qquad (D35)$$

where we restricted the terms to the lower boundary of the integral $\nu' = 0$. Equation (D32) then gives

$$\chi^{(3)}_{\gamma^t}(\omega) = \frac{u^3}{2} \sum_{\sigma, \sigma'} \int_0^{\xi_0} d\nu \ln \frac{i\nu - \sigma i\tilde{\omega}}{\sigma \xi_0}$$
$$\times \frac{-i}{i\nu - \sigma i\tilde{\omega}} \left[\ln \frac{i\tilde{\omega}}{-\xi_0} - \ln \frac{i\nu}{\sigma \xi_0} \right]. \qquad (D36)$$

The remaining expression is computed by Eq. (D1) using $\ln[i\nu/(\sigma \xi_0)] \simeq \ln[(i\nu - \sigma i\tilde{\omega})/(\sigma \xi_0)]$ and again only the lower boundary $\nu = 0$ is evaluated. This way we find the subleading-log behavior $\frac{1}{3} u^3 L^3$, given in the main text. Interpolating γ^t at $\omega = 0$ slightly improves the results for $\chi^{(3)}_{\gamma^t}$ shown in Fig. 4(c).

In analogy to our perturbative analysis, we interpolate the full t-reducible vertex $\gamma^t_{\omega, \nu, \nu'}$, Eq. (34), linearly around $\omega = 0$ to avoid further numerical instabilities during the self-consistency loop of the parquet equations.

4. Perturbative U(1) Ward identity

The U(1) Ward identity in the Matsubara formalism yields [66–68]

$$\Sigma^\sigma(\nu) - \Sigma^\sigma(\nu + \omega)$$
$$= \int_{\nu'} \sum_{\sigma'} \left([G_0^{-1}]^{\sigma'}(\nu') - [G_0^{-1}]^{\sigma'}(\nu' + \omega) \right)$$
$$\times \Gamma_{\sigma \sigma' | \sigma' \sigma}(\nu + \omega, \nu' | \nu' + \omega, \nu) G^{\sigma'}(\nu') G^{\sigma'}(\nu' + \omega). \qquad (D37)$$

In this section, we use the general notation for the vertex indices with particle types $\sigma = c, d$ introduced in Appendix F 1. For the x-ray edge singularity model with $G_0^d(\nu) \equiv G_\nu = 1/(i\nu - \xi_d)$, we get (using the notation from the main text where possible)

$$\Sigma_\nu - \Sigma_{\nu + \omega} = -i\omega \int_{\nu'} [\Gamma_{dd}]_{\nu + \omega, \nu' | \nu' + \omega, \nu} G_{\nu'} G_{\nu' + \omega}$$
$$+ \int_{\nu'} (g_{\nu'}^{-1} - g_{\nu' + \omega}^{-1}) [\Gamma_{\hat{d}c}]_{\nu + \omega, \nu' | \nu' + \omega, \nu} g_{\nu'} g_{\nu' + \omega}. \qquad (D38)$$

In second order of the interaction, the second term exactly vanishes, which can be seen as follows. First, the second-order contributions to $\Gamma_{\hat{d}c}$ are $[\gamma^t_{\hat{d}c}]^{(2)}$ and $[\gamma^p_{\hat{d}c}]^{(2)}$, which are related

to the well studied terms by crossing symmetry:

$$[\Gamma_{\hat{d}c}]^{(2)}_{\nu+\omega,\nu'|\nu'+\omega,\nu} = -[\Gamma_{dc}]^{(2)}_{\nu+\omega,\nu'|\nu,\nu'+\omega}$$
$$= -[\gamma^a]^{(2)}_{\nu'-\nu} - [\gamma^p]^{(2)}_{-\nu'-\nu-\omega}. \quad \text{(D39)}$$

From Eqs. (17), we know that those are related by a minus sign, i.e., $[\gamma^a]^{(2)}_\omega = -[\gamma^p]^{(2)}_\omega$. The clue is now that the c propagator is odd, i.e., $g_{-\nu} = -g_\nu$. By performing the substitution $\nu' \to \nu' - \omega/2$ of the integral variable ν' and then subdividing the integral for negative and positive ν', it becomes clear that the second term in Eq. (D38) vanishes:

$$\int_{\nu'} \left(g^{-1}_{\nu'-\frac{\omega}{2}} - g^{-1}_{\nu'+\frac{\omega}{2}} \right) \left(-[\gamma^a]^{(2)}_{\nu'-\frac{\omega}{2}-\nu} + [\gamma^a]^{(2)}_{-\nu'-\frac{\omega}{2}-\nu} \right)$$
$$\times g_{\nu'-\frac{\omega}{2}} g_{\nu'+\frac{\omega}{2}}$$
$$= \int_{\nu'>0} \sum_{\sigma'=\pm} \left(g^{-1}_{\sigma'\nu'-\frac{\omega}{2}} - g^{-1}_{\sigma'\nu'+\frac{\omega}{2}} \right)$$
$$\times \left(-[\gamma^a]^{(2)}_{\sigma'\nu'-\frac{\omega}{2}-\nu} + [\gamma^a]^{(2)}_{-\sigma'\nu'-\frac{\omega}{2}-\nu} \right) g_{\sigma'\nu'-\frac{\omega}{2}} g_{\sigma'\nu'+\frac{\omega}{2}}$$
$$= 0. \quad \text{(D40)}$$

The remaining first term in Eq. (D38) is simplified in second order. Here, Γ_{dd} only gives a contribution in the a channel [the p-channel diagram $[\gamma^p_{dd}]^{(2)}$ vanishes directly while $[\gamma^t_{dd}]^{(2)}$ yields a closed d bubble when integrated multiplied by the two d propagators in Eq. (D38)]. We now multiply both sides of Eq. (D38) by u and get

$$\frac{u}{i\omega} \left(\Sigma^{(2)}_{\nu+\omega} - \Sigma^{(2)}_\nu \right) = u \int_{\nu'} [\gamma^a_{dd}]^{(2)}_{\nu'-\nu} G_{\nu'} G_{\nu'+\omega} = [\gamma^t]^{(3)}_{\omega,\nu+\omega}. \quad \text{(D41)}$$

Diagrammatically, we could identify the right-hand side with the third-order diagram in the t channel in Appendix D 3. A frequency shift $\nu \to \nu' - \omega$ yields the expression (25) in the main text.

5. Multi-boson exchange diagram

Inserting the a-reducible multi-boson diagram $[M^a]^{(4)}$, Eq. (28), into the susceptibility χ yields Eq. (29) (recall $i\tilde\omega = i\omega + \xi_d$):

$$\chi^{(4)}_{M^a}(\omega) = \int_{\nu,\nu',\nu''} \Pi^a_{\omega,\nu} [\gamma^p]^{(2)}_{\omega-\nu-\nu''} \Pi^a_{\omega,\nu''} [\gamma^p]^{(2)}_{\omega-\nu''-\nu'} \Pi^a_{\omega,\nu'}$$
$$= \int_{\nu''} \Pi^a_{\omega,\nu''} \left[\int_\nu \Pi^a_{\omega,\nu} [\gamma^p]^{(2)}_{\omega-\nu-\nu''} \right]^2. \quad \text{(D42)}$$

The integrals over ν and ν', which consist each of one bubble Π^a and one vertex $[\gamma^p]^{(2)}$, could be integrated independently. They yield the same and, in fact, they coincide with the integral, Eq. (D18), which has already been performed in the context of the crossed diagram,

$$\left[\frac{1}{u^2} \int_\nu \Pi^a_{\omega,\nu} [\gamma^p]^{(2)}_{\omega-\nu-\nu''} \right]^2$$
$$\simeq \frac{1}{4} \ln^4 \frac{i\nu''-i\tilde\omega}{\xi_0} - \ln^3 \frac{i\nu''-i\tilde\omega}{\xi_0} \ln \frac{-i\tilde\omega}{\xi_0}$$
$$+ \ln^2 \frac{i\nu''-i\tilde\omega}{\xi_0} \ln^2 \frac{-i\tilde\omega}{\xi_0}. \quad \text{(D43)}$$

So in the end, one only needs to perform the integration over ν'', which can be recast according to Eq. (D10):

$$\chi^{(4)}_{M^a}(\omega) \simeq -\frac{iu^4}{2} \int_0^{\xi_0} d\nu'' \sum_\sigma \frac{1}{i\nu''-\sigma i\tilde\omega} \left[\frac{1}{4} \ln^4 \frac{i\nu''-\sigma i\tilde\omega}{\sigma\xi_0} \right.$$
$$\left. - \ln \frac{-i\tilde\omega}{\xi_0} \ln^3 \frac{i\nu''-\sigma i\tilde\omega}{\sigma\xi_0} + \ln^2 \frac{-i\tilde\omega}{\xi_0} \ln^2 \frac{i\nu''-\sigma i\tilde\omega}{\sigma\xi_0} \right]. \quad \text{(D44)}$$

This expression is solvable by Eq. (D1),

$$\chi^{(4)}_{M^a} = -\frac{iu^4}{2} \sum_\sigma \left[\frac{-i}{20} \ln^5 \frac{i\nu''-\sigma i\tilde\omega}{\sigma\xi_0} \right.$$
$$+ \frac{i}{4} \ln \frac{-i\tilde\omega}{\xi_0} \ln^4 \frac{i\nu''-\sigma i\tilde\omega}{\sigma\xi_0}$$
$$\left. - \frac{i}{3} \ln^2 \frac{-i\tilde\omega}{\xi_0} \ln^3 \frac{i\nu''-\sigma i\tilde\omega}{\sigma\xi_0} \right]$$
$$\simeq u^4 \left[-\frac{1}{20} + \frac{1}{4} - \frac{1}{3} \right] \ln^5 \frac{i\tilde\omega}{-\xi_0}, \quad \text{(D45)}$$

and yields the leading-log result $\frac{2}{15} u^4 L^5$ (cf. Eq. (29) in the main text).

APPENDIX E: NUMERICAL RESULTS FOR THE SELF-ENERGY

From Eq. (33), we concluded that inserting a leading-log vertex $\Gamma^{(n)}_{\text{lead}} \sim u^n L^{n-1}$ into the Schwinger–Dyson equation (32) yields a subleading-log contribution to the self-energy $\Sigma^{(n+1)}_{\text{sub}} \sim u^{n+1} i\tilde\nu \bar{L}^n$. Analogously, inserting a subleading-log vertex $\Gamma_{\text{sub}} \sim u^n L^{n-2}$ yields a subsubleading-log term $\Sigma^{(n+1)}_{\text{subsub}} \sim u^{n+1} i\tilde\nu \bar{L}^{n-1}$. Consequently, inserting the full leading-log vertex Γ_{lead}, solved by Eqs. (30), into the Schwinger–Dyson equation (32) reproduces the full subleading logarithm of the self-energy, while inserting the subleading-log Γ_{sub}, solved by Eqs. (32)–(36) and the full d propagator, reproduces the full subsubleading logarithm of the self-energy.

As mentioned at the end of Sec. II, the expansion of Anderson's orthogonality power law, Eq. (13), involves powers of $u^2 \bar{L}$. The second-order term $u^2 i\tilde\nu \bar{L}$ for the self-energy [cf. Eq. (21b)] involves the subleading logarithm and is thus correctly reproduced by inserting Γ_{lead} into the Schwinger–Dyson equation (32). The fourth-order term $u^4 i\tilde\nu \bar{L}^2$, in contrast, already goes beyond the subleading logarithm and can only be correctly reproduced when also the subleading contributions to Γ_{sub} and the renormalized propagator G_{sub} are included in Eq. (32). Furthermore, a complete computation of the sixth-order term $u^6 i\tilde\nu \bar{L}^3$ would already require inclusion of the envelope diagram $R^{(4)}_{\boxtimes}$.

We see that terms involving the subleading logarithm $u^n i\tilde\nu \bar{L}^{n-1}$ have to exactly cancel in higher orders of perturbation theory $\mathcal{O}(u^{n\geqslant3})$ in order to reproduce Anderson's orthogonality power law. Using our scheme, we cannot guarantee the complete reproduction of the first nonvanishing logarithmic terms at arbitrary orders of perturbation theory for the self-energy without the inclusion of totally
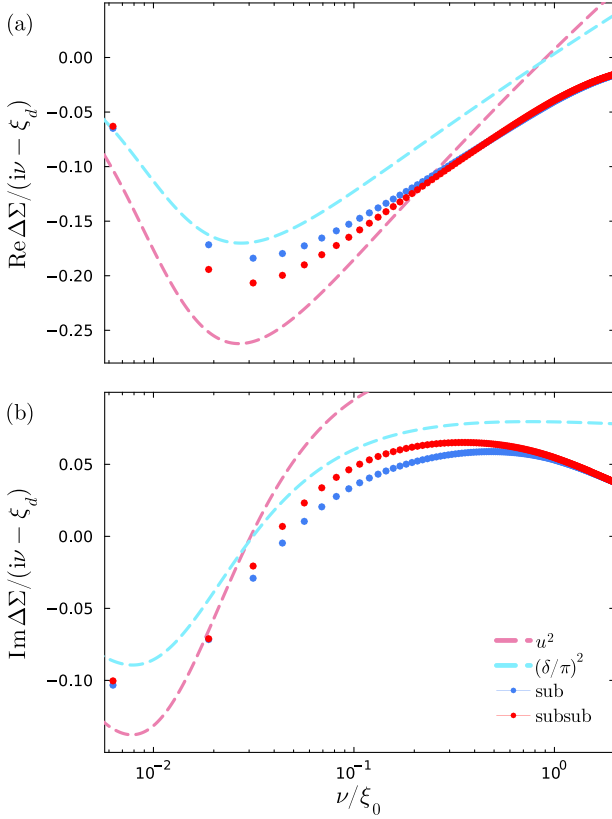
(a)

(b)

FIG. 16. Frequency dependence of Σ from self-consistent summations at $u = 0.28$, $T/\xi_0 = 0.002$, and $\xi_d/\xi_0 = -0.01$. The self-energy differences $\Delta\Sigma$, Eq. (22), are divided by $i\bar{\nu} = i\nu - \xi_d$. We compare the numerical results after inserting the leading-log vertex into the Schwinger–Dyson equation (blue dots) and after inserting the subleading-log vertex and the renormalized d propagator into the Schwinger–Dyson equation (red dots) to the analytically determined $T = 0$ power law with the subleading-log exponent $\alpha_G = u^2$ (pink, dashed) and the exact exponent $\alpha_G = (\delta/\pi)^2$ (light blue, dashed).

irreducible diagrams (beyond the bare vertex). These are beyond the scope of this work. Nonetheless, an insertion of Γ_{lead} into Eq. (32) already generates a lot of terms beyond the subleading logarithm $u^n i\bar{\nu}\bar{L}^{n-1-p}$ with $p > 0$. We evaluate them numerically, being aware that their summation is incomplete.

Although within the parquet approximation, it is impossible to capture the u^2 power law at all orders of perturbation theory, we may still compare our numerical data to the power law, Eq. (B2). Figure 16 shows the results when inserting the leading-log vertex Γ_{lead}, Eq. (30), into the Schwinger–Dyson equation (32) (blue dots) and when additionally including the subleading-log vertex Γ_{sub}, Eq. (36), and the full d propagator (red dots). The analytic power laws with $\alpha_G = u^2$ and $\alpha_G = (\delta/\pi)^2$ (pink and light blue, dashed), applicable in a rather small frequency regime, are not too far from the numerical results. Moreover, it is remarkable that the quantitative difference between inserting Γ_{lead} or Γ_{sub} into the Schwinger–Dyson equation is rather small.
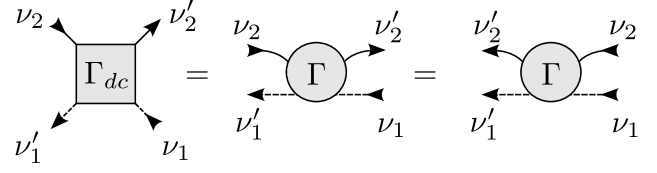
FIG. 17. Translation between the two diagrammatic conventions: The square vertex is used in Hubbard-like models. Here, the positions of the legs are fixed. This more general notation is exclusively used in this section. The round vertex on the other hand is used in the main text. There, the frequencies are defined according to the respective leg type, not its leg position.

APPENDIX F: DETAILS ON THE t-REDUCIBLE VERTEX

Here, we give details on how our expression for the t-reducible vertex, γ^t Eq. (34), can be motivated from the full parquet formalism and how we have implemented its numerical computation.

1. More general vertex conventions

The bare interaction u appearing in the action S, Eq. (6), describes only a single scattering event between the d electron with one c electron. In a general diagrammatic treatment, however, the full vertex Γ describes all scattering events between d electrons and c electrons involving two particles, in particular, also scattering events within one particle type. For this, it naturally comes with four indices $\Gamma_{1'2'|12}$ representing the four different particle types of the legs (cf. Appendix C and Ref. [43]). While in the main text only one component is needed, namely that with four distinguishable legs, in the general treatment, we have to include the particle-type in the notation. Figure 17 points out the difference between the two conventions: In Hubbard-like models, we represent the full vertex by a square, where the indices of its four legs are identified by their position ($\Gamma_{1'2'|12}$: 1' bottom-left, 2' top-right, 1 bottom-right, 2 top-left). When using only one component with four distinguishable legs, this notation becomes superfluous; so, in the main text, we always take $\Gamma \equiv \Gamma_{1'2'|12}$ (with 1' outgoing d, 2' outgoing c, 1 ingoing d, 2 ingoing c). There, the indices are identified by its particle types and the position is not decisive. To mark the difference, we represent Γ by a circle.

Following the convention with four indices of the full vertex $\Gamma_{1'2'|12}$ introduced in Ref. [43], we denote the spin components of vertices in the following way:

$$\Gamma_{dc} = \Gamma_{dc|dc}, \quad \Gamma_{\hat{d}c} = \Gamma_{dc|cd}, \quad \Gamma_{dd} = \Gamma_{dd|dd}. \quad \text{(F1)}$$

The other components Γ_{cd}, $\Gamma_{\hat{c}d}$ and Γ_{cc} are obtained by exchanging $c \leftrightarrow d$. The corresponding diagrams are illustrated in Fig. 18. In contrast to Hubbard-like models obeying SU(2) spin symmetry, Γ_{dd} cannot be retrieved from Γ_{dc} and $\Gamma_{\hat{d}c}$. Moreover, due to the advanced property of the d propagator, closed loops of dashed d lines are suppressed, so Γ_{cc} is negligible as it must contain closed dashed loops. In the main text, we exclusively use the component Γ_{dc} and drop the corresponding indices.
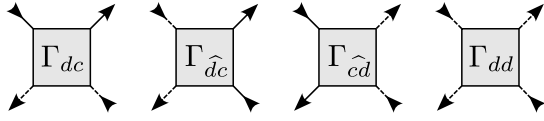
FIG. 18. Convention for the particle-type components of the full vertex Γ.

Exchanging two fermionic legs of the vertex yields an additional minus sign:

$$\Gamma_{1'2'|12} = -\Gamma_{2'1'|12} = -\Gamma_{1'2'|21} = \Gamma_{2'1'|21}. \qquad \text{(F2)}$$

An insertion of the frequencies Eqs. (C1) and spin indices Eqs. (F1) yields the so-called *crossing symmetries* [12,69]. Applying symmetries interrelates the different vertex components and heavily simplifies the numerical effort. Note that under exchange of two legs, the a and t channels are translated into each other while the p channel translates into itself.

In the main text, only bubbles including one d line G and one c line g were used [cf. Eq. (15)]. In general, however, the products of two propagators can appear in all possible combinations of particle-type indices and diagrammatic channels:

$$[\Pi^a_{ij}]_{\omega,\nu} = G^i_\nu G^j_{\nu+\omega}, \qquad \text{(F3a)}$$

$$[\Pi^p_{ij}]_{\omega,\nu} = \tfrac{1}{2} G^i_{-\nu} G^j_{\nu+\omega}, \qquad \text{(F3b)}$$

$$[\Pi^t_{ij}]_{\omega,\nu} = -G^i_\nu G^j_{\nu+\omega}. \qquad \text{(F3c)}$$

Note that in contrast to Eq. (15) in the main text, we inserted an additional factor $1/2$ in the definition of Π^p_{ij} to compensate overcounting, which appears as the additional sum over particle types in the Bethe–Salpeter equations includes both Γ_{dc} and Γ_{cd} [43]. Moreover, in the general framework, we denote $G^c_\nu = g_\nu$ and $G^d_\nu = G_\nu$.

2. Subleading-log parts of the t-reducible vertex

Here, we motivate that our expression for γ^t, Eq. (34), can be derived from the full parquet formalism [29,43] by taking into account only subleading-log diagrams. In the full parquet formalism, the dc component of the t-reducible vertex is given by [cf. Fig. 19(a)]

$$[\gamma^t_{dc}]_{\omega,\nu,\nu'} = \int_{\nu''} [\Gamma^t_{cc}]_{\omega,\nu,\nu''} [\Pi^t_{cc}]_{\omega,\nu''} [I^t_{dc}]_{\omega,\nu'',\nu'}$$

$$+ \int_{\nu''} [\Gamma^t_{dc}]_{\omega,\nu,\nu''} [\Pi^t_{dd}]_{\omega,\nu''} [I^t_{dd}]_{\omega,\nu'',\nu'}. \qquad \text{(F4)}$$

The first term does not contribute as Γ_{cc} contains closed dashed loops. According to Sec. III F, γ^t_{dc} at the most contains subleading-log terms if both the inserted vertices are leading log. Insertions of the self-energy into Π^t_{dd} and subleading contributions of the two vertices Γ_{dc} and I^t_{dd} are beyond our subleading-log scheme. Thus they are on the same footing as the higher-order totally irreducible vertices, which are anyways dropped according to the parquet approximation.

So, we focus on Γ_{dc} and I^t_{dd} in leading-log order. The irreducible vertex is given by $I^t_{dd} = \gamma^a_{dd} + \gamma^p_{dd}$. There is only one
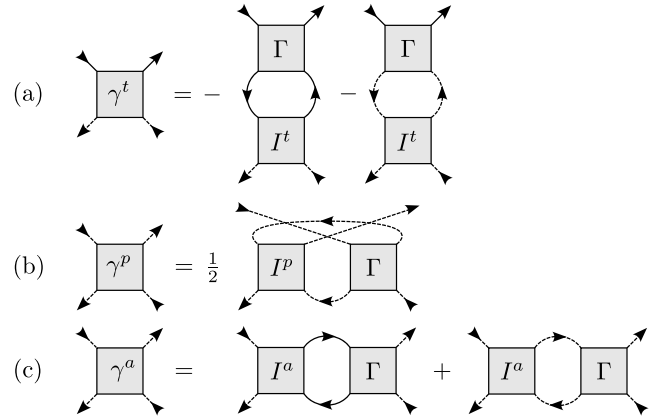
FIG. 19. Vertices appearing in the full parquet expression for the t-reducible vertex γ^t.

contribution in the p-reducible channel γ^p_{dd} [cf. Fig. 19(b)]:

$$[\gamma^p_{dd}]_{\omega,\nu,\nu'} = \int_{\nu''} [\Gamma^p_{dd}]_{\omega,\nu,\nu''} [\Pi^p_{dd}]_{\omega,\nu''} [I^p_{dd}]_{\omega,\nu'',\nu'}. \qquad \text{(F5)}$$

This eventually leads to closed dashed loops when inserted into Eq. (F4) and thus leads to a vanishing contribution. From the two contributions in the a-reducible channel γ^a_{dd} [cf. Fig. 19(c)],

$$[\gamma^a_{dd}]_{\omega,\nu,\nu'} = \int_{\nu''} [\Gamma^a_{\hat{d}c}]_{\omega,\nu,\nu''} [\Pi^a_{cc}]_{\omega,\nu''} [I^a_{\hat{c}d}]_{\omega,\nu'',\nu'}$$

$$+ \int_{\nu''} [\Gamma^a_{dd}]_{\omega,\nu,\nu''} [\Pi^a_{dd}]_{\omega,\nu''} [I^a_{dd}]_{\omega,\nu'',\nu'}, \qquad \text{(F6)}$$

the second one also leads to closed dashed loops and is therefore negligible. Hence, the remaining term includes $I^a_{\hat{d}c}$ and $\Gamma_{\hat{c}d}$. By crossing symmetry, the a-irreducible vertex is related to the t-irreducible one, i.e., $I^a_{\hat{c}d} = -I^t_{cd} = u - \gamma^a_{cd} - \gamma^p_{cd}$, which, to leading-log order coincides with the full vertex $-\Gamma_{cd}$ (there are no leading-log contributions in the transversal channel). So, only the term

$$\int_{\nu''} [\Gamma^a_{\hat{d}c}]_{\omega,\nu,\nu''} [\Pi^a_{cc}]_{\omega,\nu''} [\Gamma^a_{\hat{c}d}]_{\omega,\nu'',\nu'} \subseteq [I^t_{dd}]_{\omega,\nu,\nu'} \qquad \text{(F7)}$$

leads to the subleading logarithm of the full parquet t-reducible vertex γ^t_{dc}, Eq. (F4). Thus the remaining term in Eq. (F4) [cf. Eq. (F8)] reproduces the expression used in the main text [cf. Eq. (34)].

3. Numerical implementation of the t-reducible vertex

In the subleading-log parquet scheme, Eq. (36), the dc component of the t-reducible vertex γ^t is taken additionally, which, on the other hand, includes the dd component of the a-reducible vertex γ^a. Using the conventions introduced in Sec. F 1, the t-reducible vertex γ^t, Eq. (34), from the main text is equivalent to

$$[\gamma^t_{dc}]_{\omega,\nu,\nu'} = \int_{\nu''} [\Gamma^t_{dc}]_{\omega,\nu,\nu''} [\Pi^t_{dd}]_{\omega,\nu''} [\gamma^a_{dd}]_{\nu''-\nu',\omega+\nu',\nu'}, \qquad \text{(F8a)}$$

$$[\gamma^a_{dd}]_{\omega,v,v'} = \int_{v''} [\Gamma^a_{\hat{d}c}]_{\omega,v,v''}[\Pi^a_{cc}]_{\omega,v''}[\Gamma^a_{\hat{c}d}]_{\omega,v'',v'}, \quad \text{(F8b)}$$

$$\text{(F8c)}$$

To minimize the effort in numerical computations, the additional vertex components Γ^t_{dc}, $\Gamma^a_{\hat{d}c}$ and $\Gamma^a_{\hat{c}d}$ are expressed in terms of Γ^t_{dc} and Γ^a_{dc} by using the crossing symmetries, Eqs. (F2). Explicitly we have

$$[\Gamma^t_{dc}]_{\omega,v,v'} = -u + [\gamma^t_{dc}]_{\omega,v,v'} + [\gamma^a_{dc}]_{v-v',\omega+v',v'}$$
$$+ [\gamma^p_{dc}]_{\omega+v+v',-\omega-v',-v'}, \quad \text{(F9a)}$$

$$[\Gamma^a_{\hat{d}c}]_{\omega,v,v'} = -[\Gamma^a_{dc}]_{v'-v,v,v+\omega}$$
$$= u - [\gamma^a_{dc}]_{v'-v,v,v+\omega} - [\gamma^p_{dc}]_{\omega+v+v',-v,-v-\omega}$$
$$- [\gamma^t_{dc}]_{-\omega,v',v+\omega}, \quad \text{(F9b)}$$

$$[\Gamma^a_{\hat{c}d}]_{\omega,v,v'} = -[\Gamma^a_{dc}]_{v-v',v'+\omega,v'}$$
$$= u - [\gamma^a_{dc}]_{v-v',v'+\omega,v'} - [\gamma^p_{dc}]_{\omega+v+v',-v'-\omega,-v'}$$
$$- [\gamma^t_{dc}]_{\omega,v,v'}. \quad \text{(F9c)}$$

Note that for the first-order contribution we have $\Gamma^{(1)}_{dc} = -u = -\Gamma^{(1)}_{\hat{d}c} = -\Gamma^{(1)}_{\hat{c}d}$. By inserting Eqs. (F9) into Eqs. (F8), we receive the equations given in the main text, were everything is expressed in the dc component. For clarity, let us elaborate the derivation. In a first step, Eqs. (F9b) and (F9c) are inserted into Eq. (F8b):

$$[\gamma^a_{dd}]_{\omega,v,v'} = \int_{v''} [\Gamma^a_{dc}]_{v''-v,v,v+\omega}[\Pi^a_{cc}]_{\omega,v''}[\Gamma^a_{dc}]_{v''-v',v'+\omega,v'}, \quad \text{(F10)}$$

which is then inserted into Eq. (F8a):

$$[\gamma^t_{dc}]_{\omega,v,v'}$$
$$= \int_{v_1,v_2} [\Gamma^t_{dc}]_{\omega,v,v_1}[\Pi^t_{dd}]_{\omega,v_1}[\Gamma^a_{dc}]_{v_2-\omega-v',\omega+v',v+v_1-v'}$$
$$\times [\Pi^a_{cc}]_{v_1-v',v_2}[\Gamma^a_{dc}]_{v_2-v',v_1,v'}. \quad \text{(F11)}$$

Inserting the bubbles, Eqs. (F3), and dropping the dc indices gives Eq. (34).

In our code, we save the three vertices Γ^t_{dc}, Γ^a_{dc} and $\Gamma^a_{\hat{d}c}$ (minus their constant first-order contributions, i.e., $\tilde{\Gamma} = \Gamma - \Gamma^{(1)}$) on three-dimensional frequency grids.

To calculate γ^a_{dd}, Eq. (F8b), we subdivide the equation into contributions of different asymptotic classes [31,43], i.e., $\gamma^a_{dd} = [\mathcal{K}^a_1]^{dd} + [\mathcal{K}^a_{2'}]^{dd} + [\mathcal{K}^a_2]^{dd} + [\mathcal{K}^a_3]^{dd}$, which are

given by

$$[\mathcal{K}^a_1]^{dd}_\omega = \Gamma^{(1)}_{\hat{d}c} \int_{v''} [\Pi^a_{cc}]_{\omega,v''} \Gamma^{(1)}_{\hat{c}d}, \quad \text{(F12a)}$$

$$[\mathcal{K}^a_{2'}]^{dd}_{\omega,v'} = \int_{v''} \Gamma^{(1)}_{\hat{d}c}[\Pi^a_{cc}]_{\omega,v''}[\tilde{\Gamma}^a_{\hat{c}d}]_{\omega,v'',v'}, \quad \text{(F12b)}$$

$$[\mathcal{K}^a_2]^{dd}_{\omega,v} = \int_{v''} [\tilde{\Gamma}^a_{\hat{d}c}]_{\omega,v,v''}[\Pi^a_{cc}]_{\omega,v''} \Gamma^{(1)}_{\hat{c}d}, \quad \text{(F12c)}$$

$$[\mathcal{K}^a_3]^{dd}_{\omega,v,v'} = \int_{v''} [\tilde{\Gamma}^a_{\hat{d}c}]_{\omega,v,v''}[\Pi^a_{cc}]_{\omega,v''}[\tilde{\Gamma}^a_{\hat{c}d}]_{\omega,v'',v'}. \quad \text{(F12d)}$$

Also the numerical result for γ^t_{dc}, Eq. (34), is subdivided into asymptotic classes $\gamma^t_{dc} = [\mathcal{K}^t_{2'}]^{dc} + [\mathcal{K}^t_3]^{dc}$, which are given by

$$[\mathcal{K}^t_{2'}]^{dc}_{\omega,v'} = \int_{v''} \Gamma^{(1)}_{dc}[\Pi^t_{cc}]_{\omega,v''}[\gamma^a_{dd}]_{v''-v',v'+\omega,v'}$$

$$\text{(F13a)}$$

$$[\mathcal{K}^t_3]^{dc}_{\omega,v,v'} = \int_{v''} [\tilde{\Gamma}^t_{dc}]_{\omega,v,v''}[\Pi^t_{dd}]_{\omega,v''}[\gamma^a_{dd}]_{v''-v',v'+\omega,v'}$$

$$\text{(F13b)}$$

APPENDIX G: DETAILS ON THE NUMERICAL IMPLEMENTATION

The self-consistent schemes presented in Sec. IV A are implemented using the recently developed Julia library `MatsubaraFunctions.jl` [49]. To efficiently handle the frequency dependence, the two-particle reducible vertices γ^r are parametrized in single-boson exchange vertices [32–43]:

$$\gamma^r_{\omega,v,v'} = \bar{\lambda}^r_{\omega,v} \eta^r_\omega \lambda^r_{\omega,v'} + u + M^r_{\omega,v,v'}. \quad \text{(G1)}$$

(Note that the bare vertex is defined with an additional minus sign, i.e., $\Gamma^{(1)} = -u$.) Here the U-reducible contribution is a product of one bosonic propagator η^r_ω and two Hedin vertices $\bar{\lambda}^r_{\omega,v}$ and $\lambda^r_{\omega,v'}$ coupling fermionic degrees of freedom with exchange bosons. The remaining term is incorporated in the multi-boson vertex $M^r_{\omega,v,v'}$.

The parquet equations (30) and (36) are then solved in terms of the single-boson vertices using the following set of self-consistent equations (cf. Eqs. (41) in Ref. [43]):

$$P^r_\omega = \int_{v''} \lambda^r_{\omega,v''} \Pi^r_{\omega,v''}, \quad \text{(G2a)}$$

$$\eta^r_\omega = -u - uP^r_\omega \eta^r_\omega, \quad \text{(G2b)}$$

$$\bar{\lambda}^r_{\omega,\nu} = 1 + \int_{\nu''} T^r_{\omega,\nu,\nu''} \Pi^r_{\omega,\nu''}, \tag{G2c}$$

$$\lambda^r_{\omega,\nu'} = 1 + \int_{\nu''} \Pi^r_{\omega,\nu''} T^r_{\omega,\nu'',\nu'}, \tag{G2d}$$

$$T^r_{\omega,\nu,\nu'} = \Gamma^r_{\omega,\nu,\nu'} - \bar{\lambda}^r_{\omega,\nu} \eta^r_\omega \lambda^r_{\omega,\nu'}, \tag{G2e}$$

$$M^r_{\omega,\nu,\nu'} = \int_{\nu''} \left(T^r_{\omega,\nu,\nu''} - M^r_{\omega,\nu,\nu''} \right) \Pi^r_{\omega,\nu''} T^r_{\omega,\nu'',\nu'}$$

$$= \int_{\nu''} T^r_{\omega,\nu,\nu''} \Pi^r_{\omega,\nu''} \left(T^r_{\omega,\nu'',\nu'} - M^r_{\omega,\nu'',\nu'} \right). \tag{G2f}$$

Here, the polarization P^r is the bosonic self-energy. T^r represent the U-irreducible vertices in a respective channel. In practice, we use a symmetrized form of the two expressions for the multi-boson vertex, Eq. (G2f). We solve Eqs. (G2) self-consistently by using the Anderson acceleration method, which leads to a faster convergence involving adaptive mixing of prior solutions.

The susceptibility, Eq. (14), is directly obtained from the bosonic propagator,

$$\chi(\omega) = \frac{1}{u^2} \left(\eta^a_\omega + u \right). \tag{G3}$$

Using $-u - u \int_{\nu''} \Pi^r_{\omega,\nu''} \Gamma^r_{\omega,\nu'',\nu'} = \eta^r_\omega \lambda^r_{\omega,\nu'}$ (cf. Eq. (42b) in Refs. [43,70]), the Schwinger–Dyson equation (32) represented in single-boson exchange vertices yields

$$\Sigma_\nu = - \int_{\nu''} \eta^a_{\nu''-\nu} \lambda^a_{\nu''-\nu,\nu''} g_{\nu''}$$

$$= - \int_{\nu''} \eta^p_{-\nu''-\nu} \left(2\lambda^p_{-\nu''-\nu,-\nu''} - 1 \right) g_{\nu''}. \tag{G4}$$

Here, the Hartree term $\Sigma_H = u \int_\nu g_\nu e^{i\nu 0^+}$ is implicitly added.

We save the objects P^r_ω, η^r_ω, Σ_ν on one-dimensional frequency grids, $\bar{\lambda}^r_{\omega,\nu}$, $\lambda^r_{\omega,\nu'}$, $[\mathcal{K}^t_{2'}]^{dc}_{\omega,\nu'}$ on two-dimensional frequency grids and $M^r_{\omega,\nu,\nu'}$, $[\mathcal{K}^t_3]^{dc}_{\omega,\nu,\nu'}$ on three-dimensional frequency grids. In doing so, we ensure that the largest frequencies of the three-dimensional quantities exceed the bandwidth $\nu_{max} \simeq 1.5 \, \xi_0$. The frequency boxes corresponding to the lower-dimensional vertices are taken much larger. To represent the high-frequency asymptotics of the one-dimensional quantities P^r_ω and η^r_ω in a more sophisticated way, we approximate the Matsubara summation over bubbles outside the frequency box by an integral over the bare bubble:

$$\frac{1}{\beta} \sum_{\nu''} \Pi^r_{\omega,\nu''} \approx \frac{1}{\beta} \sum_{|\nu''| \leqslant \nu_{max}} \Pi^r_{\omega,\nu''} + \beta \int_{|\nu''| > \nu_{max}} \frac{d\nu''}{2\pi} [\Pi^r]^{(0)}_{\omega,\nu''}. \tag{G5}$$

Figures 20 and 21 show exemplary numerical results for vertex functions obtained from the subleading parquet scheme, Eqs. (32)–(36).

APPENDIX H: ANALYTICAL CONTINUATION

To test how well the minimal pole representation for analytical continuation [50,51] predicts the power-law behaviors,
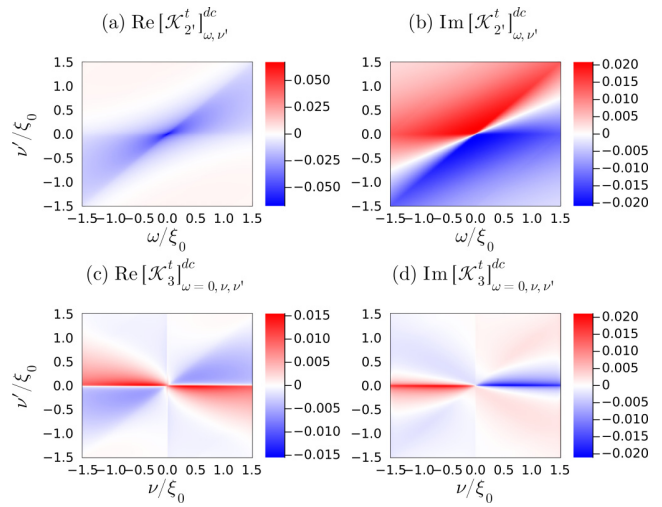
FIG. 20. Frequency dependence of the t-reducible vertices $[\mathcal{K}^t_{2'}]^{dc}$ and $[\mathcal{K}^t_3]^{dc}$, Eqs. (F13). These are obtained for $T/\xi_0 = 0.002$, $\xi_d/\xi_0 = -0.01$, and $u = 0.28$ from the subleading parquet scheme, Eqs. (32)–(36).

we start from the exact power law, Eq. (10a),

$$\chi(z) = \frac{1}{\alpha} \left[1 - \left(\frac{z - \omega_0}{-\xi_0} \right)^{-\alpha} \right], \tag{H1}$$

continued to complex variables z. The power law for $\chi(z)$ is an approximation near the threshold and does not decay to zero for $|z| \to \infty$. Nevertheless, after subtracting the offset $1/\alpha$, we find a spectral representation. By separating the power law into real and complex parts,

$$(-x - i0^+)^{-\alpha} = |x|^{-\alpha} e^{-i\alpha \arctan 2(-x, -0^+)}$$

$$= |x|^{-\alpha} [\Theta(-x) + \Theta(x) e^{i\pi\alpha}], \tag{H2}$$
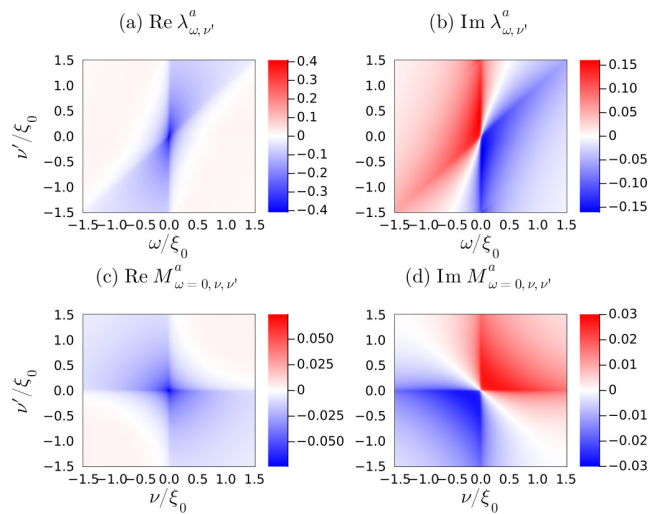
FIG. 21. Frequency dependence of the a-reducible Hedin vertex $\lambda^a_{\omega,\nu'}$ and the multi-boson vertex $M^a_{\omega,\nu,\nu'}$, Eqs. (G2), obtained for $T/\xi_0 = 0.002$, $\xi_d/\xi_0 = -0.01$, and $u = 0.28$ from the subleading parquet scheme, Eqs. (32)–(36).

with $x = (\omega - \omega_0)/\xi_0$, the spectral function $A(\omega) = -\text{Im}\,\chi(\omega + i0^+)/\pi$ yields

$$A(\omega) = \frac{\sin \pi \alpha}{\pi \alpha} \Theta(\omega - \omega_0) \left(\frac{\omega - \omega_0}{\xi_0} \right)^{-\alpha}. \qquad (H3)$$

In the Matsubara formalism, this gives

$$\chi(i\omega) - \frac{1}{\alpha} = \int_{-\infty}^{\infty} d\omega' \frac{A(\omega')}{i\omega - \omega'} = -\frac{1}{\alpha} \left(\frac{i\omega - \omega_0}{-\xi_0} \right)^{-\alpha}. \quad (H4)$$

The expression in imaginary frequencies is thus identical to a simple transformation $z \to i\omega$ in Eq. (H1).

We generated imaginary-frequency data including different levels of artificial noise. This test showed that data at a temperature $T/\xi_0 \simeq 0.002$ and with relative error 10^{-4} are sufficient to reproduce the exact power when only taking a few Matsubara frequencies, i.e., the lowest 50. From this procedure, we can be confident about the validity of the analytically continued data presented in the main text (cf. Fig. 11).

The power-law exponent is extracted from the slope of the log-log plot in Fig. 11(b). For $\omega > \omega_0$, we have

$$\frac{d}{d\ln(\omega - \omega_0)} \ln[-\text{Im}\,\chi(\omega + i0^+)]$$

$$= \frac{\omega - \omega_0}{\text{Im}\,\chi(\omega + i0^+)} \text{Im} \frac{d}{d\omega} \chi(\omega + i0^+). \qquad (H5)$$

Inserting the analytical power law, Eq. (H1), gives exactly $-\alpha$. For the logarithmic derivative of our numerical data, we use the minimal pole expansion,

$$\frac{d}{dz} \chi(z) = \frac{d}{dz} \sum_i \frac{A_i}{z - x_i} = \sum_i \frac{-A_i}{(z - x_i)^2}, \qquad (H6)$$

defined in Refs. [50,51].

[1] I. T. Diatlov, V. V. Sudakov, and K. A. Ter-Martirosian, Asymptotic meson-meson scattering theory, Sov. Phys. JETP **5**, (1957).

[2] A. A. Abrikosov, Electron scattering on magnetic impurities in metals and anomalous resistivity effects, Phys. Phys. Fiz. **2**, 5 (1965).

[3] Y. A. Bychkov, L. P. Gor'kov, and I. E. Dzyaloshinskiǐ, Possibility of superconductivity type phenomena in a one-dimensional system, Sov. Phys. JETP **23**, 489 (1966).

[4] P. W. Anderson, A poor man's derivation of scaling laws for the Kondo problem, J. Phys. C **3**, 2436 (1970).

[5] B. Roulet, J. Gavoret, and P. Nozières, Singularities in the x-ray absorption and emission of metals. I. First-order parquet calculation, Phys. Rev. **178**, 1072 (1969).

[6] P. Nozières, J. Gavoret, and B. Roulet, Singularities in the x-ray absorption and emission of metals. II. Self-consistent treatment of divergences, Phys. Rev. **178**, 1084 (1969).

[7] T. Schäfer, N. Wentzell, F. Šimkovic, Y.-Y. He, C. Hille, M. Klett, C. J. Eckhardt, B. Arzhang, V. Harkov, F.-M. Le Régent, A. Kirsch, Y. Wang, A. J. Kim, E. Kozik, E. A. Stepanov, A. Kauch, S. Andergassen, P. Hansmann, D. Rohe, Y. M. Vilk *et al.*, Tracking the footprints of spin fluctuations: A multi-method, multimessenger study of the two-dimensional Hubbard model, Phys. Rev. X **11**, 011058 (2021).

[8] M. Qin, T. Schäfer, S. Andergassen, P. Corboz, and E. Gull, The Hubbard model: A computational perspective, Annu. Rev. Condens. Matter Phys. **13**, 275 (2022).

[9] N. E. Bickers and S. R. White, Conserving approximations for strongly fluctuating electron systems. II. Numerical results and parquet extension, Phys. Rev. B **43**, 8044 (1991).

[10] N. E. Bickers and D. J. Scalapino, Critical behavior of electronic parquet solutions, Phys. Rev. B **46**, 8050 (1992).

[11] C.-X. Chen and N. Bickers, Numerical solution of parquet equations for the Anderson impurity model, Solid State Commun. **82**, 311 (1992).

[12] N. E. Bickers, Self-consistent many-body theory for condensed matter systems, edited by D. Sénéchal, A.-M Tremblay, C. Bourbonnais in *Theoretical Methods for Strongly Correlated Electrons*, CRM Series in Mathematical Physics (Springer, New York, 2004).

[13] K. Held, A. A. Katanin, and A. Toschi, Dynamical vertex approximation: An introduction, Prog. Theor. Phys. Suppl. **176**, 117 (2008).

[14] K.-M. Tam, H. Fotso, S.-X. Yang, T.-W. Lee, J. Moreno, J. Ramanujam, and M. Jarrell, Solving the parquet equations for the Hubbard model beyond weak coupling, Phys. Rev. E **87**, 013311 (2013).

[15] A. Valli, T. Schäfer, P. Thunström, G. Rohringer, S. Andergassen, G. Sangiovanni, K. Held, and A. Toschi, Dynamical vertex approximation in its parquet implementation: Application to Hubbard nanorings, Phys. Rev. B **91**, 115115 (2015).

[16] G. Li, N. Wentzell, P. Pudleiner, P. Thunström, and K. Held, Efficient implementation of the parquet equations: Role of the reducible vertex function and its kernel approximation, Phys. Rev. B **93**, 165103 (2016).

[17] G. Li, A. Kauch, P. Pudleiner, and K. Held, The victory project v1.0: An efficient parquet equations solver, Comput. Phys. Commun. **241**, 146 (2019).

[18] A. Kauch, P. Pudleiner, K. Astleithner, P. Thunström, T. Ribic, and K. Held, Generic optical excitations of correlated systems: π-tons, Phys. Rev. Lett. **124**, 047401 (2020).

[19] G. V. Astretsov, G. Rohringer, and A. N. Rubtsov, Dual parquet scheme for the two-dimensional Hubbard model: Modeling low-energy physics of high-T_c cuprates with high momentum resolution, Phys. Rev. B **101**, 075109 (2020).

[20] C. J. Eckhardt, C. Honerkamp, K. Held, and A. Kauch, Truncated unity parquet solver, Phys. Rev. B **101**, 155104 (2020).

[21] P. Lange, C. Drukier, A. Sharma, and P. Kopietz, Summing parquet diagrams using the functional renormalization group: X-ray problem revisited, J. Phys. A: Math. Theor. **48**, 395001 (2015).

[22] F. B. Kugler and J. Von Delft, Fermi-edge singularity and the functional renormalization group, J. Phys.: Condens. Matter **30**, 195501 (2018).

[23] F. B. Kugler and J. von Delft, Multiloop functional renormalization group that sums up all parquet diagrams, Phys. Rev. Lett. **120**, 057403 (2018).

[24] J. Diekmann and S. G. Jakobs, Parquet approximation and one-loop renormalization group: Equivalence on the leading-logarithmic level, Phys. Rev. B **103**, 155156 (2021).

[25] J. Diekmann and S. G. Jakobs, Leading-logarithmic approximation by one-loop renormalization group within Matsubara formalism, Phys. Rev. B **109**, 115134 (2024).

[26] P. Nozières and C. De Dominicis, Singularities in the x-ray absorption and emission of metals. III. One-body theory exact solution, Phys. Rev. **178**, 1097 (1969).

[27] K. D. Schotte and U. Schotte, Threshold behavior of the x-ray spectra of light metals, Phys. Rev. **185**, 509 (1969).

[28] F. B. Kugler and J. von Delft, Multiloop functional renormalization group for general models, Phys. Rev. B **97**, 035162 (2018).

[29] F. B. Kugler and J. von Delft, Derivation of exact flow equations from the self-consistent parquet relations, New J. Phys. **20**, 123029 (2018).

[30] P. W. Anderson, Infrared catastrophe in Fermi gases with local scattering potentials, Phys. Rev. Lett. **18**, 1049 (1967).

[31] N. Wentzell, G. Li, A. Tagliavini, C. Taranto, G. Rohringer, K. Held, A. Toschi, and S. Andergassen, High-frequency asymptotics of the vertex function: Diagrammatic parametrization and algorithmic implementation, Phys. Rev. B **102**, 085106 (2020).

[32] F. Krien, A. Valli, and M. Capone, Single-boson exchange decomposition of the vertex function, Phys. Rev. B **100**, 155149 (2019).

[33] F. Krien, Efficient evaluation of the polarization function in dynamical mean-field theory, Phys. Rev. B **99**, 235106 (2019).

[34] F. Krien and A. Valli, Parquetlike equations for the Hedin three-leg vertex, Phys. Rev. B **100**, 245147 (2019).

[35] F. Krien, A. I. Lichtenstein, and G. Rohringer, Fluctuation diagnostic of the nodal/antinodal dichotomy in the Hubbard model at weak coupling: A parquet dual fermion approach, Phys. Rev. B **102**, 235133 (2020).

[36] F. Krien, A. Valli, P. Chalupa, M. Capone, A. I. Lichtenstein, and A. Toschi, Boson-exchange parquet solver for dual fermions, Phys. Rev. B **102**, 195131 (2020).

[37] F. Krien, A. Kauch, and K. Held, Tiling with triangles: parquet and $GW\gamma$ methods unified, Phys. Rev. Res. **3**, 013149 (2021).

[38] V. Harkov, A. I. Lichtenstein, and F. Krien, Parametrizations of local vertex corrections from weak to strong coupling: Importance of the Hedin three-leg vertex, Phys. Rev. B **104**, 125141 (2021).

[39] V. Harkov, M. Vandelli, S. Brener, A. I. Lichtenstein, and E. A. Stepanov, Impact of partially bosonized collective fluctuations on electronic degrees of freedom, Phys. Rev. B **103**, 245123 (2021).

[40] F. Krien and A. Kauch, The plain and simple parquet approximation: single-and multi-boson exchange in the two-dimensional Hubbard model, Eur. Phys. J. B **95**, 69 (2022).

[41] P. M. Bonetti, A. Toschi, C. Hille, S. Andergassen, and D. Vilardi, Single-boson exchange representation of the functional renormalization group for strongly interacting many-electron systems, Phys. Rev. Res. **4**, 013034 (2022).

[42] K. Fraboulet, S. Heinzelmann, P. M. Bonetti, A. Al-Eryani, D. Vilardi, A. Toschi, and S. Andergassen, Single-boson exchange functional renormalization group application to the two-dimensional Hubbard model at weak coupling, Eur. Phys. J. B **95**, 202 (2022).

[43] M. Gievers, E. Walter, A. Ge, J. v. Delft, and F. B. Kugler, Multiloop flow equations for single-boson exchange fRG, Eur. Phys. J. B **95**, 108 (2022).

[44] G. D. Mahan, Excitons in metals: Infinite hole mass, Phys. Rev. **163**, 612 (1967).

[45] P. Nozières, The effect of recoil on edge singularities, J. Phys. I **4**, 1275 (1994).

[46] L. S. Levitov, H. Lee, and G. B. Lesovik, Electron counting statistics and coherent states of electric current, J. Math. Phys. **37**, 4845 (1996).

[47] I. Klich, An elementary derivation of Levitov's formula, in *Quantum Noise in Mesoscopic Physics*, edited by Y. V. Nazarov (Springer Netherlands, Dordrecht, 2003), pp. 397–402.

[48] R. Schmidt, M. Knap, D. A. Ivanov, J.-S. You, M. Cetina, and E. Demler, Universal many-body response of heavy impurities coupled to a Fermi sea: a review of recent progress, Rep. Prog. Phys. **81**, 024401 (2018).

[49] D. Kiese, A. Ge, N. Ritz, J. von Delft, and N. Wentzell, Matsubarafunctions.jl: An equilibrium Green's function library in the Julia programming language, SciPost Physics Codebases 24 (2024).

[50] L. Zhang and E. Gull, Minimal pole representation and controlled analytic continuation of Matsubara response functions, Phys. Rev. B **110**, 035154 (2024).

[51] L. Zhang, Y. Yu, and E. Gull, Minimal pole representation and analytic continuation of matrix-valued correlation functions, Phys. Rev. B **110**, 235131 (2024).

[52] M. Knap, A. Shashi, Y. Nishida, A. Imambekov, D. A. Abanin, and E. Demler, Time-dependent impurity in ultracold fermions: Orthogonality catastrophe and beyond, Phys. Rev. X **2**, 041020 (2012).

[53] M. Gievers, M. Wagner, and R. Schmidt, Probing polaron clouds by Rydberg atom spectroscopy, Phys. Rev. Lett. **132**, 053401 (2024).

[54] H. Shinaoka, D. Geffroy, M. Wallerberger, J. Otsuki, K. Yoshimi, E. Gull, and J. Kuneš, Sparse sampling and tensor network representation of two-particle Green's functions, SciPost Phys. **8**, 012 (2020).

[55] M. Wallerberger, H. Shinaoka, and A. Kauch, Solving the Bethe-Salpeter equation with exponential convergence, Phys. Rev. Res. **3**, 033168 (2021).

[56] J. Kaye, K. Chen, and O. Parcollet, Discrete Lehmann representation of imaginary time Green's functions, Phys. Rev. B **105**, 235115 (2022).

[57] D. Kiese, H. U. R. Strand, K. Chen, N. Wentzell, O. Parcollet, and J. Kaye, Discrete Lehmann representation of three-point functions, Phys. Rev. B **111**, 035135 (2025).

[58] M. K. Ritter, Y. Núñez Fernández, M. Wallerberger, J. von Delft, H. Shinaoka, and X. Waintal, Quantics tensor cross interpolation for high-resolution parsimonious representations of multivariate functions, Phys. Rev. Lett. **132**, 056501 (2024).

[59] Y. N. Fernández, M. K. Ritter, M. Jeannin, J.-W. Li, T. Kloss, T. Louvet, S. Terasaki, O. Parcollet, J. von Delft, H. Shinaoka, and X. Waintal, Learning tensor networks with tensor cross interpolation: new algorithms and libraries, arXiv:2407.02454.

[60] S. Rohshap, M. K. Ritter, H. Shinaoka, J. von Delft, M. Wallerberger, and A. Kauch, Two-particle calculations

with quantics tensor trains–solving the parquet equations, arXiv:2410.22975.

[61] F. B. Kugler, S.-S. B. Lee, and J. von Delft, Multipoint correlation functions: Spectral representation and numerical evaluation, Phys. Rev. X **11**, 041006 (2021).

[62] S.-S. B. Lee, F. B. Kugler, and J. von Delft, Computing local multipoint correlators using the numerical renormalization group, Phys. Rev. X **11**, 041007 (2021).

[63] J.-M. Lihm, J. Halbinger, J. Shim, J. von Delft, F. B. Kugler, and S.-S. B. Lee, Symmetric improved estimators for multipoint vertex functions, Phys. Rev. B **109**, 125138 (2024).

[64] A. Ge, N. Ritz, E. Walter, S. Aguirre, J. von Delft, and F. B. Kugler, Real-frequency quantum field theory applied to the single-impurity Anderson model, Phys. Rev. B **109**, 115128 (2024).

[65] N. Ritz, A. Ge, E. Walter, S. Aguirre, J. von Delft, and F. B. Kugler, KeldyshQFT: A C_{++} codebase for real-frequency multiloop functional renormalization group and parquet computations of the single-impurity Anderson model, J. Chem. Phys. **161**, 054118 (2024).

[66] P. Kopietz, L. Bartosch, L. Costa, A. Isidori, and A. Ferraz, Ward identities for the Anderson impurity model: derivation via functional methods and the exact renormalization group, J. Phys. A: Math. Theor. **43**, 385004 (2010).

[67] F. Krien, Conserving dynamical mean-field approaches to strongly correlated systems, Ph.D. thesis, Universität Hamburg 2018.

[68] N. Ritz, A. Ge, M. Pelz, J. von Delft, and F. B. Kugler, Numerical fulfillment of the $U(1)$ Ward identity and the parquet equations for real-frequency correlation functions from the multipoint numerical renormalization group (unpublished).

[69] G. Rohringer, New routes towards a theoretical treatment of nonlocal electronic correlations, Ph.D. thesis, TU Wien 2013.

[70] M. Patricolo, M. Gievers, K. Fraboulet, A. Al-Eryani, S. Heinzelmann, P. M. Bonetti, A. Toschi, D. Vilardi, and S. Andergassen, Single-boson exchange formulation of the Schwinger-Dyson equation and its application to the functional renormalization group, arXiv:2411.11661.

5.2. Logarithmic divergences in the fRG

In this section, we briefly elucidate how the Fermi-edge singularity in X-ray absorption spectra can be investigated by the fRG and how this analysis initiated the development of the multiloop fRG. As discussed in the last section, Nozières and his coworkers showed that a parquet summation of a- and p-reducible diagrams (so-called *first-order parquet solution*) yields the power law of the particle-hole susceptibility to leading-logarithmic accuracy [NGR69, ND69]. They use the following approximations:

1. The local Green's function $G^c(\nu)$, Eq. (5.2), of the conduction electrons is approximated by its sharp form $G^c(\nu) \simeq -i\pi \, \text{sgn}(\nu)\Theta(\xi_0 - |\nu|)$ (cf. Eq. (8) in Ref. [P3]). Hence, only energies close to the threshold frequency $|\xi_d|$ are treated correctly.

2. The t-reducible vertices γ_t are not considered and the totally two-particle irreducible vertex R is given by the parquet approximation, i.e., $R = U$.

3. Self-energy effects Σ^d are not taken into account, thus a renormalization of the threshold frequency is prevented $\omega_0 \to -\xi_d$.

4. When integrating the Bethe–Salpeter equations, the irreducible vertices I_r are equipped with a single frequency dependence $I_r(\omega, \nu, \nu') \simeq I_r(\max[\nu, \nu'])$[2]. In particular, the leading-logarithmic behaviors of integrals stem from the parts where the integration frequency of the outermost bubble is smaller than integration frequencies of the inner bubbles.

This technique provides an approximate solution of the Bethe–Salpeter equations where the power-law exponent corresponding to the Fermi-edge singularity $\alpha_\chi \simeq 2u + \mathcal{O}(u^2)$ is accurate up to linear order in the interaction u (cf. paragraph below Eqs. (10) in Ref. [P3]).

In 2015, Lange and coworkers used an fRG approach including Hubbard–Stratonovich fields to calculate the particle-hole susceptibility χ^{dc} of the model [LDSK15]. In their analysis, they obtained the leading-logarithmic power law exponent $\alpha_\chi = 2u$, however their positive results can be attributed to a "fortuitous cancellation of diagrams" (cf. Sec. 6 in Ref. [KD18a]). The one-loop fRG approach contains effects from all parquet diagrams, but only parts of their total derivatives are taken into account. Consequently, an integration of these flow equations cannot provide the parquet diagrams as a whole. This was pointed out by Fabian Kugler and Jan von Delft in the context of the Fermi-edge singularity [KD18a] who then developed the multiloop fRG approach yielding the full summation of parquet diagrams [KD18b, KD18c, KD18d].

However, it turned out that Nozières' analysis indeed can be completely carried out in a one-loop fRG scheme. Diekmann and Jakobs showed that employing a specific sharp regulator in fRG is equivalent to the mentioned steps by Nozières for integrating out

---

[2]Where $I_r(\nu)$ is a short-hand notation for $I_r(\nu, \nu, \nu)$ [NGR69, ND69].
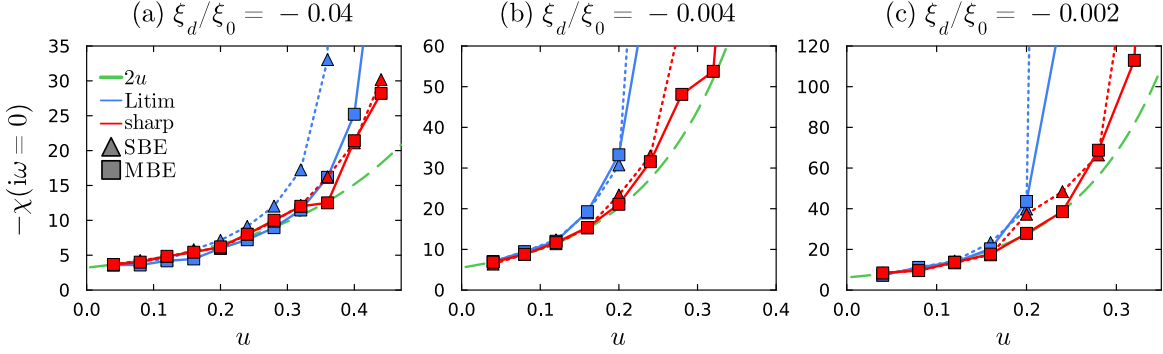
Figure 5.1.: Particle-hole susceptibility at zero Matsubara frequency $-\chi(i\omega = 0)$ at $T/\xi_0 = 0.002$ in dependence on the interaction u for different regulators and values of ξ_d/ξ_0 (similar to Fig. 10 in Ref. [P3]) using the sharp local Green's function g^{sh}. We show fRG data obtained with the Litim regulator, Eq. (5.4b), (blue) and the sharp regulator, Eq. (5.4a), (red) including MBE diagrams (squares, solid lines) and in the SBE approximation (triangles, dotted lines) and compare them to the leading-log power law with exponent $\alpha_\chi = 2u$ (dashed green line).

dominant parts of individual diagrams and finally exactly yields the logarithmic-leading power law [DJ21, DJ24]. In particular, due to Nozières' step 4, the leading-logarithmic behavior is already obtained when the outermost bubble is differentiated, which exactly corresponds to one-loop fRG diagrams. Thus, in this context, the dominant behavior of parquet diagrams can be already extracted by a one-loop fRG analysis and the multiloop extension is not necessary to obtain the leading-logarithmic power law. Still, for general applications, only the multiloop extension is equivalent to the full parquet solution and the one-loop fRG suffers from the notorious regulator dependence.

Equipped with a one-loop fRG code (see Sec. 4.2.2), we compute data for the Fermi-edge singularity presented in Fig. 5.1. As in Refs. [KD18a, KD18c], we use a sharp regulator and a Litim regulator [Lit01]:

$$\text{sharp}: \quad G_{0,\Lambda}^d(\nu) = \Theta_T(|\nu| - \Lambda)G_0^d(\nu), \qquad S_\Lambda^d(\nu) = -\delta_T(|\nu| - \Lambda)G^d(\nu), \qquad (5.4a)$$

$$\text{Litim}: \quad G_{0,\Lambda}^d(\nu) = \frac{1}{i\,\text{sgn}(\nu)\max(|\nu|, \Lambda) - \xi_d}, \quad S_\Lambda^d(\nu) = \frac{-i\,\text{sgn}(\nu)\Theta(\Lambda - |\nu|)}{[i\,\text{sgn}(\nu)\Lambda - \xi_d - \Sigma^d(\Lambda,\nu)]^2}. \qquad (5.4b)$$

While for finite temperature the Matsubara frequencies only take discrete values ν, the scale parameter Λ is defined as a continuous variable. To respect this in the sharp regulator, we use a temperature-dependent Heaviside function and delta function defined

as

$$
\Theta_T(\nu) = \begin{cases} 1 & \text{for } \nu > \pi T \\ 0 & \text{for } \nu \le -\pi T \\ [1 + \nu/(\pi T)]/2 & \text{else} \end{cases}, \quad \delta_T(\nu) = \begin{cases} 1/(2\pi T) & \text{for } -\pi T < \nu \le \pi T \\ 0 & \text{else} \end{cases}.
$$

(5.5)

The cutoff dependence, Eqs. (5.4), is only implemented in the Green's function G^d of the core electron. For the Green's function G^c of the local conduction electrons, we use the approximate sharp form $G^c(\nu) \simeq g_\nu^{\mathrm{sh}} = -\mathrm{i}\pi\,\mathrm{sgn}(\nu)\Theta(\xi_0 - |\nu|)$ (cf. Eq. (8) in Ref. [P3]) as we are only interested how close the fRG results are to the leading-log power law.

From the data shown in Fig. 5.1, we draw the following conclusions: First of all, fRG data obtained with the sharp regulator (red) seem to fit much better to the analytic leading-log behavior (dashed green) than fRG data obtained with the Litim regulator (blue). While parquet data tend to bend down for large interactions u, especially those obtained with the sharp Green's function g^{sh} (cf. purple dots in Fig. 10 of Ref. [P3]), fRG data exceed the values of the analytic leading-log behavior. In particular, the results obtained with the sharp regulator are close to the leading-log behavior, which confirms the analysis by Diekmann and Jakobs [DJ21, DJ24]. So the specific treatment of the sharp regulator is capable to extract exactly those terms from individual diagrams that characterize the leading-log behavior while parquet data in general add up the total frequency dependence, which in general excels the leading-log power law. In Sec. V. of Ref. [DJ24], it is exemplified that the leading-log behavior is reproduced exceptionally well if the sharp regulator is a function of $\mathrm{i}\nu - \xi_d$, which is not respected in our investigations [cf. Eq. (5.4a)]. Still, this explains why our fRG data from the sharp regulator are improved for smaller values of ξ_d [cf. Fig. 5.1(c)].

Another interesting observation is that fRG results excluding MBE diagrams (triangles), known as SBE approximation, are not that far off from the fRG results including MBE diagrams (squares). In our parquet analysis in Sec. 5.1, we showed that MBE diagrams are essential to reproduce the leading-log behavior of the Fermi-edge singularity. This was underlined by our numerical parquet data, which were far off when using the SBE approximation (cf. Fig. 10 in Ref. [P3]). Surprisingly, fRG results using the SBE approximation are improved compared to their parquet counterparts. We attribute this observation to the fact that the SBE approximation in our one-loop fRG scheme is made *after* the introduction of the regulator dependence, i.e., $\dot{M} = 0$ and $M = 0$ are performed at the end. So we do not use the fRG equations discussed in Sec. 3.4 of Ref. [P1], which were derived by setting $M = 0$ *before* the introduction of the flow parameter. This is in accordance to the discussion in App. A of Ref. [FHB$^+$22], where fRG results of the SBE approximation after the introduction of the flow parameter are much better than those obtained by requiring the SBE approximation before.

Finally, oscillations in the results presented in Fig. 5.1 indicate that the fRG data are less controlled than the corresponding parquet data (cf. respective plots in Ref. [P3]).

On the other hand, we receive converged results for higher values of the interaction u. So the fRG usually always gives us some results, however, their validity is not guaranteed.

To conclude, our analysis shows that the one-loop fRG may give meaningful results when using regulators that include relevant physical behavior. The SBE approximation in fRG approaches seems to be less harmful than in the parquet context. In general, however, one-loop fRG suffers from the regulator dependence inherited by the truncation of the six-point vertex. The parquet formalism, which does not dependent on artificial regulator schemes remains a valid alternative.

5.3. Connection to Fermi polarons

As discussed in Sec. 2.1.3, the most commonly used theoretical tool for the description of the Fermi polaron problem is the Chevy ansatz, Eq. (2.14) [Che06]. As it includes only a few particle-hole excitations, there, the Fermi sea is mostly left unaffected. In the limit of a static attractive impurity inserted in a Fermi sea, however, Anderson's orthogonality catastrophe applies [And67]. Here, the overlap between the non-interacting Fermi sea $|\text{FS}\rangle$ and the Fermi gas in the presence of the attractive impurity $|\text{pol}\rangle$, to use the notation from Ref. [P2], fulfills the power law $\langle \text{FS}|\text{pol}\rangle \sim N^{-\alpha_G}$, where $\alpha_G = (\delta/\pi)^2$ is the characteristic power-law exponent, introduced in Ref. [P3], and N is the number of particles in the Fermi sea. As N is macroscopic and $\alpha_G > 0$, this overlap vanishes so the addition of the impurity has a tremendous effect on the Fermi gas. Anderson's orthogonality catastrophe affects the whole Fermi sea and thus cannot be reproduced in the Chevy ansatz.

It has not yet been understood profoundly how the orthogonality catastrophe changes when the impurity is mobile. Field-theoretical approaches such as the parquet formalism, in principle, are capable of describing both the effect of a mobile impurity and a dramatically changed Fermi sea. This is a major motivation for our precise analysis of power-law exponents and logarithmic behavior in the parquet formalism. By now, we have only included the case of a static impurity in our parquet analysis, which is exactly solvable by the FDA. In this small section, we make clear that the metallic system discussed in the previous sections is equivalent to the static Fermi polaron in a cold atomic gas.

Both systems involve a non-interacting Fermi gas, either that of conduction electrons or that of majority atoms. The occupation of the core electron $|1\rangle$ in the Fermi-edge singularity model, Eq. (5.1), is equivalent to the non-interacting impurity atom $|0\rangle$ in a cold atomic gas, Eq. (2.16). Conversely, the hole in the core band $|0\rangle$ induces a local attractive interaction to the conduction electrons, which is equivalent to an inserted attractive impurity atom $|1\rangle$ in the cold atomic gas. The major difference between the two models is that for the metallic system the conduction band has a finite bandwidth and the density of states is viewed as constant $\rho(\varepsilon) = \text{const.}$ while the atomic Fermi sea is unbound to highly energetic excitations and features the usual three-dimensional density of states scaling as $\rho(\varepsilon) \sim \sqrt{\varepsilon}$. In the following, we show the tiny adaptions needed in

our code (cf. Sec. 4.2) to describe static polarons in a three-dimensional cold atomic gas using the parquet formalism.

In the Fermi polaron problem, the total density of the majority particles n_c is a characteristic quantity. In the field-theoretical description, it is related to a momentum sum over the corresponding Green's functions [cf. Eq. (4.59)]:

$$
n_c = \frac{1}{V} \sum_{\mathbf{k}} \langle \hat{c}_{\mathbf{k}}^\dagger \hat{c}_{\mathbf{k}} \rangle \simeq \int_{\mathbf{k}} \langle \bar{c}_{\mathbf{k}}(\tau = 0^+) c_{\mathbf{k}}(\tau = 0) \rangle = \frac{1}{\beta} \sum_{\nu} \int_{\mathbf{k}} \frac{\mathrm{e}^{\mathrm{i}0^+\nu}}{\mathrm{i}\nu - \varepsilon_{\mathbf{k}} - \mu_c}
$$
$$
= \frac{4\pi}{(2\pi)^3} \int_0^\infty \mathrm{d}k\, k^2 n_{\mathrm{F}}(\tfrac{k^2}{2m_c} - \mu_c). \tag{5.6}
$$

Here, we used the finite time step between the fields coming from the path integral [AS10] and expressed the momentum sum by an integral. The final expression is valid for a three-dimensional system with quadratic dispersion relation. At zero temperature, this yields $n_c(T = 0) = (2m_c\mu_c)^{3/2}/(6\pi^2)$.

The momentum integral in Eq. (5.6) turns out to be divergent if carried out first such that the introduction of an ultraviolet cutoff scale k_0 becomes crucial. Consequently, the local Green's function G^c of an atomic Fermi gas [cf. Eq. (5.2)] also depends on that cutoff scale:

$$
G^c(\nu) = \int_{|\mathbf{k}| < k_0} \frac{\mathrm{e}^{\mathrm{i}0^+\nu}}{\mathrm{i}\nu - \varepsilon_{\mathbf{k}} + \mu} = \frac{\mathrm{e}^{\mathrm{i}0^+\nu}}{2\pi^2} \int_0^{k_0} \mathrm{d}k\, \frac{2m_c k^2}{2m_c(\mu_c + \mathrm{i}\nu) - k^2}
$$
$$
= \frac{m_c}{\pi^2} \mathrm{e}^{\mathrm{i}0^+\nu} \left[-k_0 + \sqrt{2m_c(\mu_c + \mathrm{i}\nu)} \, \mathrm{atanh}\left(\frac{k_0}{\sqrt{2m_c(\mu_c + \mathrm{i}\nu)}} \right) \right]. \tag{5.7}
$$

Still, the Green's functions fulfills the typical asymptotic behavior $G^c(\nu) \overset{\nu \to \pm\infty}{\Longrightarrow} k_0^3/(6\pi^2 \mathrm{i}\nu)$, which depends on the cutoff scale as well. The momentum cutoff k_0 has to be chosen in such a way that the Matsubara sum over Eq. (5.7) yields the correct density value n_c, Eq. (5.6). By use of contour integrals, one can indeed verify that

$$
n_c = \frac{1}{\beta} \sum_{\nu} G^c(\nu) = \frac{1}{2\pi^2} \int_0^{k_0} \mathrm{d}k\, k^2 n_{\mathrm{F}}(\tfrac{k^2}{2m_c} - \mu_c), \tag{5.8}
$$

which is a good approximation as long as k_0 exceeds the energy of thermally occupied states above μ_c.

Our numerical code we described in Sec. 4.2 also offers the option to use Eq. (5.7) as an input for the bare Green's function for the parquet and fRG solver instead of Eq. (4.62c) used in our paper [P3]. From this, we can analyze how the assumption of a constant density of states and a finite bandwidth ξ_0 used in the Fermi-edge singularity model, Eq. (5.1), changes the actual properties of Fermi polarons from heavy impurities, which were briefly presented in Sec. 2.2. We leave this for future diagrammatic investigations.

6. Outlook: Fermi polarons from mobile impurities

> *"The Road goes ever on and on*
> *Down from the door where it began.*
> *Now far ahead the Road has gone,*
> *And I must follow, if I can."*
> *J. R. R. Tolkien – The Lord of the Rings*

We are equipped with a field-theoretical formalism to describe strongly correlated fermions through effective bosonic interactions. Our code computes vertex functions for models with two different particle types in the finite-temperature Matsubara formalism. Now we come back to the physics of Fermi polarons. One essential ingredient is missing so far, namely the momentum dependence of the impurity. The ultimate goal would be a full momentum-dependent description of Fermi polarons with self-consistency on the two-particle level. Due to the immense numerical effort needed for this, we cannot provide this here, but we will give some conceptional thoughts toward it.

In previous fRG studies of the Fermi polaron problem [SE11, Sch13, Mil24, MS24], the following action was used [cf. the Hamiltonian, Eq. (2.13)]:

$$S = -\int_{\boldsymbol{k},\nu} \bar{c}_{\boldsymbol{k}}(\nu)[G_0^c]^{-1}(\nu,\boldsymbol{k})c_{\boldsymbol{k}}(\nu) - \int_{\boldsymbol{k},\nu} \bar{d}_{\boldsymbol{k}}(\nu)[G_0^d]^{-1}(\nu,\boldsymbol{k})d_{\boldsymbol{k}}(\nu) - \int_{\boldsymbol{q},\omega} \bar{\phi}_{\boldsymbol{q}}(\omega)[G_0^\phi]^{-1}(\omega,\boldsymbol{q})\phi_{\boldsymbol{q}}(\omega)$$

$$- h \int_{\boldsymbol{q},\boldsymbol{k},\omega,\nu} \left[\bar{c}_{\boldsymbol{q}+\boldsymbol{k}}(\omega+\nu)\bar{d}_{\boldsymbol{q}-\boldsymbol{k}}(\omega-\nu)\phi_{\boldsymbol{q}}(\omega) + \bar{\phi}_{\boldsymbol{q}}(\omega)d_{\boldsymbol{q}-\boldsymbol{k}}(\omega-\nu)c_{\boldsymbol{q}+\boldsymbol{k}}(\omega+\nu) \right]. \quad (6.1)$$

This is a special case for the Hubbard–Stratonovich action, Eq. (3.19), with a single bosonic pairing field ϕ, describing the molecule formation of the two fermionic fields c and d. The Yukawa coupling h is considered to be real valued and constant. Here, the Matsubara frequencies ω, ν are continuous variables as the system is considered at zero temperature. The mentioned one-loop fRG studies made use of an additional constraint: The renormalization of three-point and higher vertices were completely omitted so only the self-energy flow was taken into account.

The one-loop fRG equations used in these works can be simply derived from the Schwinger–Dyson equations (3.25) by replacing the full Yukawa coupling h_ϕ with the bare one $h_{\phi,0}$ (here just the scalar parameter h) and taking the derivative with respect to a cutoff scale Λ. Additionally, on the right-hand side only single-scale propagators $S = \partial_\Lambda|_{\dot{\Sigma}=0} G$ are included. This procedure yields

$$\dot{\Sigma}^\phi(q) = h^2 \int_{k''} \partial_\Lambda|_{\dot{\Sigma}=0} \left[G^d(k'') G^c(q-k'') \right] \quad = \quad \text{⟨⟨} \dot{\Sigma}^\phi \text{⟩⟩} \quad = \quad \text{⟨⟨⟩⟩} , \quad (6.2a)$$

$$\dot{\Sigma}^d(k) = -h^2 \int_q \partial_\Lambda|_{\dot{\Sigma}=0} \left[G^\phi(q) G^c(q-k) \right] \quad = \quad \text{⟨} \dot{\Sigma}^d \text{⟩} \quad = \quad - \text{⟨⟩} . \quad (6.2b)$$

The propagator lines of the pairing field ϕ are represented by wiggly lines as in Sec. 3.2 while the propagator lines of the d particle are represented by dashed lines and those of the c particle by solid lines as in Chapters 4 and 5. The frequency and momentum dependence is combined by the four-vectors $k = (\nu, \boldsymbol{k})$ and $q = (\omega, \boldsymbol{q})$. The mentioned works directly give Eqs. (6.2) in terms of the inverse Green's functions $G^{-1} = G_0^{-1} - \Sigma$ (cf. Fig. 1 and Eq. (8) in Ref. [SE11])[1].

The overall strategy to solve the flow equations (6.2) is given by the following steps [SE11, Sch13, Mil24, MS24]: A sharp momentum regulator is implemented such that from the three-dimensional momentum integral $\int_{\boldsymbol{k}}$ only one integral over the polar angle remains. The remaining two integrals over this angle and the frequency are performed using cubic splines. The initial ultraviolet value Λ_i of the fRG flow is determined by the two-body scattering problem (cf. Sec. 2.1.2) and the flow equations are solved by a standard Runge–Kutta algorithm. Finally, the renormalized Green's functions at the end of the flow, i.e., at Λ_f, are analytically continued to real frequencies leading to the spectral functions $A^i = -\mathrm{Im}\, G^i/\pi$ using the Padé approximation. Here, the fermionic spectral functions A^c and A^d provide information on the polaron spectrum whereas the bosonic spectral function A^ϕ gives properties of the molaron branch. More recently, it was shown that for this specific problem the analytical continuation can also be performed exactly in the integrand because of the specific pole structure of the Green's functions involved in Eqs. (6.2) [MS24]. Such an analysis was also possible in a self-consistent computation for the balanced case of a two-component Fermi mixture [DHP24]. It has to be mentioned that these strategies of analytical continuation are possible because only functions of a single frequency are taken into account in the considered vertex truncation. For a general analytical continuation of vertex functions, a more elaborate method has been developed recently [GHL$^+$24].

It was shown that the results of the flow equations (6.2) strongly depend on the

---

[1]References [SE11, Sch13, Mil24, MS24] define $P(\Lambda) = G^{-1}(\Lambda) - R(\Lambda)$ as the inverse Green's function subtracted by an additive regulator $R(\Lambda)$. As the regulator dependence on the inverse bare Green's function is given by $G_0^{-1}(\Lambda) = G_0^{-1} + R(\Lambda)$, the derivative of the self-energy is directly related to the differentiated form of $P(\Lambda)$: $\dot{\Sigma}(\Lambda) = \partial_\Lambda[G_0^{-1}(\Lambda) - G^{-1}(\Lambda)] = -\partial_\Lambda[G^{-1}(\Lambda) - R(\Lambda)] = -\dot{P}(\Lambda)$. Do not confuse $P(\Lambda)$ with the bosonic self-energy or polarization P_r from the SBE formalism.

regulator [PSSW17]. This does not come as a surprise since the truncation used is crude and restricts the validity of the results. Our generalization of the SBE formalism provides a framework to compute properties of the Fermi polaron problem in a broader way. Without explicitly introducing the Hubbard–Stratonovich action, Eq. (6.1), bosonic features like that of the molecular pairing field ϕ can be computed in a purely fermionic theory. Moreover, the multiloop flow equations of SBE vertices, discussed in Sec. 3.3, offer the opportunity to calculate bosonic propagators overcoming the regulator dependence from earlier works.

As a numerical computation including the full momentum and frequency dependencies of four-point vertices is out of reach at the moment, the problem needs to be approached step by step:

1. Only the bosonic propagator η_p of the p channel is taken into account, the fermionic Green's functions G are not renormalized. This corresponds to the non-self-consistent T-matrix approach.

2. The fermionic self-energy Σ is included, which renormalizes the fermionic Green's function G. This framework is equivalent to the self-consistent T-matrix approach [PDZ09, HL24] and to the previous fRG studies [SE11, Sch13, Mil24, MS24].

3. The other diagrammatic channels a and t are taken into account such that all vertices, which depend on a single frequency and momentum, are considered. This is equivalent to the GW method [AG98].

4. To renormalize three-point interactions, the Hedin vertices $\bar{\lambda}_r$ and λ_r are included, which yields the SBE approximation [P1, BTH$^+$22, FHB$^+$22].

5. MBE vertices M_r are included, which yields the parquet approximation [P3, Bic04].

6. Contributions from the two-particle irreducible vertex R are taken into account from other methods such as the FDA or the dynamical mean-field theory (DMFT) [GKKR96, KV04].

For a static polaron (excluding the momentum dependence), we have implemented a finite-temperature parquet and fRG solver including MBE vertices, which was discussed extensively in Chapters 4 and 5. Thus, for this specific case, we have already reached step 5. For a mobile impurity (including the momentum dependence), on the other hand, we have only realized step 1 sufficiently. For this, we use a `C++` implementation within the zero-temperature Matsubara formalism. In contrast to the previous fRG studies of the Fermi polaron problem, which reached step 2, we do not rely on analytical expressions for certain regulators, but allow for a full numerical integration of the included quantities. By this, we gain flexibility, but at the same time significantly increase the numerical effort needed.
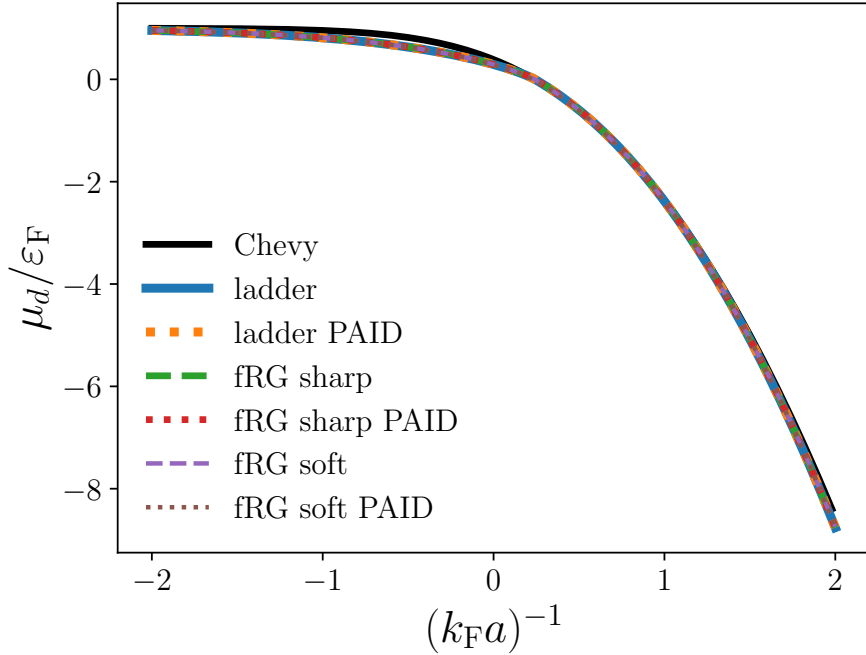
Figure 6.1.: Comparing data for the binding energy of the molecule in the Fermi polaron problem. The black line results from the variational wavefunction method known as Chevy ansatz, Eq. (2.15). The colorful dashed and dotted lines correspond to the non-self-consistent T-matrix approach, which is realized in the SBE framework when only the bosonic propagator η_p without self-energies and other vertices is included. Here, "ladder" refers to the simple ladder summation, Eq. (6.4a), and "fRG" to the solution of the respective flow equation, Eq. (6.4b), using the "sharp" and "soft" frequency regulators, Eqs. (6.3). The momentum integral of the bubble is either computed exactly (no marking) [cf. App. B.3] or by the PAID algorithm [LWP+17].

For our `C++` implementation, we use functionalities of the more general Keldysh multi-loop fRG code [RGW+24] and compute the numerical integrals by the parallel adaptive integration in higher dimensions (PAID) [LWP+17]. Hereby, we use several multiplicative frequency regulators:

$$R_{\text{sharp}}^{\Lambda}(\nu) = \Theta(|\nu| - \Lambda), \quad \dot{R}_{\text{sharp}}^{\Lambda}(\nu) = -\delta(|\nu| - \Lambda), \tag{6.3a}$$

$$R_{\text{soft}}^{\Lambda}(\nu) = \frac{\nu^2}{\nu^2 + \Lambda^2}, \qquad \dot{R}_{\text{soft}}^{\Lambda}(\nu) = -\frac{2\nu^2\Lambda}{(\nu^2 + \Lambda^2)^2}. \tag{6.3b}$$

Figure 6.1 shows our results for the binding energy using step 1 (colorful lines). To be

explicit, we take the limit $\bar{\lambda}_p = \mathbf{1}_p = \lambda_p$ in the SBE and flow equation of η_p,

$$\eta_p = U + U \circ \Pi_p \circ \eta_p \Rightarrow \eta_p^{dc}(q) = -g - g\,\eta_p^{dc}(q) \int_{k''} G^d(-k'')G^c(k''+q), \qquad (6.4\text{a})$$

$$\dot{\eta}_p = \eta_p \circ \dot{\Pi}_p \circ \eta_p \qquad \Rightarrow \dot{\eta}_p^{dc}(q) = [\eta_p^{dc}(q)]^2 \int_{k''} \partial_\Lambda|_{\dot{\Sigma}=0} \left[G^d(-k'')G^c(k''+q)\right], \qquad (6.4\text{b})$$

where $U^{dc} = -g$. This formulation is equivalent to the non-self-consistent summation of the T matrix, Eq. (2.11). The chemical potential of the minority particles μ_d is increased from a highly negative value $\mu_d/\varepsilon_{\mathrm{F}} \ll 0$ (where ε_{F} corresponds to the constant chemical potential μ_c of the majority particles) until the value of the bosonic propagator η_p^{dc} at $\omega = 0$ and $\boldsymbol{q} = \mathbf{0}$ diverges, i.e., $[\eta_p^{dc}(\omega = 0, \boldsymbol{q} = \mathbf{0})]^{-1} = 0$ is fulfilled. The obtained value of μ_d corresponds to the binding energy of the molecule for the respective interaction. We use different scattering lengths a incorporated by the relation (2.12) between the bare coupling g and the momentum integral involving the ultraviolet cutoff Λ_i, i.e., the initial condition of the fRG flow. The momentum integrals $\int_{k''}$ in Eqs. (6.4) can be performed analytically independently of the values of η_p^{dc}. Details for this are provided in App. B.3. For testing our code, we use the different regulators, Eqs. (6.3), and also include a fully numerical computation of the integral using the PAID algorithm [LWP+17]. As we consider a very primitive calculation where the self-energy is not included and the flow equation (6.4b) yields a total derivative, it is clear that the fRG results presented in Fig. 6.1 lie on top of each other, i.e., they do not depend on the respective regulator. We compare our results to the binding energy obtained from the variational wavefunctions (black line), i.e., the Chevy ansatz, Eq. (2.15). We see that these results nicely fit to those from the non-self-consistent summations. Only in the regime where the chemical potential of the impurity is positive $\mu_d > 0$, the curves differ. This is attributed to the fact that for positive μ_d it is not guaranteed anymore that only a single impurity is taken into consideration. Yet, the Chevy ansatz, Eq. (2.15), heavily relies on the zero-temperature properties of a single impurity atom.

As soon as the higher-point vertices are included, the momentum integrals also affect the vertices, which brings a tremendous complication of the problem. Due to rotational symmetry of the system, the vertex functions only depend on the absolute values of the momenta and their relative angles:

$$G(\boldsymbol{k}) \quad = G(|\boldsymbol{k}|), \qquad \qquad \eta_r(\boldsymbol{q}) \qquad = \eta_r(|\boldsymbol{q}|), \qquad (6.5\text{a})$$

$$\lambda_r(\boldsymbol{q}, \boldsymbol{k}) = \lambda_r(|\boldsymbol{q}|, |\boldsymbol{k}|, \boldsymbol{q} \cdot \boldsymbol{k}), \quad M_r(\boldsymbol{q}, \boldsymbol{k}, \boldsymbol{k}') = M_r(|\boldsymbol{q}|, |\boldsymbol{k}|, |\boldsymbol{k}'|, \boldsymbol{q} \cdot \boldsymbol{k}, \boldsymbol{q} \cdot \boldsymbol{k}', \boldsymbol{k} \cdot \boldsymbol{k}'). \quad (6.5\text{b})$$

To circumvent numerical expensive three-dimensional momentum integrals, one could develop a form-factor decomposition of the vertices, Eq. (4.104), respecting the rotational symmetries of the angular-momentum operator. For mobile impurities, i.e., the Hamiltonian, Eq. (2.13), of a two-component Fermi mixture, high angular momenta are not automatically suppressed in the vertex function. This issue is elaborated in App. B.5.

The generalization of the SBE formalism, which was the main effort of this dissertation, allows us to classify and evaluate previous diagrammatic analyses of the Fermi polaron problem, i.e., different T-matrix summations and the mentioned fRG studies, in a broader way. Although on a methodological level, it offers a clear agenda on how to extend our investigations of static polarons to the more general case of mobile polarons, the huge numerical effort needed to fully include the momentum dependencies of higher-point vertices leaves it to future research. At this point, it is obscure how to optimally handle the momentum dependence numerically. To this end, compressing methods such as the quantics tensor cross interpolation [RFW+24, FRJ+24], which has already been successfully applied to the parquet solution of the Hubbard atom [RRS+24], offer a promising tool.

7. Conclusion

"My mind and my fingers have been working around me like two lost souls. [...] Ah!
Provided I don't go mad, you will find me ~~an artist~~ [a scientist]!"
Franz Liszt[1], slightly adapted

The main motivation for the research of this dissertation was to gain a more profound understanding of Fermi polarons using field-theoretical methods. The widely used Chevy ansatz of variational wavefunctions only takes into account a few particle-hole excitations of the Fermi sea and is thus limited to zero temperatures and moderate interaction strengths. A quantum field-theoretical description *per se* is valid for arbitrary densities and temperatures. Previous analyses of Fermi polarons using the one-loop functional renormalization group (fRG) neglected the renormalization and frequency dependence of three-point vertices and suffered from a strong dependence on the regulator. The recently developed multiloop extension of the fRG offers an inviting alternative as it is built on functional differential equations including total derivatives and is equivalent to the self-consistent parquet approach, which, in principle, yields more reliable quantitative results. We classified the existing fRG analyses of Fermi polarons in a broader context and defined a general agenda how to extend and improve them. Nonetheless, a numerical implementation of the multiloop fRG analysis for Fermi polarons including the full momentum dependence of the impurity atoms has proven to be extremely demanding and thus goes beyond the scope of this work. We have rather discussed and addressed questions and problems along this more general path.

The central result of this dissertation is the generalization of the single-boson exchange (SBE) formalism. Here, the four-point vertex Γ, describing general interactions between two particles, is decomposed into bosonic propagators and three-point vertices, which represent interactions between fermionic fields and different types of exchange bosons. In contrast to previous bosonization techniques and Hubbard–Stratonovich theories, the SBE approach is formulated for a purely fermionic action and bosonic degrees of freedom arise from a new classification criterion of the two-particle vertex, namely the reducibility in the bare vertex U. The SBE allows to structure the complicated frequency dependencies of vertices in a convenient way for numerical computations and thus offers an intuitive alternative to the decomposition in asymptotic classes.

---

[1]From a letter to Pierre Wolff, written on May 2nd 1832 in Paris, translated from French: "Mon esprit et mes doigts travaillent comme deux damnés [...] Ah! pourvu que je ne devienne pas fou – tu retrouveras un artiste en moi!"

The main outcomes in the context of the SBE formalism are summarized in the following. We derived multiloop flow equations for the SBE constituents and hereby found a way how bosonic propagators and three-point vertices in the Fermi polaron problem can be computed via the fRG without a dependence on the regulator. By including a regulator dependence on the bare vertex U, we set up flow equations of the SBE constituents that allow a higher flexibility in the treatment of bosonic propagators. We implemented a code to compute SBE vertices using the self-consistent SBE equations and fRG flow equations using the finite-temperature Matsubara formalism. Our achievement is that the code is valid for local interactions between two different fermionic particle types. As a constraint, the code only involves frequency dependencies of vertex functions and is consequently applicable for the Fermi polaron problem with heavy impurities (including the Fermi-edge singularity problem), the single-impurity Anderson model and the Hubbard atom. For the latter two, we allow for general fillings and a magnetic field in z direction breaking the SU(2) spin symmetry. Our exact formulas of SBE vertices for the general Hubbard atom were essential for testing our code and can be useful for future investigations of vertex divergences, which originate from the parquet decomposition of the full vertex Γ.

Our insights into the general spin structure of the SBE formalism were useful to analyze the Schwinger–Dyson equation for the self-energy in terms of the SBE vertices in the context of the two-dimensional Hubbard model. The SBE formulation of the differentiated Schwinger–Dyson equation offers a numerically less demanding alternative to the usual fRG flow equation of the self-energy, however, the existing results are not converged in terms of the momentum dependence and differ with respect to the physical channels. It is still questionable whether neglecting multi-boson exchange (MBE) vertices is useful in the context of the Hubbard model.

An important step toward a more general description of Fermi polarons is obtained by our analysis of the Fermi-edge singularity model with respect to logarithmically scaling terms. After exciting a local deep core electron to the conduction band via X-ray absorption in a metal, there remains a local hole interacting attractively with the conduction electrons. This scenario is equivalent to an attractive impurity atom immersed in a Fermi sea and thus exhibits the formation of a static Fermi polaron. The low-energy physics is governed by the power laws corresponding to the Fermi-edge singularity in the particle-hole susceptibility and Anderson's orthogonality catastrophe in the core electron's (or impurity's) Green's function. We could demonstrate that within the parquet formalism it is possible to include all leading logarithmic and next-to-leading logarithmic terms in a perturbative expansion of the interaction vertex. We classified different self-consistent summations and went beyond previous diagrammatic approaches that predicted the characteristic power laws only up to leading-logarithmic accuracy. Our analysis is essential for the evaluation and further development of diagrammatic methods. We showed that MBE vertices are needed already at the leading-logarithmic level and the parquet approximation is not sufficient for a quantitative evaluation of the power law corresponding to Anderson's orthogonality catastrophe. On the other hand, we underlined that with a suitable choice of the regulator, the one-loop fRG is able to

provide leading-logarithmic accuracy.

Anderson's orthogonality catastrophe is correctly taken into account using another, less sophisticated method, namely the functional determinant approach (FDA). This is a numerically exact method in the limit of a static impurity atom. We used the FDA to compute absorption spectra of Fermi polarons, which can be experimentally measured using radio-frequency spectroscopy. In this context, we proposed a new measurement technique by exciting the impurity to a long-range Rydberg atom. As gas atoms can form bound states located at a specific distance to the impurity, so-called ultralong-range Rydberg molecules, our technique allows for a first *in situ* measurement of the Fermi polaron's density profile. Probing correlated quantum many-body states by the use of Rydberg excitations offers a totally new branch of experiments with ultracold quantum gases. As further applications, we elucidate how this technique allows for the observation of the time-dependent formation of a polaron cloud and for probing characteristic properties of a BCS superfluid. We hope that our suggested measurement technique can be realized experimentally using ultracold atomic gases including Rydberg excitations.

As indicated in the beginning, this dissertation does not claim to provide a full field-theoretical description of Fermi polarons. We rather extended the SBE formalism to the case of two distinct particle types and pointed out the relation to the hitherto existing fRG analyses of the Fermi polaron problem. Moreover, our findings promoted fRG analyses of the two-dimensional Hubbard model using the SBE formalism. Despite their intrinsic generality, diagrammatic approaches are not a universal remedy of describing quantum many-body systems. For numerical computations in practice, significant restrictions of multi-point correlations functions have to be applied. In particular, the vertex expansion needs to be truncated to lower-point (commonly up to four-point) correlation functions and for these only a finite resolution in frequencies and momenta can be afforded numerically. In recent years, different compression techniques have been developed to save vertex data more efficiently on sparse grids. To mention a few, there is the intermediate representation (IR) [SGW+20, WSK21] and the discrete Lehmann representation (DLR) [KCP22, KSC+25], which both give a convenient treatment of imaginary frequencies in finite-temperature Matsubara formalism. Moreover there is machine learning [SMacT+22], and finally the quantics tensor cross interpolation (QTCI) [RFW+24, FRJ+24, RRS+24], which is a more versatile method using tensor networks to compress higher-dimensional functions. Still, no matter how accurate the numerical resolution of vertex functions is, truncations in diagrammatic expansions usually make the approaches perturbative in the interaction.

By contrast, there exist other numerical methods, which are exact in certain limits like FDA for a static impurity or the dynamical mean-field theory (DMFT) [GKKR96, KV04] for the calculation of local properties. As the parquet approximation alone lacks essential properties of Fermi polarons like Anderson's orthogonality catastrophe or the precise description of the bound state for positive scattering lengths, it is tempting to combine these numerically exact methods with diagrammatic approaches to gain a more extensive

description of the characteristic physical phenomena. Thus, we should follow the spirit of Anderson who once claimed that "proofs from perturbation theory [...] ignore the possibility of anomalies, which [...] cannot be consistently treated using perturbation methods alone" [And00]. In the context of the Hubbard model, these directions are realized by diagrammatic extensions of the DMFT [TKH07, RHT$^+$18] or the combination of DMFT with fRG, which is coined DMF^{2}RG [TAB$^+$14, VTM19]. We suggest that these attempts are also appealing in the context of Fermi polarons and shed new light onto Fermi mixtures in general. To overcome the huge numerical effort, one needs to apply refined vertex decompositions as given by the SBE formalism and some of the mentioned compression techniques.

A. Conventions

For some function or operator $f = f(t, \boldsymbol{r})$ depending on the time t and the position $\boldsymbol{r}$ in d dimensions, we define the Fourier transformed function or operator $f(\omega, \boldsymbol{k})$ with the frequency ω and the momentum $\boldsymbol{k}$ as follows:

$$f(t, \boldsymbol{r}) = \int_{\omega, \boldsymbol{k}} \mathrm{e}^{-\mathrm{i}\omega t + \mathrm{i}\boldsymbol{k}\boldsymbol{r}} f(\omega, \boldsymbol{k}) = \int \frac{\mathrm{d}\omega}{2\pi} \int \frac{\mathrm{d}^d \boldsymbol{k}}{(2\pi)^d} \, \mathrm{e}^{\mathrm{i}\boldsymbol{k}\boldsymbol{r} - \mathrm{i}\omega t} f(\omega, \boldsymbol{k}), \qquad (\text{A.1a})$$

$$f(\omega, \boldsymbol{k}) = \int_{t, \boldsymbol{r}} \mathrm{e}^{\mathrm{i}\omega t - \mathrm{i}\boldsymbol{k}\boldsymbol{r}} f(t, \boldsymbol{r}) = \int \mathrm{d}t \int \mathrm{d}^d \boldsymbol{r} \, \mathrm{e}^{\mathrm{i}\omega t - \mathrm{i}\boldsymbol{k}\boldsymbol{r}} f(t, \boldsymbol{r}). \qquad (\text{A.1b})$$

The short notations, $\int_{\boldsymbol{r}}$ and $\int_{\boldsymbol{k}}$, for integrals that include adequate factors of 2π is are throughout the whole dissertation. For the operator $f^\dagger(t, \boldsymbol{r})$, the Hermitian conjugate of the above identities is taken.

The Gaussian integral with N-dimensional vectors ψ, χ of Grassmann numbers ($\bar{\psi}_n$ independent from ψ_n) and an arbitrary complex matrix A yields

$$Z[\bar{\chi}, \chi] = \int \prod_{n=1}^{N} \mathrm{d}\bar{\psi}_n \mathrm{d}\psi_n \mathrm{e}^{\sum_{n,m=1}^{N} \bar{\psi}_n A_{nm} \psi_m + \sum_{n=1}^{N} \left(\bar{\psi}_n \chi_n + \bar{\chi}_n \psi_n \right)} = \det A \, \mathrm{e}^{-\sum_{n,m=1}^{N} \bar{\chi}_n (A^{-1})_{nm} \chi_m}.$$

$$(\text{A.2})$$

In quantum field theory, the vectors of Grassmann numbers are considered in the continuous limit, i.e., they are functions.

For the free expectation value $\langle \cdot \rangle_0 = \frac{1}{Z_0} \int \mathcal{D}[\bar{\psi}, \psi] \mathrm{e}^{-\bar{\psi} A \psi}$ with Grassmann-valued ψ and the integration measure $\mathcal{D}[\bar{\psi}, \psi]$, the identity $\langle \psi_1 \bar{\psi}_2 \rangle_0 = \left. \frac{\partial^2 \ln Z[\bar{\chi}, \chi]}{\partial \bar{\chi}_1 \partial \chi_2} \right|_{\chi=0} = A_{12}^{-1}$ holds. Then *Wick's theorem* [AS10] is applicable as

$$\langle \psi_{j_1} \cdots \psi_{j_n} \bar{\psi}_{i_n} \cdots \bar{\psi}_{i_1} \rangle_0 = \langle \psi_{j_1} \bar{\psi}_{i_1} \cdots \psi_{j_n} \bar{\psi}_{i_n} \rangle_0 \quad = \sum_{P \in S^n} \mathrm{sgn}(P) \langle \psi_{j_1} \bar{\psi}_{i_{P(1)}} \rangle_0 \cdots \langle \psi_{j_n} \bar{\psi}_{i_{P(n)}} \rangle_0.$$

$$(\text{A.3})$$

The summation runs over all the permutations P of the labels $1, ..., n$ and the sign of the permutations $\mathrm{sgn}(P)$ gives additional minus signs for odd permutations considering the fermionic antisymmetric properties..

We want to calculate the continuous Fourier transform

$$f(\omega) = \int_0^T \mathrm{d}t\, f(t)\mathrm{e}^{\mathrm{i}\omega t}, \tag{A.4}$$

numerically, but we only have a discrete data set $f(t_n)$ of $N+1$ points where $t_n = nT/N$ and $n \in \{0, ..., N\}$. A symmetric spectrum $\omega \in [-\Omega, \Omega]$ with $\Omega = \pi/\mathrm{d}t$ can be arranged for $\omega_k = 2\pi k/T - N\pi/T$ where $k \in \{0, ..., N\}$. The above integral can then be identified by the following sum:

$$f(\omega_k) \simeq \sum_{n=0}^{N} \frac{T}{N} f(n\tfrac{T}{N}) \mathrm{e}^{2\pi \mathrm{i} k \frac{1}{T} n \frac{T}{N}} \mathrm{e}^{-\mathrm{i}\frac{N\pi}{T} n \frac{T}{N}} = \sum_{n=0} f_n \mathrm{e}^{2\pi \mathrm{i} k n/N}, \tag{A.5}$$

where $f_n = \frac{T}{N} f(t_n) \mathrm{e}^{-\mathrm{i}n\pi}$. This discrete sum is executable by the fast Fourier-transform algorithm.

B. Details on Fermi polarons

B.1. Physical units

For the reliable prediction of experimental measurements of a polaron cloud as presented in Sec. 2.3, it is crucial to express all the quantities in the right physical dimensions. In our paper [P2], we use natural units $\hbar = k_{\mathrm{B}} = c = 1$. The remaining scales are defined through the non-interacting values of the Fermi gas, which has a Fermi energy ε_{F} and a Fermi momentum k_{F}. Thus, our reference length scale is the inverse Fermi momentum $L^* = 1/k_{\mathrm{F}}$ and we further set the mass of the gas particles to $2m^* = 1$. Properties of the Fermi polaron can be exclusively written in units of L^* whereas introducing the Rydberg potential V_{Ryd}, Eq. (2.37), requires the correct treatment of the electron mass m_e and the s-wave scattering length a_e between the gas particles and the Rydberg electron, which is typically given in terms of the Bohr radius a_0. The latter can be expressed through the density of the Fermi gas ρ_0, which is given by

$$\rho_0 = \int_{|\boldsymbol{k}| \leq k_{\mathrm{F}}} 1 = \frac{1}{(2\pi)^3} \frac{4}{3} \pi k_{\mathrm{F}}^3 = \frac{1}{6\pi^2} k_{\mathrm{F}}^3 \Rightarrow k_{\mathrm{F}} = (6\pi^2 \rho_0)^{1/3}, \tag{B.1}$$

at zero temperature. In a two-component Fermi gas, there is an additional factor of 2. Thus, the Bohr radius in terms of the length scale L^* yields

$$a_0 = a_0 (6\pi^2 \rho_0)^{1/3} L^*. \tag{B.2}$$

When using $^{40}\mathrm{K}$ atoms as gas particles, the electron mass in terms of the reference mass m^* is given by

$$m_e = \frac{m_e}{m_{\mathrm{K}}} m^* \simeq \frac{m_e}{40 m_p} m^*, \tag{B.3}$$

where m_p is the mass of a proton. When we consider $\rho_0 = 5 \times 10^{11}\,\mathrm{cm}^{-3}$, a typical density of a cold atomic gas, the Fermi energy (in units of Planck's constant) yields

$$\frac{\varepsilon_{\mathrm{F}}}{\hbar} = \frac{\hbar}{2m_{\mathrm{K}}} (6\pi^2 \rho_0)^{2/3} \simeq 7.6\,\mathrm{kHz}. \tag{B.4}$$

B.2. Generalized version of Fermi's golden rule

In this appendix, we closely follow the steps performed in Sec. 5.7 of Ref. [SN11] and extend the discussion to derive a version of Fermi's golden rule, Eq. (2.25), where the initial and final states $|i\rangle$ and $|f\rangle$ do not need to be eigenstates of the total Hamiltonian, Eq. (2.16). This is needed to get the expression (2.44) for the absorption spectrum of a Fermi polaron during its cloud formation (cf. Sec. 2.4).

We consider the Hamiltonian $\hat{H} = \hat{H}_0 + \hat{V}$ including a perturbation $\hat{V}$. In contrast to the Hamiltonian, Eq. (2.16), used in Chapter 2, $\hat{H}_0$ corresponds to the full system so we do not make a distinction between the impurity state and the Fermi gas. Here, $\hat{V}$ is viewed as a time-dependent perturbation like the laser-induced transition operator $\hat{\Omega}$, which is switched on at a specific time t_0 and appears in Fermi's golden rule, Eq. (2.25). So $\hat{V}$ should not be mistaken with the static potential caused by an impurity.

In the Schrödinger picture, the time dependence is put onto the states $i\hbar\, d_t|\psi(t)\rangle = \hat{H}|\psi(t)\rangle$ and their time evolution is given by the full Hamiltonian, i.e., $|\psi(t)\rangle = e^{-i\hat{H}t}|\psi(0)\rangle$. For an evaluation in the interaction picture (denoted by the subscript I), the Schrödinger states and operators are transformed by the bare Hamiltonian, i.e., $|\psi_I(t)\rangle = e^{i\hat{H}_0 t}|\psi(t)\rangle$ and $\hat{A}_I(t) = e^{i\hat{H}_0 t}\hat{A}e^{-i\hat{H}_0 t}$. For the more general case of a time-dependent interaction $\hat{V}(t)$, the time evolution of the states in the interaction picture is given by the modified Schrödinger equation $i\hbar\, d_t|\psi_I(t)\rangle = \hat{V}_I(t)|\psi_I(t)\rangle$, which can be rewritten in terms of the time evolution operator $\hat{U}_I(t, t_0)$ and the Dyson series:

$$i\hbar\, d_t\hat{U}_I(t, t_0) = \hat{V}_I(t)\hat{U}_I(t, t_0), \quad U_I(t_0, t_0) = \hat{\mathbb{1}} \tag{B.5a}$$

$$\Rightarrow \hat{U}_I(t, t_0) = \hat{\mathbb{1}} - \frac{i}{\hbar}\int_{t_0}^{t} dt'\, \hat{V}_I(t')\hat{U}_I(t', t_0)$$

$$= \hat{\mathbb{1}} - \frac{i}{\hbar}\int_{t_0}^{t} dt'\, \hat{V}_I(t') + \cdots$$

$$+ \left(\frac{-i}{\hbar}\right)^n \int_{t_0}^{t} dt' \int_{t_0}^{t'} dt'' \cdots \int_{t_0}^{t^{(n-1)}} dt^{(n)}\, \hat{V}_I(t')\hat{V}_I(t'') \cdots \hat{V}_I(t^{(n)}). \tag{B.5b}$$

To evaluate Fermi's golden rule in case of the time-dependent polaron cloud formation, we need to know the overlap $\langle f|i(t)\rangle$ where $|i(t)\rangle$ is a time-evolved Schrödinger state. We can write down its time evolution with respect to the interaction picture:

$$|i(t)\rangle = e^{-i\hat{H}_0 t}|i_I(t)\rangle = e^{-i\hat{H}_0 t}\hat{U}_I(t, t_0)e^{iH_0 t_0}|i(t_0)\rangle \simeq e^{-i\hat{H}_0 t}\left[\mathbb{1} - i\int_{t_0}^{t} dt'\, \hat{V}_I(t')\right]e^{iH_0 t_0}|i(t_0)\rangle. \tag{B.6}$$

Here, we wrote the time evolution operator $\hat{U}_I(t, t_0)$ in linear response of the Dyson series,

Eq. (B.5b). Assuming that $\langle f|i(t_0)\rangle = 0^{[1]}$, we can write down the overlap as

$$\langle f|i(t)\rangle = -\mathrm{i}\int_{t_0}^{t}\mathrm{d}t'\,\langle f|\mathrm{e}^{-\mathrm{i}\hat{H}_0(t-t')}\hat{V}(t')\mathrm{e}^{\mathrm{i}\hat{H}_0(t_0-t')}|i(t_0)\rangle,\tag{B.7}$$

where the operator in the interaction picture $\hat{V}_I(t')$ from Eq. (B.6) is expressed in terms of its correspondent $\hat{V}(t')$ in the Schrödinger picture.

The absorption spectrum $A(\omega)$ is given as the long time average $\omega T \gg 1$ over the perturbation potential $\hat{V}(t) = \mathrm{e}^{\mathrm{i}\omega t}\hat{\Omega}\Theta(t-t_0)$, i.e., at a time t_0 the laser-induced transition operator $\hat{\Omega} = |1\rangle\langle 0|$ is turned on:

$$A(\omega) = \lim_{T\to\infty}\frac{1}{T}\sum_f|\langle f|i(T)\rangle|^2 = \lim_{T\to\infty}\frac{1}{T}\sum_f\left|\int_{t_0}^{T}\mathrm{d}t'\,\langle f|\mathrm{e}^{-\mathrm{i}\hat{H}_0(T-t')}\mathrm{e}^{\mathrm{i}\omega t'}\hat{\Omega}\mathrm{e}^{\mathrm{i}\hat{H}_0(t_0-t')}|i(t_0)\rangle\right|^2.\tag{B.8}$$

Here we consider only one initial state $|i(t_0)\rangle$ at the beginning so the sum only considers the final state f.

In the standard derivation of Fermi's golden rule, Eq. (2.25), the initial $|i\rangle$ and final states $|f\rangle$ are eigenstates of the Hamiltonian, i.e., $\hat{H}_0|i\rangle = E_i|i\rangle$, $\hat{H}_0|f\rangle = E_f|f\rangle$. With $t_0 = 0$, Eq. (B.8) is simplified to

$$\begin{aligned}A(\omega) &= \lim_{T\to\infty}\frac{1}{T}\sum_f\left|\int_0^{T}\mathrm{d}t'\,\langle f|\mathrm{e}^{-\mathrm{i}E_f(T-t')}\mathrm{e}^{\mathrm{i}\omega t'}\hat{\Omega}\mathrm{e}^{-\mathrm{i}E_i t'}|i\rangle\right|^2\\&= \lim_{T\to\infty}\frac{1}{T}\sum_f|\langle f|\hat{\Omega}|i\rangle|^2\frac{|\mathrm{e}^{\mathrm{i}(E_f-E_i+\omega)T}-1|^2}{(E_f-E_i+\omega)^2}\\&= \lim_{T\to\infty}\frac{1}{T}\sum_f|\langle f|\hat{\Omega}|i\rangle|^2\frac{4\sin^2[(E_f-E_i+\omega)T/2]}{(E_f-E_i+\omega)^2}.\end{aligned}\tag{B.9}$$

Fermi's golden rule, Eq. (2.25), is obtained after applying the limit

$$\lim_{\varepsilon\to 0}\frac{\varepsilon}{\pi x^2}\sin^2\left(\frac{x}{\varepsilon}\right) = \delta(x).\tag{B.10}$$

Now, we consider the case where $|i(t_0)\rangle$ is not an eigenstate of the Hamiltonian anymore. This is relevant for an absorption experiment during the polaron cloud formation (cf. Sec. 2.4). The initial state is expanded in terms of the eigenfunctions of the bare

---

[1]This is the case in Chapter 2 as $|i(t_0)\rangle$ includes the impurity state $|0\rangle$, which is orthogonal to the impurity state $|1\rangle$ included in $|f\rangle$.

Hamiltonian $|i(t_0)\rangle = \sum_n |n\rangle\langle n|i(t_0)\rangle$, where $\hat{H}_0|n\rangle = E_n|n\rangle$:

$$
\begin{aligned}
A(\omega) &= \lim_{T\to\infty}\frac{1}{T}\sum_f\left|\sum_n\int_{t_0}^T dt'\langle f|e^{-i\hat{H}_0(T-t')}e^{i\omega t'}\hat{\Omega}e^{i\hat{H}_0(t_0-t')}|n\rangle\langle n|i(t_0)\rangle\right|^2 \\
&= \lim_{T\to\infty}\frac{1}{T}\sum_f\left|\sum_n\langle n|i(t_0)\rangle\langle f|\hat{\Omega}|n\rangle\int_{t_0}^T dt'\,e^{-iE_f(T-t')}e^{i\omega t'}e^{iE_n(t_0-t')}\right|^2 \\
&= \lim_{T\to\infty}\frac{1}{T}\sum_f\left|\sum_n\langle n|i(t_0)\rangle\langle f|\hat{\Omega}|n\rangle(-i)e^{iE_f(T-t_0)-\omega t_0}\frac{e^{i(E_f-E_n+\omega)(T-t_0)}-1}{E_f-E_n+\omega}\right|^2 \\
&= \lim_{T\to\infty}\frac{1}{T}\sum_{f,m,n}\langle m|i(t_0)\rangle\langle i(t_0)|n\rangle\Omega_{fm}\Omega_{nf}\frac{e^{i(E_f-E_m+\omega)(T-t_0)}-1}{E_f-E_m+\omega}\frac{e^{-i(E_f-E_n+\omega)(T-t_0)}-1}{E_f-E_n+\omega}.
\end{aligned}
$$
(B.11)

Here, we have defined $\Omega_{nm} = \langle n|\hat{\Omega}|m\rangle$.

In order to understand the above expression, we need to examine the following limit:

$$
\begin{aligned}
F &= \lim_{T\to\infty}\frac{1}{T}\frac{e^{i(\omega-E_m)T}-1}{\omega-E_m}\frac{e^{-i(\omega-E_n)T}-1}{\omega-E_n} \\
&= \lim_{T\to\infty}\frac{1}{T}e^{i(\omega-E_m)T/2}\frac{2i\sin[(\omega-E_m)T/2]}{\omega-E_m}e^{-i(\omega-E_n)T/2}\frac{-2i\sin[(\omega-E_n)T/2]}{\omega-E_n} \\
&= \lim_{T\to\infty}\frac{4}{T}e^{i(E_n-E_m)T/2}\frac{\sin[(\omega-E_m)T/2]}{\omega-E_m}\frac{\sin[(\omega-E_n)T/2]}{\omega-E_n}.
\end{aligned}
$$
(B.12)

For brevity, we have substituted $\omega+E_f$ to ω, which can easily be reserved at the end. The expression (B.12) is analyzed in some special cases:

(i) If $E_n = E_m$, we receive the original limit from Eq. (B.10):

$$
F_{E_m=E_n} = \lim_{T\to\infty}\frac{4}{T}\frac{\sin^2[(\omega-E_m)T/2]}{(\omega-E_m)^2} = 2\pi\delta(\omega-E_m).
$$
(B.13)

(ii) If $E_m \neq \omega$ and $E_n \neq \omega$, we can replace the sine factors by another representation of the delta function:

$$
\lim_{\varepsilon\to 0}\frac{1}{\pi x}\sin\left(\frac{x}{\varepsilon}\right) = \delta(x)
$$
(B.14a)

$$
\Rightarrow F_{E_n\neq\omega\neq E_m} = \lim_{T\to\infty}\frac{1}{T}e^{i(E_n-E_m)T/2}2\pi\delta(\omega-E_m)2\pi\delta(\omega-E_n) = 0.
$$
(B.14b)

Consequently for $\omega \neq E_m$ and $\omega \neq E_n$, the whole term vanishes.

(iii) If $E_n = \omega$ or $E_m = \omega$ (excluding $E_n = E_m$), we have

$$
\begin{aligned}
F_{E_m=\omega} &= \lim_{T\to\infty} 2\mathrm{e}^{\mathrm{i}(E_n-\omega)T/2}\frac{\sin[(\omega-E_n)T/2]}{\omega-E_n} = \lim_{T\to\infty}\frac{1-\mathrm{e}^{-\mathrm{i}(\omega-E_n)T}}{\mathrm{i}(\omega-E_n)} = \int_0^\infty \mathrm{d}t\,\mathrm{e}^{-\mathrm{i}(\omega-E_n)t}, \\
F_{E_n=\omega} &= \lim_{T\to\infty} 2\mathrm{e}^{\mathrm{i}(\omega-E_m)T/2}\frac{\sin[(\omega-E_m)T/2]}{\omega-E_m} = \lim_{T\to\infty}\frac{\mathrm{e}^{\mathrm{i}(\omega-E_m)T}-1}{\mathrm{i}(\omega-E_m)} = \int_0^\infty \mathrm{d}t\,\mathrm{e}^{\mathrm{i}(\omega-E_m)t}.
\end{aligned}
\tag{B.15}
$$

The last expression can be expressed as the Fourier transform of the Heaviside function:

$$
\int_{-\infty}^\infty \mathrm{d}t\,\mathrm{e}^{\mathrm{i}\omega t}\Theta(t) = \frac{\mathrm{i}}{\omega} + \pi\delta(\omega), \quad \int_{-\infty}^\infty \mathrm{d}t\,\mathrm{e}^{-\mathrm{i}\omega t}\Theta(t) = -\frac{\mathrm{i}}{\omega} + \pi\delta(\omega), \tag{B.16a}
$$

$$
\Rightarrow F_{E_m=\omega} = -\frac{\mathrm{i}}{\omega-E_n} + \pi\delta(\omega-E_n), \quad F_{E_n=\omega} = \frac{\mathrm{i}}{\omega-E_m} + \pi\delta(\omega-E_m). \tag{B.16b}
$$

To conclude, the full function of F, Eq. (B.12), is given by

$$
\begin{aligned}
F &= \delta_{E_m,E_n} 2\pi\delta(\omega-E_n) + (1-\delta_{E_m,E_n})(\delta_{E_m,\omega}+\delta_{E_n,\omega})\left(\pi\delta(E_n-E_m) + \frac{\mathrm{i}}{E_n-E_m}\right) \\
&= \delta_{E_m,E_n} 2\pi\delta(\omega-E_n) + (1-\delta_{E_m,E_n})(\delta_{E_m,\omega}+\delta_{E_n,\omega})\frac{\mathrm{i}}{E_n-E_m}.
\end{aligned}
\tag{B.17}
$$

Importantly, δ_{E_m,E_n} and $\delta_{E_n,\omega}$ are Kronecker delta symbols not delta functions so they only give a finite contribution. The absorption function $A(\omega)$, Eq. (B.11), now yields

$$
\begin{aligned}
A(\omega) &= 2\pi \sum_{f,n} |\langle f|\hat{\Omega}|n\rangle\langle n|i(t_0)\rangle|^2 \delta(\omega+E_f-E_n) \\
&+ \sum_{f,m\neq n} (\delta_{E_m,\omega+E_f}+\delta_{E_n,\omega+E_f})\frac{\mathrm{i}}{E_n-E_m}\langle m|i(t_0)\rangle\langle i(t_0)|n\rangle\Omega_{fm}\Omega_{nf},
\end{aligned}
\tag{B.18}
$$

after substituting back $\omega \to \omega + E_f$. We assume that the second term is a subleading contribution as it does not contain a delta function $\delta(\omega+E_f-E_n)$.

Let us now specify to the case of the Rydberg spectroscopy experiment with the Hamiltonian $\hat{H} = \sum_\sigma |\sigma\rangle\langle\sigma| \otimes \hat{H}_\sigma$, Eq. (2.39), having three states for the impurity, i.e., $|0\rangle$, $|1\rangle$ and $|R\rangle$. We consider the transition operator $\hat{\Omega} = (|R\rangle\langle 1| + |1\rangle\langle R|) \otimes \hat{\mathbb{1}}$ switching between the polaron state and the Rydberg excitation. The states appearing in Eq. (B.18) can be written as

$$
|i(t_0)\rangle = |1\rangle \otimes \mathrm{e}^{-\mathrm{i}\hat{H}_1 t_0}|\mathrm{FS}\rangle, \quad |f\rangle = |R\rangle \otimes |f_{\mathrm{gas}}\rangle, \quad |n\rangle = |1\rangle \otimes |n_{\mathrm{gas}}\rangle, \tag{B.19}
$$

where by assumption the latter two are eigenstates of the Hamiltonian with $\hat{H}_R|f_{\mathrm{gas}}\rangle =$

$E_f|f_{\text{gas}}\rangle$ and $\hat{H}_1|n_{\text{gas}}\rangle = E_n|n_{\text{gas}}\rangle$. We now manipulate the absorption function, Eq. (B.18), until we get some expression that can be computed by the FDA. We start by expressing the delta function by its Fourier integral and introduce an additional summation over eigenstates m, which is expressed through a Kronecker delta $\delta_{E_m,E_n} = \frac{1}{2\pi}\int_0^{2\pi} d\tau\, e^{i(E_n-E_m)\tau}$:

$$A(\omega) = \sum_{f,n} \int dt\, \langle i(t_0)|n\rangle\langle n|\hat{\Omega}|f\rangle\langle f|\hat{\Omega}|n\rangle\langle n|i(t_0)\rangle e^{i(\omega+E_n-E_f)t}$$

$$= \sum_{f,n,m} \int dt\, \langle i(t_0)|n\rangle\langle n|\hat{\Omega}|f\rangle\langle f|\hat{\Omega}|m\rangle\langle m|i(t_0)\rangle e^{i(\omega+E_n-E_f)t}\delta_{E_n,E_m}$$

$$= \sum_{f,n,m} \int dt \int d\tau\, \langle i(t_0)|n\rangle\langle n|\hat{\Omega}|f\rangle\langle f|\hat{\Omega}|m\rangle\langle m|i(t_0)\rangle e^{i(\omega+E_n-E_f)t}e^{i(E_n-E_m)\tau}. \quad \text{(B.20)}$$

Next, we insert the Hamiltonian $\hat{H}$ at the appropriate places and remove the sums due to the completeness relations of the basis states:

$$A(\omega) = \sum_{f,n,m} \int dt\, e^{i\omega t} \int d\tau\, \langle i(t_0)|n\rangle\langle n|e^{i\hat{H}(t+\tau)}\hat{\Omega}e^{-i\hat{H}t}|f\rangle\langle f|\hat{\Omega}e^{-i\hat{H}\tau}|m\rangle\langle m|i(t_0)\rangle$$

$$= \int dt\, e^{i\omega t} \int d\tau\, \langle i(t_0)|e^{i\hat{H}(t+\tau)}\hat{\Omega}e^{-i\hat{H}t}\hat{\Omega}e^{-i\hat{H}\tau}|i(t_0)\rangle. \quad \text{(B.21)}$$

We are now able to insert the states, Eqs. (B.19), and evaluate the impurity states:

$$A(\omega) = \int dt\, e^{i\omega t} \int d\tau\, \left(\langle 1|\otimes\langle\text{FS}|e^{i\hat{H}_1 t_0} \right) e^{i\hat{H}(t+\tau)}\hat{\Omega}e^{-i\hat{H}t}\hat{\Omega}e^{-i\hat{H}\tau} \left(|1\rangle\otimes e^{-i\hat{H}_1 t_0}|\text{FS}\rangle \right)$$

$$= \int dt\, e^{i\omega t} \int d\tau\, \langle\text{FS}|e^{i\hat{H}_1(t_0+t+\tau)}e^{-i\hat{H}_R t}e^{-i\hat{H}_1(\tau+t_0)}|\text{FS}\rangle.$$

In the last expression, the integrand can be expressed as a trace over the density matrix $\hat{\rho}_0 = |\text{FS}\rangle\langle\text{FS}|$, which again can be expressed as a determinant over the single-particle Hamiltonians [cf. Eq. (2.44)].

B.3. Exact momentum integral of the bare bubble

For the two-component Fermi gas, the momentum integral over the bare bubble can be executed exactly. First, we consider the bare Green's functions in position space,

$$G_0^i(\boldsymbol{r}) = \int_{\boldsymbol{k}} e^{i\boldsymbol{k}\boldsymbol{r}} G_0^i(\boldsymbol{k}) = \int_{\boldsymbol{k}} \frac{e^{i\boldsymbol{k}\boldsymbol{r}}}{i\nu - \boldsymbol{k}^2/(2m_i) + \mu_i} = -\frac{m_i}{2\pi r}e^{-|\boldsymbol{r}|/\sqrt{-1/[2m_i(i\nu+\mu_i)]}}, \quad \text{(B.22)}$$

where we made use of the fact that the quantity is rotational symmetric, i.e., the Green's functions only depend on the absolute values of the momentum and position variables

and the three-dimensional Fourier transform is reduced to a one-dimensional integral,

$$
\begin{aligned}
f(|\boldsymbol{r}|) = \int_{\boldsymbol{k}} \mathrm{e}^{\mathrm{i}\boldsymbol{k}\boldsymbol{r}} f(|\boldsymbol{k}|) &= \frac{1}{(2\pi)^2} \int_0^\infty \mathrm{d}k\, k^2 \int_1^{-1} \mathrm{d}(\cos\theta)\, \mathrm{e}^{\mathrm{i}kr\cos\theta} f(k) \\
&= \frac{1}{(2\pi)^2} \int_0^\infty \mathrm{d}k\, \frac{2k\sin kr}{r} f(k).
\end{aligned}
\tag{B.23}
$$

The convolution integral over two Green's functions can be written as a Fourier integral of the product of the Green's functions $G^i(\boldsymbol{r})$:

$$
\mathcal{B}^{ij}(\boldsymbol{q}) = \int_{\boldsymbol{k}''} G_0^i(\boldsymbol{k}'') G_0^j(\boldsymbol{k}'' + \boldsymbol{q}) = \int_{\boldsymbol{r}} \mathrm{e}^{-\mathrm{i}\boldsymbol{q}\boldsymbol{r}} G_0^i(-\boldsymbol{r}) G_0^j(\boldsymbol{r}).
\tag{B.24}
$$

Using Eq. (B.23), this is simplified to

$$
\begin{aligned}
\mathcal{B}^{ij}(\boldsymbol{q}) &= 2\pi \int_0^\infty \mathrm{d}r\, \frac{2r\sin(|\boldsymbol{q}|r)}{|\boldsymbol{q}|} G^i(r) G^j(r) \\
&= \frac{m_i m_j}{\pi |\boldsymbol{q}|} \arctan\left[\frac{|\boldsymbol{q}|}{(-(2m_i(\mu_i + \mathrm{i}\nu_i))^{-1})^{-1/2} + (-(2m_j(\mu_j + \mathrm{i}\nu_j))^{-1})^{-1/2}} \right].
\end{aligned}
\tag{B.25}
$$

This expression is used for the fRG calculations yielding the non-self-consistent T-matrix approach (cf. Fig. 6.1). In the limit $\boldsymbol{q} \to \boldsymbol{0}$, only the argument of the arctan remains due to $\lim_{q\to 0} \alpha q^{-1} \arctan(q\beta) = \alpha\beta$.

B.4. Inclusion of the scattering length in fRG

Let us derive the relation between the bare interaction g and the scattering length a [cf. Eq. (2.12)] when including a multiplicative frequency regulator, Eq. (6.3), with the cutoff scale Λ in the fRG scheme.

In the infrared range $\Lambda \to \Lambda_f$, the bosonic propagator η_p^{dc} should correspond to the T matrix, Eq. (2.11), if both chemical potentials are taken to zero $\mu_c = 0 = \mu_d$, i.e., the two-body scattering problem is considered: $[\eta_p^{dc}]_{\mu_c=0=\mu_d}^{\Lambda_f}(q) = -(2\pi)^3 T(q)$. With the s-wave scattering amplitude $f_{k,l=0}$, Eq. (2.8), and the relation $T = -2\pi/m_r f_{l=0}$, this gives the limit $[\eta_p^{dc}]_{\mu_c=0=\mu_d}^{\Lambda_f}(q \to 0) = -2\pi a/m_r$. As in the ultraviolet range $\Lambda \to \Lambda_i$, the bosonic propagator η_p^{dc} is given by the bare coupling, i.e., $[\eta_p^{dc}]_{\mu_c=0=\mu_d}^{\Lambda_i}(q \to 0) = -g$, we can set up the following integral over the scale parameter Λ:

$$
\int_{\Lambda_f}^{\Lambda_i} \mathrm{d}\Lambda\, [\dot{\eta}_p^{dc}]_{\mu_c=0=\mu_d}^{\Lambda}(q \to 0) = -g + \frac{2\pi a}{m_r}.
\tag{B.26}
$$

We now rewrite and integrate the single-channel fRG equation (6.4b) as follows:

$$-\partial_\Lambda [\eta_p^{dc}(q)]^{-1} = \frac{\dot\eta_p^{dc}(q)}{[\eta_p^{dc}(q)]^2} = \int_{\Lambda_f}^{\Lambda_i} d\Lambda \int_{k''} \partial_\Lambda [G^d(-k'')G^c(k''+q)]$$

$$\Rightarrow -\int_{\Lambda_f}^{\Lambda_i} d\Lambda \, \partial_\Lambda [\eta_p^{dc}(q)]^{-1} = \int_{k''} [G^d]^{\Lambda_i}(-k'')[G^c]^{\Lambda_i}(k''+q)$$

$$\Rightarrow \left([\eta_p^{dc}]^{\Lambda_f}(q)\right)^{-1} - \left([\eta_p^{dc}]^{\Lambda_i}(q)\right)^{-1} = \int_{k''} \Big([G^d]^{\Lambda_i}(-k'')[G^c]^{\Lambda_i}(k''+q)$$

$$- [G^d]^{\Lambda_f}(-k'')[G^c]^{\Lambda_f}(k''+q)\Big). \qquad \text{(B.27)}$$

As we consider a multiplicative regulator, i.e., $G^\Lambda = R^\Lambda G$, the momentum integral included on the right-hand side is given by the exact expression (B.25) with $\nu_d = -\nu''$ and $\nu_c = \nu'' + \omega$. In the limit of $q = 0$ and $\mu_c = 0 = \mu_d$, we can insert Eq. (B.26) such that Eq. (B.27) yields

$$-\frac{m_r}{2\pi a} + \frac{1}{g} = \int \frac{d\nu''}{2\pi} \mathcal{B}^{dc}(\boldsymbol{q} \to 0)\big|_{\nu_d=-\nu'',\nu_c=\nu''} \left[R^{\Lambda_i}(-\nu'')R^{\Lambda_i}(\nu'') - R^{\Lambda_f}(-\nu'')R^{\Lambda_f}(\nu'')\right]$$

$$= \int \frac{d\nu''}{2\pi} \frac{m_c m_d}{2^{3/2}\pi} \frac{1}{\sqrt{\mathrm{i}m_d\nu''} + \sqrt{-\mathrm{i}m_c\nu''}} \left[R^{\Lambda_i}(-\nu'')R^{\Lambda_i}(\nu'') - R^{\Lambda_f}(-\nu'')R^{\Lambda_f}(\nu'')\right].$$
$$\text{(B.28)}$$

For the sharp regulator $R_{\text{sharp}}^\Lambda(\nu) = \Theta(|\nu| - \Lambda)$, Eq. (6.3a), this yields

$$\frac{1}{g} = \frac{m_r}{2\pi a} - \frac{m_r}{\pi^2}\left(\sqrt{m_c} + \sqrt{m_d}\right)\left(\sqrt{\Lambda_i} - \sqrt{\Lambda_f}\right). \qquad \text{(B.29)}$$

Analogously, for the soft regulator $R_{\text{soft}}^\Lambda(\nu) = \nu^2/(\nu^2 + \Lambda^2)$, Eq. (6.3a), we obtain

$$\frac{1}{g} = \frac{m_r}{2\pi a} - \frac{5}{8\sqrt{2\pi}}m_r\left(\sqrt{m_c} + \sqrt{m_d}\right)\left(\sqrt{\Lambda_i} - \sqrt{\Lambda_f}\right). \qquad \text{(B.30)}$$

B.5. Angular-momentum basis

We consider the Hamiltonian, Eq. (2.13), of the two-component Fermi gas given in Sec. 2.1.3. For this we assume an infinite system size, i.e., the momentum sum $\frac{1}{V}\sum_{\boldsymbol{k}}$ is replaced by a continuous integral $\int_{\boldsymbol{k}}$. The three-dimensional space can be represented in terms of spherical harmonics $Y_{lm}(\Omega_{\boldsymbol{r}})$ and spherical Bessel functions $j_l(kr)$, which are the eigenfunctions of the angular-momentum operator [VMK88]. The angular-momentum

states $|klm\rangle$ form an orthonormal basis spanning the total Hilbert space. We have

$$\langle \boldsymbol{r}|klm\rangle = \sqrt{\frac{2}{\pi}}k j_l(kr)Y_{lm}(\Omega_{\boldsymbol{r}}), \tag{B.31a}$$

$$\langle klm|k'l'm'\rangle = \int_{\Omega_{\boldsymbol{r}}} Y_{lm}^*(\Omega_{\boldsymbol{r}})Y_{l'm'}^*(\Omega_{\boldsymbol{r}})\frac{2}{\pi}\int_0^\infty \mathrm{d}r\, r^2 kk' j_l(kr)j_{l'}(k'r)$$

$$= \delta_{ll'}\delta_{mm'}\delta(k-k'), \tag{B.31b}$$

$$\int_0^\infty \mathrm{d}k \sum_{lm}|klm\rangle\langle klm| = \int_0^\infty \mathrm{d}k\sum_{lm}\int_{\boldsymbol{r},\boldsymbol{r}'}|\boldsymbol{r}\rangle\langle \boldsymbol{r}|klm\rangle\langle klm|\boldsymbol{r}'\rangle\langle \boldsymbol{r}'|$$

$$= \int_{\boldsymbol{r},\boldsymbol{r}'}|\boldsymbol{r}\rangle\langle \boldsymbol{r}'|\frac{2}{\pi}\int_0^\infty \mathrm{d}k\, k^2\sum_{lm}j_l(kr)j_l(kr')Y_{lm}(\Omega_{\boldsymbol{r}})Y_{lm}^*(\Omega_{\boldsymbol{r}'})$$

$$= \int_{\boldsymbol{r},\boldsymbol{r}'}|\boldsymbol{r}\rangle\langle \boldsymbol{r}'|\frac{1}{r^2}\delta(r-r')\delta(\Omega_{\boldsymbol{r}}-\Omega_{\boldsymbol{r}'}) = \int_{\boldsymbol{r},\boldsymbol{r}'}|\boldsymbol{r}\rangle\langle \boldsymbol{r}'|\delta(\boldsymbol{r}-\boldsymbol{r}')$$

$$= \int_{\boldsymbol{r}}|\boldsymbol{r}\rangle\langle \boldsymbol{r}|. \tag{B.31c}$$

For the overlap between radial-momentum states $|\boldsymbol{k}\rangle$ and angular-momentum states, we consider the plane-wave expansion,

$$\langle \boldsymbol{k}|\boldsymbol{r}\rangle = \mathrm{e}^{\mathrm{i}\boldsymbol{k}\boldsymbol{r}} = 4\pi\sum_{lm}\mathrm{i}^l j_l(kr)Y_{lm}(\Omega_{\boldsymbol{k}})Y_{lm}^*(\Omega_{\boldsymbol{r}}), \tag{B.32}$$

yielding

$$\langle \boldsymbol{k}'|klm\rangle = \int_{\boldsymbol{r}}\mathrm{e}^{-\mathrm{i}\boldsymbol{k}'\boldsymbol{r}}\langle \boldsymbol{r}|klm\rangle$$

$$= 4\pi\sqrt{\frac{2}{\pi}}k\sum_{l'm'}\mathrm{i}^{-l'}Y_{l'm'}^*(\Omega_{\boldsymbol{k}'})\int_0^\infty \mathrm{d}r\, r^2 j_{l'}(k'r)j_l(kr)\int_{\Omega_{\boldsymbol{r}}}(-1)^{m'}Y_{l',-m'}^*(\Omega_{\boldsymbol{r}})Y_{lm}(\Omega_{\boldsymbol{r}})$$

$$= 4\pi\sqrt{\frac{2}{\pi}}k\mathrm{i}^{-l}Y_{l,-m}^*(\Omega_{\boldsymbol{k}'})\frac{\pi}{2}\frac{1}{k^2}\delta(k-k')(-1)^m = (2\pi)^{3/2}\mathrm{i}^{-l}Y_{lm}(\Omega_{\boldsymbol{k}'})\frac{1}{k}\delta(k-k'). \tag{B.33}$$

The orthonormality of the angular-momentum basis can be validated as follows:

$$\langle klm|k'l'm'\rangle = \int_0^\infty \mathrm{d}q\, q^2\mathrm{i}^{l-l'}\int_{\Omega_{\boldsymbol{q}}}Y_{lm}^*(\Omega_{\boldsymbol{q}})Y_{l'm'}(\Omega_{\boldsymbol{q}})\frac{1}{q^2}\delta(k-q)\delta(k'-q)$$

$$= \int_0^\infty \mathrm{d}q\,\delta(q-k)\delta(q-k')\delta_{ll'}\delta_{mm'} = \delta_{ll'}\delta_{mm'}\delta(k-k'). \tag{B.34}$$

The Hamiltonian, Eq. (2.13), can now be expressed in terms of the fermionic operators

written with respect to angular momenta,

$$c_{\boldsymbol{k}} = \int_0^\infty \mathrm{d}k' \sum_{lm} \langle \boldsymbol{k}|k'lm\rangle c_{k'lm}, \quad c_{\boldsymbol{r}} = \int_0^\infty \mathrm{d}k' \sum_{lm} \langle \boldsymbol{r}|k'lm\rangle c_{k'lm}, \qquad (\text{B.35})$$

yielding

$$
\begin{aligned}
H &= \int_0^\infty \mathrm{d}k \sum_{lm} \left[\frac{k^2}{2m_c} c_{klm}^\dagger c_{klm} + \frac{k^2}{2m_d} d_{klm}^\dagger d_{klm} \right] \\
&+ g\frac{4}{\pi^2} \int_0^\infty \mathrm{d}r\, r^2 \int_0^\infty \prod_{i=1}^4 \left[\mathrm{d}k_i\, k_i \sum_{l_i m_i} j_{l_i}(k_i r) \right] \int_{\Omega_{\boldsymbol{r}}} Y_{l_1 m_1}^*(\Omega_{\boldsymbol{r}}) Y_{l_2 m_2}^*(\Omega_{\boldsymbol{r}}) Y_{l_3 m_3}(\Omega_{\boldsymbol{r}}) Y_{l_4 m_4}(\Omega_{\boldsymbol{r}}) \\
&\times c_{k_1 l_1 m_1}^\dagger d_{k_2 l_2 m_2}^\dagger d_{k_3 l_3 m_3} c_{k_4 l_4 m_4}.
\end{aligned}
\qquad (\text{B.36})
$$

Here, both the integral over four spherical Bessel functions as well as the integral over four spherical harmonics can be solved independently. Using the identity

$$
\begin{aligned}
Y_{l_1 m_1}(\Omega) Y_{l_2 m_2}(\Omega) &= \frac{1}{\sqrt{4\pi}} \sqrt{(2l_1+1)(2l_2+1)} \\
&\times \sum_{\tilde{l},\tilde{m}} (-1)^{\tilde{m}} \sqrt{2\tilde{l}+1} \begin{pmatrix} l_1 & l_2 & \tilde{l} \\ m_1 & m_2 & -\tilde{m} \end{pmatrix} \begin{pmatrix} l_1 & l_2 & \tilde{l} \\ 0 & 0 & 0 \end{pmatrix} Y_{\tilde{l}\tilde{m}}(\Omega),
\end{aligned}
\qquad (\text{B.37})
$$

the integral over four spherical harmonics yields

$$
\begin{aligned}
&\int_{\Omega_{\boldsymbol{r}}} Y_{l_1 m_1}^*(\Omega_{\boldsymbol{r}}) Y_{l_2 m_2}^*(\Omega_{\boldsymbol{r}}) Y_{l_3 m_3}(\Omega_{\boldsymbol{r}}) Y_{l_4 m_4}(\Omega_{\boldsymbol{r}}) \\
&= \frac{1}{4\pi} \sqrt{(2l_1+1)\cdots(2l_4+1)} \sum_{\tilde{l}} (2\tilde{l}+1) \begin{pmatrix} l_1 & l_2 & \tilde{l} \\ 0 & 0 & 0 \end{pmatrix} \begin{pmatrix} l_3 & l_4 & \tilde{l} \\ 0 & 0 & 0 \end{pmatrix} \\
&\quad \times \sum_{\tilde{m}=-\tilde{l}}^{\tilde{l}} \begin{pmatrix} l_1 & l_2 & \tilde{l} \\ m_1 & m_2 & -\tilde{m} \end{pmatrix} \begin{pmatrix} l_3 & l_4 & \tilde{l} \\ m_3 & m_4 & -\tilde{m} \end{pmatrix} \\
&= \frac{1}{4\pi} \sqrt{(2l_1+1)\cdots(2l_4+1)} \delta_{m_1+m_2, m_3+m_4} \sum_{\tilde{l}} (2\tilde{l}+1) \begin{pmatrix} l_1 & l_2 & \tilde{l} \\ 0 & 0 & 0 \end{pmatrix} \begin{pmatrix} l_3 & l_4 & \tilde{l} \\ 0 & 0 & 0 \end{pmatrix} \\
&\quad \times \begin{pmatrix} l_1 & l_2 & \tilde{l} \\ m_1 & m_2 & -m_1-m_2 \end{pmatrix} \begin{pmatrix} l_3 & l_4 & \tilde{l} \\ m_3 & m_1+m_2-m_3 & -m_1-m_2 \end{pmatrix}.
\end{aligned}
\qquad (\text{B.38})
$$

Here, the sum over angular momenta is reduced to the values $\max(|l_1-l_2|,|l_3-l_4|) \le \tilde{l} \le \min(l_1+l_2, l_3+l_4)$ and even values of $l_1+l_2+\tilde{l}$ and $l_3+l_4+\tilde{l}$. In particular, the integral, Eq. (B.38), vanishes if $\max(|l_1-l_2|,|l_3-l_4|) > \min(l_1+l_2, l_3+l_4)$. This is due to the

properties of the 2j-Wigner symbols, which are related to Clebsch-Gordon coefficients by

$$
\begin{pmatrix} j_1 & j_2 & J \\ m_1 & m_2 & M \end{pmatrix} = \frac{(-1)^{j_1-j_2-m_2}}{\sqrt{2J+1}} \langle j_1, m_1; j_2, m_2 | J, -M \rangle. \tag{B.39}
$$

The integral over four spherical harmonics, Eq. (B.38), respects the conservation of angular momentum, however, it does not decay for high angular momenta. We conclude that the general Hamiltonian written in angular-momentum basis does not involve a simpler dependence for the four-point interaction vertex.

The situation is different for the case of an immobile impurity (cf. Sec. 2.2 and Chapter 5), where the Hamiltonian takes the form

$$
\hat{H} = \int_{\boldsymbol{k}} \frac{\boldsymbol{k}^2}{2m} \hat{c}_{\boldsymbol{k}}^\dagger \hat{c}_{\boldsymbol{k}} + \varepsilon_d \hat{d}^\dagger \hat{d} - U \int_{\boldsymbol{k},\boldsymbol{k}'} \hat{c}_{\boldsymbol{k}}^\dagger \hat{c}_{\boldsymbol{k}} \hat{d} \hat{d}^\dagger. \tag{B.40}
$$

Expressing the operators in the angular-momentum basis yields

$$
\hat{H} = \int_{k_1,k_2} \sum_{l_1,l_2,m_1,m_2} \int_{\boldsymbol{k}} \varepsilon_{\boldsymbol{k}} \langle k_1 l_1 m_1 | \boldsymbol{k} \rangle \langle \boldsymbol{k} | k_2 l_2 m_2 \rangle \hat{c}_{k_1 l_1 m_1}^\dagger \hat{c}_{k_2 l_2 m_2} + \varepsilon_d \hat{d}^\dagger \hat{d}
$$
$$
- U \int_{k_1,k_2} \sum_{l_1,l_2,m_1,m_2} \int_{\boldsymbol{k}} \langle k_1 l_1 m_1 | \boldsymbol{k} \rangle \int_{\boldsymbol{k}'} \langle \boldsymbol{k}' | k_2 l_2 m_2 \rangle \hat{c}_{k_1 l_1 m_1}^\dagger \hat{c}_{k_2 l_2 m_2} \hat{d} \hat{d}^\dagger. \tag{B.41}
$$

For the kinetic term, we have

$$
\int_{\boldsymbol{k}} \varepsilon_{\boldsymbol{k}} \langle k_1 l_1 m_1 | \boldsymbol{k} \rangle \langle \boldsymbol{k} | k_2 l_2 m_2 \rangle
$$
$$
= \mathrm{i}^{l_1-l_2} \int_0^\infty \mathrm{d}k \, k^2 \frac{k^2}{2m} \frac{1}{k^2} \delta(k-k_1) \delta(k-k_2) \int_{\Omega_{\boldsymbol{k}}} Y_{l_2 m_2}(\Omega_{\boldsymbol{k}}) Y_{l_1 m_1}^*(\Omega_{\boldsymbol{k}})
$$
$$
= \frac{k_1^2}{2m} \delta(k_1-k_2) \delta_{l_1 l_2} \delta_{m_1 m_2}, \tag{B.42}
$$

and for the interacting part,

$$
\int_{\boldsymbol{k}} \langle k_1 l_1 m_1 | \boldsymbol{k} \rangle = (2\pi)^{-3/2} \int_0^\infty \mathrm{d}k \, k^2 \int_{\Omega_{\boldsymbol{k}}} \mathrm{i}^{l_1} Y_{l_1 m_1}^*(\Omega_{\boldsymbol{k}}) \frac{1}{k} \delta(k_1-k) = (2\pi)^{-3/2} k_1 \sqrt{4\pi} \delta_{l_1 0} \delta_{m_1 0}
$$
$$
= \frac{1}{\sqrt{2\pi}} k_1 \delta_{l_1 0} \delta_{m_1 0}. \tag{B.43}
$$

We used $\sqrt{4\pi} Y_{00}(\Omega_{\boldsymbol{k}}) = 1$. The final expression,

$$
\hat{H} = \int_0^\infty \mathrm{d}k \sum_{l,m} \frac{k^2}{2m} \hat{c}_{klm}^\dagger \hat{c}_{klm} + \varepsilon_d \hat{d}^\dagger \hat{d} - U \int_0^\infty \mathrm{d}k \int_0^\infty \mathrm{d}k' \frac{1}{2\pi^2} \hat{c}_{k00}^\dagger \hat{c}_{k'00} \hat{d} \hat{d}^\dagger, \tag{B.44}
$$

indeed only couples to the s-wave states as all the other angular-momentum states do not interact with the immobile impurity.

C. Details on the SBE formalism

C.1. Derivation of Schwinger–Dyson equations

In this appendix, we provide more details on the derivation of the Schwinger–Dyson equations (3.25)–(3.26) for the bosonic self-energies $\Sigma_{\psi,\phi}$, Eqs. (3.22), and Yukawa couplings $\bar{h}_{\psi,\phi}, h_{\psi,\phi}$, Eqs. (3.23), within the Hubbard–Stratonovich theory presented in Sec. 3.2.

The general strategy of how Schwinger–Dyson equations are derived is explained in Sec. 6.3.3 of Ref. [KBS10]. The generating functional $\mathcal{G}[\bar{j}, j]$, Eq. (3.3), of correlation functions is independent of shifts in the fields $\bar{c} \mapsto \bar{c} + \delta\bar{c}$, $c \mapsto c + \delta c$. Thus, a linear expansion with respect to these shifts yields

$$
\mathcal{G}[\bar{j}, j] = \frac{1}{Z} \mathcal{D}[\bar{c}, c] e^{-S[\bar{c}+\delta\bar{c}, c] + (\bar{c}_{1'}+\delta\bar{c}_{1'})j_{1'} + \bar{j}_1 c_1}
$$
$$
\overset{\delta\bar{c}\to 0}{\Longrightarrow} 0 = \frac{1}{Z} \mathcal{D}[\bar{c}, c] \left(j_{2'} - \frac{\delta S}{\delta \bar{c}_{2'}} \right) e^{-S[\bar{c}, c] + \bar{c}_{1'} j_{1'} + \bar{j}_1 c_1}, \tag{C.1a}
$$
$$
\mathcal{G}[\bar{j}, j] = \frac{1}{Z} \mathcal{D}[\bar{c}, c] e^{-S[\bar{c}, c+\delta c] + \bar{c}_{1'} j_{1'} + \bar{j}_1 (c_1 + \delta c_1)}
$$
$$
\overset{\delta c\to 0}{\Longrightarrow} 0 = \frac{1}{Z} \mathcal{D}[\bar{c}, c] \left(-\bar{j}_2 - \frac{\delta S}{\delta c_2} \right) e^{-S[\bar{c}, c] + \bar{c}_{1'} j_{1'} + \bar{j}_1 c_1}. \tag{C.1b}
$$

This procedure can be straightforwardly extended to the Hubbard–Stratonovich theory $S \mapsto S_0 + S_{\mathrm{HS}}$, Eq. (3.19), with an addition of bosonic source fields $\bar{j}^{\psi}, j^{\psi}, \bar{j}^{\phi}, j^{\phi}$ and shifts in the bosonic fields $\delta\bar{\psi}, \delta\psi, \delta\bar{\phi}, \delta\phi$ [cf. Eq. (3.24)]. The minus sign before $\bar{j}_2$ in Eq. (C.1b) is dropped when $\bar{j}_2$ is replaced by a bosonic source field since exchanging the functional derivatives does not yield an additional minus sign for bosons. Relations between correlation functions, i.e., the Schwinger–Dyson equations arise by applying functional derivatives with respect to certain source fields. This naturally relates correlation functions due to the property of the generating functional $\mathcal{G}[\bar{j}, j]$, Eq. (3.3). Corresponding terms

involve the functional derivatives:

$$\frac{\delta S_{\mathrm{HS}}}{\delta \psi_3} = -\bar{\psi}_{3'}[W_{\psi,0}^{-1}]_{3'|3} - \tfrac{1}{2}[\bar{h}_{\psi,0}]_{1'23}\bar{c}_{1'}c_2, \qquad \frac{\delta S_{\mathrm{HS}}}{\delta \bar{\psi}_{3'}} = -[W_{\psi,0}^{-1}]_{3'|3}\psi_3 - \tfrac{1}{2}[h_{\psi,0}]_{3'2'1}\bar{c}_{2'}c_1,$$

$$\tag{C.2a}$$

$$\frac{\delta S_{\mathrm{HS}}}{\delta \phi_3} = -\bar{\phi}_{3'}[W_{\phi,0}^{-1}]_{3'|3} - \tfrac{1}{2}[\bar{h}_{\phi,0}]_{1'2'3}\bar{c}_{1'}\bar{c}_{2'}, \qquad \frac{\delta S_{\mathrm{HS}}}{\delta \bar{\phi}_{3'}} = -[W_{\phi,0}^{-1}]_{3'|3}\phi_3 - \tfrac{1}{2}[h_{\phi,0}]_{3'12}c_1c_2,$$

$$\tag{C.2b}$$

$$\frac{\delta S_0}{\delta c_1} = \bar{c}_{1'}[G_0^{-1}]_{1'|1}, \qquad \frac{\delta S_{\mathrm{HS}}}{\delta c_1} = \tfrac{1}{2}[\bar{h}_{\psi,0}]_{1'13}\bar{c}_{1'}\psi_3 + \tfrac{1}{2}[h_{\psi,0}]_{3'2'1}\bar{\psi}_{3'}\bar{c}_{2'} - [h_{\phi,0}]_{3'12}\bar{\phi}_{3'}c_2, \tag{C.3a}$$

$$\frac{\delta S_0}{\delta \bar{c}_{1'}} = -[G_0^{-1}]_{1'|1}c_1, \qquad \frac{S_{\mathrm{HS}}}{\delta \bar{c}_{1'}} = -\tfrac{1}{2}[\bar{h}_{\psi,0}]_{1'23}c_2\psi_3 - \tfrac{1}{2}[h_{\psi,0}]_{3'1'1}\bar{\psi}_{3'}c_1 - [\bar{h}_{\psi,0}]_{1'2'3}\bar{c}_{2'}\phi_3.$$

$$\tag{C.3b}$$

We exemplify the derivation of the Schwinger–Dyson equations for Σ_ϕ and h_ϕ. Sending $\delta\bar{\phi} \to 0$ in Eq. (C.1) and taking the derivative with respect to $j_{3'}^\phi$ yields

$$0 = \frac{1}{Z}\int \mathcal{D}[\bar{c},c]\mathcal{D}[\bar{\psi},\psi]\mathcal{D}[\bar{\phi},\phi]\left[\delta_{2'3'} + \left(j_{2'}^\phi - \frac{\delta S_{\mathrm{HS}}}{\delta\bar{\phi}_{2'}}\right)\bar{\phi}_{3'}\right]\mathrm{e}^{-S_0[\bar{c},c]-S_{\mathrm{HS}}[\bar{c},c,\bar{\psi},\psi,\bar{\phi},\phi]+\bar{\phi}_{1'}j_{1'}^\phi}$$

$$\overset{\bar{j}^\phi\to 0}{\Longrightarrow} \delta_{2'3'} = \left\langle \frac{\delta S_{\mathrm{HS}}}{\delta\bar{\phi}_{2'}}\bar{\phi}_{3'}\right\rangle = -[W_{\phi,0}^{-1}]_{2'|3}\langle\phi_3\bar{\phi}_{3'}\rangle - \tfrac{1}{2}[h_{\phi,0}]_{2'12}\langle c_1c_2\bar{\phi}_{3'}\rangle. \tag{C.4}$$

For the correlators $[W_\phi]_{3|3'} = -\langle\phi_3\bar{\phi}_{3'}\rangle$ and $\langle c_1c_2\bar{\phi}_{3'}\rangle$, we insert Eqs. (3.22) and (3.23) and multiply the expression by the inverse propagator $[W_\phi^{-1}]_{3'|4}$ to obtain

$$[W_\phi^{-1}]_{2'|4} = [W_{\phi,0}^{-1}]_{2'|4} - \tfrac{1}{2}[h_{\phi,0}]_{3'12}G_{1|1'}G_{2|3'}[\bar{h}_\phi]_{1'2'4}. \tag{C.5}$$

This expression is equivalent to the Schwinger–Dyson equation (3.25b) of Σ_ϕ.

To obtain the Schwinger–Dyson equation of h_ϕ, we take two derivatives with respect to the fermionic source fields $j_{3'}$ and $j_{4'}$ after sending $\delta\bar{\phi} \to 0$ in Eq. (C.1b):

$$0 = \frac{\delta^2}{\delta j_{4'}\delta j_{3'}}\frac{1}{Z}\int \mathcal{D}[\bar{c},c]\left(j_{2'}^\phi - \frac{\delta S_{\mathrm{HS}}}{\delta\bar{\phi}_{2'}}\right)\mathrm{e}^{-S[\bar{c},c]+\bar{\phi}_1 j_1^\phi+\bar{c}_{1'}j_{1'}}$$

$$\overset{\bar{j}^\phi,j\to 0}{\Longrightarrow} 0 = \left\langle \frac{\delta S_{\mathrm{HS}}}{\delta\bar{\phi}_{2'}}\bar{c}_{3'}\bar{c}_{4'}\right\rangle = -[W_{\phi,0}^{-1}]_{2'|3}\langle\phi_3\bar{c}_{3'}\bar{c}_{4'}\rangle - \tfrac{1}{2}[h_{\phi,0}]_{2'12}\langle c_1c_2\bar{c}_{3'}\bar{c}_{4'}\rangle. \tag{C.6}$$

Now, we insert the expressions of the tree expansions, Eq. (3.23b) for $\langle\phi_3\bar{c}_{3'}\bar{c}_{4'}\rangle$ and for $\langle c_1c_2\bar{c}_{3'}\bar{c}_{4'}\rangle$ we insert the relation from the tree expansion in the Hubbard–Stratonovich theory (cf. Eq. (6.92) in Ref. [KBS10]), which is an extension of Eq. (3.7) and involves

the full Yukawa couplings $\bar{h}_\phi, h_\phi$:

$$\langle c_1 c_2 \bar{c}_{2'} \bar{c}_{1'} \rangle = G_{1|1'} G_{2|2'} - G_{1|2'} G_{2|1'} + G_{1|3'} G_{2|4'} \left[I^\phi_{3'4'|34} + [\bar{h}_\phi]_{3'4'5} [W_\phi]_{5|5'} [h_\phi]_{5'34} \right] G_{3|1'} G_{4|2'}. \tag{C.7}$$

Importantly, I^ϕ is irreducible with respect to the bosonic propagator $W_{\phi,0}$ in contrast to the second term, which resembles the SBE decomposition. With this, Eq. (C.6) yields

$$0 = [W^{-1}_{\phi,0}]_{4'|3} [W_\phi]_{3|3'} [h_\phi]_{3'12} G_{1|1'} G_{2|2'} - \frac{1}{2} [h_{\phi,0}]_{4'12} G_{1|1'} G_{2|2'} + \frac{1}{2} [h_{\phi,0}]_{4'12} G_{1|2'} G_{2|1'}$$

$$- \frac{1}{2} [h_{\phi,0}]_{4'12} G_{1|1'} G_{2|2'} G_{3|3'} G_{5|5'} \left(I^\phi_{3'5'|35} + [\bar{h}_\phi]_{3'5'6} [W_\phi]_{6|6'} [h_\phi]_{6'35} \right). \tag{C.8}$$

Now, we divide the expression by $G_{1|1'} G_{2|2'}$ and insert the bosonic Dyson equation (3.22b), $[W^{-1}_{\phi,0}]_{4'|3} [W_\phi]_{3|3'} = \delta_{4'3'} + [\Sigma_\phi]_{4'|3} [W_\phi]_{3|3'}$, and the Schwinger–Dyson equation (3.25b) for Σ_ϕ to cancel the last term:

$$0 = [h_\phi]_{3'12} + \frac{1}{2} [h_{\phi,0}]_{4'56} G_{5|5'} G_{6|6'} [\bar{h}_\phi]_{5'6'3} [W_\phi]_{3|3'} [h_\phi]_{3'12} - [h_{\phi,0}]_{4'12}$$

$$- \frac{1}{2} [h_{\phi,0}]_{4'12} G_{3|3'} G_{5|5'} \left(I^\phi_{3'5'|35} + [\bar{h}_\phi]_{3'5'6} [W_\phi]_{6|6'} [h_\phi]_{6'35} \right). \tag{C.9}$$

This expression is equivalent to the Schwinger–Dyson equation (3.26d) of h_ϕ.

C.2. Identity operators in the SBE formalism

For general four-point objects $A_{12|34}$ (i.e., vertices Γ or bubbles Π), we define the channel-dependent product $\circ$, which includes a summation over both frequencies and other indices (cf. Eqs. (4.6) and Eqs. (5) in Ref. [P1]). The corresponding identity operators $\mathbb{1}_r$ are defined through the relation $\Gamma = \mathbb{1}_r \circ \Gamma = \Gamma \circ \mathbb{1}_r$. In Ref. [P1], we give the following explicit form (cf. Eqs. (8) ibid.):

$$\mathbb{1}_{a;12|34} = \delta_{13} \delta_{24}, \quad \mathbb{1}_{p;12|34} = \frac{1}{2} (\delta_{13} \delta_{24} - \delta_{14} \delta_{23}), \quad \mathbb{1}_{t;12|34} = \delta_{14} \delta_{23}. \tag{C.10}$$

At this point, it is worth to mention that in the p channel the following alternative form fulfills the defining relation as well:

$$\mathbb{1}_{p;12|34} = \delta_{13} \delta_{24} = \mathbb{1}_{a;12|34}. \tag{C.11}$$

Let us now make use of the channel-dependent frequency parametrization (Eq. (17) and Fig. 3 in Ref. [P1]):

$$\Gamma_{1'2'|12} (\nu'_1 \nu'_2 | \nu_1 \nu_2) = \delta_{\nu'_1 + \nu'_2, \nu_1 + \nu_2} \Gamma_{1'2'|12} (\omega_r, \nu_r, \nu'_r). \tag{C.12}$$

Importantly, from now on, the frequency dependence is made explicit in our notation and

the indices $1'2'|12$ do not include frequencies anymore. We can also make the frequency dependence explicit in the identity operators $\mathbb{1}_r$ [cf. Eq. (C.10)]:

$$\mathbb{1}_{a;12|34}(\omega_a, \nu_a, \nu'_a) = \delta_{13}\delta_{24}\delta_{\nu_a\nu'_a}, \tag{C.13a}$$

$$\mathbb{1}_{p;12|34}(\omega_p, \nu_p, \nu'_p) = \tfrac{1}{2}(\delta_{13}\delta_{24}\delta_{\nu_p\nu'_p} - \delta_{14}\delta_{23}\delta_{\nu_p,-\nu'_p}), \tag{C.13b}$$

$$\mathbb{1}_{t;12|34}(\omega_t, \nu_t, \nu'_t) = \delta_{14}\delta_{23}\delta_{\nu_t\nu'_t}. \tag{C.13c}$$

Further, we have introduced the product •, which only contains a summation over non-frequency indices in analogy to the ∘ product defined in Eq. (4.6). The identity operators corresponding to this product are defined by $\Gamma = \mathbf{1}_r \bullet \Gamma = \Gamma \bullet \mathbf{1}_r$ and are crucial for the definition of SBE ingredients. In Ref. [P1], we have not given an explicit form of $\mathbf{1}_r$. $\mathbf{1}_r$ should not depend on frequencies as the product • does not include any frequency summation. When multiplied with a vertex, it must not change its frequency dependence. For the a and t channel, one can simply drop the delta symbols in Eq. (C.13), to get reasonable expressions for $\mathbf{1}_r$:

$$\mathbf{1}_{a;12|34} = \delta_{13}\delta_{24}, \quad \mathbf{1}_{t;12|34} = \delta_{14}\delta_{23}. \tag{C.14}$$

However, for the p channel, simply dropping the delta symbols in Eq. (C.13) in general would lead to a wrong result:

$$
\begin{aligned}
\tfrac{1}{2}\left(\delta_{15}\delta_{26} - \delta_{16}\delta_{25}\right)\Gamma_{56|34}(\omega_p, \nu_p, \nu'_p) &= \tfrac{1}{2}\left(\Gamma_{12|34}(\omega_p, \nu_p, \nu'_p) - \Gamma_{21|34}(\omega_p, \nu_p, \nu'_p)\right) \\
&= \tfrac{1}{2}\left(\Gamma_{12|34}(\omega_p, \nu_p, \nu'_p) - \Gamma_{12|34}(\omega_p, -\nu_p, \nu'_p)\right) \\
&\neq \Gamma_{12|34}(\omega_p, \nu_p, \nu'_p) \\
&\neq \tfrac{1}{2}\left(\Gamma_{12|34}(\omega_p, \nu_p, \nu'_p) - \Gamma_{12|34}(\omega_p, \nu_p, -\nu'_p)\right) \\
&= \tfrac{1}{2}\left(\Gamma_{12|34}(\omega_p, \nu_p, \nu'_p) - \Gamma_{12|43}(\omega_p, \nu_p, \nu'_p)\right) \\
&= \Gamma_{12|56}(\omega_p, \nu_p, \nu'_p)\tfrac{1}{2}\left(\delta_{53}\delta_{64} - \delta_{54}\delta_{63}\right). \tag{C.15}
\end{aligned}
$$

The defining relation $\Gamma = \mathbf{1}_p \bullet \Gamma = \Gamma \bullet \mathbf{1}_p$ is however fulfilled when just considering the first addend, i.e., with an identity operator $\mathbf{1}_p$ analogous to Eq. (C.11):

$$\mathbf{1}_{p;12|34} = \delta_{13}\delta_{24} = \mathbf{1}_{a;12|34}. \tag{C.16}$$

Eqs. (C.14) and (C.16) are reasonable expressions for the identity operators $\mathbf{1}_r$, which do not affect frequencies.

C.3. Spin components for the interaction flow

To obtain the spin components of the bosonic single-scale propagator $S_{\eta_r}(\Lambda) = \eta_r \bullet U^{-1} \bullet \dot{U} \bullet U^{-1} \bullet \eta_r$, Eq. (3.68), it is useful to compute $U^{-1} \bullet \dot{U} \bullet U^{-1}$ explicitly. We calculate its

spin components in the matrix representation. For local interactions, i.e., $U^{\uparrow\uparrow} = 0$, we get:

$$[U^{-1} \bullet \dot{U} \bullet U^{-1}]_t^{\hat{\uparrow}\downarrow} = \frac{\dot{U}^{\uparrow\downarrow}}{[U^{\uparrow\downarrow}]^2}, \tag{C.17a}$$

$$[U^{-1} \bullet \dot{U} \bullet U^{-1}]_t^{\hat{\uparrow}\downarrow} = \frac{\dot{U}^{\hat{\uparrow}\downarrow}}{[U^{\hat{\uparrow}\downarrow}]^2} = -\frac{\dot{U}^{\uparrow\downarrow}}{[2U^{\uparrow\downarrow}]^2}, \tag{C.17b}$$

$$[U^{-1} \bullet \dot{U} \bullet U^{-1}]_p^{\uparrow\downarrow} = \frac{\dot{U}^{\uparrow\downarrow}}{[2U^{\uparrow\downarrow}]^2}, \tag{C.17c}$$

$$[U^{-1} \bullet \dot{U} \bullet U^{-1}]_p^{\hat{\uparrow}\downarrow} = \frac{\dot{U}^{\hat{\uparrow}\downarrow}}{[2U^{\hat{\uparrow}\downarrow}]^2} = -\frac{\dot{U}^{\uparrow\downarrow}}{[2U^{\uparrow\downarrow}]^2}, \tag{C.17d}$$

and vanishing contributions for all the other spin components.

The prefactors $1/4$ in the p channel cancel each other when multiplied by η_p from the left and right as it is the case inside S_{η_r}. Explicitly, we have

$$[\eta_p \bullet (U^{-1} \bullet \dot{U} \bullet U^{-1}) \bullet \eta_p]^{\uparrow\downarrow} = \eta_p^{\uparrow\downarrow} 4 [U^{-1} \bullet \dot{U} \bullet U^{-1}]^{\uparrow\downarrow} \eta_p^{\uparrow\downarrow} = \eta_p^{\uparrow\downarrow} \frac{\dot{U}^{\uparrow\downarrow}}{[U^{\uparrow\downarrow}]^2} \eta_p^{\uparrow\downarrow}, \tag{C.18a}$$

$$[\eta_p \bullet (U^{-1} \bullet \dot{U} \bullet U^{-1}) \bullet \eta_p]^{\hat{\uparrow}\downarrow} = \eta_p^{\uparrow\downarrow} \frac{\dot{U}^{\uparrow\downarrow}}{[U^{\uparrow\downarrow}]^2} \eta_p^{\hat{\uparrow}\downarrow}. \tag{C.18b}$$

C.4. Asymptotic classes in spin components

Using the spin structure introduced in Sec. 4.1.1, we here give the relation between the asymptotic classes $\mathcal{K}_{1r}, \mathcal{K}_{2r}, \mathcal{K}_{3r}$ and the SBE vertices $\eta_r, \bar{\lambda}_r, \lambda_r, M_r$ for systems using the two spin components $\uparrow, \downarrow$.

The relation between the first asymptotic class $\mathcal{K}_{1r}$ and the bosonic propagator η_r is trivial, i.e., $\mathcal{K}_{1r} = \eta_r - U$ (cf. Eq. (81a) in Ref. [P1]), and does not need any further explanation for the individual spin components. Also the inverse relation $\eta_r = U + \mathcal{K}_{1r}$ is trivial.

For the second asymptotic classes $\mathcal{K}_{2r}$ and $\mathcal{K}_{2'r}$, we have discussed the products between the Hedin vertices $\bar{\tilde{\lambda}}_r, \tilde{\lambda}_r$ and the bosonic propagator η_r [cf. Eqs. (81b)–(81c) in Ref. [P1] as well as Eqs. (4.22) and (4.39)]:

$$\mathcal{K}_{2a}^{\uparrow\downarrow} = \bar{\tilde{\lambda}}_a^{\uparrow\downarrow} \eta_a^{\uparrow\downarrow}, \qquad \begin{bmatrix} \mathcal{K}_{2a}^{\uparrow\uparrow} & \mathcal{K}_{2a}^{\hat{\uparrow}\downarrow} \\ \mathcal{K}_{2a}^{\hat{\downarrow}\uparrow} & \mathcal{K}_{2a}^{\downarrow\downarrow} \end{bmatrix} = \begin{bmatrix} \bar{\tilde{\lambda}}_a^{\uparrow\uparrow} & \bar{\tilde{\lambda}}_a^{\hat{\uparrow}\downarrow} \\ \bar{\tilde{\lambda}}_a^{\hat{\downarrow}\uparrow} & \bar{\tilde{\lambda}}_a^{\downarrow\downarrow} \end{bmatrix} \begin{bmatrix} \eta_a^{\uparrow\uparrow} & \eta_a^{\hat{\uparrow}\downarrow} \\ \eta_a^{\hat{\downarrow}\uparrow} & \eta_a^{\downarrow\downarrow} \end{bmatrix}, \tag{C.19a}$$

$$\mathcal{K}_{2p}^{\uparrow\uparrow} = 0, \qquad \begin{bmatrix} \mathcal{K}_{2p}^{\uparrow\downarrow} & \mathcal{K}_{2p}^{\hat{\uparrow}\downarrow} \\ \mathcal{K}_{2p}^{\hat{\downarrow}\uparrow} & \mathcal{K}_{2p}^{\downarrow\downarrow} \end{bmatrix} = \begin{bmatrix} \tilde{\lambda}_p^{\uparrow\downarrow} & -\bar{\tilde{\lambda}}_p^{\uparrow\downarrow} \\ -\tilde{\lambda}_p^{\downarrow\uparrow} & \bar{\tilde{\lambda}}_p^{\downarrow\uparrow} \end{bmatrix} 2\eta_p^{\uparrow\downarrow}, \tag{C.19b}$$

$$\mathcal{K}_{2t}^{\uparrow\hat{\downarrow}} = \tilde{\tilde{\lambda}}_t^{\uparrow\hat{\downarrow}}\eta_t^{\uparrow\hat{\downarrow}}, \quad \begin{bmatrix} \mathcal{K}_{2t}^{\uparrow\uparrow} & \mathcal{K}_{2t}^{\downarrow\uparrow} \\ \mathcal{K}_{2t}^{\uparrow\downarrow} & \mathcal{K}_{2t}^{\downarrow\downarrow} \end{bmatrix} = \begin{bmatrix} \tilde{\tilde{\lambda}}_t^{\uparrow\uparrow} & \tilde{\tilde{\lambda}}_t^{\downarrow\uparrow} \\ \tilde{\tilde{\lambda}}_t^{\uparrow\downarrow} & \tilde{\tilde{\lambda}}_t^{\downarrow\downarrow} \end{bmatrix} \begin{bmatrix} \eta_t^{\uparrow\uparrow} & \eta_t^{\downarrow\uparrow} \\ \eta_t^{\uparrow\downarrow} & \eta_t^{\downarrow\downarrow} \end{bmatrix}, \tag{C.19c}$$

$$\mathcal{K}_{2'a}^{\uparrow\downarrow} = \eta_a^{\uparrow\downarrow}\tilde{\lambda}_a^{\uparrow\downarrow}, \quad \begin{bmatrix} \mathcal{K}_{2'a}^{\uparrow\uparrow} & \mathcal{K}_{2'a}^{\uparrow\hat{\downarrow}} \\ \mathcal{K}_{2'a}^{\downarrow\uparrow} & \mathcal{K}_{2'a}^{\downarrow\downarrow} \end{bmatrix} = \begin{bmatrix} \eta_a^{\uparrow\uparrow} & \eta_a^{\uparrow\hat{\downarrow}} \\ \eta_a^{\downarrow\uparrow} & \eta_a^{\downarrow\downarrow} \end{bmatrix} \begin{bmatrix} \tilde{\lambda}_a^{\uparrow\uparrow} & \tilde{\lambda}_a^{\uparrow\hat{\downarrow}} \\ \tilde{\lambda}_a^{\downarrow\uparrow} & \tilde{\lambda}_a^{\downarrow\downarrow} \end{bmatrix}, \tag{C.20a}$$

$$\mathcal{K}_{2'p}^{\uparrow\uparrow} = 0, \quad \begin{bmatrix} \mathcal{K}_{2'p}^{\uparrow\downarrow} & \mathcal{K}_{2'p}^{\uparrow\hat{\downarrow}} \\ \mathcal{K}_{2'p}^{\downarrow\uparrow} & \mathcal{K}_{2'p}^{\downarrow\uparrow} \end{bmatrix} = 2\eta_p^{\uparrow\downarrow} \begin{bmatrix} \tilde{\lambda}_p^{\uparrow\downarrow} & -\tilde{\lambda}_p^{\downarrow\uparrow} \\ -\tilde{\lambda}_p^{\uparrow\downarrow} & \tilde{\lambda}_p^{\downarrow\uparrow} \end{bmatrix}, \tag{C.20b}$$

$$\mathcal{K}_{2't}^{\uparrow\hat{\downarrow}} = \eta_t^{\uparrow\hat{\downarrow}}\tilde{\lambda}_t^{\uparrow\hat{\downarrow}}, \quad \begin{bmatrix} \mathcal{K}_{2't}^{\uparrow\uparrow} & \mathcal{K}_{2't}^{\downarrow\uparrow} \\ \mathcal{K}_{2't}^{\uparrow\downarrow} & \mathcal{K}_{2't}^{\downarrow\downarrow} \end{bmatrix} = \begin{bmatrix} \eta_t^{\uparrow\uparrow} & \eta_t^{\downarrow\uparrow} \\ \eta_t^{\uparrow\downarrow} & \eta_t^{\downarrow\downarrow} \end{bmatrix} \begin{bmatrix} \tilde{\lambda}_t^{\uparrow\uparrow} & \tilde{\lambda}_t^{\downarrow\uparrow} \\ \tilde{\lambda}_t^{\uparrow\downarrow} & \tilde{\lambda}_t^{\downarrow\downarrow} \end{bmatrix}. \tag{C.20c}$$

As discussed in Sec. 4.1.2, due to the crossing symmetries, the pure matrix for η_p is not invertible anymore. However, since $\mathcal{K}_{2p}$ has the same matrix structure as $\tilde{\tilde{\lambda}}_p$ (and $\mathcal{K}_{2'p}$ as $\tilde{\lambda}_p$), it is possible to give the inverse relations $\tilde{\tilde{\lambda}}_r = \mathcal{K}_{2r} \bullet \eta_r^{-1}$ and $\tilde{\lambda}_r = \eta_r^{-1} \bullet \mathcal{K}_{2'r}$ (cf. Eq. (78) in Ref. [P1]) in a unique way for all spin components:

$$\tilde{\tilde{\lambda}}_a^{\uparrow\downarrow} = \frac{\mathcal{K}_{2a}^{\uparrow\downarrow}}{\eta_a^{\uparrow\downarrow}}, \quad \begin{bmatrix} \tilde{\tilde{\lambda}}_a^{\uparrow\uparrow} & \tilde{\tilde{\lambda}}_a^{\uparrow\hat{\downarrow}} \\ \tilde{\tilde{\lambda}}_a^{\downarrow\uparrow} & \tilde{\tilde{\lambda}}_a^{\downarrow\downarrow} \end{bmatrix} = \begin{bmatrix} \mathcal{K}_{2a}^{\uparrow\uparrow} & \mathcal{K}_{2a}^{\uparrow\hat{\downarrow}} \\ \mathcal{K}_{2a}^{\downarrow\uparrow} & \mathcal{K}_{2a}^{\downarrow\downarrow} \end{bmatrix} \frac{1}{\eta_a^{\uparrow\uparrow}\eta_a^{\downarrow\downarrow} - \eta_a^{\uparrow\hat{\downarrow}}\eta_a^{\downarrow\uparrow}} \begin{bmatrix} \eta_a^{\downarrow\downarrow} & -\eta_a^{\uparrow\hat{\downarrow}} \\ -\eta_a^{\downarrow\uparrow} & \eta_a^{\uparrow\uparrow} \end{bmatrix}, \tag{C.21a}$$

$$\tilde{\tilde{\lambda}}_p^{\uparrow\uparrow} = 0, \quad \begin{bmatrix} \tilde{\tilde{\lambda}}_p^{\uparrow\downarrow} & \tilde{\tilde{\lambda}}_p^{\uparrow\hat{\downarrow}} \\ \tilde{\tilde{\lambda}}_p^{\downarrow\hat{\uparrow}} & \tilde{\tilde{\lambda}}_p^{\downarrow\uparrow} \end{bmatrix} = \begin{bmatrix} \mathcal{K}_{2p}^{\uparrow\downarrow} & -\mathcal{K}_{2p}^{\uparrow\downarrow} \\ -\mathcal{K}_{2p}^{\downarrow\uparrow} & \mathcal{K}_{2p}^{\downarrow\uparrow} \end{bmatrix} \frac{1}{2\eta_p^{\uparrow\downarrow}}, \tag{C.21b}$$

$$\tilde{\tilde{\lambda}}_t^{\uparrow\hat{\downarrow}} = \frac{\mathcal{K}_{2t}^{\uparrow\hat{\downarrow}}}{\eta_t^{\uparrow\hat{\downarrow}}}, \quad \begin{bmatrix} \tilde{\tilde{\lambda}}_t^{\uparrow\uparrow} & \tilde{\tilde{\lambda}}_t^{\downarrow\uparrow} \\ \tilde{\tilde{\lambda}}_t^{\uparrow\downarrow} & \tilde{\tilde{\lambda}}_t^{\downarrow\downarrow} \end{bmatrix} = \begin{bmatrix} \mathcal{K}_{2t}^{\uparrow\uparrow} & \mathcal{K}_{2t}^{\downarrow\uparrow} \\ \mathcal{K}_{2t}^{\uparrow\downarrow} & \mathcal{K}_{2t}^{\downarrow\downarrow} \end{bmatrix} \frac{1}{\eta_t^{\uparrow\uparrow}\eta_t^{\downarrow\downarrow} - \eta_t^{\downarrow\uparrow}\eta_t^{\uparrow\downarrow}} \begin{bmatrix} \eta_t^{\downarrow\downarrow} & -\eta_t^{\downarrow\uparrow} \\ -\eta_t^{\uparrow\downarrow} & \eta_t^{\uparrow\uparrow} \end{bmatrix}, \tag{C.21c}$$

$$\tilde{\lambda}_a^{\uparrow\downarrow} = \frac{\mathcal{K}_{2'a}^{\uparrow\downarrow}}{\eta_a^{\uparrow\downarrow}}, \quad \begin{bmatrix} \tilde{\lambda}_a^{\uparrow\uparrow} & \tilde{\lambda}_a^{\uparrow\hat{\downarrow}} \\ \tilde{\lambda}_a^{\downarrow\uparrow} & \tilde{\lambda}_a^{\downarrow\downarrow} \end{bmatrix} = \frac{1}{\eta_a^{\uparrow\uparrow}\eta_a^{\downarrow\downarrow} - \eta_a^{\uparrow\hat{\downarrow}}\eta_a^{\downarrow\hat{\uparrow}}} \begin{bmatrix} \eta_a^{\downarrow\downarrow} & -\eta_a^{\uparrow\hat{\downarrow}} \\ -\eta_a^{\downarrow\hat{\uparrow}} & \eta_a^{\uparrow\uparrow} \end{bmatrix} \begin{bmatrix} \mathcal{K}_{2'a}^{\uparrow\uparrow} & \mathcal{K}_{2'a}^{\uparrow\hat{\downarrow}} \\ \mathcal{K}_{2'a}^{\downarrow\hat{\uparrow}} & \mathcal{K}_{2'a}^{\downarrow\downarrow} \end{bmatrix}, \tag{C.22a}$$

$$\tilde{\lambda}_p^{\uparrow\uparrow} = 0, \quad \begin{bmatrix} \tilde{\lambda}_p^{\uparrow\downarrow} & \tilde{\lambda}_p^{\uparrow\hat{\downarrow}} \\ \tilde{\lambda}_p^{\downarrow\hat{\uparrow}} & \tilde{\lambda}_p^{\downarrow\uparrow} \end{bmatrix} = \frac{1}{2\eta_p^{\uparrow\downarrow}} \begin{bmatrix} \mathcal{K}_{2'p}^{\uparrow\downarrow} & -\mathcal{K}_{2'p}^{\uparrow\downarrow} \\ -\mathcal{K}_{2'p}^{\downarrow\uparrow} & \mathcal{K}_{2'p}^{\downarrow\uparrow} \end{bmatrix}, \tag{C.22b}$$

$$\tilde{\lambda}_t^{\uparrow\hat{\downarrow}} = \frac{\mathcal{K}_{2't}^{\uparrow\hat{\downarrow}}}{\eta_t^{\uparrow\hat{\downarrow}}}, \quad \begin{bmatrix} \tilde{\lambda}_t^{\uparrow\uparrow} & \tilde{\lambda}_t^{\downarrow\uparrow} \\ \tilde{\lambda}_t^{\uparrow\downarrow} & \tilde{\lambda}_t^{\downarrow\downarrow} \end{bmatrix} = \frac{1}{\eta_t^{\uparrow\uparrow}\eta_t^{\downarrow\downarrow} - \eta_t^{\downarrow\uparrow}\eta_t^{\uparrow\downarrow}} \begin{bmatrix} \eta_t^{\downarrow\downarrow} & -\eta_t^{\downarrow\uparrow} \\ -\eta_t^{\uparrow\downarrow} & \eta_t^{\uparrow\uparrow} \end{bmatrix} \begin{bmatrix} \mathcal{K}_{2't}^{\uparrow\uparrow} & \mathcal{K}_{2't}^{\downarrow\uparrow} \\ \mathcal{K}_{2't}^{\uparrow\downarrow} & \mathcal{K}_{2't}^{\downarrow\downarrow} \end{bmatrix}. \tag{C.22c}$$

The spin components of the third asymptotic class $\mathcal{K}_{3r} = M_r + \tilde{\tilde{\lambda}}_r \bullet \eta_r \bullet \tilde{\lambda}_r$ (cf. Eq. (81d) in Ref. [P1]) result from the spin components of the triple product [cf. Eqs. (4.22) and

(4.40)]:

$$\mathcal{K}_{3a}^{\uparrow\downarrow} = M_a^{\uparrow\downarrow} + \tilde{\bar{\lambda}}_a^{\uparrow\downarrow}\eta_a^{\uparrow\downarrow}\tilde{\lambda}_a^{\uparrow\downarrow},$$

$$\begin{bmatrix} \mathcal{K}_{3a}^{\uparrow\uparrow} & \mathcal{K}_{3a}^{\uparrow\hat{\downarrow}} \\ \mathcal{K}_{3a}^{\hat{\downarrow}\uparrow} & \mathcal{K}_{3a}^{\downarrow\downarrow} \end{bmatrix} = \begin{bmatrix} M_a^{\uparrow\uparrow} & M_a^{\uparrow\hat{\downarrow}} \\ M_a^{\hat{\downarrow}\uparrow} & M_a^{\downarrow\downarrow} \end{bmatrix} + \begin{bmatrix} \tilde{\bar{\lambda}}_a^{\uparrow\uparrow} & \tilde{\bar{\lambda}}_a^{\uparrow\hat{\downarrow}} \\ \tilde{\bar{\lambda}}_a^{\hat{\downarrow}\uparrow} & \tilde{\bar{\lambda}}_a^{\downarrow\downarrow} \end{bmatrix} \begin{bmatrix} \eta_a^{\uparrow\uparrow} & \eta_a^{\uparrow\hat{\downarrow}} \\ \eta_a^{\hat{\downarrow}\uparrow} & \eta_a^{\downarrow\downarrow} \end{bmatrix} \begin{bmatrix} \tilde{\lambda}_a^{\uparrow\uparrow} & \tilde{\lambda}_a^{\uparrow\hat{\downarrow}} \\ \tilde{\lambda}_a^{\hat{\downarrow}\uparrow} & \tilde{\lambda}_a^{\downarrow\downarrow} \end{bmatrix}, \tag{C.23a}$$

$$\mathcal{K}_{3p}^{\uparrow\uparrow} = M_p^{\uparrow\uparrow},$$

$$\begin{bmatrix} \mathcal{K}_{3p}^{\uparrow\downarrow} & \mathcal{K}_{3p}^{\uparrow\hat{\downarrow}} \\ \mathcal{K}_{3p}^{\downarrow\uparrow} & \mathcal{K}_{3p}^{\downarrow\uparrow} \end{bmatrix} = \begin{bmatrix} M_p^{\uparrow\uparrow} & M_p^{\uparrow\hat{\downarrow}} \\ M_p^{\hat{\downarrow}\uparrow} & M_p^{\downarrow\downarrow} \end{bmatrix} + \begin{bmatrix} \tilde{\bar{\lambda}}_p^{\uparrow\downarrow}4\eta_p^{\uparrow\downarrow}\tilde{\lambda}_p^{\uparrow\downarrow} & -\tilde{\bar{\lambda}}_p^{\uparrow\downarrow}4\eta_p^{\uparrow\downarrow}\tilde{\lambda}_p^{\downarrow\uparrow} \\ -\tilde{\bar{\lambda}}_p^{\downarrow\uparrow}4\eta_p^{\uparrow\downarrow}\tilde{\lambda}_p^{\uparrow\downarrow} & \tilde{\bar{\lambda}}_p^{\downarrow\uparrow}4\eta_p^{\uparrow\downarrow}\tilde{\lambda}_p^{\downarrow\uparrow} \end{bmatrix}, \tag{C.23b}$$

$$\mathcal{K}_{3t}^{\hat{\uparrow}\downarrow} = M_t^{\hat{\uparrow}\downarrow} + \tilde{\bar{\lambda}}_t^{\hat{\uparrow}\downarrow}\eta_t^{\hat{\uparrow}\downarrow}\tilde{\lambda}_t^{\hat{\uparrow}\downarrow},$$

$$\begin{bmatrix} \mathcal{K}_{3t}^{\uparrow\uparrow} & \mathcal{K}_{3t}^{\downarrow\uparrow} \\ \mathcal{K}_{3t}^{\uparrow\downarrow} & \mathcal{K}_{3t}^{\downarrow\downarrow} \end{bmatrix} = \begin{bmatrix} M_t^{\uparrow\uparrow} & M_t^{\downarrow\uparrow} \\ M_t^{\uparrow\downarrow} & M_t^{\downarrow\downarrow} \end{bmatrix} + \begin{bmatrix} \tilde{\bar{\lambda}}_t^{\uparrow\uparrow} & \tilde{\bar{\lambda}}_t^{\downarrow\uparrow} \\ \tilde{\bar{\lambda}}_t^{\uparrow\downarrow} & \tilde{\bar{\lambda}}_t^{\downarrow\downarrow} \end{bmatrix} \begin{bmatrix} \eta_t^{\uparrow\uparrow} & \eta_t^{\downarrow\uparrow} \\ \eta_t^{\uparrow\downarrow} & \eta_t^{\downarrow\downarrow} \end{bmatrix} \begin{bmatrix} \tilde{\lambda}_t^{\uparrow\uparrow} & \tilde{\lambda}_t^{\downarrow\uparrow} \\ \tilde{\lambda}_t^{\uparrow\downarrow} & \tilde{\lambda}_t^{\downarrow\downarrow} \end{bmatrix}. \tag{C.23c}$$

Also here, the fact that the matrix η_p is not invertible does not prevent us from finding a unique way of expressing the MBE vertices in terms of the asymptotic classes. In spin components, the relation $M_r = \mathcal{K}_{3r} - \mathcal{K}_{2r} \bullet \eta_r^{-1} \bullet \mathcal{K}_{2'r}$ (cf. Eq. (80) in Ref. [P1]) yields

$$M_a^{\uparrow\downarrow} = \mathcal{K}_{3a}^{\uparrow\downarrow} - \mathcal{K}_{2a}^{\uparrow\downarrow}\mathcal{K}_{2'a}^{\uparrow\downarrow}/\eta_a^{\uparrow\downarrow},$$

$$\begin{bmatrix} M_a^{\uparrow\uparrow} & M_a^{\uparrow\hat{\downarrow}} \\ M_a^{\hat{\downarrow}\uparrow} & M_a^{\downarrow\downarrow} \end{bmatrix} = \begin{bmatrix} \mathcal{K}_{3a}^{\uparrow\uparrow} & \mathcal{K}_{3a}^{\uparrow\hat{\downarrow}} \\ \mathcal{K}_{3a}^{\hat{\downarrow}\uparrow} & \mathcal{K}_{3a}^{\downarrow\downarrow} \end{bmatrix} - \begin{bmatrix} \mathcal{K}_{2a}^{\uparrow\uparrow} & \mathcal{K}_{2a}^{\uparrow\hat{\downarrow}} \\ \mathcal{K}_{2a}^{\hat{\downarrow}\uparrow} & \mathcal{K}_{2a}^{\downarrow\downarrow} \end{bmatrix} \begin{bmatrix} \eta_a^{\uparrow\uparrow} & \eta_a^{\uparrow\hat{\downarrow}} \\ \eta_a^{\hat{\downarrow}\uparrow} & \eta_a^{\downarrow\downarrow} \end{bmatrix}^{-1} \begin{bmatrix} \mathcal{K}_{2'a}^{\uparrow\uparrow} & \mathcal{K}_{2'a}^{\uparrow\hat{\downarrow}} \\ \mathcal{K}_{2'a}^{\hat{\downarrow}\uparrow} & \mathcal{K}_{2'a}^{\downarrow\downarrow} \end{bmatrix}, \tag{C.24a}$$

$$M_p^{\uparrow\uparrow} = \mathcal{K}_{3p}^{\uparrow\uparrow},$$

$$\begin{bmatrix} M_p^{\uparrow\uparrow} & M_p^{\uparrow\hat{\downarrow}} \\ M_p^{\hat{\downarrow}\uparrow} & M_p^{\downarrow\downarrow} \end{bmatrix} = \begin{bmatrix} \mathcal{K}_{3p}^{\uparrow\downarrow} & \mathcal{K}_{3p}^{\uparrow\hat{\downarrow}} \\ \mathcal{K}_{3p}^{\downarrow\uparrow} & \mathcal{K}_{3p}^{\downarrow\uparrow} \end{bmatrix} - \frac{1}{4\eta_p^{\uparrow\downarrow}} \begin{bmatrix} \mathcal{K}_{2p}^{\uparrow\downarrow}\mathcal{K}_{2'p}^{\uparrow\downarrow}/\eta_p^{\uparrow\downarrow} & -\mathcal{K}_{2p}^{\uparrow\downarrow}\mathcal{K}_{2'p}^{\downarrow\uparrow}/\eta_p^{\uparrow\downarrow} \\ -\mathcal{K}_{2p}^{\downarrow\uparrow}\mathcal{K}_{2'p}^{\uparrow\downarrow}/\eta_p^{\uparrow\downarrow} & \mathcal{K}_{2p}^{\downarrow\uparrow}\mathcal{K}_{2'p}^{\downarrow\uparrow}/\eta_p^{\uparrow\downarrow} \end{bmatrix}, \tag{C.24b}$$

$$M_t^{\hat{\uparrow}\downarrow} = \mathcal{K}_{3t}^{\hat{\uparrow}\downarrow} - \mathcal{K}_{2t}^{\hat{\uparrow}\downarrow}\mathcal{K}_{2't}^{\hat{\uparrow}\downarrow}/\eta_t^{\hat{\uparrow}\downarrow},$$

$$\begin{bmatrix} M_t^{\uparrow\uparrow} & M_t^{\downarrow\uparrow} \\ M_t^{\uparrow\downarrow} & M_t^{\downarrow\downarrow} \end{bmatrix} = \begin{bmatrix} \mathcal{K}_{3t}^{\uparrow\uparrow} & \mathcal{K}_{3t}^{\downarrow\uparrow} \\ \mathcal{K}_{3t}^{\uparrow\downarrow} & \mathcal{K}_{3t}^{\downarrow\downarrow} \end{bmatrix} - \begin{bmatrix} \mathcal{K}_{2t}^{\uparrow\uparrow} & \mathcal{K}_{2t}^{\downarrow\uparrow} \\ \mathcal{K}_{2t}^{\uparrow\downarrow} & \mathcal{K}_{2t}^{\downarrow\downarrow} \end{bmatrix} \begin{bmatrix} \eta_t^{\uparrow\uparrow} & \eta_t^{\downarrow\uparrow} \\ \eta_t^{\uparrow\downarrow} & \eta_t^{\downarrow\downarrow} \end{bmatrix}^{-1} \begin{bmatrix} \mathcal{K}_{2't}^{\uparrow\uparrow} & \mathcal{K}_{2't}^{\downarrow\uparrow} \\ \mathcal{K}_{2't}^{\uparrow\downarrow} & \mathcal{K}_{2't}^{\downarrow\downarrow} \end{bmatrix}. \tag{C.24c}$$

C.5. SU(2)-symmetric case

We show that in the SU(2)-symmetric case the SBE equations, given in Sec. 4.1.1, obtain a diagonal form when using the physical charge ch, spin sp, singlet si and triplet tr channels, defined by Eq. (4.102). The spin components of the Green's functions become superfluous, i.e., $G \equiv G^{\uparrow} = G^{\downarrow}$ and the same is valid for the bubbles Π_r. Still, we define physical channels of the bubbles as $\Pi^{\text{ch/sp}} = \Pi_t$ and $\Pi^{\text{tr/si}} = \Pi_p$. The SU(2) symmetry

relation (4.101) implies

$$\Gamma^{\mathrm{sp}} = \Gamma^{\hat{\uparrow\downarrow}}_t, \quad \Gamma^{\mathrm{tr}} = \Gamma^{\uparrow\uparrow}_p. \tag{C.25}$$

As $\hat{\uparrow\downarrow}$ is the diagonal component for the t channel and $\uparrow\uparrow$ for the p channel [cf. Eq. (4.7)], Eq. (C.25) makes clear that the parquet equations are diagonal in the spin and triplet channel. Explicitly, Eqs. (4.11c), (4.15c), (4.16c), (4.18c), and (4.20) imply

$$M^{\mathrm{sp}}(\omega, \nu, \nu') = \tfrac{1}{\beta} \sum_{\nu''} [T^{\mathrm{sp}}(\omega, \nu, \nu'') - M^{\mathrm{sp}}(\omega, \nu, \nu'')]\Pi^{\mathrm{sp}}(\omega, \nu'')T^{\mathrm{sp}}(\omega, \nu'', \nu'), \tag{C.26a}$$

$$\lambda^{\mathrm{sp}}(\omega, \nu') = 1 + \tfrac{1}{\beta} \sum_{\nu''} \Pi^{\mathrm{sp}}(\omega, \nu'')T^{\mathrm{sp}}(\omega, \nu'', \nu'), \tag{C.26b}$$

$$P^{\mathrm{sp}}(\omega) = \tfrac{1}{\beta} \sum_{\nu''} \lambda^{\mathrm{sp}}(\omega, \nu'')\Pi^{\mathrm{sp}}(\omega, \nu''), \tag{C.26c}$$

$$\eta^{\mathrm{sp}}(\omega) = U^{\mathrm{sp}} + U^{\mathrm{sp}}P^{\mathrm{sp}}(\omega)\eta^{\mathrm{sp}}(\omega), \text{ where } U^{\mathrm{sp}} = -U^{\uparrow\downarrow}, \tag{C.26d}$$

$$\nabla^{\mathrm{sp}}(\omega, \nu, \nu') = \lambda^{\mathrm{sp}}(\omega, \nu)\eta^{\mathrm{sp}}(\omega)\lambda^{\mathrm{sp}}(\omega, \nu'). \tag{C.26e}$$

For the triplet channel, the U-irreducible vertices vanish $\eta^{\mathrm{tr}} = 0 = \tilde{\lambda}^{\mathrm{tr}}$ according to Eq. (C.25) and the symmetry relations discussed in Sec. 4.1.2. Consequently, in this channel, only MBE vertices remain. These fulfill the Bethe–Salpeter equation

$$M^{\mathrm{tr}}(\omega, \nu, \nu') = \tfrac{1}{\beta} \sum_{\nu''} [T^{\mathrm{tr}}(\omega, \nu, \nu'') - M^{\mathrm{tr}}(\omega, \nu, \nu'')]\Pi^{\mathrm{tr}}(\omega, \nu'')T^{\mathrm{tr}}(\omega, \nu'', \nu'). \tag{C.27}$$

The crossing symmetries $\eta^{\uparrow\downarrow}_p = -\eta^{\hat{\uparrow\downarrow}}_p$ and $\lambda^{\hat{\uparrow\downarrow}}_p = 1 - \lambda^{\uparrow\downarrow}_p$ for the p channel [cf. Eqs. (4.36b) and (4.31)] further simplify the structures of the singlet channel:

$$\eta^{\mathrm{si}} = 2\eta^{\uparrow\downarrow}_p, \quad \lambda^{\mathrm{si}} = 2\lambda^{\uparrow\downarrow}_p - 1. \tag{C.28}$$

By using the SBE equations in the p channel, i.e., Eqs. (4.29), (4.15b), (4.16b), (4.20b), (4.18b), and (4.40), we conclude

$$M^{\mathrm{si}}(\omega, \nu, \nu') = \tfrac{1}{\beta} \sum_{\nu''} [T^{\mathrm{si}}(\omega, \nu, \nu'') - M^{\mathrm{si}}(\omega, \nu, \nu'')]\Pi^{\mathrm{sp}}(\omega, \nu'')T^{\mathrm{si}}(\omega, \nu'', \nu'), \tag{C.29a}$$

$$\lambda^{\mathrm{si}}(\omega, \nu') = 1 + \tfrac{1}{\beta} \sum_{\nu''} \Pi^{\mathrm{si}}(\omega, \nu'')T^{\mathrm{si}}(\omega, \nu'', \nu'), \tag{C.29b}$$

$$P^{\mathrm{si}}(\omega) = \tfrac{1}{\beta} \sum_{\nu''} \lambda^{\mathrm{si}}(\omega, \nu'')\Pi^{\mathrm{si}}(\omega, \nu''), \tag{C.29c}$$

$$\eta^{\mathrm{si}}(\omega) = U^{\mathrm{si}} + U^{\mathrm{si}}P^{\mathrm{si}}(\omega)\eta^{\mathrm{si}}(\omega), \text{ where } U^{\mathrm{si}} = 2U^{\uparrow\downarrow}, \tag{C.29d}$$

$$\nabla^{\mathrm{si}}(\omega, \nu, \nu') = \lambda^{\mathrm{si}}(\omega, \nu)\eta^{\mathrm{si}}(\omega)\lambda^{\mathrm{si}}(\omega, \nu'). \tag{C.29e}$$

Finally, the SBE equations in the t channel, i.e., Eqs. (4.11c), (4.15c), (4.16c), (4.18c), and (4.20) imply the diagonal structure for the charge channel when the individual spin components are summed over:

$$M^{\mathrm{ch}}(\omega, \nu, \nu') = \tfrac{1}{\beta} \sum_{\nu''} [T^{\mathrm{ch}}(\omega, \nu, \nu'') - M^{\mathrm{ch}}(\omega, \nu, \nu'')] \Pi^{\mathrm{ch}}(\omega, \nu'') T^{\mathrm{ch}}(\omega, \nu'', \nu'), \quad \text{(C.30a)}$$

$$\lambda^{\mathrm{ch}}(\omega, \nu') = 1 + \tfrac{1}{\beta} \sum_{\nu''} \Pi^{\mathrm{ch}}(\omega, \nu'') T^{\mathrm{ch}}(\omega, \nu'', \nu'), \quad \text{(C.30b)}$$

$$P^{\mathrm{ch}}(\omega) = \tfrac{1}{\beta} \sum_{\nu''} \lambda^{\mathrm{ch}}(\omega, \nu'') \Pi^{\mathrm{ch}}(\omega, \nu''), \quad \text{(C.30c)}$$

$$\eta^{\mathrm{ch}}(\omega) = U^{\mathrm{ch}} + U^{\mathrm{ch}} P^{\mathrm{ch}}(\omega) \eta^{\mathrm{ch}}(\omega), \quad \text{where } U^{\mathrm{ch}} = U^{\uparrow\downarrow}, \quad \text{(C.30d)}$$

$$\nabla^{\mathrm{ch}}(\omega, \nu, \nu') = \lambda^{\mathrm{ch}}(\omega, \nu) \eta^{\mathrm{ch}}(\omega) \lambda^{\mathrm{ch}}(\omega, \nu'). \quad \text{(C.30e)}$$

The formulations in Sec. 4.4 are valid for the general case, where a single Hubbard site is placed out of half filling including an external magnetic field in z direction. The specific case with $\mu = u/2$ and $h = 0$ is extensively discussed in the literature [Roh13, TGCR18, SCC+20, HSS23, Roh23, RRS+24]. Still, we briefly provide the formulas for the vertices that are consistent with our conventions and definitions from Chapter 4.

We receive a simplified form for the parameters, Eqs. (4.88), (4.89), and (4.92),

$$Z = 2(1 + \mathrm{e}^{\beta u/2}), \quad n = \tfrac{1}{2}, \quad x(\nu) = \mathrm{i}\nu + \frac{u}{2}, \quad y(\nu) = \mathrm{i}\nu - \frac{u}{2}, \quad \text{(C.31)}$$

which gives

$$G_0(\nu) = \frac{1}{\mathrm{i}\nu}, \quad G(\nu) = -\frac{4\mathrm{i}\nu}{4\nu^2 + u^2}, \quad \Sigma(\nu) = \frac{u^2}{4\mathrm{i}\nu}, \quad \Sigma_{\mathrm{H}} = 0. \quad \text{(C.32)}$$

As the chemical potential is given by the perturbation parameter u, the bare Green's function does not include $\mu = u/2$ anymore, which generates a shift of the Hartree term by $u/2$ compared to Eqs. (4.91)–(4.93).

The bosonic propagators, Eqs. (4.94), are simplified to

$$\tilde{\eta}_a^{\uparrow\downarrow}(\omega) = -\frac{u^2 \beta \delta_\omega}{Z} \mathrm{e}^{\beta u/2}, \quad \tilde{\eta}_a^{\hat{\uparrow}\downarrow}(\omega) = \frac{u^2 \beta \delta_\omega}{Z^2} (\mathrm{e}^{\beta u} - 1), \quad \text{(C.33a)}$$

$$\tilde{\eta}_a^{\uparrow\uparrow}(\omega) = -\frac{u^2 \beta \delta_\omega}{4}, \quad \tilde{\eta}_p^{\uparrow\downarrow}(\omega) = \frac{u^2 \beta \delta_\omega}{Z}. \quad \text{(C.33b)}$$

The expressions in the physical channel yield

$$\tilde{\eta}^{\mathrm{ch}}(\omega) = \frac{u^2 \beta \delta_\omega}{Z}, \quad \tilde{\eta}^{\mathrm{sp}}(\omega) = \frac{u^2 \beta \delta_\omega}{Z} \mathrm{e}^{\beta U/2}, \quad \tilde{\eta}^{\mathrm{tr}}(\omega) = 0 \quad \tilde{\eta}^{\mathrm{si}}(\omega) = 2\tilde{\eta}^{\mathrm{ch}}(\omega), \quad \text{(C.34)}$$

where the crossing symmetries $\eta_t^{\uparrow\downarrow}(\omega) = -\eta_a^{\hat{\downarrow}\uparrow}(\omega)$ and $\eta_p^{\uparrow\downarrow}(\omega) = -\eta_p^{\uparrow\downarrow}(\omega)$ [cf. Eqs. (4.26)],

were used.

In the SU(2)-symmetric case, the Hedin vertices fulfill $\bar{\lambda}_r = \lambda_r$ for all spin components (cf. Sec. 4.1.2) and can be expressed in terms of a single function $f(\omega, \nu) = u^2/[4\nu(\nu+\omega)]$. The spin components of the bosonic propagators $\tilde{\eta}^\alpha$ yield

$$\lambda^{\mathrm{ch}}(\omega, \nu') = 1 + f(\omega, \nu')\frac{\tilde{\eta}^{\mathrm{ch}}(\omega) + u}{\tilde{\eta}^{\mathrm{ch}}(\omega) - u}, \qquad \lambda^{\mathrm{sp}}(\omega, \nu') = 1 + f(\omega, \nu')\frac{\tilde{\eta}^{\mathrm{sp}}(\omega) - u}{\tilde{\eta}^{\mathrm{sp}}(\omega) + u}, \quad \text{(C.35a)}$$

$$\lambda_a^{\uparrow\downarrow}(\omega, \nu') = \lambda^{\mathrm{sp}}(\omega, \nu'), \tag{C.35b}$$

$$\lambda_a^{\hat{\uparrow\downarrow}}(\omega, \nu') = \tfrac{1}{2}\left[\lambda^{\mathrm{ch}}(\omega, \nu') - \lambda^{\mathrm{sp}}(\omega, \nu')\right], \quad \lambda_a^{\uparrow\uparrow}(\omega, \nu') = \tfrac{1}{2}\left[\lambda^{\mathrm{ch}}(\omega, \nu') + \lambda^{\mathrm{sp}}(\omega, \nu')\right], \tag{C.35c}$$

$$\lambda_p^{\uparrow\downarrow}(\omega, \nu') = \tfrac{1}{2} + \tfrac{1}{2}\lambda^{\mathrm{ch}}(\omega, \nu'), \qquad\qquad \lambda_p^{\hat{\uparrow\downarrow}}(\omega, \nu') = \tfrac{1}{2} - \tfrac{1}{2}\lambda^{\mathrm{ch}}(\omega, \nu'). \tag{C.35d}$$

The connected four-point correlation functions, Eqs. (4.99), simplify to

$$[G_{\mathrm{con}}^{(4)}]^{\uparrow\downarrow}(\nu_1, \nu_2, \nu_4, \nu_3) = \frac{-16u\nu_1\nu_2\nu_3\nu_4 + 3u^5 + 2u^3(\nu_1^2 + \nu_2 + \nu_3^2 + \nu_4^2)}{16\left(\nu_1^2 + \frac{u^2}{4}\right)\left(\nu_2^2 + \frac{u^2}{4}\right)\left(\nu_3^2 + \frac{u^2}{4}\right)\left(\nu_4^2 + \frac{u^2}{4}\right)}$$
$$- \frac{\beta u^2(\delta_{\nu_3\nu_2} + 2\delta_{\nu_3\nu_1})}{4(1 + \mathrm{e}^{-\beta u/2})}\frac{\nu_3\nu_4}{\left(\nu_3^2 + \frac{u^2}{4}\right)\left(\nu_4^2 + \frac{u^2}{4}\right)}$$
$$+ \frac{\beta u^2(\delta_{\nu_1+\nu_2} + 2\delta_{\nu_3\nu_2})}{4(1 + \mathrm{e}^{\beta u/2})}\frac{\nu_2\nu_4}{\left(\nu_2^2 + \frac{u^2}{4}\right)\left(\nu_4^2 + \frac{u^2}{4}\right)}, \tag{C.36a}$$

$$[G_{\mathrm{con}}^{(4)}]^{\uparrow\uparrow}(\nu_1, \nu_2, \nu_4, \nu_3) = \beta u^2(\delta_{\nu_2\nu_3} - \delta_{\nu_1\nu_3})\frac{4}{(4\nu_1^2 + u^2)(4\nu_2^2 + u^2)}, \tag{C.36b}$$

which yield the four-point vertices [Roh13, TGCR18]

$$\Gamma^{\uparrow\downarrow}(\nu_1, \nu_2, \nu_4, \nu_3) = -u + \frac{3u^5 + 2u^3(\nu_1^2 + \nu_2^2 + \nu_3^2 + \nu_4^2)}{16\nu_1\nu_2\nu_3\nu_4}$$
$$- \frac{\beta u^2(\delta_{\nu_3\nu_2} + 2\delta_{\nu_3\nu_1})}{4(1 + \mathrm{e}^{-\beta u/2})\nu_1^2\nu_2^2}\left(\nu_1^2 + \frac{u^2}{4}\right)\left(\nu_2^2 + \frac{u^2}{4}\right)$$
$$+ \frac{\beta u^2(2\delta_{\nu_1+\nu_2} + \delta_{\nu_3\nu_2})}{4(1 + \mathrm{e}^{\beta u/2})\nu_1^2\nu_3^2}\left(\nu_1^2 + \frac{u^2}{4}\right)\left(\nu_3^2 + \frac{u^2}{4}\right), \tag{C.37a}$$

$$\Gamma^{\uparrow\uparrow}(\nu_1, \nu_2, \nu_4, \nu_3) = \beta u^2(\delta_{\nu_2\nu_3} - \delta_{\nu_1\nu_3})\frac{1}{4\nu_1^2\nu_2^2}\left(\nu_1^2 + \frac{u^2}{4}\right)\left(\nu_2^2 + \frac{u^2}{4}\right). \tag{C.37b}$$

D. Details on the logarithmic analysis of the Fermi-edge singularity

D.1. Perturbation theory

In this section, we complete the discussion on the perturbation theory of the Fermi-edge singularity given in App. D of our paper [P3] by providing diagrams up to fourth-order perturbation theory $\mathcal{O}(u^4)$ and indicate their logarithmic behavior.

Let us first neglect the self-energy and hence the renormalization of the Green's function G and bubble Π_r. The nth-order contributions of SBE vertices can be deduced from the SBE equations involving lower-order contributions. The nth-order Bethe–Salpeter equation for the two-particle reducible vertex γ_r can be constructed from lower-order contributions of the involved vertices:

$$\gamma_r^{(n\geq 2)} = \sum_{k=1}^{n-1} I_r^{(n-k)} \circ \Pi_r \circ \Gamma^{(k)}, \tag{D.1}$$

where the lowest contribution of the vertices is given by the bare vertex $I_r^{(1)} = \Gamma^{(1)} = U$. The perturbative expressions of the SBE vertices are

$$\eta_r^{(n>2)} = U \circ \Pi_r \circ \Gamma^{(n-2)} \circ \Pi_r \circ U, \qquad \eta_r^{(2)} = \gamma_r^{(2)} = U \circ \Pi_r \circ U, \tag{D.2a}$$

$$\bar{\lambda}_r^{(n\geq 2)} = \mathbf{1}_r \circ \Pi_r \circ T_r^{(n)}, \qquad \lambda_r^{(n\geq 2)} = T_r^{(n)} \circ \Pi_r \circ \mathbf{1}_r, \tag{D.2b}$$

$$\nabla_r^{(n\geq 1)} = \sum_{i+j+k=n} \bar{\lambda}_r^{(i)} \bullet \eta_r^{(j)} \bullet \lambda_r^{(k)}, \qquad T_r^{(n\geq 2)} = \Gamma^{(n)} - \nabla^{(n)}, \tag{D.2c}$$

$$M^{(n\geq 4)} = \sum_{k=1}^{n-1} (T_r^{(n-k)} - M_r^{(n-k)}) \circ \Pi_r \circ T_r^{(k)}, \tag{D.2d}$$

and the trivial contributions $\eta_r^{(1)} = U$, $\bar{\lambda}_r^{(0)} = \mathbf{1}_r = \lambda_r^{(0)}$. All the other terms vanish.

The diagrams for the particle-hole susceptibility are formed as (cf. Eq. (14) in Ref. [P3])

$$\chi_a^{dc} = [\mathbf{1}_a \circ \Pi_a \circ \mathbf{1}_a]^{dc} + [\mathbf{1}_a \circ \Pi_a \circ \Gamma \circ \Pi_a \circ \mathbf{1}_a]^{dc}, \tag{D.3}$$

and result from the diagrams of η_a^{dc} by dividing through the squared bare vertex $[U^{dc}]^2 = (-u)^2$ [cf. Eq. (4.83a)].

The simplest diagrams are ladder diagrams $\gamma_{a,\mathrm{lad}}$, which all belong to the bosonic propagator η_r and whose logarithmic behavior was discussed in Eqs. (17) of our paper [P3]:

$$[\gamma_{a,\mathrm{lad}}^{(n\geq 2)}]^{dc}(\omega) = \ \text{<image>} \ \simeq (-u)^n[L(\omega)]^{n-1}, \tag{D.4a}$$

$$[\gamma_{p,\mathrm{lad}}^{(n\geq 2)}]^{dc}(\omega) = \ \text{<image>} \ \simeq (-u)^n[-L(-\omega)]^{n-1}. \tag{D.4b}$$

Note that we draw the diagrams according to the more general notation introduced in Chapter 4 and App. F in Ref. [P3]. Also the logarithmic term in the p channel deviates from the expressions in the paper due to the other frequency convention [cf. Eqs. (4.1) and Eqs. (5.3)]. This leads to the following ladder diagrams for the susceptibility (cf. Eq. (18) in Ref. [P3]):

$$[\chi_{a,\mathrm{lad}}^{(n)}]^{dc} = \ \text{<image>} \ \simeq (-u)^n L^{n+1}. \tag{D.5}$$

The crossed diagrams are constructed from the third-order contributions of the Hedin vertices $[\bar{\lambda}_a^{(2)}]^{dc} = [\lambda_a^{(2)}]^{dc}$:

$$[\bar{\lambda}_a^{(2)}]^{dc} = [\gamma_p^{(2)} \circ \Pi_a \circ \mathbf{1}_a]^{dc} = \ \text{<image>} \ = \ \text{<image>} \ = [\mathbf{1}_a \circ \Pi_a \circ \gamma_p^{(2)}]^{dc} = [\lambda_a^{(2)}]^{dc}. \tag{D.6}$$

In the paper [P3], the corresponding logarithmic behavior is computed in Eqs. (D14)–(D16). For the particle-hole susceptibility, the crossed diagram has the following leading-log behavior (cf. Eq. (19) in Ref. [P3]):

$$[\chi_{a,\times}^{(2)}]^{dc} = [\mathbf{1}_a \circ \Pi_a \circ \gamma_p^{(2)} \circ \Pi_a \circ \mathbf{1}_a]^{dc} = \ \text{<image>} \ \simeq -\tfrac{1}{3}u^2 L^3. \tag{D.7}$$

Together with the ladder diagrams $\chi_{a,\mathrm{lad}}^{dc}$, Eq. (D.7), we can describe the leading-log contributions up to second order: $\chi_{a,\mathrm{lead}}^{dc} = L - uL^2 + \tfrac{2}{3}u^2 L^3 + \mathcal{O}(u^3)$ (cf. Eq. (11) in Ref. [P3]).

In third order, besides the ladder diagram $[\chi_{a,\mathrm{lad}}^{(3)}]^{dc} \simeq -u^3 L^4$, we deduce the logarithmic behavior of the two diagrams involving a-reducible eye diagrams using the crossed diagram $[\chi_{a,\times}^{(2)}]^{dc}$, Eq. (D.7),

$$\text{<image>} \ = \ \text{<image>} \ = [\chi_{a,\times}^{(2)}]^{dc} U^{dc} [\chi_a^{(0)}]^{dc} = \tfrac{1}{3}u^3 L^4. \tag{D.8}$$

Since the leading-log term for $\chi_{a,\mathrm{lead}}^{dc}$ is $-\tfrac{1}{3}u^3 L^4$, this suggests that the logarithmic contributions from the two p-reducible eye diagrams and the p-reducible ladder diagram
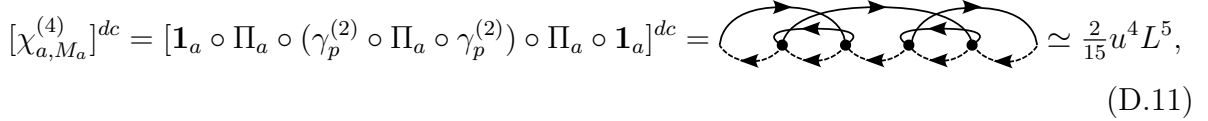
cancel:
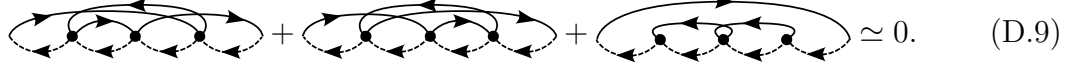
$$\simeq 0. \qquad (\text{D}.9)$$

All subleading-log contributions in third order are discussed in the paper [P3] (in particular see Eqs. (26)–(27) therein):


$$\simeq -\tfrac{1}{3}u^3 L^3. \qquad (\text{D}.10)$$

The first contribution includes the *t*-reducible diagram $[\gamma_t^{(3)}]^{dc}$ of third order and the two other contributions include the self-energy diagram $[\Sigma^{(2)}]^d$ of second order. When self-energy contributions are taken into account, the bare bubbles in Eqs. (D.2) are replaced by higher-order contributions involving higher-order contributions of the Green's functions.

In fourth-order perturbation theory, besides the ladder diagram $[\chi_{a,\text{lad}}^{(4)}]^{dc} \simeq u^4 L^5$, Eq. (D.7), we explicitly computed the contribution arising from the multi-boson exchange vertex (cf. Eq. (29) in Ref. [P3]),

$$[\chi_{a,M_a}^{(4)}]^{dc} = [\mathbf{1}_a \circ \Pi_a \circ (\gamma_p^{(2)} \circ \Pi_a \circ \gamma_p^{(2)}) \circ \Pi_a \circ \mathbf{1}_a]^{dc} = \quad \text{} \quad \simeq \tfrac{2}{15}u^4 L^5,$$

$$(\text{D}.11)$$

and two contributions that contain *a*-reducible eye diagrams and thus involve the crossed diagram, similarly to Eq. (D.12),
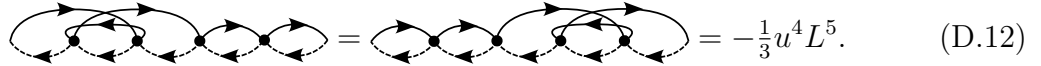
$$= \quad \text{} \quad = -\tfrac{1}{3}u^4 L^5. \qquad (\text{D}.12)$$

Further leading-log contributions at fourth order are missing to obtain the complete behavior $\tfrac{2}{15}u^4 L^5$ appearing in the power law of the susceptibility (cf. Eq. (11) in Ref. [P3]), not to mention subleading contribution involving the self-energy, *t*-reducible diagrams and the envelope diagrams.

Let us finally give an exact summation of the bare bubble Π_a^{dc} at finite temperature T involving the sharp local Green's function $G^c(\nu) = -\mathrm{i}\pi\rho\,\mathrm{sgn}(\nu)\Theta(\xi_0 - |\nu|)$:

$$\tfrac{1}{\beta}\sum_{\nu''}\Pi_a^{dc} = \tfrac{1}{\beta}\sum_{\nu''}G^c(\nu'')G^d(\nu''+\omega) = -\tfrac{\mathrm{i}\pi\rho}{\beta}\sum_{|\nu''|<\xi_0}\frac{\mathrm{sgn}(\nu'')}{\mathrm{i}(\nu''+\omega)-\xi_d}$$

$$= \tfrac{\rho}{2}\left[\psi(\tfrac{1}{2\pi T}(\pi T + \mathrm{i}\xi_d + \omega)) + \psi(\tfrac{1}{2\pi T}(\pi T - \mathrm{i}\xi_d - \omega))\right. \qquad (\text{D}.13)$$

$$\left. -\psi(\tfrac{1}{2\pi T}(3\pi T + 2\pi T\tilde{\xi}_0 + \mathrm{i}\xi_d + \omega)) - \psi(\tfrac{1}{2\pi T}(3\pi T + 2\pi T\tilde{\xi}_0 - \mathrm{i}\xi_d - \omega))\right].$$

Here, $\psi(z) = \mathrm{d}\ln\Gamma(z)/\mathrm{d}z$ is the digamma function and the parameter $\tilde{\xi}_0 = \lfloor \frac{1}{2\pi T}(\xi_0 - \pi T)\rfloor$ rounds the gap parameter ξ_0 off to the integer value corresponding to the closest Matsubara frequency. This formula is useful to test functionalities of our code.

D.2. Functional determinant approach

In App. A of our paper [P3], we mainly discuss how we compute benchmark data for the Fermi-edge singularity problem using the functional determinant approach (FDA). In this section, we provide some additional information that were not included there.

First of all, for zero interactions $U = 0$, where the single-particle Hamiltonians $\hat{h}_0$ and $\hat{h}_1$ (cf. Eq. (2.16) and Eq. (A1) in Ref. [P3]) coincide, the Green's function G^d of the core electron, G in the paper, yields (cf. Eq. (A7) in Ref. [P3])

$$G_0^d(t) = \mathrm{i}\Theta(-t)\mathrm{e}^{-\mathrm{i}\xi_d t}, \quad G_0^d(\nu) = [\nu - \mathrm{i}0^+ - \xi_d]^{-1}, \tag{D.14}$$

with $\mu = \xi_0$ and $\xi_d = \varepsilon_d - \xi_0$. This agrees with the bare Matsubara Green's function, Eq. (4.62c), and has a simple spectral function $A_0^d(\nu) = -\mathrm{Im}\, G_0^d(\nu)/\pi = \delta(\nu - \xi_d)$.

Also our FDA expression for the particle-hole susceptibility X_a^{dc}[1], X in the paper, (cf. Eq. (A18) in Ref. [P3]) is simplified for zero interactions,

$$X_{a,0}^{dc}(t) = -\mathrm{i}\Theta(t)\mathrm{e}^{\mathrm{i}\varepsilon_d t}\frac{1}{V}\sum_{\boldsymbol{k},\boldsymbol{k}'}\left[\mathrm{e}^{-\mathrm{i}\hat{h}_0 t}\left(\hat{\mathbb{1}} - f(\hat{h}_0)\right)\right]_{\boldsymbol{k}\boldsymbol{k}'} = -\mathrm{i}\Theta(t)\mathrm{e}^{\mathrm{i}\varepsilon_d t}\frac{1}{V}\sum_{\boldsymbol{k},\boldsymbol{k}'}\mathrm{e}^{-\mathrm{i}\varepsilon_{\boldsymbol{k}} t}\left[1 - \Theta(\xi_0 - \varepsilon_{\boldsymbol{k}})\right]$$

$$\simeq -\mathrm{i}\Theta(t)\mathrm{e}^{\mathrm{i}\varepsilon_d t}\rho\int_0^{2\xi_0}\mathrm{d}\varepsilon\,\mathrm{e}^{-\mathrm{i}\varepsilon t}\left[1 - \Theta(\xi_0 - \varepsilon)\right] = \frac{\rho}{t}(\mathrm{e}^{-2\mathrm{i}\xi_0 t} - \mathrm{e}^{-\mathrm{i}\xi_0 t}), \tag{D.15}$$

where in the last line the constant density of states $\rho(\varepsilon)$ (cf. Eq. (5) in Ref. [P3]) is inserted. The frequency representation follows as

$$X_{a,0}^{dc}(\omega) = -\mathrm{i}\,\rho\int_{\xi_0}^{2\xi_0}\mathrm{d}\varepsilon\int\mathrm{d}t\,\Theta(t)\mathrm{e}^{\mathrm{i}(\omega+\varepsilon_d-\varepsilon)t} = \rho\ln\frac{\omega + \mathrm{i}0^+ + \xi_d}{\omega + \mathrm{i}0^+ + \xi_d - \xi_0}, \tag{D.16}$$

which agrees with the imaginary-frequency result (cf. Eq. (D8) in Ref. [P3]). For a reliable check, we successively verified Eqs. (D.14)–(D.16) with our numerical FDA data[2].

---

[1] Following the conventions of the paper, i.e., Eq. (9), $X_a^{dc} = \rho\chi_a^{dc}$.

[2] As mentioned at the end of App. A of our paper [P3], the FDA requires a finite system size and we include a broadening of the spectra when performing their Fourier transform.

Bibliography

[P1] M. Gievers, E. Walter, A. Ge, J. von Delft, and F. B. Kugler, *Multiloop flow equations for single-boson exchange fRG*, Eur. Phys. J. B **95** (2022), no. 7, 1–22.

[P2] M. Gievers, M. Wagner, and R. Schmidt, *Probing polaron clouds by Rydberg atom spectroscopy*, Phys. Rev. Lett. **132** (2024), 053401.

[P3] M. Gievers, R. Schmidt, J. von Delft, and F. B. Kugler, *Subleading logarithmic behavior in the parquet formalism*, Phys. Rev. B **111** (2025), 085151.

[P4] M. Patricolo, M. Gievers, K. Fraboulet, A. Al-Eryani, S. Heinzelmann, P. M. Bonetti, A. Toschi, D. Vilardi, and S. Andergassen, *Single-boson exchange formulation of the Schwinger-Dyson equation and its application to the functional renormalization group*, SciPost Phys. **18** (2025), 078.

[P5] T. Müller, M. Gievers, H. Fröml, S. Diehl, and A. Chiocchetta, *Shape effects of localized losses in quantum wires: Dissipative resonances and nonequilibrium universality*, Phys. Rev. B **104** (2021), 155431.

[P6] M. Gievers, T. Müller, H. Fröml, S. Diehl, and A. Chiocchetta, *Quantum wires with local particle loss: Transport manifestations of fluctuation-induced effects*, Phys. Rev. B **110** (2024), 205419.

[AEM+95] M. H. Anderson, J. R. Ensher, M. R. Matthews, C. E. Wieman, and E. A. Cornell, *Observation of Bose-Einstein condensation in a dilute atomic vapor*, Science **269** (1995), no. 5221, 198–201.

[AG98] F. Aryasetiawan and O. Gunnarsson, *The GW method*, Reports on Progress in Physics **61** (1998), no. 3, 237.

[AGHW10] T. Amthor, C. Giese, C. S. Hofmann, and M. Weidemüller, *Evidence of antiblockade in an ultracold Rydberg gas*, Phys. Rev. Lett. **104** (2010), 013001.

[ALS+20] H. S. Adlong, W. E. Liu, F. Scazza, M. Zaccanti, N. D. Oppong, S. Fölling, M. M. Parish, and J. Levinsen, *Quasiparticle lifetime of the repulsive Fermi polaron*, Phys. Rev. Lett. **125** (2020), 133401.

[And65] D. G. Anderson, *Iterative procedures for nonlinear integral equations*, J. ACM **12** (1965), no. 4, 547–560.

[And67] P. W. Anderson, *Infrared catastrophe in Fermi gases with local scattering potentials*, Phys. Rev. Lett. **18** (1967), no. 24, 1049–1051.

[And00] P. W. Anderson, *Brainwashed by Feynman?*, Physics Today **53** (2000), no. 2, 11–12.

[ARR20] G. V. Astretsov, G. Rohringer, and A. N. Rubtsov, *Dual parquet scheme for the two-dimensional Hubbard model: Modeling low-energy physics of high-Tc cuprates with high momentum resolution*, Phys. Rev. B **101** (2020), no. 7, 075109.

[AS10] A. Altland and B. D. Simons, *Condensed matter field theory*, Cambridge University Press, 2010.

[BBN$^+$09] V. Bendkowsky, B. Butscher, J. Nipper, J. P. Shaffer, R. Löw, and T. Pfau, *Observation of ultralong-range Rydberg molecules*, Nature **458** (2009), no. 7241, 1005–1008.

[BCS57] J. Bardeen, L. N. Cooper, and J. R. Schrieffer, *Theory of superconductivity*, Physical Review **108** (1957), no. 5, 1175.

[BDN12] I. Bloch, J. Dalibard, and S. Nascimbene, *Quantum simulations with ultracold quantum gases*, Nature Physics **8** (2012), no. 4, 267–276.

[BDZ08] I. Bloch, J. Dalibard, and W. Zwerger, *Many-body physics with ultracold gases*, Rev. Mod. Phys. **80** (2008), 885–964.

[BHF$^+$24] C. Baroni, B. Huang, I. Fritsche, E. Dobler, G. Anich, E. Kirilov, R. Grimm, M. A. Bastarrachea-Magnani, P. Massignan, and G. M. Bruun, *Mediated interactions between Fermi polarons and the role of impurity quantum statistics*, Nature Physics **20** (2024), no. 1, 68–73.

[Bic04] N. E. Bickers, *Self-consistent many-body theory for condensed matter systems*, in: Sénéchal D., Tremblay A.-M., Bourbonnais C. (eds), Theoretical methods for strongly correlated electrons, CRM Series in Mathematical Physics, Springer, New York, 2004.

[BPD12] I. Boettcher, J. M. Pawlowski, and S. Diehl, *Ultracold atoms and the functional renormalization group*, Nuclear Physics B-Proceedings Supplements **228** (2012), 63–135.

[BPR11] J.-P. Blaizot, J. M. Pawlowski, and U. Reinosa, *Exact renormalization group and Φ-derivable approximations*, Phys. Lett. B **696** (2011), no. 5, 523–528.

[BPR21] J.-P. Blaizot, J. M. Pawlowski, and U. Reinosa, *Functional renormalization group and 2PI effective action formalism*, Annals of Physics **431** (2021), 168549.

[Bra12]   J. Braun, *Fermion interactions and universal behavior in strongly interacting theories*, Journal of Physics G: Nuclear and Particle Physics **39** (2012), no. 3, 033001.

[BTH+22] P. M. Bonetti, A. Toschi, C. Hille, S. Andergassen, and D. Vilardi, *Single boson exchange representation of the functional renormalization group for strongly interacting many-electron systems*, Phys. Rev. Res. **4** (2022), no. 1, 013034.

[BW91]   N. E. Bickers and S. R. White, *Conserving approximations for strongly fluctuating electron systems. II. Numerical results and parquet extension*, Phys. Rev. B **43** (1991), no. 10, 8044–8064.

[CB92]   C.-X. Chen and N. E. Bickers, *Numerical solution of parquet equations for the Anderson impurity model*, Solid State Communications **82** (1992), no. 5, 311–315.

[CBA+04] C. Chin, M. Bartenstein, A. Altmeyer, S. Riedl, S. Jochim, J. Hecker Denschlag, and R. Grimm, *Observation of the pairing gap in a strongly interacting Fermi gas*, Science **305** (2004), no. 5687, 1128–1130.

[CGJT10] C. Chin, R. Grimm, P. Julienne, and E. Tiesinga, *Feshbach resonances in ultracold gases*, Rev. Mod. Phys. **82** (2010), 1225–1286.

[Che06]   F. Chevy, *Universal phase diagram of a strongly interacting Fermi gas with unbalanced spin populations*, Phys. Rev. A **74** (2006), no. 6, 063628.

[Chr23]   A. Christianen, *Chemistry in a quantum medium: Bose polarons, ultracold molecules, and quantum computing*, PhD Thesis, TU München, 2023.

[CJL+16] M. Cetina, M. Jag, R. S. Lous, I. Fritsche, J. T. M. Walraven, R. Grimm, J. Levinsen, M. M. Parish, R. Schmidt, M. Knap, and E. Demler, *Ultrafast many-body interferometry of impurities coupled to a Fermi sea*, Science **354** (2016), no. 6308, 96–99.

[CJT74]   J. M. Cornwall, R. Jackiw, and E. Tomboulis, *Effective action for composite operators*, Phys. Rev. D **10** (1974), 2428–2445.

[CMS24]   C.-C. Chien, S. I. Mistakidis, and H. R. Sadeghpour, *Breaking and trapping Cooper pairs by Rydberg-molecule spectroscopy in atomic Fermi superfluids*, Phys. Rev. A **110** (2024), L051303.

[CRLC07] R. Combescot, A. Recati, C. Lobo, and F. Chevy, *Normal state of highly polarized Fermi gases: Simple many-body approaches*, Phys. Rev. Lett. **98** (2007), no. 18, 180402.

[CSPR⁺18] G. Calvanese Strinati, P. Pieri, G. Röpke, P. Schuck, and M. Urban, *The BCS–BEC crossover: From ultra-cold Fermi gases to nuclear systems*, Physics Reports **738** (2018), 1–76.

[CSW⁺18] F. Camargo, R. Schmidt, J. D. Whalen, R. Ding, G. Woehl, S. Yoshida, J. Burgdörfer, F. B. Dunning, H. R. Sadeghpour, E. Demler, and T. C. Killian, *Creation of Rydberg polarons in a Bose gas*, Phys. Rev. Lett. **120** (2018), 083401.

[DAD⁺15] B. J. DeSalvo, J. A. Aman, F. B. Dunning, T. C. Killian, H. R. Sadeghpour, S. Yoshida, and J. Burgdörfer, *Ultra-long-range Rydberg molecules in a divalent atomic system*, Phys. Rev. A **92** (2015), no. 3, 031403.

[DCE⁺21] N. Dupuis, L. Canet, A. Eichhorn, W. Metzner, J. M. Pawlowski, M. Tissier, and N. Wschebor, *The nonperturbative functional renormalization group and its applications*, Physics Reports **910** (2021), 1–114.

[DG87] N. Y. Du and C. H. Greene, *Interaction between a Rydberg atom and neutral perturbers*, Phys. Rev. A **36** (1987), no. 2, 971.

[DHP24] E. Dizer, J. Horak, and J. M. Pawlowski, *Spectral properties and observables in ultracold Fermi gases*, Phys. Rev. A **109** (2024), no. 6, 063311.

[Die23] O. K. Diessel, *Polaron physics and phase transitions in light-matter systems*, PhD Thesis, TU München, 2023.

[DJ21] J. Diekmann and S. G. Jakobs, *Parquet approximation and one-loop renormalization group: Equivalence on the leading-logarithmic level*, Phys. Rev. B **103** (2021), no. 15, 155156.

[DJ24] J. Diekmann and S. G. Jakobs, *Leading-logarithmic approximation by one-loop renormalization group within Matsubara formalism*, Phys. Rev. B **109** (2024), no. 11, 115134.

[DM64] C. de Dominicis and P. C. Martin, *Stationary entropy principle and renormalization in normal and superfluid systems. I. Algebraic formulation*, Journal of Mathematical Physics **5** (1964), no. 1, 14–30.

[DMA⁺95] K. B. Davis, M.-O. Mewes, M. R. Andrews, N. J. van Druten, D. S. Durfee, D. M. Kurn, and W. Ketterle, *Bose-Einstein condensation in a gas of sodium atoms*, Phys. Rev. Lett. **75** (1995), 3969–3973.

[DMCS24] O. K. Diessel, J. von Milczewski, A. Christianen, and R. Schmidt, *Probing molecular spectral functions and unconventional pairing using Raman spectroscopy*, Phys. Rev. Res. **6** (2024), 023239.

[Dup14] N. Dupuis, *Nonperturbative renormalization-group approach to fermion systems in the two-particle-irreducible effective action formalism*, Phys. Rev. B **89** (2014), no. 3, 035113.

[EGS09] A. Eichhorn, H. Gies, and M. M. Scherer, *Asymptotically free scalar curvature-ghost coupling in quantum Einstein gravity*, Phys. Rev. D **80** (2009), 104003.

[EHF⁺24] A. Al-Eryani, S. Heinzelmann, K. Fraboulet, F. Krien, and S. Andergassen, *Screening and effective RPA-like charge susceptibility in the extended Hubbard model*, 2024, arXiv:2412.07323.

[EHHK20] C. J. Eckhardt, C. Honerkamp, K. Held, and A. Kauch, *Truncated unity parquet solver*, Phys. Rev. B **101** (2020), no. 15, 155104.

[Eil19] M. T. Eiles, *Trilobites, butterflies, and other exotic specimens of long-range Rydberg molecules*, Journal of Physics B: Atomic, Molecular and Optical Physics **52** (2019), no. 11, 113001.

[EKKH23] C. J. Eckhardt, P. Kappl, A. Kauch, and K. Held, *A functional-analysis derivation of the parquet equation*, SciPost Physics **15** (2023), no. 5, 203.

[ERST24] H. Eßl, M. Reitner, G. Sangiovanni, and A. Toschi, *General Shiba mapping for on-site four-point correlation functions*, Phys. Rev. Res. **6** (2024), no. 3, 033061.

[ESEH18] C. J. Eckhardt, G. A. H. Schober, J. Ehrlich, and C. Honerkamp, *Truncated-unity parquet equations: Application to the repulsive Hubbard model*, Phys. Rev. B **98** (2018), no. 7, 075143.

[FBD⁺21] I. Fritsche, C. Baroni, E. Dobler, E. Kirilov, B. Huang, R. Grimm, G. M. Bruun, and P. Massignan, *Stability and breakdown of Fermi polarons in a strongly interacting Fermi-Bose mixture*, Phys. Rev. A **103** (2021), 053314.

[Fey82] R. P. Feynman, *Simulating physics with computers*, International Journal of Theoretical Physics **21** (1982), no. 6, 467–488.

[FGH⁺14] M. M. Forbes, A. Gezerlis, K. Hebeler, T. Lesinski, and A. Schwenk, *Neutron polaron as a constraint on nuclear density functionals*, Phys. Rev. C **89** (2014), 041301.

[FHB⁺22] K. Fraboulet, S. Heinzelmann, P. M. Bonetti, A. Al-Eryani, D. Vilardi, A. Toschi, and S. Andergassen, *Single-boson exchange functional renormalization group application to the two-dimensional Hubbard model at weak coupling*, Eur. Phys. J. B **95** (2022), no. 12, 202.

[FHS20] C. Fey, F. Hummel, and P. Schmelcher, *Ultralong-range Rydberg molecules*, Molecular Physics **118** (2020), no. 2, e1679401.

[FKW10] S. Friederich, H. C. Krahl, and C. Wetterich, *Four-point vertex in the Hubbard model and partial bosonization*, Phys. Rev. B **81** (2010), no. 23, 235108.

[FPR20] W.-J. Fu, J. M. Pawlowski, and F. Rennecke, *QCD phase structure at finite temperature and density*, Phys. Rev. D **101** (2020), 054032.

[Frö54] H. Fröhlich, *Electrons in lattice fields*, Advances in Physics **3** (1954), no. 11, 325–361.

[FRJ+24] Y. Núñez Fernández, M. K. Ritter, M. Jeannin, J.-W. Li, T. Kloss, T. Louvet, S. Terasaki, O. Parcollet, J. von Delft, H. Shinaoka, and X. Waintal, *Learning tensor networks with tensor cross interpolation: new algorithms and libraries*, 2024, arXiv:2407.02454.

[FSIS20] C. Fey, P. Schmelcher, A. İmamoğlu, and R. Schmidt, *Theory of exciton-electron scattering in atomically thin semiconductors*, Phys. Rev. B **101** (2020), no. 19, 195417.

[FW09] S. Floerchinger and C. Wetterich, *Exact flow equation for composite operators*, Physics Letters B **680** (2009), no. 4, 371–376.

[GDS00] C. H. Greene, A. S. Dickinson, and H. R. Sadeghpour, *Creation of polar and nonpolar ultra-long-range Rydberg molecules*, Phys. Rev. Lett. **85** (2000), no. 12, 2458.

[GHL+24] A. Ge, J. Halbinger, S.-S. B. Lee, J. von Delft, and F. B. Kugler, *Analytic continuation of multipoint correlation functions*, Annalen der Physik (2024), 2300504.

[GKKR96] A. Georges, G. Kotliar, W. Krauth, and M. J. Rozenberg, *Dynamical mean-field theory of strongly correlated fermion systems and the limit of infinite dimensions*, Rev. Mod. Phys. **68** (1996), 13–125.

[GRS+12] G. Günter, M. Robert-de Saint-Vincent, H. Schempp, C. S. Hofmann, S. Whitlock, and M. Weidemüller, *Interaction enhanced imaging of individual Rydberg atoms in dense gases*, Phys. Rev. Lett. **108** (2012), 013002.

[GRJ03] M. Greiner, C. A. Regal, and D. S. Jin, *Emergence of a molecular Bose–Einstein condensate from a Fermi gas*, Nature **426** (2003), no. 6966, 537–540.

[GRW+24] A. Ge, N. Ritz, E. Walter, S. Aguirre, J. von Delft, and F. B. Kugler, *Real-frequency quantum field theory applied to the single-impurity Anderson model*, Phys. Rev. B **109** (2024), no. 11, 115128.

[Hed65] L. Hedin, *New method for calculating the one-particle Green's function with application to the electron-gas problem*, Phys. Rev. **139** (1965), no. 3A, A796–A823.

[HGS12] C. Husemann, K.-U. Giering, and M. Salmhofer, *Frequency-dependent vertex functions of the (t,t') Hubbard model at weak coupling*, Phys. Rev. B **85** (2012), no. 7, 075121.

[HJY24] M. Homenda, P. Jakubczyk, and H. Yamase, *Generalized Hertz action and quantum criticality of two-dimensional Fermi systems*, Phys. Rev. B **110** (2024), no. 12, L121102.

[HKE$^+$20] C. Hille, F. B. Kugler, C. J. Eckhardt, Y.-Y. He, A. Kauch, C. Honerkamp, A. Toschi, and S. Andergassen, *Quantitative functional renormalization group description of the two-dimensional Hubbard model*, Phys. Rev. Res. **2** (2020), 033372.

[HKT08] K. Held, A. A. Katanin, and A. Toschi, *Dynamical vertex approximation: An introduction*, Progress of Theoretical Physics Supplement **176** (2008), 117–133.

[HL24] H. Hu and X.-J. Liu, *Spectral function of Fermi polarons at finite temperature from a self-consistent many-body T-matrix approach in real frequency*, Phys. Rev. A **109** (2024), no. 6, 063313.

[HLK21] V. Harkov, A. I. Lichtenstein, and F. Krien, *Parametrizations of local vertex corrections from weak to strong coupling: importance of the Hedin three-leg vertex*, Phys. Rev. B **104** (2021), no. 12, 125141.

[HRAE04] C. Honerkamp, D. Rohe, S. Andergassen, and T. Enss, *Interaction flow method for many-fermion systems*, Phys. Rev. B **70** (2004), no. 23, 235115.

[HRHA20] C. Hille, D. Rohe, C. Honerkamp, and S. Andergassen, *Pseudogap opening in the two-dimensional Hubbard model: A functional renormalization group analysis*, Phys. Rev. Res. **2** (2020), 033068.

[HS09] C. Husemann and M. Salmhofer, *Efficient parametrization of the vertex function, ω scheme, and the t,t' Hubbard model at van Hove filling*, Phys. Rev. B **79** (2009), no. 19, 195125.

[HSS23] J. Halbinger, B. Schneider, and B. Sbierski, *Spectral representation of Matsubara n-point functions: Exact kernel functions and applications*, SciPost Physics **15** (2023), no. 5, 183.

[HVB$^+$21] V. Harkov, M. Vandelli, S. Brener, A. I. Lichtenstein, and E. A. Stepanov, *Impact of partially bosonized collective fluctuations on electronic degrees of freedom*, Phys. Rev. B **103** (2021), no. 24, 245123.

[JL23] P. Jentsch and C. F. Lee, *Critical phenomena in compressible polar active fluids: Dynamical and functional renormalization group studies*, Phys. Rev. Res. **5** (2023), no. 2, 023061.

[JW03] J. Jaeckel and C. Wetterich, *Flow equations without mean field ambiguity*, Phys. Rev. D **68** (2003), 025020.

[Kat04] A. A. Katanin, *Fulfillment of Ward identities in the functional renormalization group approach*, Phys. Rev. B **70** (2004), no. 11, 115109.

[Kat19] A. A. Katanin, *Extended dynamical mean field theory combined with the two-particle irreducible functional renormalization-group approach as a tool to study strongly correlated systems*, Phys. Rev. B **99** (2019), no. 11, 115112.

[KBC$^+$10] P. Kopietz, L. Bartosch, L. Costa, A. Isidori, and A. Ferraz, *Ward identities for the Anderson impurity model: derivation via functional methods and the exact renormalization group*, Journal of Physics A: Mathematical and Theoretical **43** (2010), no. 38, 385004.

[KBS10] P. Kopietz, L. Bartosch, and F. Schütz, *Introduction to the functional renormalization group*, Lecture Notes in Physics, vol. 798, Springer Berlin Heidelberg, Berlin, Heidelberg, 2010.

[KCP22] J. Kaye, K. Chen, and O. Parcollet, *Discrete Lehmann representation of imaginary time Green's functions*, Phys. Rev. B **105** (2022), 235115.

[KD18a] F. B. Kugler and J. von Delft, *Fermi-edge singularity and the functional renormalization group*, Journal of Physics: Condensed Matter **30** (2018), no. 19, 195501.

[KD18b] F. B. Kugler and J. von Delft, *Multiloop functional renormalization group for general models*, Phys. Rev. B **97** (2018), 035162.

[KD18c] F. B. Kugler and J. von Delft, *Multiloop functional renormalization group that sums up all parquet diagrams*, Phys. Rev. Lett. **120** (2018), 057403.

[KD18d] F. B. Kugler and J. von Delft, *Derivation of exact flow equations from the self-consistent parquet relations*, New J. Phys. **20** (2018), no. 12, 123029.

[Kel22] C. T. Kelley, *Solving nonlinear equations with iterative methods: Solvers and examples in Julia*, SIAM, 2022.

[KGR$^+$24] D. Kiese, A. Ge, N. Ritz, J. von Delft, and N. Wentzell, *MatsubaraFunctions.jl: An equilibrium Green's function library in the Julia programming language*, SciPost Physics Codebases (2024), 024.

[KK22] F. Krien and A. Kauch, *The plain and simple parquet approximation: single-and multi-boson exchange in the two-dimensional Hubbard model*, Eur. Phys. J. B **95** (2022), no. 4, 69.

[KKH21] F. Krien, A. Kauch, and K. Held, *Tiling with triangles: parquet and GWγ methods unified*, Phys. Rev. Res. **3** (2021), 013149.

[KLD21] F. B. Kugler, S.-S. B. Lee, and J. von Delft, *Multipoint correlation functions: Spectral representation and numerical evaluation*, Phys. Rev. X **11** (2021), no. 4, 041006.

[Kli03] I. Klich, *An elementary derivation of Levitov's formula*, Quantum Noise in Mesoscopic Physics (Yuli V. Nazarov, ed.), Springer Netherlands, Dordrecht, 2003, pp. 397–402.

[KLR20] F. Krien, A. I. Lichtenstein, and G. Rohringer, *Fluctuation diagnostic of the nodal/antinodal dichotomy in the Hubbard model at weak coupling: A parquet dual fermion approach*, Phys. Rev. B **102** (2020), no. 23, 235133.

[KMI+22] D. Kiese, T. Müller, Y. Iqbal, R. Thomale, and S. Trebst, *Multiloop functional renormalization group approach to quantum spin systems*, Phys. Rev. Res. **4** (2022), 023185.

[KP14] P. Kroiss and L. Pollet, *Diagrammatic Monte Carlo study of quasi-two-dimensional Fermi polarons*, Phys. Rev. B **90** (2014), no. 10, 104510.

[KP15] P. Kroiss and L. Pollet, *Diagrammatic Monte Carlo study of a mass-imbalanced Fermi-polaron system*, Phys. Rev. B **91** (2015), no. 14, 144507.

[KPA+20] A. Kauch, P. Pudleiner, K. Astleithner, P. Thunström, T. Ribic, and K. Held, *Generic optical excitations of correlated systems: π-tons*, Phys. Rev. Lett. **124** (2020), no. 4, 047401.

[KPV+12] M. Koschorreck, D. Pertot, E. Vogt, B. Fröhlich, M. Feld, and M. Köhl, *Attractive and repulsive Fermi polarons in two dimensions*, Nature **485** (2012), no. 7400, 619–622.

[Kri18] F. Krien, *Conserving dynamical mean-field approaches to strongly correlated systems*, PhD Thesis, Universität Hamburg, 2018.

[KSC+25] D. Kiese, H. U. R. Strand, K. Chen, N. Wentzell, O. Parcollet, and J. Kaye, *Discrete Lehmann representation of three-point functions*, Phys. Rev. B **111** (2025), 035135.

[KSN+12] M. Knap, A. Shashi, Y. Nishida, A. Imambekov, D. A. Abanin, and E. Demler, *Time-dependent impurity in ultracold fermions: Orthogonality catastrophe and beyond*, Phys. Rev. X **2** (2012), no. 4, 041020.

[Kug21] F. B. Kugler, *Renormalization group approaches to strongly correlated electron systems*, PhD Thesis, Ludwig-Maximilians-Universität München, 2021.

[KV04]   G. Kotliar and D. Vollhardt, *Strongly correlated materials: Insights from dynamical mean-field theory*, Physics Today **57** (2004), no. 3, 53–59.

[KV19]   F. Krien and A. Valli, *Parquetlike equations for the Hedin three-leg vertex*, Phys. Rev. B **100** (2019), no. 24, 245147.

[KVC19]   F. Krien, A. Valli, and M. Capone, *Single-boson exchange decomposition of the vertex function*, Phys. Rev. B **100** (2019), 155149.

[KVC+20]   F. Krien, A. Valli, P. Chalupa, M. Capone, A. I. Lichtenstein, and A. Toschi, *Boson-exchange parquet solver for dual fermions*, Phys. Rev. B **102** (2020), no. 19, 195131.

[KWK+24]   D. Kiese, N. Wentzell, I. Krivenko, O. Parcollet, K. Held, and F. Krien, *Embedded multi-boson exchange: A step beyond quantum cluster theories*, Phys. Rev. Res. **6** (2024), 043159.

[KZJ+12]   C. Kohstall, M. Zaccanti, M. Jag, A. Trenkwalder, P. Massignan, G. M. Bruun, F. Schreck, and R. Grimm, *Metastability and coherence of repulsive polarons in a strongly interacting Fermi mixture*, Nature **485** (2012), no. 7400, 615–618.

[Lan33]   L. D. Landau, *Electron motion in crystal lattices*, Phys. Z. Sowjet. **3** (1933), 664.

[LC24]   R. Liu and X. Cui, *Competing few-body correlations in ultracold Fermi polarons*, AAPPS Bulletin **34** (2024), no. 1, 29.

[LDSK15]   P. Lange, C. Drukier, A. Sharma, and P. Kopietz, *Summing parquet diagrams using the functional renormalization group: X-ray problem revisited*, Journal of Physics A: Mathematical and Theoretical **48** (2015), no. 39, 395001.

[Lit01]   D. F. Litim, *Optimized renormalization group flows*, Phys. Rev. D **64** (2001), 105007.

[LKD21]   S.-S. B. Lee, F. B. Kugler, and J. von Delft, *Computing local multipoint correlators using the numerical renormalization group*, Phys. Rev. X **11** (2021), no. 4, 041007.

[LKPH19]   G. Li, A. Kauch, P. Pudleiner, and K. Held, *The victory project v1.0: An efficient parquet equations solver*, Computer Physics Communications **241** (2019), 146–154.

[LLL96]   L. S. Levitov, H. Lee, and G. B. Lesovik, *Electron counting statistics and coherent states of electric current*, Journal of Mathematical Physics **37** (1996), no. 10, 4845–4866.

[LLP19] W. E. Liu, J. Levinsen, and M. M. Parish, *Variational approach for impurity dynamics at finite temperature*, Phys. Rev. Lett. **122** (2019), no. 20, 205301.

[LP48] L. D. Landau and S. I. Pekar, *Effective mass of a polaron*, Zh. Eksp. Teor. Fiz. **18** (1948), no. 5, 419–423.

[LPR+17] J. Lichtenstein, D. de la Peña, D. Rohe, E. di Napoli, C. Honerkamp, and S. A. Maier, *High-performance functional renormalization group calculations for interacting fermions*, Computer Physics Communications **213** (2017), 100–110.

[LWP+16] G. Li, N. Wentzell, P. Pudleiner, P. Thunström, and K. Held, *Efficient implementation of the parquet equations: Role of the reducible vertex function and its kernel approximation*, Phys. Rev. B **93** (2016), no. 16, 165103.

[LWP+17] J. Lichtenstein, J. Winkelmann, D. Sánchez de la Peña, T. Vidović, and E. di Napoli, *Parallel adaptive integration in high-performance functional Renormalization Group computations*, High-Performance Scientific Computing: First JARA-HPC Symposium, JHPCS 2016, Aachen, Germany, October 4–5, 2016, Revised Selected Papers 1, Springer, 2017, pp. 170–184.

[MC09] C. Mora and F. Chevy, *Ground state of a tightly bound composite dimer immersed in a Fermi sea*, Phys. Rev. A **80** (2009), 033607.

[Mil24] J. von Milczewski, *Quasiparticle formation and induced correlations in strongly coupled Bose-Fermi mixtures*, PhD Thesis, Universität Heidelberg, 2023.

[Mor94] T. R. Morris, *The exact renormalization group and approximate solutions*, International Journal of Modern Physics A **09** (1994), no. 14, 2411–2449.

[MPY+19] B. Mukherjee, P. B. Patel, Z. Yan, R. J. Fletcher, J. Struck, and M. W. Zwierlein, *Spectral response and contact of the unitary Fermi gas*, Phys. Rev. Lett. **122** (2019), 203402.

[MRS22] J. von Milczewski, F. Rose, and R. Schmidt, *Functional-renormalization-group approach to strongly coupled Bose-Fermi mixtures in two dimensions*, Phys. Rev. A **105** (2022), no. 1, 013317.

[MS24] J. von Milczewski and R. Schmidt, *Momentum-dependent quasiparticle properties of the Fermi polaron from the functional renormalization group*, Phys. Rev. A **110** (2024), 033309.

[MSH+12] W. Metzner, M. Salmhofer, C. Honerkamp, V. Meden, and K. Schönhammer, *Functional renormalization group approach to correlated fermion systems*, Rev. Mod. Phys. **84** (2012), no. 1, 299–352.

[MZB14] P. Massignan, M. Zaccanti, and G. M. Bruun, *Polarons, dressed molecules and itinerant ferromagnetism in ultracold Fermi gases*, Reports on Progress in Physics **77** (2014), no. 3, 034401.

[ND69] P. Nozières and C. T. de Dominicis, *Singularities in the X-ray absorption and emission of metals. III. One-body theory exact solution*, Physical Review **178** (1969), no. 3, 1097.

[NGR69] P. Nozières, J. Gavoret, and B. Roulet, *Singularities in the X-ray absorption and emission of metals. II. Self-consistent treatment of divergences*, Physical Review **178** (1969), no. 3, 1084.

[NNJ+09] S. Nascimbène, N. Navon, K. J. Jiang, L. Tarruell, M. Teichmann, J. McKeever, F. Chevy, and C. Salomon, *Collective oscillations of an imbalanced Fermi gas: Axial compression modes and polaron effective mass*, Phys. Rev. Lett. **103** (2009), 170402.

[NO98] J. W. Negele and H. Orland, *Quantum many-particle systems*, Westview Press Boulder, CO, 1998.

[NSF+20] G. Ness, C. Shkedrov, Y. Florshaim, O. K. Diessel, J. von Milczewski, R. Schmidt, and Y. Sagi, *Observation of a smooth polaron-molecule transition in a degenerate Fermi gas*, Phys. Rev. X **10** (2020), 041019.

[PDZ09] M. Punk, P. T. Dumitrescu, and W. Zwerger, *Polaron-to-molecule transition in a strongly imbalanced Fermi gas*, Phys. Rev. A **80** (2009), no. 5, 053605.

[PG18] D. Pimenov and M. Goldstein, *Spectra of heavy polarons and molecules coupled to a Fermi sea*, Phys. Rev. B **98** (2018), 220302.

[PS08] N. Prokof'ev and B. Svistunov, *Fermi-polaron problem: Diagrammatic Monte Carlo method for divergent sign-alternating series*, Phys. Rev. B **77** (2008), 020408.

[PSSW17] J. M. Pawlowski, M. M. Scherer, R. Schmidt, and S. J. Wetzel, *Physics and the choice of regulators in functional renormalisation group flows*, Annals of Physics **384** (2017), 165–197.

[PST00] S. Pairault, D. Sénéchal, and A.-M. S. Tremblay, *Strong-coupling perturbation theory of the Hubbard model*, Eur. Phys. J. B **16** (2000), no. 1, 85–105.

[Pun09] M. Punk, *Many-particle physics with ultracold gases*, PhD Thesis, TU München, 2009.

[RFW+24] M. K. Ritter, Y. Núñez Fernández, M. Wallerberger, J. von Delft, H. Shinaoka, and X. Waintal, *Quantics tensor cross interpolation for high-resolution, parsimonious representations of multivariate functions in physics and beyond*, Phys. Rev. Lett. **132** (2024), no. 5, 056501.

[RGN69] B. Roulet, J. Gavoret, and P. Nozières, *Singularities in the X-ray absorption and emission of metals. I. First-order parquet calculation*, Phys. Rev. **178** (1969), no. 3, 1072–1083.

[RGW+24] N. Ritz, A. Ge, E. Walter, Santiago Aguirre Lamus, J. von Delft, and F. B. Kugler, *KeldyshQFT: A C++ codebase for real-frequency multiloop functional renormalization group and parquet computations of the single-impurity Anderson model*, The Journal of Chemical Physics **161** (2024), no. 5, 054118.

[RHT+18] G. Rohringer, H. Hafermann, A. Toschi, A. A. Katanin, A. E. Antipov, M. I. Katsnelson, A. I. Lichtenstein, A. N. Rubtsov, and K. Held, *Diagrammatic routes to nonlocal correlations beyond dynamical mean field theory*, Rev. Mod. Phys. **90** (2018), 025003.

[RJM15] J. F. Rentrop, S. G. Jakobs, and V. Meden, *Two-particle irreducible functional renormalization group schemes—a comparative study*, Journal of Physics A: Mathematical and Theoretical **48** (2015), no. 14, 145002.

[RKM+22] M. K. Ritter, D. Kiese, T. Müller, F. B. Kugler, R. Thomale, S. Trebst, and J. von Delft, *Benchmark calculations of multiloop pseudofermion fRG*, Eur. Phys. J. B **95** (2022), no. 7, 102.

[RMJ16] J. F. Rentrop, V. Meden, and S. G. Jakobs, *Renormalization group flow of the Luttinger-Ward functional: Conserving approximations and application to the Anderson impurity model*, Phys. Rev. B **93** (2016), no. 19, 195160.

[Roh13] G. Rohringer, *New routes towards a theoretical treatment of nonlocal electronic correlations*, PhD Thesis, TU Wien, 2013.

[Roh23] S. Rohshap, *Analytical calculation of two-particle vertices for multiorbital Hubbard atom*, Master's Thesis, TU Wien, 2023.

[RRS+24] S. Rohshap, M. K. Ritter, H. Shinaoka, J. von Delft, M. Wallerberger, and A. Kauch, *Two-particle calculations with quantics tensor trains – solving the parquet equations*, 2024, arXiv:2410.22975.

[SBC+17] M. Sidler, P. Back, O. Cotlet, A. Srivastava, T. Fink, M. Kroner, E. Demler, and A. İmamoğlu, *Fermi polaron-polaritons in charge-tunable atomically thin semiconductors*, Nature Physics **13** (2017), no. 3, 255–261.

[SCC+20] D. Springer, P. Chalupa, S. Ciuchi, G. Sangiovanni, and A. Toschi, *Interplay between local response and vertex divergences in many-fermion systems with on-site attraction*, Phys. Rev. B **101** (2020), no. 15, 155148.

[Sch13] R. Schmidt, *From few- to many-body physics with ultracold atoms*, PhD Thesis, TU München, 2013.

[SE11]   R. Schmidt and T. Enss, *Excitation spectra and rf response near the polaron-to-molecule transition from the functional renormalization group*, Phys. Rev. A **83** (2011), no. 6, 063620.

[SGW⁺20] H. Shinaoka, D. Geffroy, M. Wallerberger, J. Otsuki, K. Yoshimi, E. Gull, and J. Kuneš, *Sparse sampling and tensor network representation of two-particle Green's functions*, SciPost Physics **8** (2020), no. 1, 012.

[Sha94]   R. Shankar, *Renormalization-group approach to interacting fermions*, Rev. Mod. Phys. **66** (1994), 129–192.

[SKI⁺18] R. Schmidt, M. Knap, D. A. Ivanov, J.-S. You, M. Cetina, and E. Demler, *Universal many-body response of heavy impurities coupled to a Fermi sea: a review of recent progress*, Reports on Progress in Physics **81** (2018), no. 2, 024401.

[SLE⁺16] M. Schlagmüller, T. C. Liebisch, F. Engel, K. S. Kleinbach, F. Böttcher, U. Hermann, K. M. Westphal, A. Gaj, R. Löw, S. Hofferberth, T. Pfau, J. Pérez-Ríos, and C. H. Greene, *Ultracold chemical reactions of a single Rydberg atom in a dense gas*, Phys. Rev. X **6** (2016), 031020.

[SLN⁺16] M. Schlagmüller, T. C. Liebisch, H. Nguyen, G. Lochead, F. Engel, F. Böttcher, K. M. Westphal, K. S. Kleinbach, R. Löw, S. Hofferberth, T. Pfau, J. Pérez-Ríos, and C. H. Greene, *Probing an electron scattering resonance using Rydberg molecules within a dense and ultracold gas*, Phys. Rev. Lett. **116** (2016), no. 5, 053001.

[SMacT⁺22] D. di Sante, M. Medvidović, A. Toschi, G. Sangiovanni, C. Franchini, A. M. Sengupta, and A. J. Millis, *Deep learning the functional renormalization group*, Phys. Rev. Lett. **129** (2022), 136402.

[SN11]   J. J. Sakurai and J. Napolitano, *Modern quantum mechanics*, 2. ed., international ed ed., Addison-Wesley, Pearson, Boston, Mass., 2011.

[SSD16]   R. Schmidt, H. R. Sadeghpour, and E. Demler, *Mesoscopic Rydberg impurity in an atomic quantum gas*, Phys. Rev. Lett. **116** (2016), no. 10, 105302.

[SVM⁺17] F. Scazza, G. Valtolina, P. Massignan, A. Recati, A. Amico, A. Burchianti, C. Fort, M. Inguscio, M. Zaccanti, and G. Roati, *Repulsive Fermi polarons in a resonant mixture of ultracold ^{6}Li atoms*, Phys. Rev. Lett. **118** (2017), 083602.

[SWD⁺18] R. Schmidt, J. D. Whalen, R. Ding, F. Camargo, G. Woehl, S. Yoshida, J. Burgdörfer, F. B. Dunning, E. Demler, H. R. Sadeghpour, and T. C. Killian, *Theory of excitation of Rydberg polarons in an atomic quantum gas*, Phys. Rev. A **97** (2018), no. 2, 022707.

[SWS⁺21] T. Schäfer, N. Wentzell, F. Šimkovic, Y.-Y. He, C. Hille, M. Klett, C. J. Eckhardt, B. Arzhang, V. Harkov, F.-M. Le Régent, A. Kirsch, Y. Wang, A. J. Kim, E. Kozik, E. A. Stepanov, A. Kauch, S. Andergassen, P. Hansmann, D. Rohe, Y. M. Vilk, J. P. F. LeBlanc, S. Zhang, A.-M. S. Tremblay, M. Ferrero, O. Parcollet, and A. Georges, *Tracking the footprints of spin fluctuations: A multimethod, multimessenger study of the two-dimensional hubbard model*, Phys. Rev. X **11** (2021), 011058.

[SWSZ09] A. Schirotzek, C.-H. Wu, A. Sommer, and M. W. Zwierlein, *Observation of Fermi polarons in a tunable Fermi liquid of ultracold atoms*, Phys. Rev. Lett. **102** (2009), no. 23, 230402.

[TAB⁺14] C. Taranto, S. Andergassen, J. Bauer, K. Held, A. Katanin, W. Metzner, G. Rohringer, and A. Toschi, *From infinite to two dimensions through the functional renormalization group*, Phys. Rev. Lett. **112** (2014), no. 19, 196402.

[TC12] C. Trefzger and Y. Castin, *Impurity in a fermi sea on a narrow Feshbach resonance: A variational study of the polaronic and dimeronic branches*, Phys. Rev. A **85** (2012), 053612.

[TFY⁺13] K.-M. Tam, H. Fotso, S.-X. Yang, T.-W. Lee, J. Moreno, J. Ramanujam, and M. Jarrell, *Solving the parquet equations for the Hubbard model beyond weak coupling*, Phys. Rev. E **87** (2013), no. 1, 013311.

[TGCR18] P. Thunström, O. Gunnarsson, S. Ciuchi, and G. Rohringer, *Analytical investigation of singularities in two-particle irreducible vertex functions of the Hubbard atom*, Phys. Rev. B **98** (2018), no. 23, 235107.

[THK⁺19] A. Tagliavini, C. Hille, F. B. Kugler, S. Andergassen, A. Toschi, and C. Honerkamp, *Multiloop functional renormalization group for the two-dimensional Hubbard model: Loop convergence of the response functions*, SciPost Physics **6** (2019), no. 1, 009.

[TKH07] A. Toschi, A. A. Katanin, and K. Held, *Dynamical vertex approximation: A step beyond dynamical mean-field theory*, Phys. Rev. B **75** (2007), no. 4, 045118.

[TRK⁺20] J. Thoenniss, M. K. Ritter, F. B. Kugler, J. von Delft, and M. Punk, *Multiloop pseudofermion functional renormalization for quantum spin systems: Application to the spin-1/2 Kagome Heisenberg model*, November 2020, arXiv:2011.01268.

[Tsi11] C. Tsitouras, *Runge–Kutta pairs of order 5(4) satisfying only the first column simplifying assumption*, Computers & Mathematics with Applications **62** (2011), no. 2, 770–775.

[VMK88] D. A. Varshalovich, A. N. Moskalev, and V. K. Khersonskii, *Quantum theory of angular momentum*, World Scientific, 1988.

[VRH14] J. Vlietinck, J. Ryckebusch, and K. van Houcke, *Diagrammatic Monte Carlo study of the Fermi polaron in two dimensions*, Phys. Rev. B **89** (2014), 085119.

[VST⁺15] A. Valli, T. Schäfer, P. Thunström, G. Rohringer, S. Andergassen, G. Sangiovanni, K. Held, and A. Toschi, *Dynamical vertex approximation in its parquet implementation: Application to Hubbard nanorings*, Phys. Rev. B **91** (2015), no. 11, 115115.

[VTM19] D. Vilardi, C. Taranto, and W. Metzner, *Antiferromagnetic and d-wave pairing correlations in the strongly interacting two-dimensional Hubbard model from the functional renormalization group*, Phys. Rev. B **99** (2019), no. 10, 104501.

[Wag24] M. Wagner, *Many-body physics with atomically thin semiconductors and ultracold atoms*, PhD Thesis, Universität Heidelberg, 2024.

[Wal21] E. Walter, *Real-frequency dynamics of quantum impurity models studied with fRG, NRG, CFT*, PhD Thesis, Ludwig-Maximilians-Universität München, 2021.

[Wan23] J. Wang, *Functional determinant approach investigations of heavy impurity physics*, AAPPS Bulletin **33** (2023), no. 1, 20.

[Wet93] C. Wetterich, *Exact evolution equation for the effective potential*, Phys. Lett. B **301** (1993), no. 1, 90–94.

[Wil75] K. G. Wilson, *The renormalization group: Critical phenomena and the Kondo problem*, Rev. Mod. Phys. **47** (1975), 773–840.

[WLH22] J. Wang, X.-J. Liu, and H. Hu, *Exact quasiparticle properties of a heavy polaron in BCS Fermi superfluids*, Phys. Rev. Lett. **128** (2022), 175301.

[WLT⁺20] N. Wentzell, G. Li, A. Tagliavini, C. Taranto, G. Rohringer, K. Held, A. Toschi, and S. Andergassen, *High-frequency asymptotics of the vertex function: Diagrammatic parametrization and algorithmic implementation*, Phys. Rev. B **102** (2020), no. 8, 085106.

[WML⁺10] H. Weimer, M. Müller, I. Lesanovsky, P. Zoller, and H. P. Büchler, *A Rydberg quantum simulator*, Nature Physics **6** (2010), no. 5, 382–388.

[WSK21] M. Wallerberger, H. Shinaoka, and A. Kauch, *Solving the Bethe-Salpeter equation with exponential convergence*, Phys. Rev. Res. **3** (2021), no. 3, 033168.

[YPM⁺19] Z. Yan, P. B. Patel, B. Mukherjee, R. J. Fletcher, J. Struck, and M. W. Zwierlein, *Boiling a unitary Fermi liquid*, Phys. Rev. Lett. **122** (2019), 093401.

[Zha21] H. Zhai, *Ultracold atomic physics*, Cambridge University Press, 2021.

[Zwe11] W. Zwerger, *The BCS-BEC crossover and the unitary Fermi gas*, vol. 836, Springer Science & Business Media, 2011.